POSITION ESTIMATION AND PERFORMANCE PREDICTION FOR PERMANENT-MAGNET MOTOR DRIVES

by Nesimi ERTUĞRUL B.Sc., M.Sc.

Submitted to the Faculty of Engineering for the degree of

Doctor of Philosophy

Department of Electrical and Electronic Engineering

The University of Newcastle upon Tyne

May 1993

Abstract

This thesis presents a theoretical and experimental development of a novel position estimator, a simulation model, and an analytical solution for brushless PM motor drive. The operation of the drive, the position estimation model of the test motor, development of hardware, and basic operation of inverter are discussed. Starting with the well-known continuous-time model of brushless PM motor, a sampled-data model is developed that is suitable for the application of real-time position estimator.

An analytical method of calculating the steady-state behaviour of the brushless PM motor for 120° inverter operation is presented. The analysis assumes that the machine air gap is free of saliency effects, and has sinusoidal back EMF. The analytical solution is derived for 60° electrical of the whole period. By experimental results, it is shown that the method of analysis is adequate to predict the motor's performance for typical operating points including phase advance and phase delay operation.

A computer simulation model for prediction of the performance of brushless PM motors is presented. The model is formulated entirely in the natural **abc** frame of reference, which allows direct comparison of the simulation and corresponding experimental results. The equations and diagrams are put into a convenient form for the simulation and future developments and library modules. The simulation model and corresponding experimental data of the brushless PM motor drive is given.

The thesis describes a modern solution to real-time rotor position estimation, which has been subject to intense research activity for the last 15 years. The implemented new algorithm for shaft position sensorless operation of PM motors is based on the flux linkage and line current estimation. The position estimation algorithm has also been verified by both off-line and on-line experiments (accomplished by a DSP, TMS320C30), and a wide range of steady-state and transient results have been given including starting from rest. The position estimation method effectively moves the position measurement point in the drive from the mechanical side to the motor's terminals. As well as eliminating the mechanical shaft position sensor, the investigated method can be used for high performance torque control of brushless PM motors. The thesis demonstrates that, in contrast to many other "sensorless" schemes, the new position estimation method is able to work effectively over the full operating range of the drive, and is applicable to a wide range of motor/converter types. Since the hardware is straightforward, only the new position estimation algorithm differentiates a system. Therefore, if a DSP control system is already implemented in the drive, the position estimator can be implemented at low cost.

Acknowledgements

I would like to thank my supervisor, Dr.Paul P.Acarnley, for his accessibility, insights, support, and above all these for his friendship during my research. He has made this project both challenging and energetic. I have thoroughly enjoyed working with him.

I would like to acknowledge my former supervisor Dr. Pragasen Pillay and Prof. Alan Jack. I also would like to acknowledge the Istanbul Technical University and Higher Education Council, Turkey, for funding my Ph.D. research.

Much of my time over the past several years has been spent in the UG Lab. I am grateful to staff for their assistance. In particular, I would like to thank my friend and colleague Peter Freere, for ever ready help and good humour at all hours of the day, night, and Tuesdays !. I would also like to thank my other colleagues, Chris, Kanti, Teresa, Mark, Dave and my former officemate Hamid for their friendship, listening, and discussions.

My deepest love and appreciation goes out my wife, for the unending support, encouragement, and understanding during my late night working hours. I am also deeply grateful to my family who are in Turkey and all my friends. Their faith in me has been a constant source of inspiration. To them and to all teachers, I am forever grateful.

Nesimi ERTUĞRUL

May 1993, Newcastle upon Tyne

ABBREVIATIONS

List of variables used throughout this thesis

Abbr.	Variable Name	Unit
'	Superscript denoting second estimation	—
(k)	Subscript denotes order numbers in real-time	—
B	Damping coefficient	Nm.s
BSPM	Brushless Sinusoidal Permanent Magnet	—
BTPM	Brushless Trapezoidal Permanent Magnet	—
Δ	Prefix denoting small variation	—
Δh	Hysteresis bandwidth in current controller	A
ΔT	Sampling interval	s
e	Base of natural logarithms	(2.718...)
e	Subscript denoting estimated values	—
$e_{1,2,3}$	Instantaneous values of back EMFs	V
E1, E2	Errors in flux linkage equations	Wb
E_m	Maximum value of trapezoidal back EMF	V
$E_{T(rms)}$	rms value of trapezoidal back EMF	V
f	Chopping frequency	Hz
$i_{1,2,3}$	Instantaneous line currents	A
I_{dc}	DC current	A
I_{mr}	Maximum value of rectangular current	A
I_{ms}	Maximum value of sinusoidal current	A
I_o	Initial value of current	A
i_{ref}	Instantaneous value of reference current	A
J	Moment of inertia	$kg.m^2$
$J_{1,2}$	Measured system inertias	$kg.m^2$

Abbr.	Variable Name	Unit
K	Constant used in the simulation model	—
k_e	Back EMF constant	V/rad/s
$k_{e1,e3,e5,e7,e9}$	Harmonic coefficients of back EMF	V/rad/s
k_{es}	Constant in sinusoidal back EMF	V/rad/s
k_{eT}	Constant in trapezoidal back EMF	V/rad/s
L	Equivalent winding inductance	H
L_m	Amplitude of variable winding inductance	H
I_m	Maximum value of current	A
L_o	Average value of variable winding inductance	H
L_{xx}	Self inductance of winding x	H
M_{xy}	Mutual inductance between two windings x and y	H
n	Speed of the motor	rpm
p	Pole pair	—
p	Subscript denoting predicted values	—
$\theta_{1,2,3}$	Electrical positions in three-phase windings	rad
θ_c	Angle showing the commutation instant	rad
θ_e	Electrical position	rad
θ_o	Initial mechanical position	rad
θ_r	Mechanical rotor position	rad
R	Winding resistance	Ω
T_{ave}	Average value of electromagnetic torque	Nm
t_c	Commutation time	s
T_e	Electromagnetic torque	Nm
$T_{e1,e2,e3}$	Single phase electromagnetic torque	Nm
T_L	Load torque	Nm
T_{L2}	Speed dependent part of the load torque	Nm
T_{LO}	Constant part of the load torque	Nm

Abbr.	Variable Name	Unit
TR	Torque ripple	(%)
$v_{1,2,3}$	Instantaneous phase-to-star point voltages	V
$v_{a,b,c}$	Terminal voltages reference to midpoint of DC rail	V
V_{dc}	DC rail voltage	V
v_s	Star point voltage reference to midpoint of DC rail	V
ω_e	Electrical angular speed	rad/s
ω_r	Angular speed of the rotor	rad/s
$\psi_{1,2,3}$	Total flux linkages	Wb
$\psi_{pm1,pm2,pm3}$	Magnet flux linkages	Wb
∂	Denotes partial differentiation	—

CONTENTS

CHAPTER I

INTRODUCTION

1. OVERVIEW

Permanent magnet machines have received considerable attention in recent years for variable-speed drives in the low (1W, *Shipley*, 1982) to high (1.1MW, *Nerowski* et al 1990) power range. The stator of a brushless permanent magnet machine has the conventional winding of a three-phase machine. The rotor magnetic field excitation is provided by permanent magnets instead of a discrete field winding carrying DC current. The absence of a field winding helps to improve the machine efficiency while reducing copper loss and the rotor inertia [*Henneberger*, 1987], and makes these motors the preferable option in variable-speed drive applications.

Moreover, in some industrial applications such as in plastic manufacturing, the presence of PVC dust or particles is extremely damaging to the brushes [*Bartos*, 1990] of a conventional DC motor. Eliminating brushes and a mechanical commutator is probably a prime benefit of brushless PM motors, since it reduces the maintenance requirement.

Permanent magnet motors are also used as prime movers in a wide variety of commercial and industrial drives as in robots, numerical controlled equipment, and machine tools. In all these applications, controllers designed

around nominal operating parameters are typically used to meet performance specifications.

There are basically three types of brushless PM motor: Brushless Sinusoidal Permanent Magnet (BSPM) motor, Brushless Trapezoidal Permanent Magnet (BTPM) motor, and hybrid brushless PM motors. However BSPM and BTPM motors are the two major categories which are the subject of this research. Basically, two types of control are used to drive brushless PM motors: either rectangular or sinusoidal. From the control point of view, they differ only in the method used to generate and control torque. Sinusoidal or rectangular reference current waveforms are generated with rotor position information. Similar control techniques apply to both, although performance may differ. High performance torque controllers, whether trapezoidal or sinusoidal, use current feedback to regulate motor currents.

The most common way of controlling the current is the use of three individual current controllers. For the case of a hysteresis current regulator, the current control is done using three hysteresis controllers that compare the line currents with their commands (generated by the rotor position data), and based on the polarity of the error, change the state of the power switches in the inverter. The line currents are usually measured by Hall-effect current transducers that also provide isolation between power and control circuits. Although, in a star-connected stator winding with isolated neutral, measuring two line currents is sufficient, three independent current transducers are used for better performance.

The BTPM motors have higher maximum torques than the BSPM motors using the same magnetic material and operating from inverters with the same

current ratings [*Stefanovic*, 1986]. The reason is that, for the same peak value, the 120° square wave current block has a higher RMS value than the corresponding sinewave current. It is also interesting to observe that the type of magnetic material (ferrite or samarium-cobalt) does not affect in practice the ratio of peak torque to rated torque [*Stefanovic*, 1986]. The reason for this is, that for cost effective drive designs, the inverter current capability is the limiting factor and is normally met before the demagnetisation of the motors with ferrite magnets becomes a factor.

Generation of ripple free torque in brushless PM motors depends on how well the motor's back EMF is matched to the controller's current waveform. For example, a 120° inverter operated controller (rectangular current excited) driving a three-phase BSPM motor will produce 13% peak-to-peak torque ripple with a frequency equal to the commutation frequency. A sinusoidal current excitation will also generate torque ripple if the motor's back EMF is not sinusoidal. The BTPM motors controlled with rectangular current also creates torque ripple since winding inductance prevents current changing instantly. However, in practice, the reference current waveform can be modified simply by changing the contents of a EPROM.

It is simple to shape the current waveforms to match a given motor and thereby practically eliminate torque ripple assuming that the back EMF waveforms are unaffected by stator currents. Unfortunately stator currents can cause back EMF distortion, especially in motors using ferrite magnets [*Comstock*, 1990], which can introduce torque ripple even if the current is matched to the no-load back EMF.

The 120° inverter operated controller can be designed to allow shaping of the current waveform within the commutation division. Although, the

brushless PM motors, which use the position information only for current commutation, can tolerate several degrees of inaccurate measurement [*Stefanovic*, 1986], the shaping current waveform needs a higher resolution position feedback (as in the sinusoidal current excitation in BSPM motor control), and removes a major cost advantage.

Both rectangular fed and sinusoidal fed brushless PM drives require some form of position sensing device in order to generate a reference current which should simultaneously follow the rotor flux position. Requirement of position sensor force the developer and user to agree the need for the sensors to be integrated into the machine or/and controller package. While the general need of position sensor is common to both rectangular and sinusoidal excitation, the requirements are somewhat different. As will be explained later in the thesis, while the sinusoidal current excited BSPM motor needs continuous (relatively continuous) position information, 120° inverter operated (rectangular current excited) brushless PM motors require the position signals at intervals of 60° electrical.

In brushless PM motors, when a mechanical position sensor is used, the angular mechanical alignment must be set to the absolute electrical null position to a high accuracy. Furthermore, to avoid mechanical alignment errors, the position sensor should be rigidly attached to the rotor shaft.

The position sensor technology offers many alternatives (e.g. resolver, encoders). However, beside the accurate and high resolution position sensing, most of the mechanical shaft position sensors have disadvantages arising mainly from environmental limitations, increased complexity of the control circuit, and increased number of connections between the motor and the control system.

Recently there has been much interest in techniques for eliminating mechanical shaft position sensors, and determining position by observing the motor's voltages and currents. Such approaches are based on observer models such as Kalman Filter [*Schroedl*, 1990; *Dhaouadi* et al, 1991; *Liu* and *Stiebler*, 1990; *Sattler and Starker*, 1989], sliding observer [*Furuhashi*, 1992], state observer [*Jones and Lang*, 1989; *Sepe and Jeffrey* 1992]. In the paper reported by *Min-Ho* and *Hong-Hee* (1989), a sensorless vector control of a PM synchronous motor has been introduced using a model reference adaptive system, which was initially developed for the induction motor. One successful observer method has been implemented by *Wu* and *Slemon* (1991). The method uses two line-to-line voltages and two stator currents to determine the rotor position.

The sensorless operation requirements are similar to those in other switched drives (such as switched reluctance motors) since they also need position information to generate commutation signals. Various methods for estimation of rotor position in reluctance machines and step motors have been presented in the literature by monitoring the time variations of terminal voltage and current, by monitoring a carrier voltage in a non-conducting phase, or by measuring and analysing the mutually induced voltage in the *off* phase, [*Acarnley et al*, 1985; *Ehsani and Husain*, 1992; *Ehsani et al*, 1992-A; *Lumsdaine et al*, 1985; *Mvungi et al*, 1990; *Ehsani et al*, 1992-B; *Panda and Amaratunga*, 1993; *Bass et al*, 1986; *Siefert*, 1985; *Kuo et al*, 1979].

However many of the methods given in the literature work for some, but not all, brushless PM motors. Furthermore, some of the reported methods are only in the simulation stage, and have not been implemented since they involve very math intensive calculations, or use idealised machine models.

1.1 OBJECTIVES AND CONTRIBUTIONS

Nowadays, manufacturers of industrial control systems are looking for higher levels of systems integration, coupled with increasing sophistication in control techniques, at lower costs. However, the task of direct interfacing between the electronic system and electromechanical loads still remains. Traditionally, interfacing has been achieved by using large numbers of discrete components. However, some higher levels of system integration are now possible using modern building block products.

While only a few years ago thyristors were exclusively used in industrial drives, a wide choice of power devices is now available. Although the dividing lines between different power switches are changing every year, the inverter-motor combinations can be grouped depending on the drive power rating.

For many applications, light weight, small size, low acoustic noise, and high efficiency modular inverters are demanded. High voltage and high current bipolar power transistor modules are available but switching speeds are not satisfactory. Power MOSFET switching speeds are satisfactory but high voltage and current modules are not available [*Fuji Electric*, 1992; *International Rectifier*, 1990]. The IGBT is expected to be further developed as a new type of switching device that has the high switching speed of the power MOSFET and the high voltage and high current switching capability (1200V, 400A) with the low saturation voltage of the bipolar transistor. Recently, they have been used widely in inverter applications. Their high frequency switching capabilities also allow the inverter to operate above the audible frequency range.

The thesis has three major objectives: implementation of an adaptable drive system to investigate any desired behaviour of the brushless PM motor, developing a simulation model, and developing a position estimation method which might be used in a wide range of switched drives.

This thesis develops a simulation model and semi-digital control hardware which can be modified easily to get any desired performance from a brushless PM motor. In the context of developing the simulation, this thesis makes contributions in several areas: the performance prediction, the analysis, and the tool to develop the position estimation method. Since the difference in modelling of brushless PM motor drive is in the waveforms of the reference current and back EMF , the developed simulation model should cover all motor (BTPM and BSPM motors with constant or variable inductance) and excitation types (sinusoidal or rectangular current excitation).

Although, some aspects of the simulation model have appeared in the literature [*Benkhoris et al*, 1990; *Bosch and Visser*, 1990; *Pillay*, 1987; and *Baudon et al*, 1992], there has yet to be a complete, compatible, general, and well connected analysis of brushless PM motor drives. The developed modular approach and **abc** simulation model allows this target to be met. On the other hand, if it is desired to add an extra control loop, such as velocity control, to the drive, a section concerning velocity control can be added without difficulty.

As is well known, the conventional way of measuring rotor position involves mechanical position sensors usually attached to the motor shaft. However, in practice, the shaft position sensing devices have limited resolution and operating characteristics, Besides the basic need to accurately

determine the rotor position, the shaft position sensor must operate under the same environmental conditions as the motor. This requirement often limits the performance and application type.

Recently, there has been much interest in techniques for eliminating the rotor position sensing device and deducing position by analysing the motor's voltage and/or current waveforms. Although the processing power required is still expensive, the cost is reducing rapidly, and in the near future, the high performance control of any type of brushless PM motor will be achieved only by monitoring the motor's power terminals.

This thesis describes the first shaft position sensorless method applicable to a wide range of brushless PM motors and excitation types. Furthermore, the method is potentially valuable for other switched drives such as switched reluctance motor drives.

In addition, this thesis describes one of the first implemented position estimation methods on a practical system in real-time, using existing hardware technology.

The fundamental feedback devices in the brushless PM drive are a resolver and current sensors which provide position information and actual current information to the controller. The ultimate goal of the position estimation algorithm is to eliminate the mechanical position sensing device on the motor shaft, or in the motor's housing, and to use only the motor's power terminals. **Fig. 1.1** shows a possible illustration of the operation block diagram when the motor terminals are used to obtain rotor position in brushless PM motor drives. As indicated in the figure, the position estimation method using motor terminal quantities basically removes the position sensing device from the mechanical side to electrical side.

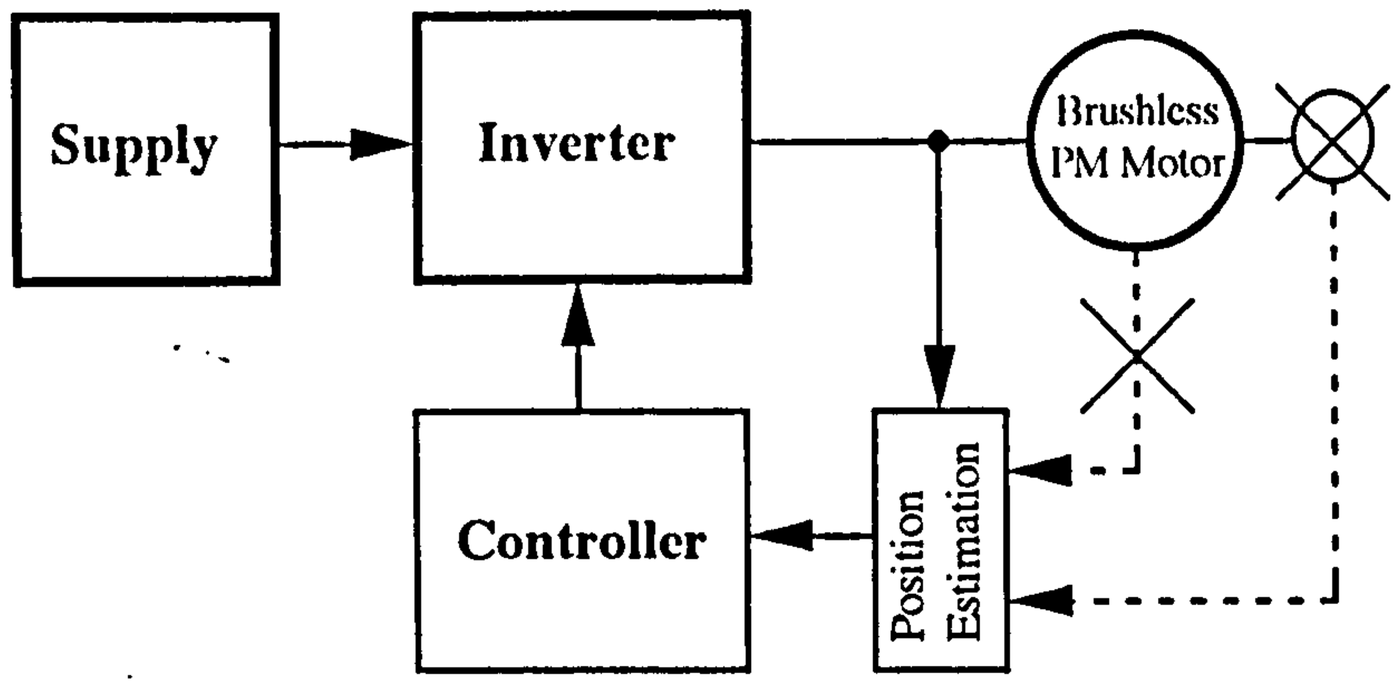

Figure 1.1 Schematic diagram showing the modification in the control for mechanical position sensorless operation.

Following the recent progress in power electronics and microelectronics, more advanced brushless PM motor control is possible. In particular, digital signal processors (DSP), although developed for application in the field of communications, are being used as motor controllers because of their fast computational capability and suitable architecture.

The more fundamental problems are based on implementation limitations and are less affected by the theoretical limitations which effectively increase the size of algorithm. The technology driven problems on the implementation of the new position estimation method can often be reduced by employing advance digital signal processors (such as TMS320xx). For computationally intensive advance control algorithms, which consist mostly of multiply-and-accumulate operations, this is a big advantage. Using the DSP will make possible the overall real-time control of brushless PM motors including position estimation, and various kinds of control strategies can be served. This can also help to update or change the control strategies during operation.

1.2 OUTLINE OF THESIS

The contents of this thesis are divided into seven chapters:

Chapter II deals with the concepts of PM motor modelling, and explains them in a simple and schematic manner which was already developed by earlier researchers. To start with, the chapter discusses the vital first step of understanding of PM motor and goes on to briefly describe some of the control options, and also provides a control overview with block diagrams of similar systems. A mathematical model is given for the brushless PM motor and this can be used for direct comparison with the actual drive developed during this research. The derivation of the model is briefly reviewed along with the necessary transformations to convert between the variable winding inductance and the constant winding inductance assumptions. Having established the form of the brushless PM motor model, experimental procedures are outlined to evaluate its electrical and mechanical parameters. Overall implementation details of the brushless PM motor drive are also given with corresponding circuit diagrams which are illustrated in Appendices.

Chapter III focuses on the analytical solution of the brushless PM motor model developed in **Chapter II** for 120° inverter operation. Firstly, ideal operation of the inverter is reviewed from the point of view of basic switching instants. The assumptions and simplifications are addressed. The analytical equations are developed for one 60° electrical interval, and comparisons with experimental results are given.

Chapter IV provides a simulation model for brushless PM motor drives. It is instructive to consider the operation of the BTPM and BSPM motor from

the same control point of view. Therefore, the simulation model is developed and principal differences in drive modelling are explained. The chapter gives basic simulation block diagrams, and explains them for specific motor parameters. Simulation tools are developed and both steady-state and dynamic results are compared with experimental results.

Chapter V starts by classifying shaft position sensorless methods developed for PM motor drives. The chapter provides a mathematical model for the new position estimation method for switched PM drives. Here, problems are simultaneously addressed with the ambitious goal of developing a position estimation model. Consequently, in this chapter, possible disturbances and imperfect starting conditions will be examined by data acquired from the simulated drive in **Chapter IV.**

Chapter VI completes the development of the position sensorless operation algorithm by describing its implementation and giving a wide range of experimental results. The algorithm is used with the test motor parameters, and the results are presented with a number of operation conditions including starting from standstill and excitation with sinusoidal current. Finally, the performance of the algorithm is illustrated by several experiments obtained from a real-time system. While a composite error analysis is derived, real-time implementation issues such as resolution, scaling, and quantisation are discussed.

Chapter VII provides a brief summary, conclusion, and recommendation for future work based upon the insights and experience gained in each of the previous chapters. It is designed to enhance the conclusions that are at the end of each chapter, and give a better understanding of the overall picture.

The appendices are used to supplement the work found in the chapters. They include additional data and hardware details. **Appendix 1** contains some numerical data used in determining back EMF constant of the motor, and a graph showing the variation of the winding inductance. **Appendix 2** derives the average electromagnetic torques for better understanding of the excitation differences in brushless PM motor. Some developed hardware details are given in **Appendix 3.** Useful trigonometric relations used in the analytical solution are summarised in **Appendix 4.** Unless otherwise stated, all equations in this thesis are in SI units.

CHAPTER II

BRUSHLESS PM MOTORS: Modelling and Control

2. INTRODUCTION

The brushless PM motor is a motor technology that has been rapidly increasing in popularity over recent years. It has the advantage of being relatively maintenance free while keeping the benefits of a closed loop brushed DC motor. The rotor field flux of a brushless PM motor is produced by permanent magnets, and various iron, nickel, and cobalt based alloys can be permanently magnetized to provide a source of rotor flux. Ferrite and rare earth (samarium cobalt) materials are also widely used as permanent magnets.

The most popular brushless PM motor configuration is probably the three-phase star-connected motor. The stator winding is a conventional distributed three phase winding located in the stator slots and energized by a three phase AC supply usually via a conventional inverter. The permanent magnets can be located either at the airgap (surface permanent magnets) or within the body of the rotor (interior permanent magnets).Today's technology offers basically three different types of brushless PM motors: Brushless Sinusoidal

Permanent Magnet (BSPM) motor, Brushless Trapezoidal Permanent Magnet (BTPM) motor, and hybrid brushless PM motors. Both BSPM motor and BTPM motor are essentially a synchronous motor with rotor position feedback, and the difference is in the winding arrangement of the stator and shaping of the magnets. The hybrid brushless PM motor is a motor combination of the permanent magnet and variable reluctance types, features both high efficiency and small stepping angle [*Kenjo*, 1991].

As will be explained in the later sections, the drive characteristics and control methods of brushless PM motors are very similar for conventional servo drive applications. Permanent magnet motors with direct line-starting capability are also increasingly being considered as alternative solutions to induction motor applications, but they are not going to be discussed here.

This chapter examines the requirements which determine the choice and the performance of brushless PM motor drive control, and gives an equivalent circuit model. The system equations are also given in general form and will be widely used to determine overall behaviour of the brushless drive. The chapter classifies the control methods and explains them in a systematic manner and presents an overview of practical considerations in the application of brushless PM motor drives. While the discussions presented in the following sections apply to most variable frequency drives, the emphasis in this chapter is on overall drive design and key points. For more detailed design information the reader should refer to the related sections in **Appendices.**

2.1 BRUSHLESS PERMANENT MAGNET MOTORS

In this discussion, the applications for which PM motors are the preferable option are explained, and fundamental differences among the brushless PM motors are summarized. Attention is mainly focused on three-phase star-connected brushless PM motors, and selection criteria are summarized. The brushless hybrid PM motors are motor combinations which include permanent magnets, and they are not discussed here.

2.1.1 Fundamental Distinctions and Applications

Although, in the literature the BSPM motor and BTPM motor are treated as different kinds of brushless PM motors, the only real difference is in the winding arrangement of the stator and shaping of the magnets.

The BSPM motor and BTPM motor have many similarities. They both have permanent magnets on the rotor and require alternating stator currents to produce constant torque. This makes these two motors have similar operating characteristics and control requirements. A distinguishing feature of the BSPM motor is that it generates a sinusoidal back EMF while the BTPM motor generates trapezoidal back EMF which usually has a 120° electrical flat top. The magnets at the rotor of the BSPM and BTPM motors can be either buried or surface mounted. Both types of motor can be classified into subgroups with radial or axial field designs.

Although most machines on the market are of the radial field (cylindrical rotor) type, the axial field design is claimed to have some advantages over the conventional radial field designs especially in terms of power density, torque-to-inertia ratio, and peak torque [*Krishnan and Beutler*, 1985]. In the axial field design, an axially directed magnetic field from the rotor magnets

interacts with radially directed currents, whereas a radially directed field interacts with axially directed current in the radial field design.

Fig.2.1. shows two types of commonly used brushless PM motor construction with permanent magnet positions. Overall test results in this thesis are based on a three-phase axial field BSPM motor, and its cross section and magnet position are given in **Fig.2.1a**. The same construction is also known as a pancake, disk, or sandwich type of brushless PM motor. It has a rotating magnet system and a double sided stator. The stator windings are embedded in slots as in conventional motor. As illustrated in **Fig.2.1a.**, magnets are mounted on the rotor to create an axial magnetic field that is parallel rather than perpendicular to the shaft. So, an axially directed magnetic field from the rotor magnets interacts with radially directed currents to produce torque. The rotor has no iron, giving the motor a low inertia, and the magnets are encapsulated in a resin or plastic. In **Fig.2.1b.**, a cylindrical motor having a radial field is shown. Depending on the desired flux linkage waveform, the magnets on the rotor can have different shape and position (buried or surface). The rotor laminations usually have cutouts which improve the flux conduction and decrease inertia [*Henneberg, 1987*], and the housing usually consists of an extrusion moulded profile which often has cooling fins.

A primary advantage of axial field brushless PM motors is that they require less magnet weight than radial field motors for an equivalent torque rating [*Bartos, 1988*]. From the control point of view, the only difference between these two types comes from the typically low inductance in the axial field brushless PM motor, due to its short winding turns and large number of poles [*Henneberg, 1987*]. The choice between the two designs depends on the installation situation and application requirements (such as low inertia).

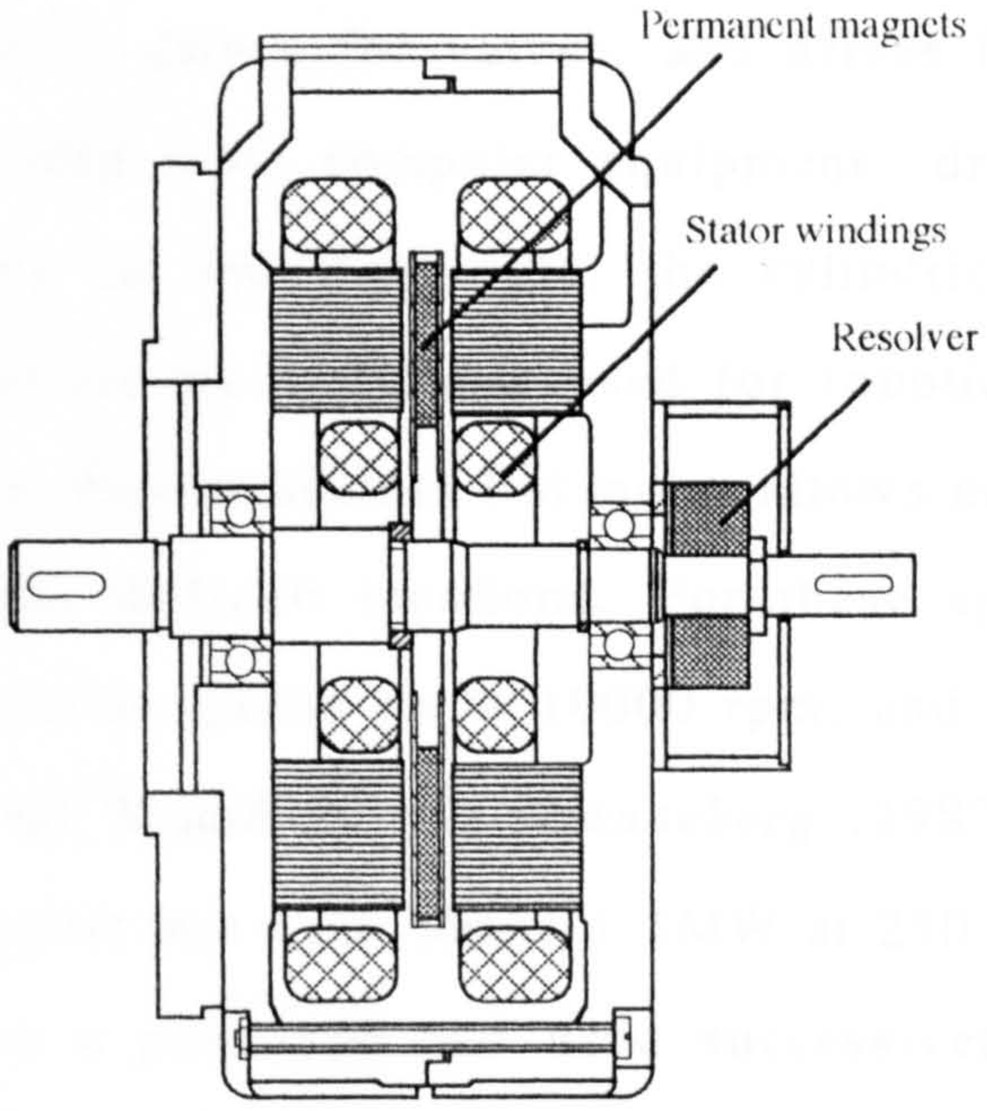

a

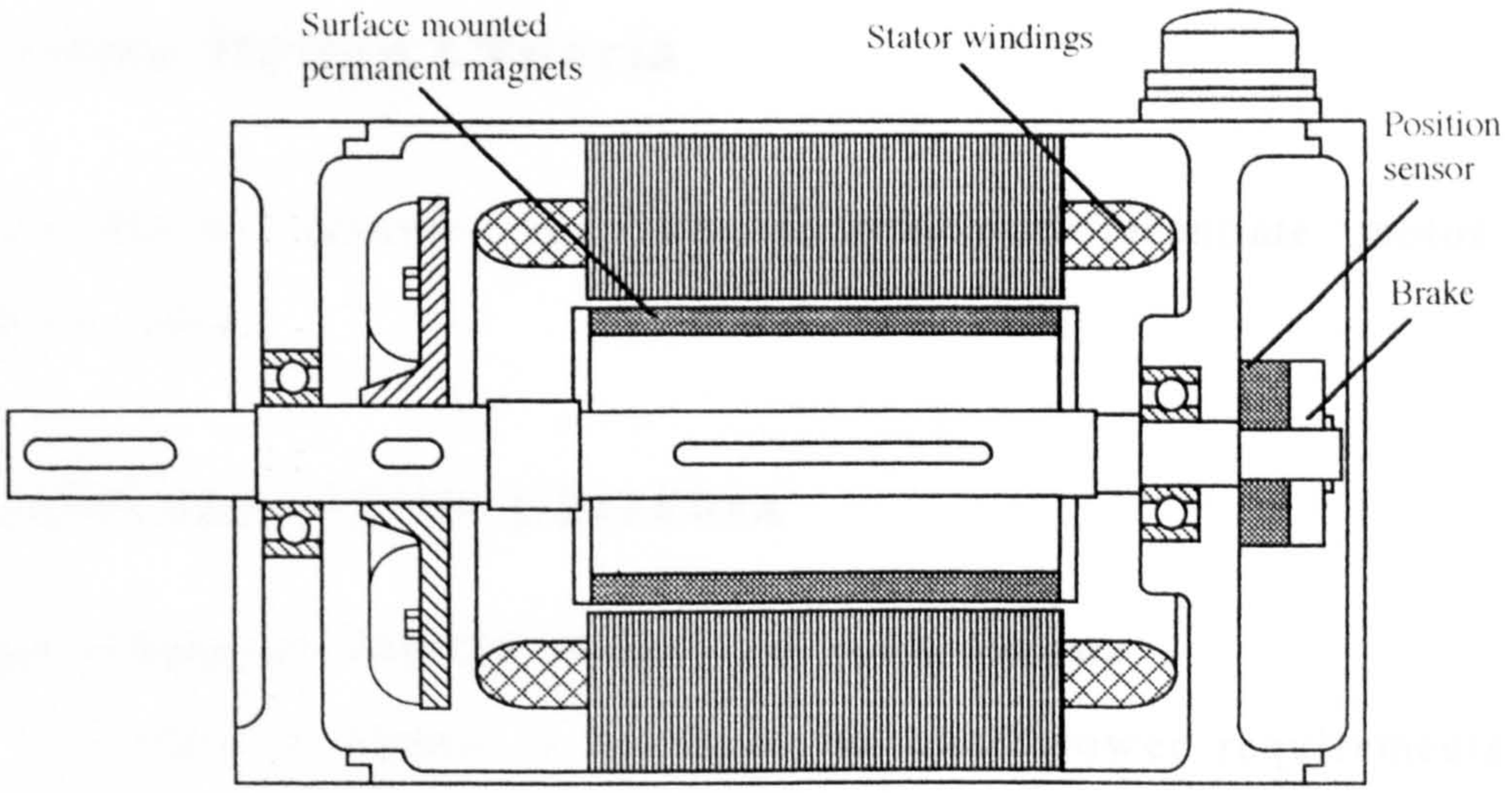

b

Figure 2.1. Cross-Sections of Two Popular Brushless PM Motors.

a) 1.9KW Axial Field Brushless PM Motor (Mavilor).

b) Brushless Radial Field PM Motor.

The following examples for the broad applications of brushless PM motors may be given: spindle drives for machine tools, drives for robots, drives for aerials and telescopes, servo drives for valves, and drives for x-y tables. Applications can be extended from computer equipment drives to textile machines. In servo drives for machine tools, the cylindrical design has prevailed whereas disc motors are preferably used for robotics drives. The compact design of the axial field brushless PM motor allows motor mounting on robot arms and in other difficult locations. For these applications the torque range is 0.1-100 Nm at speeds up to 10000 rpm, and rated power is approximately between 100 W and 20 kW [*Henneberg* ,1987]. However , *Nerowski et al* (1990) report that a six phase 1.1MW at 230 rpm brushless PM motor is in use. It is a prototype and used successively as a ship's propulsion drive.

2.1.2 Drive Design Criteria

This subsection discusses the factors, which differentiate motor and application types.

A. MOTOR SELECTION CRITERIA

1. High torque-to-inertia ratios and peak torque

When very rapid movement is required, the shaft power requirements can become extremely high. **Fig.2.2** shows how the various PM motor technologies compare in terms of peak-to-nominal torque ratio for about 7Nm rated torque and 3000 rpm rated speed brushless PM motors. Although, performance and values of specific designs from various manufacturers can vary significantly due to design and magnetic material improvement, this

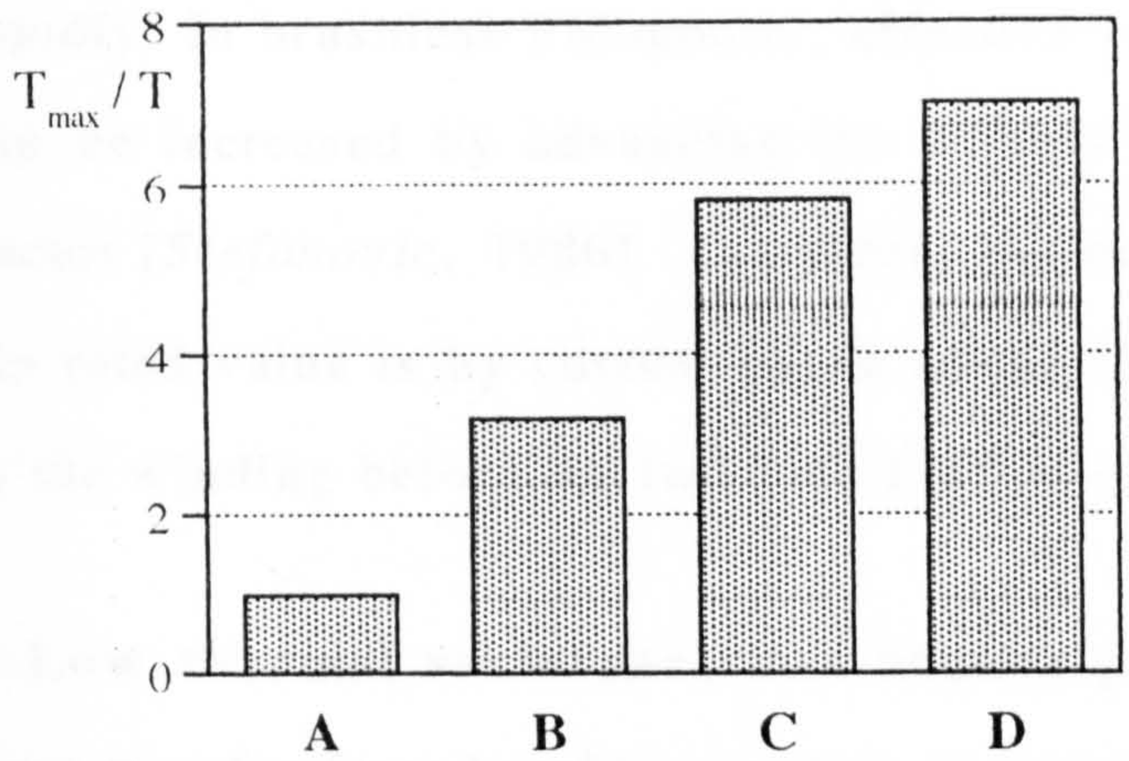

A: Ferrite magnet (radial field)

B: Rare earth, Neodymium Iron Boron Magnet (radial field)

C: Rare earth, Samarium Cobalt Magnet (radial field)

D: Rare earth, Samarium Cobalt Magnet (axial field)

Figure 2.2. Various Brushless Motor Technologies Comparing Peak Torque Values

graphic was compiled from a sample of manufacturers data [*Electro-Craft*, 1990; *Pacific Scientific*, 1990; *Mavilor Motors*, 1991]. The figure is a measure of acceleration performance and therefore relates to move time. Clearly the axial field brushless PM motors delivers a very high peak output, so in applications with a modest duty cycle, it can return very fast positioning times with the aid of low inertia.

2. High torque over wide speed range and operation above rated speed

Servo drives operate in the constant torque mode of operation from zero to rated speed [*Pillay and Krishnan 1991*]. The rated speed in brushless PM motors is the speed at which the back EMF equals to the maximum available terminal voltage set by the source voltage. The operation above the rated speed is also possible in brushless PM motors. Since the motor's back EMF increases linearly with speed, as the difference between the source voltage and back EMF voltage decreases, the current controller gradually loses its ability to control the current [*Jahns*, 1989] and the motor current drops

rapidly. In brushless PM motors, effective voltage across the motor winding can be increased by advancing the current vector ahead of the back EMF vector [*Stefanovic*, 1986]. Therefore, the only way to increase speed above the rated value is by current phase advancing, so that the current builds up in the winding before the full back EMF is established.

3. Low thermal resistance and higher power density

Heat transfer from brushless motors is greatly improved by comparison with conventional brush DC motors [*Bartlett*, 1984], by the direct thermal coupling, and consequently much lower thermal resistance from armature to the outer surface. Therefore, since the heat arising in the copper of the stator can be dissipated more efficiently, the power per unit volume also increases [*Weinmann et al*, 1984]. In certain applications (such as aerospace, robotics), it is preferable to have as low a weight as possible for a given output power. The power density is limited by the heat dissipation capability of the machine [*Pillay and Krishnan*, 1991], and it is usually the case that the BTPM motor is capable of supplying 15% more power than the BSPM motor from the same size.

4. Motor geometry and location flexibility

The motor geometry is a factor where the operating requirements specify a desired ratio between the motor axial length and the diameter. The shape of the housing is also important. Generally, the mounting problems are not significant because of the closed rectangular construction form, so that brushless PM motors are widely built in the same form.

5. Reduced electromagnetic interference.

Electromagnetic interference due to brush arcing can be avoided by choosing brushless motors.

6. Cogging torque

Cogging torque is possible in the brushless PM motor due to the PM excitation and slotting of the stator teeth. It may be minimized by anti-cogging torque magnet design. It is shown by *Ackerman et al* (1992) and *Carlson et al* (1989) that the cogging torque in brushless PM motors can be reduced by correct choice of magnet pole arc and skewing. *Favre and Jufer* (1990) proposed a current control method to eliminate the effect of cogging torque on the resultant electromagnetic torque. Cogging torque free operation gives smooth low speed operation of the brushless PM motor.

7. Efficiency and motor size for a given power rating

At high power levels, the motor's efficiency is directly related to the drive operating cost. There is little difference between either efficiency or motor size of BSPM and BTPM motors for given power rating. BSPM motors are marginally more efficient due to somewhat higher losses associated with the squarewave currents in BTPM motors.

B. APPLICATION CRITERIA

1. Motor/inverter choice

To obtain the desired performance from a drive system the load must be characterized and its motion profile (in terms of intermittent and continuous duty) must be defined. Torque/speed curves of the motor should be used to select and design the optimum brushless PM motor/inverter combination as a function of the drive power rating.

2. Torque ripple

Some applications may require torque ripple free operation. The interaction between rotor flux and winding current may produce torque ripple. Imperfect

sensor position and non ideal motor winding distribution in brushless PM motors are other torque ripple sources. The torque ripple can be minimized by controlling the input stator current, and proper design [*Murai et al*, 1987; *Le-Huy et al*, 1985; *Bolton and Ashen*, 1984; *Carlson et al*, 1989]

3. Choice of feedback devices

The appropriate type of position and speed sensors changes with the type of brushless permanent magnet motor and its application. Highly accurate position control applications may require special position sensors, and good speed control may require a separate speed sensor. Due to environmental factors, such as temperature and humidity, which may effect the performance of the control and motor, using specially designed sensors should be taken into consideration. Operation without the shaft position sensor is possible, and several schemes have been reported as given in **Chapter I.**

4. Braking

In drives where four quadrant operation is required the machine works as a generator during braking. The generated energy is either dissipated or given to the supply. If the energy is dissipated in a resistor, used in parallel drive system, it is called as dynamic braking. However, in the regenerative braking, the generated energy is recovered in the power supply. The designer needs to specify the controlled rate at which the motor may stop or slow down. Apart from regenerative braking, in many brushless PM motor applications, the dynamic braking is preferred (see **Section 2.5.2** and **Appendix A-3.3**). While that may not be difficult, it increases the cost of the system.

5. Reliability of the system

Reliability of any control system is a fundamentally important factor. Although advance control methods with the help of external sensors increase the performance of the drive system, considerable extra complexity in the control circuit may reduce the reliability, particularly if good starting and running performance is to be achieved with a wide range of load torques and inertias.

2.2 THE MATHEMATICAL MODEL

The electrical behaviour of the star connected (floating neutral) brushless PM machine is modelled by a star connected three-phase network consisting of a series connected resistance, inductance, and voltage source per phase, see **Fig.2.3.** The justification for this rather simple model was given earlier in references such as *Nehl et al* (1982), and *Pillay and Krishnan* (1987). In the rotor of brushless PM motor, since both the magnet and the stainless steel retaining sleeves (resin or plastic in axial field brushless PM motors) have high resistivity, rotor induced currents is ignored and no damper windings are modelled. It has also been assumed that the stator resistances of all the windings are equal. As reported by *Nehl et al* (1982), the stator currents have little (or negligible) effects on the magnet flux distributions under normal operating conditions. In this research, it is also supported by the static torque measurement tests that, the developed torque is not effected by the applied current to the windings, and no significant demagnetization is experienced above the rated current value in the test motor. Both the steady-state and dynamic behaviour of the brushless PM motor can be studied using this model, and the same model is used

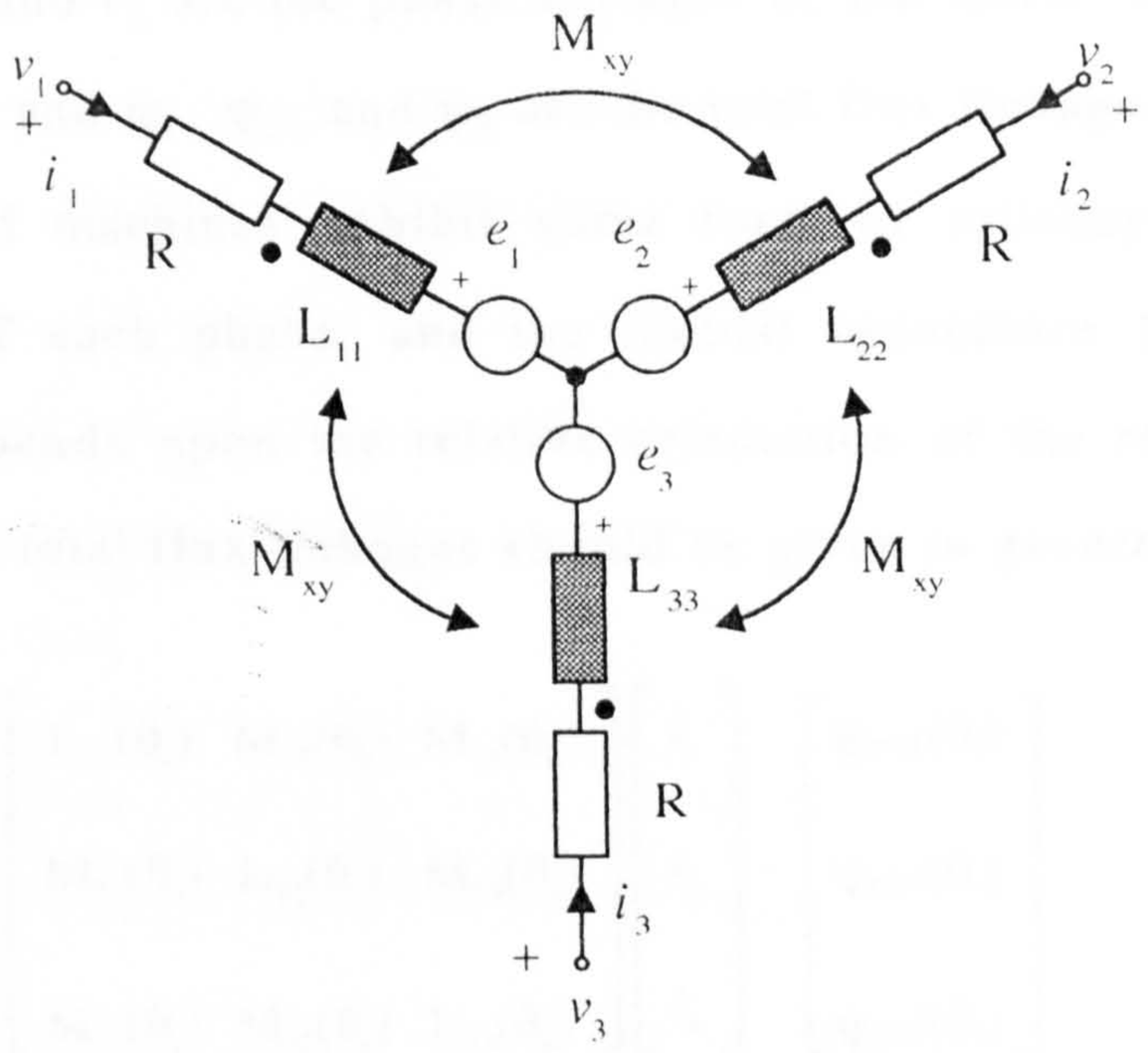

Figure 2.3. An equivalent circuit of the three-phase balanced brushless PM motor.

successfully for both dynamic and steady-state analysis of brushless PM motors in this thesis.

2.2.1 Voltage Equations

It is assumed that the stator windings of the brushless PM motor are identical windings displaced 120° electrical, and having resistance R. In terms of total flux linkages, the general voltage equations in the matrix form for the three-phase brushless PM motor are,

$$\begin{bmatrix} v_1 \\ v_2 \\ v_3 \end{bmatrix} = \begin{bmatrix} R & 0 & 0 \\ 0 & R & 0 \\ 0 & 0 & R \end{bmatrix} \begin{bmatrix} i_1 \\ i_2 \\ i_3 \end{bmatrix} + \frac{d}{dt} \begin{bmatrix} \psi_1 \\ \psi_2 \\ \psi_3 \end{bmatrix} \qquad (2.1)$$

Here, v_1, v_2, and v_3 are the phase voltages of the motor; i_1, i_2, and i_3 are the line currents; and ψ_1, ψ_2, and ψ_3 are the total flux linkages. Many designs of brushless PM machines exhibit some form of saliency, in that the self inductance of each phase, and the mutual inductance between the phase windings depends upon the relative orientation of the rotor and stator. In this case, the total flux linkages should be given in general form,

$$\begin{bmatrix} \psi_1 \\ \psi_2 \\ \psi_3 \end{bmatrix} = \begin{bmatrix} L_{11}(\theta_e) & M_{12}(\theta_e) & M_{13}(\theta_e) \\ M_{21}(\theta_e) & L_{22}(\theta_e) & M_{23}(\theta_e) \\ M_{31}(\theta_e) & M_{32}(\theta_e) & L_{33}(\theta_e) \end{bmatrix} \begin{bmatrix} i_1 \\ i_2 \\ i_3 \end{bmatrix} - \begin{bmatrix} \psi_{pm1}(\theta_e) \\ \psi_{pm2}(\theta_e) \\ \psi_{pm3}(\theta_e) \end{bmatrix} \qquad (2.2)$$

Where $\Psi_{pm1}(\theta_e)$, $\Psi_{pm2}(\theta_e)$, and $\Psi_{pm3}(\theta_e)$ are the flux linkages established by the permanent magnet as viewed from the stator phase windings. In other words, the magnitude of $d/dt(\Psi_{pm})$ would be the magnitude of the open-circuit voltage (e_1, e_2, and e_3 in **Fig.2.3.**) induced in each stator phase winding. $M_{xy}(\theta_e)$ is the mutual inductance between two windings **x** and **y**. $L_{xx}(\theta_e)$ is the self inductance of winding **x**. Here **x** and **y** are the notations that express the number of phases and varies from 1 to 3 for the three-phase motor. The term θ_e in the equations is the electrical position in radians, and is given by:

$$\theta_e = p\,\theta_r = p\,(\omega_r t + \theta_o) \qquad (2.3)$$

Here p is the number of pole pairs, θ_r is the mechanical rotor position in radian, ω_r is the rotor speed in rad/s, and θ_o is the initial position of the rotor or phase advance/delay angle in rad/s.

The main model difference between BSPM and BTPM motor appears in this stage of the electrical model. If the voltage induced in the stator windings by the permanent magnet is sinusoidal, the motor is described as a BSPM motor, whereas the induced voltage has a trapezoidal waveform in the BTPM motor. **Fig.2.4.** illustrates these two types of typical back EMF waveforms. These profiles are termed "*sinusoidal* " and "*trapezoidal* " due to their respective shapes.

A more complex equation can be given by differentiating **Eq.2.2**, substituting it into **Eq.2.1**, and rearranging,

$$\begin{bmatrix} v_1 \\ v_2 \\ v_3 \end{bmatrix} = \begin{bmatrix} R & 0 & 0 \\ 0 & R & 0 \\ 0 & 0 & R \end{bmatrix} \begin{bmatrix} i_1 \\ i_2 \\ i_3 \end{bmatrix} + \begin{bmatrix} L_{11}(\theta_e) & M_{12}(\theta_e) & M_{13}(\theta_e) \\ M_{21}(\theta_e) & L_{22}(\theta_e) & M_{23}(\theta_e) \\ M_{31}(\theta_e) & M_{32}(\theta_e) & L_{33}(\theta_e) \end{bmatrix} \frac{d}{dt} \begin{bmatrix} i_1 \\ i_2 \\ i_3 \end{bmatrix}$$

$$+ \frac{d}{dt} \begin{bmatrix} L_{11}(\theta_e) & M_{12}(\theta_e) & M_{13}(\theta_e) \\ M_{21}(\theta_e) & L_{22}(\theta_e) & M_{23}(\theta_e) \\ M_{31}(\theta_e) & M_{32}(\theta_e) & L_{33}(\theta_e) \end{bmatrix} \begin{bmatrix} i_1 \\ i_2 \\ i_3 \end{bmatrix} - \frac{d}{dt} \begin{bmatrix} \psi_{pm1}(\theta_e) \\ \psi_{pm2}(\theta_e) \\ \psi_{pm3}(\theta_e) \end{bmatrix} \qquad (2.4)$$

The performance of nearly all types of brushless PM motors may be adequately described by straightforward modifications of the **Eq.2.4**. In some cases, e.g. salient-pole brushless PM motors, the self and mutual inductance terms can be expressed explicitly as regular sin or cos functions. Similarly, the same approach may be done for the magnet flux linkage variables in BTPM motors. Where this is not convenient or appropriate, look-up tables or other calculation techniques could be employed. As seen in **Eq.2.4**, inductances of some motors are functions of θ_e and therefore a function of the rotor speed ω_r. Hence, the coefficients of the voltage

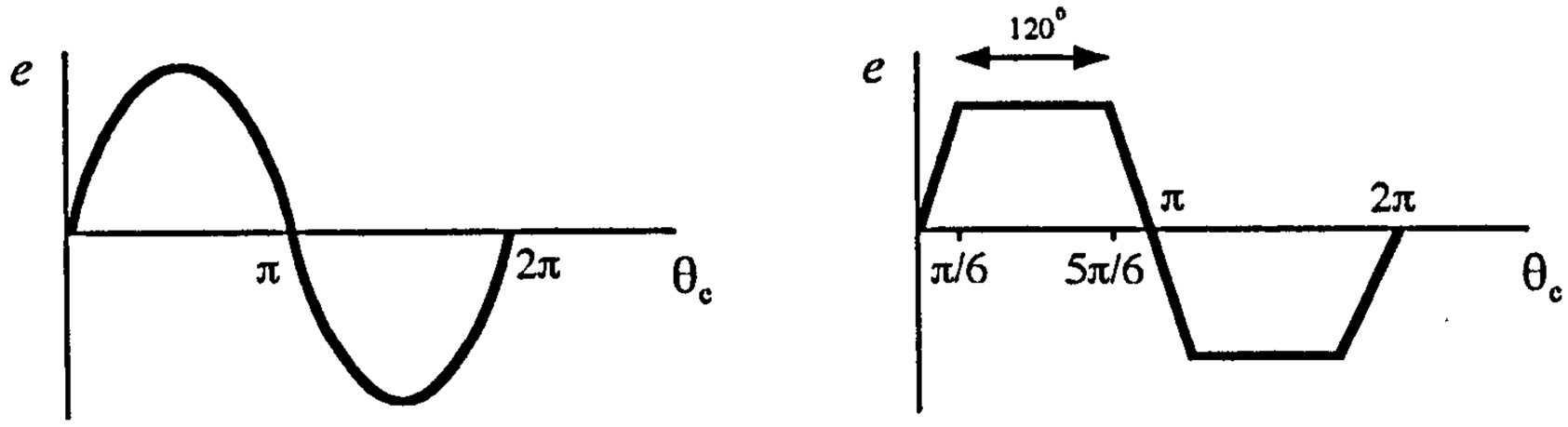

Figure 2.4. Typical back EMF waveforms in brushless PM motors.

a) BSPM motor.

b) BTPM motor.

equations are time varying except when the rotor is stalled. Moreover, as it will be seen in the next subsection, rotor speed is also a function of the electric torque. Clearly, the solution of the voltage equations is very involved. In fact, a computer is required in order to determine dynamic behaviour of the motor for specific situations.

If the motor displays the round rotor characteristic (no reluctance variations around the rotor surface with angle), then the self inductance of each stator phase winding depends upon a combination of leakage flux linkages and flux linkages shared equally with stator phases,

$$L_{11} = L_{22} = L_{33} = L_l \tag{2.5}$$

It follows that the mutual inductances being independent of rotor position are given by

$$M_{12} = M_{21} = M_{13} = M_{31} = M_{23} = M_{32} = M_l \tag{2.6}$$

And, since the sum of the line currents is equal to zero ($i_1+i_2+i_3 = 0$) in the star connected with isolated star point motor, the following equation can be written,

$$M_1 i_1 + M_1 i_2 = - M_1 i_3 \tag{2.7}$$

Linear three-phase coupled systems are magnetically symmetrical if the diagonal elements of the inductance matrix are also equal [*Krause*, 1986]. Hence, with the assumptions in **Eqs.2.5-2.7**, the voltage equations may be simplified,

$$\begin{bmatrix} v_1 \\ v_2 \\ v_3 \end{bmatrix} = \begin{bmatrix} R & 0 & 0 \\ 0 & R & 0 \\ 0 & 0 & R \end{bmatrix} \begin{bmatrix} i_1 \\ i_2 \\ i_3 \end{bmatrix} + \begin{bmatrix} L & 0 & 0 \\ 0 & L & 0 \\ 0 & 0 & L \end{bmatrix} \frac{d}{dt} \begin{bmatrix} i_1 \\ i_2 \\ i_3 \end{bmatrix} + \begin{bmatrix} e_1 \\ e_2 \\ e_3 \end{bmatrix} \tag{2.8}$$

Here, $L=L_1-M_1$, and e_1, e_2, and e_3 are the back EMFs of the brushless PM motor.

As seen in **Eq.2.8**, the change of variables allows us to eliminate the time-varying inductances and thereby reduces complexity of the voltage equations. However, the resulting differential equations still require a computer to simulate the transient behaviour of the motor.

2.2.2. Torque Equations

As in all types of drives, the brushless PM motor is normally coupled to a mechanical system. So, the complete dynamic model is described by a set of four first order differential equations, three electrical (**Eq.2.8**) in state variables i , and one mechanical in state variable ω_r,

$$T_e = J \frac{d\omega_r}{dt} + B\omega_r + T_L \tag{2.9}$$

Eq.2.9 is known as "*the equation of motion* ", and here, T_e is the electromagnetic torque of the motor, J is the inertia of the motor and the connected load in kgm^2. The constant B is a damping coefficient associated with the rotational system of the motor and mechanical load. It has the units Nms/rad. It is generally small and often neglected. T_L is the load torque in Nm.

When magnetic saturation is present, the flux linkages in brushless PM machine are not linear functions of the phase currents ($\psi_k=\psi_k(i_1,i_2,i_3,\theta_e$; k=1,2,3). To derive the electromagnetic torque equation, a set of mathematical representation of the flux linkages has to be obtained. In this case, the electromagnetic torque expression can be given by the coenergy function, W_c [*Hemati and Leu*, 1992],

$$T_e(i_1,i_2,i_3,\theta_e) = \frac{\partial W_c(i_1,i_2,i_3,\theta_e)}{\partial \theta_e} \qquad (2.10)$$

In brushless PM motors, because of the large low-permeability gaps between stator and rotor, the magnetic circuits in the motor are generally operated in their linear region. Therefore, if the saturation is neglected, the flux linkages become linear function of the phase currents. Hence, after the phase currents have been determined from **Eq.2.8**, the electromagnetic torque in brushless PM motors can be obtained easily from,

$$T_e = \frac{1}{\omega_r}(e_1 i_1 + e_2 i_2 + e_3 i_3) \qquad (2.11)$$

and here, back EMFs are,

$$\begin{aligned} e_1 &= \omega_r k_e e_1(\theta_e) \\ e_2 &= \omega_r k_e e_2(\theta_e) \\ e_3 &= \omega_r k_e e_3(\theta_e) \end{aligned} \qquad (2.12)$$

where k_e is the maximum value of back EMF constant, and $e_1(\theta_e)$, $e_2(\theta_e)$, and $e_3(\theta_e)$ are functions of rotor position with a maximum magnitude of ±1.

As seen in **Eq.2.11**, the electromagnetic torque is inversely proportional to motor speed ω_r, and directly proportional with the line currents and back EMFs of the phases. Due to **Eq.2.12**, back EMFs are also proportional with rotor angular speed ω_r. Therefore, giving electromagnetic torque in terms of maximum value of back EMF constant k_e may be convenient,

$$T_e = k_e\left(e_1(\theta_e)i_1 + e_2(\theta_e)i_2 + e_3(\theta_e)i_3\right) \qquad (2.13)$$

The more specific expressions for electromagnetic torque of BSPM and BTPM motors are given in the later chapters on specific control and excitation.

2.3 PARAMETER DETERMINATION AND STATIC TORQUE CHARACTERISTICS

The modelling of the motor is idealized (**Fig.2.3**) in that it is necessary to assume symmetry of motor phases, balanced phase quantities, sinusoidal variations (for the BSPM motor) and trapezoidal variations (for the BTPM motor) of induced voltages, and constant or sinusoidally varying winding inductances. Since the field excitation cannot be removed from a brushless PM motor, measurement of its electrical parameters requires test procedures that differ from the conventional methods. Procedures for measurements of brushless PM motor parameters are available in the literature (such as *Gorman et al*, (1988); *Wallace and Spee*, (1987); and *Mellor et al*, (1991)).

Although some details of the brushless PM motor parameters are usually supplied by the motor manufacturer, these parameters can be measured experimentally and used for simulation and control purposes. This subsection describes a series of tests which can be used to determine the parameters of the PM motor needed to apply dynamic and steady-state analysis. Attention in this work is mainly focused on the determination of back EMF constant and static torque characteristics. Other motor parameters such as winding resistance R, winding inductance L and moment of inertia J are defined as usual in the literature. All experimental tests in this thesis have been performed on the axial field BSPM motor which has the specifications in **Table 2.1**.

Table 2.1 Axial field BSPM test motor plate data

Torque constant	: 0.31 Nm/A
Peak Stall Torque	: 52 Nm
Continuous Stall Torque	: 3.4 Nm
Back EMF	: 143 V
Maximum Speed	: 6000 rpm
Number of poles	: 8

2.3.1 Parameter Determinations

Resistance, R

The winding resistance R was obtained in the usual manner from its DC value, and corrected by an appropriate factor to allow for skin effects. A series of experiments have been carried out to measure winding resistance. A DC voltage supply was connected in parallel to one phase winding of the motor and terminal voltage and current were measured at time intervals of 5 minutes, until the windings reached a steady temperature.

Inductance, L

A Wayne Kerner LCR bridge instrument was placed across the terminals of the motor, and inductance variations were measured directly with changing the rotor position at 5° mechanical intervals. The series inductance per phase in the equivalent circuit model is nearly independent of the rotor position, as determined by inductance measurement in the experimental setup. This is mainly due to the large effective airgap in the test motor. The value of inductance variation for the test motor was estimated to be 1.3%.

Although, the inductance representations were simplified to constant values (as in **Eqs.2.5** and **2.6**), being the mean of the exact values, the exact inductance variation may be represented by idealized cosinusoidal variation. The construction of motors with unusual magnetic circuits can result in winding inductances which are neither constant nor vary in an idealized manner. For modelling purposes of the axial field PM test motor, the inductance variations may be represented in the computer simulation by the following expressions:

$$L = L_0 + L_m |\cos \theta_e|^k \qquad (2.14)$$

or

$$L = L_0 + L_m \cos(2\theta_e) \qquad (2.15)$$

Fig.2.5 presents two variable inductance waveform which were defined in **Eq.2.14** and **Eq.2.15**. Here, L_0 is the mean value of the inductance, and L_m is a maximum value which determines the inductance variation, and k is a constant. For the test motor, the nature of the small inductance variations as a function of the rotor position is given in **Appendix A.1**. As will be seen, the variation of the inductance approximates the waveform which is given in **Fig.2.5a**.

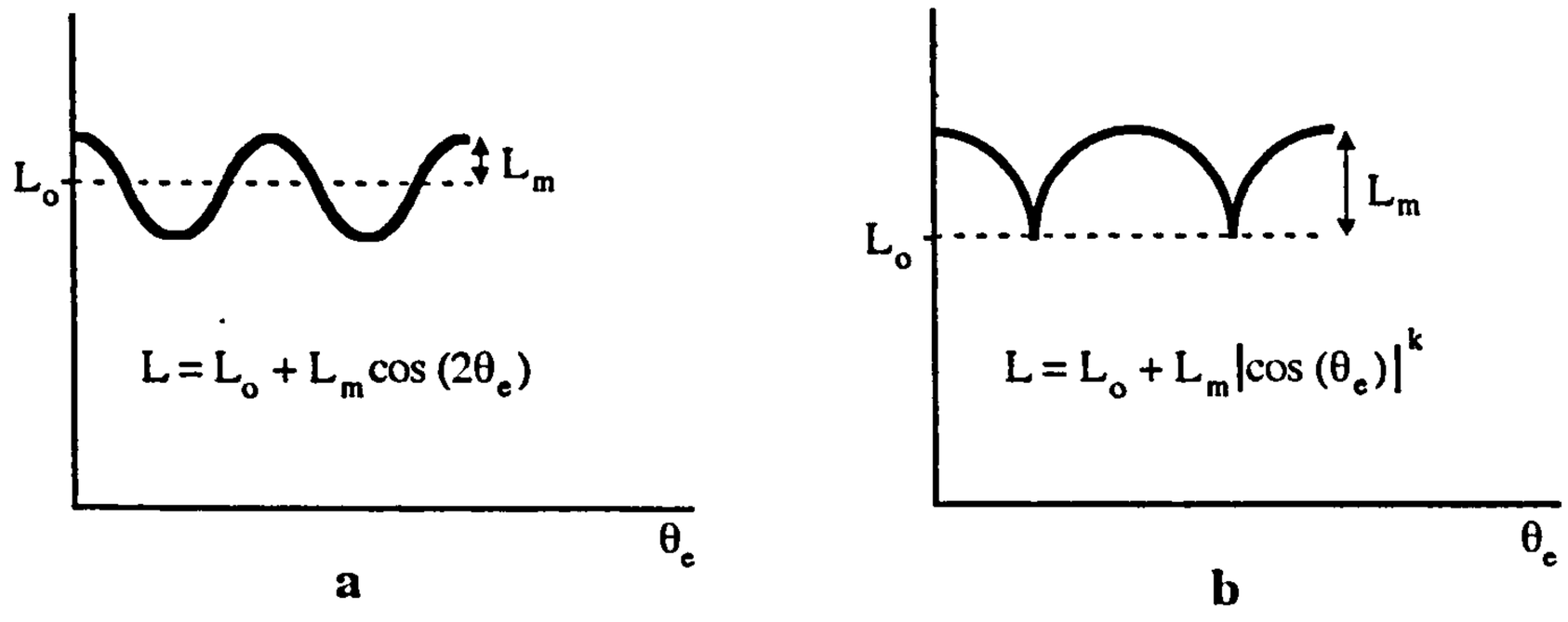

Figure 2.5 Two variable inductance representations in brushless PM motors.

a) Cosinusoidal variable inductance approximation.

b) Absolute value approximation.

Back EMF Constant k_e

It has been shown in earlier work by *Fouad et al* (1981), and explained in **Section 2.2** that, for some brushless PM motors, since the currents have little (or negligible) effects on the magnet flux distributions under normal operating conditions, the back EMFs are relatively independent of the current levels. Therefore, it is also assumed that, there is practically no difference between the no load and load back EMFs in the test motor used in this research.

The back EMF constant is measured while driving the motor as a generator at different speeds and is expressed as a peak value. The open-circuit phase voltage of the generator is equal to the induced voltage (back EMF).

In the commercially available axial field BSPM motors, the phase-to-phase back EMF approximates a sinusoidal waveform whereas the phase-to-star point back EMF approximates a quasi trapezoidal waveform (**Fig.2.6**). In practice, the trapezoidal waveform of back EMF can be approximated by a

sinusoidal back EMF of the fundamental period and peak value. However more accurate expressions may be given by fourier series or look-up tables.

In practice, since measuring the peak value is difficult, the measured **true rms** value of the voltage can be directly used to estimate maximum value of the back EMF, and this approach is more convenient for estimating back EMF constant in BTPM motors. For this reason, **Fig.2.7** was used to find a relationship between the rms and maximum value of a trapezoidal back EMF waveform of the BTPM motor (with 120° electrical flat-top) which was given in **Eq.2.16**. However, it should be noted here that, this assumption is true if the motor has a good trapezoidal back EMF waveform.

From **Fig.2.7**, the rms value of the trapezoidal waveform can be estimated in terms of the maximum value E_m,

$$E_{T(rms)} = \left\{ \frac{1}{\pi} \left[\int_0^{\pi/6} \left(\frac{E_m}{\pi/6} \theta_e \right)^2 d\theta_e + \int_{\pi/6}^{5\pi/6} (E_m)^2 d\theta_e + \int_{5\pi/6}^{\pi} \left(-\frac{E_m}{\pi/6} (\theta_e - \pi) \right)^2 d\theta_e \right] \right\}^{1/2}$$

$$E_{T(rms)} = 0.882\ E_m \qquad (2.16)$$

The solution of **Eq.2.16** gives a direct result for the maximum value of the trapezoidal waveform which has a 120° flat top. The only requirement for this measurement is a true rms voltmeter. The maximum value of back EMF, E_m is given by,

$$E_m = k_e\ \omega_r \qquad (2.17)$$

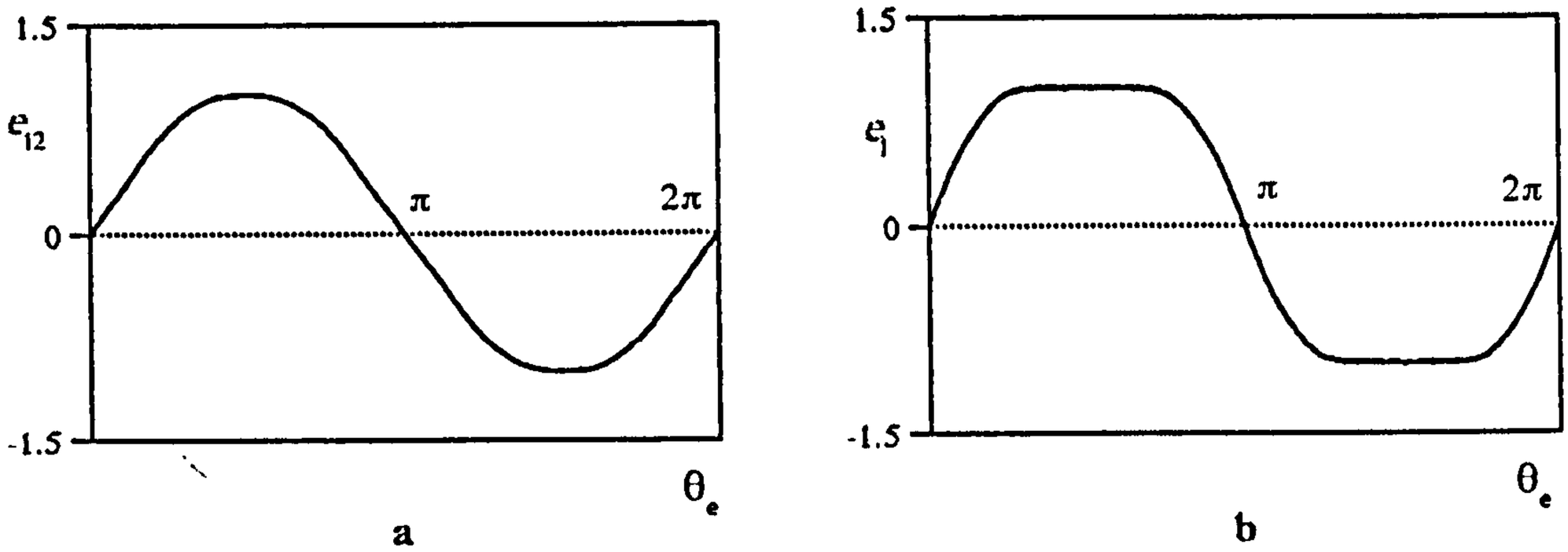

Figure 2.6 Measured back EMF waveforms in a commercial BSPM motor.

a) Phase-to-phase back EMF voltage (normalized).

b) Phase-to-star point back EMF voltage (normalized).

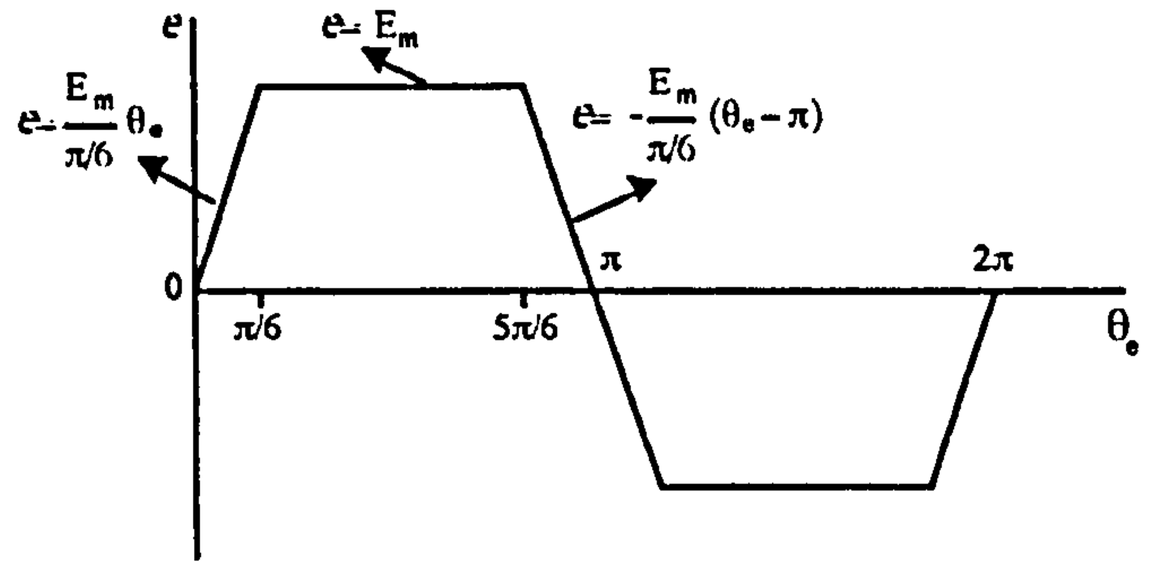

Figure 2.7 Ideal back EMF waveform of a BTPM motor.

In Fig.2.7, an ideal trapezoidal back EMF voltage waveform was shown for the BTPM motor. The waveform has a 120° electrical flat top and magnitude E_m . However, apart from fourier series, giving a straightforward equation for the back EMF of the BTPM motor is not possible. Therefore, it can be given in piecewise form for a single phase as,

$$e = \begin{cases} \dfrac{E_m}{\pi/6}\theta_e & 0 < \theta_e \le \dfrac{\pi}{6} \\ E_m & \dfrac{\pi}{6} < \theta_e \le \dfrac{5\pi}{6} \\ -\dfrac{E_m}{\pi/6}\left(\theta_e - \pi\right) & \dfrac{5\pi}{6} < \theta_e \le \dfrac{7\pi}{6} \\ -E_m & \dfrac{7\pi}{6} < \theta_e \le \dfrac{11\pi}{6} \\ E_m\left(\dfrac{\theta_e}{\pi/6} - 12\right) & \dfrac{11\pi}{6} < \theta_e \le 2\pi \end{cases} \qquad (2.18)$$

The instantaneous back EMF equations for the three-phase BSPM motor can be derived easily. Assuming balanced windings,

$$\begin{bmatrix} e_1 \\ e_2 \\ e_3 \end{bmatrix} = \begin{bmatrix} E_m \sin(\theta_e) \\ E_m \sin(\theta_e - 2\pi/3) \\ E_m \sin(\theta_e - 4\pi/3) \end{bmatrix} \qquad (2.19)$$

Moment of Inertia, J

Moment of inertia, usually referred to simply as inertia, is an indication of resistance to change in speed. A large inertia will require greater torque to achieve a given acceleration rate. It is not an easy parameter to visualize, and to measure, particularly if there is friction present. The moment of inertia of a brushless PM motor is usually given in manufacturer's catalogues. The motor inertia was measured with a deceleration test by using the long time scale of a storage oscilloscope, and the measured moment of inertia was checked against the published data. A similar test was done to measure system (motor+load) inertia. The measured values are used in the dynamic analysis of the drive in **Chapter IV.**

Table 2.2 Measured motor parameters.

Winding resistance, R	: 0.8 Ω
Equivalent winding inductance, L	: 3.12 mH
Back EMF constant, k_e	: 0.417 V/rad/s
Moment of inertia, J	: 0.0008 kgm^2

2.3.2 Static Torque Characteristics

In general, the torque resulting from excitation of a phase winding is a function of phase current and rotor position as given in **Eq.2.13**. If a constant DC current supplied to a stator winding, and the rotor is rotated by an external force incrementally, the resultant torque due to interaction between the winding current and the magnet flux will vary periodically with rotor position. This characteristic is known as the *static torque characteristic*. Ideally, the static torque characteristic has trapezoidal shape for BTPM motors, whereas it varies sinusoidally in BSPM motors. An examination of the static torque characteristic shows which excitation method is more appropriate for the control of a particular brushless PM motor.

In the BTPM motor, the static torque characteristic has a 120° flat-top region that can be utilized to produce torque. Thus, if the motor phases are excited sequentially with a constant current during each 120° interval of constant phase torque, the motor develops a constant total torque.

Similarly, in the three phase BSPM motor, the sinusoidal torque waveforms for each of the phases are displaced by 120°. Assuming that the phase currents are varied sinusoidally with position, the resultant torque becomes

constant. Hence, as will be shown in **Table 2.4**, the developed torque becomes independent of rotor position, and is linearly related to current amplitude.

The measured static torque characteristics for the individual phases of the experimental BSPM motor are shown in **Fig.2.8**. In the **Fig.2.8**, it is shown that the static torque varies with rotor position at I=4A constant current excitation. Since the test motor has 8 poles, the measurements were repeated at 2° intervals up to 90° mechanical rotor position. Small fluctuations at the top of the torque waveform may be due to measurement errors or small saliency in the test motor.

Fig.2.9 gives more detailed experimental results to show the effect of current levels in the static torque characteristics. The measurements were carried out for various levels of current from 2A to 12A, which is above the rated current value of the motor. It was found that there was no noticeable difference in the torque waveforms due to current level. However, the results for the BSPM motor are surprising because they confirm the fact that the static torque characteristics of individual phases have about 90° flat-top region. This practical imperfection of the static torque characteristic will result in fluctuation (ripple) in shaft torque with both sinusoidal and rectangular excitation. It is also clearly seen that the torque ripple is mainly due to position varying part of the static torque (see **Fig.2.8**). Nevertheless, third harmonic torque ripple can cancel out in the balanced three-phase star connected motor.

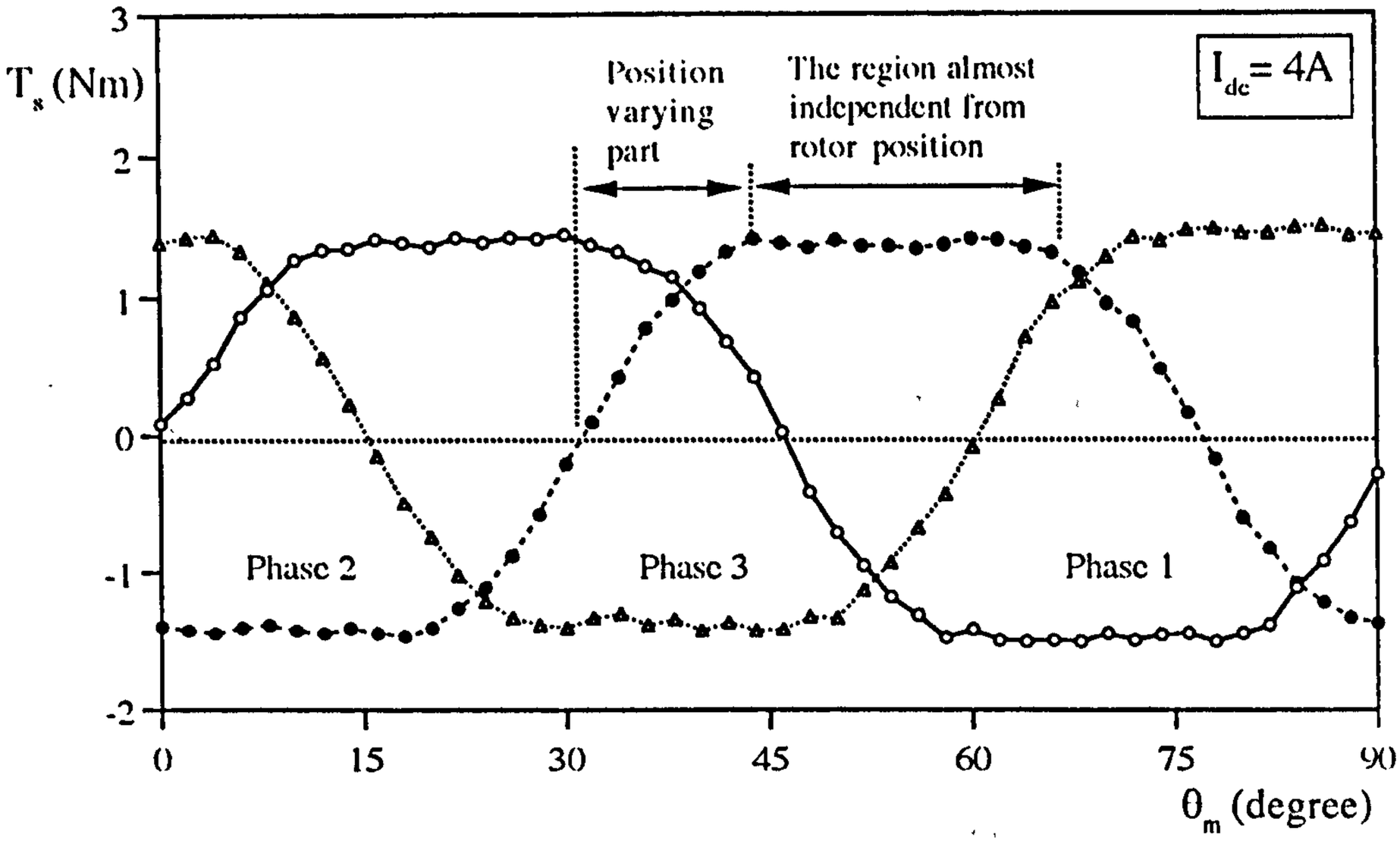

Figure. 2.8 Measured static torque characteristics for the BSPM test motor, I_{dc}=4A

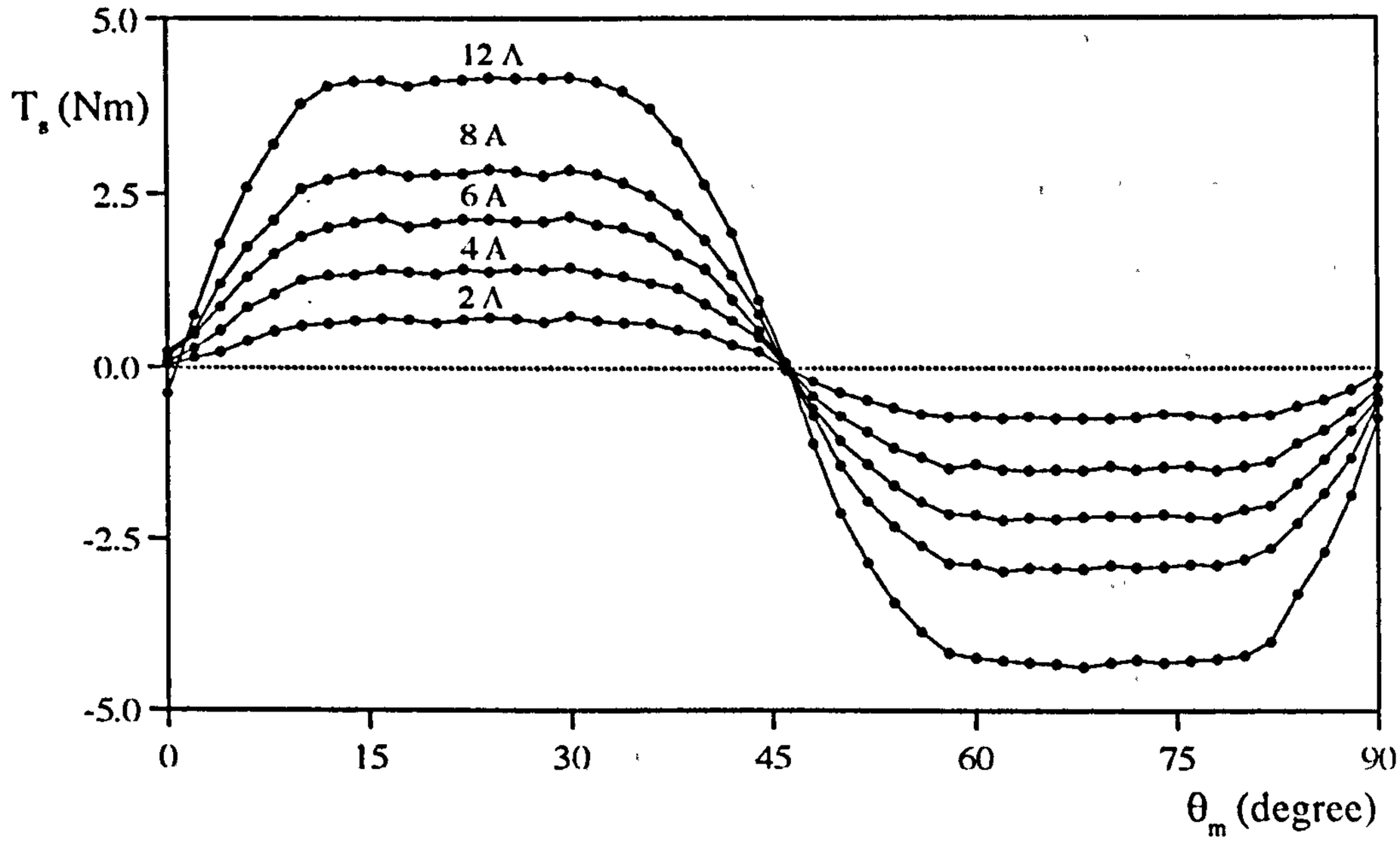

Figure 2.9 The static torque characteristics for various DC current values in the BSPM test motor.

2.4 DRIVE CONTROL

In this section, a brief review of torque, speed, and position control in brushless PM motors is presented. The section examines the requirements which determine the choice and the performance of brushless PM motor drive control, and goes on to explain the auxiliary control units in the experimental drive.

2.4.1 Control Instrumentation

The control techniques used in BTPM and BSPM motor drives are very similar to those used in a conventional controller. **Fig.2.10** shows a block diagram of a complete drive system for brushless PM motors. From the control point of view, the only difference between BTPM and BSPM motors is the control electronics and the resolution of the rotor position information.

In brushless PM motor applications, the drive system consists of two main components, a controller and a motor. The controller provides electrical energy to the motor which converts electrical energy to mechanical energy.

As seen in **Fig.2.10**, a required motor voltage must usually be controlled by means of a power converter (inverter) which accepts the DC voltage supplied by a rectifier. The rectifier and inverter can be arranged in various configurations, but the most common one for a three phase drive is given in **Section 2.5.**

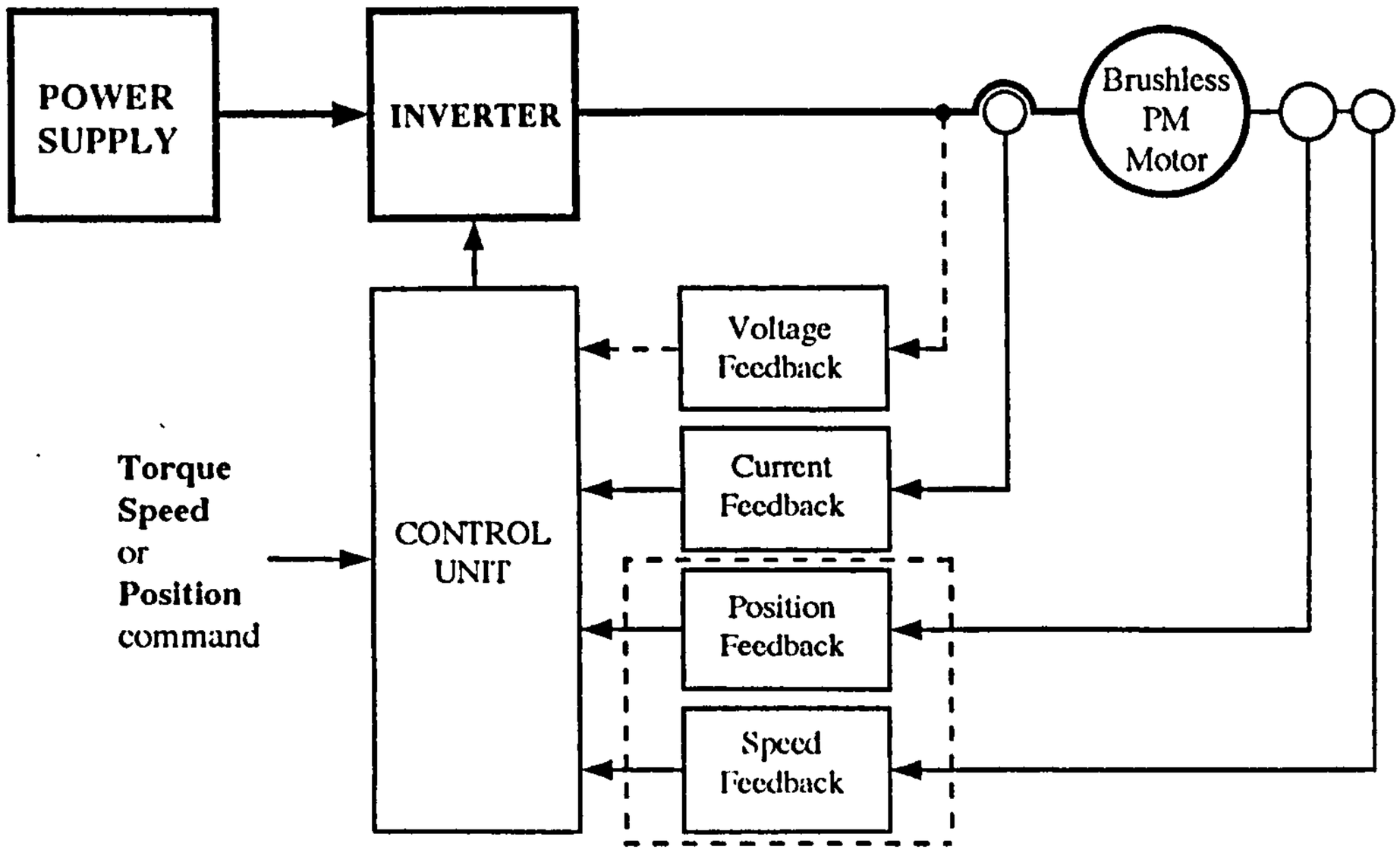

Figure 2.10 The complete drive system block diagram for brushless PM motors.

2.4.1.1. Feedback Devices in Drive Implementation

In this section, the rotor position sensors and other feedback devices are discussed briefly as an aid to understanding the conventional drive system and its control. Basically, all output signals from the sensors are processed to provide the logic signals required for the base drive signals in the inverter. In order to implement the PM motor control, at least two out of four variables shown below have to be measured:

a) Motor line currents

b) Motor terminal voltages

c) Shaft position

d) Shaft speed

a) All current control applications require a measurement unit which measures actual current. In measuring the motor line currents, one normally has to provide isolation between power and control circuitry. For that reason, Hall-effect current transducers are most often used to measure actual line currents of the motor.

b) The requirements for voltage measurement are basically for back EMF sensing (for BTPM motor or 120° current conduction) and advance real time control applications. It is relatively easy and cheap, but the requirement for an isolation amplifier increases the cost while reducing robustness.

c) The rotor flux position in brushless PM motors is defined by the mechanical angle of rotation, which is obtained from some form of rotor position sensor as indicated in **Table.2.2**. Shaft position is usually measured using either resolver or encoders. However, BTPM motors require less accurate shaft position sensing for current commutation. Simple electro-optical sensors are appropriate for trapezoidal type of PM (BTPM) motors or 120° electrical current excitation of a BSPM motors (see **Table 2.3**).

d) Shaft speed measurement is used for the outer loop (**Fig.2.10**). A range of devices, from a conventional DC tachogenerator to AC tachogenerators are used. If a position sensor is used, the speed signal is often derived from the position information at low speed range.

Table 2.3 summaries the popular feedback devices with their related application areas, and the following paragraphs give brief explanations of the devices.

Hall-effect current transducers can detect the magnitude and direction of the line currents. Today these devices are integrated, and provide sensitive current sensing. Three-phase systems may have three of these sensors to measure the alternating and rapidly changing line current. Hall effect devices can also be mounted on the stator to detect the position of the main rotor magnets.

The tachsyn is an air gap reluctance sensitive 3 phase alternator with PM field and trapezoidal output waveforms [*Luneau*, 1985]. It is used for position and velocity sensing, and signal outputs are analog. The tachsyn is available in 4,6, and 8 pole configurations which are designed for 4,6, and 8 pole motors.

Synchros are the sensors which are used in positioning systems. The synchro is essentially a three phase version of the resolver [*Analog Devices*, 1980]. Internally almost all synchros are similar in construction, having a rotor, with one or three windings capable of revolving inside a fixed stator. In general, the rotor winding of a synchro is excited by the reference voltage (at 60 Hz or 400 Hz), and the induced voltages in the stator windings are processed by a resolver digital converter through a special transformer.

Resolver operation is based on inductive coupling between stator and rotor windings. The resolver with its resolver-to-digital (R/D) converter gives precise absolute digital position information. The Inductive Modular Absolute System (IMAS) is a transducer designed for very high position information requirements [*Horner and Freund*, 1991]. The IMAS transducer appears to the outside electronics world to look identical to a resolver. Whilst the resolver has a wound rotor and stator, it has a rotor without windings. The amplitude of the output voltages of the IMAS changes as a

Table 2.3 System comparison of feedback devices in PM motor applications

DEVICE	TECHNOLOGY	MEASURED QUANTITIES	APPLICATIONS
Hall-Effect devices	Electronic, magnetic	Coarse rotor position Current	Brushless motor commutation Current measuring Limited velocity feedback
Tachsyn	Electromagnetic	Coarse rotor position Velocity	Brushless motor commutation Analog velocity feedback
Synchro	Electromagnetic	Fine/Coarse rotor position Velocity	Brushless motor commutation Analog velocity feedback Digital velocity feedback
Resolver and IMAS Transducer	Electromagnetic Electromagnetic -Electronic	Fine/Coarse rotor position Limited velocity Very fine rotor position	Brushless motor commutation Analog velocity Analog velocity feedback Digital velocity feedback
Electro-Optical Devices	LED and Phototransistor combination	Coarse rotor position	Brushless motor commutation
Encoder (Absolute or Incremental)	Electronic-Optical	Fine rotor position Limited velocity	Digital rotor position Velocity feedback
Isolation Amplifier	Electronic	Voltage	Isolated voltage measurement
DC Tachometer and Brushless Tachometer	Electromagnetic	Velocity	Analog velocity feedback

function of the angular position of the rotor. Unlike the sin and cos signal from a resolver, the IMAS's output signals are provided in a triangular form dependent on rotor position.

The electro-optical sensor consists of a light-emitting diode (LED) and photo-transistor, which act as a light transmitter and detector respectively. A slotted wheel is mounted on the motor shaft with a number of stator mounted sensors. Three phase BTPM motors require three of these sensors properly mounted on the stator to define current commutation instants. The sensor must be mechanically adjusted so that the pole pieces are aligned with the optical switching point.

An encoder is an electro-mechanical device which converters mechanical rotation into an electrical output. This output is in digital form, allowing direct interfacing with other digital equipment. Position information is obtained from incremental encoders by counting. The pattern in this case consists of a number of radial lines, equally spaced to give a specified number of *"increments"* per revolution. An absolute encoder provides a series of uniquely coded positions. This is achieved by arranging a number of incremental patterns of varying resolution concentrically on the same disk. Absolute encoders can interface directly with computer equipment.

An isolation amplifier consists of an input and output stage that are isolated from one another. Its primary function is to pass analogue signals without degradation between the stages. Isolation amplifiers serve many critical applications including data acquisition and conversion, and process control. It should prevent ground loop problems and noise related inaccuracies.

The DC Tachometer and Brushless Tachometer are used to sense motor velocity. They provide an analog DC voltage that is proportional to shaft velocity. The polarity of the output voltage in both types of tachometer is determined by the direction of rotation. Unlike the DC tachometer, the brushless tachometer does not have brushes or a commutator.

2.4.2. Controlled Parameters and Methods

In brushless PM motors, the electromagnetic interaction between the magnet field and stator winding results in two basic outputs: electric torque proportional to the winding currents (**Eq.2.11**), and an induced voltage proportional to rotor speed (**Eq.2.17**). The proportional relationship between the motor current and electromagnetic torque provides a direct control of torque in PM motors. **Table 2.4** gives the torque-current relations for different current excitation cases. More detailed information about the derivation of the torque equations will be given in **Appendix.A.2.**

Basically, two types of control are used to drive brushless PM motors; either rectangular or sinusoidal. The relationship between the motor's peak back EMF voltage constants (k_{eT} or k_{es}) and peak torque constant depends on which type of drive is used. Motor operation is always in the constant torque region if the phases are supplied with rectangular wave currents or sinusoidal wave currents of amplitudes I_{mr} and I_{ms} respectively which are normally in phase with the back EMFs of the windings.

Sinusoidal or rectangular reference current waveforms are generated with rotor position information, and the actual phase currents track the reference currents in a current controlled inverter, as will be described in the next subsection.

The complete control system, as described in **Fig.2.10**, gives operation over the full ranges of speed and torque of the brushless PM motor. There are basically three desired controllable outputs for a brushless PM motor drive : torque, speed and position, as discussed in the following section.

Table 2.4 Preferred ideal current conduction patterns and total electromagnetic torque in 3-phase star connected brushless PM motors

DESCRIPTIONS	SINUSOIDAL EXCITATION	RECTANGULAR EXCITATION	
	BSPM Motor	**BSPM** Motor	**BTPM** Motor
Back EMF Waveforms for a Single Phase	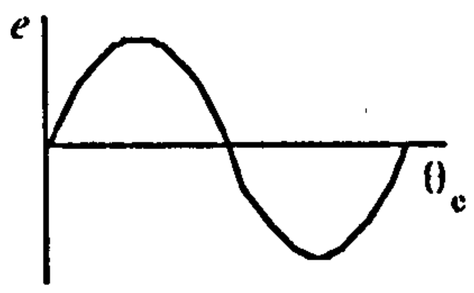	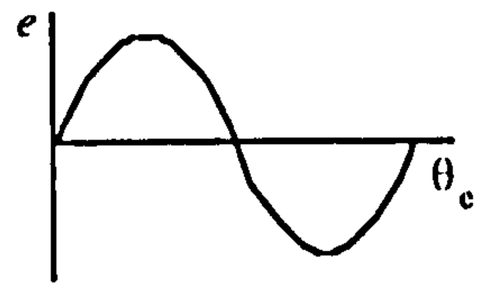	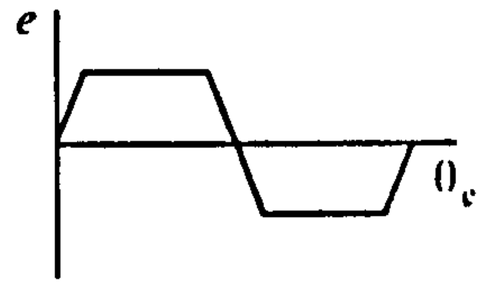
Ideal Current Waveforms for a Single Phase	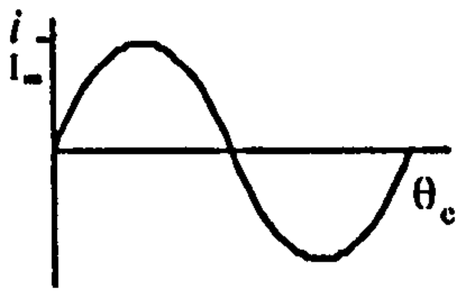	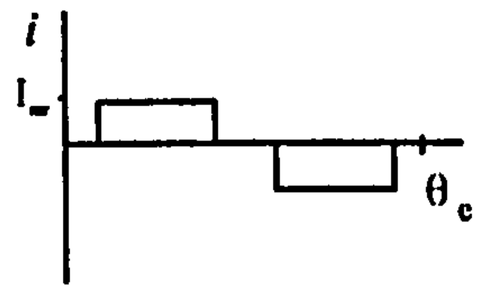	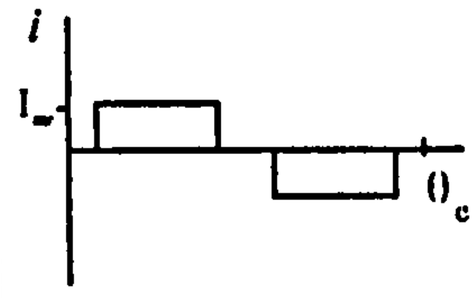
Ideal Total Electromagnetic Waveforms	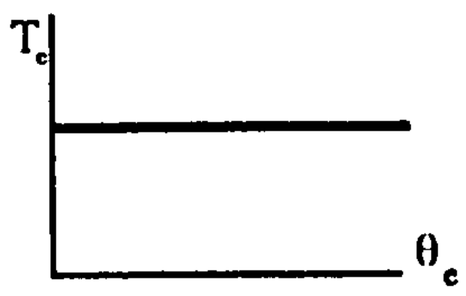	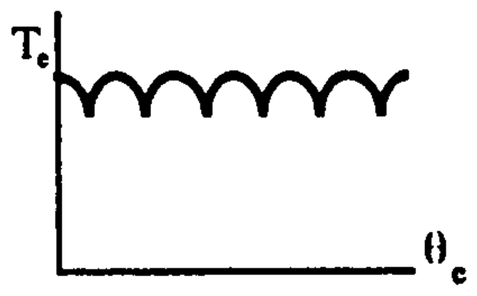	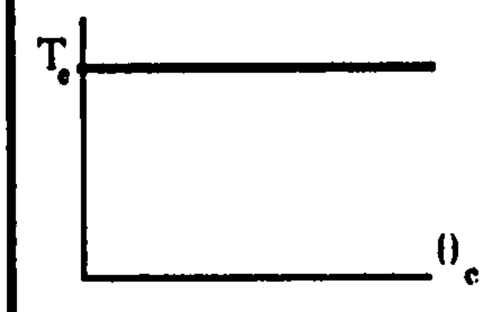
Total Average Electromagnetic Torques	$T_e = \frac{3}{2} k_{es} I_{ms}$ $= 1.5\, k_{es} I_{ms}$	$T_e = \frac{3\sqrt{3}}{\pi} k_{es} I_{mr}$ $= 1.65\, k_{es} I_{mr}$	$T_e = 2\, k_{eT} I_{mr}$

2.4.2.1 Torque Control

As explained in the introduction of **Section 2.4.2**, for direct torque control, the requirement is to be able to control the winding current. Thus, torque can be adjusted as accurately and as rapidly as the motor current can be adjusted and controlled. The current can also be controlled by varying

conduction angle, phase advancing or delaying, and amplitude regulation. However, these control methods may cause torque ripple. In this section, the discussion is mainly going to cover torque ripple free control of brushless PM motor drive. In practice, various schemes can be employed in current controllers [*Freere and Pillay*, 1990]. Hysteresis and pulse width modulated (PWM) control methods are discussed here.

a) Hysteresis Current Controller

Although technological advances in current sensing and more sophisticated current regulator schemes assist for solving current control problems, this method is the simplest. It is also known as *bang-bang* control. **Fig.2.11** illustrates the hysteresis current controller technique, and the control method for one leg of a three-phase inverter. Three of these controllers should be used to control a three phase drive.

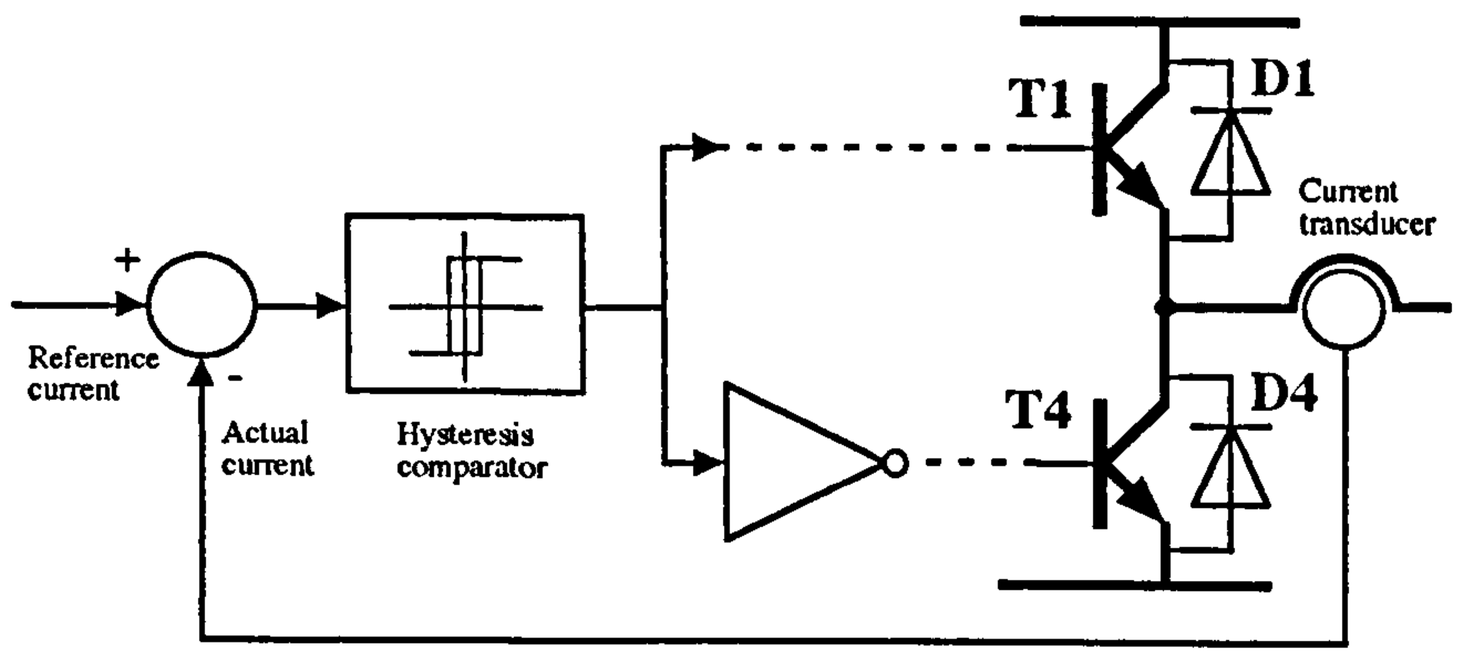

Figure 2.11. Hysteresis current control technique.

It is essential for the controller to force the actual current to follow the reference signal within a narrow band. The function of the hysteresis controller (or any other controller) is to generate logic signals that will drive the power devices in such a way that this requirement is satisfied.

Firstly, the reference current and actual current obtained from a current transducer are compared in a single current loop. Then the current error signal is used to generate drive signals for the inverter power switches so that the current error is reduced. **Fig. 2.12** illustrates the type of waveform produced with a simple hysteresis current controller for a rectangular reference current. If the actual current is more positive than the reference current value, the upper transistor (**T1**) is turned off and the lower transistor (**T4**) is turned on (complementary switching) causing the motor current to decrease by applying negative voltage to related phase, and vice versa.

The hysteresis comparator has a bandwidth (ΔH) that determines the permitted deviation of actual phase current from the reference value before a switching is initiated. Thus, the actual current tracks the reference (sinusoidal, rectangular or any other form) value without significant amplitude error or phase delay.

As clearly seen in **Fig. 2.12**, a small hysteresis bandwidth (Δh) gives a near rectangular (or sinusoidal for sinusoidal excitation) phase current with a small current ripple, but requires a high switching frequency in the inverter. In brushless PM motor drive applications for a given hysteresis bandwidth, the switching frequency is not constant. It varies because of variations in the motor back EMF and inductance (if the motor has variable winding inductance). For a given supply voltage, when the back EMF of the motor is low, the switching frequency may rise excessively.

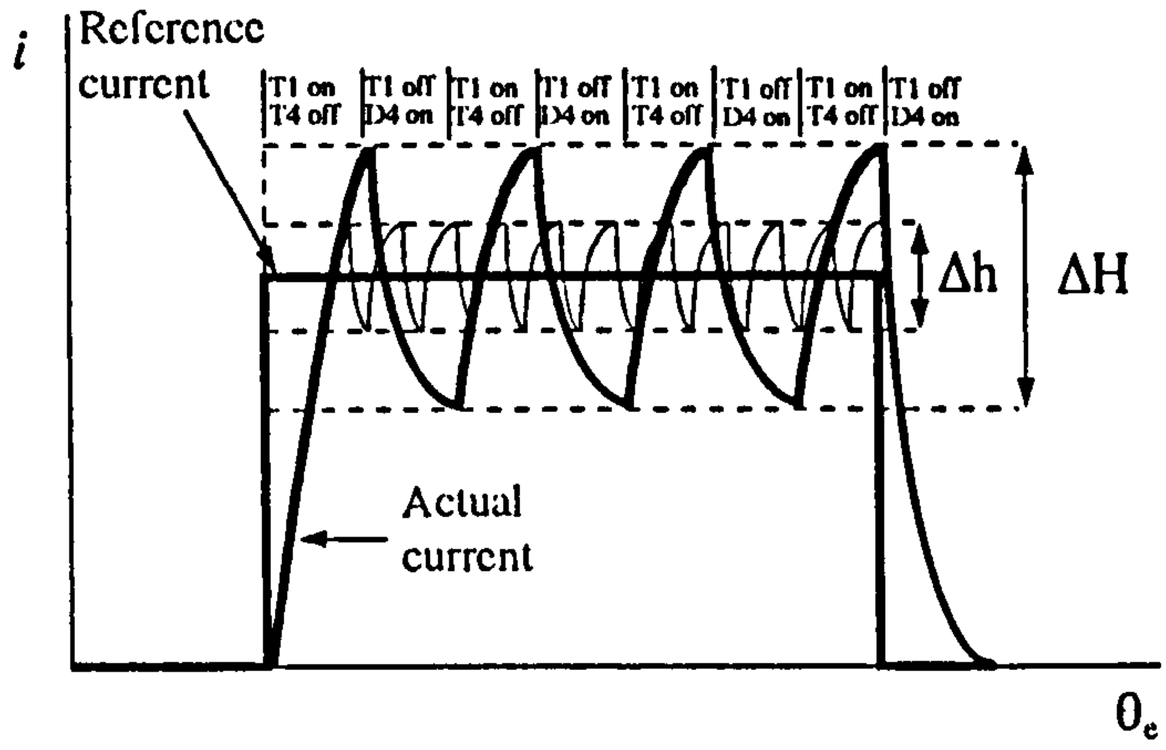

Figure 2.12 Principle of hysteresis current controller.

b) PWM Current Controller

Fig.2.13 shows the schematic of a PWM current controller. The error between the current reference and actual current in each phase is compared to a fixed sawtooth voltage waveform, and the output is passed into a zero crossing detector to generate the switching state of the transistors [*Brod and Novotny*, 1985].

The switching procedure for a PWM current controller is illustrated in **Fig.2.14**. If the reference current is more positive than the actual current, the resulting error is positive. Regions **1** and **2** in **Fig.2.14** show two typical operating conditions of a PWM current controller. If the resulting current error is positive (the reference current bigger than the actual current), and smaller than the sawtooth , the DC voltage is switched to the negative rail voltage ①. Similarly, if the current error is positive and larger than the sawtooth, the DC rail voltage is switched positively ②. The switching frequency in the PWM controller is defined by the sawtooth signal. It is preset and therefore it is easy to ensure that the inverter switching capability is not exceeded.

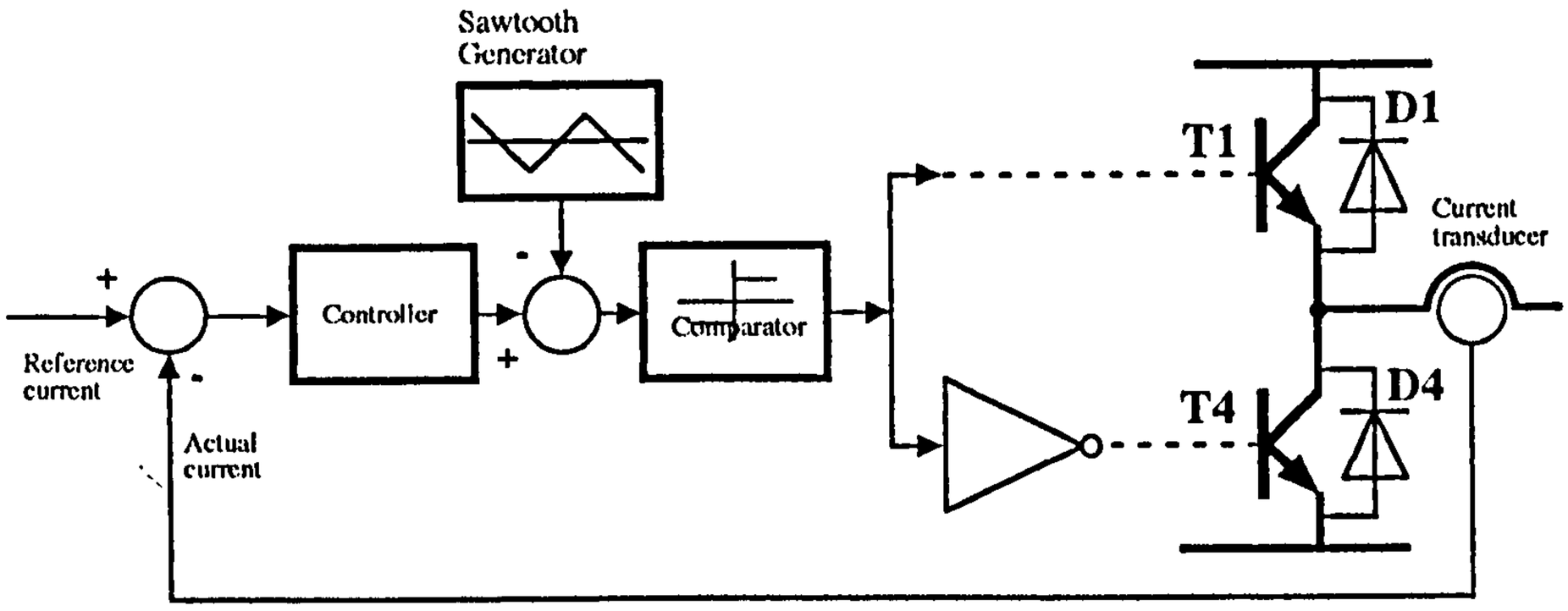

Figure 2.13. PWM current controller.

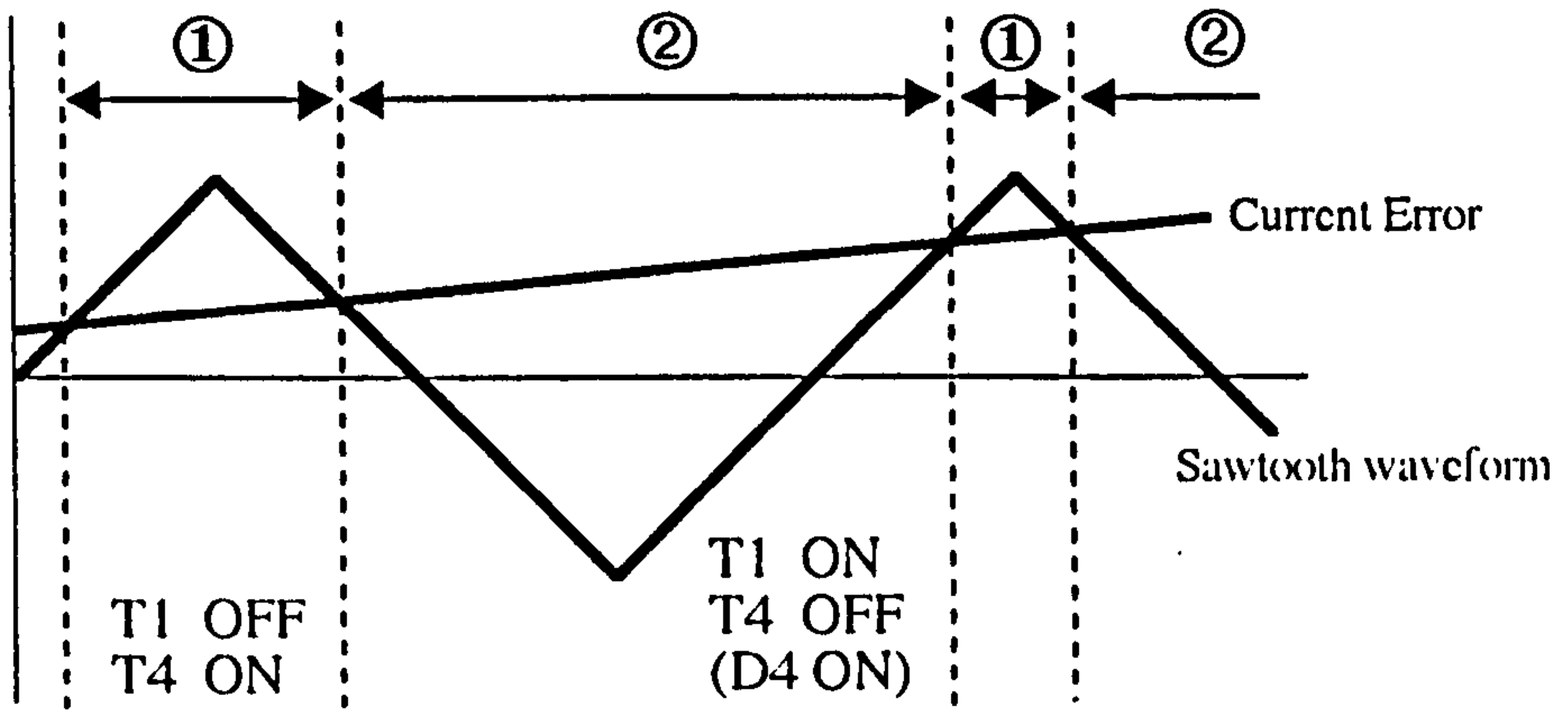

Figure 2.14 Switching procedure of PWM current controller

2.4.2.2 Speed Control

Fig.2.15 shows motor speed being controlled by a classical double loop control scheme with an outer speed loop and an inner current loop. As usual, the magnitude of the speed command represents the desired motor speed. The signal is compared with the speed sensor signal to produce a speed error that is fed to the current loop. As in the classical drive, the speed error becomes the demanded current after the speed controller, and hence the demanded torque in the motor. Furthermore, proportional-integral (PI) speed controllers are often used in the industry [*Pillay*, 1989], and to avoid steady-state speed error, proportional gain of the speed controller is chosen high.

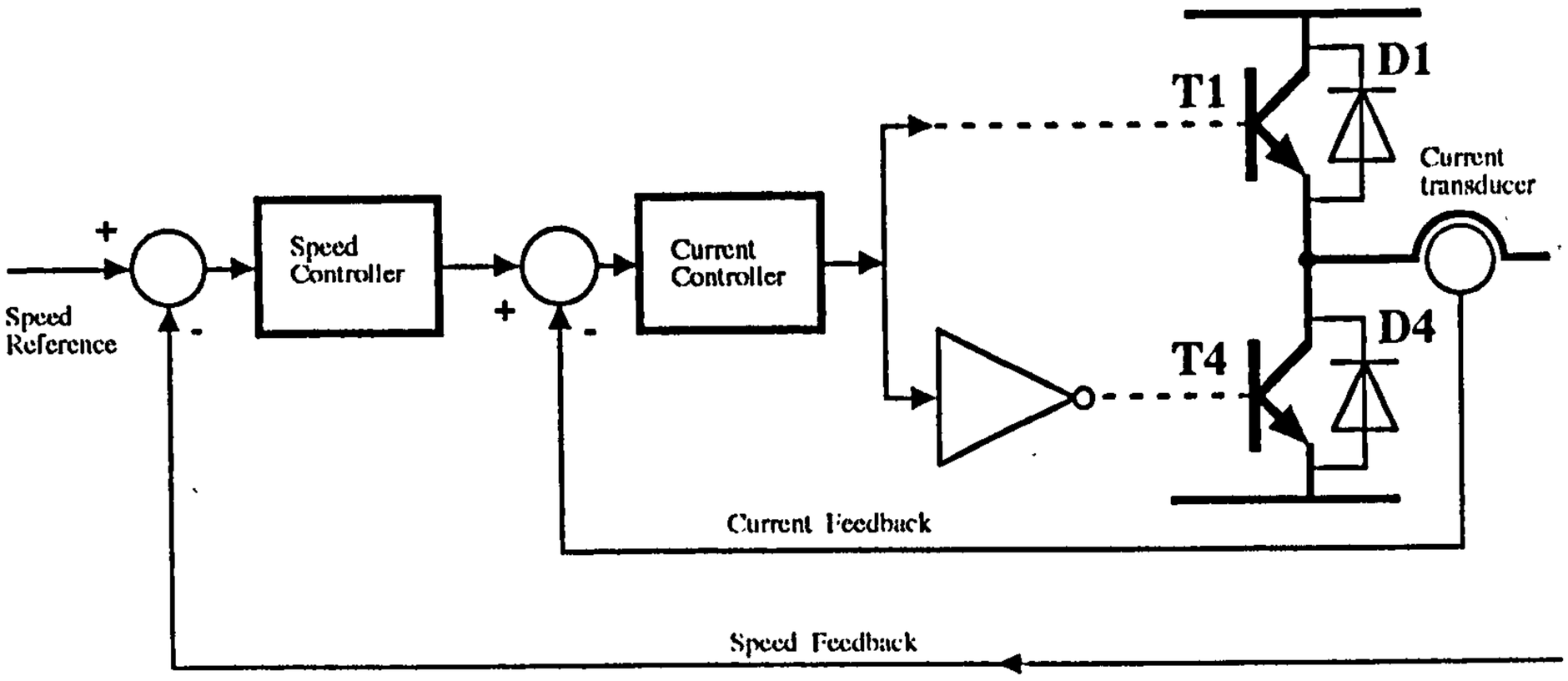

Figure. 2. 15 Speed control block diagram.

2.4.2.3 Position Control

A position control loop may be needed in the brushless PM motor drive, if the drive is employed in a positioning application. With a position loop as shown in **Fig.2.16**, the controller can receive the desired motor position input via another controller (such as a computer). A resolver, or any other standard position sensor (**Table 2.2**), or a position estimation algorithm may produce the position feedback signal, as well as speed information or commutation signals. The speed signal can extracted from the position signal [*Krishnan and Rim*, 1989] for position control applications (dashed box in **Fig.2.16**).

In **Fig.2.16**, electrical servodrives have a position feedback control with inner speed loop derived from the position (or measured separately) and torque feedback control loop in order to get a good transient behaviour [*Naunin and Reuss*, 1988]. In this cascade structure, the torque control loop is superimposed by a position-speed controller providing the torque command values.

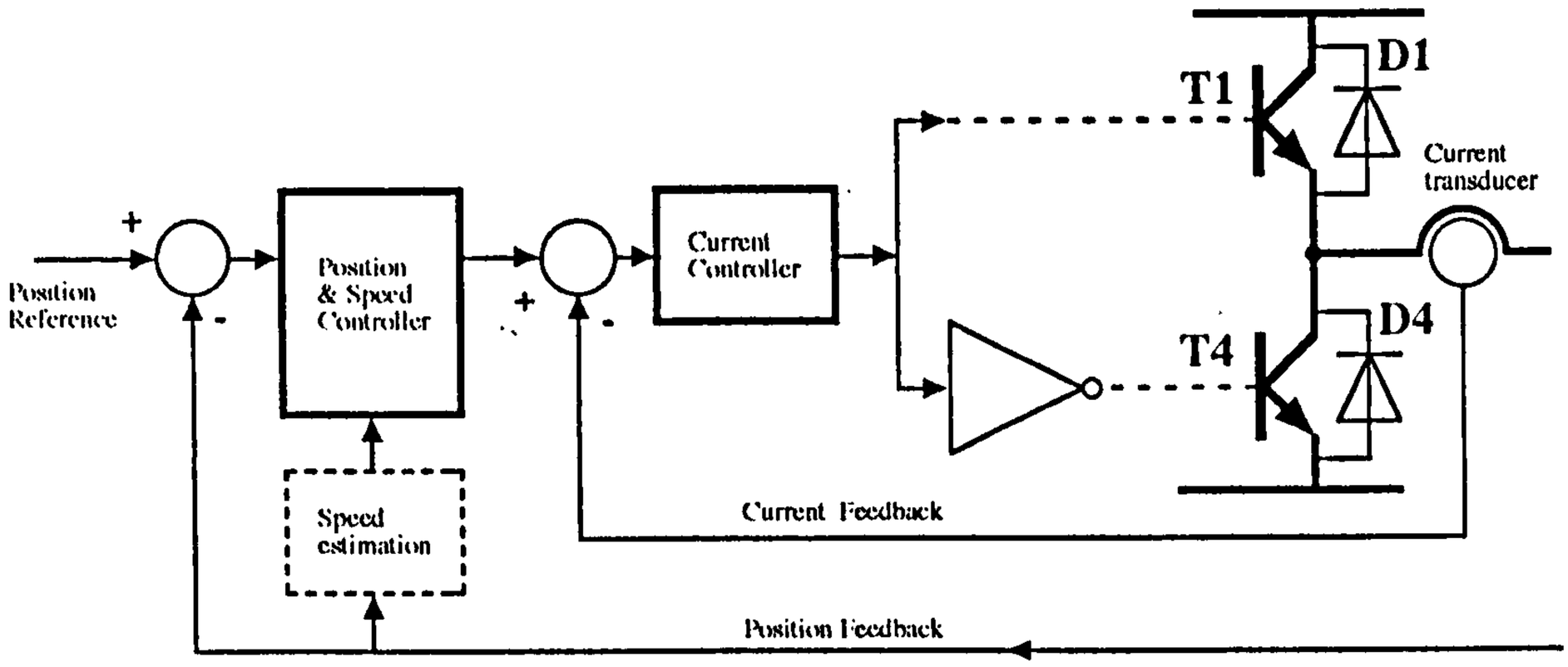

Figure 2.16 Position control block diagram

2.5 IMPLEMENTATION OF A DRIVE

This section describes the process for specifying the inverter and other power circuits for brushless PM motor applications. The implementation of brushless PM motor drives in the literature display a wide variety of control schemes. The most common control scheme and circuits have been used in this research to implement the drive. A block diagram representation of the control circuits has been presented along with a summary of the components.

2.5.1 Power Circuit

Typical converter structures for brushless PM motor applications consist of four parts: rectifier, filter, dynamic braking circuit, and inverter as shown in **Fig.2.17**. DC power is obtained by rectification of the fixed frequency alternating supply voltage with usually a diode rectifier circuit (three phase uncontrolled bridge rectifier), and the DC bus voltage is smoothed (in the voltage fed inverter) by using a filter, and is inverted by power switches. Power switches are the key elements in all of the power circuits which can

be used for motor control, and a wide choice of power devices is now available. Although, the dividing lines between different power switches are changing every year, the overall design of the motor/inverter combination should be considered to get optimum performance from the drive.

The performance characteristics of a brushless PM motor/inverter combination are described by a torque/speed operating envelope. Torque/speed curves help to select the optimum brushless PM motor/inverter combination.

The availability of new and improved switching devices (such as IGBTs) has not greatly affected the basic switching circuits and techniques which are used for brushless PM motor drives. Although the basic requirements for auxiliary commutation circuits are similar, the availability of higher switching frequencies increase in power limits for use of a particular switching device. More detailed design information about the power circuit which has the schematic diagram in **Fig.2.17** is given in **Appendix A.3**. During this research, two types of inverter (bipolar and IGBT) have been designed and used successfully. The rectifier design, the selection of the diodes and the filter components (LC), and heat sink design are discussed in **Appendix A.3**. The choice of dynamic braking resistor is explained, and two types of inverter are discussed in the same appendix. Although, detailed design information is given in the appendix, the key points in the converter design may be summarized as follows:

1. The rectifier and the filter must be capable of supplying the DC voltage and current to the inverter. Therefore, the rectifier diodes must be chosen to handle the required peak current and voltage.

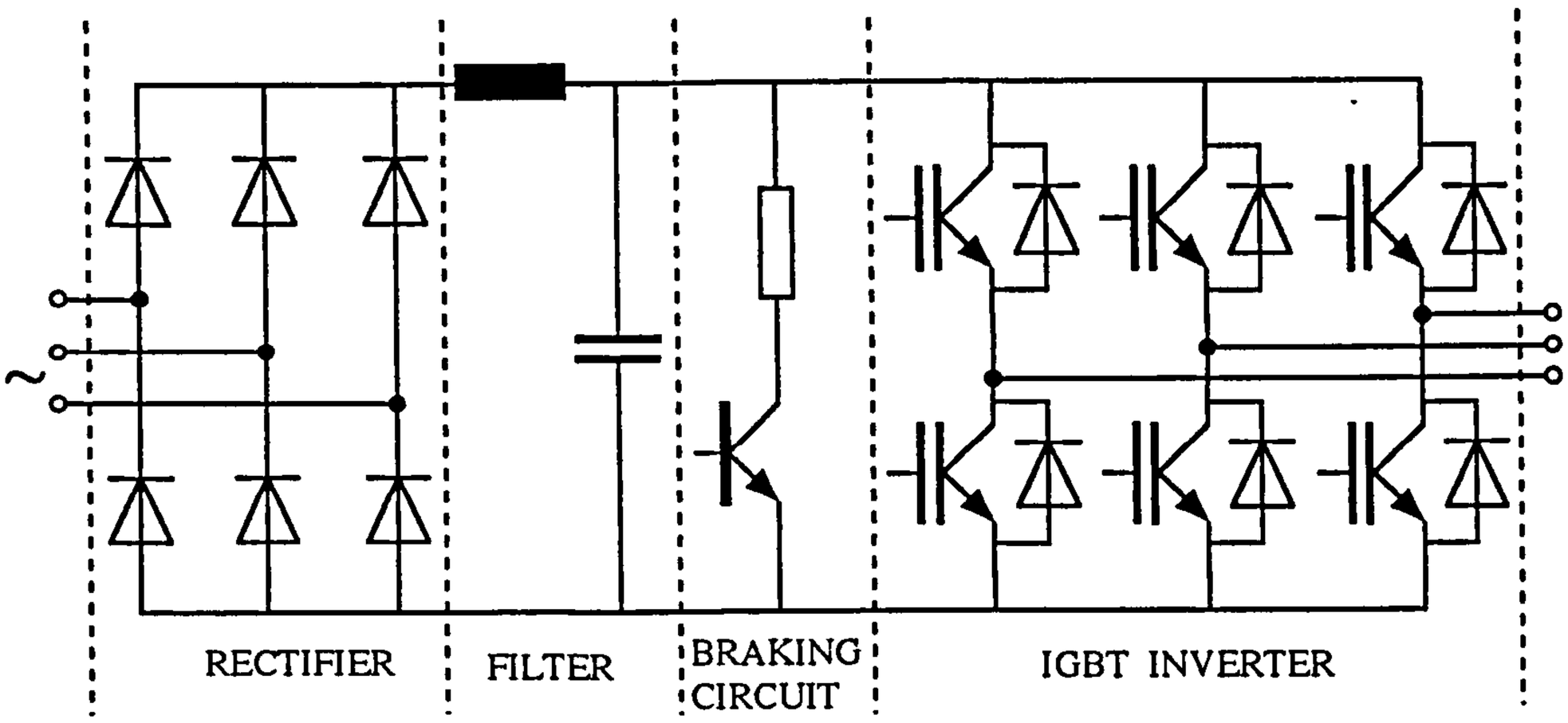

Figure 2.17 Three-phase rectifier/inverter bridge for the brushless PM motor drive.

2. The filter inductor gives the advantage of continuous diode conduction. This results in reduced peak forward current rating of the rectifier diodes.

3. Due to high DC voltage ripple, rectifiers without a capacitor (for the voltage fed inverter) find limited application. The capacitor filter is used to hold the load voltage almost constant.

4. Drives such as brushless PM motors in robotics, machine tools, etc. require braking action. Moreover, DC link voltage may rise excessively at above the rated speed operation of brushless PM motor. Preventing overvoltage and achieving braking action are simply implemented by an external resistance in the DC link (dynamic braking). The braking energy (motor-load kinetic energy) is dissipated as heat in the resistor designed for that purpose.

5. The important power switch ratings in the inverter are forward voltage blocking and on-state current. In many applications brushless PM motors have to occasionally provide torques which are several times their rated

value. Therefore, inverter current rating depends on the maximum torque required from the motor. In both BSPM motor and BTPM motor drive design, the peak motor current is the important parameter.

6. Inverters with IGBTs are used reasonable high power range (1200V, 400A) in brushless PM motor drive [*Control Techniques*, 1992]. Inverters with bipolar transistors are also very popular for the brushless PM motor drive where the power requirement is very high. It should be noted here that multiple stage darlington transistors are used up to 1200V blocking voltages and current ratings of 1000A [*Nerowski et al*, 1990]. In inverters with very low power ratings, FET switches may be selected [18V, 80mA; *Shipley*, 1982].

7. To achieve very fast switching with low switching losses requires different type of power switches. The new power switches (such as IGBTs) allow operation of the inverter with very high chopping frequencies, permitting nearly ideal waveforms of motor current in brushless PM motor drives.

8. Due to the inductive nature of the PM motor load, free wheeling action occurs in the inverter. If the power switch has no inherent reverse parallel diode, an external fast recovery diode must be selected to match the performance of the switch. In addition to this, a diode in series with the power switch may be required to prevent conduction of the parasitic diode which is in the power device.

9. A snubber may be required to damp unwanted oscillations and to prevent the power switch from the overvoltage which might occur during switching.

10. In the inverter design, all calculations of component values should include a reasonable safety margin.

2.5.2 Control Electronics and Auxiliary Circuits

To be able to build a complete brushless PM motor drive system which has a general block diagram given in **Fig.2.10** requires a variety of tools and auxiliary hardware to perform the following functions: monitoring the motor currents, finding the rotor position, producing commanded current waveform, implementing the current controller, interfacing circuits between the control and the power side of the drive, and controlling dynamic braking. In the following paragraphs, these units will be briefly described: design and circuit details are given in **Appendix A.3**.

The complete block diagram of the drive is shown in **Fig.2.18**. This drive employs an 8 pole axial field BSPM motor. As explained in the previous section, the motor is supplied by a three phase bridge voltage source inverter, and the motor currents are regulated by a hysteresis current controller for each phase of the motor. Both rectangular and sinusoidal excitation schemes can be implemented by changing the EPROMs which may have rectangular, sinusoidal or any other stored waveforms. The drive has been built using both digital and analog subassemblies, and it operates as an open-loop system. It can be easily converted into a closed-loop system by adding an outer speed loop as shown in **Fig.2.10**.

As described earlier, the principle employed in this system consists of controlling the inverter switches in such a way to force the currents in the motor to follow reference currents generated from a resolver. This type of control is easy to realize with an IGBT inverter where high switching frequencies are possible. The principal system diagram is composed of the following elements:

1. ROTOR POSITION SENSING CIRCUIT: The rotor position sensor is a resolver combined with a R/D converter. The resolver together with the R/D converter provides highly accurate binary rotor position information which is used to address the EPROMs.

2. COMMANDED CURRENT WAVEFORM GENERATOR: The commanded current generating circuit using the rotor position, produces two analog signals with 120° phase difference. The digital value of position serves as address for EPROMs where the reference values of the current components (Rectangular or Sinusoidal) for two phases are stored in a normalized form. With the stored data format, it is possible to choose the current waveform which is best suited to the motor control. The 120° phase shifting circuit which is placed between the R/D converter output and EPROMs uses a binary adder-latch. The circuit produces a second commanded current waveform by shifting the position data by 120°. The signals which are stored in EPROMs are read by two multiplier D/A converters, and converted to analog form. By changing the D/A converter control voltage, the amplitude of the commanded currents can be adjusted. A third commanded current is reconstructed by adding and inverting the output of the two generated commanded current waveforms.

3. ACTUAL CURRENT MONITORING: An inner current loop, and current sensing is required in the brushless PM motor drive to use in the hysteresis current controller, hence for torque control. Although, in a star-connected stator winding with isolated neutral, measuring two line currents is sufficient, for proper operation, three independent LEM current transducers are used to measure actual motor currents.

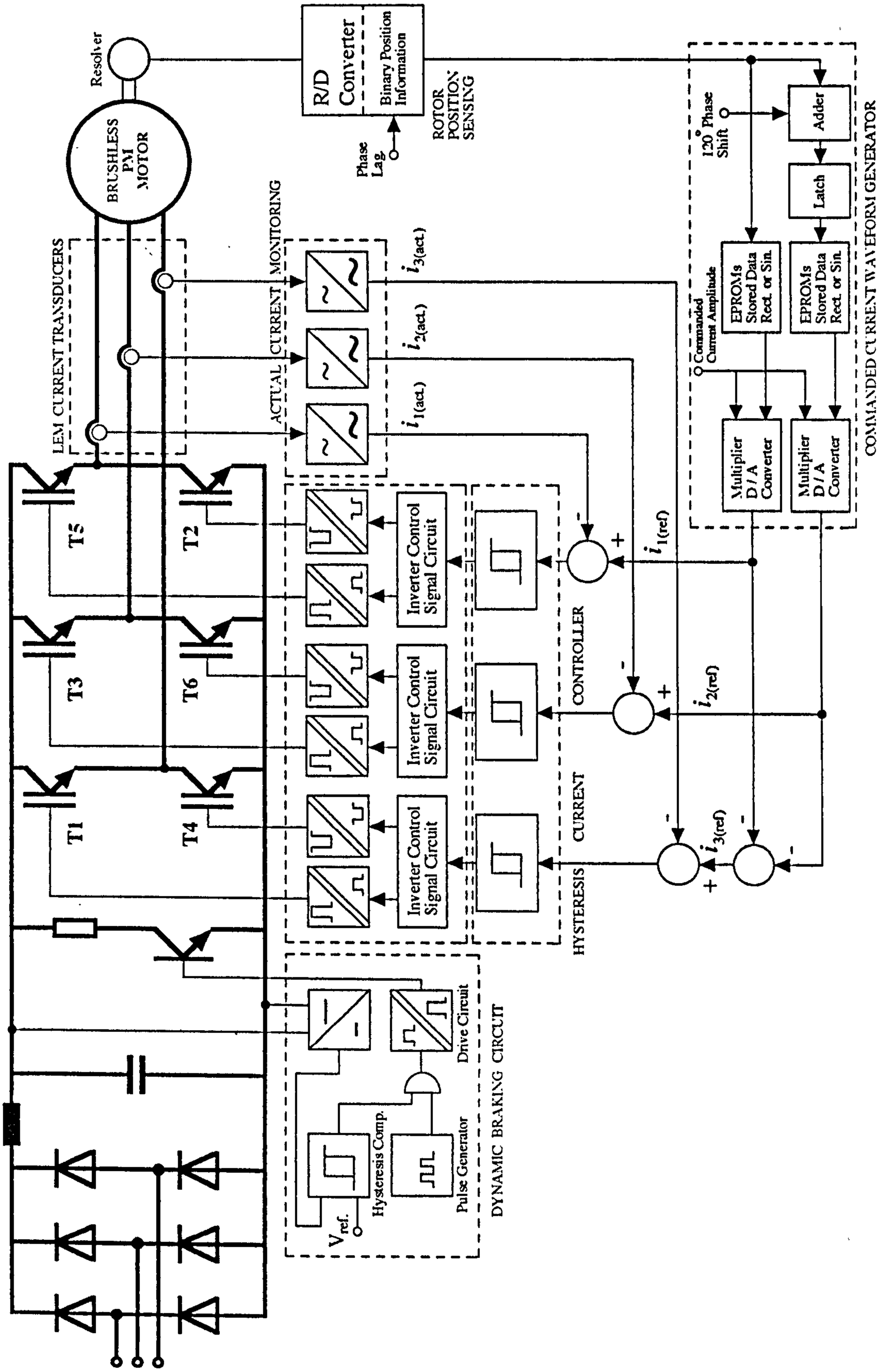

Figure 2.18 Functional System Configuration of Implemented Brushless PM Motor Drive

4. HYSTERESIS CURRENT CONTROLLER: A bus connects the multiplier D/A converters with the hysteresis current controllers. The most common way of controlling the current is the use of three individual current controllers. This current control is done using a hysteresis controller that compares the actual line currents with their commands, and based on the polarity of the error, produces a switching signal. The basic operation of hysteresis current controller was given in **Section 2.4.2.1.**

5. DRIVE AND INVERTER CONTROL SIGNAL UNIT: The switching procedure, which is defined by the current controllers, is applied to the inverter switches in a complementary manner by the inverter control signal circuit. Delay times and switching times in both the IGBT and the bipolar transistor are determined by the need for charge to be established and removed. For use at high switching frequencies, the IGBT delay times can be reduced to very low values by hard driving of the gate. Moreover, for circuits where the motor supply is greater than 50V DC, then it is also advisable to provide some form of electrical isolation. The simplest and most popular way is to use opto-couplers. All requirements which are explained above, can be implemented in the drive circuit. Two suitable drive circuits for interfacing the control circuit with the power switches (bipolar and IGBT) are given in **Appendix A.3.4** and **A.3.5.**

6. DYNAMIC BRAKING CIRCUIT: The dynamic braking circuit works as an overvoltage protection unit. Braking operation is obtained by a transistor controlled resistor as shown in **Fig.2.18.** The DC link voltage is attenuated by a voltage divider, and is compared to the reference voltage in the comparator with hysteresis. The voltage V_{ref} is referred to no-load DC link voltage. The switching signals are produced by a pulse generator

separately. In the case of over voltage on the DC link, the braking transistor is switched on or off by the drive circuit to keep the DC link voltage almost constant within the hysteresis tolerance.

The described method guarantees the control of the three phase currents of the motor within the given hysteresis bandwidth. Using the implemented drive in **Fig.2.18**, the magnitude of current (hence the torque) can be easily adjusted since the inverter switching signals are derived from the rotor position. It is also possible to control the phase angle between the current and the back EMF by giving phase shift which is shown in the rotor position sensing unit **in Fig.2.18**.

2.6 RECENT DEVELOPMENTS IN BRUSHLESS PM MOTOR DRIVE

A modern drive incorporates an impressive range of technology: new materials, motors, sensors, power and control electronics, and software. Traditionally, interfacing the control circuit with the power circuit has been achieved by using large number of discrete components. However, higher levels of system integration are now possible using compact products and ICs. Very large scale integrated (VLSI) circuits and application specific integrated circuits (ASICs) are becoming popular in brushless PM motor drive applications. Nowadays, manufacturers of industrial control systems are looking for higher levels of systems integration, coupled with increasing sophistication in control techniques at lower costs. Depending on the application, driver and control products for brushless PM motor drives are available with voltages up to 600 V and varying degrees of control and logic complexity. To achieve very fast switching in the motor control applications

requires a low inductance as well as a low impedance gate drive to ensure rapid charging and discharging of the input capacitance. Today, most of the requirements for brushless PM motor drives can be supplied by semiconductor producers. Some of these products and features of them which are available in the market, may be summarized as in the following paragraphs.

Toshiba produces an IGBT module. Six IGBTs with their inverse parallel diodes are built into one package. The MP6750 module has 600V voltage and 15A current ratings, and can be used for high power switching motor control applications. Moreover, current sensing MOSFETs have been developed to meet the need of current monitoring in the power device.

The **International Rectifier** IR2130 is a complete 28 pin chip for high voltage MOS gate drive. It can be used as a high power switch driver in motor control. The driver is used in inverters which have DC rail voltages up to 600V. Due to a floating output, the IR2130 can drive six switching devices in the three phase inverter using a single supply. It has a built-in overvoltage protection circuit, a shoot through current monitoring circuit, and fault and current sensing circuits. The IR2110 is a MOS gate driver with 14 pins, but it can give only 2 floating outputs (useful for one inverter leg), and operates up to 500V DC rail voltage.

Harris SP600 is another high voltage integrated circuit to drive two MOS gated (such as IGBT) power devices. It has 22 pin packaging, and provides all necessary control and protection with a single power supply. The SP600 has overcurrent protection and 500V maximum rating.

Ericson PBM3961 is a CMOS control circuit for three phase DC brushless motors in constant speed applications. It uses Hall devices as position sensors. The IC and a small number of external components provide all necessary functions to start, drive control, brake, and current limit during start up.

The **National Semiconductor** LM621 is designed for commutation of brushless DC motors. The IC is compatible with both three and four phase motors. It can directly drive the power switching devices from a 40V supply used in the inverter. It uses Hall logic sensors. The controller chip can incorporate six output power transistors, with a PWM control circuit. LM621 provides a dead-time circuit to eliminate shoot through current spikes, and overcurrent detection circuit.

The **Siliconix** Si9985CY [*Nicholson*, 1991] is a comprehensive device, sensorless and 3-phase brushless PM motor drive. This is achieved by sensing the back EMF signal from the motor terminals. It also incorporates functions such as a fault indicator, temperature sensing, 4-8 pole motor selection, f/V conversion circuitry for speed control, and a charge pump voltage generator for level shifting and driving the output switching transistors in the inverter.

The **Philips** SA/SE/NE 5570 [*Philips*, 1989] is a CMOS controller for three phase brushless PM motors. It provides full operation of the motor. The switching power transistors (power MOSs) are connected directly to the IC outputs. It can accept logic compatible serial interface to control rotation direction, run,, brake lock, enable, and motor voltage. Three Hall sensor inputs are provided to enable correct current commutation.

The **AD2S100/2S110** [*Flett*, 1991] integrated circuit is produced by Analog Devices. It performs the combined function of Clarke and Park transforms to control the brushless PM synchronous motor. It is a three port device provides a digital port accommodating the most popular sensors used for rotor position and velocity measurement in brushless PM synchronous machines. The position inputs can be either absolute serial binary or incremental encoder format.

2.7 CONCLUSIONS

A simple but comprehensive study of different features of brushless PM motors and drive systems has been presented in this chapter. Firstly, the study provides background knowledge which will help both the author and the reader in successful launching into the other chapters. Secondly, some of the concepts which had been briefly discussed here will appear in considerable detail in the following chapters, so unnecessary repetition will be avoided in the forthcoming discussions.

The subsection on "The Mathematical Model" will help the reader to understand the motor model which is going to be used in both steady-state and dynamic analysis of the drive system. The accurate steady-state and dynamic analysis of the drive needs correct parameter measurement. Some practical considerations about measuring of the motor parameters, and initial ideas about the control system have been explained.

It is fundamentally important to recognise that drive design cannot be isolated from application requirements. The drive system, comprising control circuits and motor must be designed as a whole. The designed complete and

flexible drive system will give the opportunity to verify the algorithms which are developed in the next chapters.

Although, a complete drive system for brushless PM motors has been developed and implemented in this work, the author believes that the major remaining problems in this area relate to establishing the best techniques for proper control and position sensing in brushless PM motor by using higher level system integration. The material presented here, and in related appendices, will be of assistance in advancing towards this objective.

CHAPTER III

A NEW ANALYTICAL APPROACH TO DETERMINING STEADY-STATE PERFORMANCE

3. INTRODUCTION

The differential equations which describe the behaviour of a brushless PM motor had been conveniently expressed in **Section 2.2**. The general set of state equations given in **Eqns.2.8** and **2.9** apply to the brushless PM motor, and can be solved using numerical methods (e.g. Runge-Kutta) or an analytical method.

In this chapter, the solution of the first order differential equations of a star connected BSPM motor by analytical calculation will be explained in the case of 120° steady-state inverter operation. The chapter describes a new analytical approach, which, although more complicated than the numerical method, leads to a shorter computation time, since only one iterative process (Newton-Raphson) is involved. A numerical method (such as Runge-Kutta) requires several iterations, and it is possible to obtain a precise solution only if the current on time is a multiple of the time step. When this solution is not met, it is necessary to start the procedure again but with another time

step. Moreover, if the number of time steps is increased in the numerical method, the computation time also increases. However, when the state equations are nonlinear (see **Eq.2.4**), and transient behaviour of the brushless PM motor is being investigated, a numerical method should be used.

The analytical solution of the brushless PM motor for 120° inverter operation requires, the following assumptions to be made:

1. In the axial field BSPM motor, the effective air gap length is constant and large since the motor magnets and their supporting disk have the same permeability as air. Therefore, it can be assumed that the machine inductance is independent of the rotor position.

2. For the analytical calculation method, it is necessary that all motor parameters are constant during the calculation step [*Deleroi and Woudtsra*, 1990], so the system is in the steady-state. In particular, the rotor speed is assumed to be constant. Although harmonic torques, resulting from imperfect operation of the drive, tend to induce speed oscillations, it is assumed that the rotor inertia is sufficiently large so as to minimize this effect.

3. The stator windings of the motor are identical and, as will be explained in the next section, since the inverter is switched symmetrically, it is clear that the three stator winding currents are both three-phase and half-wave symmetric.

4. It is assumed that the back EMFs of the motor vary sinusoidally. If the assumption is not adequate, the fundamental component of back EMF can be used for the analysis.

In fact we need four differential equations (one is mechanical) to describe the behaviour of the three-phase brushless PM motor. However, three differential equations are enough for the case of constant speed operation. The developed electrical torque of the motor can be easily estimated at constant speed using **Eq.2.13** which was given in **Section 2.2.2.**

The following sections describe the basic switching procedure of the inverter driven brushless PM motor, explain the procedure in a schematic manner, and give the analytical solution of the differential equations in detail. To verify the solution, comprehensive experimental and computed results are also given in **Section 3.4.**

3.1 PRINCIPLES OF THE EXCITATION SCHEME AND THE SYMMETRY RELATIONSHIP

3.1.1 Switching Procedure for 120° Inverter Operation

The bipolar version of the inverter connected with the load is illustrated in **Fig.3.1a.** As explained briefly in the previous chapter (**Section 2.4**) for 120° inverter operation, motor line currents are obtained by switching the transistors at 60° intervals in the sequence in which they are numbered in **Fig.3.1b.** Each transistor switching occurs in response to the rotor position sensor signal. The idealized quasi-square waveform currents of **Fig.3.1b.** imply instantaneous switching of current from one phase combination to the next. Although the line current waveforms in **Fig.3.1b** are idealised, this is not possible in a practical voltage fed system, because of non-ideal inverter switches and the inductances of the phase windings. Due to the presence of inductance of winding, the build up of current delay,

and also the current conduction continues after the theoretical turn-off instant. As a result of this imperfection, during the current commutation from one phase to another, all three phases of the motor are connected to the DC rail voltage by means of inverse parallel diodes of related power switches.

Typical steady-state motor currents showing "*the commutation interval*" are given in **Fig.3.1c**. A diagram illustrating the transistor switching sequence with on-state of the reverse parallel diodes, and six fundamental switching states has also been represented in the same figure.

The machine model voltage differential equations which were given in **Eq.2.8**, are dependent on the switching states of the inverter. For every combination of the inverter switching and the motor windings, it is necessary to make a new model. Basically for 120° inverter operation, it is possible to describe 6 inverter states in the drive.

During the intervals which are shown as inverter states in **Fig.3.1c** , it is clear that two distinct circuit states exist:

1. "*The commutation interval*", all three phases of the motor are connected to the DC rail voltage by means of the inverter ($0<\theta_e\leq\theta_c$).

2. "*The conduction interval*", two of the motor windings are connected to the DC rail voltage, and remaining phase is open-circuit ($\theta_c<\theta_e\leq\pi/3$).

In both modes of connection, since the motor is star connected, the sum of all three /or/ two stator currents are zero (see **Eq.2.7**).

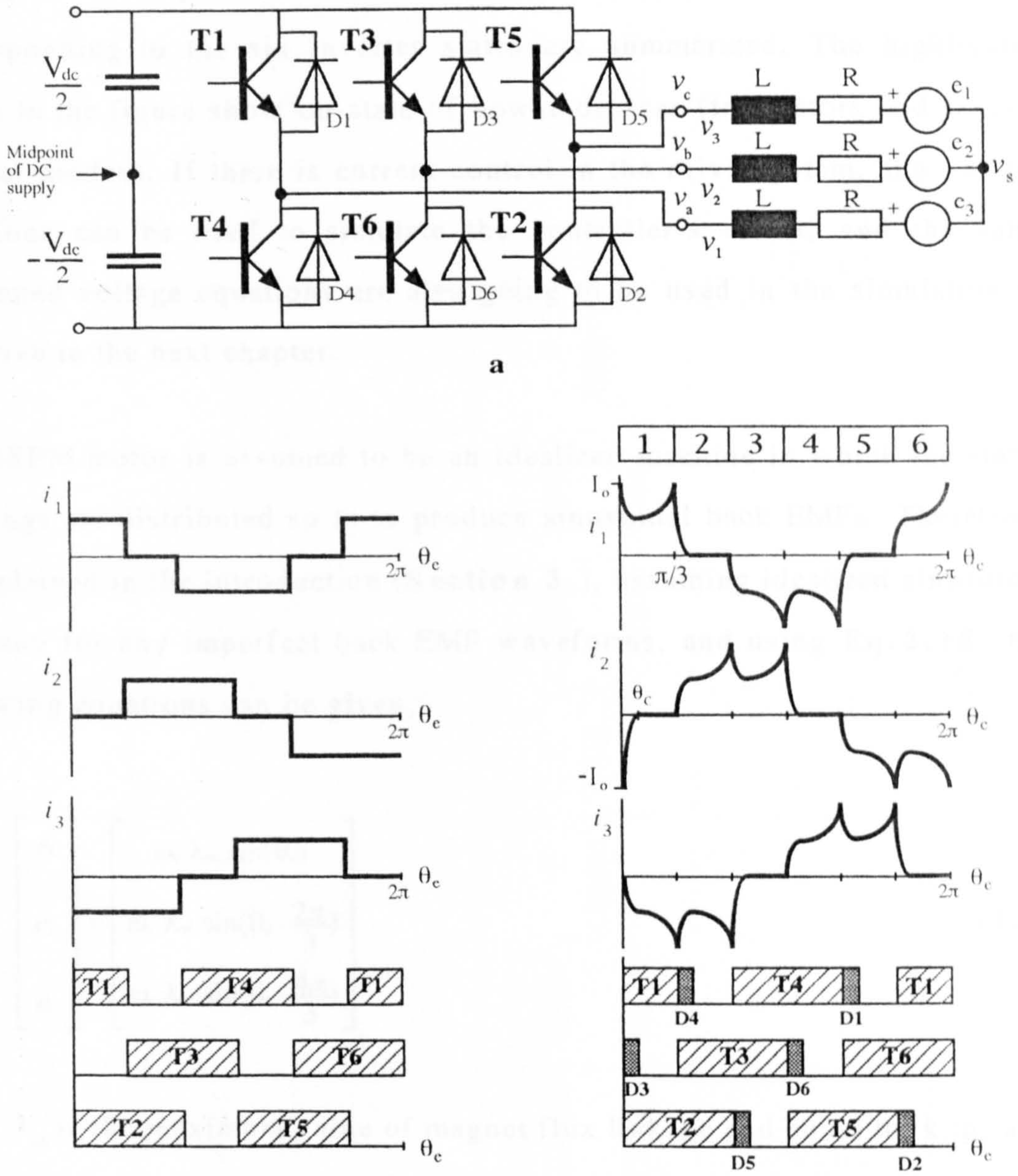

Figure 3.1 Idealized and typical current waveforms of brushless PM motor drive for 120° inverter operation.

a) Three phase inverter

b) Idealized waveforms of line currents, and switching devices.

c) Typical steady state line current waveforms, and conducting devices in the inverter.

In **Fig.3.2**, the possible circuit connections and phase voltage equations corresponding to the six inverter states are summarized. The highlighted letters in the figure show on-state of power devices (transistors and reverse parallel diodes). If there is current control in the drive system, the voltage equations can be used to simulate the controller's effect, and the same developed voltage equations are also going to be used in the simulation of the drive in the next chapter.

The BSPM motor is assumed to be an idealized machine in which the stator windings are distributed so as to produce sinusoidal back EMFs. Therefore, as explained in the introduction (**Section 3.**), assuming idealized sinusoidal variation for any imperfect back EMF waveforms, and using **Eq.2.18**, the following equations can be given,

$$\begin{bmatrix} e_1 \\ e_2 \\ e_3 \end{bmatrix} = \begin{bmatrix} \omega_e \lambda_m \sin(\theta_e) \\ \omega_e \lambda_m \sin(\theta_e - \frac{2\pi}{3}) \\ \omega_e \lambda_m \sin(\theta_e - \frac{4\pi}{3}) \end{bmatrix} \qquad (3.1)$$

Here, λ_m is the maximum value of magnet flux linkage and equal to k_e/p, and ω_e is the electrical speed in rad/s.

Due to the back EMFs of the phases, the star point voltage v_s changes with the position of rotor. The **State 1** in **Fig.3.2** will be used to show the estimation method of the star point voltages, hence the phase-to-star point voltages of the motor windings.

STATE NO.	THE COMMUTATION INTERVAL		THE CONDUCTION INTERVAL	
1	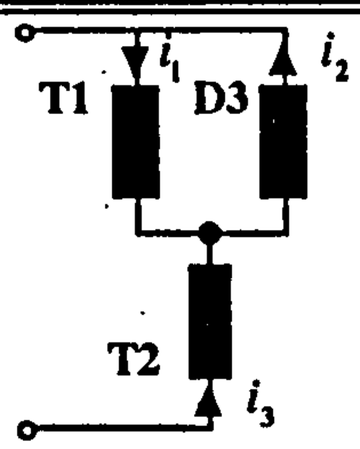	$v_1=\frac{V_{dc}}{3}$ $v_2=\frac{V_{dc}}{3}$ $v_3=-\frac{2V_{dc}}{3}$	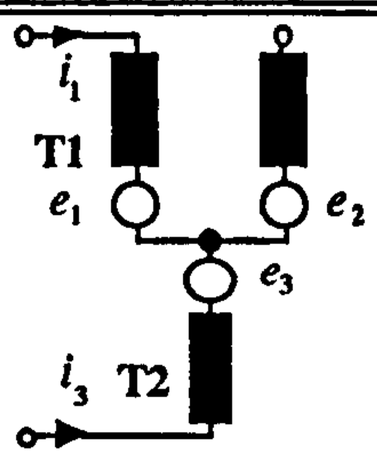	$v_1=\frac{V_{dc}}{2}+\frac{e_1+e_3}{2}$ $v_2=e_2$ $v_3=-\frac{V_{dc}}{2}+\frac{e_1+e_3}{2}$
2	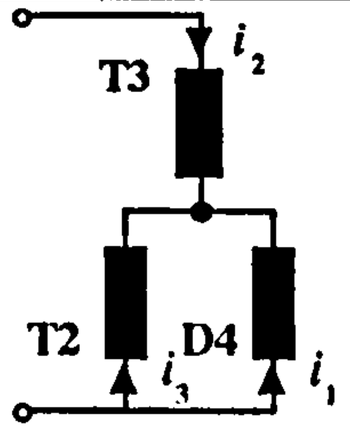	$v_1=-\frac{V_{dc}}{3}$ $v_2=\frac{2V_{dc}}{3}$ $v_3=-\frac{V_{dc}}{3}$	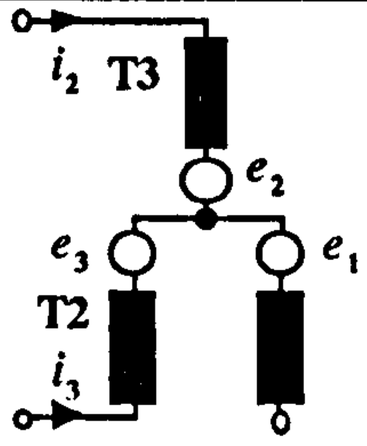	$v_1=e_1$ $v_2=\frac{V_{dc}}{2}+\frac{e_2+e_3}{2}$ $v_3=-\frac{V_{dc}}{2}+\frac{e_2+e_3}{2}$
3	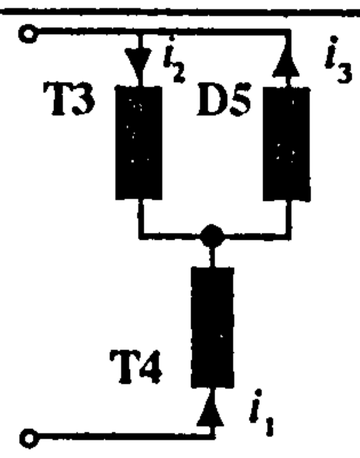	$v_1=-\frac{2V_{dc}}{3}$ $v_2=\frac{V_{dc}}{3}$ $v_3=\frac{V_{dc}}{3}$	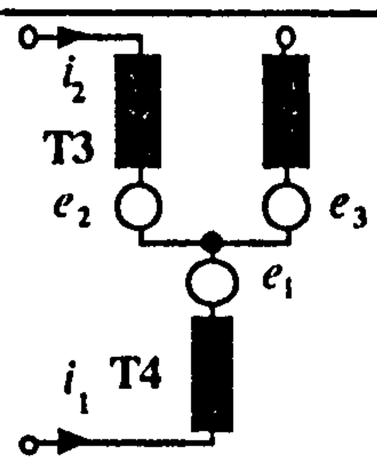	$v_1=-\frac{V_{dc}}{2}+\frac{e_1+e_2}{2}$ $v_2=\frac{V_{dc}}{2}+\frac{e_1+e_2}{2}$ $v_3=e_3$
4	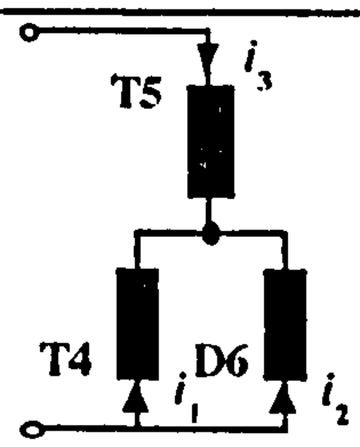	$v_1=-\frac{V_{dc}}{3}$ $v_2=-\frac{V_{dc}}{3}$ $v_3=\frac{2V_{dc}}{3}$	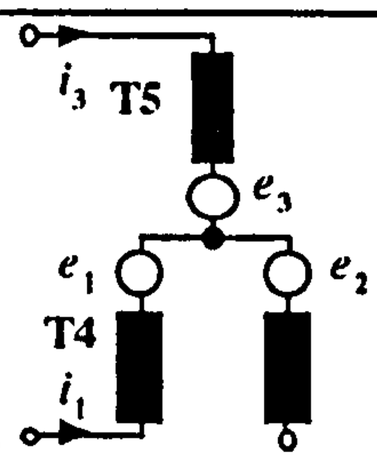	$v_1=-\frac{V_{dc}}{2}+\frac{e_1+e_3}{2}$ $v_2=e_2$ $v_3=\frac{V_{dc}}{2}+\frac{e_1+e_3}{2}$
5	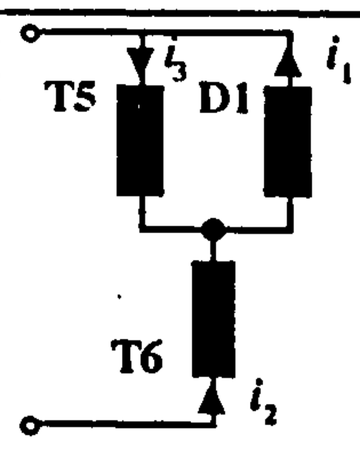	$v_1=\frac{V_{dc}}{3}$ $v_2=-\frac{2V_{dc}}{3}$ $v_3=\frac{V_{dc}}{3}$	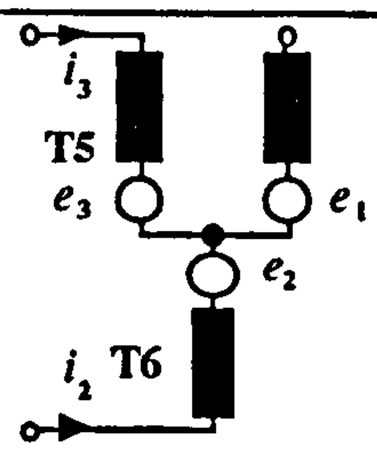	$v_1=e_1$ $v_2=-\frac{V_{dc}}{2}+\frac{e_2+e_3}{2}$ $v_3=\frac{V_{dc}}{2}+\frac{e_2+e_3}{2}$
6	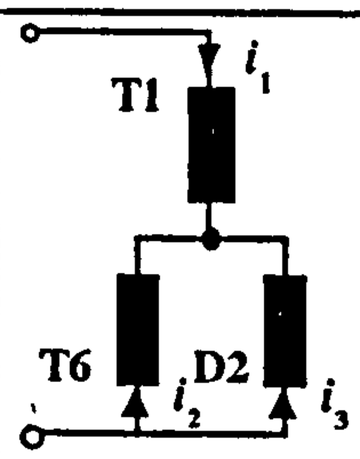	$v_1=\frac{2V_{dc}}{3}$ $v_2=-\frac{V_{dc}}{3}$ $v_3=-\frac{V_{dc}}{3}$	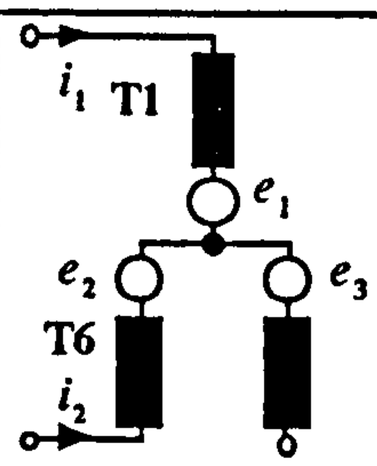	$v_1=\frac{V_{dc}}{2}+\frac{e_1+e_2}{2}$ $v_2=-\frac{V_{dc}}{2}+\frac{e_1+e_2}{2}$ $v_3=e_3$

Figure 3.2 Six inverter states of the three phase brushless PM motor for 120° current conduction

a) THE CONDUCTION INTERVAL:

Using the **Eq.2.8** and **Figs.3.1-2**, the voltage equations with respect to the midpoint of the DC rail voltage can be written as,

$$\frac{V_{dc}}{2} = L\frac{di_1}{dt} + Ri_1 + e_1 + v_s$$

$$-\frac{V_{dc}}{2} = L\frac{di_3}{dt} + Ri_3 + e_3 + v_s \qquad (3.2)$$

and since $i_1 = -i_3$, if we sum these two equations, we get the star point voltage for this particular connection,

$$v_s = -\frac{(e_1+e_3)}{2} \qquad (3.3)$$

Then, the phase-to-star point voltages can be given,

$$v_1 = \frac{V_{dc}}{2} - v_s = \frac{V_{dc}}{2} + \frac{(e_1+e_3)}{2}$$

$$v_2 = e_2 \qquad (3.4)$$

$$v_3 = -\frac{V_{dc}}{2} - v_s = -\frac{V_{dc}}{2} + \frac{(e_1+e_3)}{2}$$

b) THE COMMUTATION INTERVAL:

Unlike the conduction interval, in the case of commutation interval, the estimation of the phase voltages is much easier. Similarly a set of equations as **Eq.3.2** can be written for three phases of the motor,

$$\frac{V_{dc}}{2} = L\frac{di_1}{dt} + Ri_1 + e_1 + v_s$$

$$\frac{V_{dc}}{2} = L\frac{di_2}{dt} + Ri_2 + e_2 + v_s \qquad (3.5)$$

$$-\frac{V_{dc}}{2} = L\frac{di_3}{dt} + Ri_3 + e_3 + v_s$$

As in the previous estimation, using the relations of $i_1+i_2+i_3=0$ and $e_1+e_2+e_3=0$ for a star connected balanced brushless PM motor, if we sum these three equations, we find,

$$v_s = \frac{1}{6} V_{dc} \tag{3.6}$$

Eq.3.6 indicates that, for balanced operation, the star point voltage is always equal to 1/6 DC rail voltage. Therefore, the phase-to-star point voltages of the motor can be easily estimated:

$$v_1 = \frac{V_{dc}}{2} - v_s = \frac{1}{3} V_{dc}$$

$$v_2 = \frac{V_{dc}}{2} - v_s = \frac{1}{3} V_{dc} \tag{3.7}$$

$$v_3 = -\frac{V_{dc}}{2} - v_s = -\frac{2}{3} V_{dc}$$

The same estimation procedure was repeated and resultant phase-to-star point equations were summarized in **Fig.3.2** for the remaining inverter states and connection modes.

3.1.2 Symmetry Relationship and Reconstruction of Line Current

It can be observed from **Fig.3.1c** that the input currents of the motor are in piecewise continuous form over a period, and because of the symmetric nature of the inverter switching, it can be shown that it is not necessary to obtain the solution over an entire cycle.

By reference to **Fig.3.1c** and references [*Lipo*, 1981; *Lipo and Cornell*, 1981; *Nucera and Krause*, 1986], three stator currents are halfwave symmetric. That is, for any two time instants relatively displaced by 180° electrical,

$$\begin{aligned} i_1(\theta_e) &= -\, i_1(\theta_e+\pi) \\ i_2(\theta_e) &= -\, i_2(\theta_e+\pi) \\ i_3(\theta_e) &= -\, i_3(\theta_e+\pi) \end{aligned} \tag{3.8}$$

Also, because of phase symmetry in the three phase star connected motor, the three line currents are displaced by 120° electrical . The assumption of three phase symmetry implies,

$$\begin{aligned} i_1(\theta_e+2\pi/3) &= i_3(\theta_e) \\ i_2(\theta_e+2\pi/3) &= i_1(\theta_e) \\ i_3(\theta_e+2\pi/3) &= i_2(\theta_e) \end{aligned} \tag{3.9}$$

Adding $(\pi/3)$ to **Eq.3.9** and substituting the resultant into **Eq.3.8** respectively, yields,

$$\begin{aligned} i_1(\theta_e) &= -i_3(\theta_e+\pi/3) \\ i_2(\theta_e) &= -i_1(\theta_e+\pi/3) \\ i_3(\theta_e) &= -i_2(\theta_e+\pi/3) \end{aligned} \tag{3.10}$$

These resultant equations imply that, if the current is specified at any time instant, than the currents 60° electrical later can be specified. Because of this symmetry, it can be seen that the solution of a 60° electrical interval is enough to define entire period of the current variations in the three-phase star connected brushless PM motor.

Fig.3.3 indicates schematically that a solution over 60° electrical of line current can be used to reconstruct the entire period. **Fig.3.3a** represents typical variation of three line currents over a 60° electrical interval for 120° inverter operation. Here θ_c is the commutation angle in rad as indicated in **Fig.3.1a**. The reconstruction of one cycle of line current is represented in **Fig.3.3b** with six equal intervals which are given to show the current variations required for the reconstruction. After reconstructing one period of line current, the other remaining line currents can be easily achieved using three phase symmetry (**Eq.3.9**).

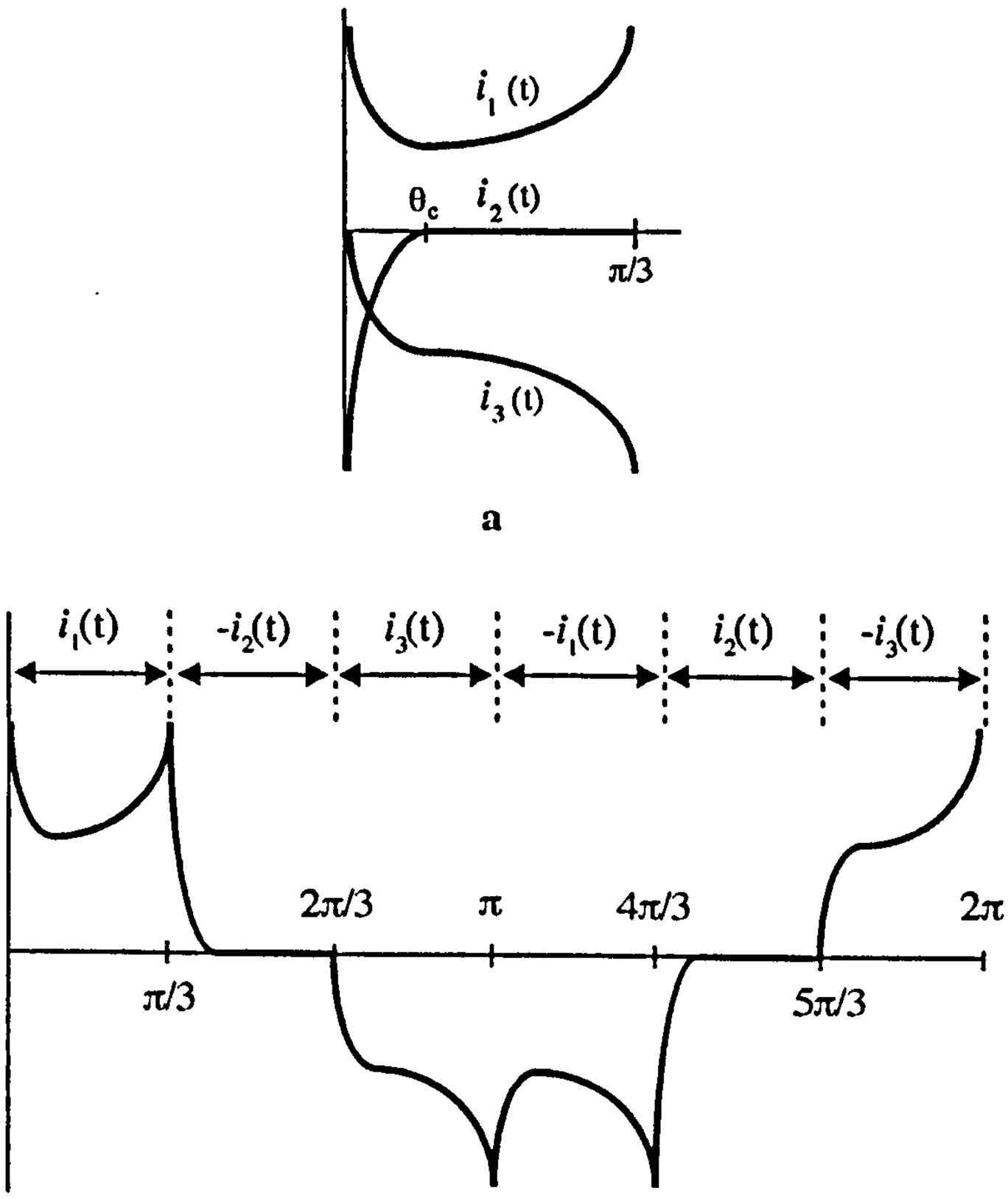

Figure 3.3 Reconstruction of line current using symmetry relationship.

a) Typical variations of three line currents for 60° interval.

b) The reconstructed line current waveform for a single phase.

3.2 THE SOLUTION OF THE STATE EQUATIONS

In this section, complete solutions of the differential equations for 120° current conduction of an inverter driven brushless PM motor have been developed.

Using the assumptions given in **Section 3**, and the matrix form of equations in **Eq.2.8** which was developed in **Section 2.2**, the three differential equations can be rearranged in state variable form as,

$$\frac{d}{dt}\begin{bmatrix} i_1(t) \\ i_2(t) \\ i_3(t) \end{bmatrix} = \begin{bmatrix} -\frac{R}{L} & 0 & 0 \\ 0 & -\frac{R}{L} & 0 \\ 0 & 0 & -\frac{R}{L} \end{bmatrix} \begin{bmatrix} i_1(t) \\ i_2(t) \\ i_3(t) \end{bmatrix} + \begin{bmatrix} \frac{1}{L} & 0 & 0 \\ 0 & \frac{1}{L} & 0 \\ 0 & 0 & \frac{1}{L} \end{bmatrix} \begin{bmatrix} v_1 - e_1(t) \\ v_2 - e_2(t) \\ v_3 - e_3(t) \end{bmatrix} \qquad (3.11)$$

or they can be expressed with a matrix form of state variables,

$$\frac{d\mathbf{i}(t)}{dt} = \mathbf{A}\mathbf{i}(t) + \mathbf{B}\mathbf{u}(t) \qquad (3.12)$$

Where, $e_1(t)$, $e_2(t)$, and $e_3(t)$ are time dependent sinusoidally varying back EMFs as given in **Eq.2.19**. The solution of the differential equations can be written in state-transition matrix form [*Kassakian* et al, 1991],

$$\mathbf{i}(t) = e^{\mathbf{A}t}\mathbf{i}_o + \int_0^t e^{\mathbf{A}(t-\tau)}\mathbf{B}\mathbf{u}(\tau)\, d\tau \qquad (3.13)$$

Here,

$$\mathbf{i}(t)=\begin{bmatrix} i_1(t) \\ i_2(t) \\ i_3(t) \end{bmatrix} \qquad \mathbf{A}=\begin{bmatrix} -\frac{R}{L} & 0 & 0 \\ 0 & -\frac{R}{L} & 0 \\ 0 & 0 & -\frac{R}{L} \end{bmatrix} \qquad \mathbf{i}_0=\begin{bmatrix} i_1(0) \\ i_2(0) \\ i_3(0) \end{bmatrix}$$

$$\mathbf{B}=\begin{bmatrix} \frac{1}{L} & 0 & 0 \\ 0 & \frac{1}{L} & 0 \\ 0 & 0 & \frac{1}{L} \end{bmatrix} \qquad \mathbf{u}(\tau)=\begin{bmatrix} v_1-e_1(\tau) \\ v_2-e_2(\tau) \\ v_3-e_3(\tau) \end{bmatrix}$$

As clearly seen in **Eq.3.11**, the three differential equations are first order equations. In general, the state variables $i_1(t)$, $i_2(t)$, and $i_3(t)$ must contain enough information about the past history of the system to determine its future behaviour. As given in **Eq.3.13**, the past history of the system is defined by the initial state vector $\mathbf{i}_0$. Probably the most difficult part of the analytical solution is to define the initial conditions. However, as will be shown later, this can be solved by using the symmetry feature of the system.

The solution of **Eq.3.12** involves some trigonometric relations and integrations which are given in **Appendix A-4**.

As explained in **Section 3.1.2**, only 1/6 of a complete cycle is used for solution, and **State 1** in **Fig.3.2** has been chosen as the 60° interval over which the differential equations are solved:

a) The Solution Within the Commutation Interval

After performing the integration in **Eq. 3.13** within the commutation interval $0 \le t < t_c$, the complete solution for the line currents can be given as,

$$i_1(t) = i_1(0)\, e^{-(R/L)t} + \frac{V_{dc}}{3R}\left(1 - e^{-(R/L)t}\right) - \frac{\omega_e L \lambda_m}{(R^2+\omega_e^2 L^2)}$$

$$\cdot\left\{\left[\left(\frac{\sqrt{3}R}{2L}+\frac{\omega_e}{2}\right)\cos(\theta_e-\phi) + \left(\frac{\sqrt{3}\omega_e}{2}+\frac{R}{2L}\right)\sin(\theta_e-\phi)\right]\right.$$

$$\left. - \left[\left(\frac{\sqrt{3}R}{2L}+\frac{\omega_e}{2}\right)\cos(\phi) + \left(\frac{R}{2L}-\frac{\sqrt{3}\omega_e}{2}\right)\sin(\phi)\right] e^{-(R/L)t}\right\} \quad (3.14)$$

$$i_2(t) = i_2(0)\, e^{-(R/L)t} + \frac{V_{dc}}{3R}\left(1 - e^{-(R/L)t}\right) - \frac{\omega_e L \lambda_m}{(R^2+\omega_e^2 L^2)}$$

$$\cdot\left\{\left[\left(\frac{R}{L}\right)\sin(\theta_e-\phi) - \omega_e \cos(\theta_e-\phi)\right]\right.$$

$$\left. - \left[\left(\frac{R}{L}\right)\sin(-\phi) - \omega_e \cos(-\phi)\right] e^{-(R/L)t}\right\} \quad (3.15)$$

$$i_3(t) = -\left(i_1(t) + i_2(t)\right) \quad (3.16)$$

Where, ϕ is the phase angle between the back EMF and line current, t_c is the commutation time and is equal to (θ_c/ω_e). Since the current waveform has been shifted $(\pi/6)$ electrical radian, $\phi = -(\pi/6)$ corresponds to 0° phase advance of the current.

b) The Solution Within the Conduction Interval

Similarly, the integration in **Eq.3.13** is performed within the interval $t_c \le t < (\pi/3\omega_e)$, and the solution is given by,

$$i_1(t) = i_1(t_c)\, e^{-(R/L)(t-t_c)} + \frac{V_{dc}}{2R}\left(1 - e^{-(R/L)(t-t_c)}\right) + \frac{\omega_e L \lambda_m}{(R^2+\omega_e^2 L^2)}$$

$$\cdot\left\{\left[\left(-\frac{\sqrt{3}R}{2L}\right)\cos(\theta_e-\phi) + \left(-\frac{\sqrt{3}\omega_e}{2}\right)\sin(\theta_e-\phi)\right]\right.$$

$$\left. + e^{-(R/L)(t-t_c)}\left[\left(\frac{\sqrt{3}R}{2L}\right)\cos(\phi-\theta_c) - \left(\frac{\sqrt{3}\omega_e}{2}\right)\sin(\phi-\theta_c)\right]\right\} \qquad (3.17)$$

$$i_2(t) = 0 \qquad (3.18)$$

$$i_3(t) = -\, i_1(t) \qquad (3.19)$$

As can be seen in **Eq.3.14-19**, we have only three independent equations whereas there are six unknown variables: $i_1(t)$, $i_1(0)$, $i_2(t)$, $i_2(0)$, $i_1(t_c)$, and t_c. Therefore, it is necessary to eliminate some of the unknowns, which can be done by using the boundary conditions of the currents.

From **Fig.3.1c**, we can write,

$$i_1(0) = I_0 \qquad (3.20)$$

$$i_2(0) = -\, I_0 \qquad (3.21)$$

$$i_2(t_c) = 0 \qquad (3.22)$$

With **Eqs.3.17-19**, if we rearrange the **Eq.3.15**, we find,

$$0 = I_0\, e^{-(R/L)\,t_c} + \frac{V_{dc}}{3R}\left(1 - e^{-(R/L)\,t_c}\right) + \frac{\omega_e L \lambda_m}{(R^2+\omega_e^2 L^2)}$$

$$\cdot\left\{\left[\left(-\frac{R}{L}\right)\sin(\theta_e-\phi) + \omega_e\cos(\theta_e-\phi)\right]\right.$$

$$\left.-\left[\left(\frac{R}{L}\right)\sin(\phi) + \omega_e\cos(\phi)\right]\right\} e^{-(R/L)\,t_c} \qquad (3.23)$$

Moreover, it can be given that the value of line current i_1 is equal to the initial value I_o at the time instant $\pi/3\omega_e$,

$$i_1\left(\frac{\pi}{3\omega_e}\right) = I_o \qquad (3.24)$$

Similarly, using **Eq.3.24**, **Eq.3.17** can be rearranged as,

$$I_o = i_1(t_c)\, e^{-(R/L)((\pi/3\omega e)-t_c)} + \frac{V_{dc}}{2R}\left(1 - e^{-(R/L)((\pi/3\omega e)-t_c)}\right) + \frac{\omega_e L \lambda_m}{2(R^2+\omega_e^2 L^2)}$$

$$\cdot\left\{\left[\left(-\frac{\sqrt{3}R}{L}\right)\cos\left(\frac{\pi}{3}-\phi\right) - \sqrt{3}\omega_e\sin\left(\frac{\pi}{3}-\phi\right)\right] + e^{-(R/L)((\pi/3\omega e)-t_c)}\right.$$

$$\left.\cdot\left[\left(\frac{\sqrt{3}R}{L}\right)\cos(\phi-\theta_c) - \sqrt{3}\omega_e\sin(\phi-\theta_c)\right]\right\} \qquad (3.25)$$

Eq.3.25 has three unknowns I_o, $i_1(t_c)$, and t_c. By setting $t=t_c$ and $i_1(0)= I_o$ (**Eq.3.20**) in **Eq.3.14**, we can find another relation which gives the value of $i_1(t_c)$ with two unknowns I_o and t_c in **Eq.3.25**. Both the resultant equation and **Eq.3.23** has only two unknowns I_o and t_c. If we solve the commutation time, we finally get a complex multivariable function which only includes constant motor parameters: R, L, λ_m, and operating parameters: V_{dc}, ω_e and ϕ.

$$0 = \frac{V_{dc}}{6R}\ \frac{(2-e^{-(R/L)(\pi/3\omega_e)})}{(1-e^{-(R/L)(\pi/3\omega_e)})}$$

$$+\left\{\frac{\omega_e\ \lambda_m}{4(R^2+\omega_e^2\ L^2)}\ \frac{(1-2e^{-(R/L)(\pi/3\omega_e)})}{(1-e^{-(R/L)(\pi/3\omega_e)})}\right.$$

$$\cdot\left[(\sqrt{3}R-\omega_e L)\cos(\phi)-(\sqrt{3}\omega_e L+R)\sin(\phi)\right]$$

$$-\frac{V_{dc}}{3R}\ \frac{(1-2e^{-(R/L)(\pi/3\omega_e)})}{(1-e^{-(R/L)(\pi/3\omega_e)})}$$

$$\left.-\frac{V_{dc}}{2R(1-e^{-(R/L)(\pi/3\omega_e)})}\right\}e^{-(R/L)t_c}$$

$$+\frac{\omega_e\ \lambda_m}{2(R^2+\omega_e^2\ L^2)}\ \frac{(2-e^{-(R/L)(\pi/3\omega_e)})}{(1-e^{-(R/L)(\pi/3\omega_e)})}$$

$$\cdot(\omega_e L\cos(\omega_e t_c-\phi)-R\sin(\omega_e t_c-\phi)) \qquad (3.26)$$

3.3 THE NEWTON-RAPHSON METHOD AND COMPUTER SOLUTION

As described in **Section 3.1.1**, each 60° electrical inverter state is made up of two parts; the commutation interval and the conduction interval. Since commutation interval is defined by t_c , to find the value of t_c must be estimated from **Eq.3.26**. The t_c is a root of the function in **Eq.3.26**, and is impossible to solve analytically. Therefore an iterative method can be used. After finding the root (t_c) of the function (**Eq.3.26**), the value of it is used to obtain the initial value of the current I_o by using **Eq.3.23** Using the initial value I_o for a specific working condition, the solution over the interval $0<t_c<\pi/3\omega_e$ can be completely defined through **Eqs.3.14-19** which have the variations illustrated in **Fig.3.3a.**

In this work, the Newton-Raphson method had been used to find a solution for **Eq.3.26**. The Newton-Raphson method finds the root of a function known to lie in an interval. Clearly, the required value of t_c must lie in the interval $0<t_c\leq\pi/3\omega_e$, and as will be given in next section, practical results show that the commutation angle varies between 0° and 30° electrical. The conventional Newton-Raphson method does not adjust the bound, and works only on local information at the initial interval for t_c. The bounds are only used to pick the midpoint as the first guess, and if the solution wanders outside the bound, it is rejected. Because of the poor properties of the conventional method [*Press et al*, 1992], a combination of bisection and Newton-Raphson has been used in the computer algorithm to solve **Eq.3.26**. This hybrid algorithm takes a bisection step whenever Newton-Raphson would take the solution out of bounds, or whenever Newton-Raphson is not reducing the size of interval rapidly enough.

A computer program for the hybrid Newton-Raphson method can be readily obtained from the books [such as *Press et al*, 1992]. However, due to requirement of first derivative of the function, the program must also be modified to compute the first derivative of the function. This can be simply accomplished by the inclusion of a user-defined function for the derivative:

$$y'(t_c) = \frac{\omega_e \lambda_m}{(R^2+\omega_e^2 L^2)} \frac{[2-e^{-(R/L)(\pi/3\omega_e)}]}{[1-e^{-(R/L)(\pi/3\omega_e)}]}$$

$$\cdot[(\omega_e^2 L \sin(\omega_e t_c-\phi)+R\cos(\omega_e t_c-\phi)] - \frac{[1-2e^{-(R/L)(\pi/3\omega_e)}]\, R\, e^{-(R/L)t_c}}{L[1-e^{-(R/L)(\pi/3\omega_e)}]}$$

$$\cdot\left\{\frac{\omega_e \lambda_m}{4(R^2+\omega_e^2 L^2)}[(\sqrt{3}R-\omega_e L)\cos(\phi) - (\sqrt{3}\omega_e L+R)\sin(\phi)] - \frac{V_{dc}}{3R}\right.$$

$$\left. - \frac{(V_{dc}/2R)}{e^{-(R/L)(\pi/3\omega_e)}}\right\} \qquad (3.27)$$

The flowchart given in **Fig.3.4** describes the solution for 1/6 of a period and the reconstruction for a line current estimation of 120° inverter operated brushless PM motor drive. The flowchart describes the logical flow of the software routine.

The flowchart presented in **Fig.3.4** can be broken down into four parts: initialization of motor parameters, the Newton-Raphson routine, the line currents and electrical torque computation routine, and reconstruction routine.

The execution of the program begins by a start up procedure which initializes the constant motor parameters; the winding resistance **R** in ohm, the winding inductance **L** in mH, the maximum value of magnet flux linkage λ_m in Wb.t, the number of pole pairs **p**, and reads operation parameters; the speed of the motor **n** in rpm, the phase advance or delay angle ϕ in electrical degree, and DC rail voltage V_{dc} in volt. The number of periods for reconstruction can also be given as input parameter.

Secondly, the program reads the input reference for the hybrid Newton-Raphson routine. The routine does the calculations to determine the root of the function which is the commutation time in this work, and to do that needs an initial interval of commutation. The program also needs the maximum number of iteration to get the desired accuracy from the computation. If the estimated value of the commutation time (the root) wanders outside the initial interval, the programs returns to the beginning of the routine.

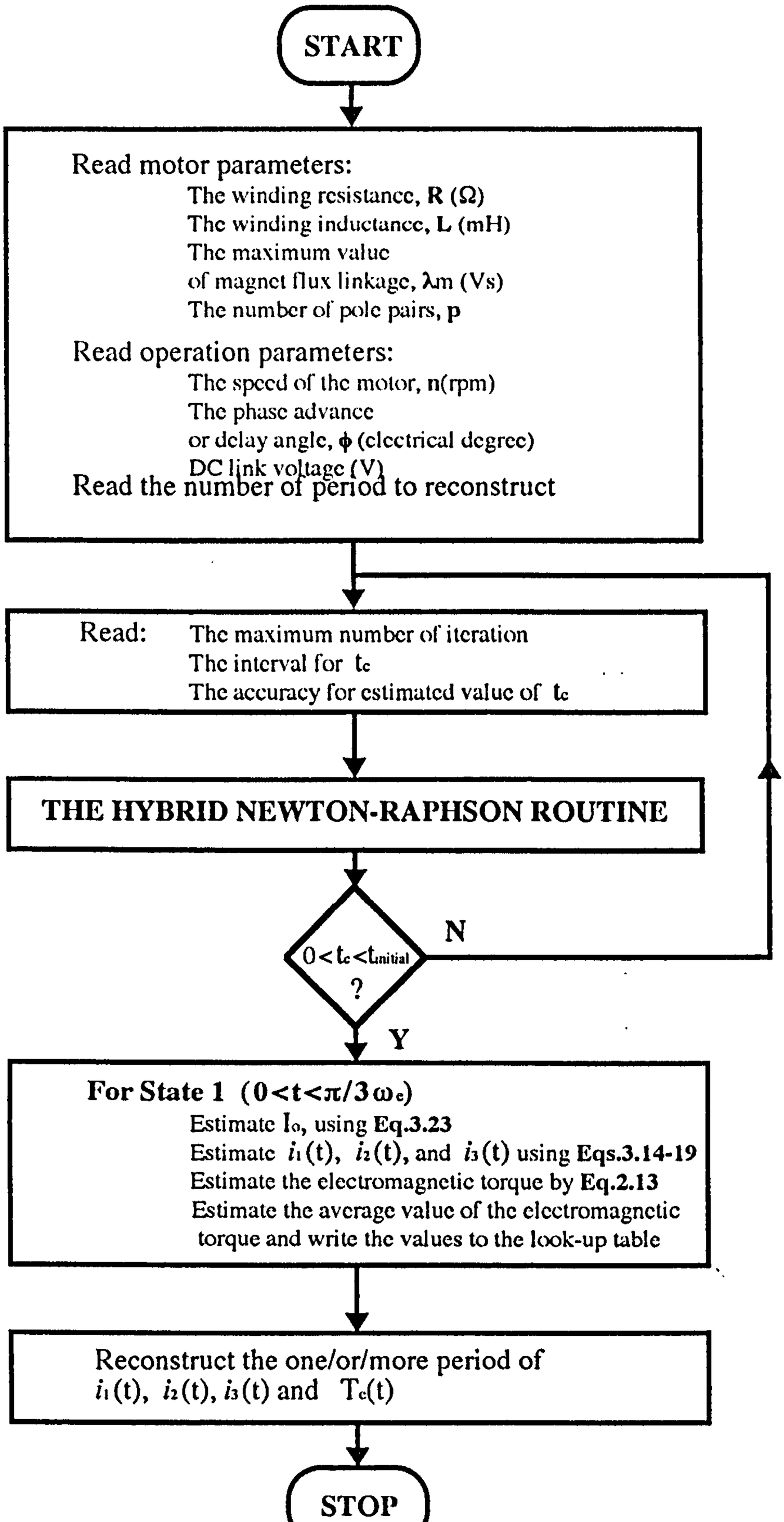

Figure 3.4 The flowchart of the analytical solution.

After determination of the commutation time, the value is passed to the third routine where the initial value of current, line currents, and electrical torque calculations are done. The number of data point for estimation is adjusted in this routine. The calculated results are stored in a look-up table to use in the last routine.

Finally, the reconstruction routine executes. The line currents and electromagnetic torque over the entire period are reconstructed using a look-up table. Some other calculations, such as average torque, for performance prediction of the motor are also done in the routine.

3.4 COMPUTED AND EXPERIMENTAL RESULTS

In order to verify the equations which have been developed, the solution obtained from the computer solution which has the flowchart given in **Fig.3.4**, was compared with the experiment results. The experimental drive system was shown in **Eq.2.18** , and the inverter with bipolar transistors was connected to the control system. For the tests of recommended steady-state calculation method, a star connected axial field BSPM motor is used which has the parameters given in **Tables 2.1-2**. The maximum value of the magnet flux linkage λ_m is found 0.104 V/rad/s.

It is of interest to compare the difference in performance of various operation modes from the implemented drive. Three typical operation modes were selected to reflect a wide variation in performance characteristics of the motor: no phase advance, 30° electrical phase advance, and 30° electrical phase delay.

The first set of results are presented in **Fig.3.5** show how the commutation time changes with the speed of the motor at different DC rail voltage levels. Initially, the commanded current amplitude is set to the maximum level (10A), and the test carried out at three different voltage levels (40V, 60V, and 80V). By loading the motor externally from no load speed, the commutation time was measured until current control limits. Afterwards, the commutation time has been estimated for every particular operating point, and both measured and estimated values are given in **Fig.3.5**. Due to reading difficulty, it was not possible to measure the commutation time for 80V DC rail voltage in the case of 30° electrical phase delay operation. Therefore, only the results for 40V and 60V are given for comparison purposes (**Fig.3.5c**).

As said earlier, the measurements are taken from no load speed to the control limit (up to current controlled operation). As seen in **Fig.3.5** there is a very good match between the estimated and measured commutation times. The effect of current level on the forward voltage drop of the transistors is not taken into consideration in **Fig.3.5a**. Since the voltage drop across each transistor was assumed constant (3V), it should be noted that the difference becomes bigger at higher speeds in **Fig.3.5a**. This is effectively due to less voltage across the motor winding, and it can be recovered by reducing the value of voltage drop with increasing speed.

In **Fig.3.6a**, the measured line current of the motor is given. The DC rail voltage was adjusted to 46.5V. The motor was running in the steady-state with a speed of 447 rpm. In this case, the angle between back EMF and the commanded current was zero. Referring to **Fig.3.1c**, the commutation time, the conducting and non-conducting intervals of the current can be seen clearly in **Fig.3.6a** for 120° inverter operation.

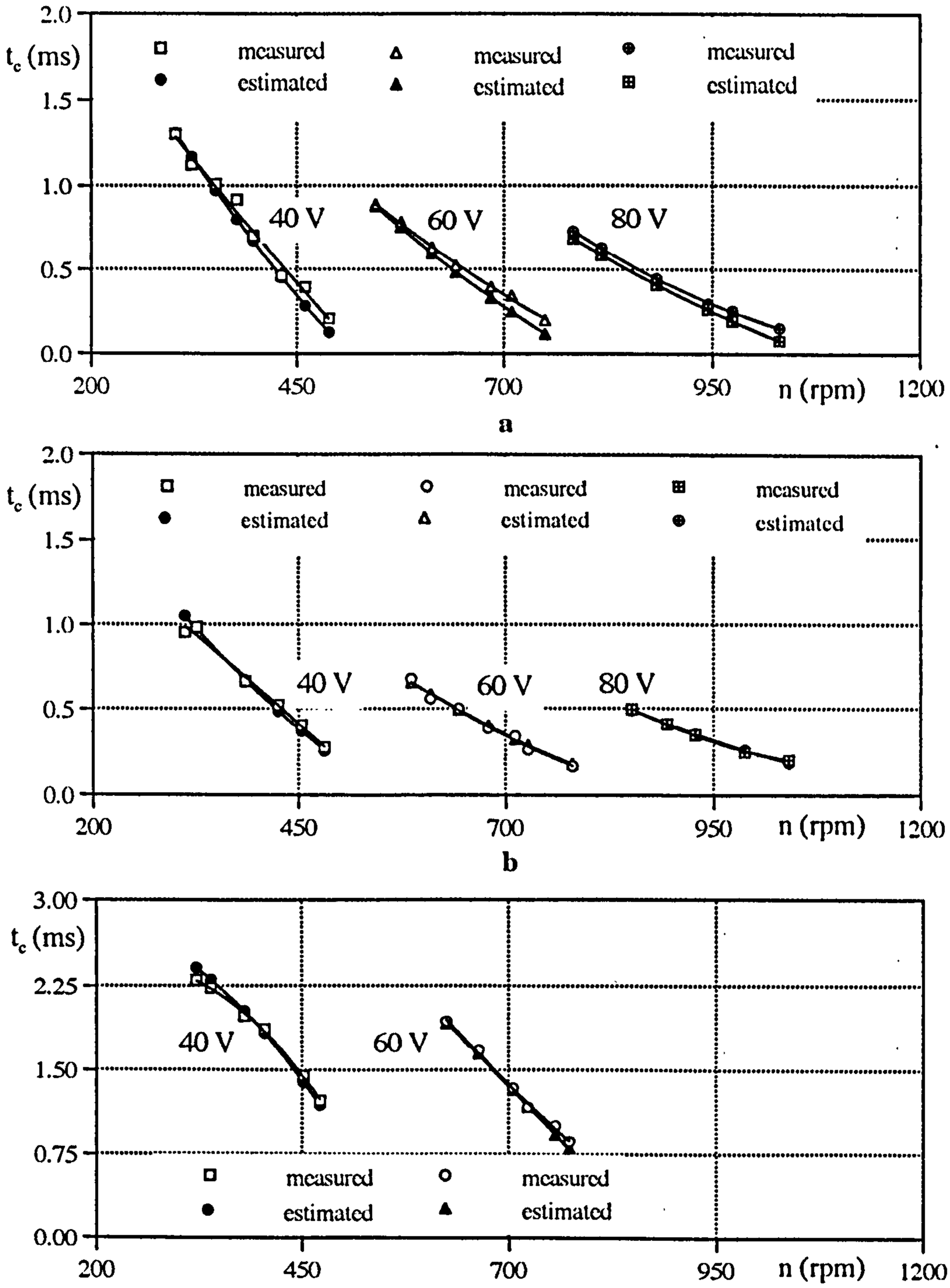

Figure 3.5 The comparison of the commutation time at typical operation conditions for V_{dc}= 40V, 60V, and 80V.

a) No phase advance

b) 30° electrical phase advance

c) 30° electrical phase delay

As explained earlier in **Section 3.1.2**, and shown in **Fig.3.3.** the zero current interval and the commutation angle θ_c between the phase voltage and the line current zero crossings are identical in all three phases. Because of the symmetry, it has been shown that only 1/6 of a complete cycle needs to be solved in detail. The solution over this interval (**State 1**) was done with 150 samples, and the entire cycle is defined and the result is given in **Fig.3.6b.** The same time scaling is used for overall comparison of the line currents, and as seen, a very good agreement between the measured and calculated line current waveforms exists in **Fig.3.6.**

Fig.3.7a shows the current waveform that is obtained from the experimental drive for a particular case of 30° electrical phase advance operation. Again, comparing the measured current waveform with the estimated current (**Fig.3.7b**), it is evident that there is close agreement.

Referring to the **Fig.3.7a**, the current variation is small on the top of the waveform. This may be due to fluctuation in the DC rail voltage and small variation in the winding inductance by position, or the flat-top of the actual back EMF waveform (**Fig.2.6b**) which may effectively cause equal phase-to-neutral voltage within a defined interval.

Fig.3.8 also shows a comparison of the results of the computer solution of the motor line current with the actual current. A 30° electrical phase delay angle was supplied to the control system, and the DC rail voltage adjusted to 46V. Similarly, in this condition, the motor was operating in the steady-state at a speed of 485 rpm. Effects due to fluctuations of the DC rail voltage tend to give very small variations in the peak values of the measured line current as seen in **Fig.3.8a**. However, a good overall comparison is evident.

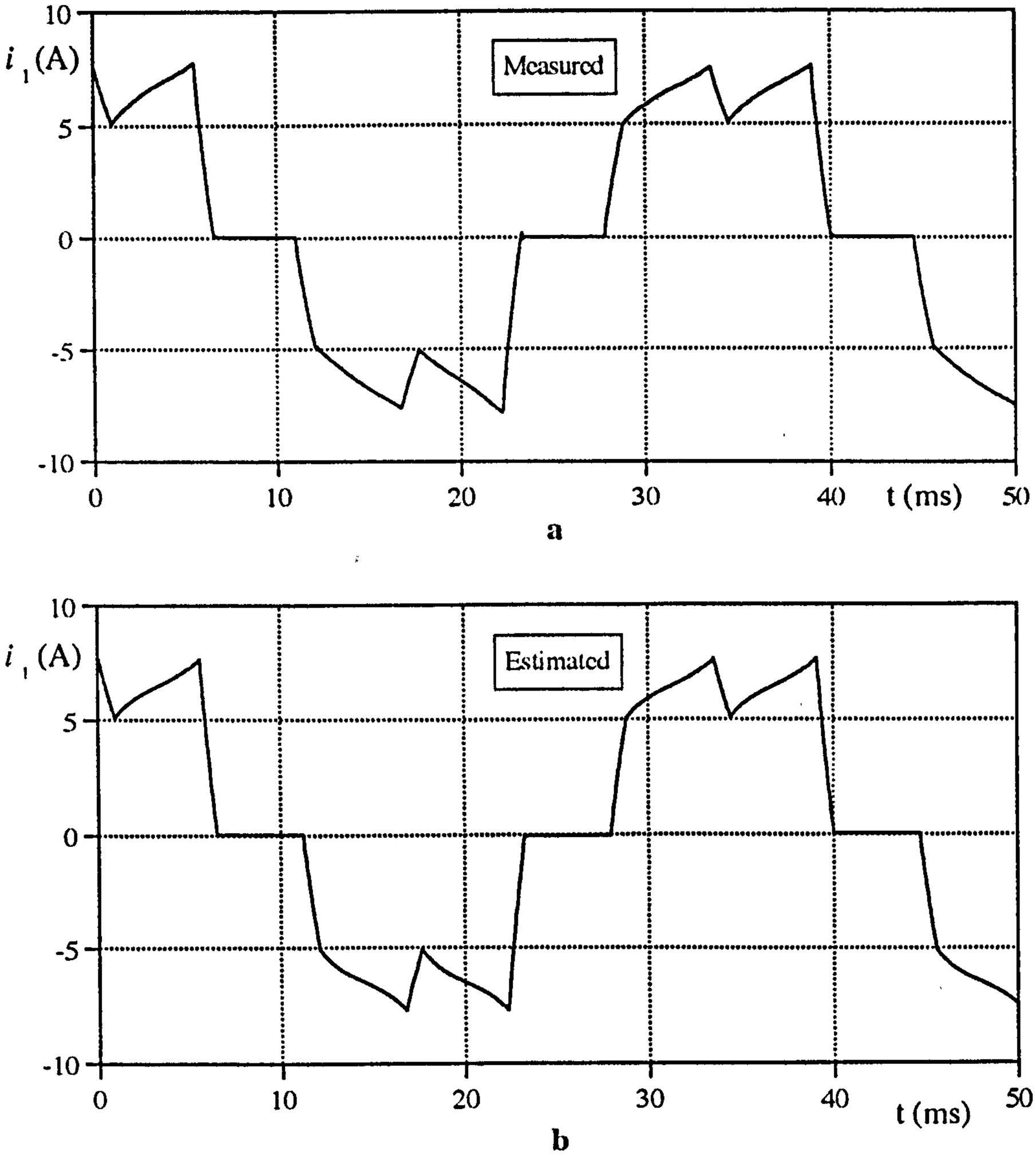

Figure 3.6 The measured and estimated current waveforms, no phase advance, V_{dc}= 46.5V, n= 447 rpm.

a) Measured line current of Phase 1

b) Estimated line current of Phase 1

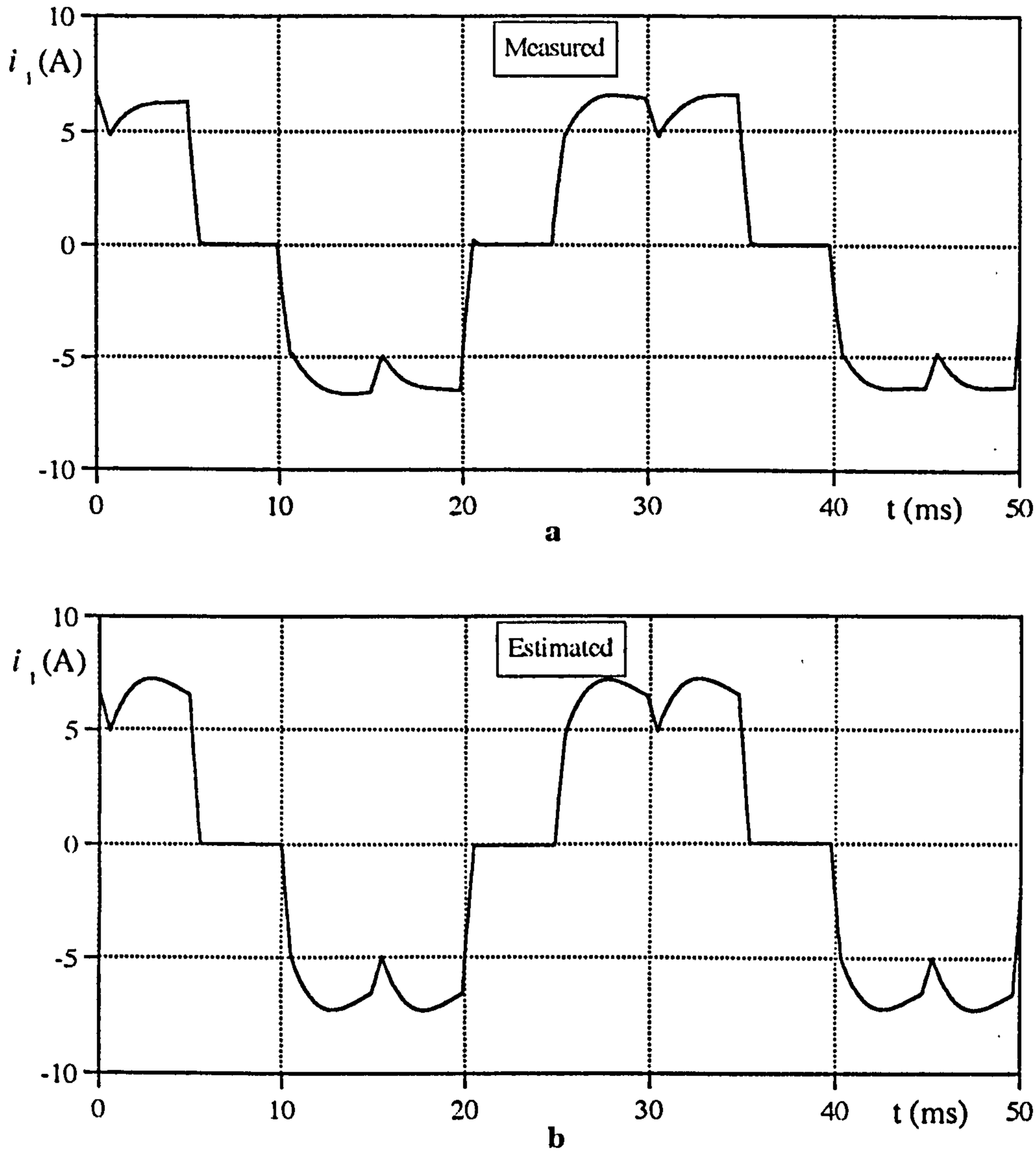

Figure 3.7 The measured and estimated line currents, 30° electrical phase advance, V_{dc}= 46V, n= 503 rpm.

a) Measured line current for Phase 1.

b) Estimated line current for Phase 1.

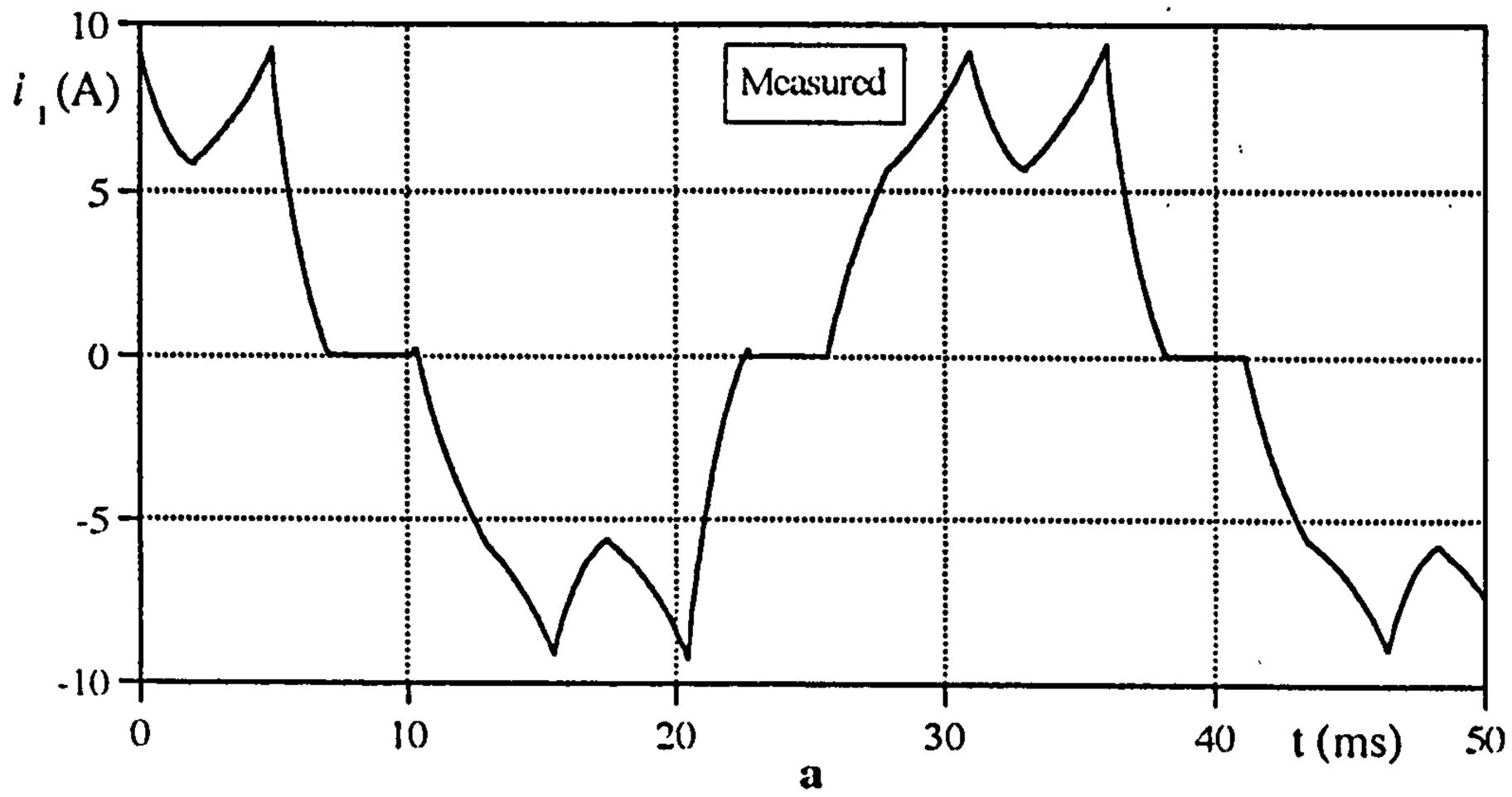

Figure 3.8 The measured and estimated line currents for 30° electrical delay operation, V_{dc}= 46V, n= 485 rpm.

a) Measured line current for Phase 1.

b) Estimated line current for Phase 1.

In **Fig.3.9**, the measured and the estimated phase-to-star point voltages are given for Phase 1. The computation of phase voltage is based on the equations which were given in **Fig.3.2**. The switching transients (the commutation time) in the measured phase voltage waveform indicates that the estimated waveform differs from the measured voltage in terms of both amplitude and phase. As will be explained in the next chapter, this may be due to the sinusoidal back EMF assumption and the low inertia of the motor-load which may create speed fluctuations. An imperfect drive system is another source of mismatch. As seen in the measured phase voltage waveform in **Fig.3.9**, the star point voltage is superimposed on the back EMF waveform during the conduction period, and since the actual back EMF waveform is non-sinusoidal, the phase voltage has a flat profile.

Fig.3.10 shows a comparison of the measured total instantaneous electromagnetic torque (**Fig.3.10a**) with the estimated torque (**Fig.3.10b**). The measured torque was taken from an electronic circuit where the electromagnetic torque measurement is implemented. The circuit is based on multiplication of the actual line current with the related back EMF variation (see **Eq.2.11**). As explained in the commanded current generating circuit (**Section 2.5.2**), the digital value of position serves as the address for EPROMs where the actual values of the back EMFs for three phases are stored in a normalized form. The output of each EPROM is connected to a multiplier D/A converter to multiply the back EMF with the related line current, and then the analog variation of the electromagnetic torque for each phase is added to get the total torque (**Fig.3.10a**).

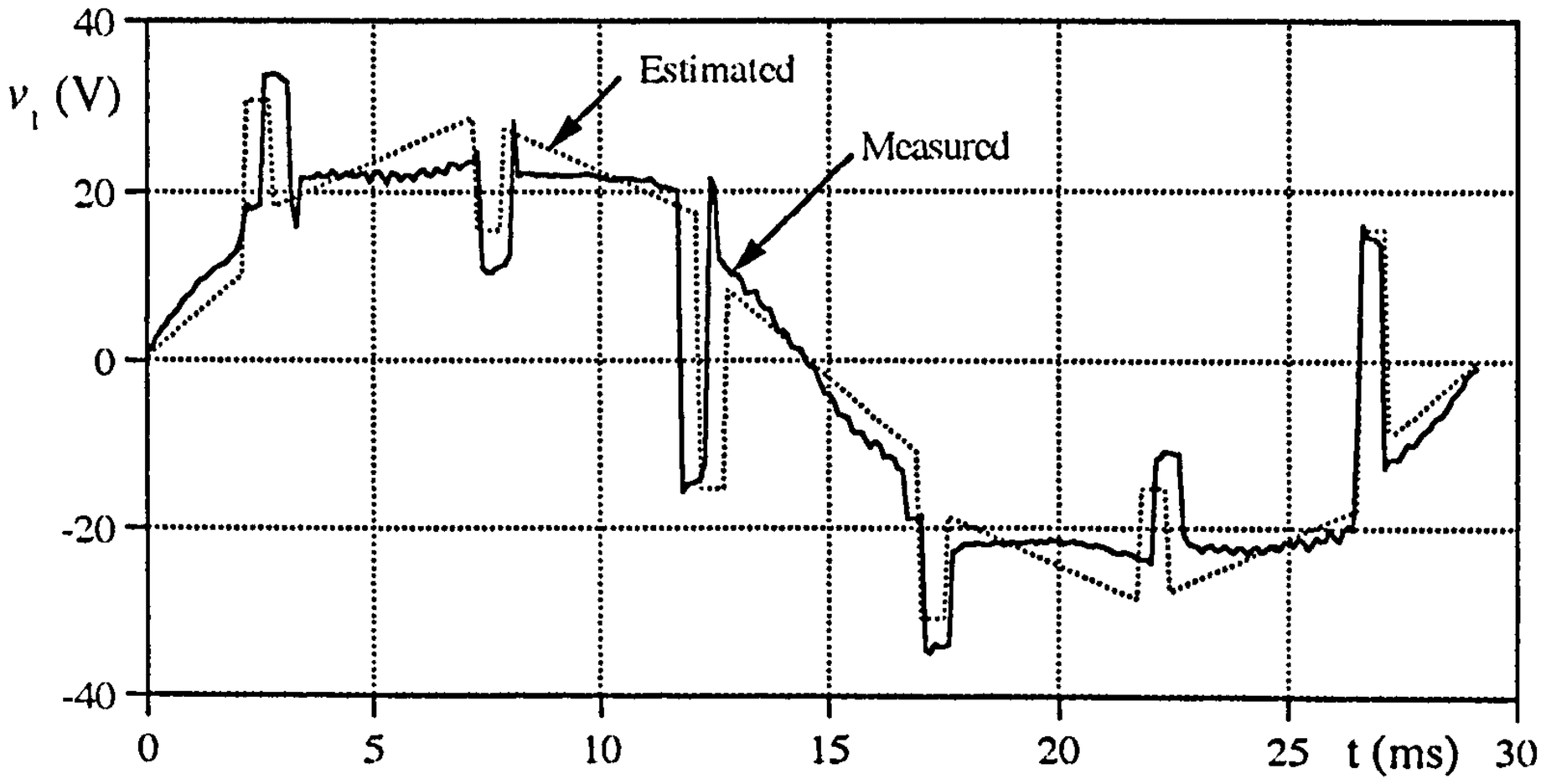

Figure 3.9 Comparison of a typical phase-to-neutral point voltage, no phase advance, V_{dc}= 50V, n= 515 rpm.

Fig.3.10 shows the electromagnetic torque varying six times per electrical period. Note that in terms of the waveforms of instantaneous torque, correlation is not very satisfactory. However, the average torque values are very close. Discrepancies in the measured and estimated torque waveforms are mainly due to fluctuations in DC rail voltage and non ideal motor parameters.

To experimentally verify the proposed solution, the theoretical average electromagnetic torque, T_e is calculated, and the average shaft torque, T_s is measured (by a *Sensor Technology Torque Transducer, D3B*) at various operating speeds, with the result shown in **Fig.3.11.** The electromagnetic torque was also measured by the electromagnetic torque board in the implemented drive and presented as a comparison to the estimated result. As noticed, the torque profiles have almost linear decline with the motor speed.

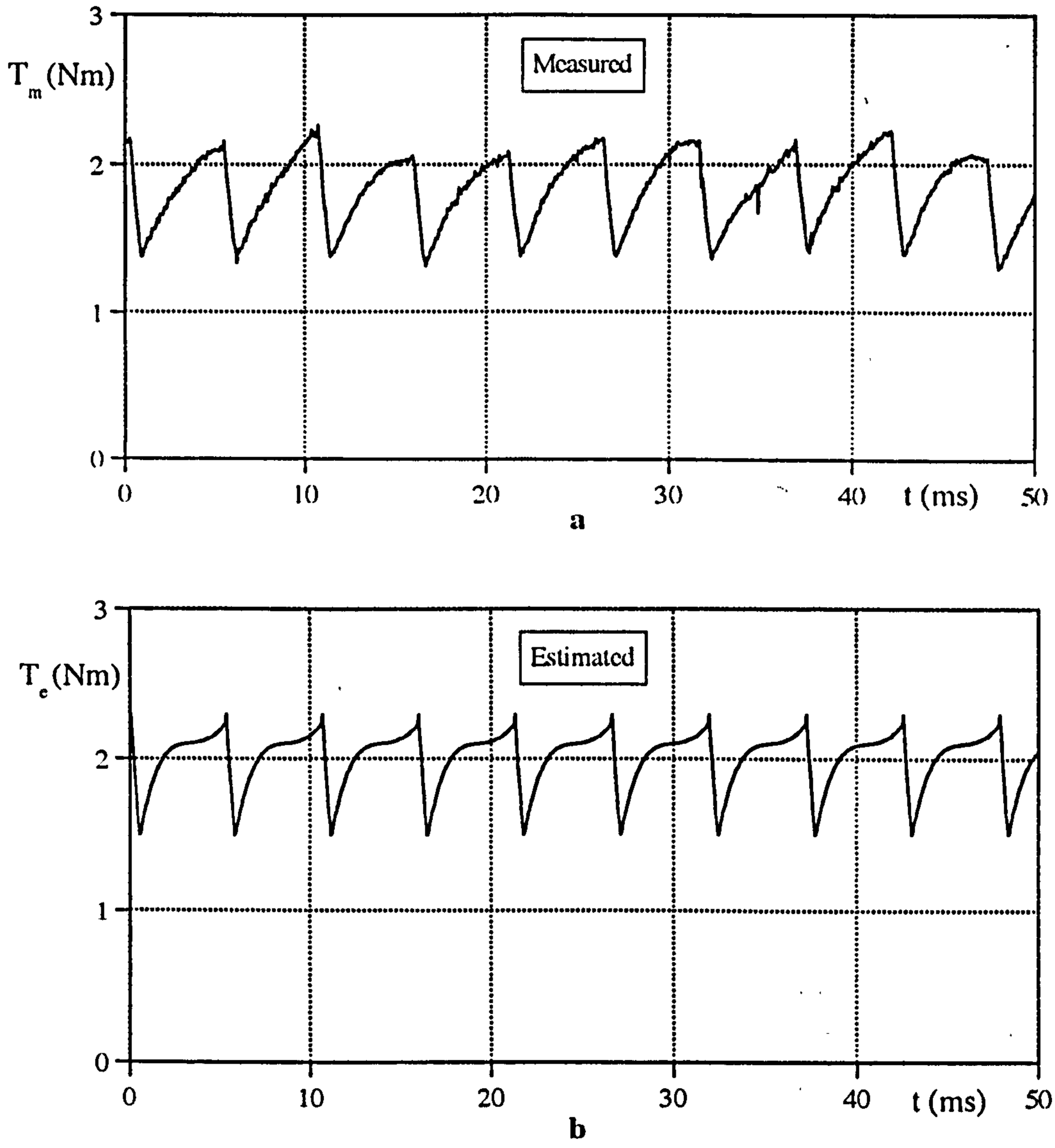

Figure 3.10 The electromagnetic torque waveforms for typical operation, no phase advance, V_{dc}= 40.8, n=480 rpm.

a) Measured total electromagnetic torque waveform.

b) Estimated total electromagnetic torque waveform.

As expected, the fall in the torque (**Fig.3.11**) is due to the reduction in the motor current. Since the motor's back EMF increases linearly with speed, as the difference between the source voltage and back EMF voltage decreases, the motor current drops while the load is removed.

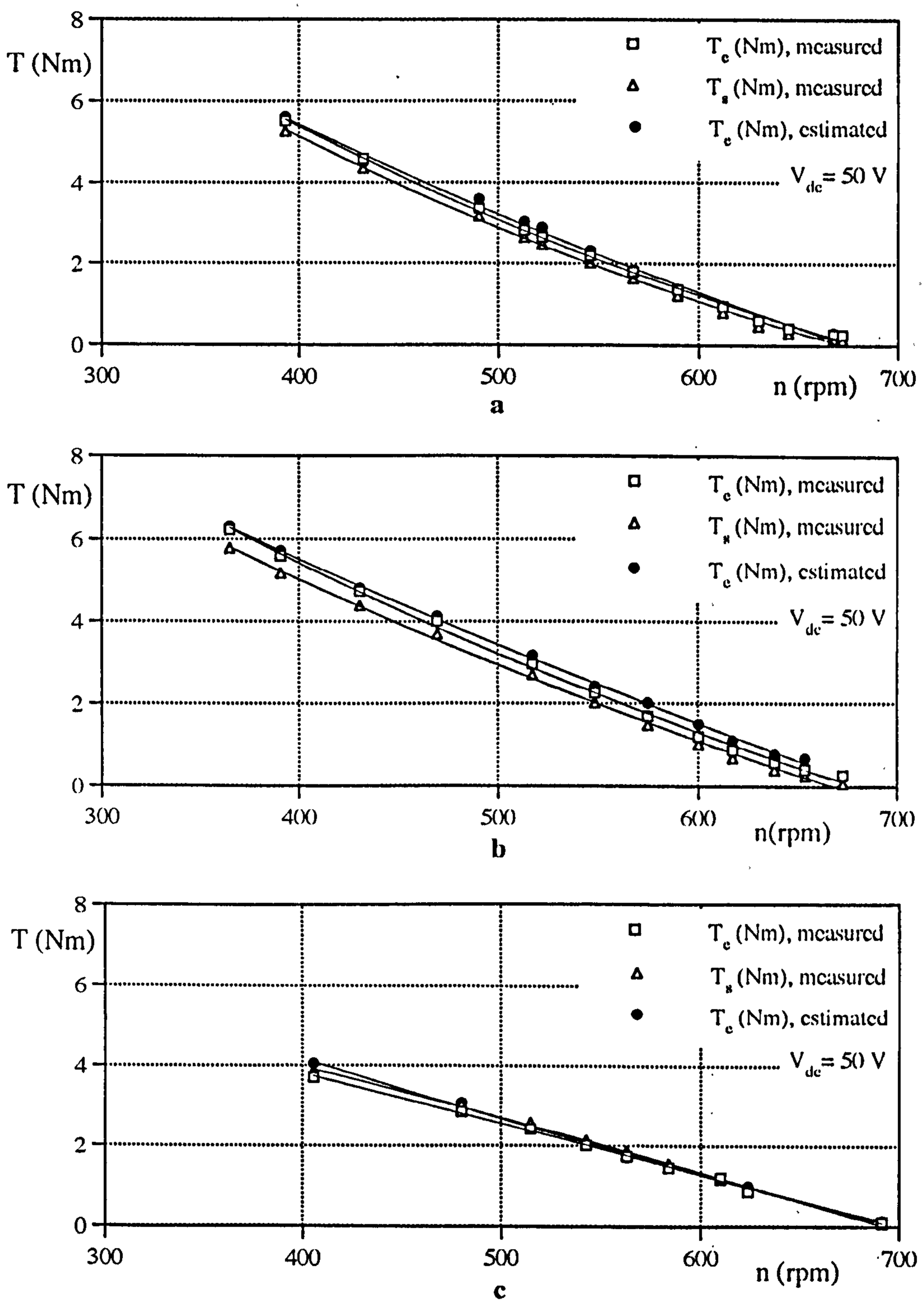

a

b

c

Figure 3.11 The comparison of Torque-Speed curves, V_{dc}= 50V

a) No phase advance

b) 30° electrical phase advance.

c) 30° electrical phase delay.

3.5 CONCLUSIONS

This chapter has presented a straightforward method of calculating the steady-state behaviour of the brushless PM motor for 120° inverter operation. As shown in previous sections, because of the symmetrical nature of the applied voltages in the inverter driven brushless PM motor and resulting symmetry of line currents, a considerable reduction is possible in the computing effort needed to obtain a solution.

A solution for any $\pi/3$ interval is sufficient to uniquely define all variables over an entire period. One or more periods of the waveforms are reconstructed by using the look-up table. It is possible to start computation at any convenient moment, the needed initial value of current can be estimated first. The number of samples can be changed with the desired resolution of the graphics.

It has to be noted that the Runge-Kutta method can be used over 60° electrical also, but to get an accurate initial value of current, the estimation should be repeated over at least 2 or 3 such periods.

It is seen that the assumptions which were given in **Section 3** make the test motor ideal, any deviations from the actual motor and drive system will present some form of discrepancies in the measured values. Discrepancies in the measured and estimated values of waveforms are mainly due to fluctuations in DC rail voltage, non ideal motor parameters, small variations in winding inductance (1.3%), imbalance between phases, and the assumption of ideal power switches (such as equal and constant voltage drop).

It can be concluded that the analytical calculation method gives good results even for a large calculation step. As a result of the comparison, it appears that the method of analysis presented in this chapter is adequate to predict the instantaneous line currents and the electromagnetic torque of the motor for typical steady-state operating points.

CHAPTER IV

DRIVE SIMULATION: Results and Verification

4. INTRODUCTION

In the previous chapter, the analytical method has been used to predict the steady-state performance of brushless PM motors for various modes of operation under the assumptions made in **Chapter III, Section 3.** However, any deviation from these assumptions makes the performance prediction inadequate or impossible. Moreover, the dynamic behaviour of the motor cannot be examined by the analytical method. A simulation model for the transient performance prediction of brushless PM drives is described which does not require assumptions of the phase balance of either the power electronic converter or the motor, nor idealized waveforms for back EMFs, or inductance terms.

It is convenient to represent the dynamic motor model by using the equations which were developed in **Chapter II, Section 2.2.** The derivatives of state equations for currents have been given in **Eq:3.11.** The complete dynamic model of the brushless PM motor and drive consists of:

a) the differential equations for current (**Eq.3.11**),

b) the developed torque expression (**Eq.2.11**),

c) the rotor dynamic equations:

from the equation of motion in **Eq.2.9**,

$$\frac{d\omega_r}{dt} = \frac{1}{J}(T_e - B\omega_r + T_L) \tag{4.1}$$

and differentiating the rotor position with respect to time in **Eq.2.3**, the rotor speed can be obtained by

$$\frac{d\theta_r}{dt} = \omega_r \tag{4.2}$$

Dynamic characteristics of the drive respond to operational commands which are generated by a control circuit. In the simulation, above given equations should be solved simultaneously for dynamic performance prediction of the drive. The simulation of dynamic behaviour is based on providing the numerical solution of the motor model differential equations for the different existing modes of operation. Since the mathematical model has been made available in the previous chapters it becomes a relatively simple matter to program these in a computer.

The **abc** modelling approach is used to simulate the drive. The model allows a direct and detailed examination of the motor's current, speed, position and torque behaviour that will not be possible if any simplifying assumption is made. Moreover, since the back EMF is non sinusoidal in BTPM motors (or non ideal in commercially available BSPM motors), **d-q** transformation does not seem advantageous. A possibility is to find a Fourier series for back EMF. However, the back EMF in the **d-q** reference frame would also consist of more than one term. Therefore, the **abc** model developed in previous

chapters can be used directly without further transformation in both BTPM motors and BSPM motors. It is also important to note that using the **abc** model in the simulation allows direct comparison of the variables and output quantities without inverse transformations. All the numerical values in the simulation were represented in one system of units (SI).

In this chapter, a simulation method for a brushless PM motor fed by a voltage source inverter is derived. The back EMFs may have trapezoidal or sinusoidal waveforms, and the current in each phase of the motor may vary as shown in **Table 2.4**. The chapter will focus on the dynamic modelling and performance prediction of the drive. Specifically, the drive simulation computer program is developed for the 120° inverter driven BSPM motor, and as will be explained in next sections, simple modifications can be introduced to extend the simulation to any other excitation and control method.

In the present study, the saturation effect is neglected and the power transistors in the inverter are assumed to be ideal switches. The study did not examine speed regulation and, the reference current is used to regulate the line current by means of a hysteresis current controller. **Section 4.1** gives basic simulation block diagrams, and explains the differences in the blocks for specific motor parameters. The complete dynamic model is described in **Section 4.2.** The developed computer simulation is explained in **Section 4.3.** Simulation tools are developed to study various aspects of the brushless PM motor drive. Both steady-state and dynamic analysis are available. The results of the simulation are illustrated by various operation characteristics and compared to actual operation characteristics in **Section 4.4. Section 4.5** is the conclusion.

4.1 PRINCIPAL SIMULATION APPROACH

There are numerous ways of the simulating the brushless PM motor drive. The simulation block model is very similar to the implemented drive in **Fig.2.18 (Chapter II)** which has a three-phase current regulation loop. However, because of three-phase symmetry, it is sufficient to derive one block diagram for one phase of the motor. Then, the simulation blocks can be appropriately modified for all other phases.

The system under simulation can be represented as a block diagram, and divided into functional components as shown in **Fig.4.1**. The model can be derived easily from the physical circuit diagram of **Fig.3.1a**, and by using **Eq.3.2**. Basically, two different models can be given to show the effect of equivalent winding inductance in the simulation model.

For **Phase 1**, the basic voltage equation can be written as in **Eq.4.3**, and so that the simulation model can be derived as in **Fig.4.1a** for constant winding inductance.

$$\pm \frac{V_{dc}}{2} + v_s = R i_1 + L \frac{di_1}{dt} + e_1 \qquad (4.3)$$

Similarly, for the variable inductance (**Fig.4.1b**), the simulation voltage equations can be given by,

$$\pm \frac{V_{dc}}{2} + v_s = R i_1 + L \frac{di_1}{dt} + i_1 \frac{dL}{dt} + e_1 \qquad (4.4)$$

Here L is the equivalent variable winding inductance, and can be modelled as in **Eqs.2.14-15**.

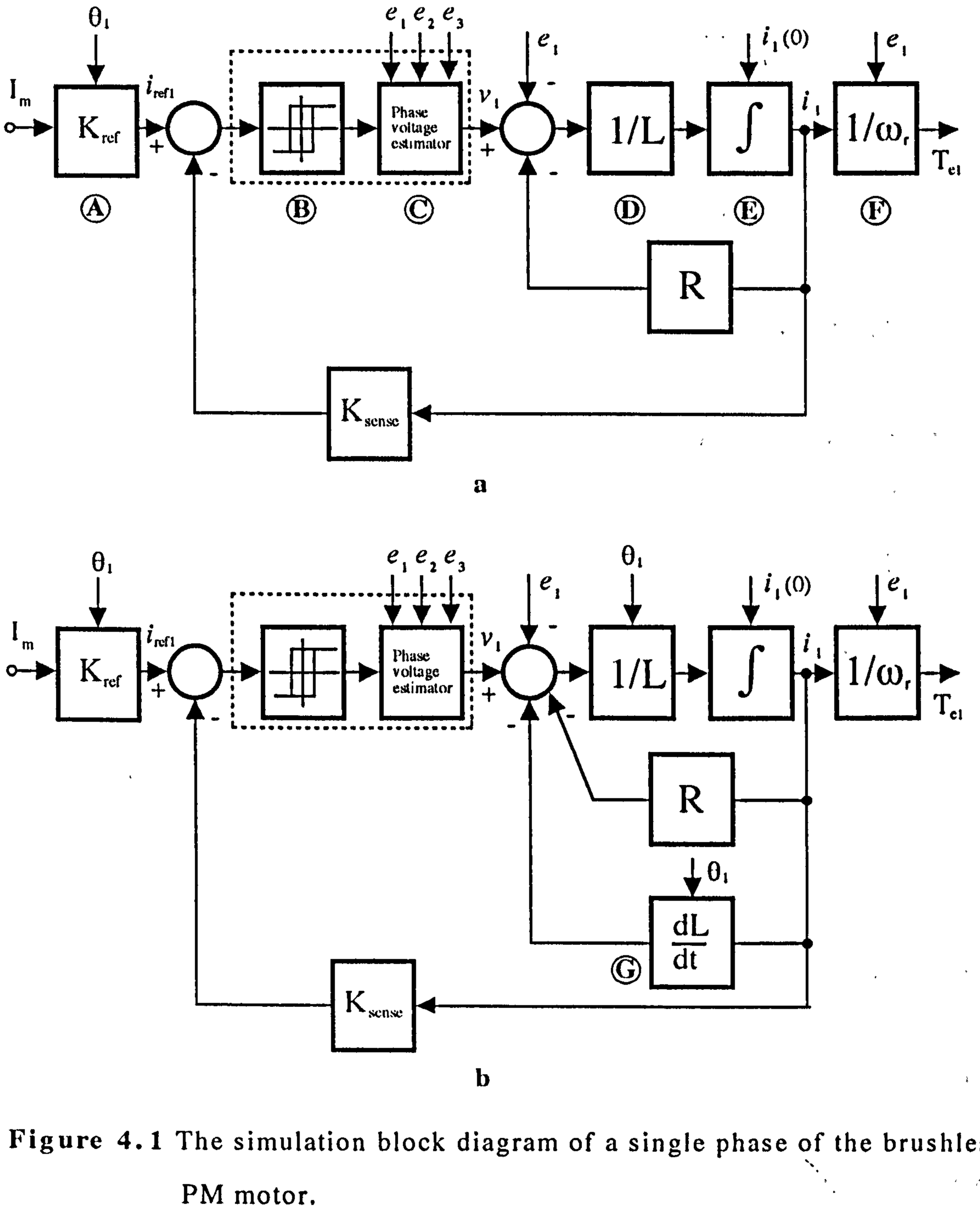

Figure 4.1 The simulation block diagram of a single phase of the brushless PM motor.

a) The constant inductance model

b) The variable inductance model

As seen in **Fig.4.1b**, the difference from **Fig.4.1a** is one extra feedback which comes from the multiplication of the actual current with the

differentiation of variable inductance term. In both cases assuming no saturation (see **Eq. 2.11**), the developed electromagnetic torque for a single phase (Phase 1) is given by,

$$T_{e1} = \frac{1}{\omega_r}(e_1 i_1) \tag{4.5}$$

The three-phase motor drive requires the solution of a system of simultaneous five differential equations (three currents, two rotor dynamic equations) rather than a single equation as represented in **Eq. 4.3** or **Eq. 4.4**. All the explanations in this section for a single phase can be extended to the three-phase drive by shifting 120° electrical.

In the next subsections, the functions of each block in **Fig. 4.1** will be explained, and modification details will be given to understand the drive and to help future developments.

4.1.1 Generating Commanded Currents

As described earlier in **Chapter II, Section 2.4.2**, the current excitation type defines the form of commanded current, and basically it can be rectangular or sinusoidal form. More specific commanded current generating methods may be given as below. In the **block** Ⓐ K_{ref} is the input signal gain, and is equal to 1 in the simulation model. I_m is the commanded current amplitude.

a) 120° Current Conduction: The commanded current is always synchronized with the instantaneous rotor position which is produced by integrating the estimated rotor speed (**Eq. 4.2**) (during transient operation)

or by equal increment of position as a function of time (for steady-state operation) Referring to **Fig.3.1b**, the simulation logic of the commanded current for a single phase can be given as:

$$\text{If} \quad 0 \le \theta_e < \frac{\pi}{6} \quad \text{then} \quad i_{ref} = 0$$

$$\text{If} \quad \frac{\pi}{6} \le \theta_e < \frac{5\pi}{6} \quad \text{then} \quad i_{ref} = I_m$$

$$\text{If} \quad \frac{5\pi}{6} \le \theta_e < \frac{7\pi}{6} \quad \text{then} \quad i_{ref} = 0$$

$$\text{If} \quad \frac{7\pi}{6} \le \theta_e < \frac{11\pi}{6} \quad \text{then} \quad i_{ref} = -I_m$$

$$\text{If} \quad \frac{11\pi}{6} \le \theta_e < 2\pi \quad \text{then} \quad i_{ref} = 0$$

b) Sinusoidal Commanded Current: The reference current should be represented as a sinusoidal function of the position:

$$i_{ref} = I_m \sin(\theta_e) \tag{4.6}$$

c) Stored Waveform: As explained in **Chapter II, Section 2.3.2,** examination of the static torque characteristics shows which commanded current waveform is more convenient for torque-ripple free control. On the basis of static torque characteristics, if the same profile is used to generate the commanded current in the actual drive, the torque ripple can be minimized. The desired commanded current waveform can be stored in a normalized form in a table, so that the simulation model of commanded current may have the same variation. In this case, due to the practical limitation of the number of data points, an interpolation method may be required to get the value in a certain position which is not in the table.

4.1.2 Modelling of Inverter Switching And Hysteresis Current Controller

This section describes how the inverter switches are operated and how the hysteresis current controllers are modelled in the simulation. Although the given model has common features to both excitation and motor control methods, it is specifically modelled for 120° excitation of the brushless PM motor.

Firstly, it is worth examining the switching procedure in a little more detail. As seen in **Fig.3.1a**, the DC voltage source is connected to the motor windings through a three-phase inverter composed of six transistors with their reverse parallel diodes allowing reverse current conduction.

Each leg of a three phase inverter consists of two switches which may not be "ON" simultaneously. Therefore, referring to the mid-point of the DC rail voltage as shown in **Fig.3.1a**, the output of each inverter leg may be either at $+V_{dc}/2$ (when the upper reverse parallel diode or the power switch is ON) or at $-V_{dc}/2$ (when the lower reverse parallel diode or the power switch is ON). Considering these two states and commutation instants (**Fig.3.1.c**) for each inverter leg, and combining them yields twelve possible connections as illustrated in **Fig.4.2**. The load is not shown in the figure. The solid lines in the figure show the *active devices*, and in the related tables a "1" indicates a "ON" position whilst a "0" indicates an "OFF" position.

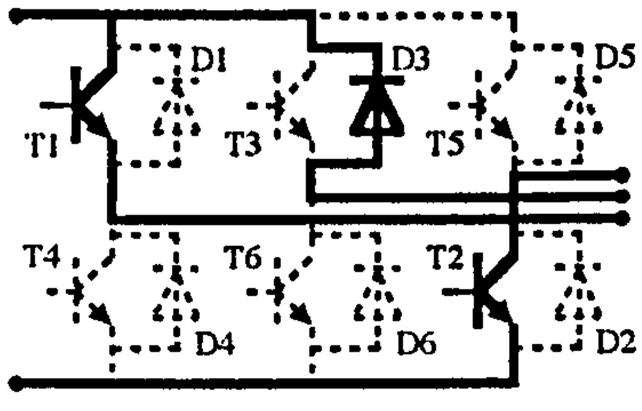

T1	1	D1	0
T2	1	D2	0
T3	0	D3	1
T4	0	D4	0
T5	0	D5	0
T6	0	D6	0

a

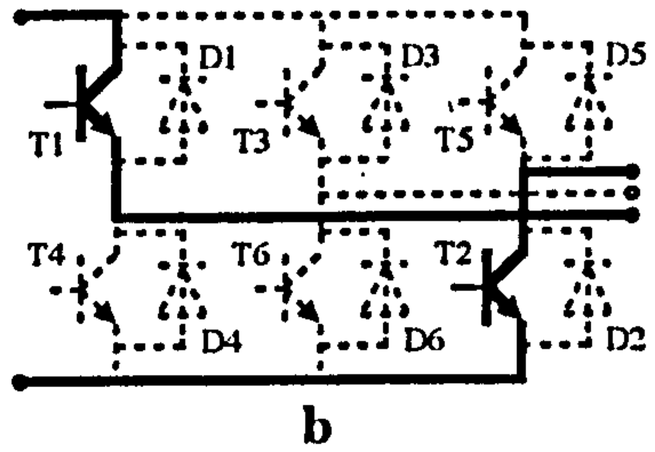

T1	1	D1	0
T2	1	D2	0
T3	0	D3	0
T4	0	D4	0
T5	0	D5	0
T6	0	D6	0

b

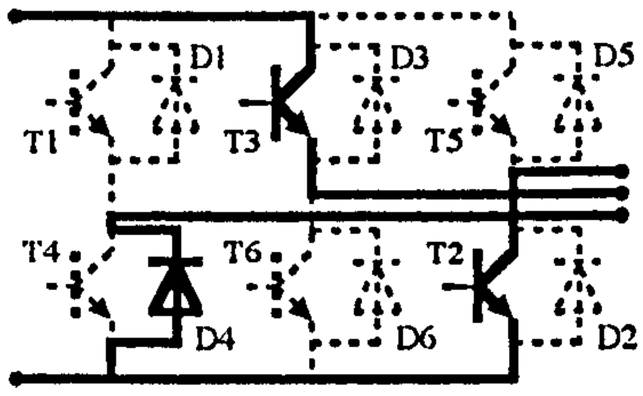

T1	0	D1	0
T2	1	D2	0
T3	1	D3	0
T4	0	D4	1
T5	0	D5	0
T6	0	D6	0

c

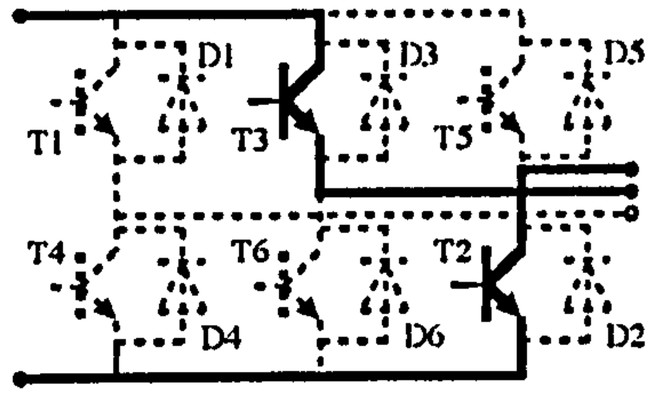

T1	0	D1	0
T2	1	D2	0
T3	1	D3	0
T4	0	D4	0
T5	0	D5	0
T6	0	D6	0

d

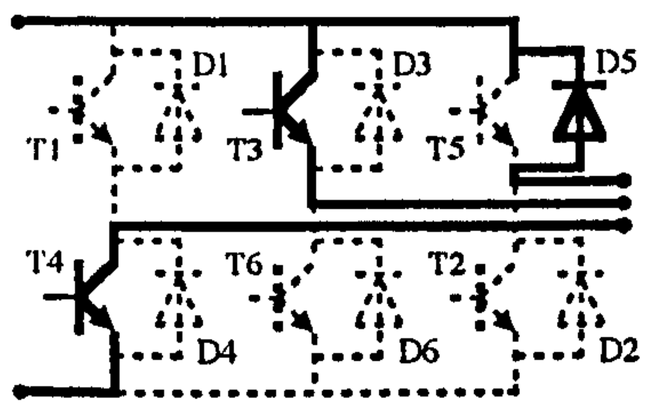

T1	0	D1	0
T2	0	D2	0
T3	1	D3	0
T4	1	D4	0
T5	0	D5	1
T6	0	D6	0

e

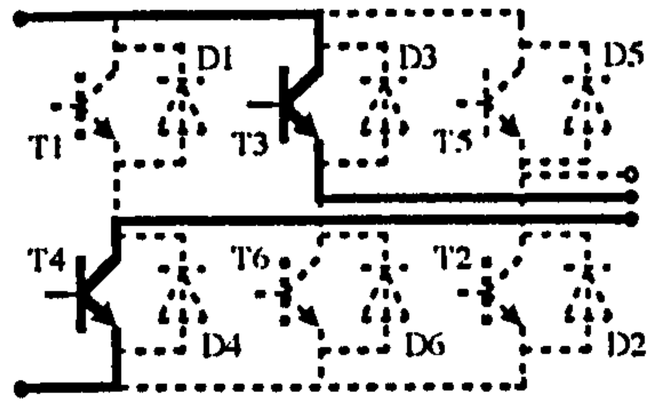

T1	0	D1	0
T2	0	D2	0
T3	1	D3	0
T4	1	D4	0
T5	0	D5	0
T6	1	D6	0

f

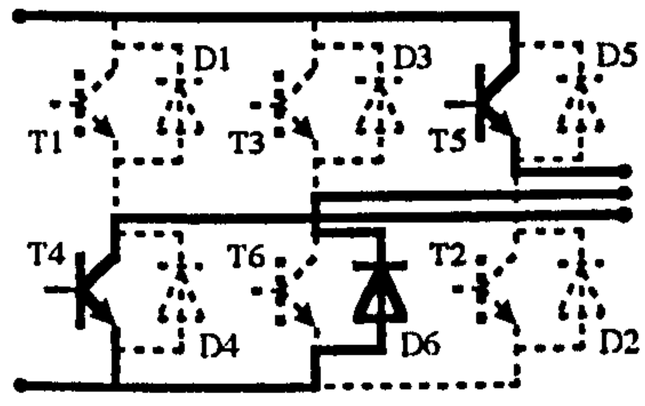

T1	0	D1	0
T2	0	D2	0
T3	0	D3	0
T4	1	D4	0
T5	1	D5	0
T6	0	D6	1

g

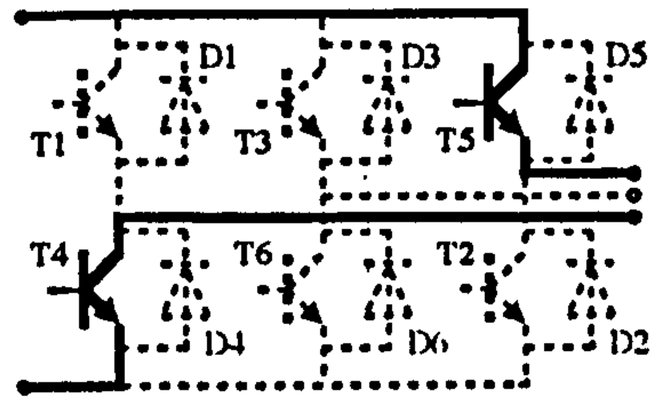

T1	0	D1	0
T2	0	D2	0
T3	0	D3	0
T4	1	D4	0
T5	1	D5	0
T6	0	D6	0

h

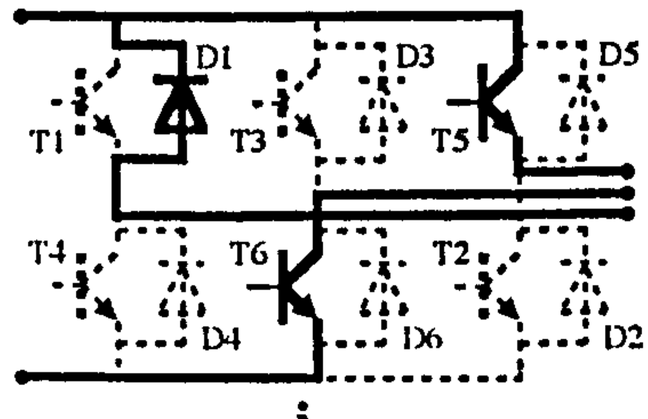

T1	0	D1	1
T2	0	D2	0
T3	0	D3	0
T4	0	D4	0
T5	1	D5	0
T6	1	D6	0

i

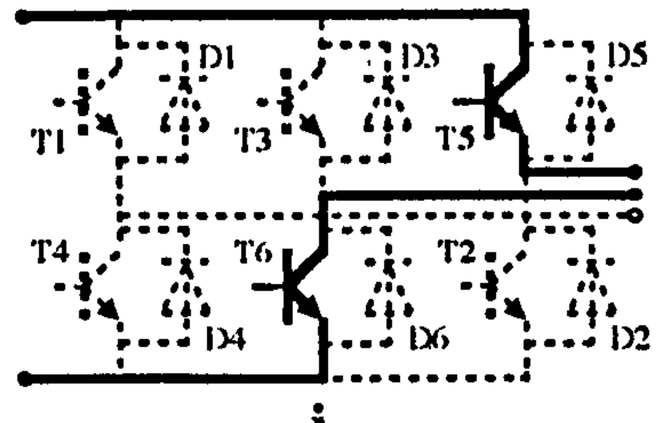

T1	0	D1	0
T2	0	D2	0
T3	0	D3	0
T4	0	D4	0
T5	1	D5	0
T6	1	D6	0

j

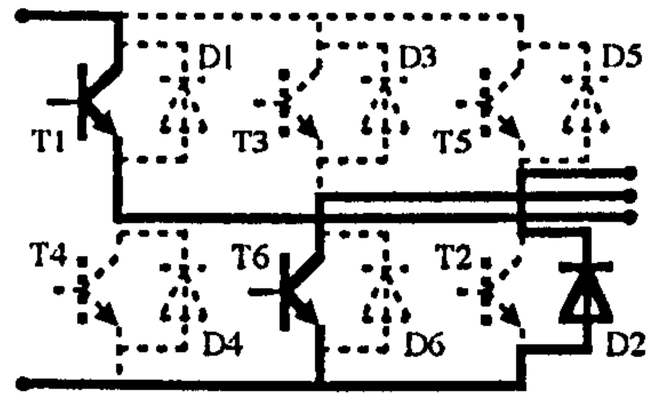

T1	1	D1	0
T2	0	D2	1
T3	0	D3	0
T4	0	D4	0
T5	0	D5	0
T6	1	D6	0

k

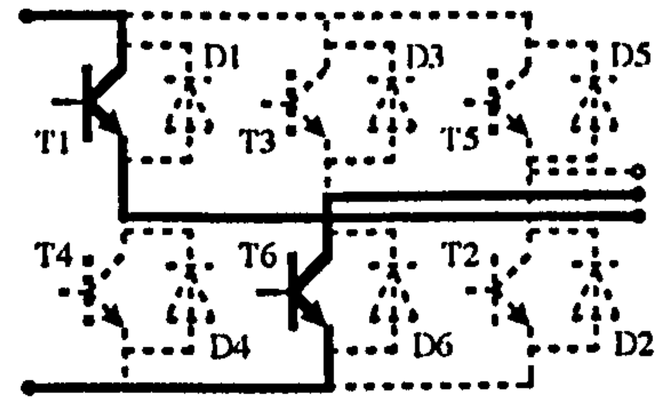

T1	1	D1	0
T2	0	D2	0
T3	0	D3	0
T4	0	D4	0
T5	0	D5	0
T6	1	D6	0

l

Figure 4.2 Twelve basic switching instants showing *active devices* in 120° inverter operation.

Each winding carries current for 120° electrical of each half period, before repetition of the switching sequence. As seen in the right column of **Fig.4.2**, two power transistors are "ON" at any time (during a conduction interval). The load current flows via either a pair of phase windings or three phase windings (during commutation time). The active reverse parallel diodes (in the left column of **Fig.4.2**) have an important role during commutation and switching instants permitting the phase current to decay naturally.

In the actual drive, due to non ideal power switches, inevitable delays occur between the time of commanding a switching event and the time when it actually happens. Although these delays may create more switching combinations, they are not shown in **Fig.4.2**. Moreover, as will be explained later, in connection with the modelling of the hysteresis current controller, each current decay instant activates the complementary reverse parallel diode.

The main aim of a hysteresis current controller is to control the torque of the brushless PM motor. To control the torque of the motor, the stator currents must follow the references which have amplitude proportional to the desired torque and are in phase with the rotor position. In order to regulate the motor current accurately within a given hysteresis bandwidth **Δh**, a control **block** Ⓑ must be added to the simulation (**Fig.4.1a**). The current controller in this method needs the actual line current which is connected to a summation point. For 120° inverter operation, a discontinuous rectangular commanded current is produced as explained in **Section 4.1.1.**

When the actual current exceeds specified error limits (**±Δh/2**) relative to its reference, the state of the corresponding inverter pole is changed, as described shortly in **Section 2.4.2.1a. Fig.4.3** illustrates a typical phase

current waveform for one electrical period controlled by a hysteresis controller. The logical senses and the reference are also given in **Fig.4.3a**. In **Fig.4.3b**, the single phase current is shown with the variation of terminal voltage with respect to the mid-point of the DC supply voltage.

Referring to **Fig.4.2** and **Fig.4.3**, for **Phase 1**, whenever T1 is "ON", terminal voltage v_a becomes $+V_{dc}/2$, and i_1 increases positively using either T2 or T6 as a return path. As soon as the current reaches the upper hysteresis limit, T1 switches from "ON" to an "OFF" position and the complementary reverse parallel diode (D4) begins to conduct allowing the current decay. When this occurs, the voltage of **Phase 1** switches from $+V_{dc}/2$ to $-V_{dc}/2$ where the mid-point of the DC supply is taken as reference. A similar switching procedure is repeated throughout the 120° conduction in the first half cycle. After 120° controlled current conduction, the current is allowed to decay to zero. The switching procedure is repeated for negative half cycle of the current as shown in **Fig.4.3**.

The hysteresis current controller is modelled in terms of the above described logic, and shown in **Fig.4.3**. Similar logic can be applied to other phases or reference current waveforms (such as sinusoidal). After defining the value of terminal voltage which can be either $+V_{dc}/2$ or $-V_{dc}/2$, the phase voltage v_1 should be estimated by using the logic described in the next section (**Section 4.1.3**).

Fig.4.4 is given to show the actual current variation with respect to the measured pulses in the transistor gates. If we analyse **Fig.4.4b**, we can say that the current rises as soon as **T1** is **ON**. Since there is current control in the drive, when the actual current reaches the upper current limit, **T1** is switched to the **OFF** position, and reverse parallel diode **D4** starts conducting allowing current to decay naturally to the lower hysteresis limit.

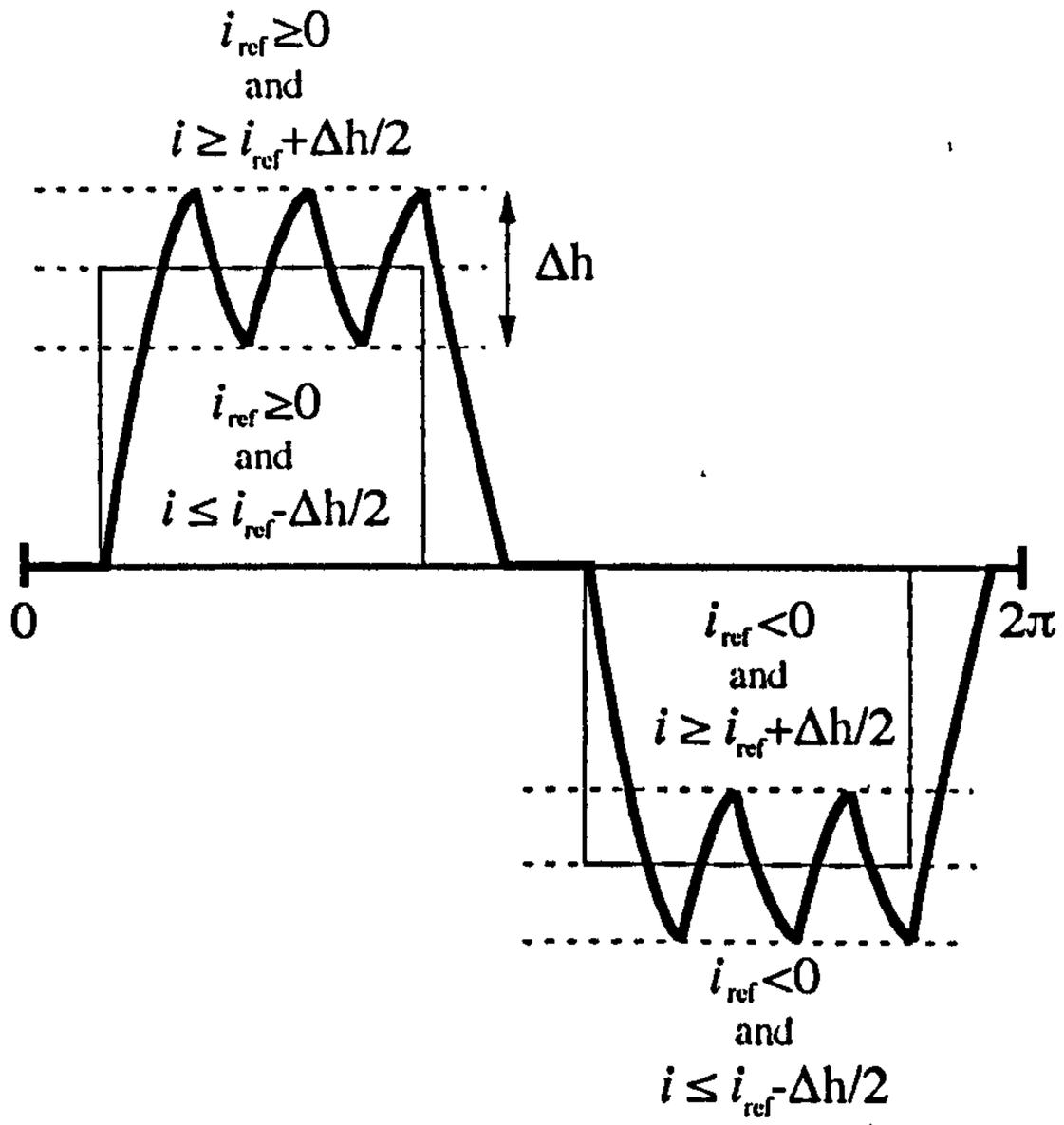

a

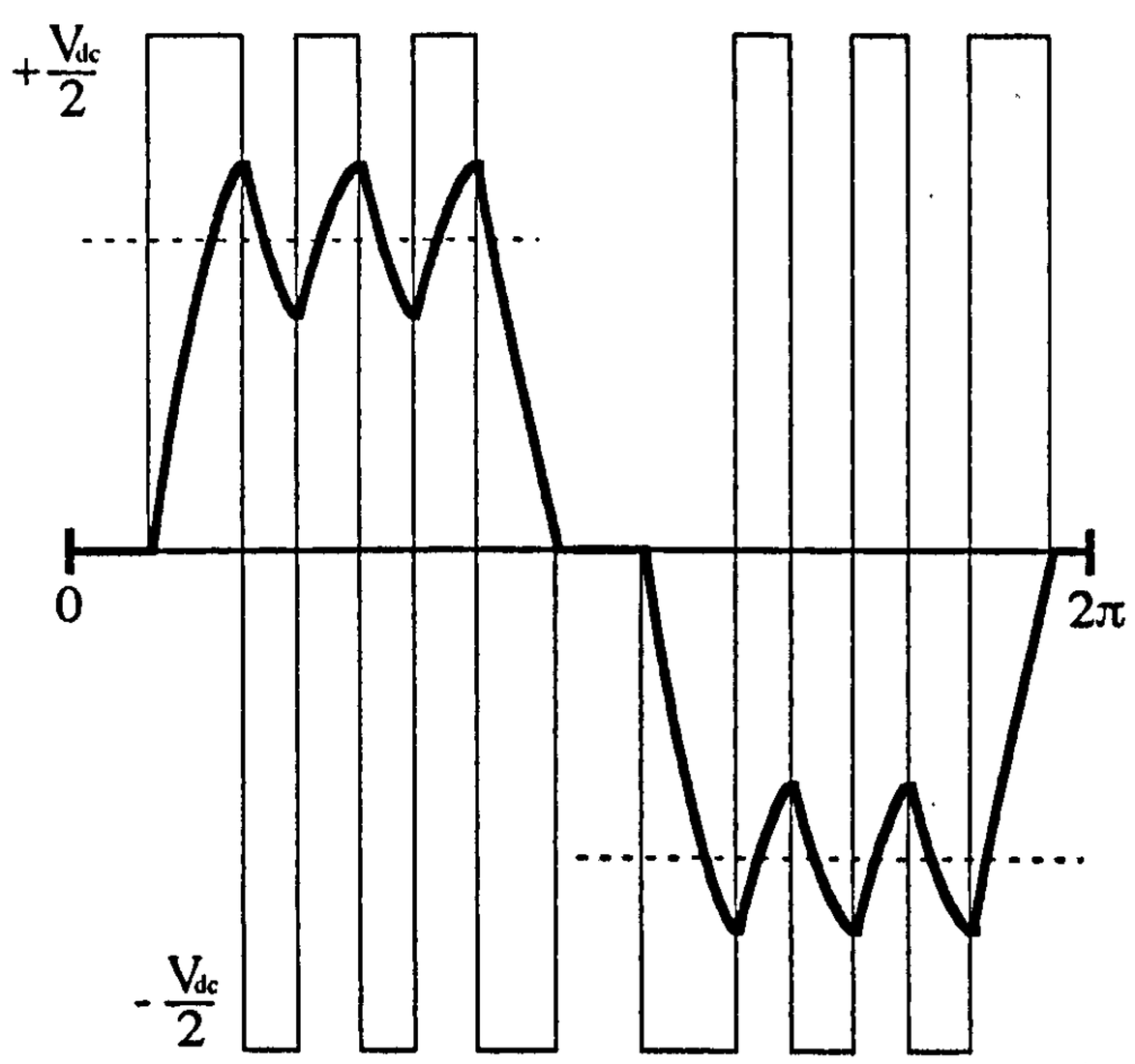

b

Figure 4.3 Typical single phase current variation and terminal voltage waveforms

a) The logical representation of the hysteresis current control

b) Changing of terminal voltage during hysteresis current control

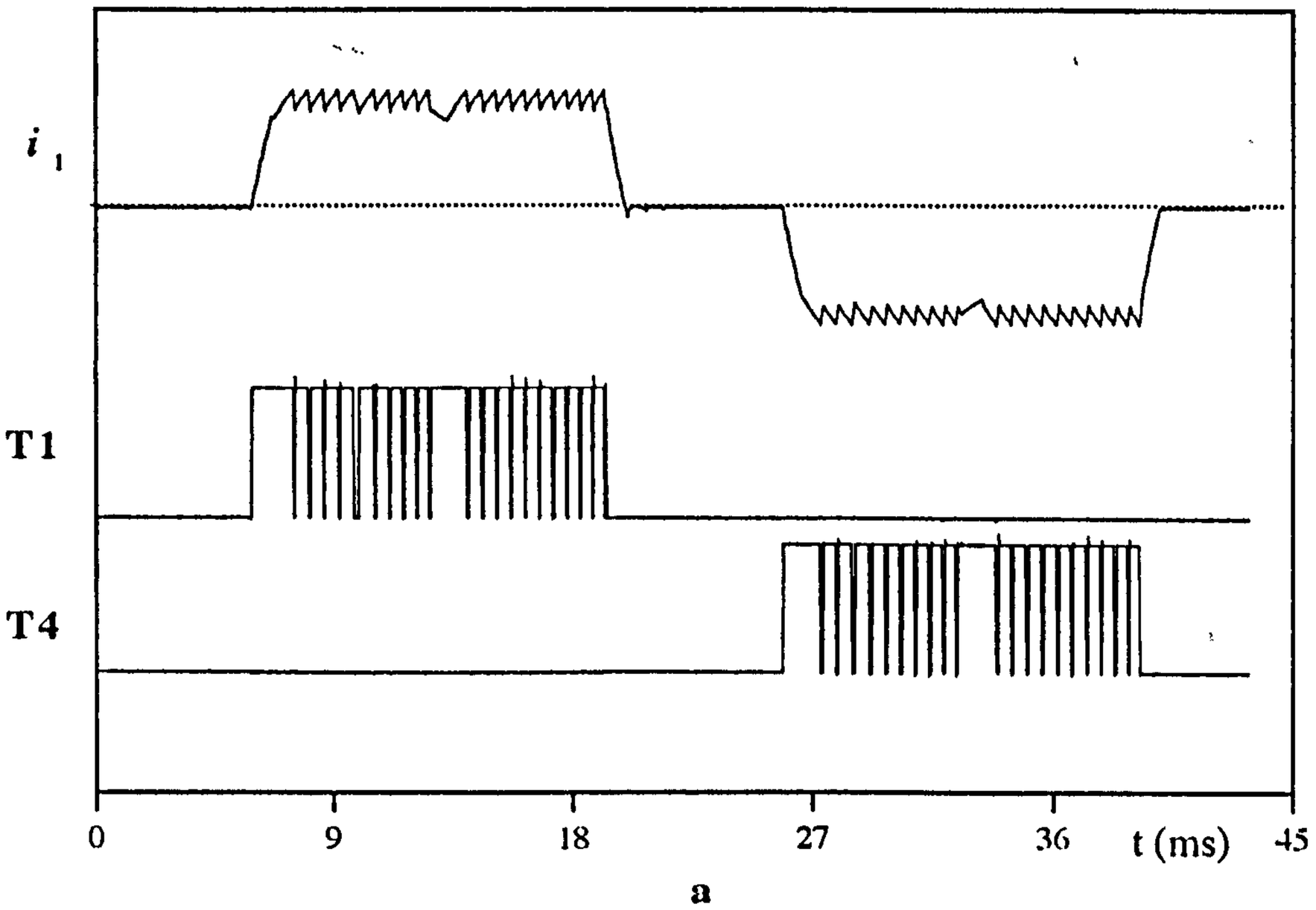

Figure 4.4 Observed line current waveform reference to the gate signals of the related power transistors, no phase advance, $V_{dc} = 57.2V$, $\pm\Delta h/2 = \pm 0.3A$.

a) The line current and base signals

b) Enlarged waveform for the interval 4-10ms in (**a**).

4.1.3 Phase-to-Star Point Voltage Estimator

The **block** Ⓒ in **Fig.4.1** shows the phase-to-star point voltage estimator. As shown, the **block** Ⓒ reads out the terminal voltages ($\pm V_{dc}/2$) from the **block** Ⓑ to estimate the phase voltage v_1.

As explained in **Section 3.1.1**, for the motors having isolated star-connected windings, the star-point voltage v_s must be calculated for every winding combinations and motor speed. For modelling purposes, the phase voltages of the motor may be represented in the computer simulation by the expressions given in **Fig.3.2**. However more general expressions are going to given below to model any excitation type.

Basic difference in estimation of phase voltage for simulation purpose comes from back EMF variations in brushless PM motors. **Fig.4.5** illustrates two typical idealized back EMF waveforms in three-phase brushless PM motors. As marked in **Fig.4.5**, the summation of back EMFs in motors which have sinusoidal back EMF (**Fig.4.5a**) is different than that of the trapezoidal back EMF motors (**Fig.4.5b**). This difference presents an extra term in the star-point voltage estimations as shown below:

Using **Fig.3.1a** and the developed equations in **Eq.2.8**, the terminal voltage equations can be given by,

$$\begin{aligned} v_a &= Ri_1 + L\frac{di_1}{dt} + e_1 + v_s \\ v_b &= Ri_2 + L\frac{di_2}{dt} + e_2 + v_s \\ v_c &= Ri_3 + L\frac{di_3}{dt} + e_3 + v_s \end{aligned} \tag{4.7}$$

or in terms of phase voltages,

$$\begin{aligned} v_a &= v_1 + v_s \\ v_b &= v_2 + v_s \\ v_c &= v_3 + v_s \end{aligned} \tag{4.8}$$

Here v_a,v_b, and v_c are the terminal voltages with respect to the midpoint of the DC supply voltage, and can be $\pm V_{dc}/2$. For the three-phase inverter operated brushless PM motor, it is always true that the summation of line currents is zero. Therefore, if we sum three equations in **Eq.4.7**, we get the star-point voltage as a function of terminal voltages and back EMFs.

$$v_s = \left(\frac{v_a+v_b+v_c}{3}\right)-\left(\frac{e_1+e_2+e_3}{3}\right) \tag{4.9}$$

The difference in modelling phase voltage appears in the last term of **Eq.4.9**. If the simulated motor model has sinusoidal back EMF variations, at any time instant, the term $(e_1+e_2+e_3)$ is equal to zero. However, it is not true when the trapezoidal (**Fig.4.5b**) or quasi trapezoidal back EMF approximation is taken into account (except zero crossing instants).

Since the controlled parameter is line current, from the phase windings point of view, there are two possibilities:

a) If one phase is not conducting (because the other two phases are conducting), the current in that phase will be zero, and the back EMF voltage will be seen in that phase.

b) All three phases may conduct.

Table 4.1 summarizes the estimated star point and phase voltages for two typical back EMF variations with the simulation logic statements.

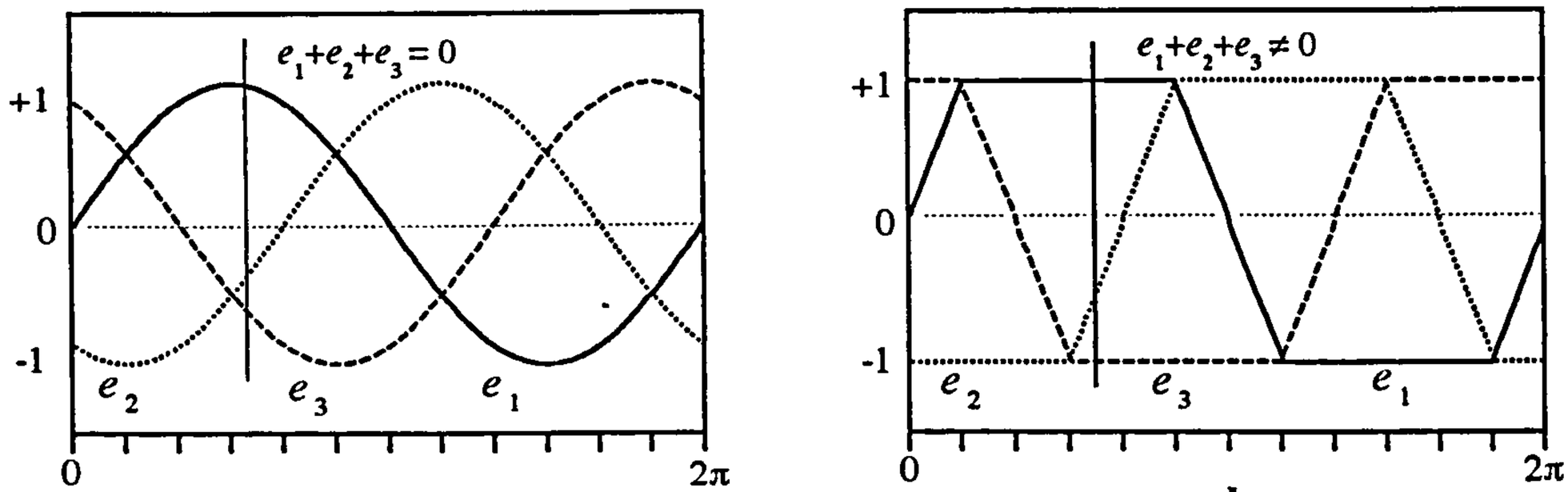

Figure 4.5 Typical three-phase back EMF variations

a) Sinusoidal back EMFs

b) Trapezoidal back EMFs (120° flat top, BTPM motor)

In this work, the harmonic analysis of the back EMF at different operating speed was done, and the back EMF constants (k_{en}, n=1,2,...) of each dominant harmonic component were estimated as in **Eq.2.17 (Chapter II)**. The estimations were repeated within a speed variation between 150 rpm and 2856 rpm. As expected, the resulting analysis (by Brüel&Kjær, Signal Analyzer, Type 2034) shows that the actual back EMF variation contains odd harmonics only. After the harmonic analysis, ignoring the harmonics higher than 9th, the Fourier series to represent the actual back EMF variation can be expressed as a periodic function of θ_e,

$$e(\theta_e) = \omega_r [k_{e1}\sin(\theta_e) + k_{e3}\sin(3\theta_e) + k_{e5}\sin(5\theta_e) + k_{e7}\sin(7\theta_e) + k_{e9}\sin(9\theta_e)] \quad (4.10)$$

or

$$e(\theta_e) = \omega_r \sum_{n=1}^{9} k_{en}\sin(n\theta_e) \quad (4.11)$$

Here n is a positive integer and varies as 1,3,5,7,9, and k_{en} can be interpreted as the Fourier coefficients of the function (in V/rad/s) which were measured and given as below:

$k_{e1} = 0.407$

$k_{e3} = 0.07$

$k_{e5} = 0.008$

$k_{e7} = 0.0009$

$k_{e9} = 0.00318$

Table 4.1 Estimation of phase voltages in the simulation

SINUSOIDAL BACK EMFs	TRAPEZOIDAL BACK EMFs
$e_1+e_2+e_3 = 0$	$e_1+e_2+e_3 \neq 0$ (except zero crossing instants)
$v_a, v_b, v_c = \pm\frac{V_{dc}}{2}$ or e_1, e_2, e_3 and	$v_a = v_1 + v_s$ $v_b = v_2 + v_s$ $v_c = v_3 + v_s$
$v_s = K[(v_a+v_b+v_c) - (e_1+e_2+e_3)]$	
If $i_1=0$ then	$v_1=v_a=e_1$ $v_2=v_b-v_s$ K=1/2 $v_3=v_c-v_s$
If $i_2=0$ then	$v_1=v_a-v_s$ $v_2=v_b=e_2$ K=1/2 $v_3=v_c-v_s$
If $i_3=0$ then	$v_1=v_a-v_s$ $v_2=v_b-v_s$ K=1/2 $v_3=v_c=e_3$
If $i_1\neq0$, $i_2\neq0$, $i_3\neq0$ then	$v_1=v_a-v_s$ $v_2=v_b-v_s$ K=1/3 $v_3=v_c-v_s$

It is worth explaining here the difference between estimated and measured phase voltage waveforms shown in **Fig.3.9**. Since the back EMFs are not sinusoidal in the actual system, the summation of back EMFs is not zero. During the commutation instants, the difference between measured and estimated phase voltage becomes bigger. At these instants, the estimated star point voltage varies between $\pm E_m/3$. Referring to the positive cycle of a single phase current, if this difference is $+E_m/3$ (at the starting instant of current conduction), the star-point voltage reduces. As a result of this reduction, the value of phase voltage increases with same difference. The opposite happens when the value of $(e_1+e_2+e_3)/3$ is equal to $-E_m/3$ (at 90° electrical position of back EMF).

For comparative purposes, the simulation and experimental phase voltage and the star-point voltage (with respect to mid-point of DC rail voltage) waveforms are shown in **Fig.4.6**. As seen in the Figure, the assumption of non sinusoidal back EMF waveform in the simulation (**Eqns.4.10-11**) makes the estimated phase voltage (**Fig.4.6a**) very close to the measured waveform. In **Fig.4.6**, the small spikes, fluctuations, phase differences during commutation instants and small DC offset are due to switching transients in the inverter, fluctuations on DC rail voltage, unsymmetrical commutation in the system, and error in the measurement unit respectively. As explained earlier, in the three phase isolated star-point brushless PM drive, the instantaneous value of the terminal voltage changes between the commutation instants considerably. This effect can be attributed to one cause corresponding to the star-point voltage. In **Fig.4.6b**, the measured and estimated star point voltages are given at the motor speed of 479.23 rpm, and V_{dc}= 54 V.

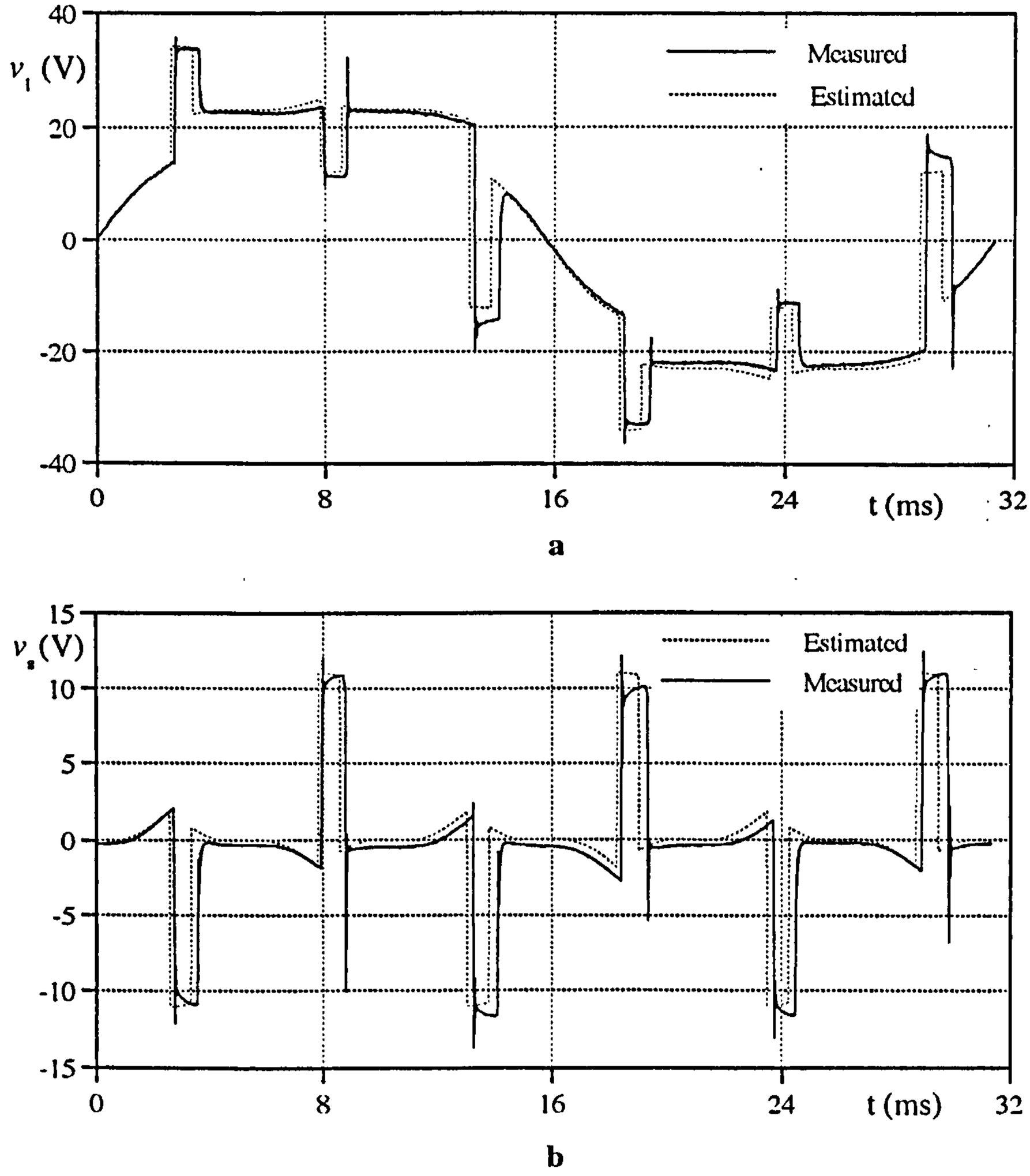

Figure 4.6 Observed and estimated typical voltage waveforms, n= 479.23 rpm, V_{dc}= 54V, no phase advance.

a) Phase 1 estimated and measured voltages

b) Star-point voltages with respect to the mid-point of DC rail voltage.

4.1.4 Equivalent Inductance Modelling

The model used in **Fig.4.1a** for constant winding inductance can be extended to study the influence of variable winding inductance (**Fig.4.1b**). The general approximation equations in **Eq.2.14-15** may be used to model variable winding inductance in the simulation..

Although in practice, the inductance of each phase is not a pure cosine function of position, the use of the inductance expression of **Eq.2.14-15** generally gives satisfactory results. If more accuracy is desired, it is possible to include some of the higher harmonics in the model. When the variable winding inductance model is used in the simulation, for simplicity, the inductance expression should be differentiated with respect to time, and replaces **block** Ⓖ in **Fig.4.1b**. As seen in **Eq.2.14-15**, the rotor position should also be used as a parameter to define incremental inductance variation in the simulation. However, the constant inductance modelling does not require the position data, and does not present any modelling difficulties as shown in **Fig.4.1a**.

4.1.5 Integration

The integration **block** Ⓔ is placed between the block Ⓓ and block Ⓕ to estimate state variables (currents, or speed and position for dynamic performance). Therefore, a numerical method should be selected to be used in integrating the system of differential equations which represent the drive. Many methods are available, and the accuracy of the simulation depends on the sophistication of the integration method. The "integration" subroutine packages are widely available in the literature.

The numerical integration methods are not going to discussed here, however it is worth giving some explanation about the integration method implemented in the simulation. The method used in the simulation is a fixed-increment Kutta-Merson method.

In general, the first order differential equation $\frac{dy}{dt} = f(t,y)$ with the initial condition $y(t_0)=y_0$ is solved. The solution is in the form:

$$y = \int_{t_n}^{t_{n+1}} f(t)dt \qquad (4.12)$$

Similar to the popular Runge-Kutta integration method, the Kutta-Merson integration formula also involves a weighted average of values f(t,y) taken at different points in the interval $t_n \le t \le t_{n+1}$, and it is given by [*Ledermann* 1981; *Hopkins and Phillips*, 1988],

$$y_{n+1} = y_n + \Delta t \left(\frac{1}{6} k_1 + \frac{2}{3} k_4 + \frac{1}{6} k_5\right) \qquad (4.13)$$

or

$$y_{n+1} = y_n + \Delta t \left(\frac{1}{2} k_1 + \frac{3}{2} k_3 + 2k_5\right) \qquad (4.14)$$

where $\Delta t = t_{n+1} - t_n$ is the time increment, t is the time, y is the state variable, and

$$k_1 = f(t_n,\ y(t_n))$$

$$k_2 = f\left(t_n + \frac{1}{3}\Delta t,\ y(t_n) + \frac{1}{3} k_1\right)$$

$$k_3 = f\left(t_n + \frac{1}{3}\Delta t,\ y(t_n) + \frac{1}{6} k_1 + \frac{1}{6} k_2\right)$$

$$k_4 = f\left(t_n + \frac{1}{2}\Delta t,\ y(t_n) + \frac{1}{8} k_1 + \frac{3}{8} k_3\right)$$

$$k_5 = f(t_n + \Delta t,\ y(t_n) + \frac{1}{2}k_1 - \frac{3}{2}k_3 + 2k_4)$$

The sum $(\frac{1}{6}k_1 + \frac{2}{3}k_4 + \frac{1}{6}k_5)$ in **Eq. 4.13** can be interpreted as an average slope in the Kutta-Merson method.

4.1.6 Electromagnetic Torque Estimator

The basic block diagram (**block** Ⓕ) for instantaneous electromagnetic torque estimation is presented in **Fig. 4.1**. It assumes no saturation. However, the model can be modified to account for the effects of saturation.

It is relatively easy to take into account the effect of saturation in the torque, and because of symmetry, it is sufficient to derive new expressions for the torque just for one phase of the motor. These can be appropriately modified for all phases.

For computer simulation of the three-phase brushless PM motor, the total electromagnetic torque can be easily obtained by adding in a summation point as will be shown in the next section using the derived equations in **Eq. 2.11**.

4.2 THE COMPLETE DYNAMIC MODEL OF THE DRIVE TO BE SIMULATED

The expression "dynamic" means that the components of the system, electrical and mechanical, are changing continuously. The system variables, such as speed, position or load, may change continuously. With the appropriate inputs and parameters, any operation of the drive should be simulated with the model, and the model should be flexible for further developments. Therefore the developed dynamic model should cover all possible operation conditions and should predict the state variables correctly. The dynamic model equations of the drive given in the introduction are used to derive a complete model.

In the previous section, a single phase simulation model was developed. However, as said earlier, the model should be modified for a three-phase drive. **Fig.4.7** shows the functional dynamic simulation block diagram of the model for a three-phase brushless PM motor drive. The input to the model consists of the amplitude of commanded current. The summation point and next blocks in the figure represent the conversion of the developed motor torque according to **Eq.4.1**. The following integral element evaluates the resultant equation and finds instantaneous rotor speed ω_r. The rotor speed ω_r is integrated (**Eq.4.2**), and the rotor position is calculated.

As is well known, the time phase of back EMF is also directly proportional to the rotor position. Comparing with the actual drive, the integration block (in **Fig.4.7**) for position estimation functions as a rotor position sensor in the simulation. Thus, the rotor position can be used to estimate three-phase back EMFs (**block Ⓗ**)in terms of the desired back EMF model.

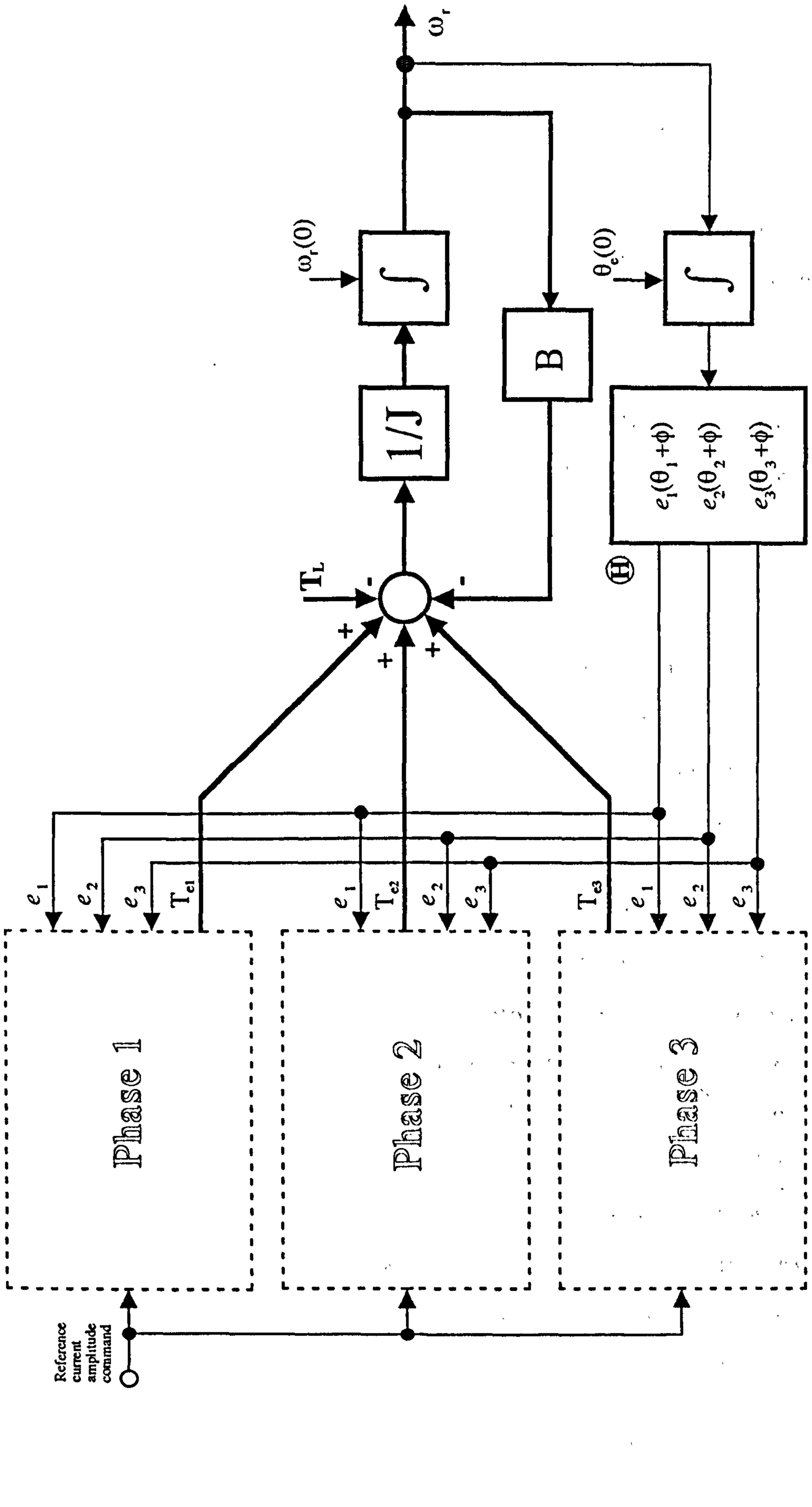

Figure 4.7 The functional complete block diagram of the dynamic simulation of the brushless PM motor drive

4.3 THE COMPUTER SIMULATION

We can now consider the actual computer simulation program. The main task of the simulation is the investigation of transient and steady-state speed, torque, voltage, and current characteristics of the motor. As will be seen in the next chapter, the computer simulation will also give opportunity to test the position sensorless operation algorithm for different operation conditions and motor types.

Fig.4.8 shows the basic structure of the computer program for simulating the brushless PM motor drive. The computer simulation program was written in FORTRAN, and executed on an IBM PC compatible and Apple Macintosh computers.

The complete program consists of a main program and three auxiliary subroutines. The rectangular boxes indicate the simulation "routines", ellipses are control commands, and the diamond is the comparison routine. The main processing program has starting and stopping commands.

The execution of the main program begins by a start-up procedure which initializes the state-variables (speed, position, and currents) and switching positions, and defines the operation and motor parameters. The program in this routine allows the selection of motor model parameters: the winding inductance **L** in mH (or L_o and L_m, when the motor has variable winding inductance), the back EMF constant $\mathbf{k_e}$ in V/rad/s, the number of poles **2p**. The routine also reads the input references: the corresponding values of phase advance or delay angles ϕ in electrical degrees, the hysteresis bandwidth $\pm\Delta\mathbf{h/2}$ in Amperes, the load torque parameters in Nm, the inertia of the system **J** in kgm^2, the DC rail voltage $\mathbf{V_{dc}}$ in Volt, and the time step

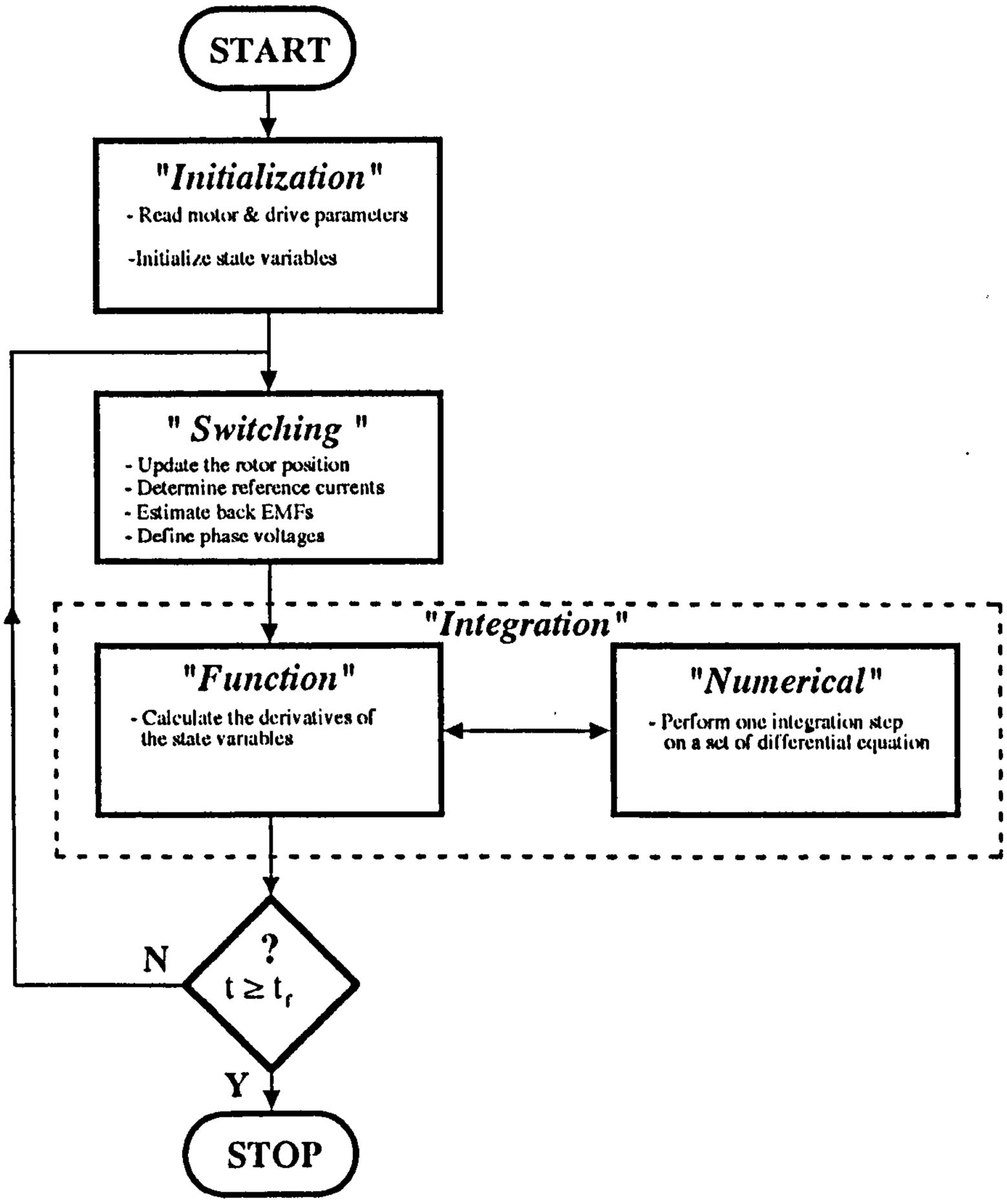

Figure 4.8 Flow chart illustrating the brushless PM motor drive simulation program.

Δt and the final time t_f in second. The number of parameters in the program may increase with the type of block models used in the simulation (**Fig.4.1**).

The set of logical operations (in **Section 4.1.1**, **Fig.4.3**, and **Table 4.1**) are located prior to the "*Integration* " subroutine. Basically, the subroutine "*Switching* " defines the phase voltages, and update the rotor position. The

estimated rotor position in the "*Integration* " routine passes to this routine to reset the position value when it exceeds the value 2p. The routine also does the calculations to determine the reference currents and back EMFs. The switching operations are defined in this routine. The star (or neutral)-point voltage is computed using the logical operations given in **Table 4.1**, and phase voltages are calculated. The process is continued throughout the drive operation up to the maximum simulation time.

The phase voltages (v_1,v_2, and v_3) are transferred to the "*Integration* " subroutine. To integrate the dynamic equations (**Section 4**) of the system simultaneously, the routine works between the "*Function* " subroutine and the "*Numerical* " subroutine. The subroutine "*Function* " calculates the derivatives of the variables (three electrical and two mechanical equations) at each time instant and passes the information to the "*Numerical* " integration routine. The routine carries out one numerical integration step on a set of five differential equations. The values of the independent variables (phase voltages) are entered as inputs and new values are got out which are stepped by a step size Δt. After the completion of each integration step, the output of the "*Numerical*" subroutine is stored in the "*Switching*" routine for later plotting according to the format requirements.

Finally, the program enters a "*Comparison*" routine. The program runs from an initial time t_o to a final time t_f in a specified number of steps. The method treats every step in a sequence of steps in an identical manner. The routine compares the time with maximum execution time (t_f). If the time is not exceeded, the program returns to the beginning, otherwise it stops.

Steady-state simulation results are also taken from the same simulation program. However the number of state equations reduces in this case. Due to

equivalent increment of the rotor position at the constant speed operation, the estimation of position and speed can be employed easily. The computer model is modified for fixed increments of position (as a function of time), and only three voltage equations are solved simultaneously in the "*Integration* " routine. As mentioned in **Chapter III**, since the initial values of current will be wrong, the estimation is repeated over several electrical cycles.

4.4 COMPARISON OF SIMULATION AND EXPERIMENTAL RESULTS

The simulation and experimental results presented in this section have been specifically chosen to understand the drive as described earlier, and to demonstrate some capabilities of the model, and to provide confirmation of the validity of current and voltage estimation which will be used in the next chapter. Experimental confirmation of voltage waveform will be helpful to simulate the shaft position sensorless operation of the drive in **Chapter V.**

The simulation results with the corresponding test data are compared, and results are given under two subsections: The steady-state operation and transient operation. The electrical quantities (such as voltage, current, electromagnetic torque...) were measured by a 5 channel data acquisition system which has a 10 μs sampling period with 16 bit data resolution, as will be described later in **Chapter VI.**

The validity of the model will be verified by applying it to the prediction of the performance of an axial field brushless PM motor which has the parameters given in **Table 2.2.** Overall measured results are taken under a variety of operation conditions using the test setup shown in **Fig.4.7.** The

setup has the feature of fine adjustable load and low/high inertia load. The setup system consisted of a separately excited DC machine (as high inertia load) or an axial field brushless PM machine (as low inertia load). Using a variable power resistor across the DC machine's armature, and a variable field supply, the mechanical load on the system was controlled. As mentioned above, another axial field brushless PM machine was also used as a low inertia load. Similar to the DC machine load, the terminals of the brushless PM generator were connected to a variable power resistor via a three-phase diode rectifier to give the effect of adjustable mechanical load.

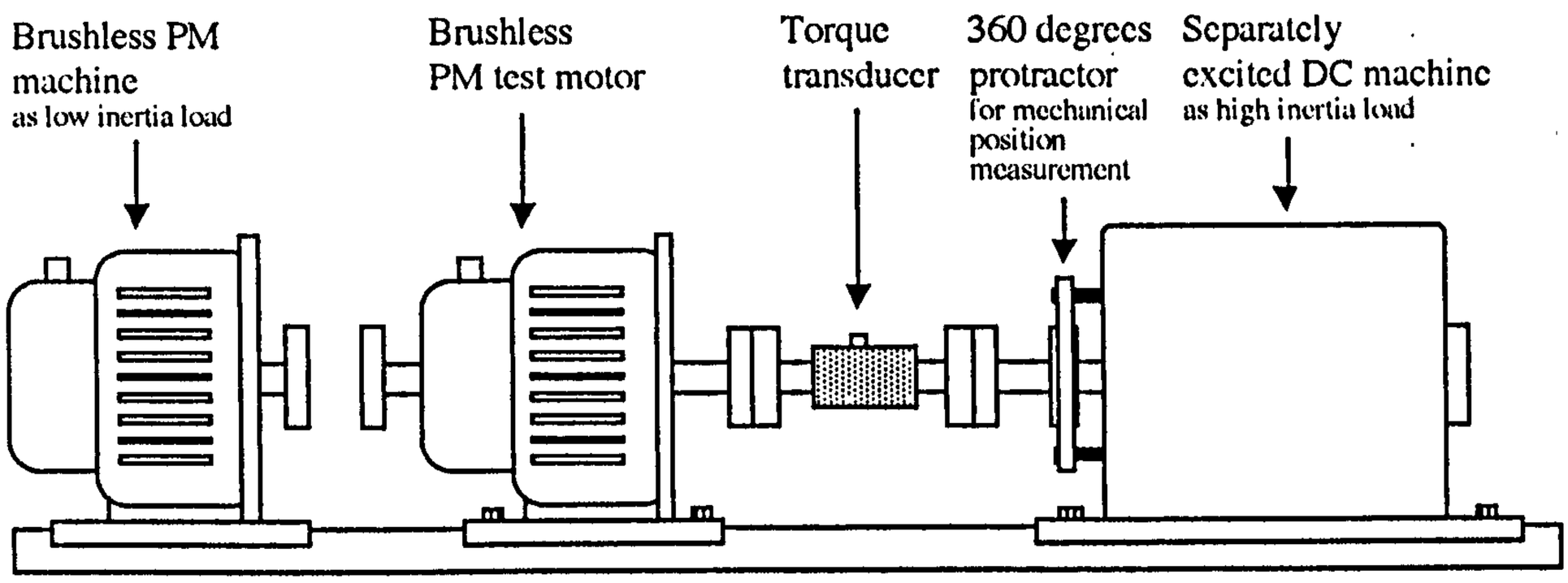

Figure 4.9 The schematic representation of the experimental setup.

The brushless PM motor drive system under test and a torque transducer were linked via couplings to a mechanical load as shown in **Fig. 4.9**. The torque transducer (see **Chapter III, Section 3.4**) was used to measure the average shaft torque of the system. The speed of the motor was estimated accurately by measuring the period of the current waveform. The measured system inertias in the experimental setup are:

$$J_1 = 4.757 \times 10^{-2} \text{ kgm}^2$$

$$J_2 = 4.839 \times 10^{-3} \text{ kgm}^2$$

Here J_1 is the inertia of the test motor+the couplings+the torque transducer+DC machine, and J_2 is the inertia of the test motor+the couplings+the torque transducer. The values of inertia were used in the simulation for dynamic performance prediction.

4.4.1 The Steady-State Results

Extensive steady-state experimental investigations on the drive system were made. Some selected experimental results were presented and emphasized special features of the brushless PM motor drive, and control. In the following pages, the experimental results corresponding to typical operation modes are shown at the left column of the related figure. The right column of the figures presents the simulated results for easy comparison.

Fig. 4.10 shows a comparison of the computed results with measurement from the actual drive system. For the case shown in the figure, the DC rail voltage of the inverter was set at 50V, and the motor was operated with no phase advance angle at steady-state (500.5 rpm).

Since the actual back EMF variation was modelled in the simulation (with Fourier coefficients), the comparison between the measured phase voltage and back EMF profile in **Fig.4.10a** will also give extra information to test the saturation effect during operation. As seen in **Fig.4.10a**, there is a very good match between the measured phase voltage and back EMF voltage within the non conducting interval of the line current, and no noticeable distortion is seen in the back EMF profile.

The measured line current waveform (Phase 1) is given in **Fig.4.10b**. As will be seen in later figures, under all conditions the line current does not retain a conduction angle of 120° electrical (for 120° inverter operation). As described earlier (see **Section 3.1, Chapter III**), this is due to the winding inductance. The computer-simulated current for Phase 1 is given in **Fig.4.10f**. Excellent agreement between the two currents is evident in both amplitudes and overall waveshapes. Notice also that in this operation mode the phase current failed to reach the maximum commanded current limit of 10A. Therefore, no current control is achieved by the hysteresis current controller.

The single phase and total electromagnetic torque were measured for a constant operation speed and DC rail voltage and compared with the estimated electromagnetic torques in **Fig.4.10c,g** and **d,h** respectively. The single phase and total simulated electromagnetic torques were plotted to give a perspective of expected performance from the drive. Notice that, the unsymmetrical electromagnetic torque profile in the single phase is due to variations in the actual back EMF and line current, and no negative torque was observed in this operation mode.

The brushless PM motor with a typical step type commutation (in this work, 120° inverter operation) will have a torque curve with lower torque values at the points in which the phases commutate.

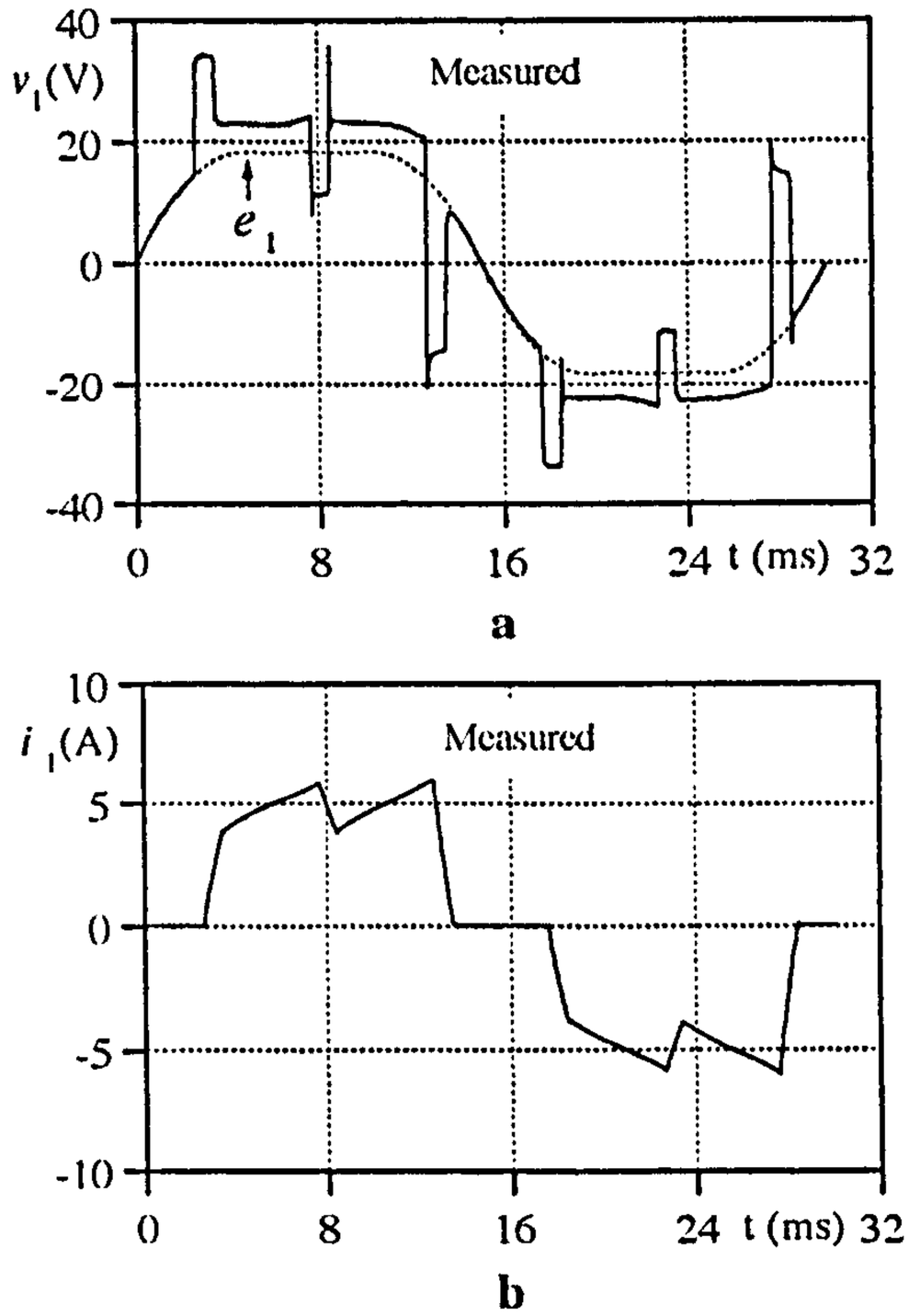

Figure 4.10 Typical steady-state measured and estimated waveforms, no phase advance, V_{dc}= 50V, n=500.5 rpm.

Very good agreements between the test results and the simulation were achieved, including predicting torque ripple (TR). The torque ripple was calculated from the instantaneous electromagnetic torque $T_e(t)$, and average torque T_{ave} [*Wallace and Spee*, 1987],

$$TR = \frac{\sqrt{\frac{1}{T}\int_0^T [T_e(t)-T_{ave}]\,dt}}{T_{ave}} 100\% \qquad (4.15)$$

Brushless PM motor drives can be operated in two operating modes: with and without current control. Since the amplitude of torque is proportional to the amplitude of the current, in practice, good torque control can be achieved by controlling the current. **Figs. 4.11** and **12** illustrates how the computer simulation was used to investigate the effects of the current control.

The current regulation in the drive demands a positive voltage difference between the DC rail voltage and instantaneous line-to-line back EMF to drive the line currents. In fact, in brushless PM motors, the voltage required to supply the controlled current is always the sum of the speed dependent induced voltage (back EMF), the $R{\cdot}i$ resistive voltage drop, and L(di/dt) (and i(dL/dt) for variable winding inductance) voltage of the equivalent winding circuit. Since the amplitude of the back EMFs are proportional to the rotor speed (**Eq. 2.17**), the available voltage difference across the motor winding reduces to zero as the speed of the motor increases. Rapid current changes require large transient winding voltages to overcome the effects summarised above.

Fig. 4.11-12 consist of two sets of results comparing the current controlled operation of the drive at two hysteresis bandwidths: **±1A** and **±0.5A**. In

both cases, the reference current amplitude was set to 5A limit, and regulated around the hysteresis bandwidth.

As stated in previous chapters, the actual line current waveform approximates the reference current only at very low hysteresis bandwidth. However, the switching frequency may reach very high values. Two sets of results given in **Figs. 4.11-12** show both the effect of small hysteresis bandwidth and the torque ripple. The first thing to note in the figures is that reducing the hysteresis bandwidth reduces the torque ripple in the drive, while it increases the switching frequency as can be seen visually.

The measured and estimated torque ripple values representing the total electromagnetic torque waveforms were summarised in **Table 4.2**. Although, the estimated torque ripple rate may be high for some applications, the small torque ripple on the shaft of the motor can be smoothed by the large system inertia, so that torque ripple will reduce on the shaft. Low hysteresis bandwidth in the controller will also reduce the torque ripple **(Table 4.2)**.

As can be seen in **Figs. 4.11-12**, the measured phase voltage waveforms contain small spikes within non conducting intervals. These spikes may be due either to the effects of change of the line currents at the hysteresis switching intervals of the other phases, or to the experimental setup (the control system and the data acquisition system). The effect of small inductance of the motor windings can also be seen during the commutation instants in the line currents (small dips). The calculated waveforms indicate good agreement with the measured ones. So this analysis is suitable for the prediction of the performance of the drive for current controlled operation.

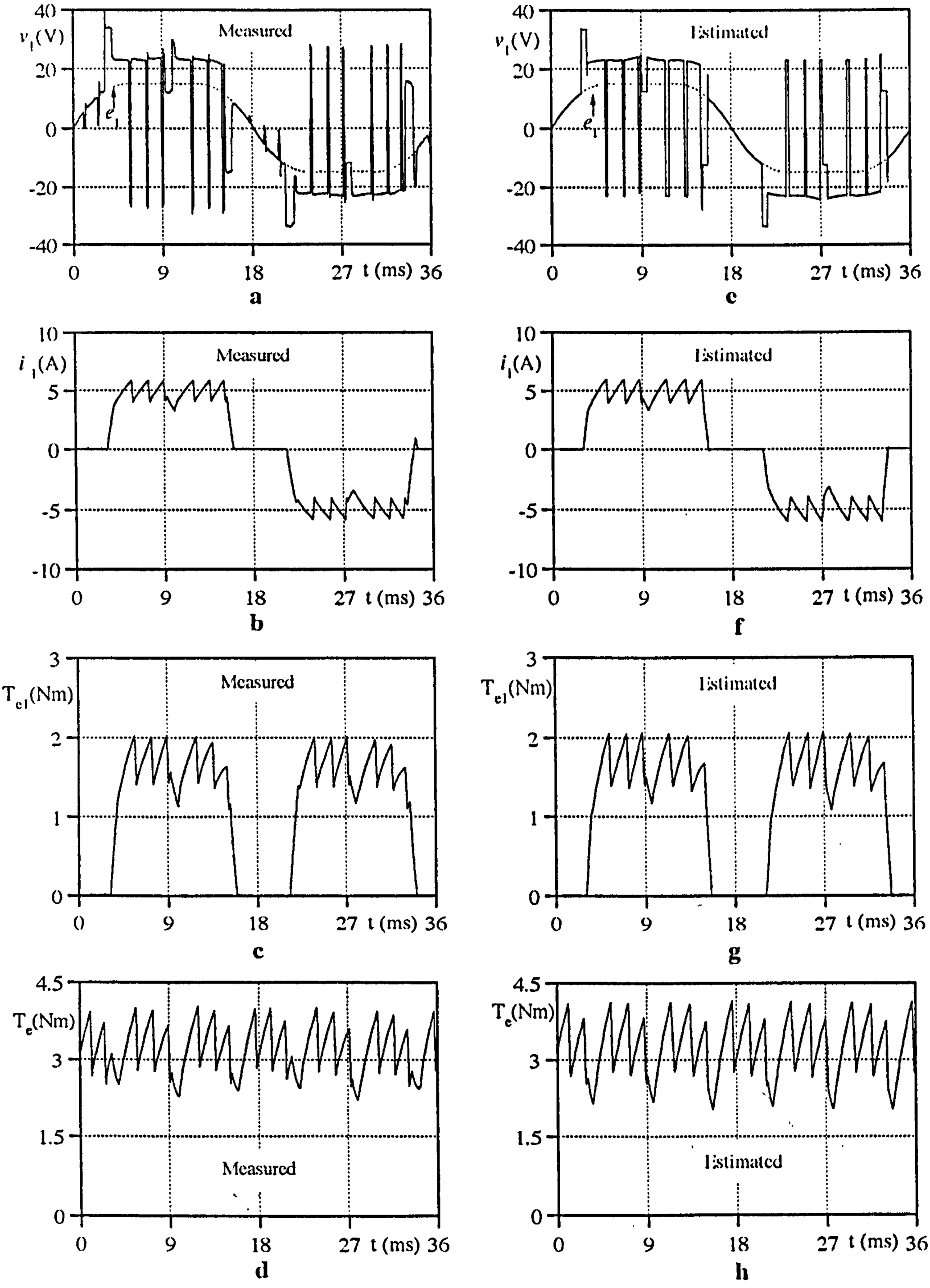

Figure 4.11 Measured and estimated waveforms in current limiting operation, n= 414.94 rpm, V_{dc}= 50V, $\pm\Delta h/2 = \pm 1$A.

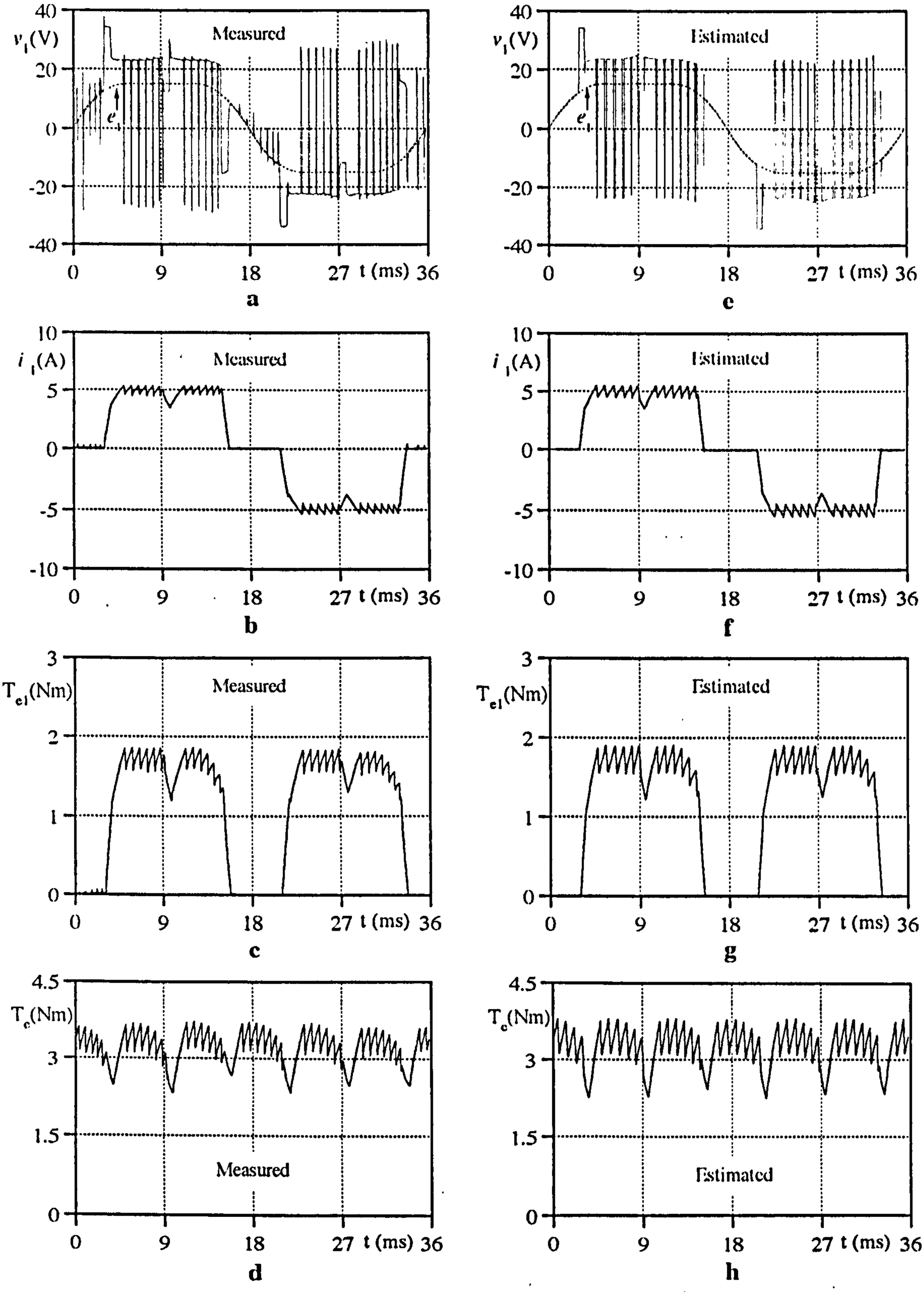

Figure 4.12 Measured and estimated waveforms in current limiting operation, n= 419.46 rpm, V_{dc}= 50V, $\pm\Delta h/2= \pm 0.5$A.

As described earlier, the switching of the six transistors of the inverter bridge is activated by signals generated from a rotor position sensing circuit (by a resolver), which was designed to allow normal as well as any value of phase advance/delay current commutation (see **Fig.2.18**). Three sets of results in **Figs.4.13-15** were given at the operation of the drive below the current control limit. The first figure (**Fig. 4.13**) shows how the drive operates at 30° phase advance angle. Comparing with **Fig.4.10**, it can be seen that, 30° phase advancing increases the torque ripple.

Fig.4.14 (60° phase advancing) shows a different profile for single phase electromagnetic torque than that of **Fig.4.13**. In this operation mode, since the resultant electromagnetic torque approximates to zero level at commutation instants, the torque ripple rises to around 50% (see **Table 4.2**). This is mainly due to the negative torque developed by each individual phase of the motor (**Fig.4.13c** or **g**).

Reconsidering **Eq.4.5**, since the back EMF and the actual current have opposite sign, the developed electromagnetic torque becomes negative. The regions showing the opposite sign variations and negative torque are represented with shaded areas in **Fig. 4.14**.

Fig. 4.15 shows another set of measured and estimated results. In this operation mode, phase angle was set to 30° delay, and the motor was working with the speed of 356.38 rpm and 36V DC rail voltage. Similar to the earlier results, since the net voltage across the phase winding is insufficient, the output current is unable to reach and track the reference current. Comparing with the case in **Fig. 4.13**, visual inspection of **Fig. 4.15** draws two main points to attention: the negative electromagnetic torque of a single phase, and torque ripple rate.

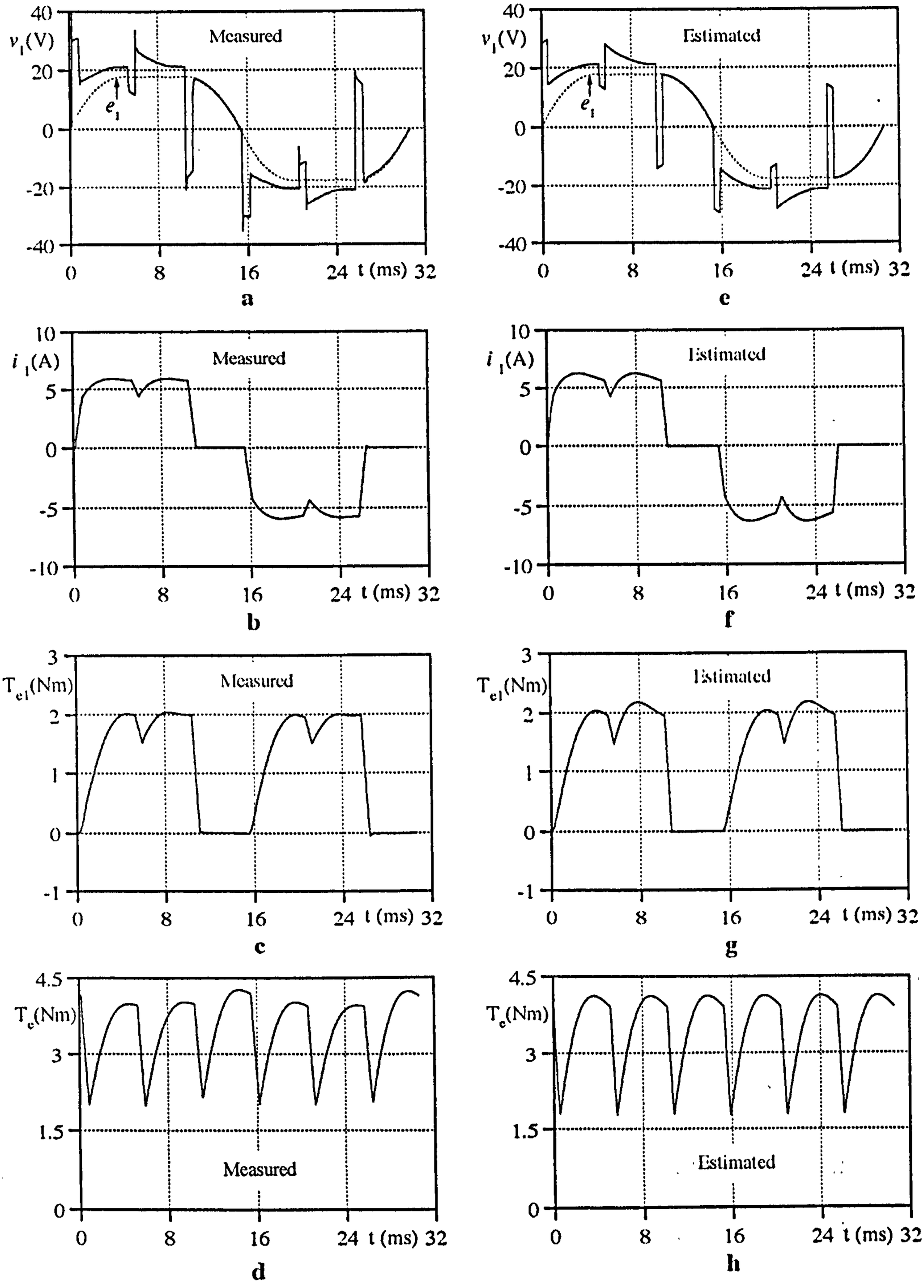

Figure 4.13 A set of measured and estimated waveforms, no current control, V_{dc}= 47V, n= 489.72 rpm, 30° phase advance.

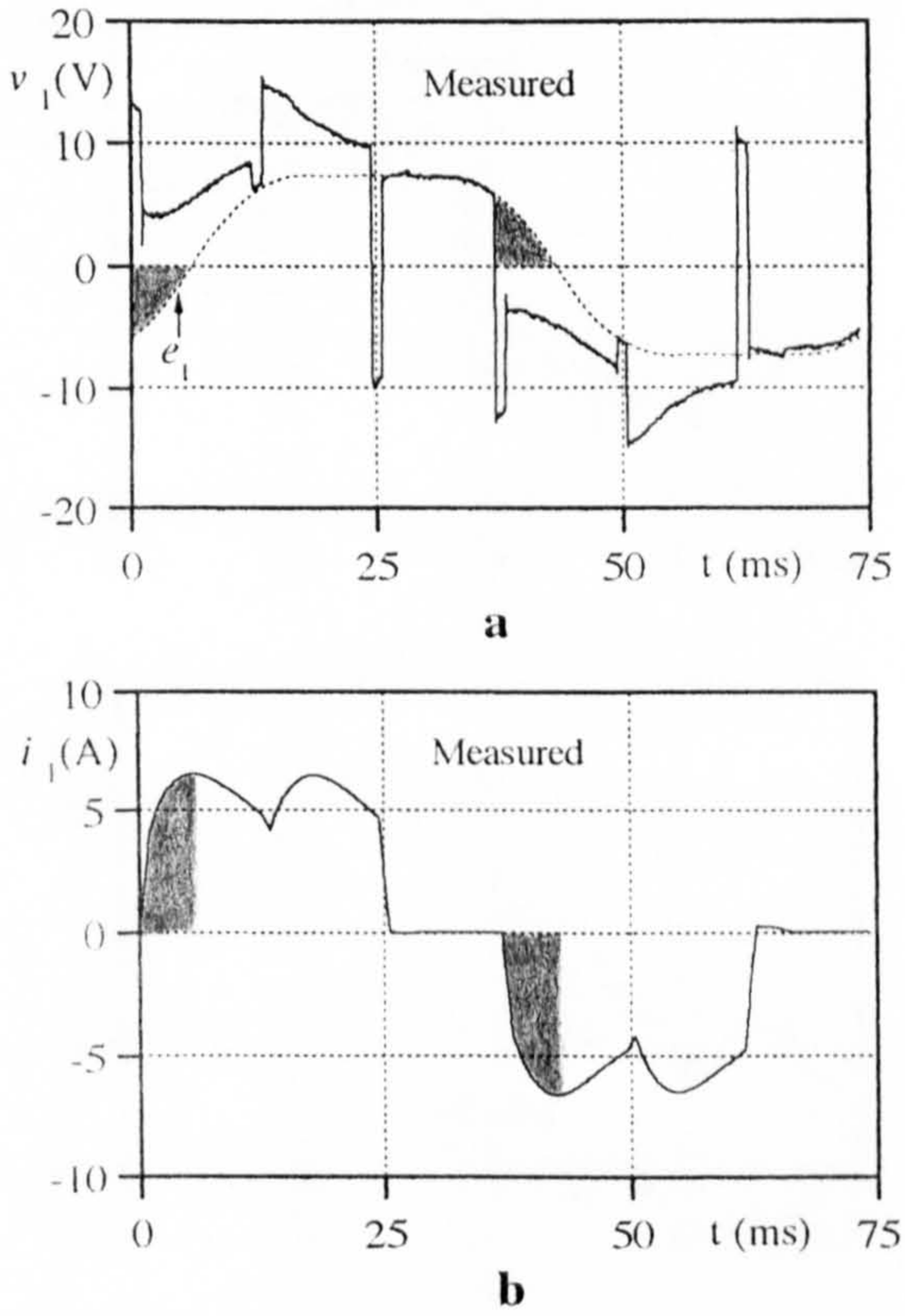

a

b

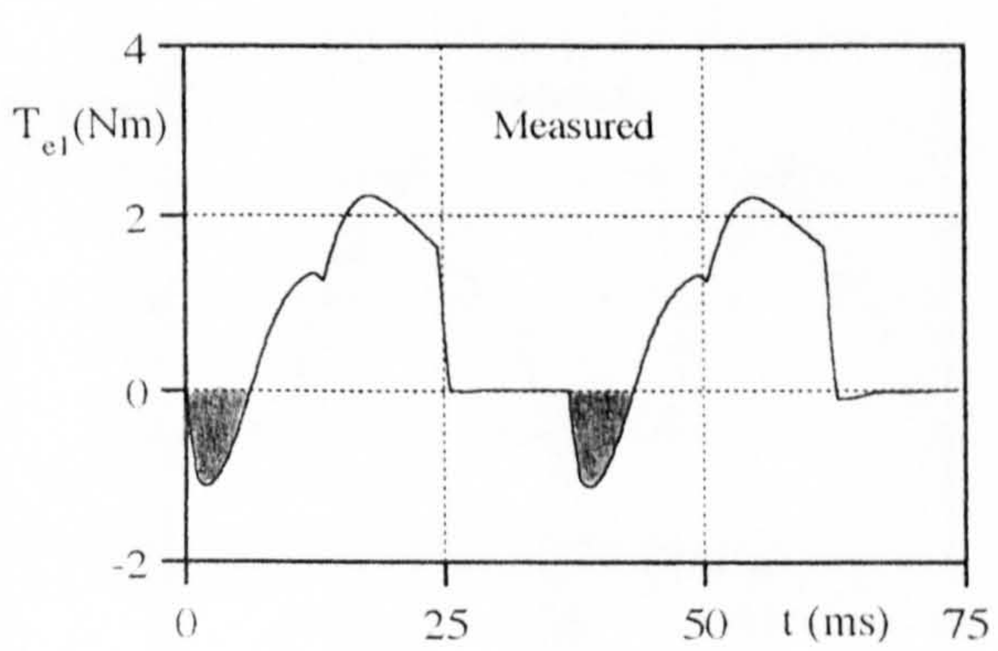

c

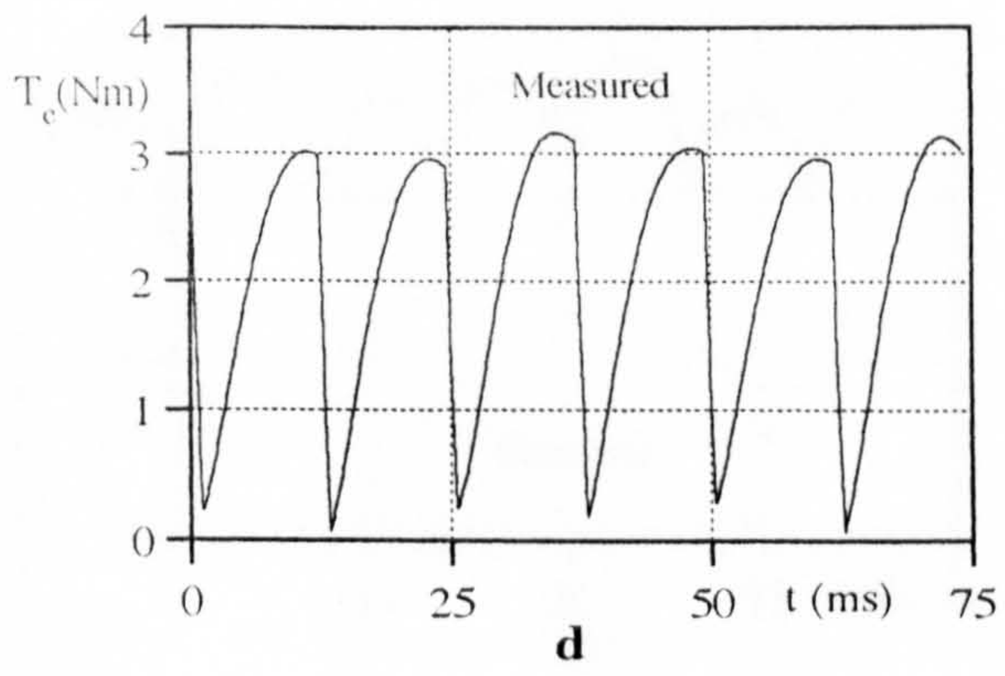

d

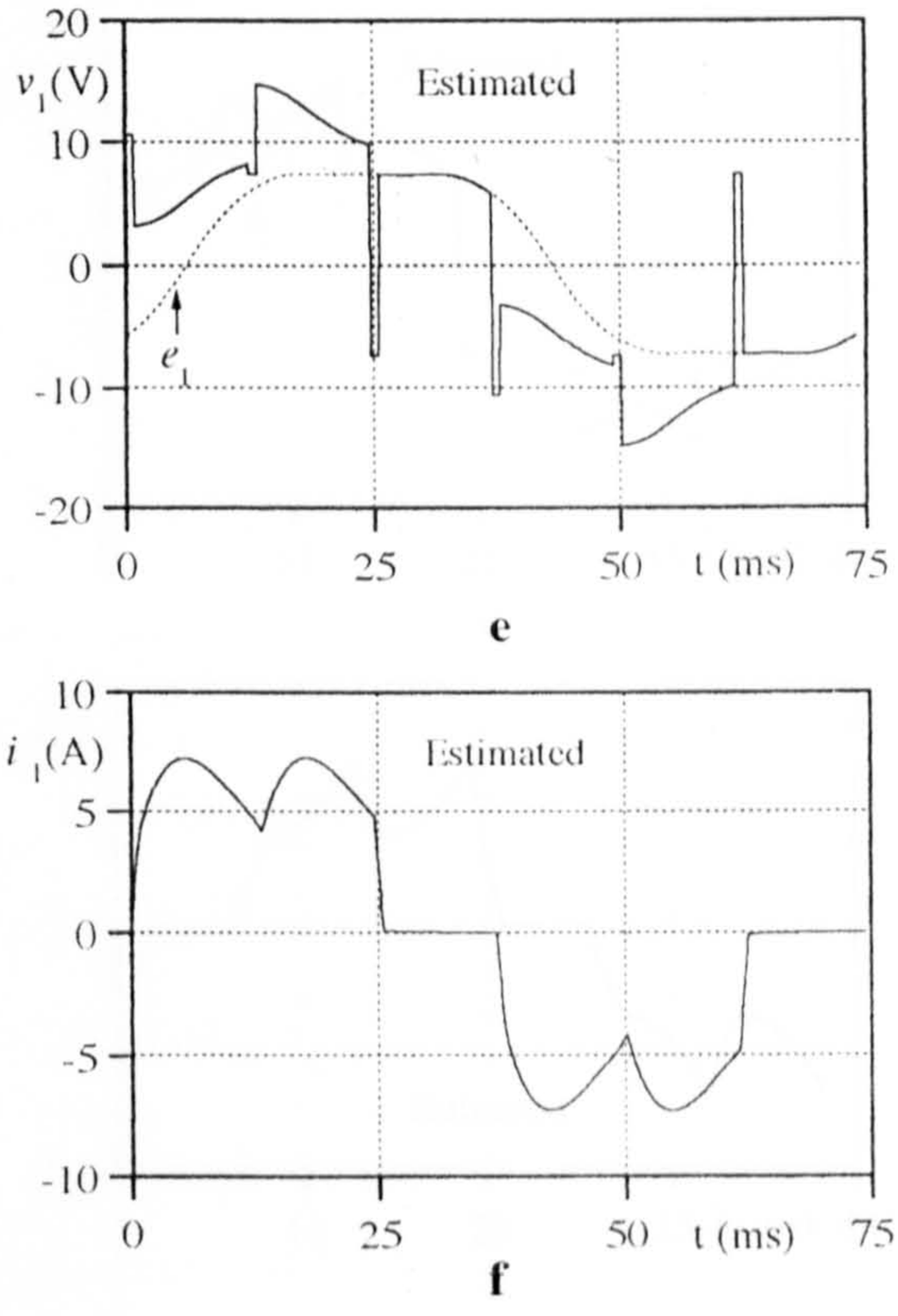

e

f

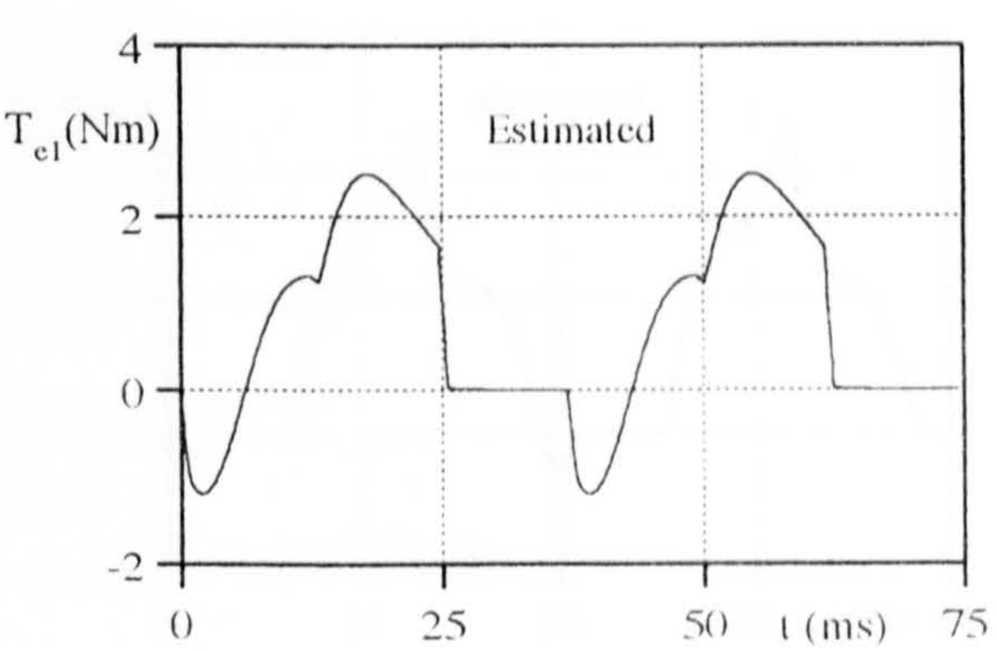

g

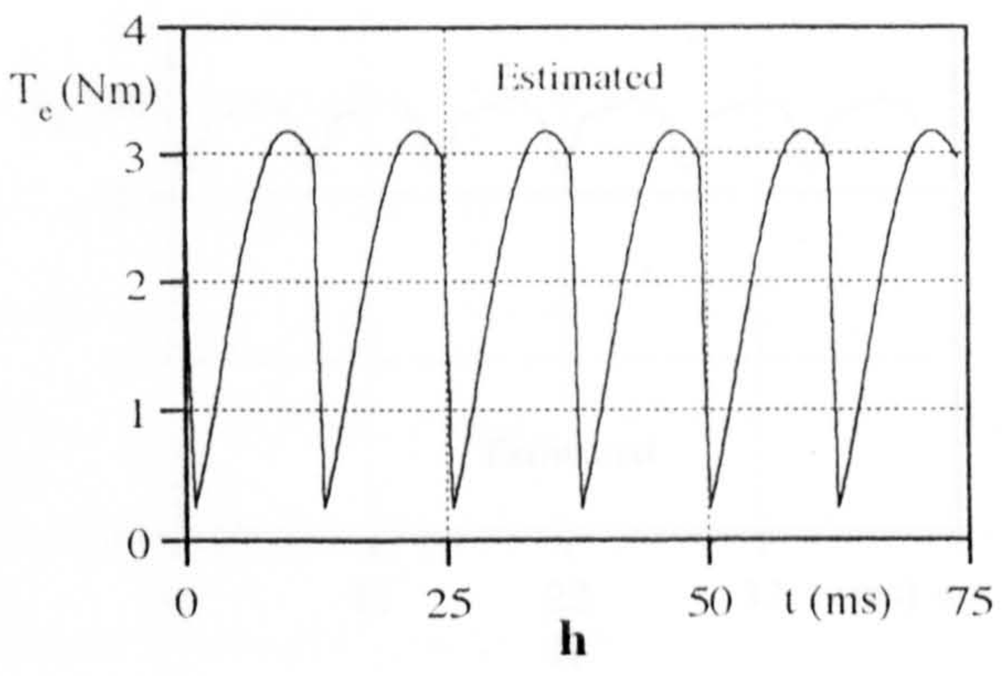

h

Figure 4.14 A set of measured and estimated waveforms, no current control, V_{dc}= 23V, n= 202.7 rpm, 60° phase advance.

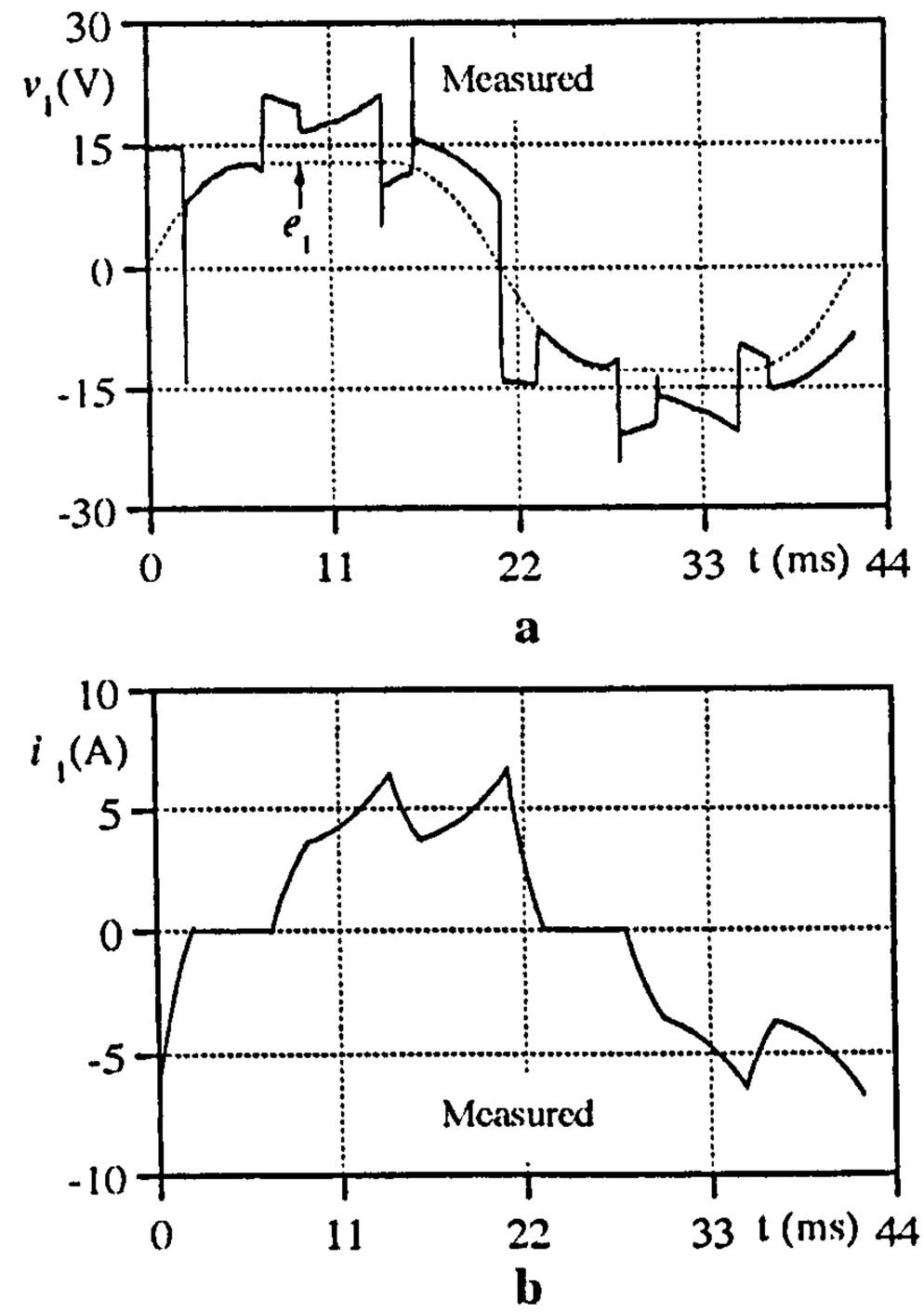

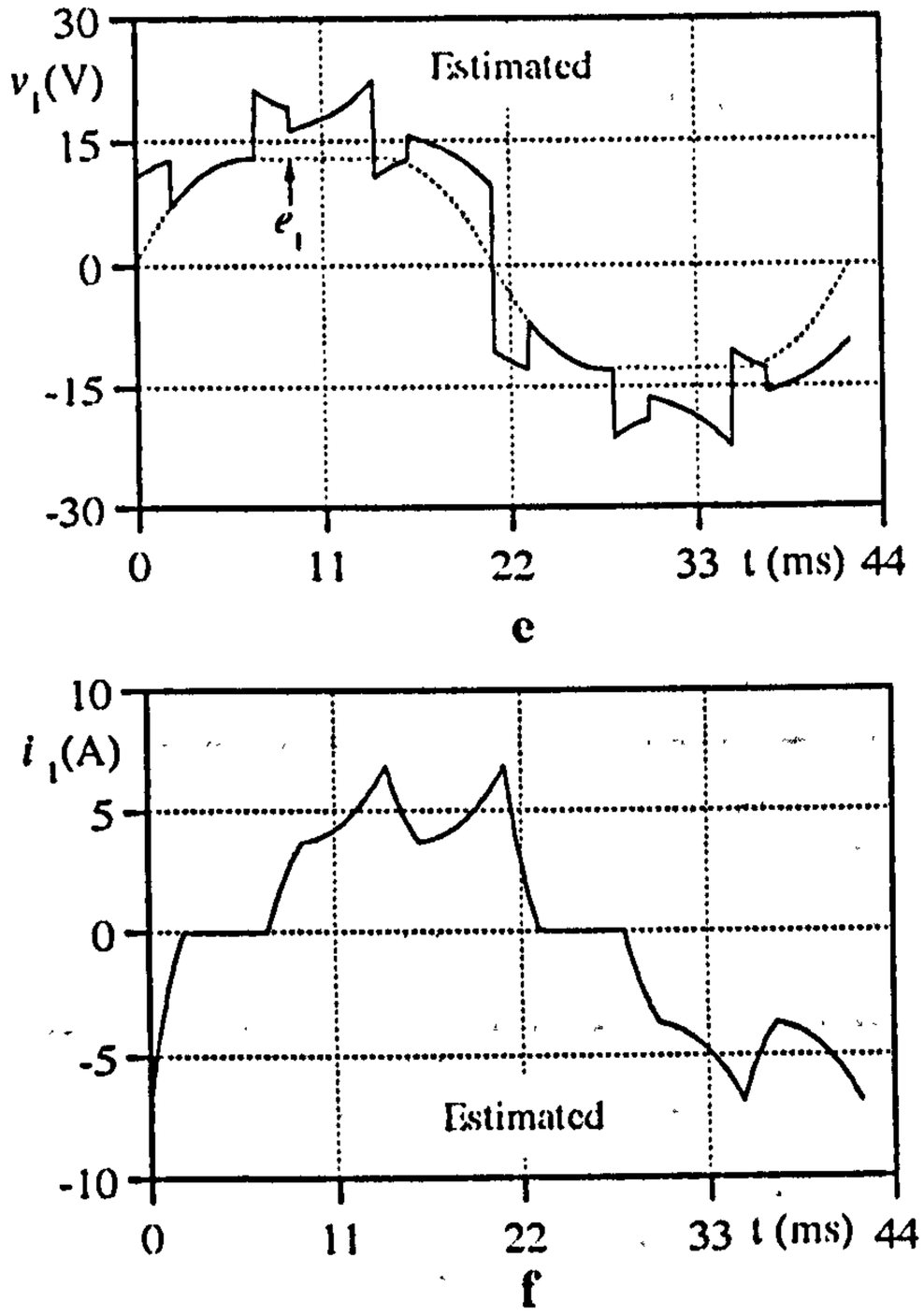

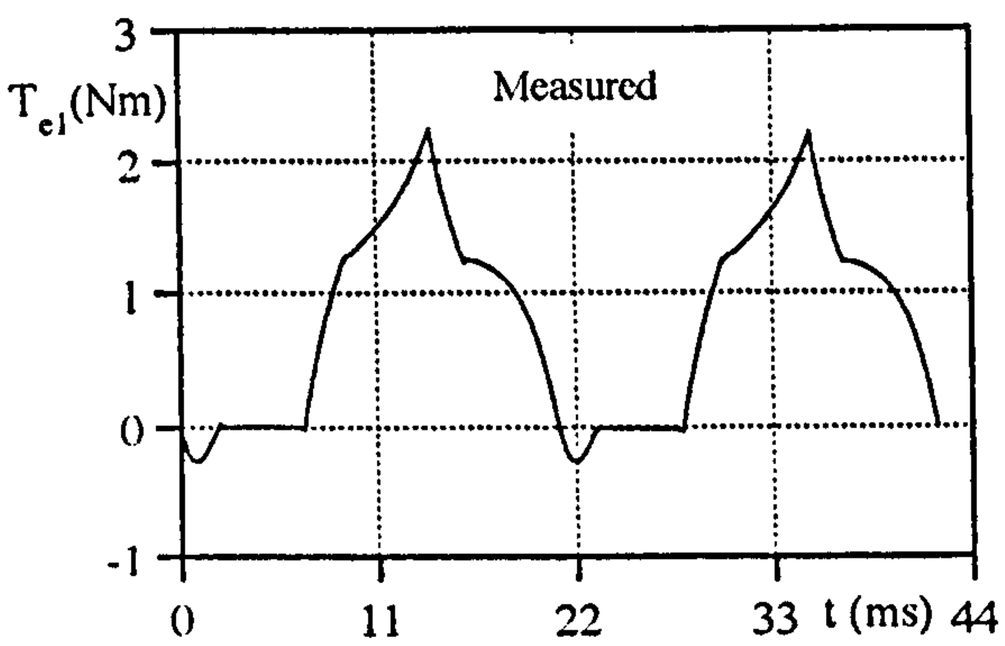

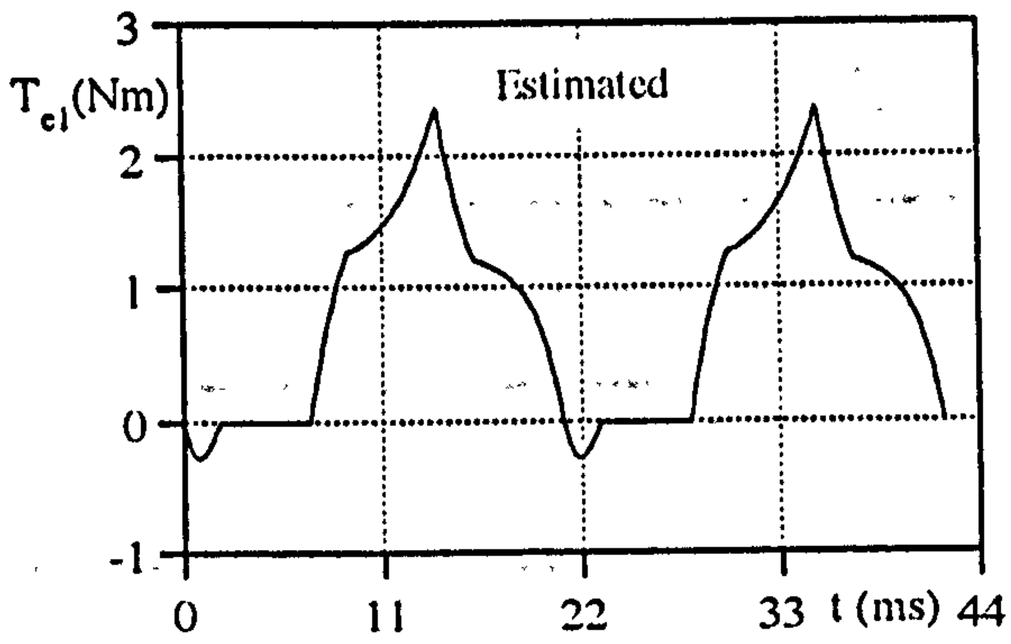

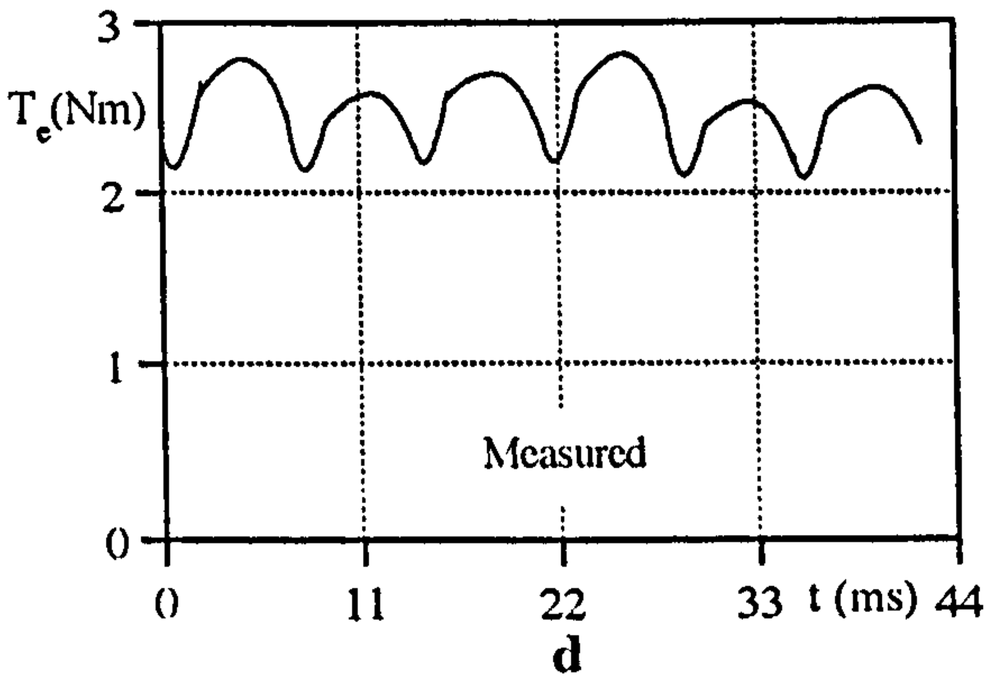

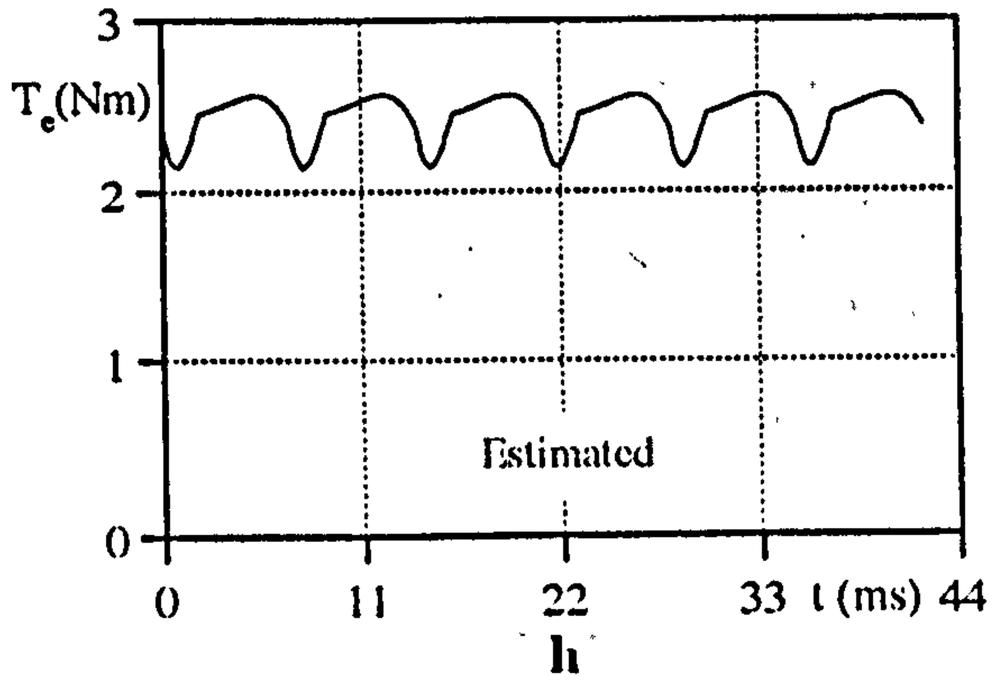

Figure 4.15 A set of measured and estimated waveforms, no current control, V_{dc}= 36V, n= 356.38 rpm, 30° phase delay.

Apart from 30° phase advance operation (**Fig.4.13**), 30° phase delay operation produce negative torque due to the falling part of the line current after the 120° electrical conduction limit. However, the torque ripple rate reduced since the single phase torque profile differs.

Table 4.2 The summary of average torque and torque ripple estimations representing some typical operations.

		T_{ave} (Nm)	TR %
No current control No phase advance (**Fig.4.10**)	Estimated from the measured waveform	3.296	10.227
	Estimated from the simulation	3.455	10.659
±1A hysteresis current control No phase advance (**Fig.4.11**)	Estimated from the measured waveform	3.206	13.801
	Estimated from the simulation	3.236	16.740
±0.5A hysteresis current control No phase advance (**Fig. 4.12**)	Estimated from the measured waveform	3.201	9.949
	Estimated from the simulation	3.241	11.393
30° phase advance No current control (**Fig. 4.13**)	Estimated from the measured waveform	3.507	18.329
	Estimated from the simulation	3.520	19.936
60° phase advance No current control (**Fig. 4.14**)	Estimated from the measured waveform	2.045	46.520
	Estimated from the simulation	2.192	44.260
30° phase delay No current control (**Fig. 4.15**)	Estimated from the measured waveform	2.494	7.822
	Estimated from the simulation	2.440	5.544

Although, the torque-speed (T-n) plot is created for a speed control strategy, measured T-n characteristics of the drive can also be used to determine how well the torque predictions within a wide speed range (from no load speed to the current limit) of the drive. In **Fig. 4.16**, the measured average shaft torque was compared with the estimated electromagnetic torque from no phase advance angle up to 40° phase advance angle operation.

To determine the T-n relationships, the test motor was loaded using a DC generator (as explained in **Section 4.1**) at constant DC rail voltage (59V), and variations (**Fig. 4.16a**) were compared with those obtained from a computer simulation (**Fig. 4.16b**). The average torque in the simulation was estimated by integrating the instantaneous electromagnetic torque within an electrical period.

The comparison of T-n characteristics which were given in **Fig. 4.16** shows good agreement at higher speeds with increasing errors at lower speeds. The inverter model used does not allow variable voltage drop with current level which may be significant in non-ideal inverter switches. So that when the small losses and variable voltage drop in the power switches are taken into account, the difference between the two results should not be considered excessive as discussed earlier in **Chapter III (Fig.3.11)**.

Fig. 4.17 illustrates the variation of the motor torque at constant speed as a function of phase advance/delay angles. The experiment was performed by changing the load to reach predetermined constant speed (410 rpm and 460 rpm) while observing current control limit at constant DC rail voltage (39V). The same procedure was repeated at different phase advance and delay angles.

As can be seen in **Fig. 4.17**, the variation of motor torque at constant speed operation has two critical points on the profile. Maximum torque can be achieved at 50° phase advance operation. From **Fig. 4.17**, it can be seen that the simulation provides a fairly good representation of the actual drive except near the critical operating point.

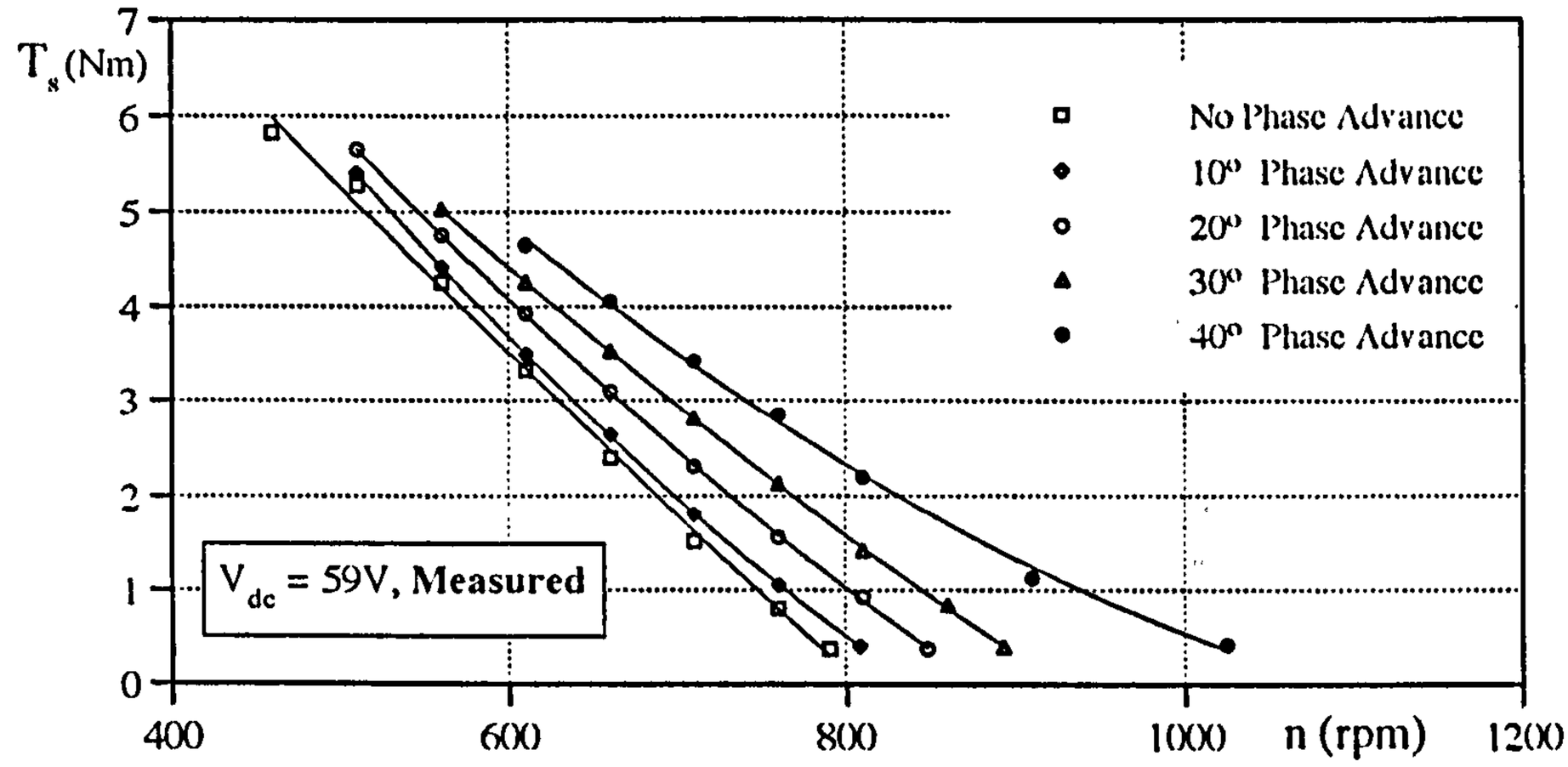

a

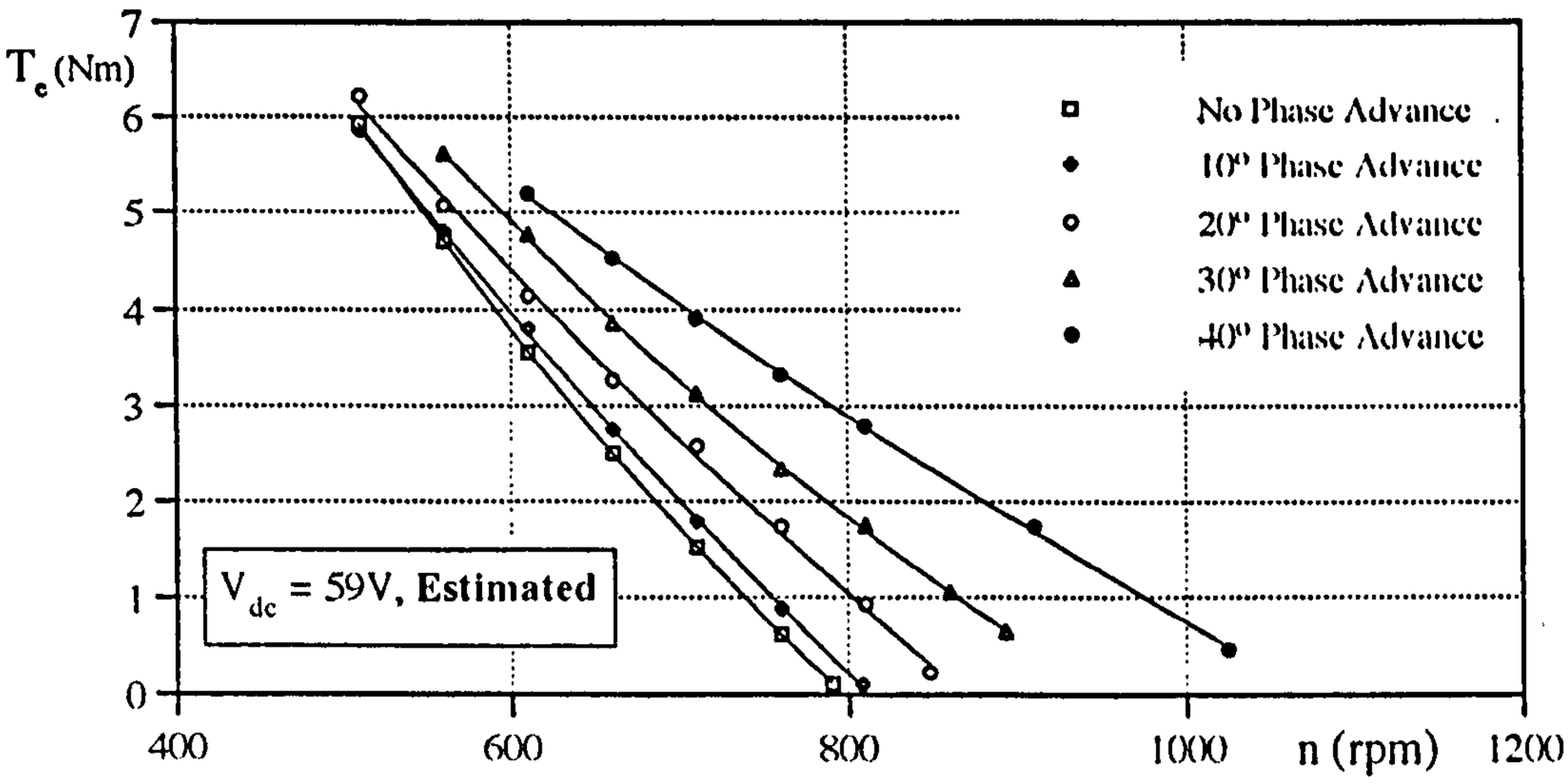

b

Figure 4.16 Typical average Torque-Speed curves for different values of the phase advance angles, no current control, V_{dc} = 59V.

a) Measured average shaft Torque-Speed curves

b) Estimated average electromagnetic Torque-Speed Curves

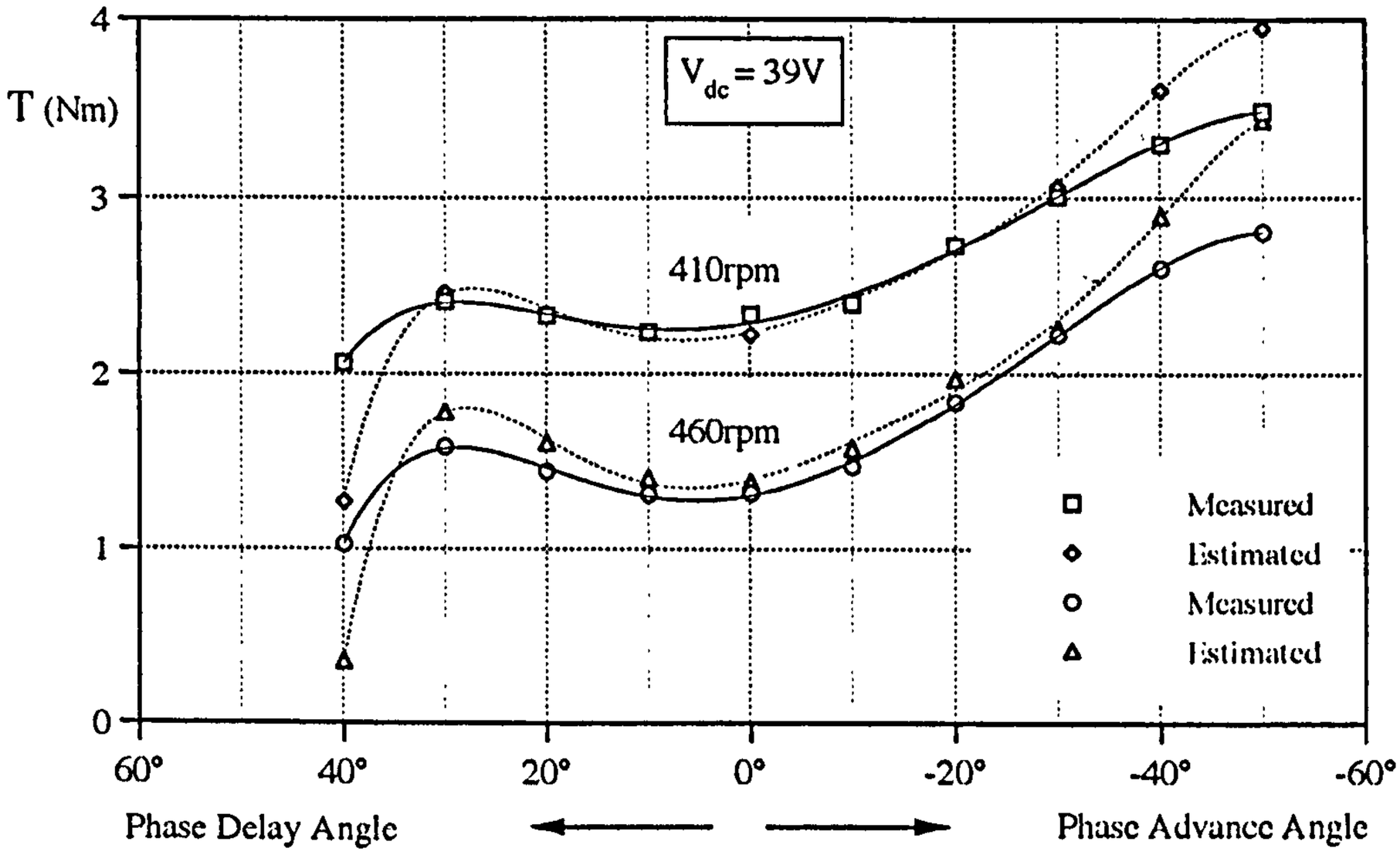

Figure 4.17 Torque versus phase advance/delay angle at two motor speeds.

4.4.2 The Transient Results

As an example of the numerical simulation, the dynamic performance of a brushless PM motor drive is examined in the case of free acceleration with load (proportional with the motor speed), and low inertia load as described in **Section 4.4**. The load torque in the simulation can be expressed as a function of the square of the per-unit motor speed,

$$T_L = T_{LO} + T_{L2}\, n_p^2 \qquad (4.16)$$

Here T_{LO} is the constant part of the load torque and T_{L2} is the speed dependent part of the load torque. The n_p is the per-unit value of the motor speed and is equal to n/n_s, where n_s is the desired steady-state speed of the motor.

Fig. 4.18 shows the variation of some motor characteristics when the motor started up from standstill to a speed of 530 rpm with steady-state DC rail voltage 50V. The electromagnetic torque Te(t) produced by the motor has been described in **Eq. 2.9**.

In practice, the maximum motor torque is limited by the inverter ratings. For a specific inverter rate, the peak torque should be large enough to accelerate the motor in any state of load T_{LO} and inertia J. In the actual system, the commanded current setted to the maximum level (10A) with the hysteresis bandwidth ±0.35A. The measurements are taken by keeping the initial resistive load constant which was connected to the terminals of the PM machine via a three phase diode rectifier (**Section 4.4**). Since the current demand was set to a maximum, and DC rail voltage was kept constant (except transient voltage drop), after starting of the motor, the current profile reduces while the speed increases.

Fig. 4.18b illustrates the transient speed characteristics measured by a *Sensor Technology Torque Transducer*. The actual transient speed profile gives an idea about acceleration time of the motor which may also be used to test the measured inertia of the system. As seen in the actual speed waveform, since the speed measurement is not as accurate as the position measurement (by a resolver), fluctuations have been observed. Discontinuous current conduction (120° inverter operation) may be another source for the speed fluctuations. The flat part in **Fig. 4.18** is due to initial measurement error at low speeds in the actual setup which was measured at about 50 rpm.

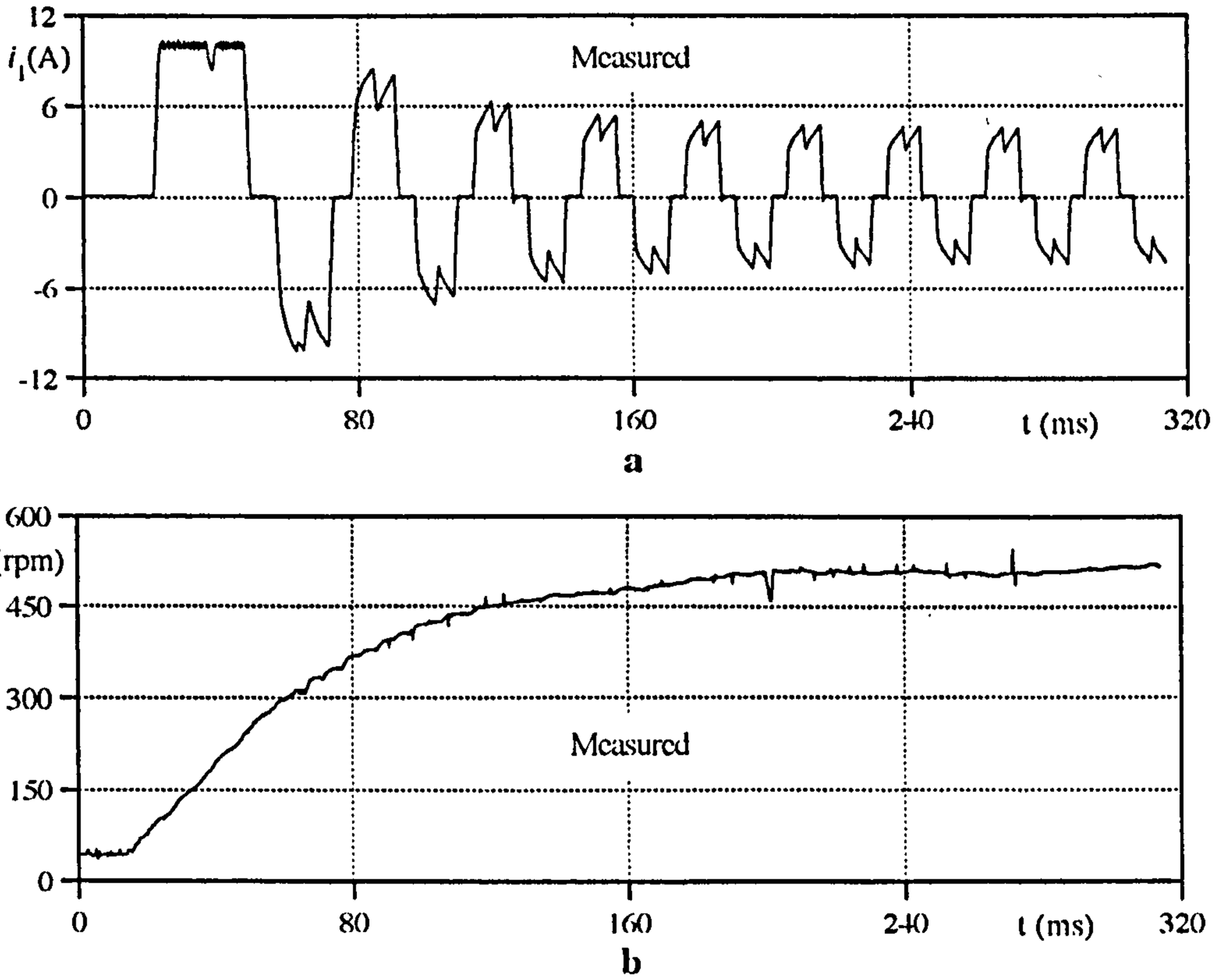

Figure 4.18 Measured transient waveforms, no phase advance, acceleration with load, V_{dc}=54.6V (at standstill), V_{dc}=50V (steady-state).

As seen in **Fig. 4.18**, during the starting, a rather violent transient occurs in the waveforms of both the electromagnetic torque (**Fig. 4.18c**) and the measured shaft torque (**Fig. 4.18d**). The electromagnetic torque was measured from the actual system assuming sinusoidal back EMF variations, and the instantaneous shaft torque is observed by the torque transducer mentioned earlier.

In practice, mechanical systems usually yield nonlinear problems. The motor is linked via a torque transmission mechanism to a mechanical load with high or low inertia, and vibration problems due to these changes and inertias arises.

The following vibration characteristics [*Dote*, 1990] should be considered in the mechanical system:

Natural vibration frequency is variable due to the load variation and mechanism attitude changes.

Multi-vibration frequencies are observed due to interactions among mechanisms.

Fig. 4.19 shows a typical interaction between the produced torque and the load torque. It is observed in **Fig. 4.19** that imperfect mechanical connections and speed dependent vibrations may cause torque ripple on the shaft, and may be cancelled out for some operating conditions. **Fig.4.19b** demonstrates a smoother shaft torque profile with the speed of 465 rpm and current controlled operation. In this mode of operation, it is found that , while the electromagnetic torque ripple is 14.62%, the shaft torque ripple is reduced down to 4.72% by the interaction of the mechanical vibration on the system inertia.

The simulation results corresponding to the operation in **Fig. 4.18** are shown in **Fig. 4.20**. Comparison of the computed results with the experimental results of **Fig. 4.18** demonstrate that it is possible to achieve good agreement in the simulation even under transient operation.

Fig. 4.21 and **22** are included to illustrate transient effects caused by phase advance operation (30° electrical). As illustrated in **Fig. 4.22**, the simulated drive is operated in a transient mode of operation. The motor accelerates from standstill up to constant speed. The actual current, the speed, and the electromagnetic torque (with modelled load torque) are shown when the DC rail voltage is 46.5V constant.

Close observation of **Figs. 4.21-22** again demonstrates that good correlation between computed and experimental results is possible. From the comparison of transient simulation results with test results, it is noted that, since the model takes the total system inertia (J=0.0097 Kgm^2) into account, the starting time (the time to reach constant speed) is slightly different. This is mainly due to imperfect inertia measurement and the assumption of zero friction in the system.

From **Fig. 4.18** and **Fig. 4.21**, it can be seen that no phase advance during starting provides slightly faster response, and better shaft torque profile. It has to be emphasised here that, in order to obtain the same acceleration profile and equal number of electrical periods of the current waveform during starting, the load parameters have been adjusted for each test.

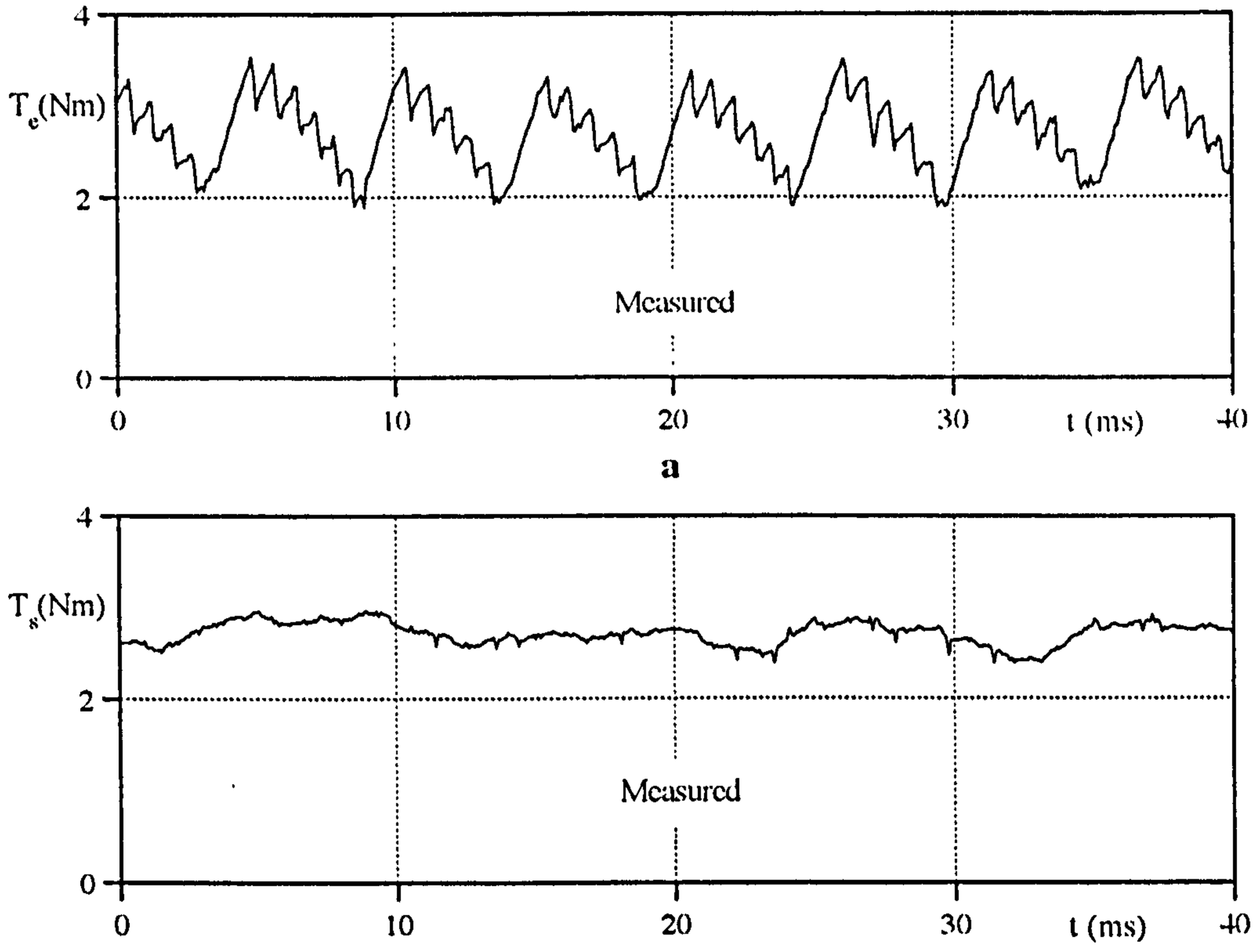

Figure 4.19 Measured torque waveforms showing the effect of torque interaction, n=465 rpm, $\Delta h = \pm 0.35A$.

Agreement between measured and predicted performance of transient operation is very much dependent on the accuracy of the motor and drive parameters, specifically, the inertia of the system and variable voltage drop on the DC rail which can not be modelled easily.

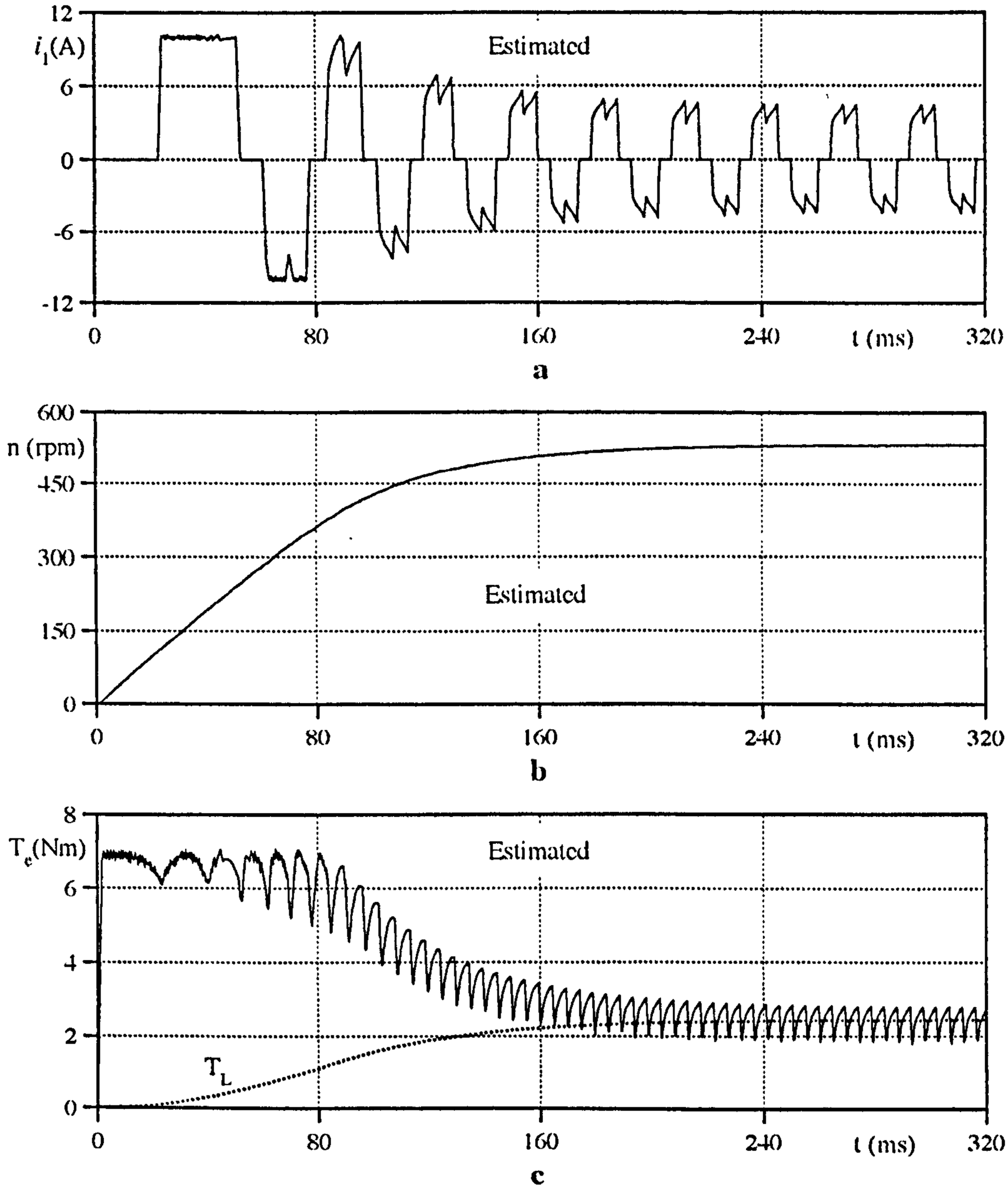

Figure 4.20 Corresponding results to **Fig. 4.18** from the simulation showing the current, the speed, and electromagnetic torque.

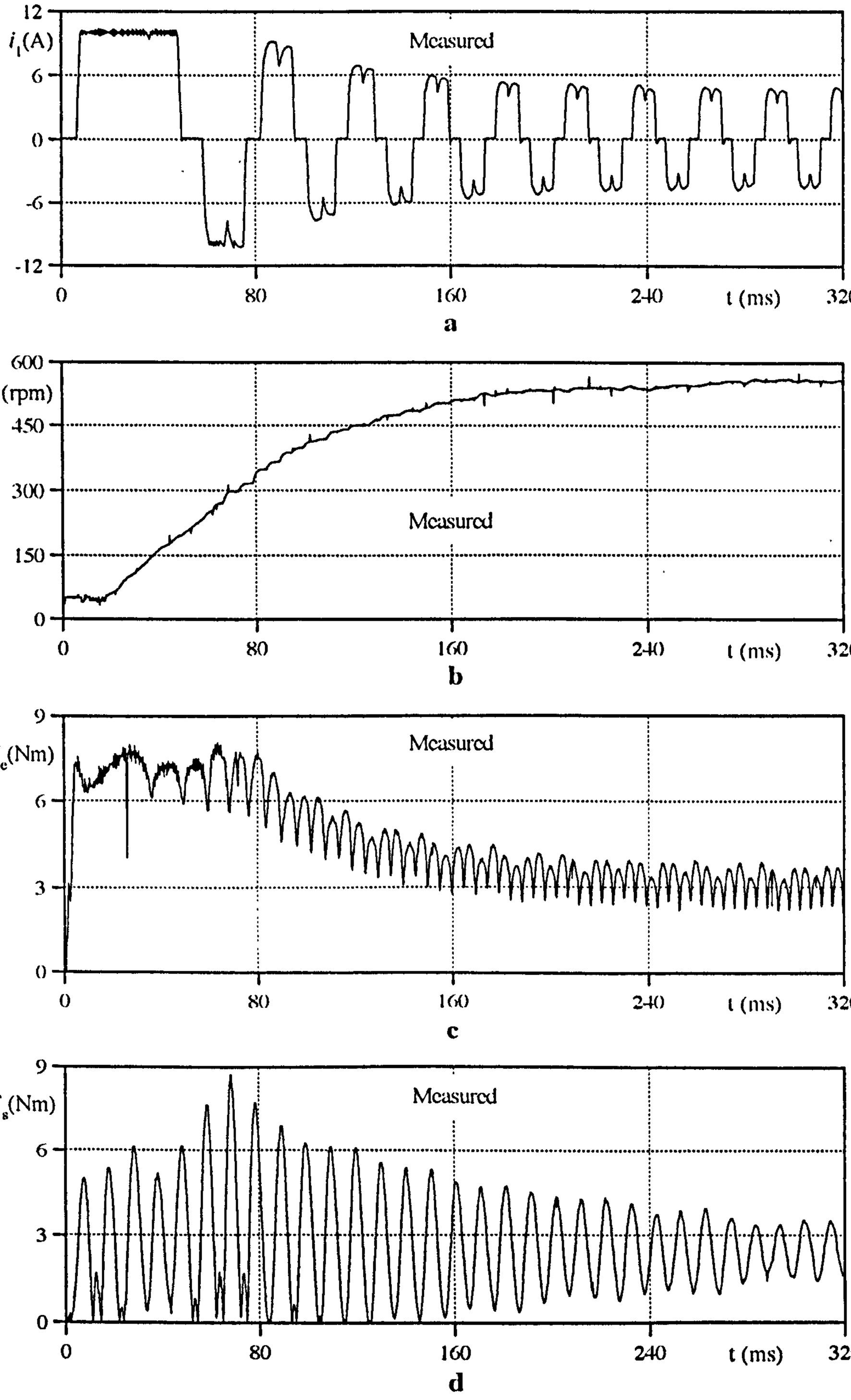

Figure. 4.21 Measured transient results with the drive operating at 30° electrical phase advance.

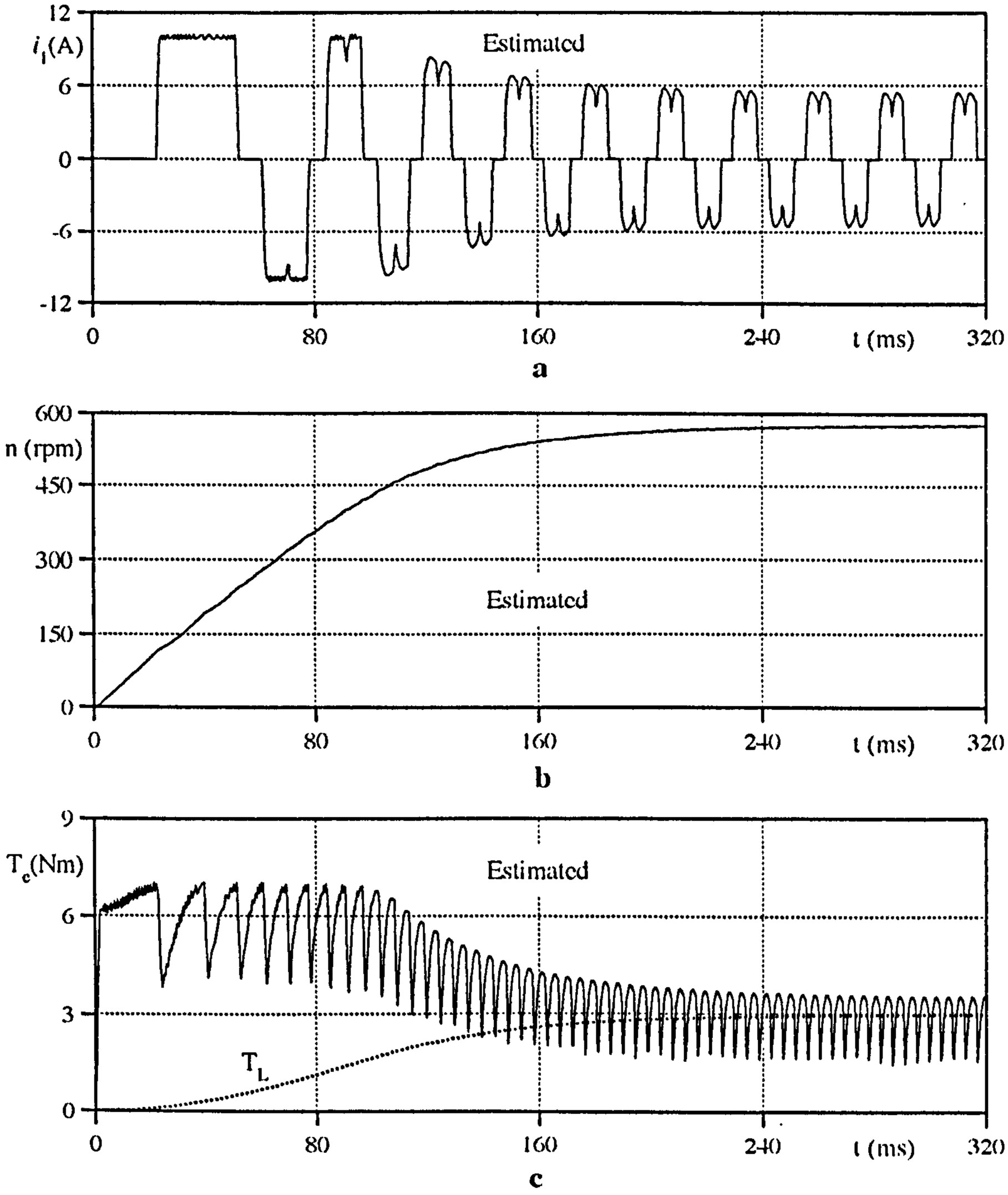

Figure 4.22 Transient results from the simulation corresponding to **Fig. 4.21.**

4.5 CONCLUSIONS

A computer simulation model for prediction of the performance of brushless PM motors was presented. As seen, a three-phase brushless PM motor was considered for numerical simulation. The developed mathematical model in the previous chapters was used, and the model was formulated entirely in the natural **abc** frame of reference, which allows direct comparison of the simulation and corresponding experimental results.

It is important that the differential equations accurately represent the system. However the simulation results are only as valid as the model which is used to generate them.

Although some effort may be required at the programming stage, numerical computer simulation offers a great deal of flexibility. The equations and diagrams are put into a convenient form for the simulation and future developments and library modules. One of the effects not included in the simulation program was the off-times of the power transistors (IGBTs). Investigation of the delay time shows that the IGBTs used in the inverter have a maximum 150ns delay time. Comparing with the usual time step in the simulation (2μs), the delay time can be ignored.

Due to the large number of available motor sizes and drive ratings, it would be a large and expensive task to obtain experimentally T-n characteristics and phase current variations for all possible operation conditions including the dynamic operation. The computer package can be an excellent tool for simulating the complete drive without implementing the actual system.

The results are an illustration of different characteristics of the drive for the 120° current conduction mode. The demonstrated results shows the close agreement between the results of the simulation model and corresponding experimental data from the brushless PM motor drive. Therefore, these results presented in this chapter clearly demonstrate the ability of the developed model which includes quasi-trapezoidal (Fourier approximation) back EMFs to accurately predict both steady-state and dynamic performance of the brushless PM motor drive under investigation.

The simulation is also a useful tool for simulating the shaft position sensorless operation algorithm which will be explained and analysed in the next chapters.

CHAPTER V

NOVEL POSITION SENSORLESS OPERATION:
Theory and Simulation

5. INTRODUCTION

A brushless PM synchronous motor with a rotor cage can be started without any information on the rotor position because it can be operated initially as an induction motor. However, a position sensor is required for any other brushless PM motor to synchronise the phase excitation pulses to the rotor position.

As described in the previous chapters, the whole set-up of brushless PM motor drives is basically equivalent to an orthodox brush type DC motor. In other words, a brushless PM motor drive is an inverted conventional DC motor with the mechanical commutator replaced by the controller and with excitation replaced by the permanent magnets. In brushless PM motor drives, the main function of the drive circuits is to synchronise the PM motor's current to the rotor position so that the stator back EMF is maintained at a fixed angle referred to the rotor. Since the inverter switching frequency is derived from the rotor, the motor cannot lose synchronism. If there is no speed feedback on the drive, it slows down when loaded.

While the sinusoidal current excited BSPM motor needs continuous position information, 120° inverter operated brushless PM motors require the position signals at interval of 60° electrical. In fact, a 120° inverter operated brushless PM motor drive is equivalent to a conventional DC motor with a number of commutator segments equal to **6p**, where **p** is the number of pole pairs. When a similar approach is applied to the sinusoidal current excited BSPM motor, continuous position information makes this type of drive similar to the DC motor with an infinite number of segments.

However, in practice, the shaft position sensing devices have limited resolution and operating characteristics. Besides the need to accurately determine the rotor position, the shaft position sensor must operate under the same environmental conditions where the motor is used.

Basically, the control system in PM motor drives requires position information for two reasons:

1. To indicate to the control circuit which position the motor is at and to switch on the correct phase or phases.

2. Although servo applications use a separate velocity sensor, a speed signal can also be delivered from the position information.

The position sensor constitutes a substantial fraction of the total drive cost and tends to reduce the drive reliability. For small drives of less than one **hp**, a position sensor may add a considerable cost to the system [*Krishnan and Ghosh*, 1989]. For applications, such as air conditioning [*Iikuza et al*, 1985], where the motor is built in a completely sealed housing, direct position sensing may increase the number of leads while reducing reliability in high temperature and refrigerant environments. For small motors as those

used in computer peripherals [*Kuo* and *Butts*, 1982], and compact headphone stereo players [*Akiyama et al*, 1990], the space limitation might make difficult the using of mechanical shaft position sensors.

Some of the drawbacks of using a mechanical shaft position sensor may be summarised as below:

a) Number of connections between the motor and control system increases.

b) Interference increases

c) Limitations in accuracy of the sensor because of environmental factors such as temperature, humidity, vibration.

d) Additional system cost (including sensor and electronic circuit) which is most meaningful when compared with the motor cost and a given level of resolution of the sensor [*Boyes*, 1980].

e) All shaft position sensors present a certain degree of static and dynamic friction to the input shaft, and the moment of inertia adds to the motor shaft inertia.

f) Additional space requirement for the position sensor in the motor housing.

Because of these drawbacks, shaft position sensor elimination techniques have received attention. The shaft position sensorless operation of PM motor, stepper motors and switched reluctance (SR) motors has been described by many earlier researches. However many of the methods work for some PM motors, but not all. Recently, there has been much interest in techniques for eliminating the rotor position sensing device, and deducing position by analysing the motor's voltage and current waveforms.

This chapter describes an alternative method of position detection in switched brushless PM motors based on the terminal voltages and the line currents with the aim of estimating the winding flux linkages. **Section 5.1** summarises the earlier developed methods of shaft position sensorless operation, and classifies them by giving brief explanations. The mathematical basis of the proposed method is discussed in **Section 5.2**. **Section 5.3** gives the block diagram of position estimator, and presents the details of the algorithm in terms of mathematical equations. In the subsections of **Section 5.3**, approximated quantities, which are used in the simulation, are compared with the directly or indirectly measured waveforms. The section also discusses the algorithm's key features. In order to verify the algorithm and show the effect of special adjustments, the estimated results using the terminal quantities of the drive which was simulated in **Chapter 4** are presented in **Section 5.4** with the flow chart of the position estimator. **Section 5.5** is the conclusions which are drawn from the new method.

5.1 METHODS OF POSITION SENSING IN THE BRUSHLESS PM MOTOR DRIVES

5.1.1 Measuring Rotor Position with Attachments on the Motor Shaft

As described earlier in **Chapter II, Section 2.4.1.1**, the rotor flux position in brushless PM motors can be obtained from some form of mechanical position sensor. The conventional ways of rotor position sensing (such as using resolver, encoder or optical devices) have been described in the same section. To avoid repetition they are not discussed here.

The rotary sensors attached to a brushless PM motors, in combination with an appropriate control circuit, detect the position. However, in spite of the sensorless operation methods, the rotary sensors still cover a wide range of applications in the industry, and the selection of the sensor is mainly defined by the type of application and desired performance from the drive. Detailed information about particular mechanical sensor devices can be found in the manufacturers' catalogues.

5.1.2 An Overview of Sensorless Operation Methods in Brushless PM Drives

Position sensorless control of brushless PM motors, which eliminates the direct shaft position sensors, has been studied by many researchers, and a number of schemes have been suggested, using either special arrangement or monitoring of the motor terminal quantities. Although dividing lines among the sensorless methods, and classification criteria may vary, basically the reported works so far can be divided into subsections, such as the terminal quantities directly used or analysed to evaluate the rotor position. In this work, the sensorless operation methods are classified as follows:

a) Evaluation or estimation of back EMF

<u>DIRECT BACK EMF DETECTION</u>

Initially, the phase voltage sensing method was applied by *Le-Huy et al* (1980) to the synchronous motor drive. The most popular sensorless operation method is the direct back EMF sensing method. The method was also applied to many industrial applications including the disk drive [*Kuo and Butts*, 1982], the compact stereo player [*Akiyama et al*, 1990], and the room air conditioner [*Endo et al*, 1983, and *Iikuza et al*, 1985]. Moreover,

availability of the commercial integrated circuits (see **Chapter II, Section 2.6**) increases the popularity of the method as it is easy to implement.

As shown in the earlier chapters, the 120° inverter operated brushless PM motor is only energised for 2/3 of each electrical period, and ideally there is always one phase which is not energised. Direct detection of the back EMF is based upon the fact that the open-circuit voltage across the phase winding is equal to the back EMF. Therefore , during no phase advance operation (see **Fig.4.10**), the zero crossings of back EMF signals can be detected from the motor terminals and used to commutate the related phases of the motor.

During current controlled operation, the brushless PM motor has important transients in the phase-to-star point voltages (see **Fig.4.11a** and **4.12a**). Since the amplitude and frequency of this voltage varies over a wide range as a function of motor speed and high di/dt at the instants of switching in the drive, more complex signal processing (such as filtering) is required in order to obtain usable signals. However, the filtering can introduce a phase shift which may be significant at high speed operation. Moreover, for some operation conditions (such as high speed, uncontrolled), the commutation duration may increase up to the commanded current open-circuit interval (30° electrical for 120° inverter operated drive) causing continuous current conduction. This makes the back EMF measurement impossible.

In the case where the motor speed is low, and therefore the back EMFs are small, it is hard to distinguish the measured values from noise.

Back EMF sensing is an elegant method of position detection. However, it suffers from the disadvantages summarised above, and requires:

1. Discontinuous current controlled operation (such as 120° inverter operation).

2. Sufficiently small current decay time during phase commutation, so that the open-circuit condition is met prior to the zero crossing of the back EMF.

3. Sufficiently high speed to distinguish the zero crossings of the back EMF.

4. Adequately clear zero crossings during the OFF period of each phase.

Antognini and Veignat (1990) investigated the improvements offered by a technique of self synchronisation for brushless PM motors based on direct monitoring of back EMF signals when all the motor phases are energised. However the method can be applied only to motors which have two phase with four windings and constant winding inductance.

ESTIMATION OF BACK EMF

The position can also be estimated by an analog circuit or numerical calculation. The main idea in this method is the reconstruction of the back EMF by using the voltage equation of the motor. Recalling **Eq.2.8**, and rearranging for a single phase

$$e = v - Ri - L\frac{di}{dt} \qquad (5.1)$$

Reconstruction of the back EMF involves either simulating the right hand side of **Eq.5.1** with operational amplifiers [*Kuo*, 1982] or by solving the equation [*Watanabe et al*, 1987]. The operational amplifier method requires

matching of gain coefficients in the reconstruction circuitry with the accurate motor parameters, and an extra resistor is need in the phase to measure the actual current.

In the method, the terminal voltage and line current are measured directly. Since the method is sensitive to changing winding resistance, the effect of temperature should be considered in the value of the winding resistance. The term di/dt involves the determination of the line current derivative and is very much dependent on measurement noises.

The method which was explained by *Antognini* (1985) is based on high frequency sampling of the phase currents to estimate the back EMF. This technique offers a particular immunity to the switching noise.

b) Third harmonic voltage detection

In the star connected brushless PM motors, the third harmonic voltage can be measured between the star-point and an artificial star-point created by three high value external resistors which are connected to the motor terminals. It is clear that the method needs a reasonable amount of third harmonic voltage. Similar to the direct back EMF sensing, since the amplitude of third harmonic is proportional with motor speed, it is difficult to sense the zero crossings at low speeds. The amplitude of third harmonic is also directly related to the motor type.

Such a voltage defines 6 zero crossings in the three phase motor. However, the zero crossings should be synchronised with the zero crossings of the actual back EMF variation to produce proper commutation signals.

c) By monitoring current or calculation of the phase inductance

Acarnley et al (1985) first suggested monitoring the current waveform to detect the rotor position in stepping and switch reluctance motors, and applied the technique successfully to variable reluctance step motors. The fundamental idea behind this technique is that the rate of change of current in a phase depends on the incremental inductance which is rotor position dependent. *Kulkarni and Ehsani* (1992) have proposed an elimination technique for the position sensor of an interior PM synchronous motor drive by calculating the phase inductance which is a function of the rotor position.

In order to overcome the problems associated with phase shift in the direct detection of back EMF zero crossings, the phase current sensing method is proposed by *Lin et al* (1989).

The accuracy of the method of estimation of winding inductance is compromised at higher currents and speeds by resistance and back EMF respectively.

d) Injecting diagnosis signal to the stator windings

The method proposed by *Binns et al* (1991) uses a PWM carrier frequency and inductance bridge to measure the rotor flux path reluctance. The method operates on a bridge principle by monitoring the inductance difference in two phase, and is sensitive to small variations in reluctance. A starting method is also proposed which uses the same detection circuit, and requires the microprocessor to drive the inverter in a different mode from normal running.

e) Observer methods

An observer reconstructs a physical variable (such as position) which is not directly measurable. The methods classified under this section basically use the phase voltages and the line currents to perform calculations to derive the rotor position.

One successful application is implemented by *Wu and Slemon* (1991). They described a control method for brushless PM motor drives without use of a shaft position sensor. The method uses two line-to-line voltages and two stator currents to produce the stator flux linkage space vector (in analog form). The drift introduced by analog circuits is compensated by a program, and it needs an open-loop starting program to accelerate the motor up to a limit frequency (1Hz, 30rpm)

The observer methods proposed by *Dhauadi and Mohan* (1990), *Liu and Stiebler* (1990), use the Kalman Filter technique to estimate the speed and position from measurements of stator voltages and currents. The methods need a motor which is **dq** transformable.

In the paper by *Spee and Lang* (1992), a discrete-time observer based controller and adaptive controller are developed for sensorless operation of a PM synchronous motor. *Furuhashi et al* (1992) have also proposed and studied an estimation technique for position and velocity sensorless control of brushless PM motors using an observer. However, the method is not satisfactory where the velocity of the motor is small.

Jones and Lang (1989) investigated a state observer for surface mounted brushless PM motor which reconstructs the electrical and mechanical states by measuring the motor currents and voltages. However, the observer is

sensitive to the flux linkage of a permanent magnet, and it estimates the states during steady-state operation.

f) By using a special windings or electromagnetic devices

A number of schemes have been suggested, using either special laminations with embedded search coils, or the addition of search coils on the stator teeth of the motor.

The method proposed by *Binns et al* (1990-A,B) requires modification by the addition of search coils on the stator teeth of the motor, and suitable additional cabling is required between the motor and controller. Induced voltages in the special windings are in phase with back EMF, and have no commutation transients.

Using an electromagnetic device to sense the rotor position is introduced by *Hesmondhalgh and Tipping* (1990). The method provides an alternative to other position sensing methods. The electromagnetic device consists of pickup coils around a special stator which is made of magnetically nonlinear material. The pickup coil is excited by a high frequency sinusoidal current. In principle, the device detects the phase change of the second harmonic component of induced voltage in the pickup coils. Construction difficulties, volume and high cost are the disadvantages of the method.

g) Monitoring switching states in the inverter

The method is reported by *Ogasawara and Akagi* (1991) where the ON/OFF states of the inverter switching devices is used for the rotor position estimation. The method is based on the motor with a trapezoidal back EMF. The position information is given on the basis of the conducting state of

free-wheeling diodes in an open phase over a wide speed range from 45 to 2300 rpm.

Another method developed by *Matsui and Shigyo* (1992) is also for position sensorless brushless DC motor control. The method needs measurements of line currents. The three-phase voltage of the motor is obtained by calculation in the controller using the DC rail voltage, PWM pattern and dead time information, and then rotor position is estimated.

5.1.3 The Starting Problem in Shaft Position Sensorless Operation

In brushless PM motors, a back EMF signal is only available when the motor is actually rotating, not at rest. Therefore, where the back EMF signal is used to determine the rotor position, the initial starting of the system from rest poses special problems.

The lack of a special starting procedure (except in the case of the incremental encoder) is probably the main advantage of the rotary position sensors. The most critical aspect of starting is from standstill to a certain speed at which the back EMF can be reliably detected and used as a substitute for the position information. *Krishnan and Ghosh* (1989) reported that the threshold speed at which the back EMFs are detectable is around 250 rpm (8 pole motor).

The minimum speed limit is reduced down to 30 rpm (4 pole motor) by *Wu and Slemon* (1991) using an observer method. Although these speed limits may not effect the low performance applications (such as fan and pump loads), most of the brushless PM drive applications require starting with a

load which varies as a function of the speed and may require fine speed control.

In the shaft position sensorless applications, the initial rotor position cannot be determined unless special techniques are used. These techniques can be classified as follows:

1. An excitation current can be imposed in order to bring the rotor to a known position (with different combinations of excitation). However, in some applications, the value of current may be high to overcome the static friction and total system inertia.

2. The initial position can be indirectly determined by measuring the phase inductance [*Schroeld*, 1988], or by injecting diagnosis signals and analysing them [*Binns*, 1991].

3. A possible solution to the initial starting problem is to give a slowly rotating current space vector without reference to back EMF which causes uncontrolled motion of the motor (open-loop starting) [*Endo et al*, 1983]. However, for some applications (such as precise position control) this uncontrolled motion during initialisation could be unacceptable.

4. Injecting the diagnosis signal to a special winding and analysing the induced voltage.

5. At standstill, the motor can be locked mechanically in a known position.

Table 5.1 Summary of indirect position sensing methods in brushless PM motors

METHODS	MOTOR TYPES	LIMITATIONS
EVALUATION OR ESTIMATION OF BACK EMF	Discontinuous current controlled drives, BTPM and BSPM motors	
Direct back EMF detection		Sensitive to switching transients Suffers at low operating speeds Needs a special starting method
Estimation of back EMF		Method is sensitive to change of winding resistance, and measurement noise
THIRD HARMONIC VOLTAGE DETECTION	Star connected BTPM motors	The method needs a motor which has reasonable amount of third harmonic voltage Requires a reference back EMF zero crossings It is difficult to sense the third harmonic voltage at low speeds
MONITORING CURRENT OR CALCULATION METHOD OF THE PHASE INDUCTANCE	BSPM and BTPM motors	Requires a starting method from standstill Limitations at higher currents and speeds Motors which have variable winding inductance
INJECTING DIAGNOSIS SIGNAL TO THE STATOR WINDINGS	BTPM motor control	Requires a starting method from rest Motors with some degree of variable winding inductance
OBSERVER METHODS	BSPM and BTPM motors	Needs a starting method from standstill Motors d-q transferable Mainly suffer from complex estimation techniques
MONITORING SWITCHING STATES IN THE INVERTER	BTPM motors	Requires a starting method from rest
USING A SPECIAL WINDINGS OR ELECTROMAGNETIC DEVICES	BTPM motors	Requires modification in the motor Number of connection increases between the motor and controller

5.2 THE MATHEMATICAL BASIS OF THE NEW POSITION ESTIMATION METHOD

5.2.1 The Flux Linkage Model for Variable Winding Inductance

The equivalent circuit for the three-phase brushless PM machine has been presented and the differential equations have been given in terms of flux linkage variables in **Chapter II, Section 2.2.** If we recall **Eq.2.1** and rearranging it in the matrix form as a function of phase voltage and line currents, we get

$$\frac{d}{dt}\begin{bmatrix}\psi_1\\ \psi_2\\ \psi_3\end{bmatrix}=\left\{\begin{bmatrix}v_1\\ v_2\\ v_3\end{bmatrix}-\begin{bmatrix}R & 0 & 0\\ 0 & R & 0\\ 0 & 0 & R\end{bmatrix}\begin{bmatrix}i_1\\ i_2\\ i_3\end{bmatrix}\right\} \tag{5.2}$$

The general flux linkage variables were defined in **Eq.2.2** in the case of saliency. Rewriting the **Eq.2.2,**

$$\begin{bmatrix}\psi_1\\ \psi_2\\ \psi_3\end{bmatrix}=\begin{bmatrix}L_{11}(\theta_e) & M_{12}(\theta_e) & M_{13}(\theta_e)\\ M_{21}(\theta_e) & L_{22}(\theta_e) & M_{23}(\theta_e)\\ M_{31}(\theta_e) & M_{32}(\theta_e) & L_{33}(\theta_e)\end{bmatrix}\begin{bmatrix}i_1\\ i_2\\ i_3\end{bmatrix}-\begin{bmatrix}\psi_{pm1}(\theta_e)\\ \psi_{pm2}(\theta_e)\\ \psi_{pm3}(\theta_e)\end{bmatrix} \tag{5.3}$$

We realise that the inductance matrix in **Eq.5.3** is position dependent and describes the self and mutual inductance relations of the stator phases of a symmetrical PM machine. As described in the **Chapter II,** $\psi_{pm1}(\theta_e)$, $\psi_{pm2}(\theta_e)$, and $\psi_{pm3}(\theta_e)$ are the flux linkages established by the permanent magnet.

If saturation is present, the total flux linkage consists of a number of sources, and is defined as a function of three line currents (i_1, i_2, i_3), and position θ_e. In other words the flux linkages define a set of 4 dimensional surfaces in 5 dimensional space (+ time). As will be explained later, it is possible to experimentally obtain these flux linkage surfaces in PM machines.

5.2.2 The Flux Linkage Model for Constant Winding Inductance

In the absence of saturation, the governing differential equations given in **Eq.5.2** do not change. However, for the machine which has no variable inductance, **Eq.5.3** can be rearranged to give more simple system equations for the flux linkages.

Using the assumptions given in **Chapter II, Section 2.2.1** the flux linkage equations can be given,

$$\begin{bmatrix} \psi_1 \\ \psi_2 \\ \psi_3 \end{bmatrix} = \begin{bmatrix} L & 0 & 0 \\ 0 & L & 0 \\ 0 & 0 & L \end{bmatrix} \begin{bmatrix} i_1 \\ i_2 \\ i_3 \end{bmatrix} - \begin{bmatrix} \psi_{pm1}(\theta_e) \\ \psi_{pm2}(\theta_e) \\ \psi_{pm3}(\theta_e) \end{bmatrix} \tag{5.4}$$

This matrix form can be separated as,

$$\psi_n(i_n, \theta_e) = \psi_{Ln}(i_n, \theta_e) - \psi_{pmn}(\theta_e) \qquad n = 1,2,3 \tag{5.5}$$

Here ψ_{Ln} is the flux linkage associated with the equivalent phase inductance L in phase **n**. As seen in **Eq.5.5** for each individual phase, the flux linkage ψ_n now represents a 2 dimensional surface rather than 4 dimensional surface.

5.2.3 Performing The Total Flux Linkages

The surfaces representing the total flux linkages can be reconstructed by sampling the phase voltages and the line currents. This can be done based on **Eq.5.2.**, and the function of flux linkage to be evaluated is in the following form,

$$\begin{bmatrix} \psi_1(t) \\ \psi_2(t) \\ \psi_3(t) \end{bmatrix} = \int_0^t \left\{ \begin{bmatrix} v_1(\tau) \\ v_2(\tau) \\ v_3(\tau) \end{bmatrix} - \begin{bmatrix} R & 0 & 0 \\ 0 & R & 0 \\ 0 & 0 & R \end{bmatrix} \begin{bmatrix} i_1(\tau) \\ i_2(\tau) \\ i_3(\tau) \end{bmatrix} \right\} d\tau \qquad (5.6)$$

and for a fixed value of $\theta_e=\theta_e^*$, we can give the general form of estimated flux linkage by,

$$\psi_n(i_1, i_2, i_3, \theta_e^*) = \int_0^t [v_n(\tau) - R i_n(\tau)]\, d\tau \qquad n=1,2,3 \qquad (5.7)$$

However, since the continuously measured data is used to perform the integration, the function $[v_n(\tau)-Ri_n(\tau)]$ does not have a closed form integral. **Eq.5.7** can be used in constructing the flux linkage surfaces, either by analog measurement or numerical technique.

By sampling of the values of phase voltage and line current, the integral can be computed. The corresponding values of the integral will then define a set of discrete data points that lie on the flux linkage surfaces. It is usually necessary to approximate the integral using numerical techniques. Although, for cases where extremely high accuracy is required, different integration methods can be used, it is found that two of the integration methods shown

in **Fig.5.1** are adequate to perform the integration in **Eq.5.7**. Both methods effectively estimate the area defined by strip **ΔT**. Function heights or average heights (for trapezoidal method) are multiplied by strip widths, and summed in order to estimate the integral. While the first method (rectangular rule) gives slightly poor accuracy, it requires less computing effort. In **Fig.5.1**, y(k) is the integrated value of the function x(k) at the sampling instant **k**, and **ΔT** is the sampling interval. Since the integration starts at k=1, y(k-1) plays the role of the initial condition.

If we rewrite the integration in **Fig.5.1a**, the discrete form of the flux linkages for three-phase PM motor can be given by

$$\begin{bmatrix} \psi_{1(k)} \\ \psi_{2(k)} \\ \psi_{3(k)} \end{bmatrix} = \Delta T \left\{ \begin{bmatrix} v_{1(k)} \\ v_{2(k)} \\ v_{3(k)} \end{bmatrix} - \begin{bmatrix} R & 0 & 0 \\ 0 & R & 0 \\ 0 & 0 & R \end{bmatrix} \begin{bmatrix} i_{1(k)} \\ i_{2(k)} \\ i_{3(k)} \end{bmatrix} \right\} + \begin{bmatrix} \psi_{1(k-1)} \\ \psi_{2(k-1)} \\ \psi_{3(k-1)} \end{bmatrix} \tag{5.8}$$

Here $\psi_1(k-1)$, $\psi_2(k-2)$ and $\psi_3(k-1)$ are the initial conditions of the integral, and if the initial rotor position is known they can be defined with reference to a single phase while the line current value is zero. At starting, the initial value of the flux linkages are proportional with the maximum value of magnet flux linkage λ_m.

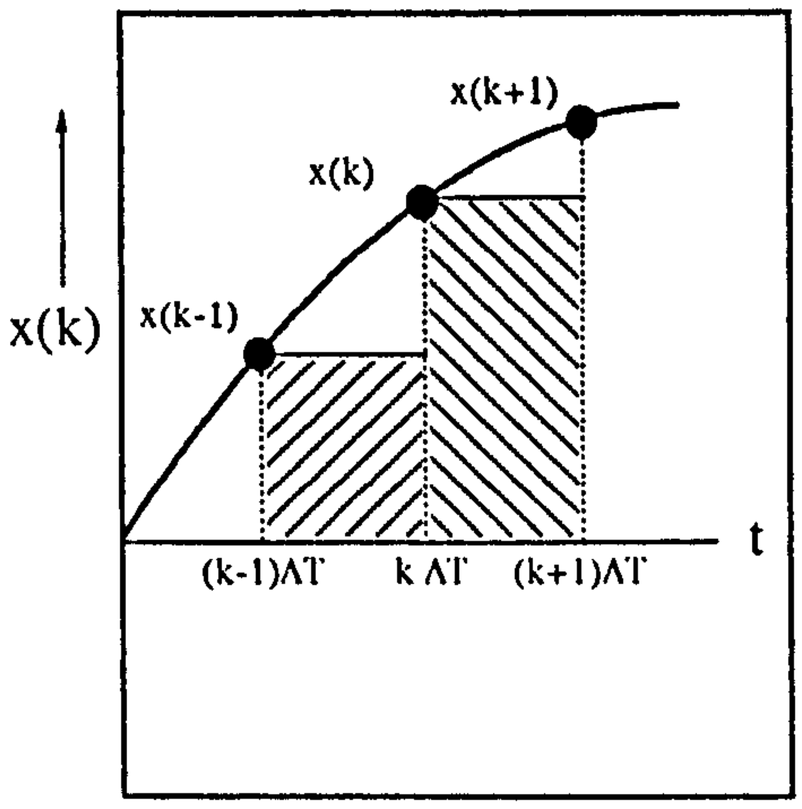

$$y(k) = \Delta T\ x(k) + y(k-1)$$

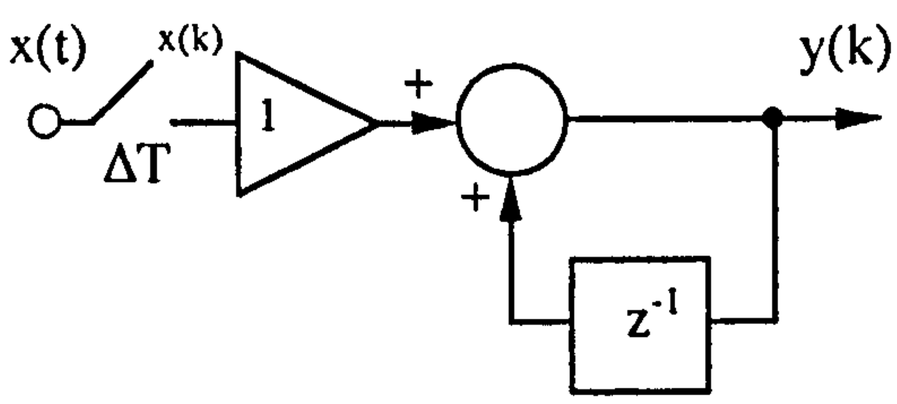

a

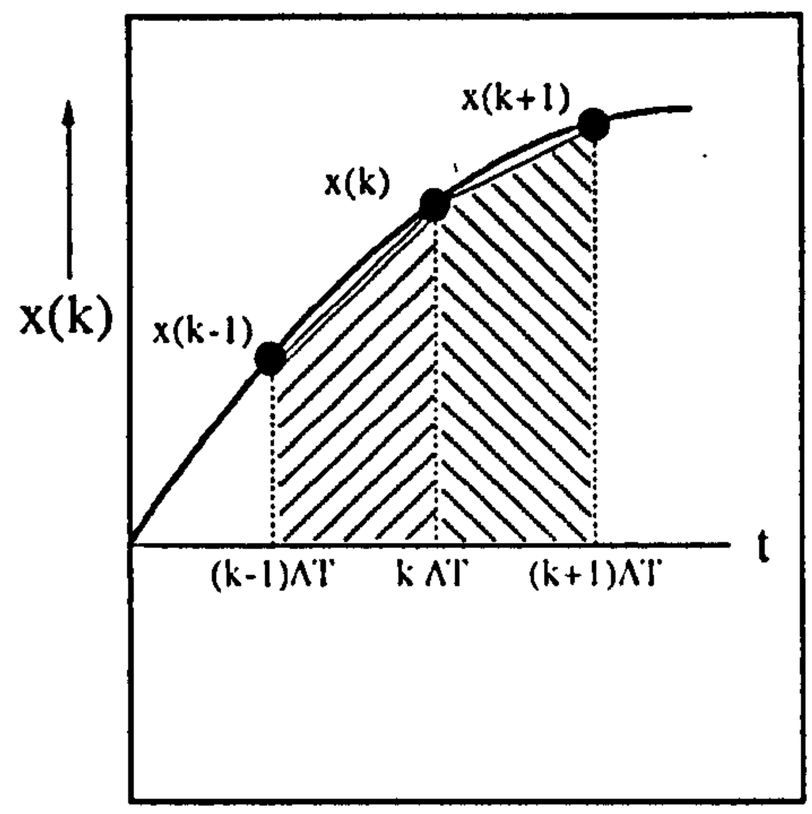

$$y(k) = \Delta T\ [x(k-1) + x(k)]\ /\ 2\ + y(k-1)$$

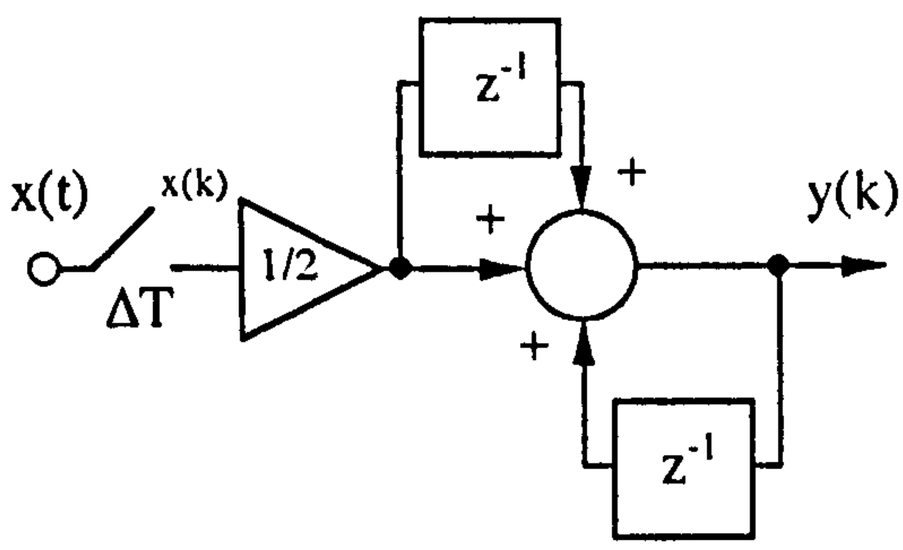

b

Figure. 5. 1 Schematic and flow diagram of two integration methods

a) Rectangular integration method

b) Trapezoidal method

5.3 DEFINITION OF THE POSITION ESTIMATOR

As mentioned earlier, the position estimator is to be incorporated with in the drive, so that the mechanical shaft position sensor can be eliminated. Using an estimation technique, discrete data points of the measured total flux linkages, can be estimated by the methods given in **Section 5.2.3**, can be

used to obtain the rotor position. It should be considered here that, the term "*measured flux linkage*" is going to be used to indicate the estimated value of the flux linkage by performing the integration in **Eq.5.8** before the flux linkage correction routine is involved.

As will be explained in this section, the position estimation based on the flux linkages is achieved by **Eq.5.8**, and **Eq.5.3** and **Eq.5.4** (whether the machine has variable winding inductances or constant inductances). In general, **Eq.5.2** and **5.3** are the centre of the position estimation algorithm. By evaluating **Eq.5.8**, the three phase flux linkages can be estimated using the measured terminal quantities (phase voltages and line currents). **Eq.5.3** is equivalent to the rate of change with time of the flux linked with each phase.

Fig.5.2 illustrates the block diagram of the shaft position sensorless algorithm which is used in both simulation and real data analysis. The following sections describe the individual blocks, and give application hints with the waveforms compiled from the actual or simulated drive. However, it is though that an overwiev explanation might be helpful to understand the algorithm. If we summarise **Fig.5.2**, the following processes are performed in sequence within the position estimator:

1. Three line currents (or two, since the third phase current can be reconstructed in the three-phase star-connected motor) and three phase-to-star point voltages are measured, and the discrete form of the integration in **Eq.5.8** is performed to estimate the total flux linkages.

2. Three phase flux linkage values are transformed by the first current estimation loop to estimate the current values ($i_{1e(k)}$, $i_{2e(k)}$, $i_{3e(k)}$, by **Eq.5.3** or **Eq.5.4**) using the previously predicted rotor position $\theta_{p(k)}$.

3. Since the actual current values are known (measured) at the instant of estimation, the estimated values of currents are used to calculate the current errors (Δi_1 ,Δi_2 ,Δi_3).

4. The position errors for each individual phases are calculated, and an averaging method is used to get a unique position error from the three position error values. Then, the previously predicted position is corrected by using the estimated position error $\theta_{e(k)}$, and the following position $\theta_{p(k+1)}$is predicted by a second order polynomial curve fitting (see **Section 5.3.3**). During the position estimation, the predicted position value is updated when it exceeds the value 2π.

5. In order to avoid error in the flux linkages, second estimations are done by using one of the methods explained in **Section 5.3.4.**

6. The estimation cycle is repeated from (**1**) capturing new voltage and current values at the following instant.

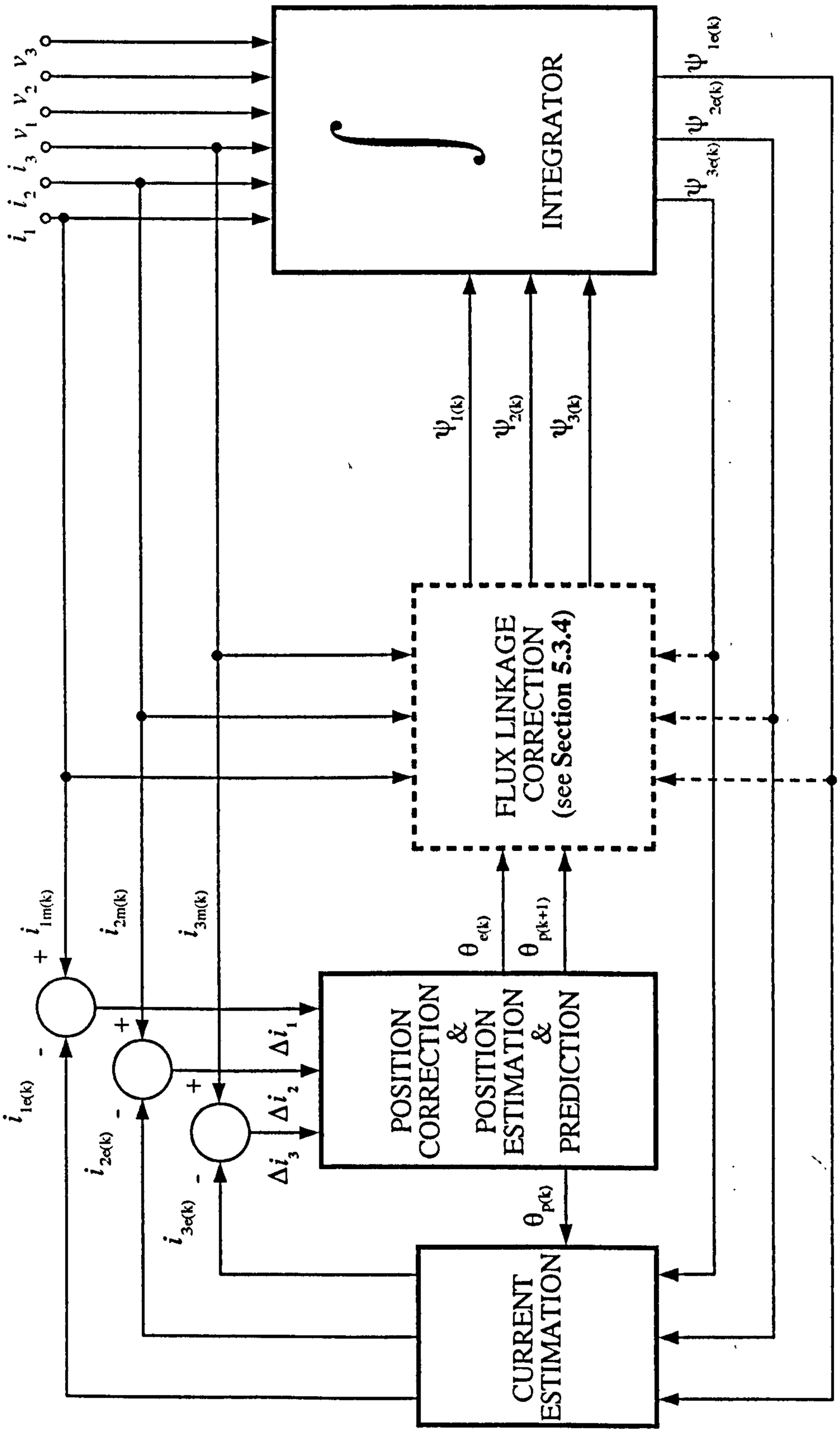

Figure 5.2 Schematic representation of the position detection algorithm

5.3.1 Analysing Flux Linkage Waveforms

THE TOTAL FLUX LINKAGES

Using the package described in **Chapter 4**, the motor's performance can be simulated for any operating condition, and resulting terminal quantities can be input to the sensorless operation algorithm. For example, the drive may be operated without current control in the steady-state and at different DC rail voltage levels. **Fig.5.3a** represents typical single phase voltage and current waveforms for one of these operating conditions. As can be seen in **Eq.5.8**, the variations of the total flux linkage is sensitive to the current level as well as the rotor position. **Fig.5.3b** shows expected variations of the flux linkages with current level, keeping the speed of the motor constant for the condition shown in **Fig.5.3a**.

As seen in **Fig.5.3b**, the flux linkage due to the winding current is superimposed on the magnet flux linkage, which is shown by the solid line. In 120° inverter operated PM motors, the value and the sign of the line current changes with position, and during current commutation instants variations becomes very position dependent. For 120° inverter operation, the dips around the maximum value of the total flux linkage indicates the starting position of the zero commanded current interval in the related phase, and end of the zero commanded current interval can be distinguished by the starting instant of negative currents.

Similar to the total flux linkage waveforms in **Fig.5.3b**, during current controlled operation (**Fig.5.4**), the total flux linkage waveform becomes a much more linear characteristic within the current conduction interval. However, the waveforms are also sensitive to rotor position in the commutation region.

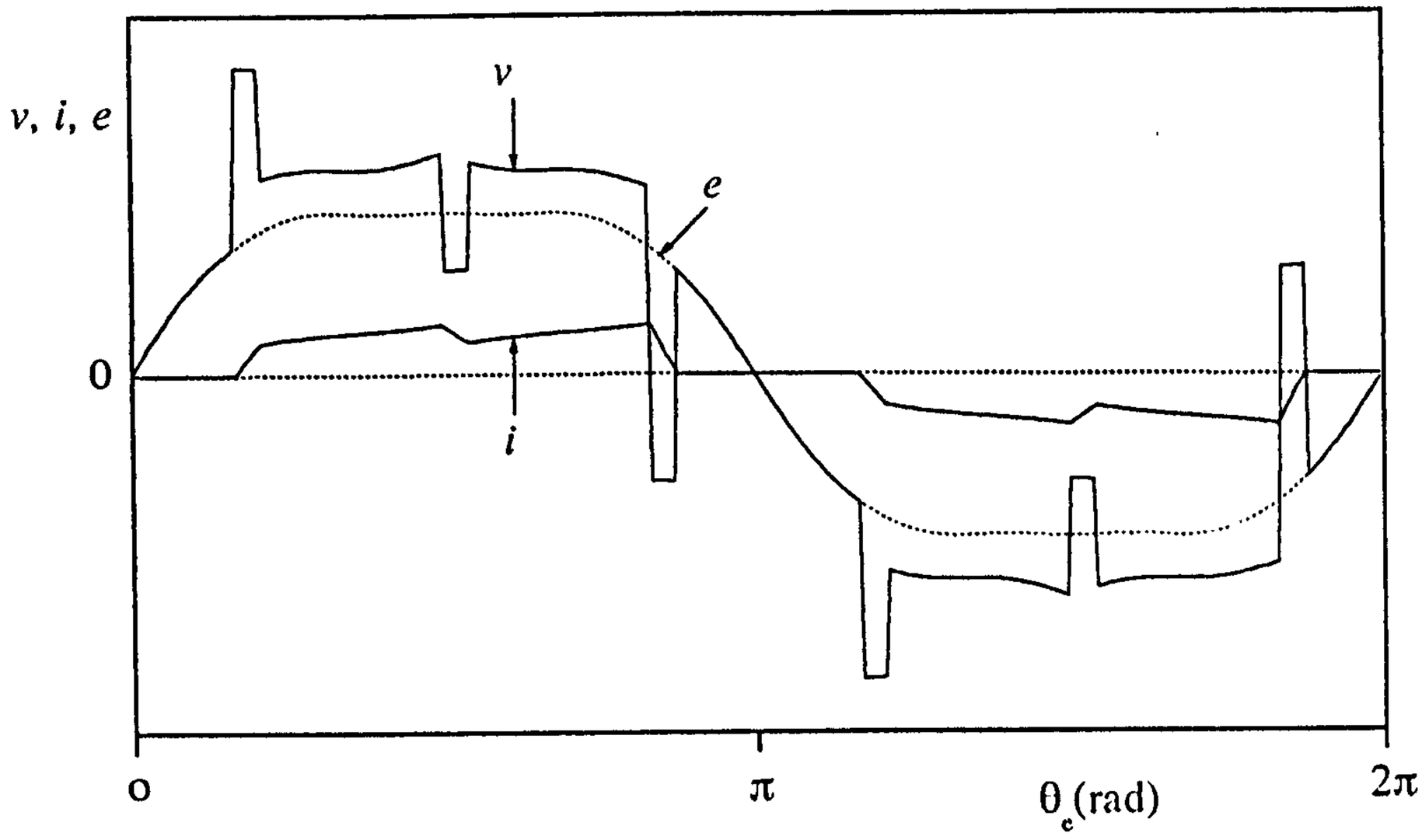

Figure 5.3 Typical voltage, current waveforms and family of the total flux linkages, no current control.

a) Motor terminal quantities for a single phase at 120° inverter operation.

b) Representation of the family of total flux linkage curves.

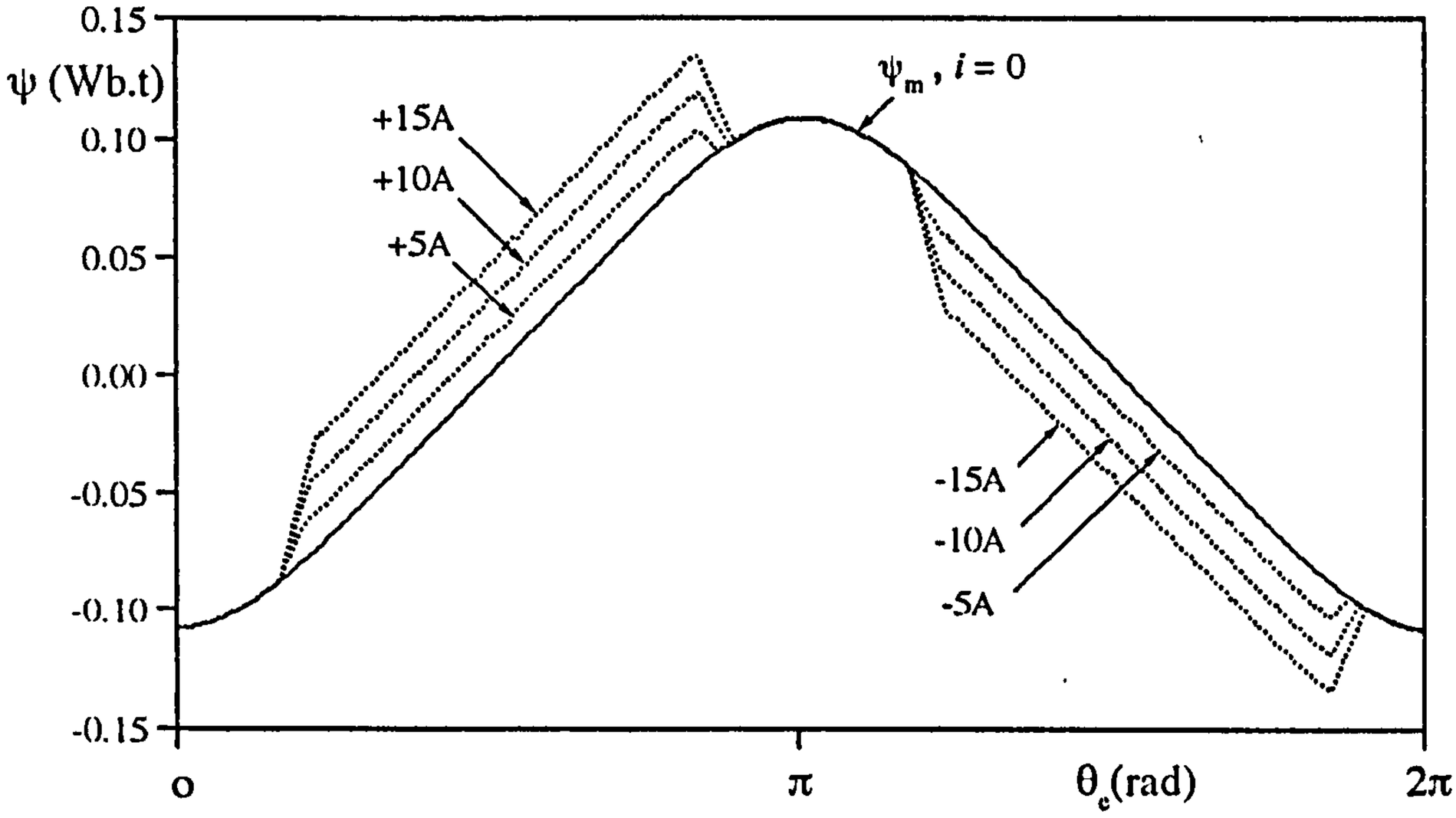

Figure 5.4 The family of total flux linkage curves, current controlled operation.

THE MAGNET FLUX LINKAGES

As explained in **Section 5.2**, the rate of change with time of the flux linked in each phase depends on a number of sources including magnet flux linkage which is a function of the rotor position. It can be seen easily in **Eq.5.4** that the magnitude of $d/dt(\psi_{pmn})$ would be the magnitude of the open circuit voltages, induced in each stator phase windings (back EMFs). To relate the back EMF at the motor terminals, we can use Faraday's Law:

$$e = \frac{d\psi}{dt} \tag{5.9}$$

In words, the derivative of magnet flux linkage is equal to the induced voltage (back EMF) in the stator winding, **or** the integration of the back EMF over an electrical period gives the magnet flux linkage. The minus signs of the magnet flux linkages in **Eqns.5.3-5** have been taken into account by the assignment of voltage polarity.

The experimental identification process is performed for each phase winding independently in the test motor, and back EMFs are measured by the data acquisition system. It is found that, in BTPM motors, or commercial BSPM motors, the magnet flux linkages give a linear characteristic over a flat-top interval of back EMFs as expected.

For comparison purpose and to help the analysis, the actual magnet flux linkage waveforms with reference to the back EMFs are given in **Fig.5.5**. As seen in **Fig.5.5**, for phase **1**, the back EMF is zero while the magnet flux linkage is maximum (λ_m), and back EMF is maximum at 90° electrical angle (90° out of alignment of magnet position).

However, the modelling procedure of the magnet flux linkage stated previously and shown in **Fig.5.5** may cause difficulties which are also computationally unattractive. **Fig.5.6** illustrates the comparison of the actual magnet flux linkage variation with an ideal cosine approximation. From **Fig.5.6**, it is found that the magnet flux linkages can be assumed to vary sinusoidally,

$$\begin{bmatrix} \psi_{pm1} \\ \psi_{pm2} \\ \psi_{pm3} \end{bmatrix} = \begin{bmatrix} \lambda_m \cos(\theta_e) \\ \lambda_m \cos(\theta_e - \frac{2\pi}{3}) \\ \lambda_m \cos(\theta_e - \frac{4\pi}{3}) \end{bmatrix} \tag{5.10}$$

Although, the sinusoidal assumption of magnet flux linkage is attractive for easy modelling, a more robust model of the magnet flux linkage might use a look-up table for real time estimation.

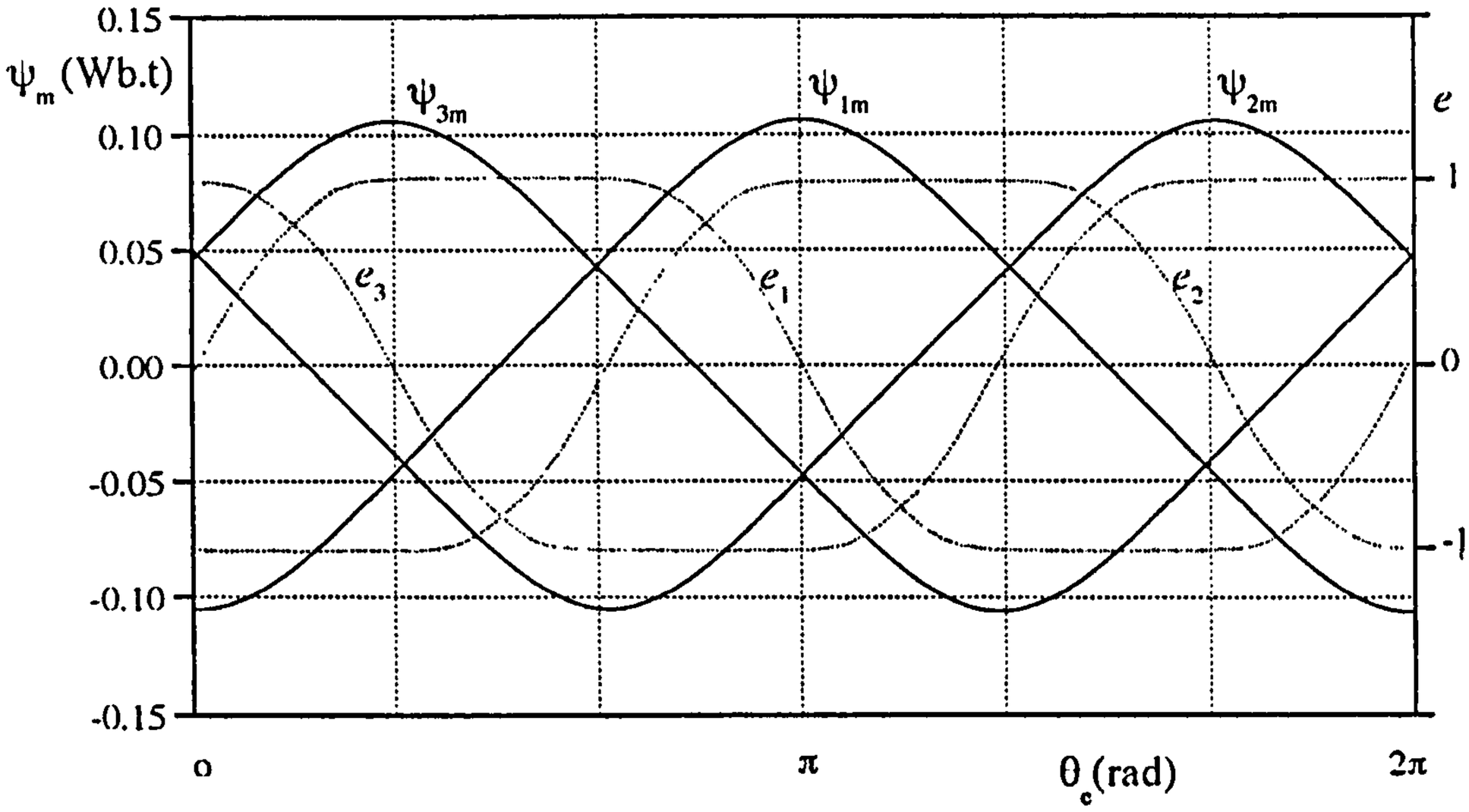

Figure 5.5 The comparison of the estimated magnet flux linkages with the actual back EMFs (per-unit) for three-phase brushless PM motor.

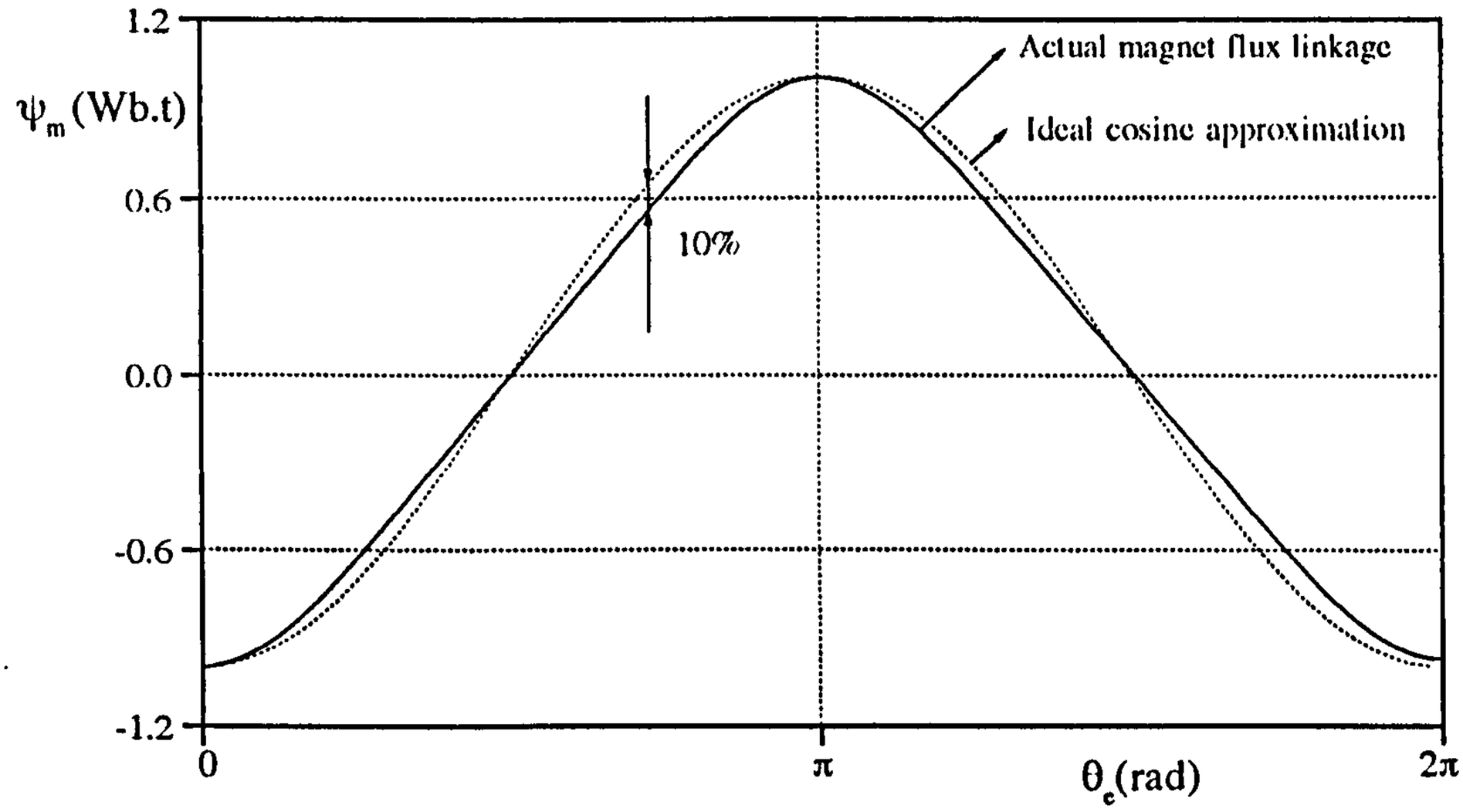

Figure 5.6 The estimated magnet flux linkage from the measured back EMF and cosine approximation for **Phase 1**.

It is found that, in the position estimator, the crucial point in the magnet flux linkage is the maximum value λ_m, not the profile of it. **Fig.5.7** shows both schematic and mathematical relation to be use in modelling of magnet flux linkage. In this approach, if the back EMF is trapezoidal in form, the maximum of magnet flux linkage can be approximated without integrating the actual back EMF profile.

The initial stage of modelling involves measuring the angle 0_{nee} (beginning of the flat-top of the back EMF). Assuming area**A1**=area**A2**, **Eq.5.11** can be produced which gives a relation between the maximum value of the trapezoidal back EMF and sinusoidal approximation of the waveform as a function of the angle θ_{nee}.

$$E_{m(s)} = E_{m(T)} \frac{(\pi - \theta_{nee})}{2} \qquad (5.11)$$

Here $E_{m(T)}$ is the maximum value of the actual trapezoidal back EMF, and $E_{m(s)}$ is the magnitude of approximated sinusoidal waveform.

If the peak value of the back EMF and speed are measured, the sinusoidal approximation of back EMF using **Eq.5.11** gives a very close approximation which is produced on the basis of the equal areas. For instance, in 120° flat-top back EMF waveform, the amplitude of sinusoidal waveform should be bigger than the actual back EMF's amplitude by a factor of 1.31. As given in **Eq.2.17**, and explained in **Chapter III, Section 3.1.1**, the maximum magnet flux linkage can be estimated directly using the maximum value of the back EMF constant ke ($\lambda_m = k_e/p$).

In Fig.5.7, A1 represents the total area of a quarter wave of trapezoidal back EMF, and **A2** is the area under a quarter sinusoidal waveform.

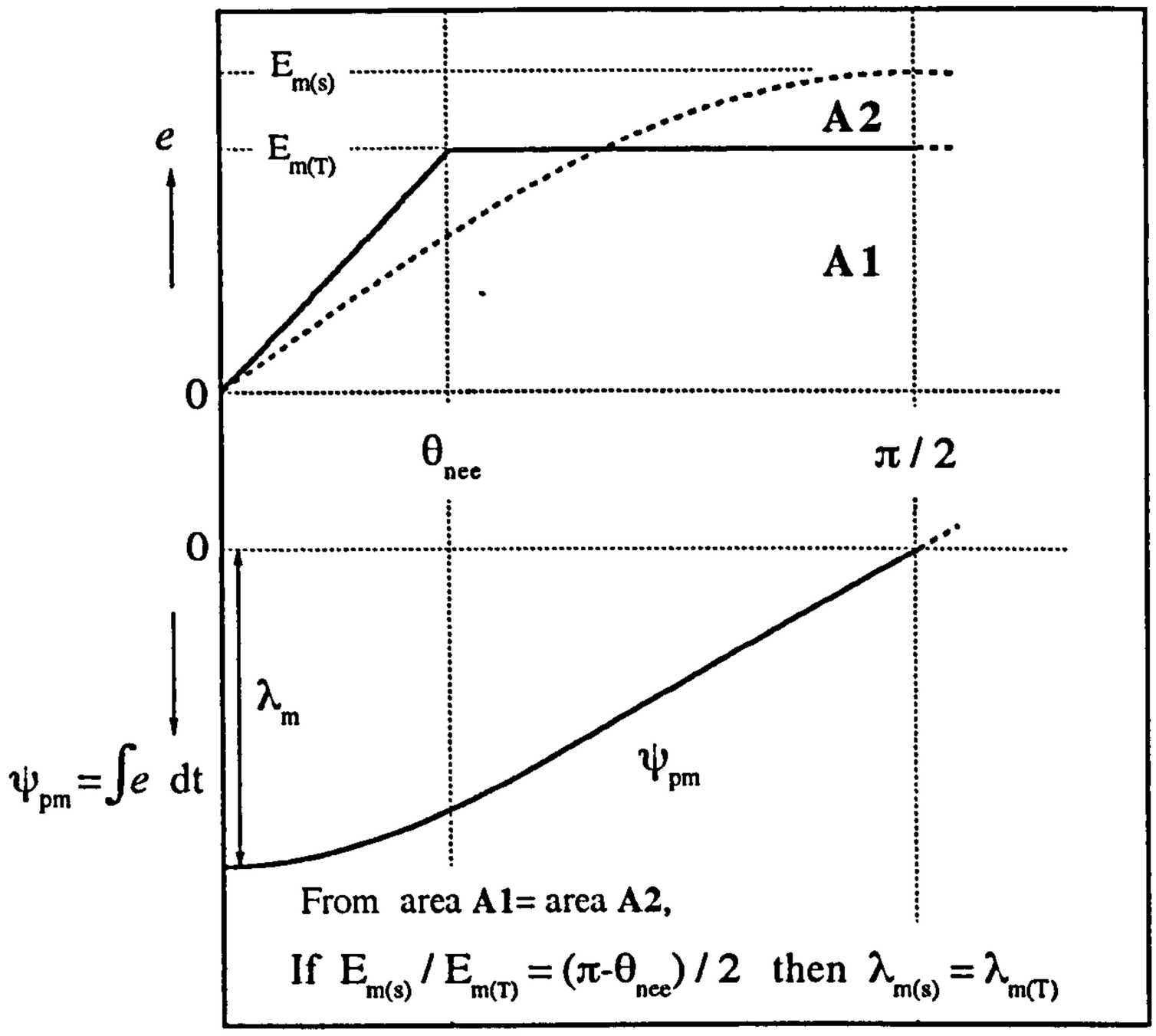

Figure 5.7 Modelling of the magnet flux linkage from the back EMF profile.

5.3.2 Line Current And Current Error Estimations

The algorithm shown in the block diagram of **Fig.5.2** has a two current-loop structure. Both loops effectively estimate the line current which is obtained by using the flux linkage relations given either in **Eq.5.3** or **Eq.5.4**. If **Eq.5.3** is used, three line currents should be solved simultaneously. Since the flux linkages can be estimated and the value of the magnet flux linkages can be defined for a known rotor position, the set of equations in **Eq.5.3** are in the form of algebraic equations with three unknowns (i_1, i_2, i_3),

$$\begin{bmatrix} L_{11}(\theta_e) & M_{12}(\theta_e) & M_{13}(\theta_e) \\ M_{21}(\theta_e) & L_{22}(\theta_e) & M_{23}(\theta_e) \\ M_{31}(\theta_e) & M_{32}(\theta_e) & L_{33}(\theta_e) \end{bmatrix} \begin{bmatrix} i_1 \\ i_2 \\ i_3 \end{bmatrix} = \begin{bmatrix} \psi_1+\psi_{pm1}(\theta_e) \\ \psi_2+\psi_{pm2}(\theta_e) \\ \psi_3+\psi_{pm3}(\theta_e) \end{bmatrix} \qquad (5.12)$$

Eq.5.12 can also be written in the matrix form as,

$$\mathbf{A}.\mathbf{x} = \mathbf{B} \tag{5.13}$$

Here, the dot denotes matrix multiplication, **A** is the matrix of coefficients (inductances), **x** is the unknown current vector, and **B** is the right hand side in **Eq.5.12** written as a column vector which includes summation of flux linkage and magnet flux linkage for related phases. We should keep in mind that the standard subroutine packages are available in the books to solve the set of equation described in **Eq.5.12**.

However, in the absence of saturation, the total flux linkage equations take the form given in **Eq.5.4**. If we rearrange **Eq.5.4**,

$$\begin{bmatrix} i_1 \\ i_2 \\ i_3 \end{bmatrix} = \begin{bmatrix} \dfrac{\psi_1+\psi_{pm1}(\theta_e)}{L} \\ \dfrac{\psi_2+\psi_{pm2}(\theta_e)}{L} \\ \dfrac{\psi_3+\psi_{pm3}(\theta_e)}{L} \end{bmatrix} \tag{5.14}$$

As seen, the new form of the matrix equation is much more simple than that of **Eq.5.12**. Direct calculation of line currents can be achieved by replacing the discrete values of the measured flux linkage and the magnet flux linkage for a given predicted position.

For each phase, a current estimate can be obtained from **Eq.5.12** or **Eq.5.14** (whether the motor has variable or constant winding inductance) using the measured flux linkages and the initial predicted position. The current estimates are then compared with the measured currents to achieve a set of current errors,

$$\begin{bmatrix} \Delta i_1 \\ \Delta i_2 \\ \Delta i_3 \end{bmatrix} = \begin{bmatrix} i_{1m}-i_{1e} \\ i_{2m}-i_{2e} \\ i_{3m}-i_{3e} \end{bmatrix} \tag{5.15}$$

Here i_{1m}, i_{2m}, and i_{3m} are the measured line currents, and i_{1e}, i_{2e}, and i_{3e} are the estimated currents described in the above paragraphs.

5.3.3 Position Correction, Estimation And Prediction

POSITION CORRECTION AND ESTIMATION

Once current errors have been estimated, we can perform a mathematical calculation for each phase, to estimate the position error. As seen in **Eq.5.3** or **Eq.5.4**, we have flux linkage functions of several variables either $\psi=\psi(i_1,i_2,i_3,\theta)$ or $\psi=\psi(i_n,\theta)$ respectively. Therefore, changes in flux linkage can be written in terms of changes in the variables.

In general, in the case of the flux linkages with four variables as in **Eq.5.3**, the changes in the flux linkages can be given by,

$$\begin{bmatrix} \Delta\psi_1 \\ \Delta\psi_2 \\ \Delta\psi_3 \end{bmatrix} = \begin{bmatrix} \frac{\partial\psi_1}{\partial i_1} & \frac{\partial\psi_1}{\partial i_2} & \frac{\partial\psi_1}{\partial i_3} \\ \frac{\partial\psi_2}{\partial i_1} & \frac{\partial\psi_2}{\partial i_2} & \frac{\partial\psi_2}{\partial i_3} \\ \frac{\partial\psi_3}{\partial i_1} & \frac{\partial\psi_3}{\partial i_2} & \frac{\partial\psi_3}{\partial i_3} \end{bmatrix} \begin{bmatrix} \Delta i_1 \\ \Delta i_2 \\ \Delta i_3 \end{bmatrix} + \begin{bmatrix} \frac{\partial\psi_1}{\partial\theta_1} & 0 & 0 \\ 0 & \frac{\partial\psi_2}{\partial\theta_2} & 0 \\ 0 & 0 & \frac{\partial\psi_3}{\partial\theta_3} \end{bmatrix} \begin{bmatrix} \Delta\theta_1 \\ \Delta\theta_2 \\ \Delta\theta_3 \end{bmatrix} \tag{5.16}$$

Here $\Delta\psi_n$ is the changing of flux linkage, $\Delta\theta_n$ is the position error, and θ_1, θ_2, and θ_3 represent the position in the related phase. Since **Eq.5.16** is a

measure of the change in the function $\psi=\psi(i_1,i_2,i_3,\theta)$, it is assumed that the values $\Delta\psi_n$, Δi_1, Δi_2, Δi_3, $\Delta\theta_n$ are small.

Assuming that the flux linkage estimate is correct and does not change ($\Delta\psi_n=0$) within the measurement interval, for constant winding inductance, the position errors can be given in terms of line current error estimations,

$$\begin{bmatrix} \Delta\theta_1 \\ \Delta\theta_2 \\ \Delta\theta_3 \end{bmatrix} = \begin{bmatrix} \frac{\partial\theta_1}{\partial i_1} & 0 & 0 \\ 0 & \frac{\partial\theta_2}{\partial i_2} & 0 \\ 0 & 0 & \frac{\partial\theta_3}{\partial i_3} \end{bmatrix} \begin{bmatrix} \Delta i_1 \\ \Delta i_2 \\ \Delta i_3 \end{bmatrix}. \qquad (5.17)$$

Fig.5.8 gives a schematic representation for the position and flux linkage correction by enlarging the dotted box in **Fig.5.3b**. It is clear from **Fig.5.8** that the assumption of constant flux linkage does not uniquely define the rotor position, as there are at least two possible positions ($\theta_{c(1)}$, $\theta_{c(2)}$) corresponding to the measured value of flux linkage for a given phase. To resolve this, a position error should be introduced which can be either positive ($+\Delta\theta_c$) or negative ($-\Delta\theta_c$) depending on the flux linkage surface.

Comparison of the estimated (i_c) and measured (i_m) currents (to generate current errors) gives the opportunity to correct the position by using the relation given in **Eq.5.17**. The logical expressions are shown in **Fig.5.8** to indicate the comparison of the estimated and the measured current values, and sign of the resultant current error (Δi). In **Fig.5.8** $i_{c(1)}$ and $i_{c(2)}$ shows two possible estimated current values with corresponding total flux linkage waveforms, and ΔT is the increment or sampling period of the continuously varying data.

If the estimated current is bigger than the actual (measured) current ($i_e > i_m$), the current error (Δi) becomes negative, so the position error becomes positive ($+\Delta\theta_e$) and corrects the initial predicted position. The opposite happens when the estimated current is smaller than the measured current ($i_e < i_m$).

Although, in the ideal motor, the incremental position effects all three phases equally, as can be seen in **Eq. 5.17**, for the three-phase PM motor, three position corrections ($\Delta\theta_1, \Delta\theta_2, \Delta\theta_3$) are produced.

Since the rotor movement in the drive is defined by the total electromagnetic torque produced at the defined time and position, it is found that, in both 120° and 180° inverter operation, at certain current levels (and resulting torques), and corresponding position, some of the phases are better indicators of position error than others. Therefore, the quality of estimation for a single position error can be improved by appropriate weighting of the position errors according to the current levels.

A single revised position is obtained by taking the average of three position corrections,

$$\Delta\theta_{(k)} = \frac{(\Delta\theta_{1(k)} + \Delta\theta_{2(k)} + \Delta\theta_{3(k)})}{3} \qquad (5.18)$$

or by taking the average of two position correction depending upon the current level in the other phase. Here the subscript "k" shows the estimation of discrete data at the kth instant of time.

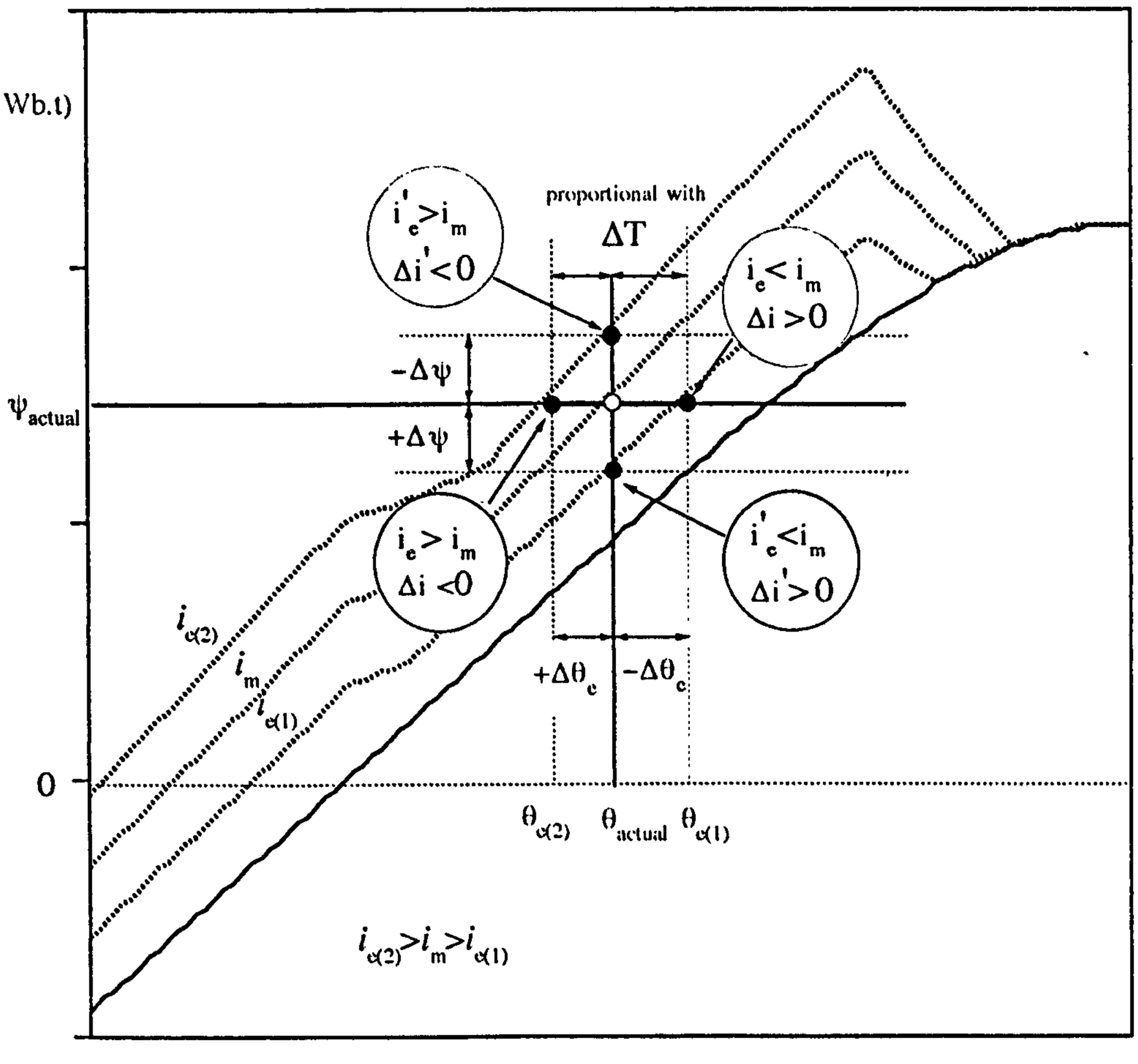

Figure 5.8 Enlarged form of **Fig.5.3b** for schematic representation of the position and the flux linkage correction.

An updated position is calculated by adding the resultant position error to the previous predicted position.

$$\theta_{e(k)} = \theta_{p(k)} + \Delta\theta_{(k)} \tag{5.19}$$

Here $\theta_{p(k)}$ represents the predicted position.

POSITION PREDICTION

As seen in **Fig.5.2**, the outer current loop is used to estimate the line current, and predicted position is utilised with estimated flux linkage. A position prediction is obtained by extrapolation of position data at previous time intervals. **Fig.5.9** shows the structure of the position prediction algorithm both schematically and with a flow chart. In **Fig.5.9**, three already known points are shown as filled dots. These are polynomial extrapolated to obtain the predicted position shown as an open dot.

Since the measured value of flux linkage will not be very accurate, the predicted rotor position is not necessarily coincident with the actual rotor position. Therefore, in **Fig.5.9**, two estimated values of position ① and ② indicate possible correct positions dependent upon the sign of estimated current error (as also shown in **Fig.5.8**).

The method records the past three position values and extrapolates them (via second order polynomial extrapolation) to predict position at the next time step. This is called the "*predictor*" step. The extrapolated value may not be exact, but it may be corrected by using the current errors as explained previously.

As said in earlier paragraphs, a second order polynomial is "fitted" to previous data, since an exact fit is possible in the cases of constant speed and constant acceleration (**Fig.5.9a**). In **Fig.5.9a**, $\theta_{e(k-2)}$, $\theta_{e(k-1)}$, and $\theta_{e(k)}$ are the values of position estimated in the previous three sampling instants, and $\theta_{p(k+1)}$ is the predicted value of position at the next sampling instant.

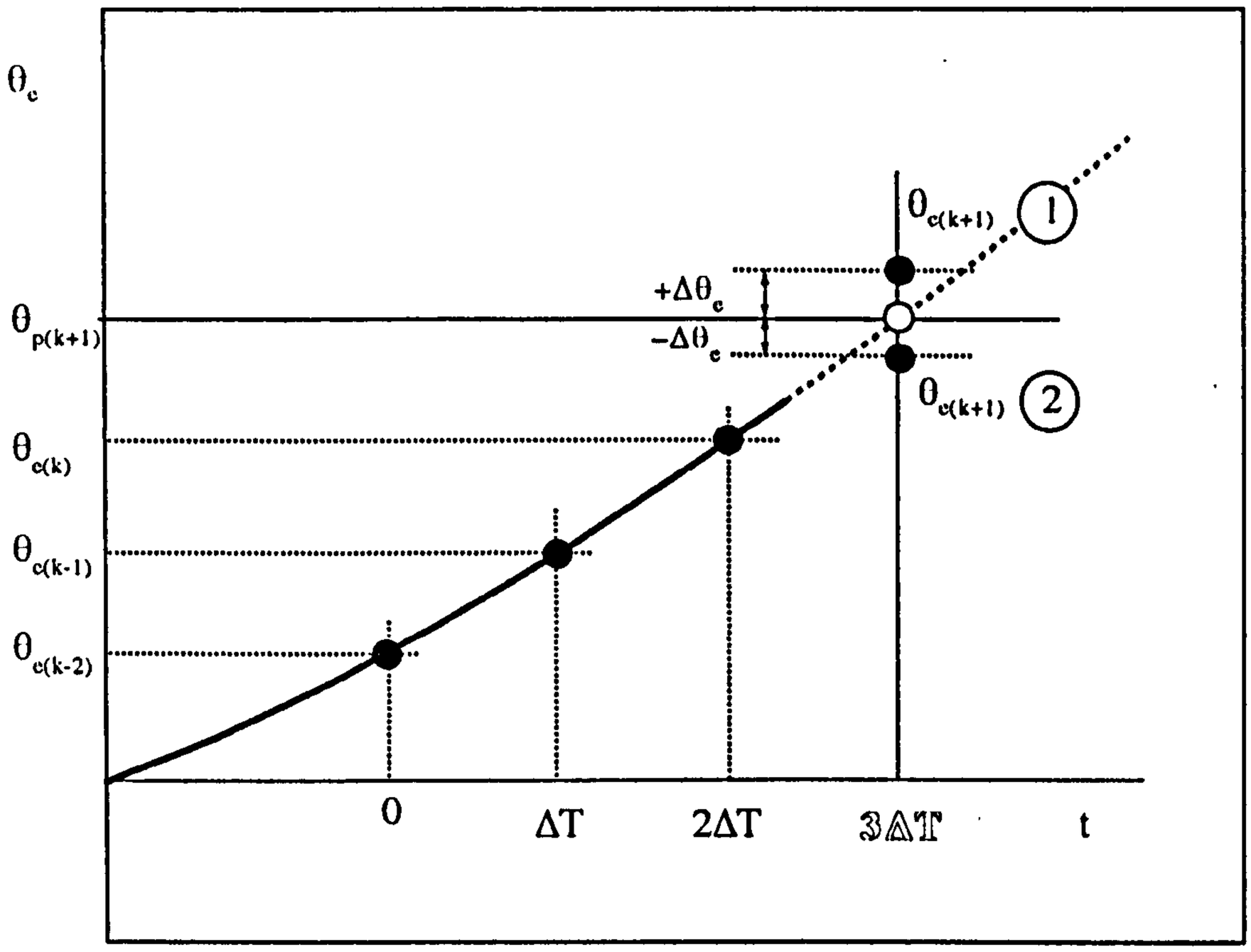

a

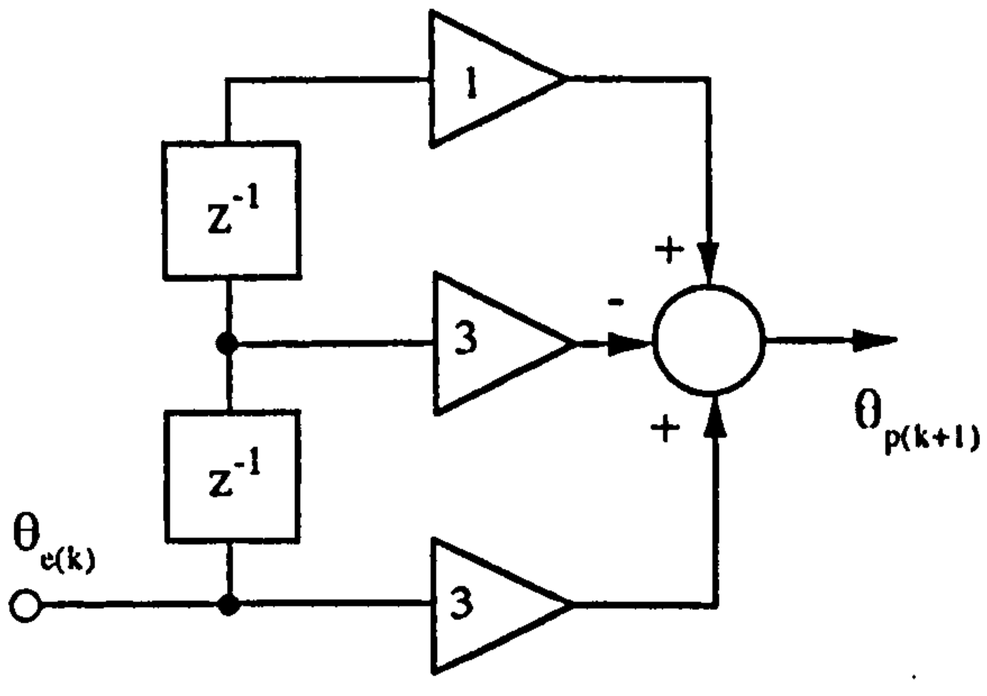

b

Figure 5.9 Position prediction algorithm and schematic diagram

a) Schematic representation of polynomial curve fitting.

b) Prediction algorithm

Assuming $\theta_e = At^2+Bt+C$ in **Fig.5.9a**, we can write the relations as shown below, at the instants of:

If $t(k-2) = 0$, then $\theta_{e(k-2)} = C$

If $t(k-1) = \Delta T$, then $\theta_{e(k-1)} = A(\Delta T)^2+B(\Delta T)+C$

If $t(k) = 2\Delta T$, then $\theta_{e(k)} = 4A(\Delta T)^2+2B(\Delta T)+C$

and,

for $t(k+1)=3\Delta T$, $\theta_{p(k+1)} = 9A(\Delta T)^2+3B(\Delta T)+C$

The simultaneous solution of these equations gives a unique equation to predict the rotor position using the previous three positions as indicated in **Fig.5.9**.

$$\theta_{p(k+1)} = 3\theta_{e(k)} - 3\theta_{e(k-1)} + \theta_{e(k-2)} \qquad (5.20)$$

As seen, to compute the predicted position $\theta_{p(k+1)}$ requires two multiplication and three additions which has the flow chart given in **Fig.5.9b**.

5.3.4 Flux Linkage Correction

It is found that, flux linkage correction is necessary because the continuous estimation of flux linkage, using an integration process, creates unwanted effects in the flux linkage waveform. Offset is a common problem faced in the implementation of integration. Moreover, as will be explained in **Chapter VI**, other effects, such as the temperature dependent winding resistance, and inaccuracies in the measurement of current and voltage, and inaccurate motor parameters also corrupt the flux linkage estimation. During this research, two possible ways of correcting flux linkage are found: correcting by current error estimation and estimation of flux linkage using

the estimated position. The following two sections are going to examine these two ways of flux linkage correction. While the first approach has been used in overall transient and steady-state results of the simulation and off-line real-data processing, the second approach has been applied to the on-line position estimation.

5.3.4.1 Correcting Flux Linkage by Current Error Estimation

The schematic diagram of the flux linkage correction was shown in **Fig.5.2**. Assuming the errors in the flux linkages occur only because of current errors, and without affecting the rotor position values ($\Delta\theta_n=0$), from **Eq.5.16**, we can write,

$$\begin{bmatrix} \Delta\psi_1 \\ \Delta\psi_2 \\ \Delta\psi_3 \end{bmatrix} = \begin{bmatrix} \frac{\partial\psi_1}{\partial i_1} & \frac{\partial\psi_1}{\partial i_2} & \frac{\partial\psi_1}{\partial i_3} \\ \frac{\partial\psi_2}{\partial i_1} & \frac{\partial\psi_2}{\partial i_2} & \frac{\partial\psi_2}{\partial i_3} \\ \frac{\partial\psi_3}{\partial i_1} & \frac{\partial\psi_3}{\partial i_2} & \frac{\partial\psi_3}{\partial i_3} \end{bmatrix} \begin{bmatrix} \Delta i_1' \\ \Delta i_2' \\ \Delta i_3' \end{bmatrix} \tag{5.21}$$

and for constant inductance,

$$\begin{bmatrix} \Delta\psi_1 \\ \Delta\psi_2 \\ \Delta\psi_3 \end{bmatrix} = \begin{bmatrix} \frac{\partial\psi_1}{\partial i_1} & 0 & 0 \\ 0 & \frac{\partial\psi_2}{\partial i_2} & 0 \\ 0 & 0 & \frac{\partial\psi_3}{\partial i_3} \end{bmatrix} \begin{bmatrix} \Delta i_1' \\ \Delta i_2' \\ \Delta i_3' \end{bmatrix} \tag{5.22}$$

Here, the current errors are redefined by,

$$\begin{bmatrix} \Delta i_1' \\ \Delta i_2' \\ \Delta i_3' \end{bmatrix} = \begin{bmatrix} i_{1m}-i_{1e}' \\ i_{2m}-i_{2e}' \\ i_{3m}-i_{3e}' \end{bmatrix} \tag{5.23}$$

Where i_{1e}', i_{2e}', and i_{3e}' indicate the second current estimations based on **Eq.5.12** or **Eq.5.14**, and the latest predicted position data in the prediction routine.

The inner estimation loop in **Fig.5.2** (the dashed box) corrects and updates the measured flux linkage. **Fig.5.10** illustrates the modified position estimator block based on above explained flux linkage correction method.

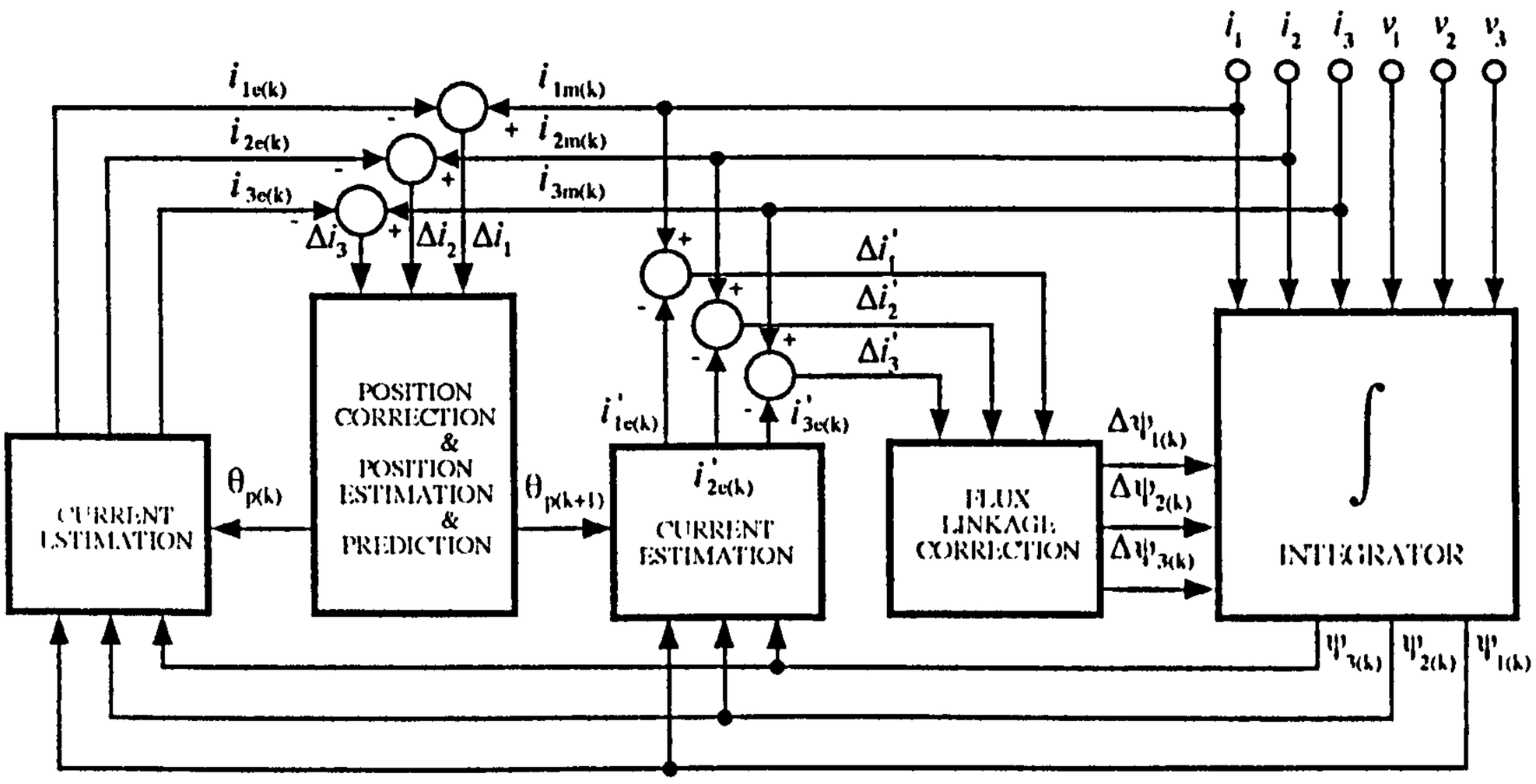

Figure 5.10 Correcting Flux Linkage by Current Error Estimation

The estimated flux linkage errors in **Eq.5.21** are used to update the integration in **Eq.5.8**,

$$\begin{bmatrix} \psi_{1(k)} \\ \psi_{2(k)} \\ \psi_{3(k)} \end{bmatrix} = \begin{bmatrix} \psi_{1(k)}+\Delta\psi_{1(k)} \\ \psi_{2(k)}+\Delta\psi_{2(k)} \\ \psi_{3(k)}+\Delta\psi_{3(k)} \end{bmatrix} \tag{5.24}$$

Here $\Delta\psi_{1(k)}$, $\Delta\psi_{2(k)}$, and $\Delta\psi_{3(k)}$ are the flux linkage errors at the time instant **k**.

5.3.4.2 Correcting Flux Linkage by an Estimation Based on Estimated Position

It is found that, in order to avoid errors in the initial values of flux linkages used to perform the integration given in **Eq.5.8**, the flux linkages can be updated by **Eq.5.3** or **Eq.5.4**. Assuming constant winding inductances in the motor, and substituting the estimated position (**Eq.5.19**) into **Eq.5.4**, the total flux linkages are calculated,

$$\begin{bmatrix} \psi_{1(k)} \\ \psi_{2(k)} \\ \psi_{3(k)} \end{bmatrix} = \begin{bmatrix} Li_{1m(k)} - \psi_{pm1(k)}(\theta_{e(k)}) \\ Li_{2m(k)} - \psi_{pm2(k)}(\theta_{e(k)}) \\ Li_{3m(k)} - \psi_{pm3(k)}(\theta_{e(k)}) \end{bmatrix} \tag{5.25}$$

The estimation routine is executed to correct the measured flux linkages in **Eq.5.8** which may be in error due to the effect of non-ideal motor parameters, and measurement errors. It is found that, the correction requires less computing effort, but suffers from high position error since the measured currents are used in the estimation. Any error in the measured currents may introduce significant position errors. Therefore, for a better performance, position error tolerance checking should also be considered in the algorithm.

Position error tolerance checking is performed after the position errors are calculated for each phase. When the estimated position error is higher than a predefined limit, it is ignored and the last position error is used to estimate the position in **Eq.5.19**. **Fig.5.11** illustrates the modified (from **Fig.5.2**) position estimation block representation for flux linkage correction based on the estimated position.

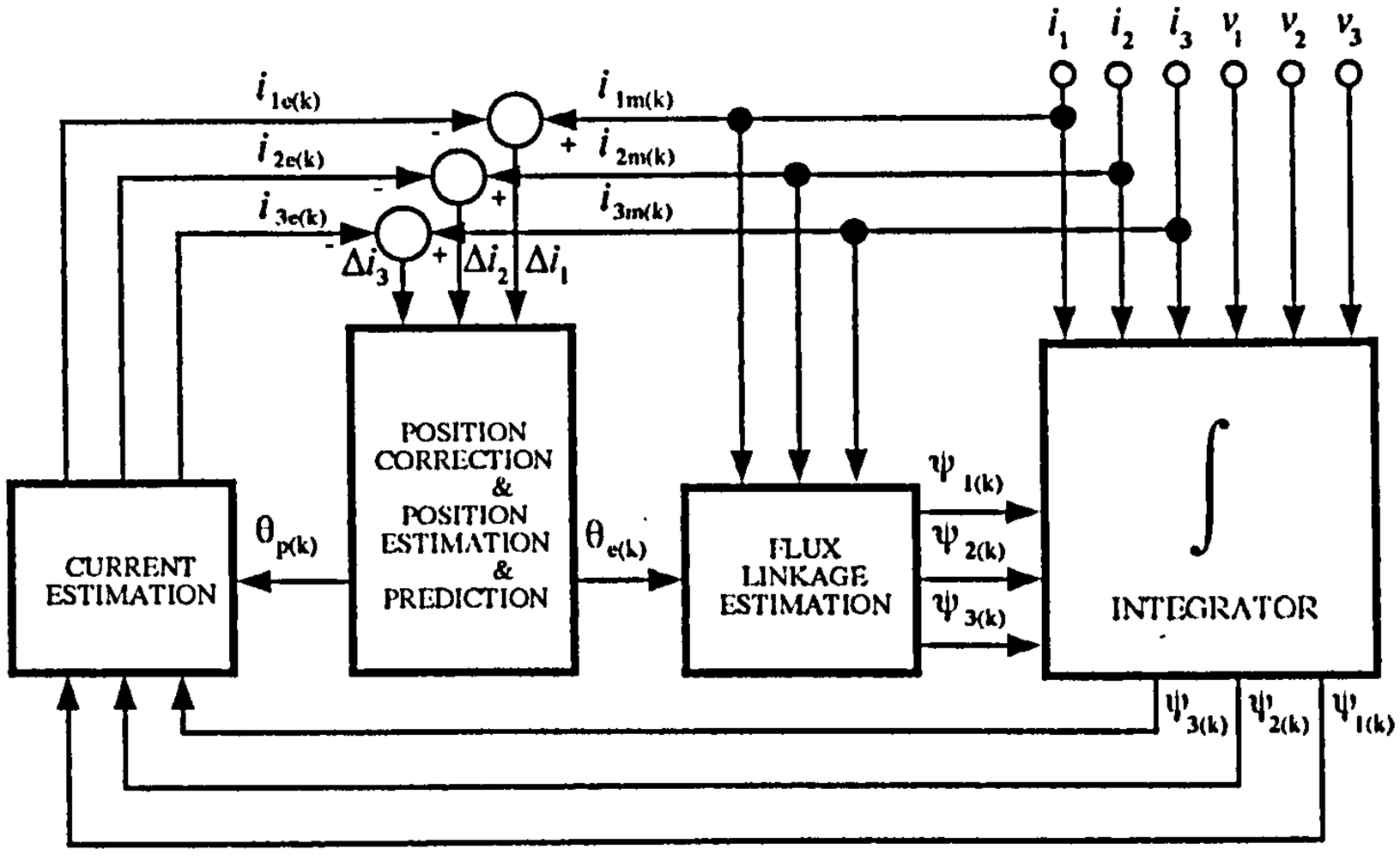

Figure 5.11 Using the estimated position for flux linkage correction in real-time estimation.

5.4 THE FLOWCHART AND SIMULATED RESULTS OF THE POSITION ESTIMATOR

5.4.1 The Flowchart of the Position Estimator

A flowchart describing the logical flow of the software routine is shown in **Fig.5.12.** The simplified flowchart of the position estimator can execute continuously. However, for reasons of limited data handling capability in the off-line data processing, it is stopped when the data limit is exceeded Basically, the computer algorithm can be divided into six parts:

a) Initialisation

b) Data capturing

c) Integration

d) Current estimation loop

e) Position error estimation, correction and prediction

f) Flux linkage correction loop

The *Initialisation* routine of the program reads the motor parameters and assumes that the motor is being started from standstill and sets inputs according to the reference phase. For instance, when the *Phase 1* is taken as reference, the initial values of flux linkages of the three phases should be $-\lambda_m$, $0.5\lambda_m$ and $0.5\lambda_m$ respectively.

The second routine reads the motor terminal quantities (the phase-to-star point voltages, and two line currents). As is well known, for three-phase star connected motors, the third line current can be calculated using the other two line currents. Therefore, in this routine, the third line current can be estimated without measuring it.

The next routine is the first computation routine. The discrete values of three-phase total flux linkages are obtained by using one of the integration methods described in **Section 5.2.3**. The rectangular integration rule has been used in the simulated drive. Three phase-to-star point voltages and line current are read in this routine, and the integration is performed using a given value of winding resistance (assumed equal and constant for all three phases).

At starting, since the current is zero, the initial values of the total flux linkages ($\psi_{1(k-1)}$, $\psi_{2(k-1)}$, $\psi_{3(k-1)}$) are proportional with the magnitude of magnet flux linkage λ_m as defined in the *Initialisation* routine, and as will be explained later, these values are updated by the flux linkage correction routine.

The *Current Estimation Loop* routine accepts the discrete values of the flux linkages ($\psi_{1(k)}$, $\psi_{2(k)}$, $\psi_{3(k)}$) and estimates the line currents ($i_{1c(k)}$, $i_{2c(k)}$, $i_{3c(k)}$) based on **Eq.5.12** or **Eq.5.14** whether the motor has variable or constant winding inductance. In the simulation, it is assumed that the motor has constant winding inductance (see **Table 2.2**), so **Eq.5.14** is evaluated to estimate the line currents. The estimated line currents are then compared with the measured currents ($i_{1m(k)}$, $i_{2m(k)}$, $i_{3m(k)}$), and the current errors ($\Delta i_{1(k)}$, $\Delta i_{2(k)}$, $\Delta i_{3(k)}$) are calculated. These current errors are used in the *Position* routine.

The *Position Error Estimation* routine is executed to correct the initially predicted rotor position ($\theta_{p(k)}$). The position errors are estimated for every single phase based on the **Eq.5.17**. However, as explained earlier, at certain rotor positions and line current levels some phases are better indicators of rotor position error than others. Therefore, a single revised position is obtained by appropriate weighting of the separate errors according to the current levels. The revised single position is used to update the position by adding the position error to the previous predicted position (see **Eq.5.19**). The *Prediction* method explained in detail in **Section 5.3.3**, uses three position data and extrapolates to find the 4th value of the position which does not lie within the measured time interval. In the simulation and real-time analysis, the routine then predicts the next discrete position value by second order polynomial curve fitting.

Finally, the *Flux Linkage Correction Loop* routine is executed for the flux linkage correction (see **Section 5.3.4**). As will be shown later, this correction has the important effect of eliminating DC offset in the integration of voltage and current signals.

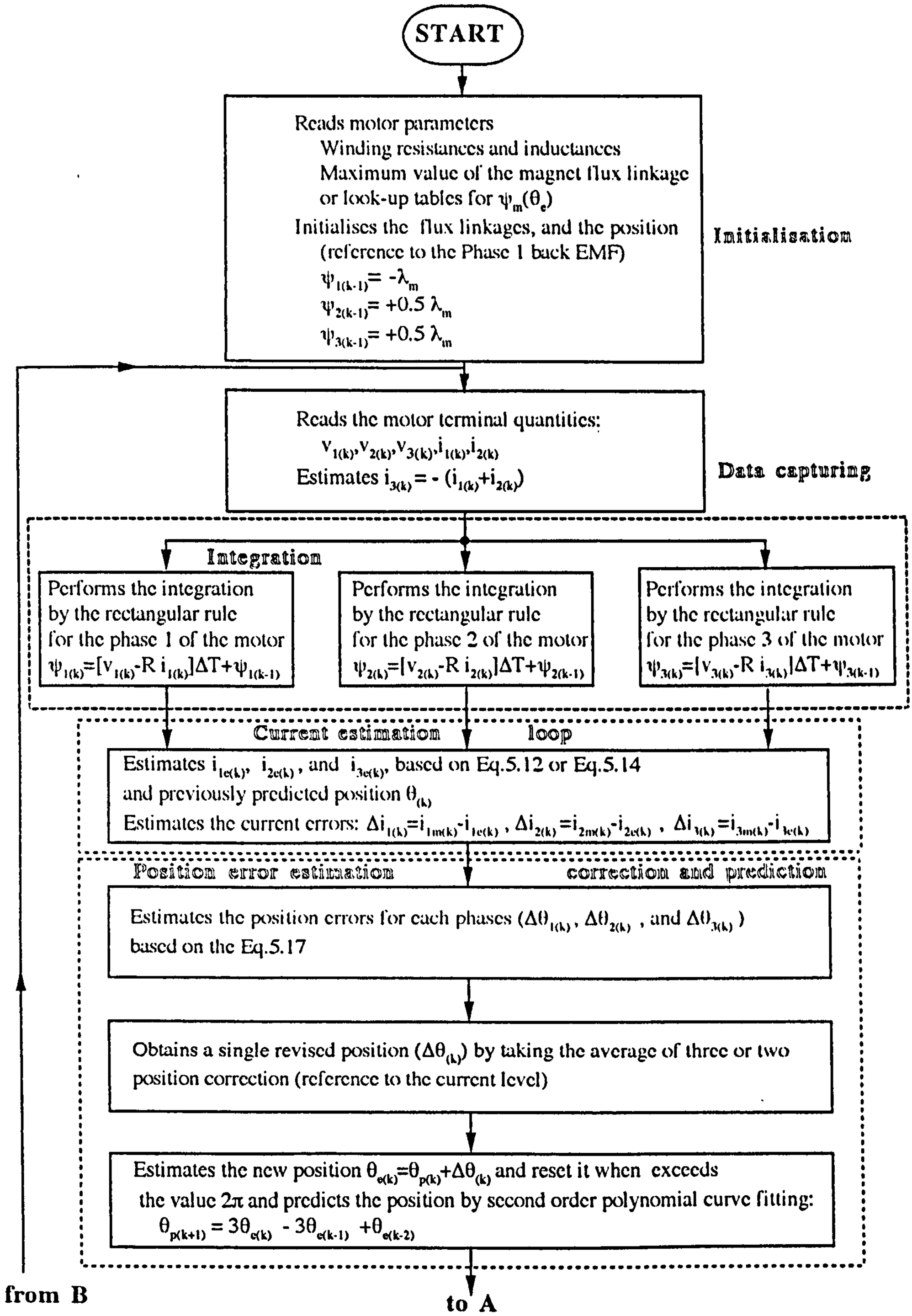

Figure 5.12 The flowchart for the position estimator **(continued...)**

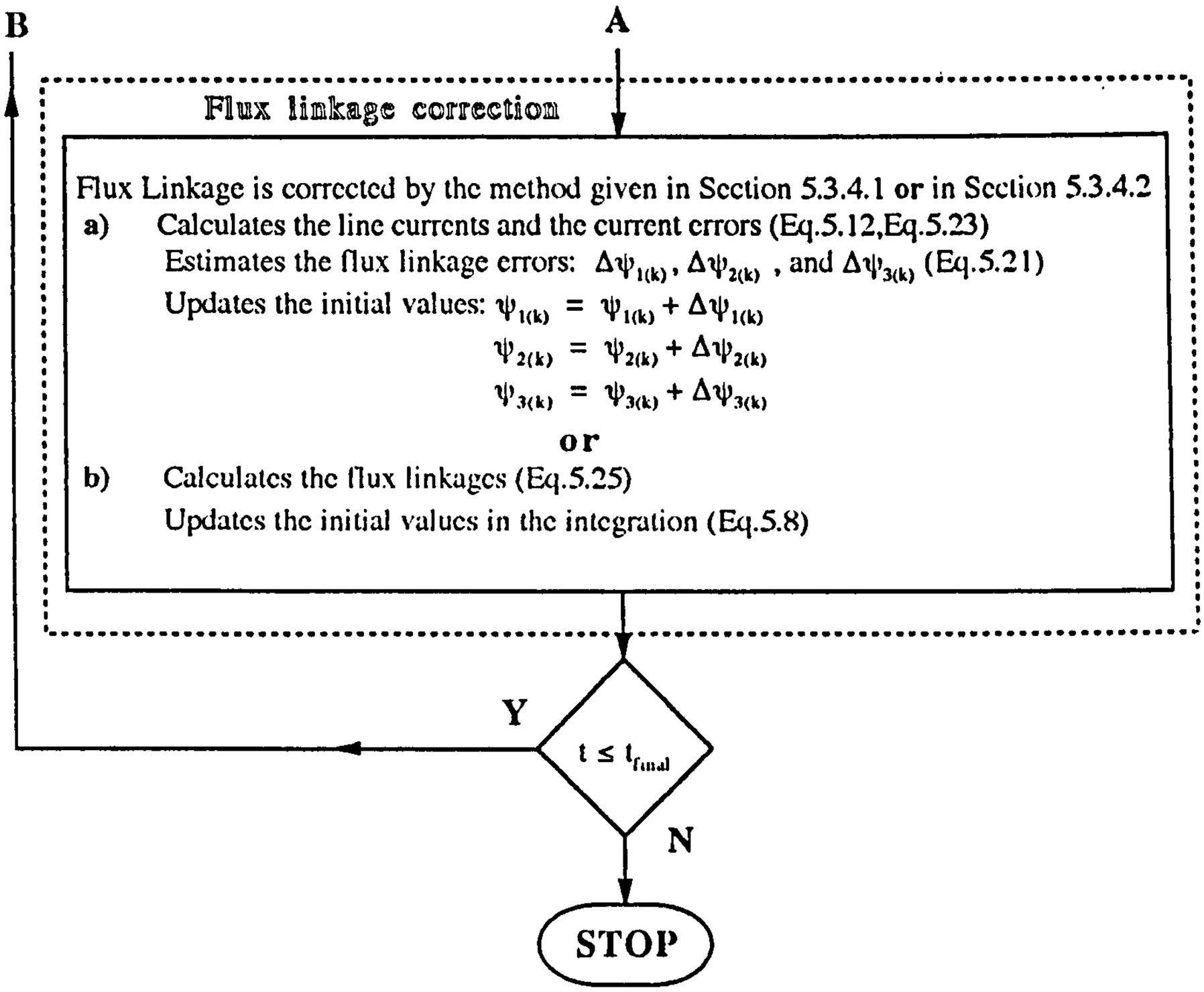

Figure 5.12 The flowchart for the position estimator

The estimation routine is repeated when the new terminal quantities are obtained from the drive. The measurement in the simulated drive has been done at every 10μs sampling time, because the value is equal to the capability of the actual data acquisition system as will be explained in **Chapter VI**. Although the sampling time can be increased to test the limit of the estimator for this particular application, it is going to examined and discussed in the next chapter.

5.4.2 The Simulated Results

The objective of this section is to verify the method described in the earlier sections. As shown in **Chapter IV**, the dynamic or any desired performance of the drive can be simulated in detail. This avoids building a complete drive and allows special adjustments required by the simulation to be implemented easily.

It is important to consider the performance of the estimator in the presence of modelling uncertainties and noise due to measurement. Modelling uncertainties include incorrect parameter values or assumptions for simplifications in the motor model. The parameters in the estimator should be identical to the physical parameters of the motor. If they are different, the performance of the algorithm will suffer. However, in this section, only certain effects will be analysed, and the generalised error analysis will be left to **Chapter VI** and discussed using the actual data.

To prove the ability of the algorithm, the simulated drive is operated very close to the actual drive, and the results are given under five distinct operating conditions:

a) Normal operating condition, no phase advance/delay, no errors in the initial conditions and measured quantities.

b) Effect of DC offset on the measured terminal quantities.

c) Effect of incorrect initial values of the flux linkages.

d) Starting the position estimation with wrong initial position.

e) Position estimation while the drive operates with 30° electrical advance.

All of the above operating conditions are performed at the transient case while the motor starts from standstill and accelerates with load. The DC rail voltage is 70V, and the hysteresis bandwidth of the current controller has been adjusted to ±0.5A. The sampling time of the estimator is 10μs.

Although the simulated drive (in **Chapter IV**) uses the actual back EMF profile (trapezoidal), the position estimation algorithm assumes sinusoidal magnet flux linkage variation in the motor as shown in **Fig.5.6.**

The first set of results are presented in **Figs.5.13-15.** The simulated drive was operated as described above, and the position estimation was performed without any adjustment in the initialisation routine. **Figs.5.13a** and **13b** show the single phase (**Phase 1**) phase-to-star point voltage and line current. Both measured and corrected flux linkage variations are shown in **Fig.5.13c.** As seen in **Fig.5.13c,** the assumption of sinusoidal magnet flux linkage in the algorithm is reflected onto the total flux linkage waveform. Therefore, the corrected flux linkage deviates form the actual flux linkage slightly.

Figs.5.14a-14b show the actual rotor position and the estimated position in rad respectively. As seen , the position estimator is able to follow the actual position with very small deviations. Fluctuations in the estimated positions are due to the sinusoidal magnet flux linkage assumption.

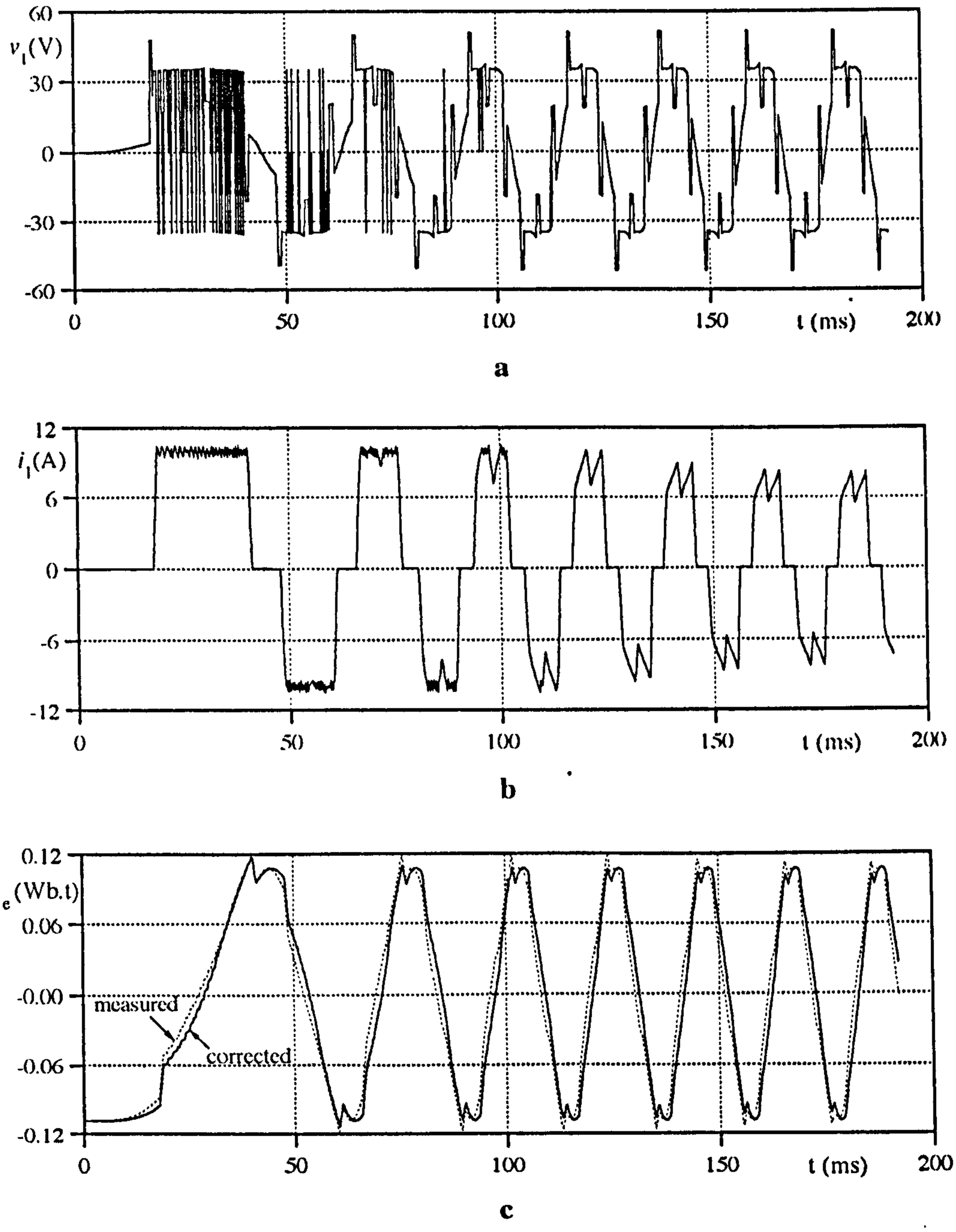

Figure 5.13 Simulated results showing the flux linkage estimations reference to the single phase voltage and the line current. Starting from standstill with DC rail voltage 70V and the maximum commanded current limit 10A.

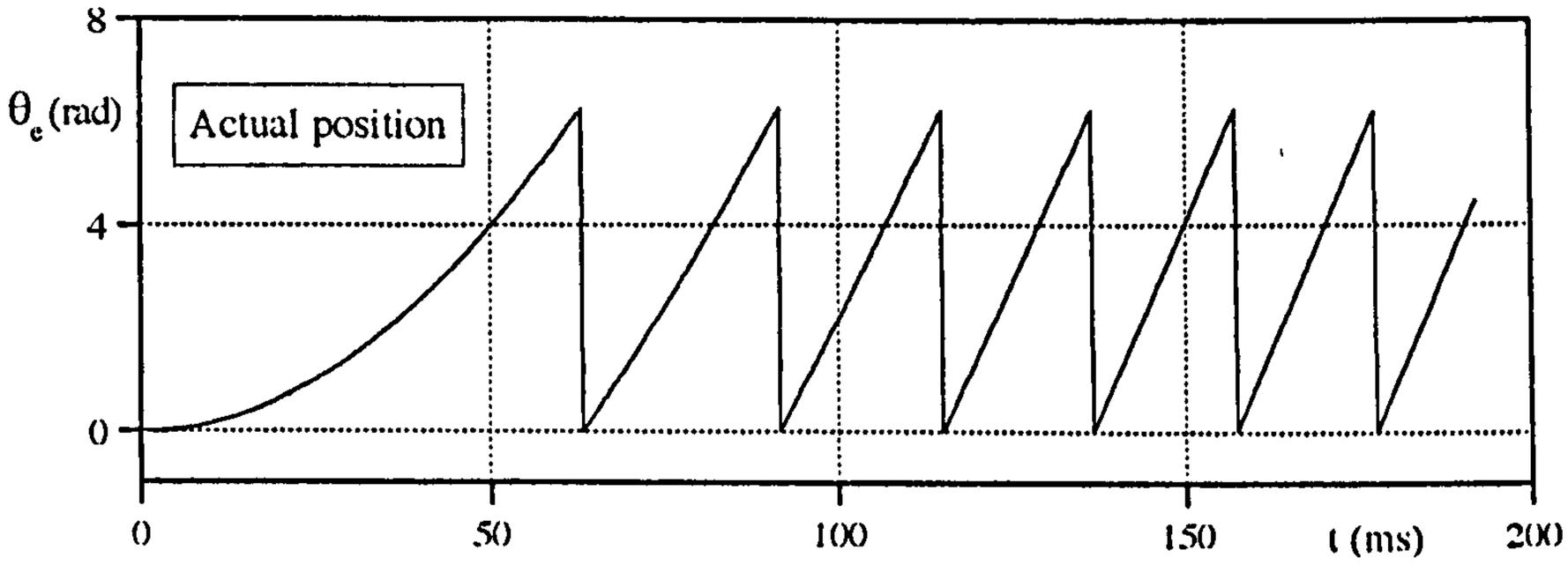

a

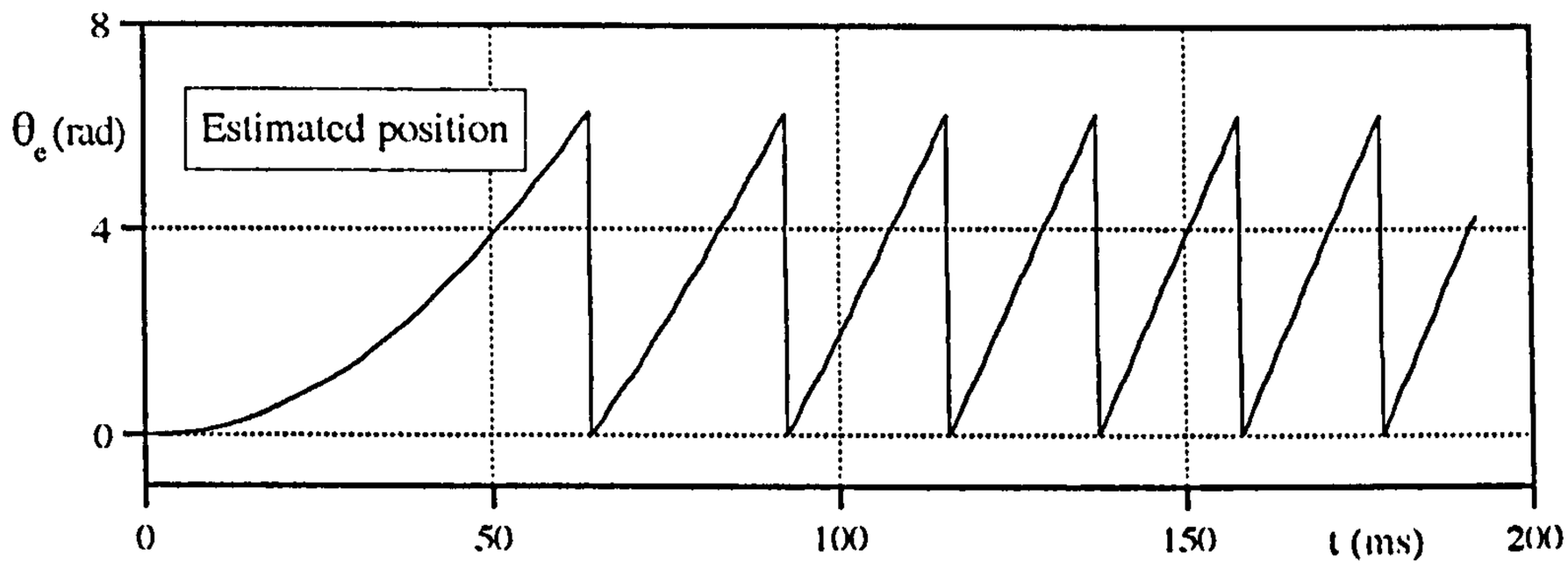

b

Figure 5.14 Actual and estimated rotor positions for the operating condition given in **Fig.5.13**.

Although the detailed estimated error waveforms are going to be given in **Chapter VI**, two waveforms of error estimations are shown in **Fig.5.15**. Referring to **Fig.5.8**, the estimated current error (**Fig.5.15a**) in the first current loop defines the position error, and corrects according to the weighting factor defined by motor's current level. The single revised position error is given in **Fig.5.15b**. The peaks on the position error waveform indicate the starting position of current conduction in the related phase.

As explained in **Section 5.2.3**, and expressed in **Section 5.4.1**, the initial conditions of the total flux linkages should be defined correctly to

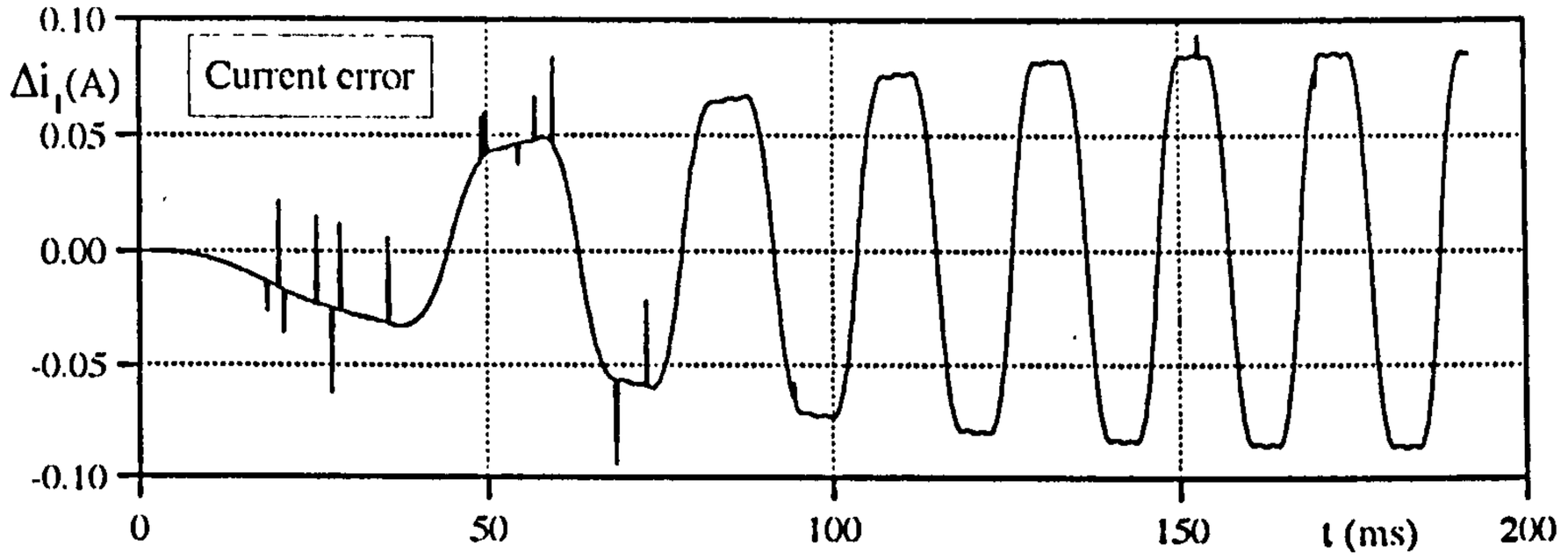

a

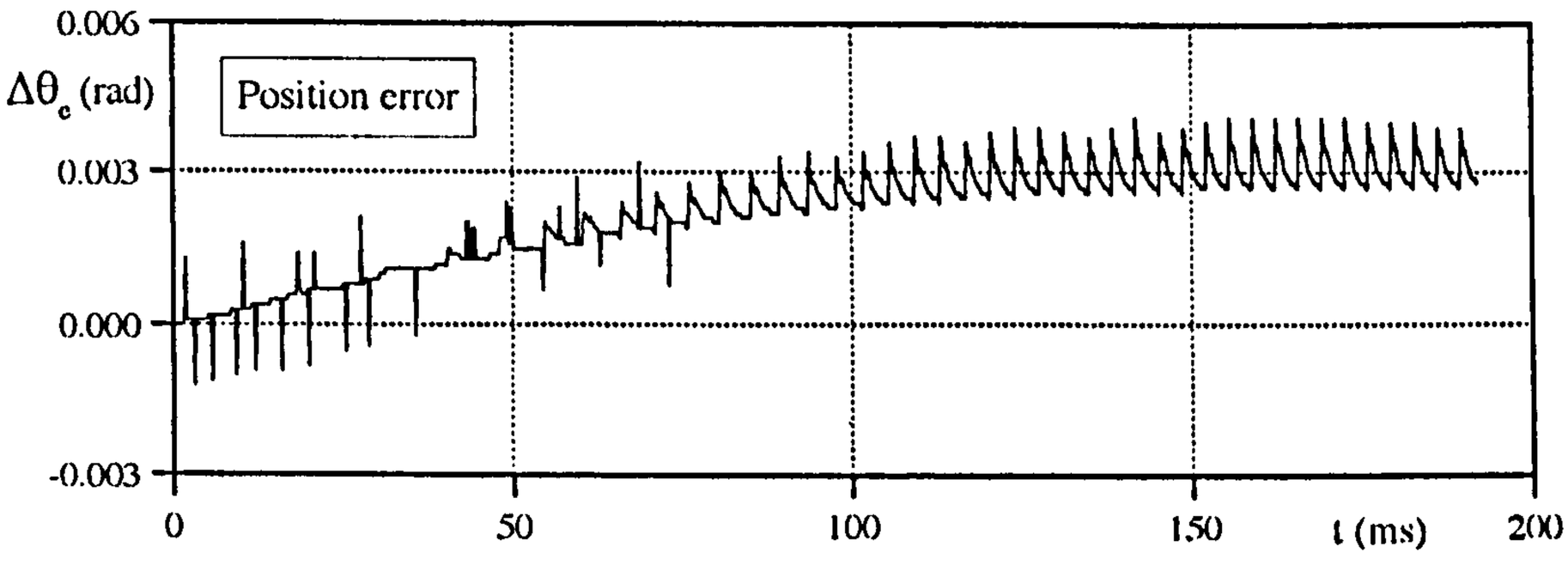

b

Figure 5.15 Estimated current and position errors representing the operation condition shown in **Figs.5.13** and **5.14**.

perform the integration given in **Eq.5.8**. If all signals (voltages and currents) have no DC offset, then the time integral values of the total flux linkages will not have a DC component. However, in real time applications, due to nature of measurement, there is always some degree of DC offset in the measured quantities. For continuous integration this may be a problem especially at low motor speeds. In the simulation, for the same operating condition as described earlier, 2% DC offsets were introduced to the terminal quantities of the motor before applying the position estimation algorithm. **Fig.5.16c** shows the effect of DC offset on the estimated flux linkage for **Phase 1.**

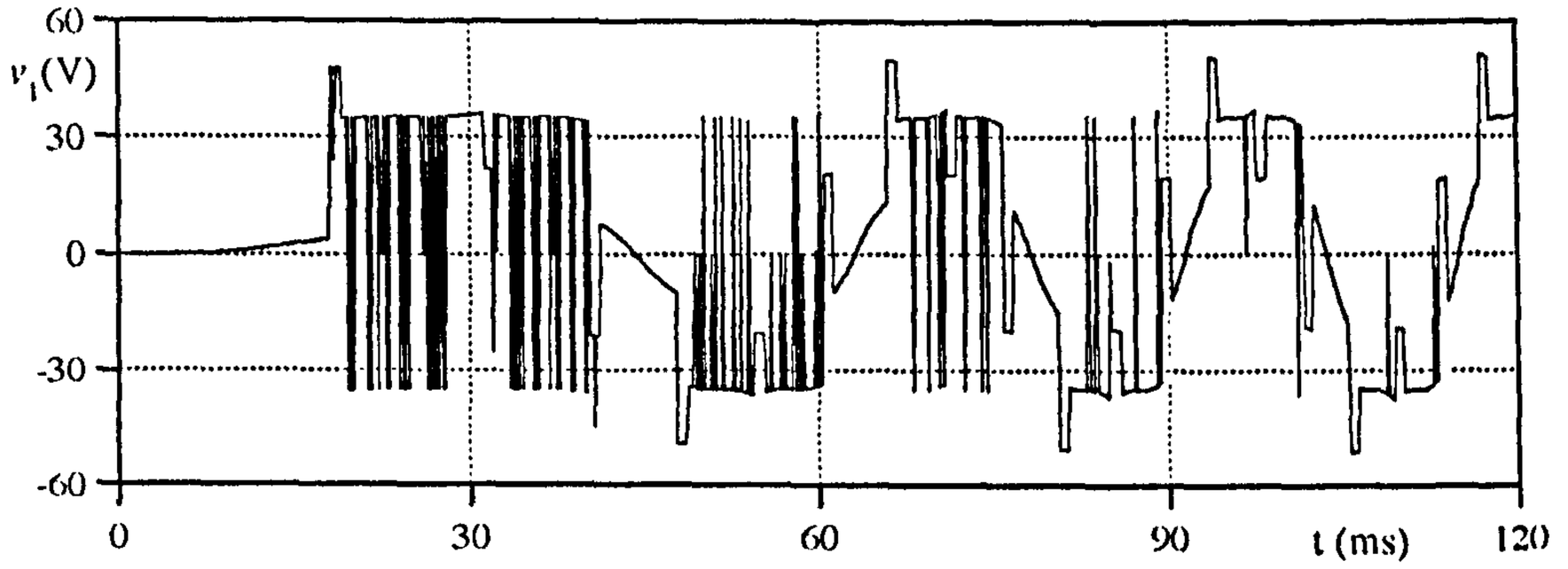

a

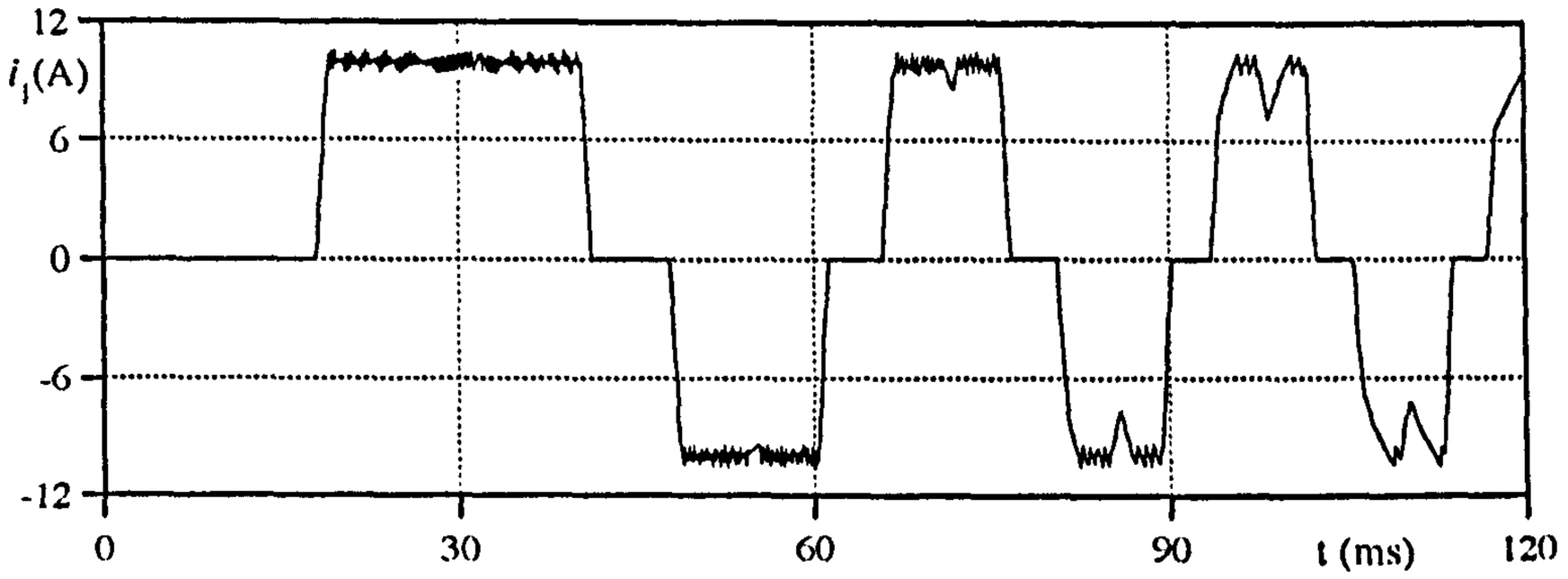

b

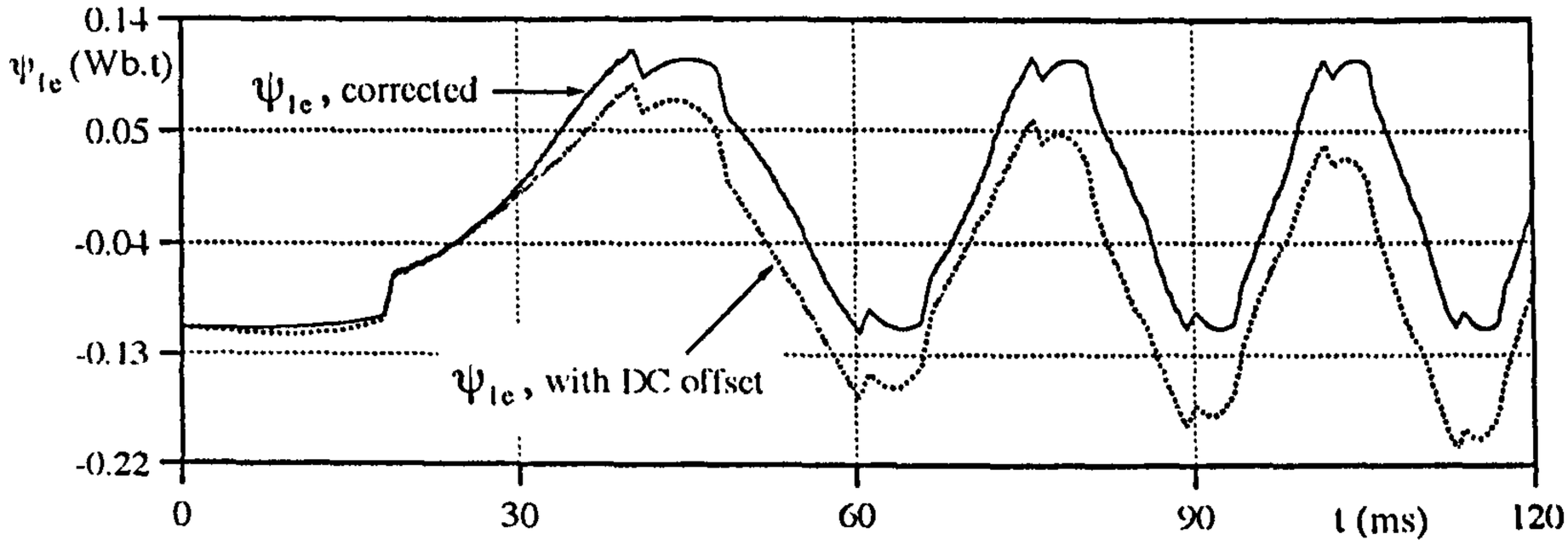

c

Figure 5.16 The effect of 2% DC offset in the measure terminal quantities onto the flux linkage waveform. $i_{1(DC)}$=-0.2A, $i_{2(DC)}$=-0.2A, $i_{3(DC)}$=+0.2A, $v_{1(DC)}$=-0.94V, $v_{2(DC)}$=-0.94V, $v_{3(DC)}$=-0.94V.

a) Phase 1 voltage waveform

b) Phase 1 current waveform

c) Estimated flux linkages

As can be seen in **Fig.5.16c**, if the flux linkage is not corrected, after few cycles, the effect of DC offset on the measured voltage and current makes the measured flux linkage impossible to use for analysis. However, the measured flux linkage is updated every time increment by the flux linkage correction ($\Delta\psi$). The corrected flux linkage waveform is illustrated with solid line in **Fig.5.16c** for the same phase.

The simulated results for the rotor position are given in **Fig.5.17**. As seen, the result is satisfactory. Since the sampling time is small (10μs), and the flux linkage correction routine is involved, the effect of DC offset on the estimated rotor position can be ignored in the position estimator.

It is found that, when the initial values of flux linkages are not the same as the real values ($\psi_{1(k-1)}=-\lambda_m$, $\psi_{2(k-1)}=+0.5\lambda_m$, $\psi_{3(k-1)}=+0.5\lambda_m$) defined in **Fig.5.13**, the estimated position deviates from the actual position initially. The simulated results for this mode of operation are illustrated in **Fig.5.18**. As seen in **Fig.5.18**, the initial condition to estimate the integration for **Phase 1** has been taken as $-1.2\lambda_m$ rather than the original value of $-\lambda_m$. As a result of this imperfection, it is found that the average value of the measured flux linkage is not zero as expected. However, the correction for the measured flux linkage can overcome this problem, and since the initial value of the integration is updated at the end of each discrete time calculation, the resultant flux linkage does not show a DC component in its overall variation.

Although, as summarised in the beginning of this section, many of the imperfect starting and operating conditions can occur together (such as wrong initial values of flux linkages together with DC offset) in the real time applications, the simulation provides a clear idea of the seperate effects. For the fourth type of transient result (**Fig.5.19**), the position

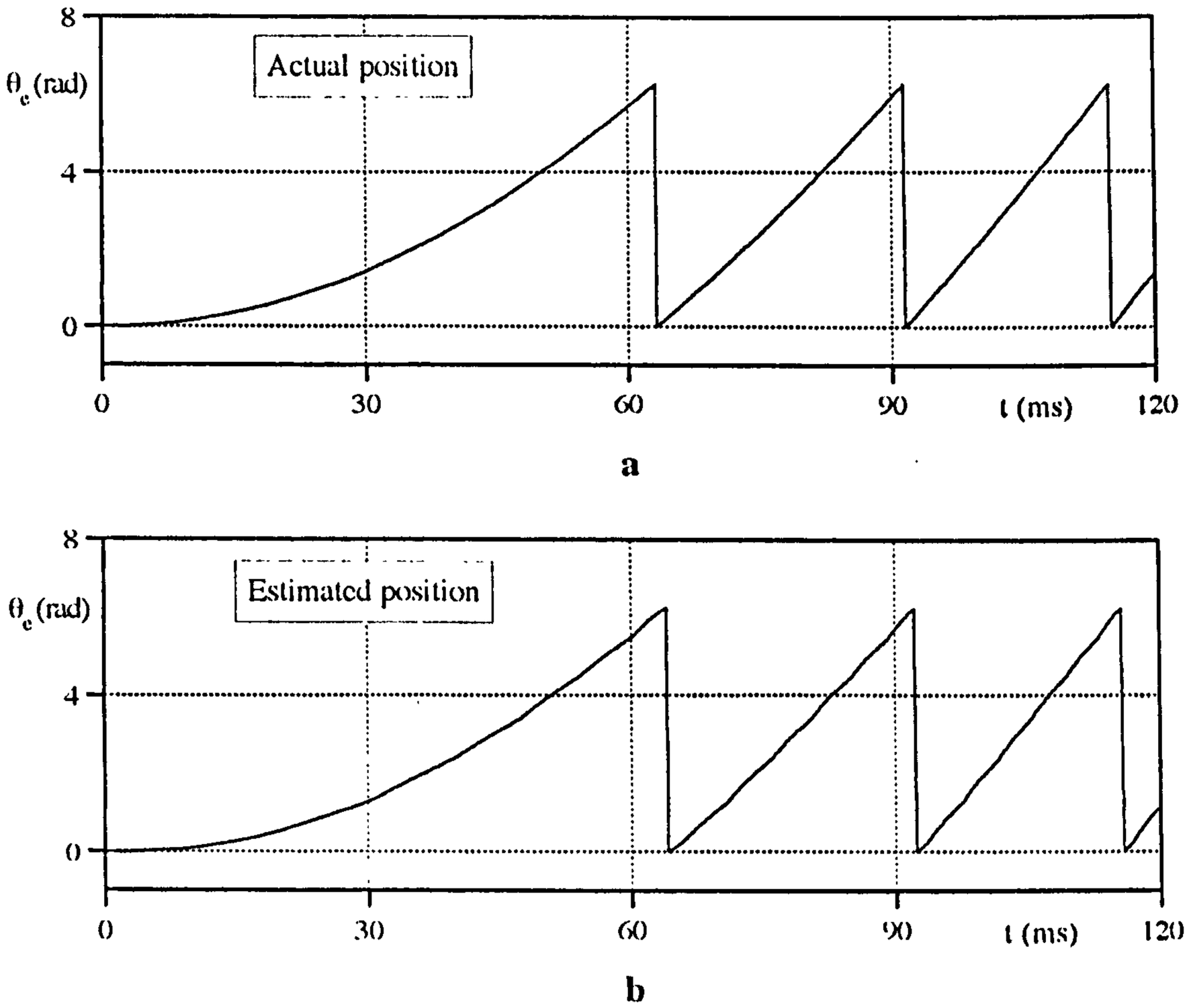

a

b

Figure.5.17 Actual and estimated rotor position waveforms for the case in **Fig.5.16.**

estimator assumes only a wrong initial position even though it may be correct in the actual (simulated) drive. As seen in **Fig.5.19a**, the measured flux linkage does not introduce any deviation from the ideal. However, due to the initial incorrect position, the corrected flux linkage deviates from the measured flux linkage to recover the effect of incorrect starting position within the first half cycle.

The small deviations on the following cycles of the flux linkages (**Fig.5.19a**) are due to the sinusoidal magnet flux linkage assumption as explained earlier. **Figs.5.19b** and **5.19c** show the actual and estimated positions respectively when the algorithm starts with an incorrect initial rotor position value (20° electrical ≈ 0.349 rad).

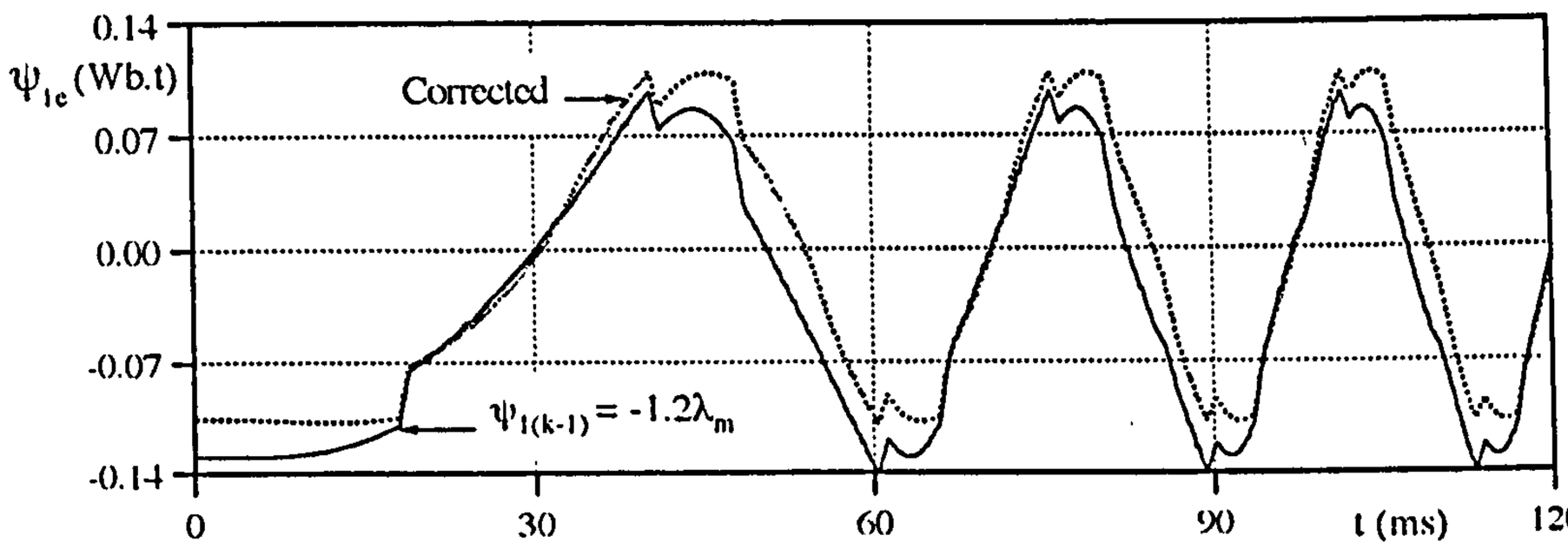

a

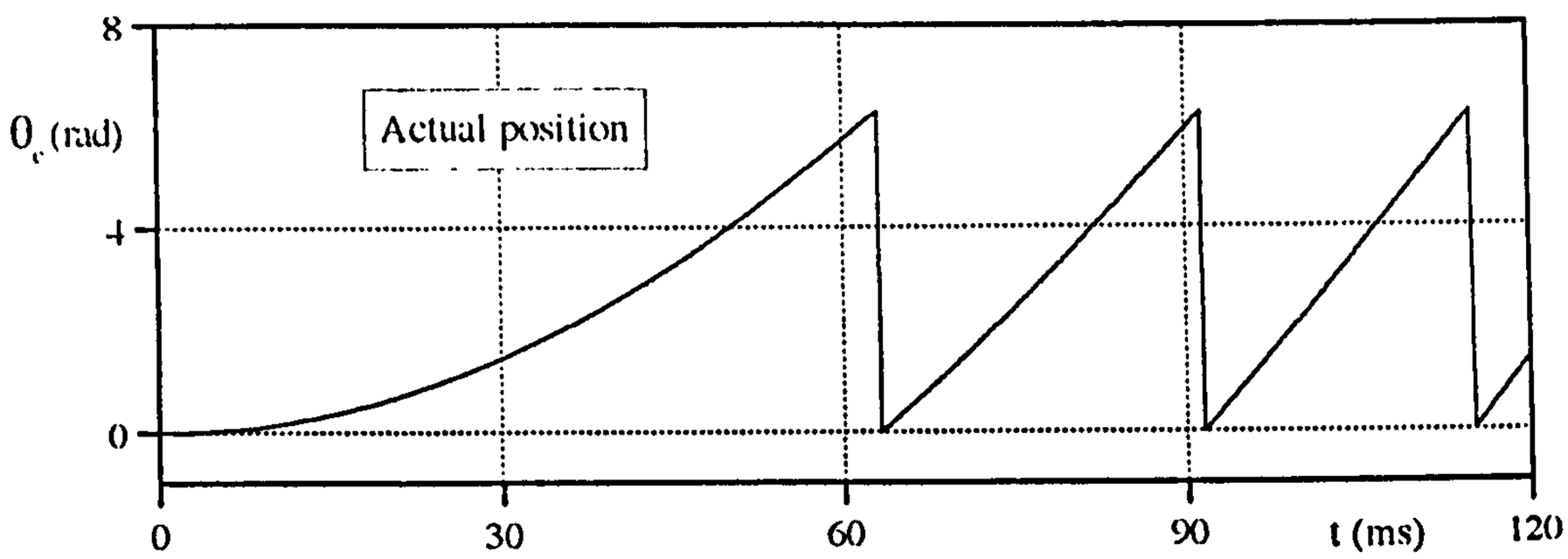

b

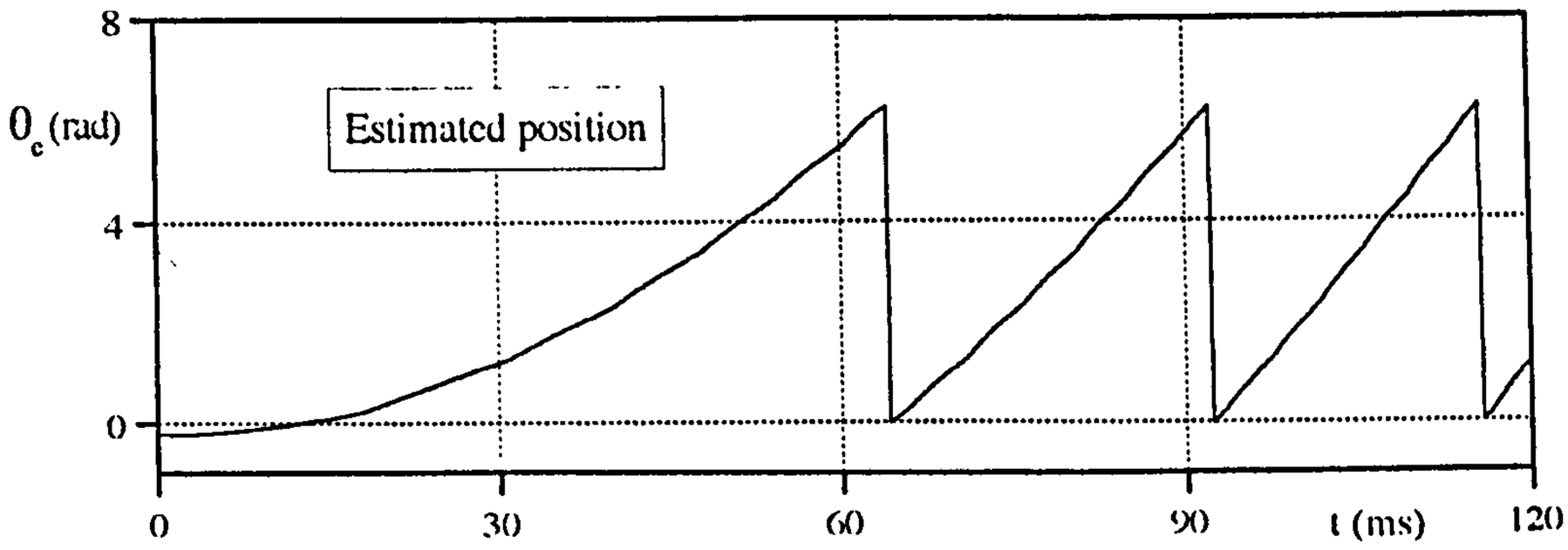

c

Figure 5.18 The position estimation with incorrect initial values of the flux linkages for the operation condition described in **Fig.5.16.** $\psi_{1(k-1)}=-1.2\lambda_m$, $\psi_{2(k-1)}=0.7\lambda_m$,. $\psi_{3(k-1)}=0.3\lambda_m$

a) Measured and corrected flux linkages for **Phase 1.**

b) Actual rotor position in the simulated drive.

c) Estimated position in the estimator.

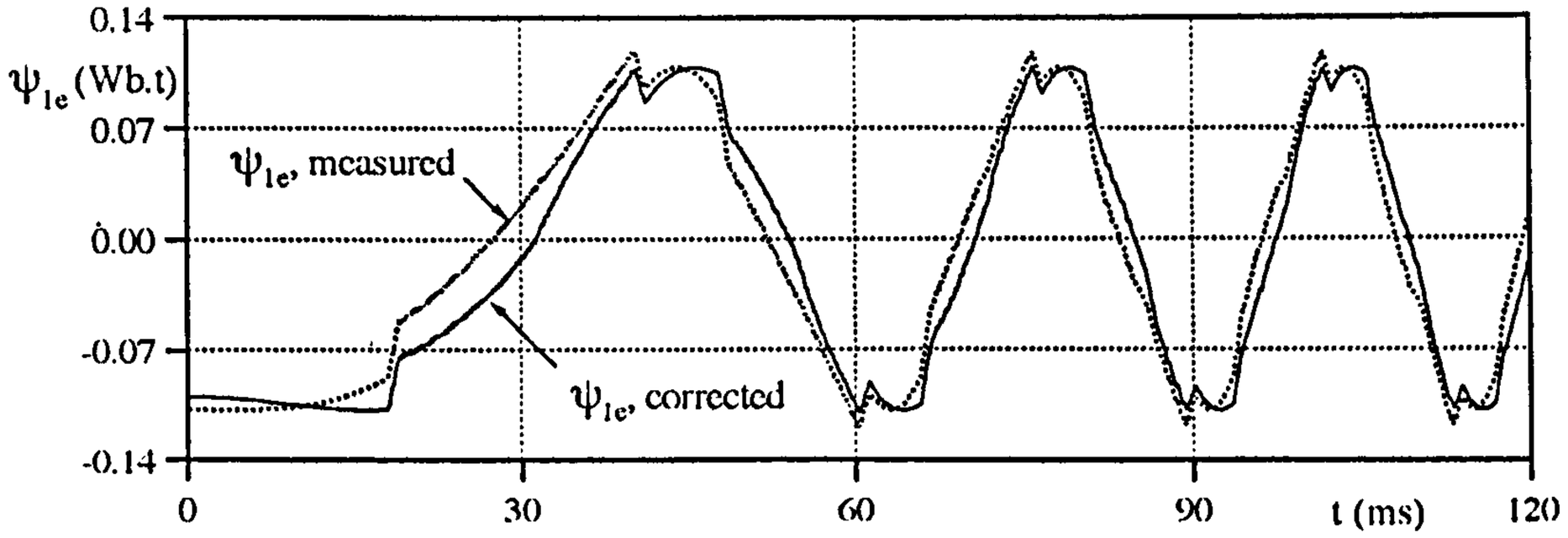

a

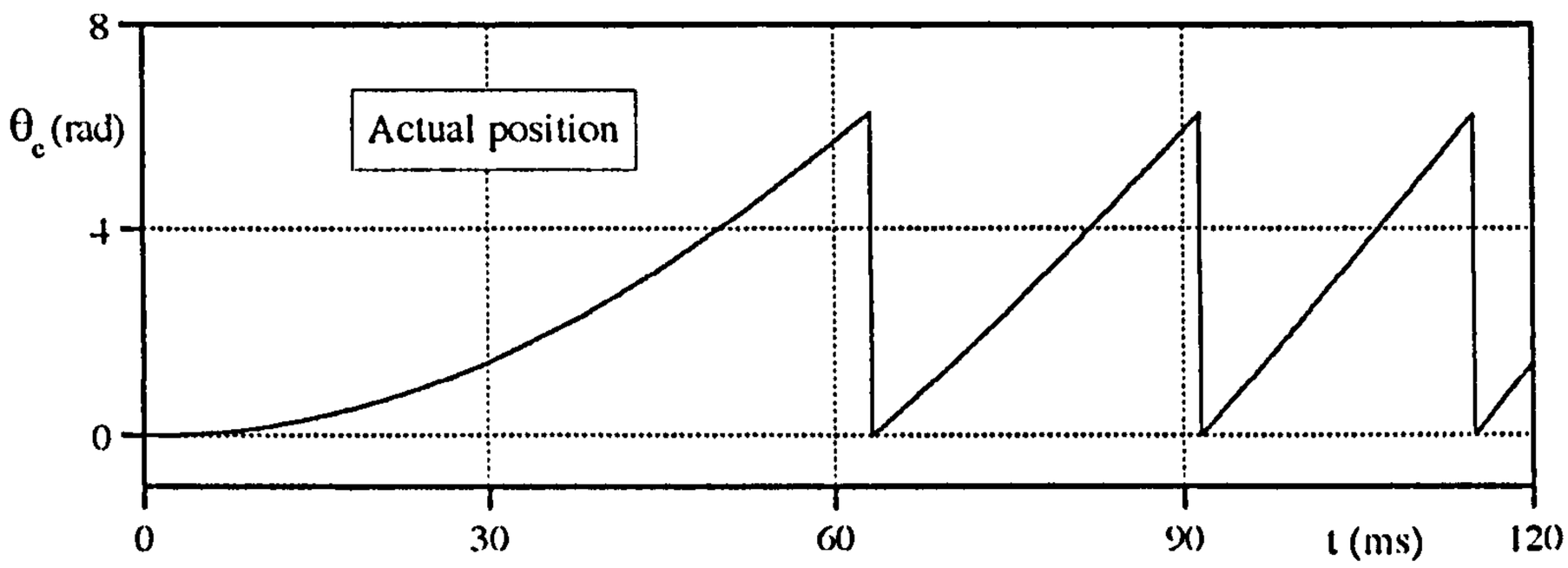

b

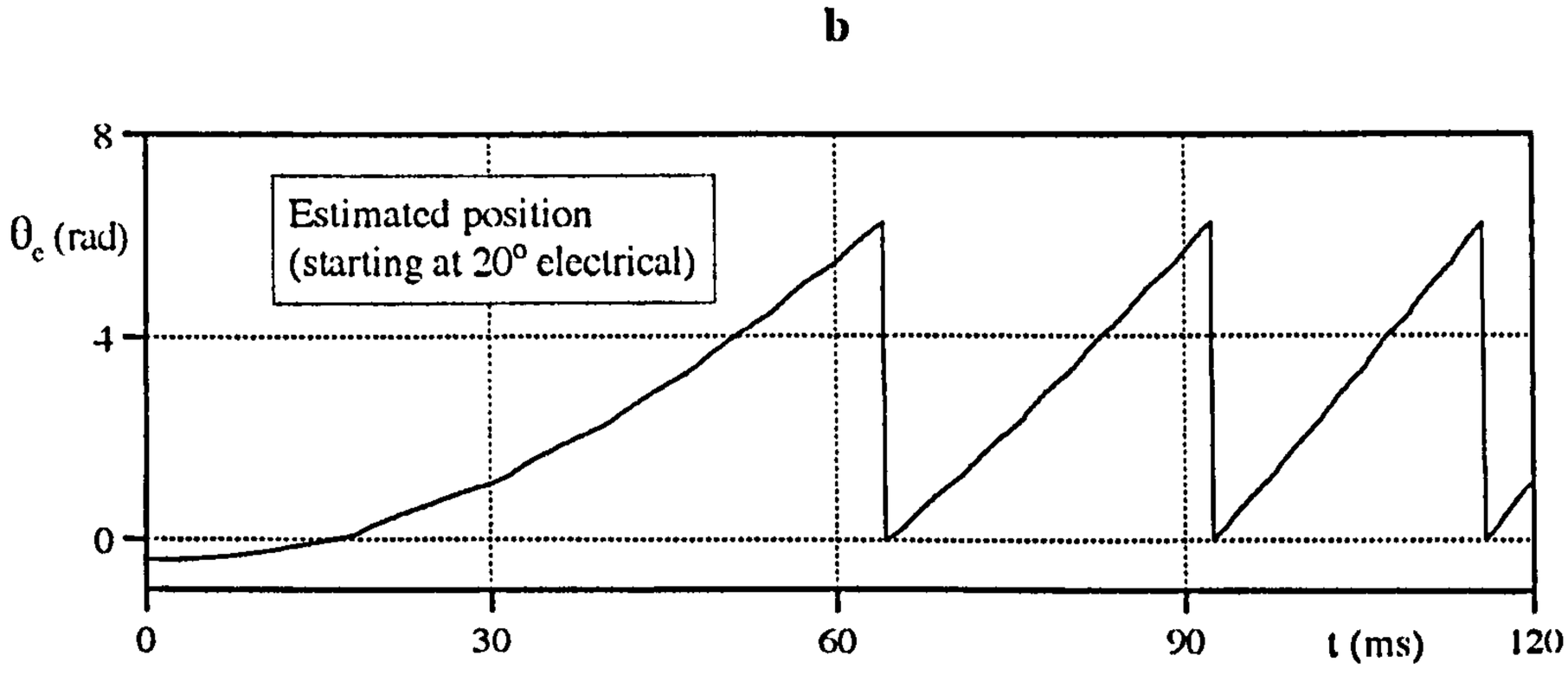

c

Figure 5.19 The results showing the flux linkages and rotor positions for the operation condition given in **Fig.5.16** while the initial position is 20° electrical (0.349 rad).

a) The measured and corrected flux linkages

b) Actual position

c) Estimated position starting with incorrect initial position

The last unique operation of the drive examines phase advancing in the controller, and the effect of it on the estimated position. **Fig.5.20** represents the voltage, the current, and the estimated flux linkages while the simulated drive operates with 30° electrical phase advance. The effect of phase advance (or delay) reflects to the total flux linkage waveform by shifting the current conduction angle with reference to the magnet flux linkage. As seen in **Fig.5.20c**, the assumption of only the changing of phase advance angle, effectively makes the initial values of flux linkages incorrect. ($\psi_{1(k-1)} \neq -\lambda_m$, $\psi_{2(k-1)} \neq 0.5\lambda_m$, and $\psi_{3(k-1)} \neq 0.5\lambda_m$). However, the flux linkage correction routine can shift the measured flux linkage to overcome the resultant DC value on the flux linkage (**Fig.5.20c**).

In this mode of operation, since the position estimation algorithm effectively follows the magnet flux linkage waveform, comparison of the actual and estimated position (**Fig.5.21**) confirms the ability of the algorithm. It should be noted here that, the actual position given in **Fig.5.21a** represent the position with reference to the actual line current (for **Phase 1**). The 30° electrical phase difference (reference to the **Fig.5.21a**) in the estimated position in **Fig.5.21b** clarifies the actual operation mode in the drive.

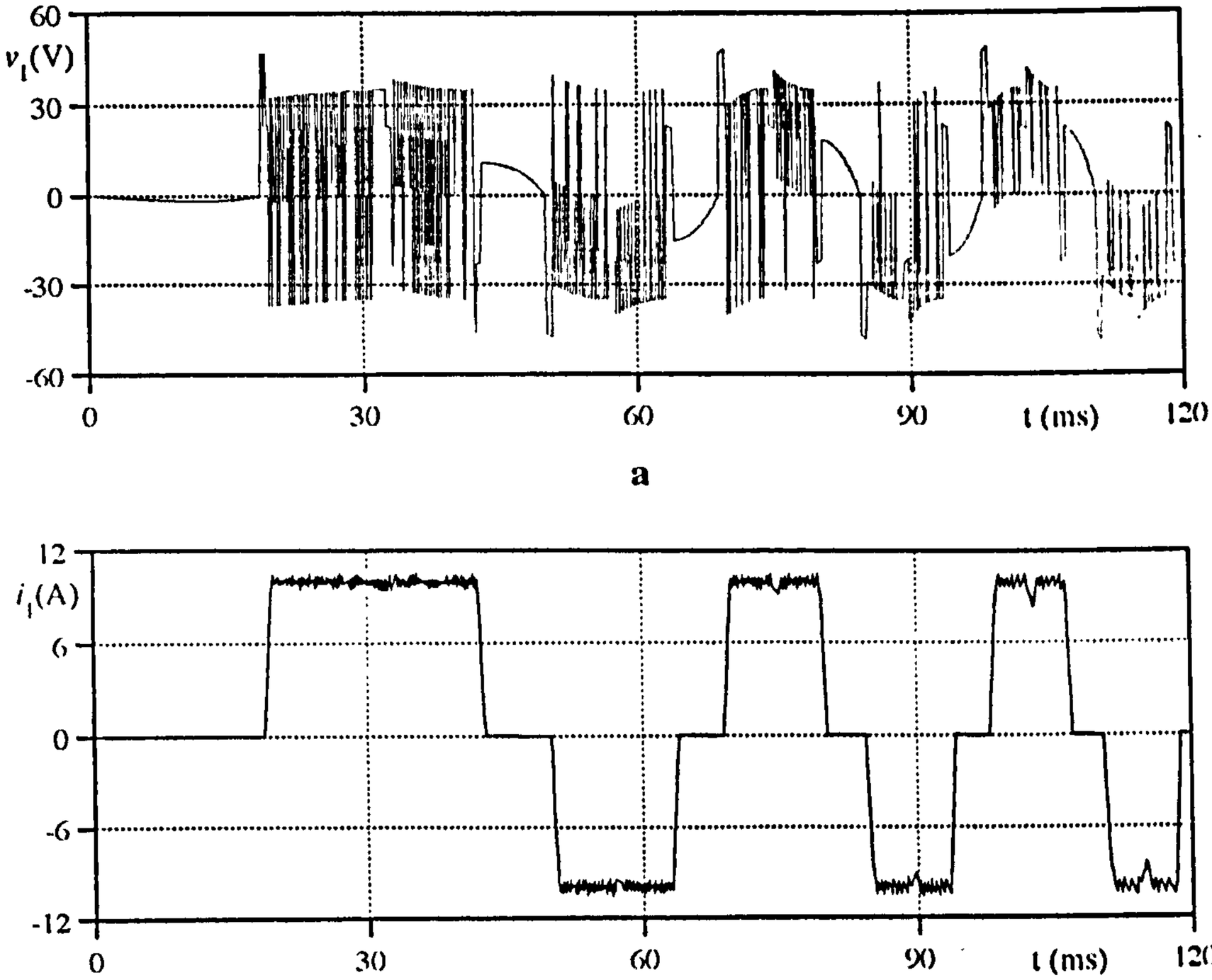

Figure 5.20 Operation with 30° electrical phase advance of the simulated drive.

a) Phase 1 voltage waveform

b) Line 1 current waveform

c) Measured and corrected flux linkages for **Phase 1**

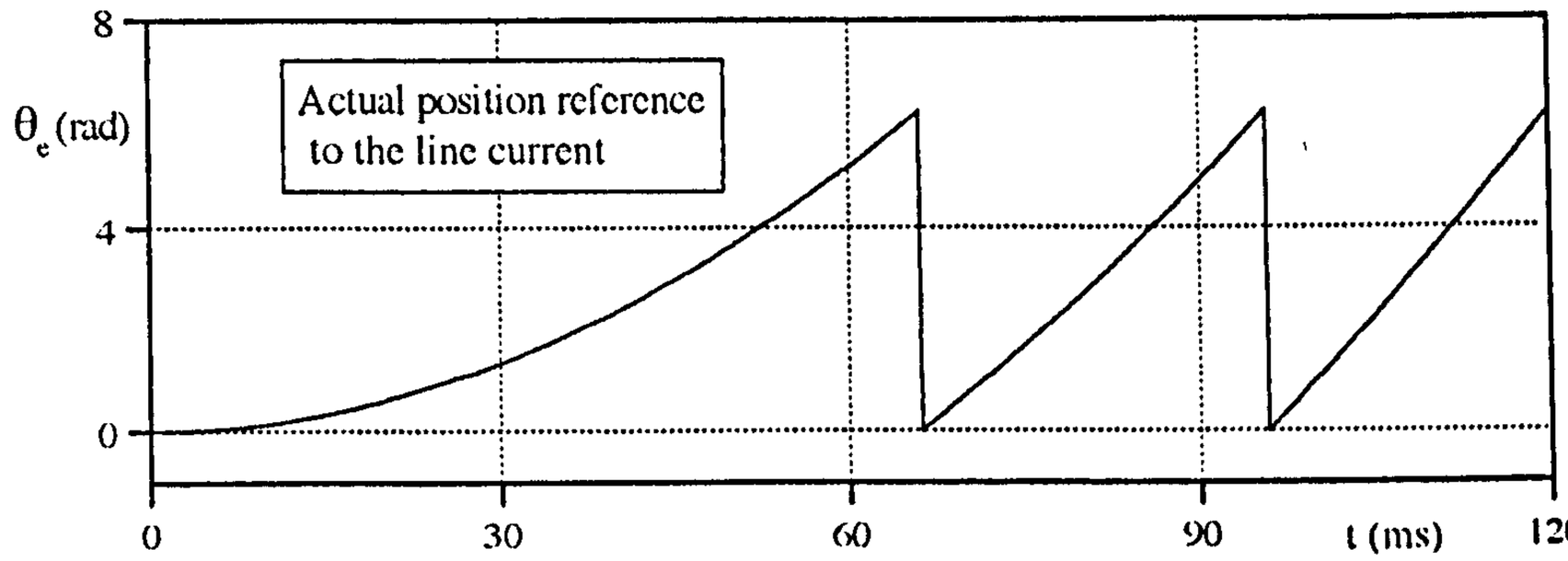

a

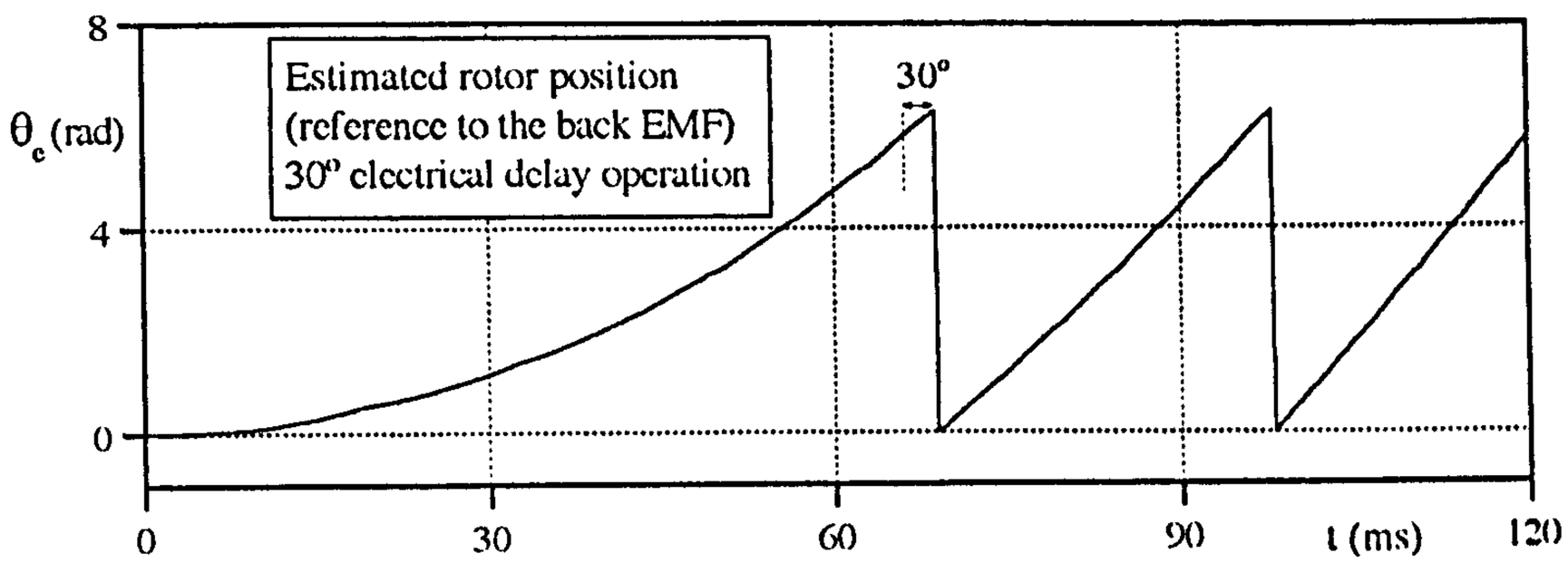

b

Figure 5.21 Waveforms for 30° electrical phase advance operation of the drive corresponding to **Fig. 5.20**.

a) The actual position reference to the **Phase 1** current

b) Estimated position reference to the **Phase 1** back EMF

5.5 CONCLUSIONS

The brushless PM motors can be commutated in different ways as explained in the introduction and previous chapters. The conventional way of measuring rotor position involves mechanical position sensors usually attached to the motor shaft. When a mechanical position sensor or a position deducing method is chosen, the price, the reliability, the resolution, the ruggedness of the system and its limitations must be considered. Besides the basic need to accurately determine the rotor position, the shaft position sensor must operate under the same environmental conditions as the motor. The choice of method may also depend on the control system implementation such as a microprocessor.

Recently, there has been much interest in techniques for eliminating the rotor position sensing device, and deducing position by analysing the motor's voltage and/or current waveforms. Although, a number of position detection techniques have been proposed in the literature, their application areas and operation are limited.

The new method proposed in this chapter gives an alternative position detection technique The proposed method senses the motor's phase voltages and currents to determine the rotor position, and can be classified under the subsection "*Observer Methods*" given in **Section 5.1.2**. The method has been discussed in detail using the state-space model of the brushless PM motor, and the mathematical process of the sensorless operation algorithm has been presented in a generalised form.

It was shown that once a discrete data point on the flux linkage surface has been estimated, the mathematical calculations can be performed for each

phase to estimate the rotor position. The method has been verified using the computer simulation of the overall drive, and a wide range of simulated results have been given showing the algorithm's ability in the case of incorrect starting conditions as well as in normal operation. In the next chapter, the developed method will be verified by experimental results obtained from the implemented drive.

CHAPTER VI

NOVEL POSITION SENSORLESS OPERATION: Implementation and Experimental Results

6. INTRODUCTION

The main purpose of **Chapter V** was to describe the mathematical model for sensorless operation which is able to deal with the actual drive for any motor type, excitation type, and operating condition. The method was explained in detail, and simulated in the same chapter. Although, the given results analysed the operation with faulty parameters, and demonstrated the algorithm's ability, they do not represent the actual drive which is the subject of this chapter.

In the chapter, the proposed sensorless operation algorithm is executed by using on-line real-data as well as off-line real data captured by a data acquisition system.

The real-time results are subject to further developments for future applications. The chapter presents a wide range of experimental results demonstrating the reliability of the method. The effect of parameter deviations and measurement sensitivity of the method are discussed.

6.1 EXPLANATION OF HARDWARE DEVELOPED TO ACQUIRE REAL-DATA

The whole measurement and evaluation setup for off-line data analysis is illustrated in **Fig.6.1**. The data acquisition system used in the work was a commercially available *Datalab 6000* module, and has the key features shown in **Table 6.1**.

Table 6.1 Some key features of the data acquisition system

5 single-ended, 10 differential input channels
Programmable input voltage range:
±50V maximum for Channel 1
±20V maximum for Channel 2-5
12-bit resolution analog-to-digital converters (A/Ds):
External trigger input
10μs minimum sample rate for five channel measurements

As known, sampling rate, resolution range, accuracy, and noise immunity, all affect the quality of the digitised signal in real-time systems. The available minimum sampling rate (10μs) was used in the data acquisition system to acquire more data points. Since the whole control system in the experimental setup was isolated from the mains it can be assumed that all input signals have a common reference. Moreover, the leads from the signal source to analog input hardware are short. Therefore, the single-ended inputs are used.

The five input channels of the data acquisition system are used to measure three phase-to-star point voltages and two line currents. In the system shown in **Fig.6.1**, the voltage and current signals are measured directly by the sensors: current transducers and voltage dividers (**Fig.6.2**).

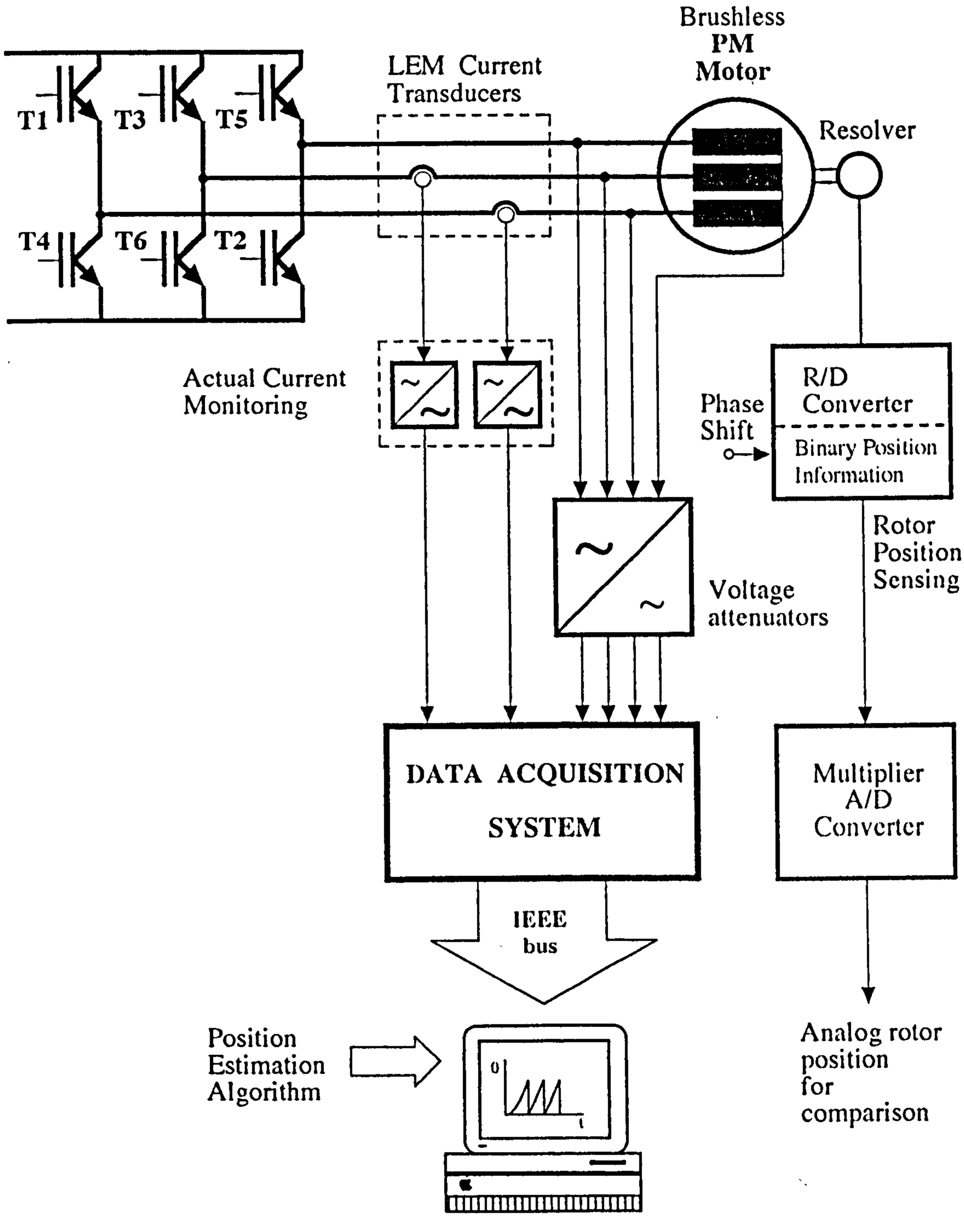

Figure 6.1 The complete block diagram of the data acquisition experimental setup.

The line currents are measured by LEM 25 current transducers which have 0 to 150kHz bandwidth, and the output voltage, which is proportional to the measured current, is amplified up to ±5V (at maximum current level) by the

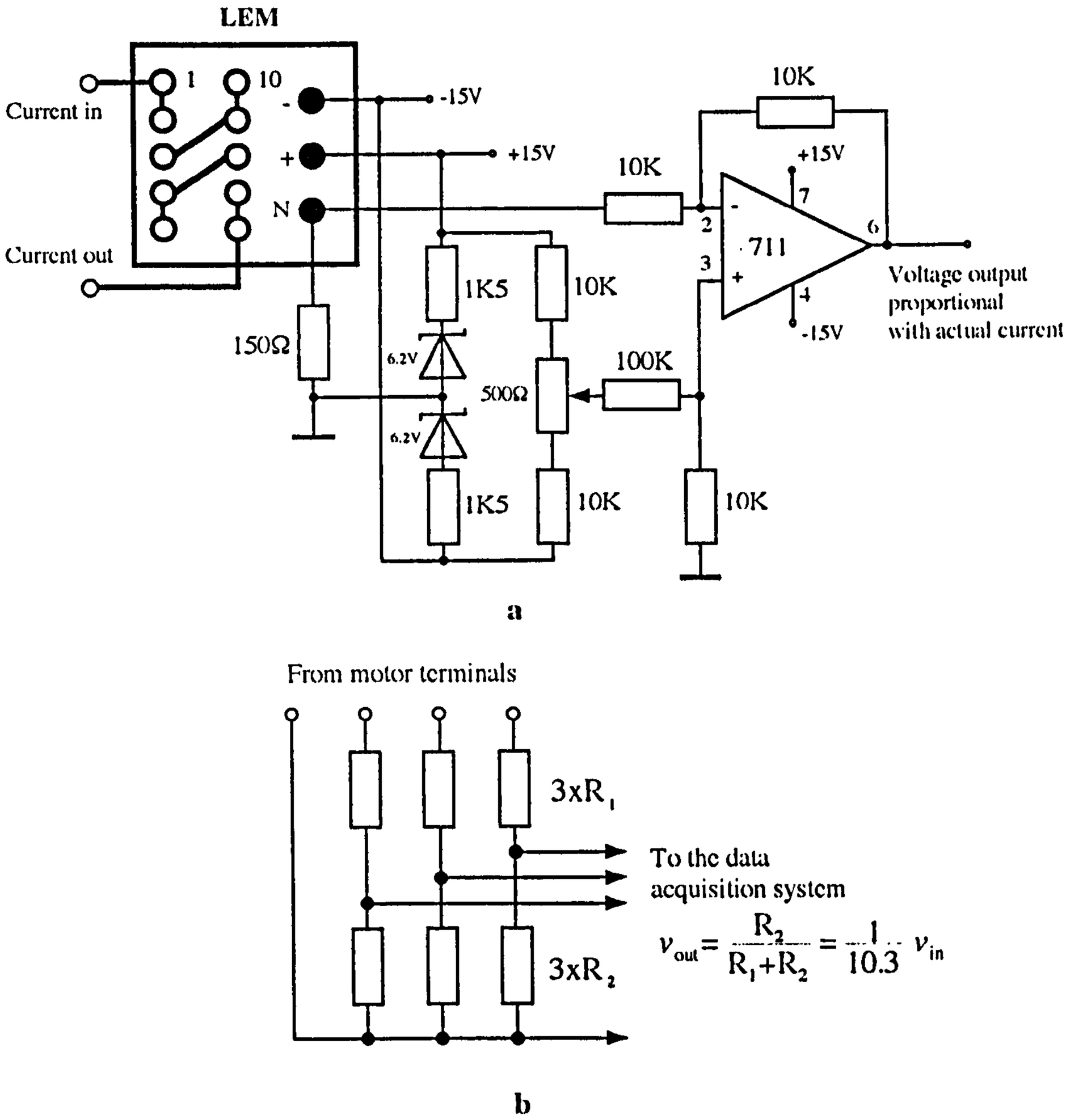

Figure 6.2 Implementation of current and voltage measurement

a) The circuit for single phase current measurement

b) Three-phase voltage dividers

circuit given in **Fig.6.2a**. Since the input impedance of the data acquisition system is high (1MΩ) , simple voltage dividers (**Fig.6.2b**) are used to measure phase-to-star point voltages. The voltages are attenuated with a predefined gain. The input signal gains for the current and the voltage measurements are 2 and ~10.3 respectively.

The actual rotor position signal is made available as an analog signal which is obtained from the output of the R/D converter by a multiplying D/A converter (**Fig.6.3**). The adders are used in the circuit to shift or to adjust the actual position signal reference to the desired line current. The actual analog position signal was also used to indicate the known initial position for starting from standstill. However, in the off-line test, due to lack of channels in the data acquisition system, the actual rotor position was measured with a second test keeping all operating conditions constant for a particular case.

For the highest possible resolution, the current and voltage signals should be equal to the maximum input range of the channels. Therefore, the programmable input voltages of the data acquisition system are adjusted for every operating condition in the drive.

The three-phase inverter was constructed with IGBTs, and the inverter is fed from the AC mains through a three-phase diode rectifier The transistor base signals are generated from a hysteresis current controller. The algorithm has been tested with a three phase axial field PM machine which has parameters shown previously in **Table.2.2**. The motor is star connected internally, and with access to the star point.

Although applications requiring an on-line process need a high speed processor, the PC used in the system determines overall off-line data processing. The voltage and current data blocks acquired by the data acquisition system are transferred to the PC through an IEEE parallel bus, then converted to a data file which represents the actual values after multiplying by the gains. The off-line processing of the position algorithm is performed continuously by reading the created data file at every desired time interval (equal to or bigger than 10μs).

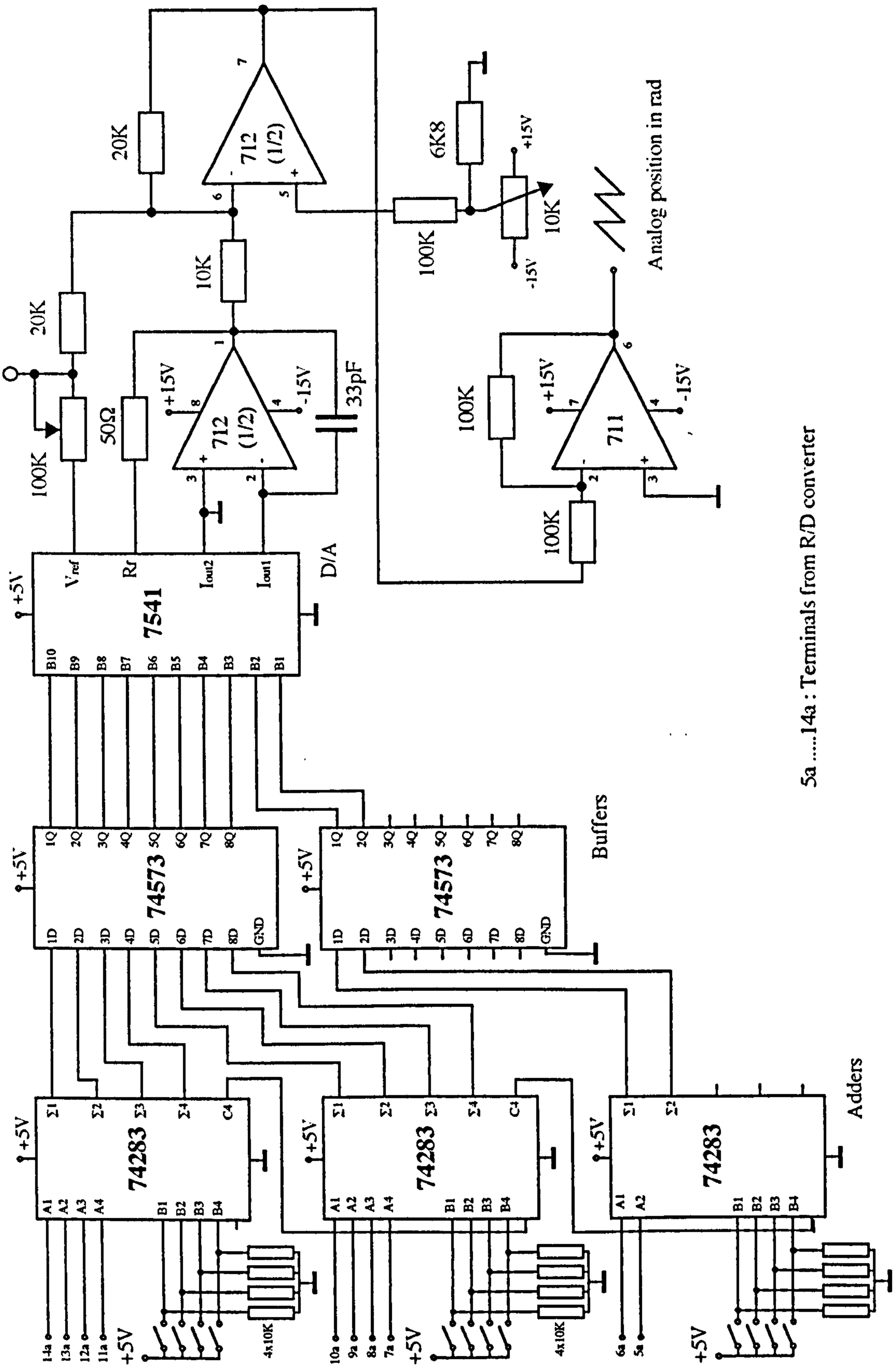

Figure 6.3 The circuit diagram for the analog position monitoring

6.2 EXPERIMENTAL RESULTS

A number of experimental results given in this section were tested in the brushless PM drive implemented during this research. The selected results represent transient operation as well as the steady-state. As explained in **Chapter IV**, the total system inertia was reduced (J_{total}=0.0097kgm²) to give fast mechanical response to the drive by using another axial field brushless PM machine as a load. **Fig.6.4** and **Fig.6.5** illustrate two basic experimental setups used to give the desired load performance.

In both operating conditions (transient or steady-state), the PM motor is loaded or unloaded through a three phase diode rectifier which is connected to the PM generator's terminals as shown in **Figs.6.4-5**. The system shown in **Fig.6.4** was used for the steady-state test and loading or unloading the motor. The desired amplitude of line current of the motor is achieved by adjusting the value of the power resistor R. The resistor R_{step} indicates the step load resistor. While the drive is operating, the power resistor R_{step} is connected in parallel to the original resistor to increase (or to reduce by disconnecting) the load, giving the effect of a step load change.

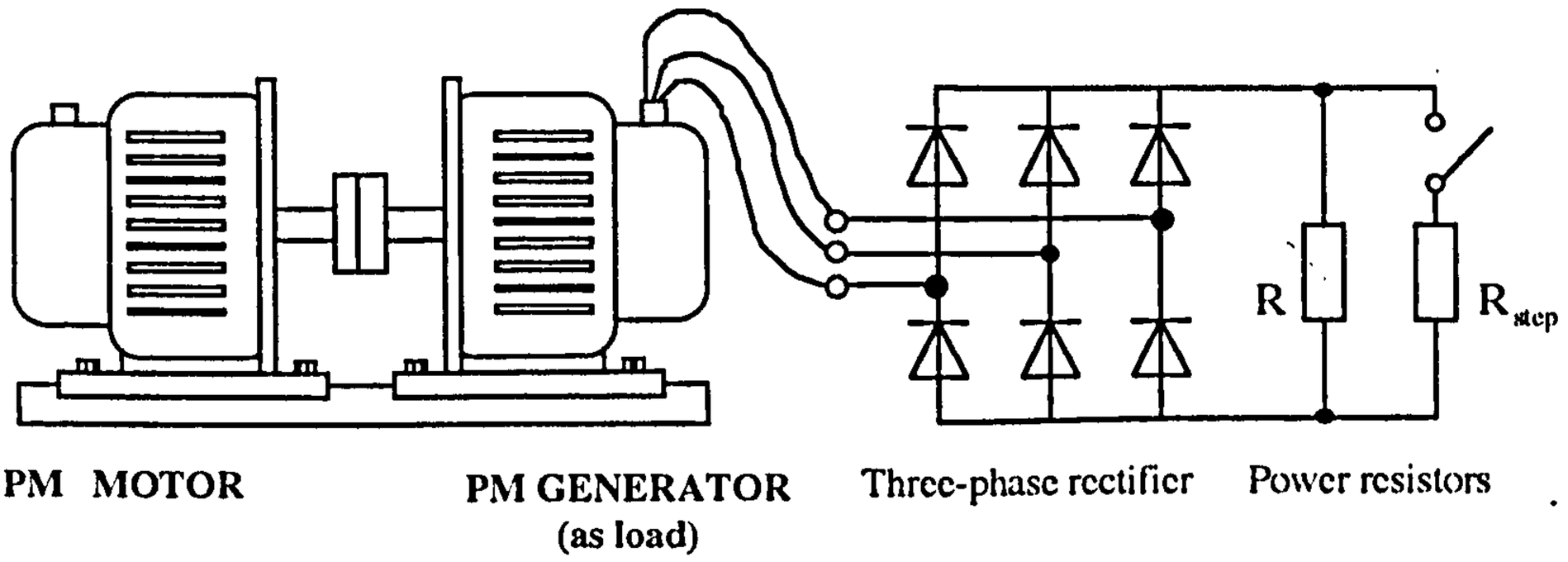

Figure 6.4 The experimental setup for loading and unloading of the brushless PM motor through the brushless PM generator.

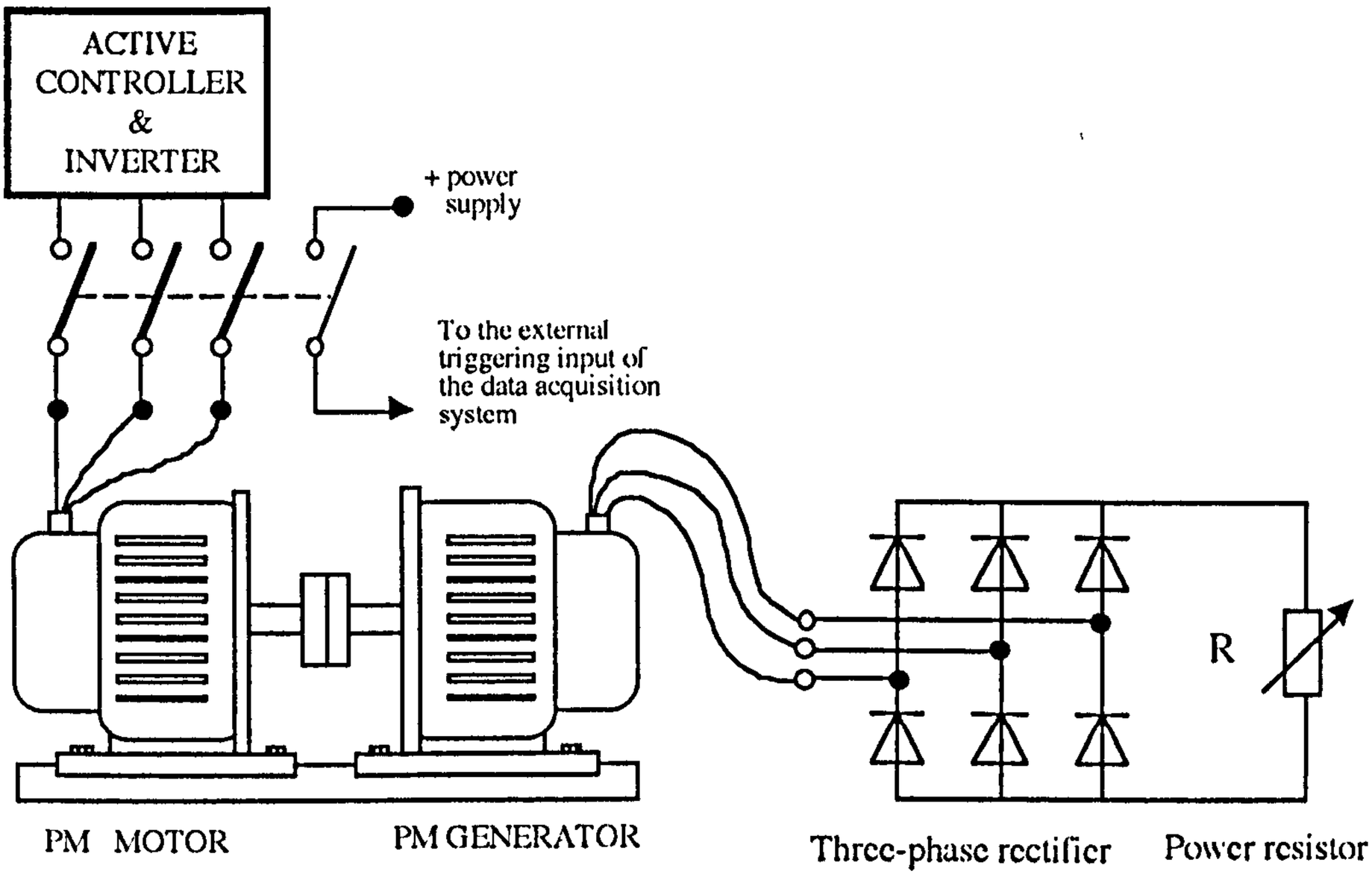

Figure 6.5 The experimental setup for starting from standstill with external triggering

The diagram given in **Fig.6.5** is used for acceleration tests from standstill. The requirement of known rotor position in the algorithm is achieved by moving the rotor and observing the analog position signal on the oscilloscope. While the inverter and whole control system are active, after the rotor is brought to a known position, the three-phase switch is switched on to trigger the data acquisition system externally via an auxiliary contact as shown in **Fig.6.5**.

In this section, the sensorless operation algorithm developed in **Chapter V** has been validated using off-line real data obtained with a 10 μs sampling time by the data acquisition experimental setup. The results arise from the position estimation algorithm's processing of data acquired with the drive operating in a number of alternative modes. Results are presented for a wide range of operating modes: steady-state and transient speed (starting from standstill and step load change), with and without current control.

6.2.1 Steady-State Off-Line Results

The first set of steady-state results are given in **Fig.6.6 and Fig.6.7. Fig.6.6a** represents a typical actual voltage waveform during steady-state operation of the 120° inverter operated PM motor without current control. The effect of the back EMF voltages appears superimposed on phase voltage because of the floating star point voltage. As also explained in **Chapter IV**, the rising and falling parts of the phase voltage are the actual back EMF waveform which occur when the phase is unexcited. Upward and downward spikes in the voltage waveform of **Fig6.6a** occur at the commutation intervals where all three phases of the motor are conducting. Since the motor was loaded lightly, the actual current waveform given in **Fig.6.6b** is unable to reach the current limiting level, and is only limited by the back EMFs of the motor. **Fig.6.6c** illustrates the estimated flux linkages for three-phases using the actual currents and the actual phase voltages. Since there is discontinuous current conduction and no current control in this mode of operation, small dips and fluctuations occur in the flux linkage waveforms as indicated in **Chapter V.**

Fig.6.7 shows the corrected flux linkages and the estimated rotor position waveforms produced by the position estimation algorithm. The comparison of **Fig.6.6c** and **Fig.6.7a** show that, the effect of DC off-set in the measured quantities is recovered by the flux linkage correction loop in the algorithm. The estimated position is given in rad in **Fig.6.7b**. Since the motor was operating at steady-state, the overall profile of estimated position has a linear characteristic within a period, and is able to track the actual current and voltage waveform which was in phase with the back EMF in this case.

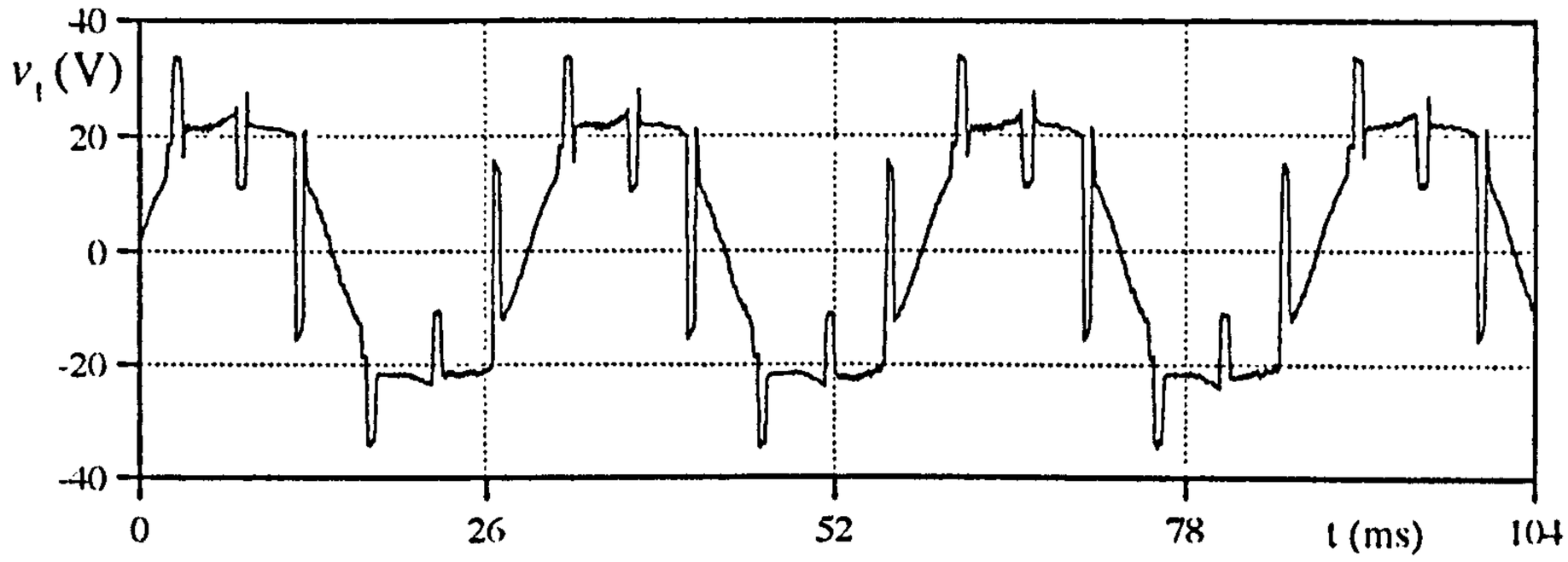

a

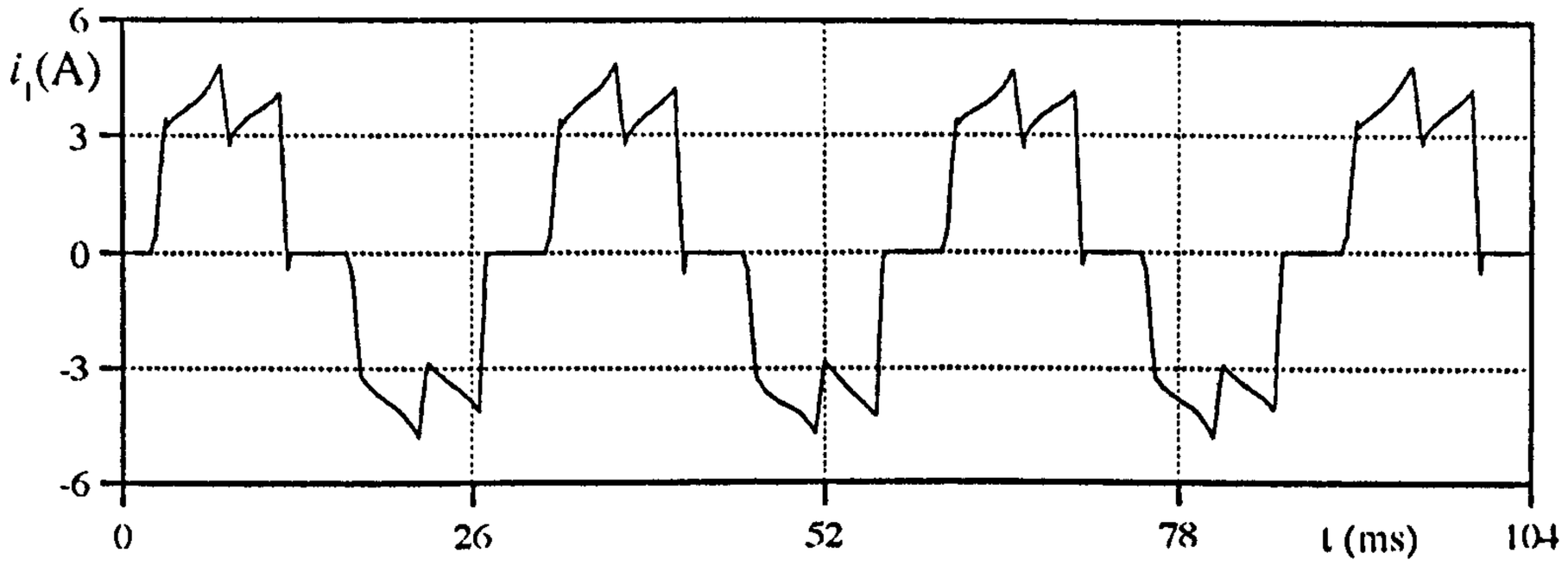

b

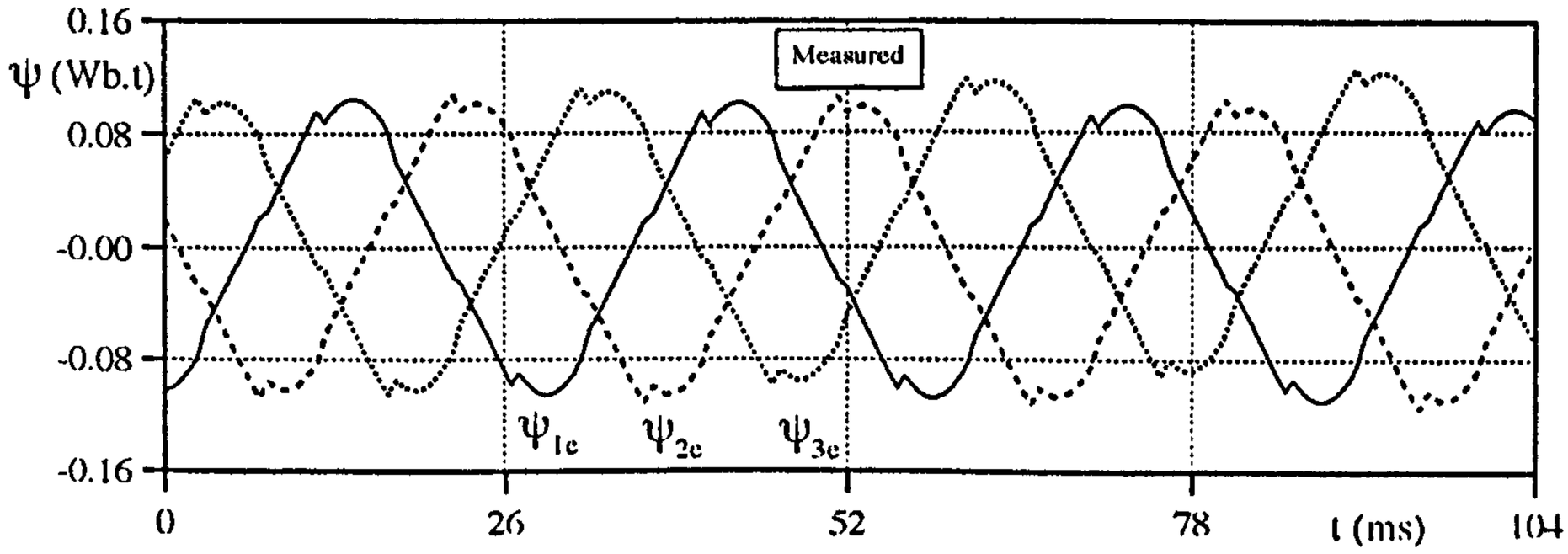

c

Figure 6.6 The steady-state experimental results, no current control, rectangular demand current, V_{dc}= 50.6V, n= 502rpm.

a) Phase 1 voltage waveform

b) Line 1 current waveform

c) Estimated three-phase flux linkage waveforms

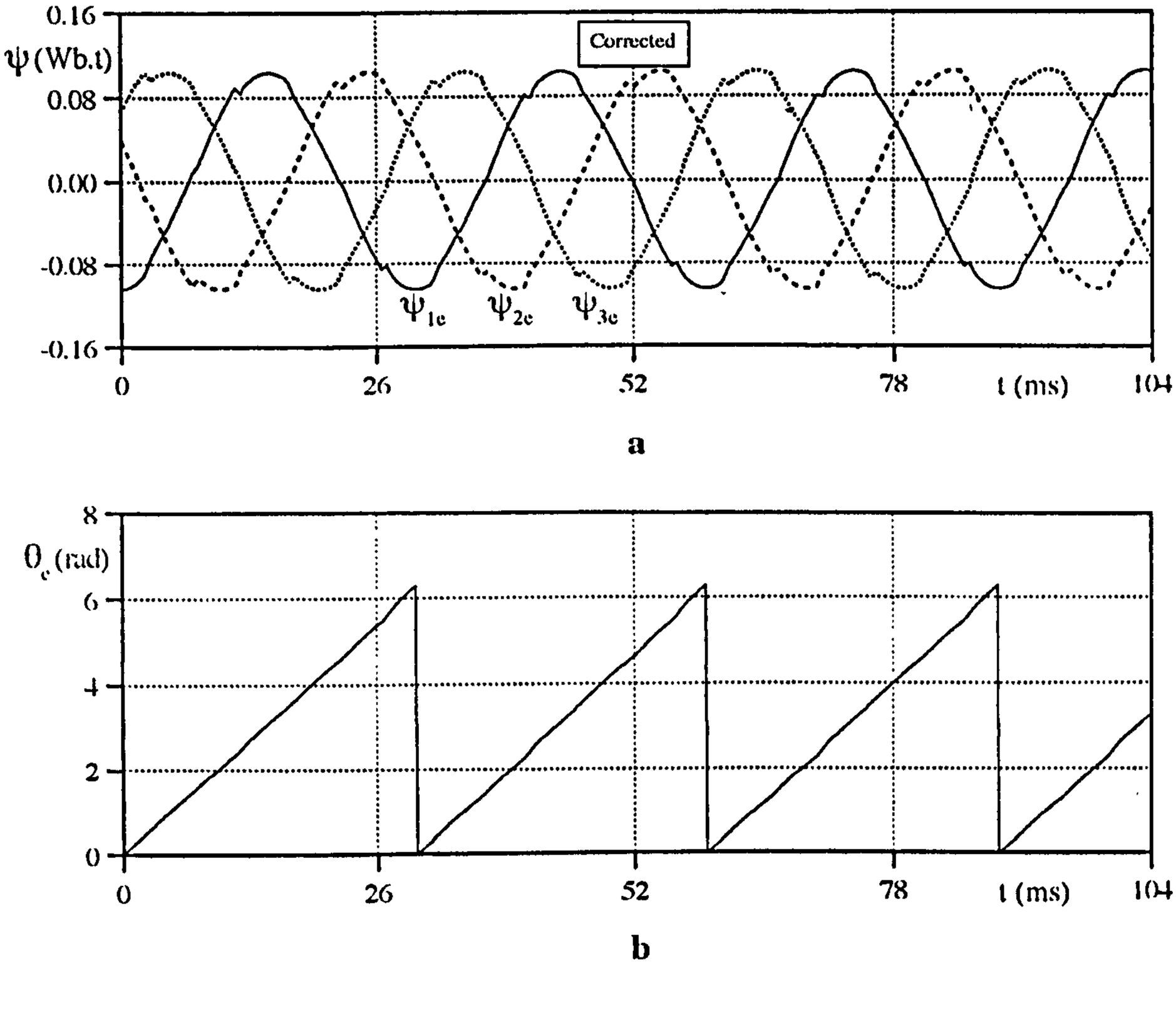

Figure 6.7 The steady-state experimental results corresponding to **Fig.6.6.**

a) Three-phase corrected flux linkage waveforms.

b) Estimated rotor position in rad.

Figs.6.8-9 give a second set of experimental results showing the current controlled during 120° conduction at constant speed. As seen in **Fig.6.8a**, the phase voltage waveform is more complicated than in **Fig.6.6a**. The actual current is limited by a commanded current level and the line current is regulated (**Fig.6.8b**) within a hysteresis band ($\Delta h=\pm 0.35A$). As in the previous case, the speed is constant since DC rail voltage and the load are constant. However, the estimated flux linkage waveforms (**Fig.6.8c**) have a slightly different profile than that of **Fig.6.6c.**

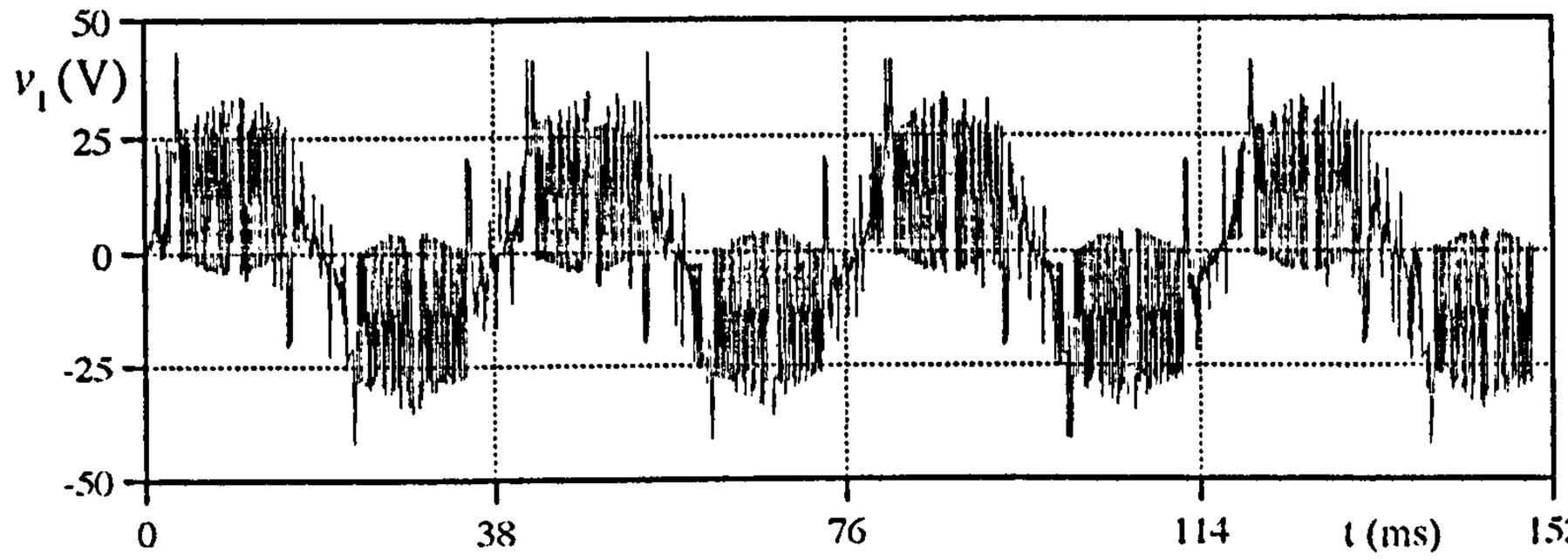

a

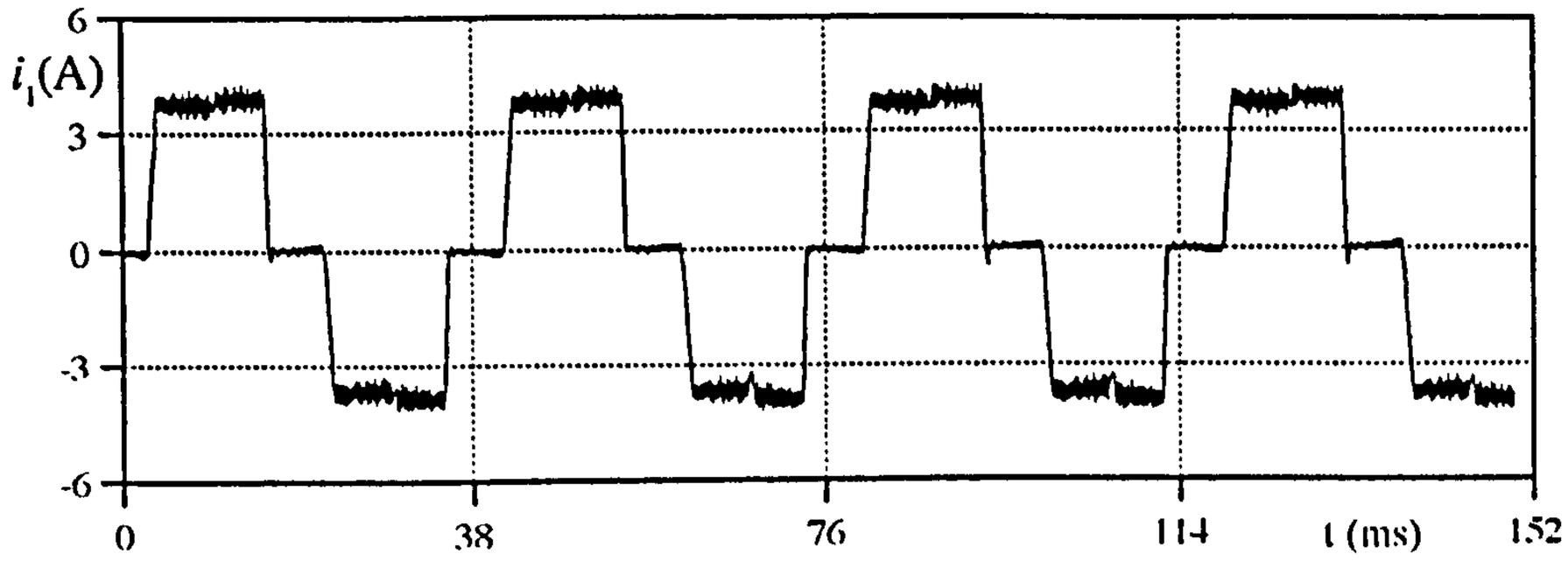

b

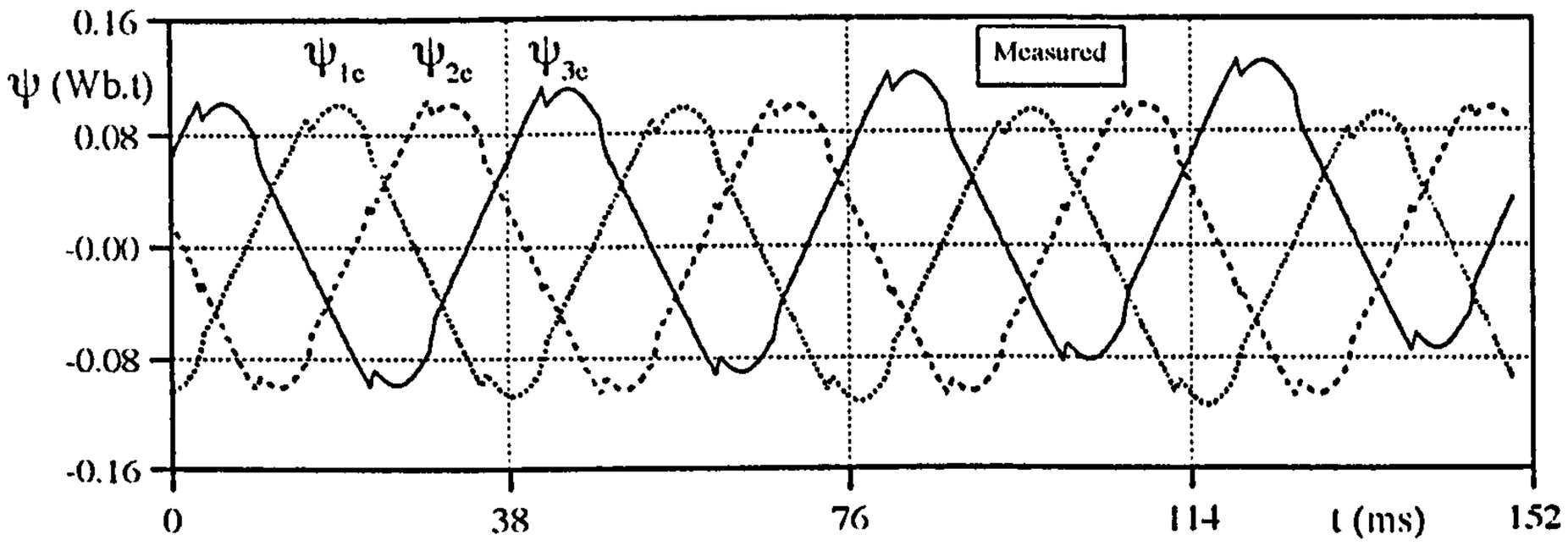

c

Figure 6.8 The steady-state experimental results, with current control ($\Delta h = \pm 0.35A$), rectangular demand current, $V_{dc} = 63.8V$, n= 381rpm.

a) Phase 1 voltage waveform

b) Line 1 current waveform

c) Three-phase estimated flux linkage waveforms

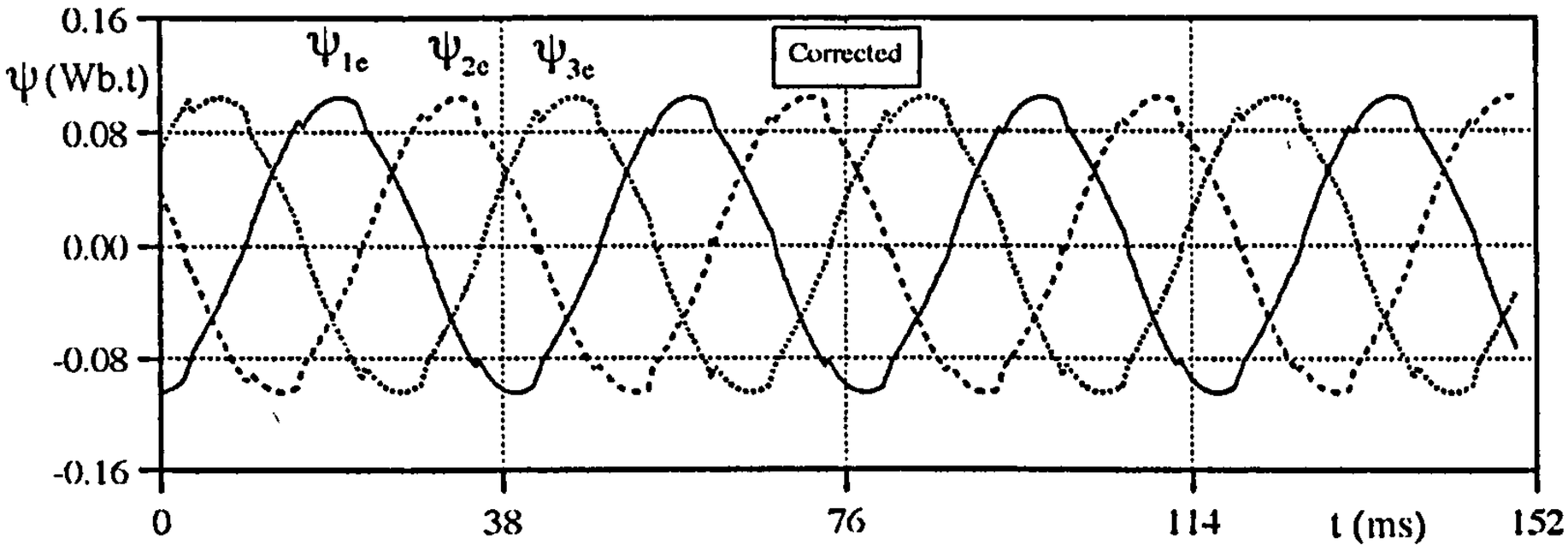

a

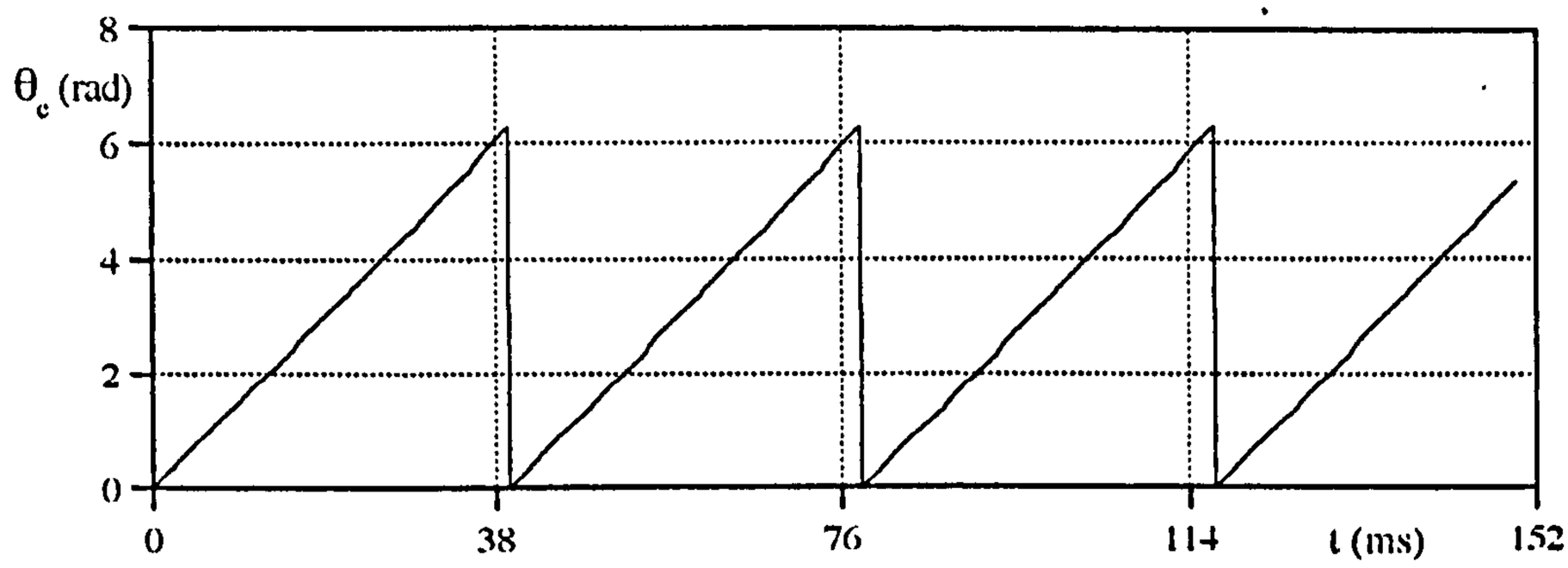

b

Figure 6.9 The steady-state experimental results corresponding to **Fig.6.8**

a) Three-phase corrected flux linkage waveforms

b) The estimated position

Since current control is involved in **Fig.6.8**, the flux linkage waveforms (**Fig.6.8c**) appear in a linear form within the current control interval as expected, and due to different DC offset values in the input channels of the data acquisition system, the estimated flux linkage waveforms present a rising or falling characteristics with time.

The corrected and the estimated position waveforms in **Fig.6.9** clarify the position estimation method for the current controlled drive. **Fig.6.9b** gives the estimated position which also matches with the actual waveforms.

The results given in **Fig.6.10** and **Fig.6.11** are very typical. The operating condition involves a sinusoidal current excited brushless PM motor. The implemented drive (**Fig.2.17, Chapter II**) was operated by storing sinusoidal commanded currents in EPROMs, and was regulated around a hysteresis bandwidth. The actual phase voltage and the sinusoidal current waveforms are shown in **Fig.6.10a** and **Fig.6.10b** respectively.

The actual current is regulated around a sinusoidal demand current by the hysteresis current controller. The main difference from previous results is that the estimated flux linkages have smooth waveforms (**Fig.6.10c**). No dips appear in this waveform because current conduction is continuous.

The flux linkages are corrected and shown in **Fig.6.11a**. Again, the position estimation (**Fig.6.11b**) gives adequately good results. As explained earlier, the demand current is in phase (no phase advance or delay) with the back EMF waveform. Therefore agreement between the actual current and the estimated position demonstrates the algorithm's ability in the sinusoidally excited brushless PM drive.

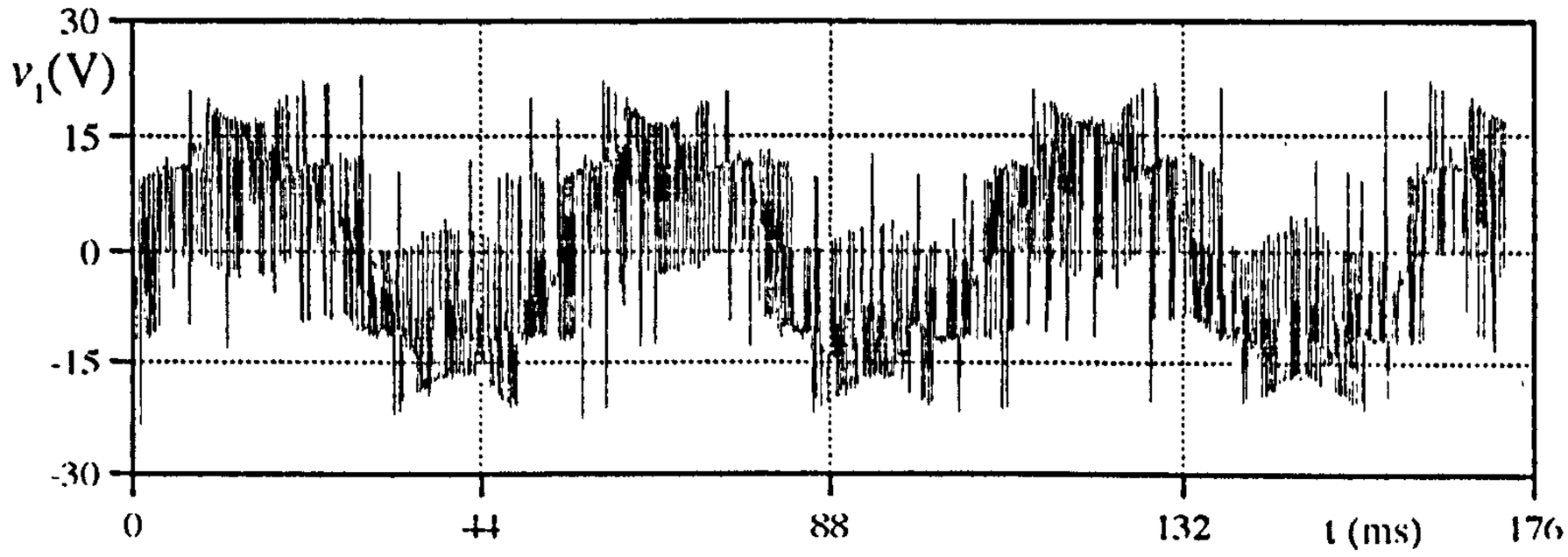

a

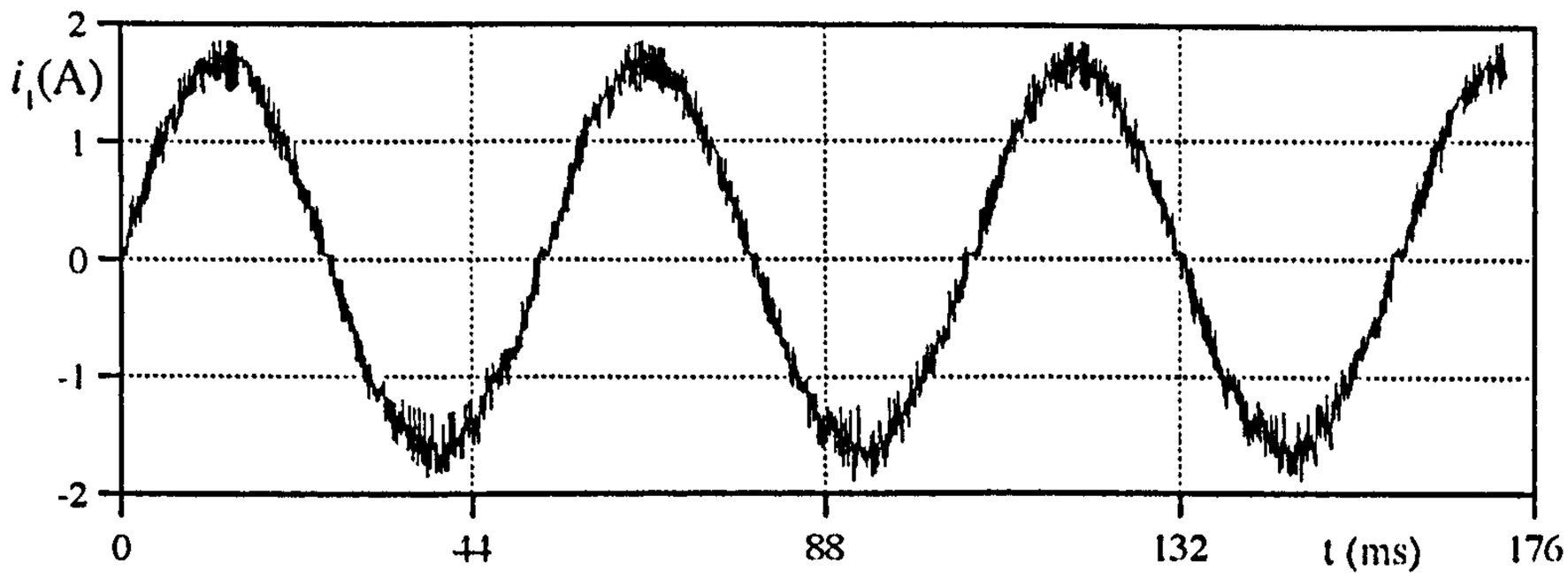

b

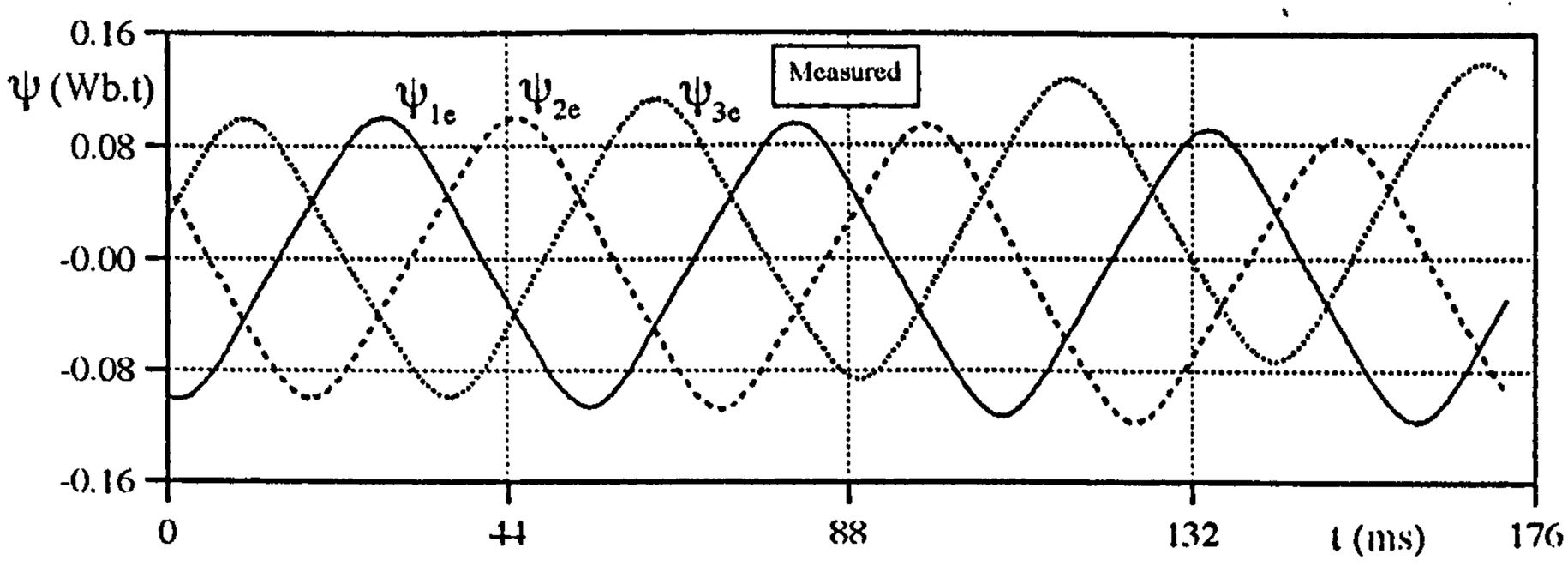

c

Figure 6.10 The steady-state experimental results, with current control ($\Delta h = \pm 0.35A$), sinusoidal demand current, $V_{dc} = 32.2V$, n= 230rpm.

a) Phase 1 voltage waveform

b) Line 1 current waveform

c) Three-phase estimated flux linkage waveforms

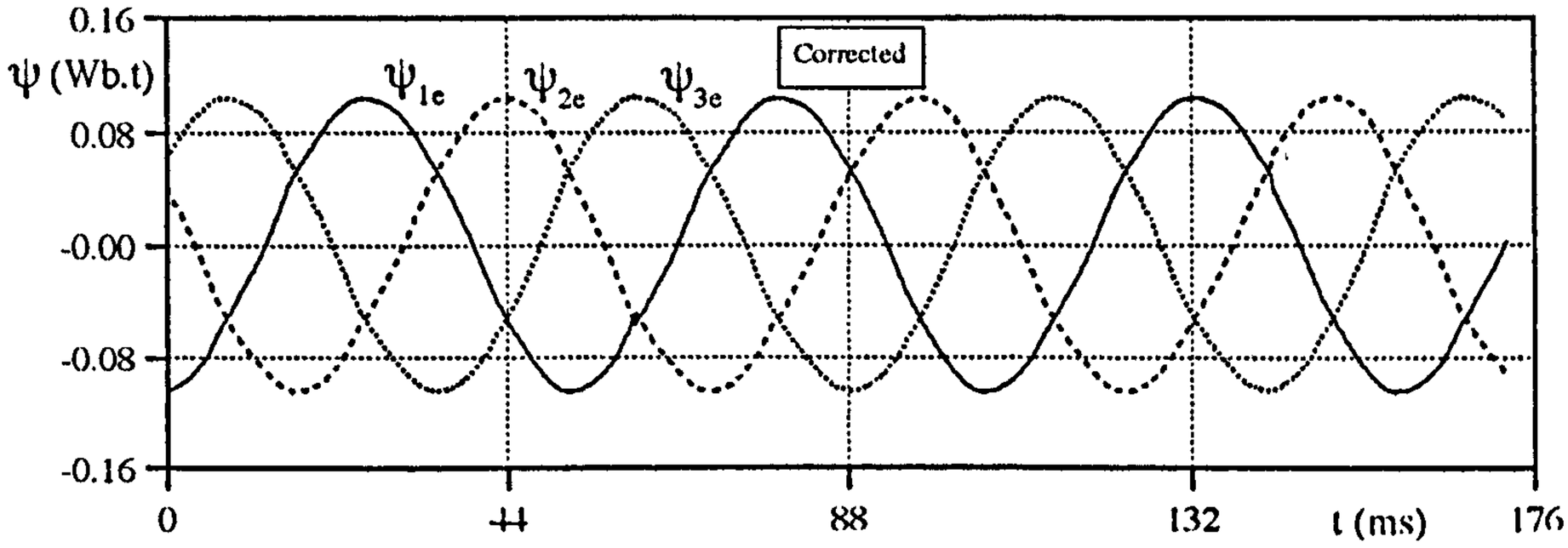

a

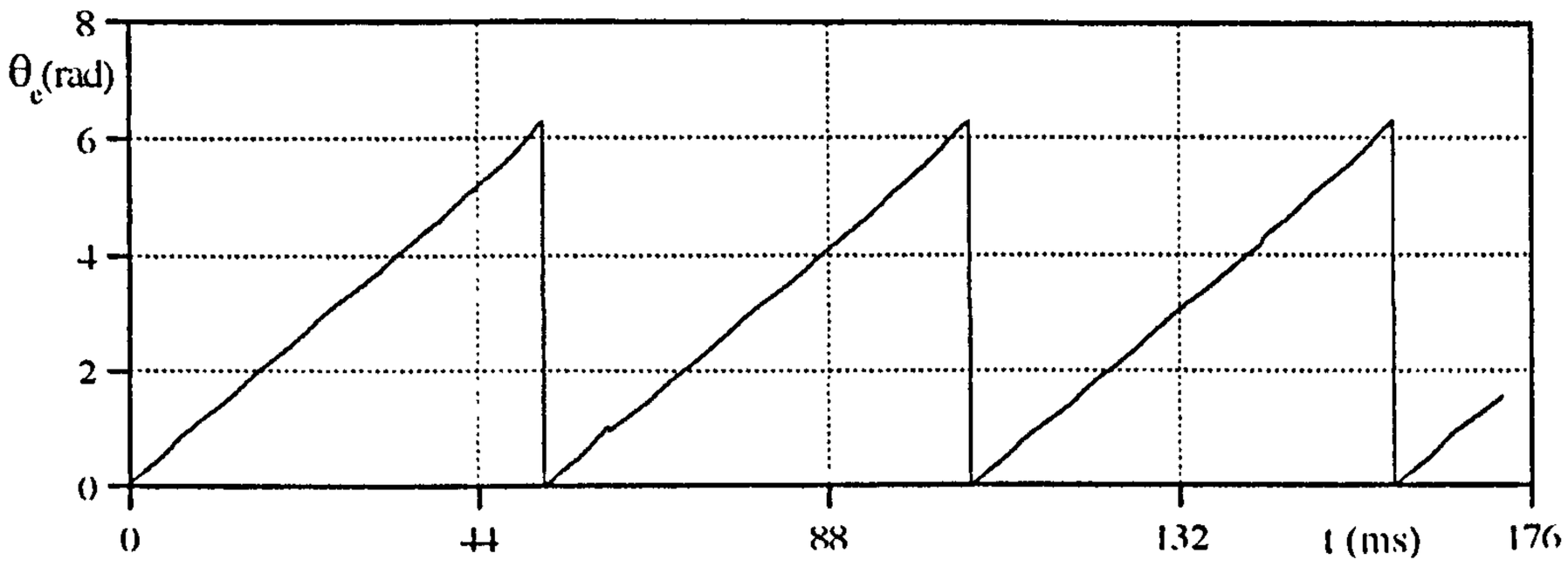

b

Figure 6.11 The steady-state experimental results corresponding to **Fig.6.10**

a) Three-phase corrected flux linkage waveforms

b) The estimated position

6.2.2 Transient Operation Results

As shown in the previous chapter, the angular position of the PM motor must be continuously determined with acceptable accuracy even during speed transients. The results in **Figs.6.12-14** demonstrate the reliability of the method during acceleration of the motor from rest for 120° current conduction and no current control. It should be noted that the high starting current (**Fig.6.12b**) diminishes the DC rail voltage (**Fig.6.12a**) slightly, and causes a bigger dip in the flux linkage waveforms (**Fig.6.12c**) initially.

Fig.6.12c illustrates the total flux linkages. As expected in the brushless PM motor, the magnitude of the magnet flux linkage remains constant with speed, but is influenced by the stator current level and inverter switching. The effect of high current level (**Fig.6.12b**) can be seen clearly in the first period of the measured flux linkages.

In **Fig.6.13**, the estimated position, current and flux linkage errors are illustrated. Due to the high switching voltage and current transients and possible wrong starting position, initially the estimated position error is bigger in amplitude. However it is relatively small when compared with the actual position.

The effect of the flux linkage correction can be seen in **Fig.6.14a**. To examine the accuracy of the position estimation, the measured and estimated rotor positions are shown in **Fig.6.14b** and **Fig.6.14c** respectively. As seen in **Fig.6.14b**, there is a small error in the starting value of the actual position. Since the starting position error is reflected to the estimated position, the estimated position deviates initially, but there is very close agreement in the overall position profiles.

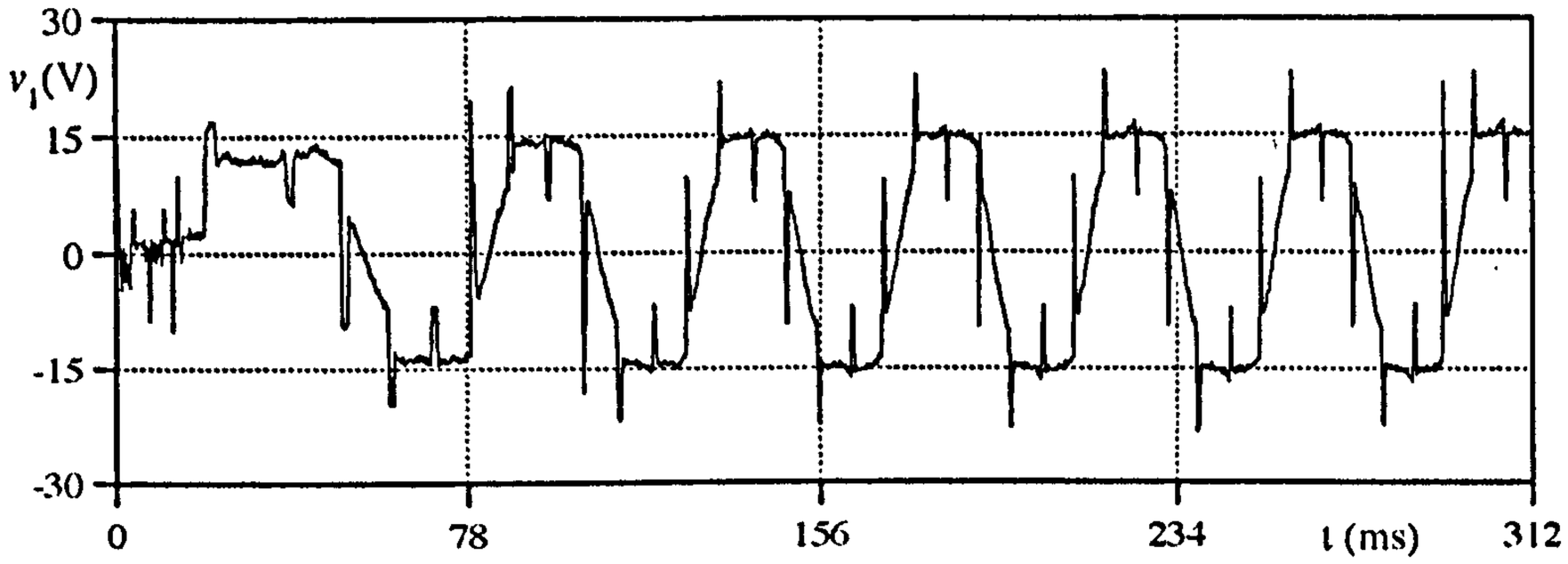

a

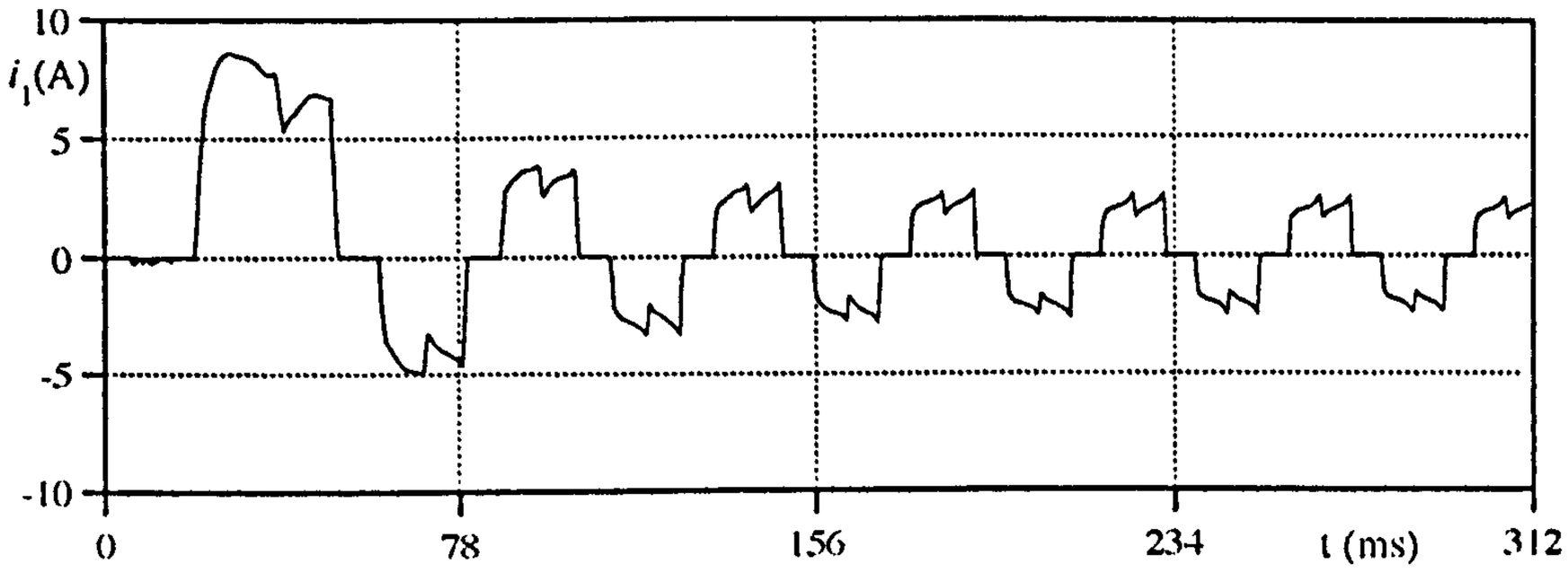

b

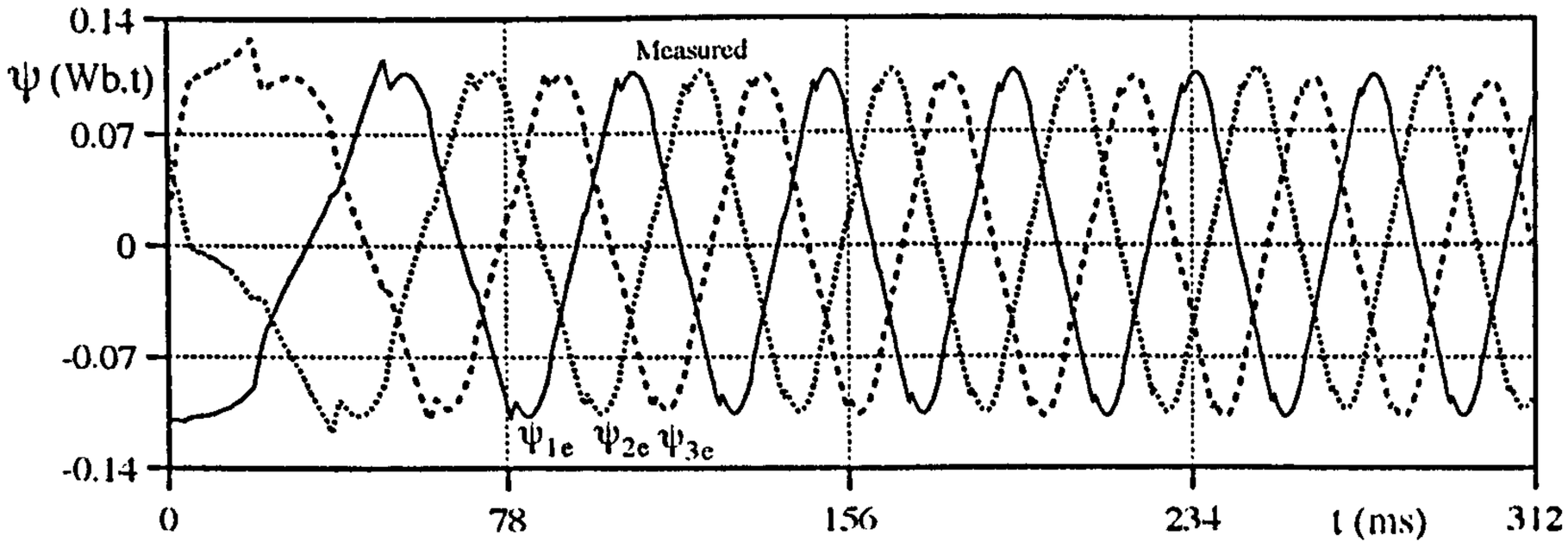

c

Figure 6.12 The transient experimental results, starting from rest, no current control, rectangular demand current, V_{dc}= 40.5V (at rest), V_{dc}= 33.7V (at steady-state).

a) Phase 1 voltage waveform

b) Phase 1 current waveform

c) Three-phase estimated flux linkage waveforms

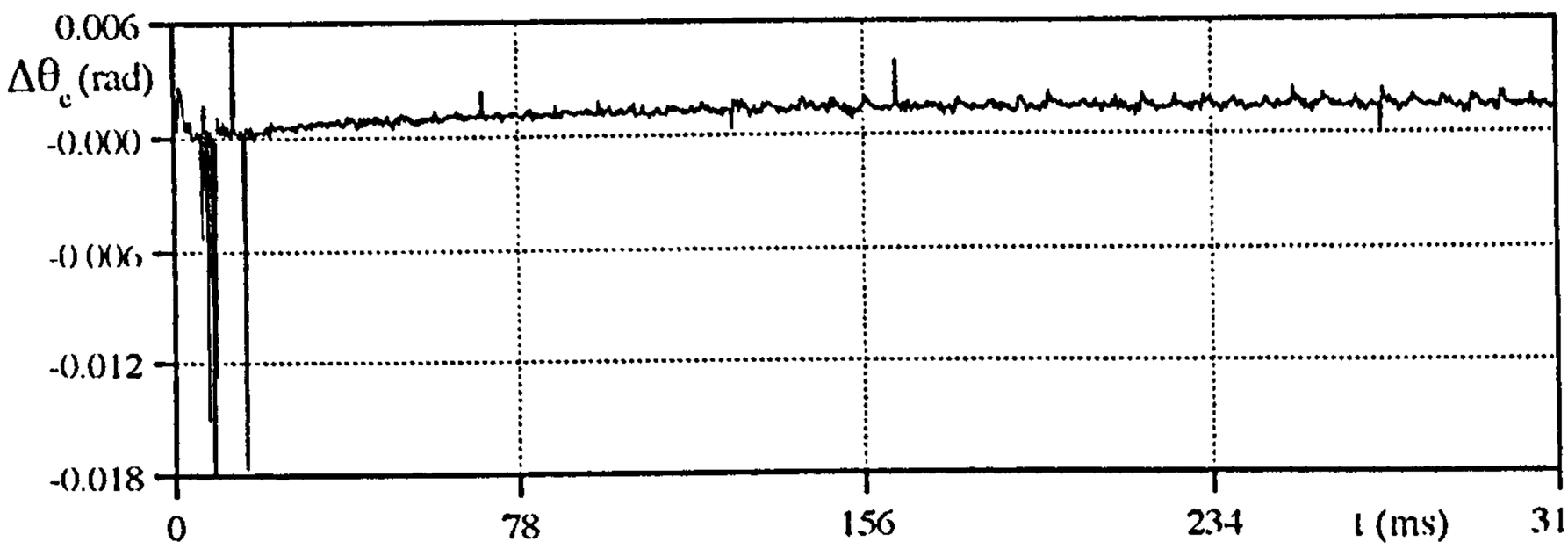

a

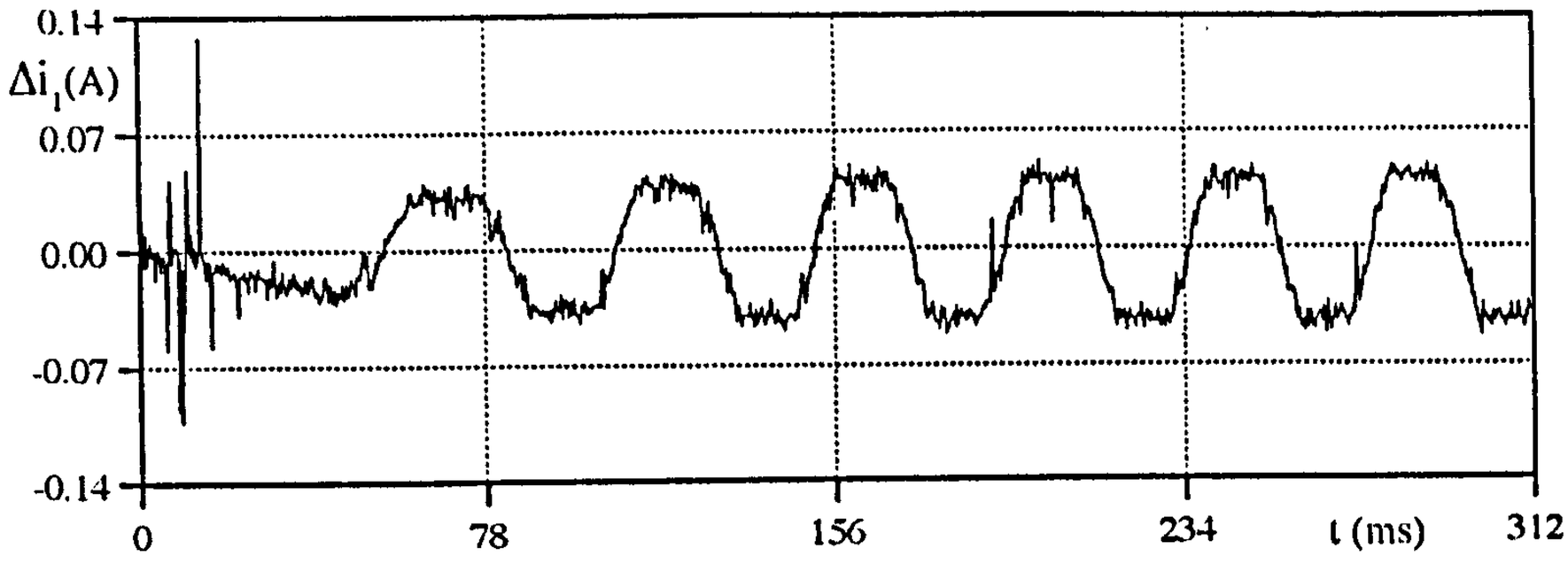

b

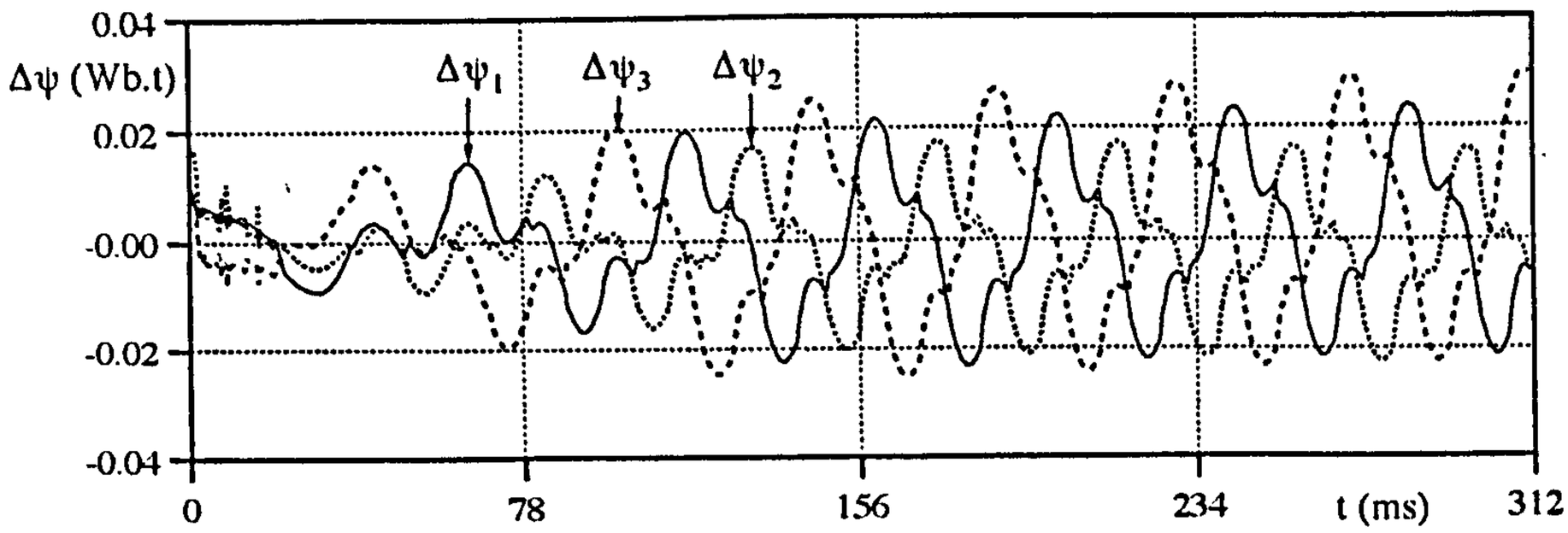

c

Figure 6.13 The transient experimental results for the operating condition shown in **Fig.6.12.**

a) Position error

b) Current error variation with time

c) Three-phase estimated flux linkage errors

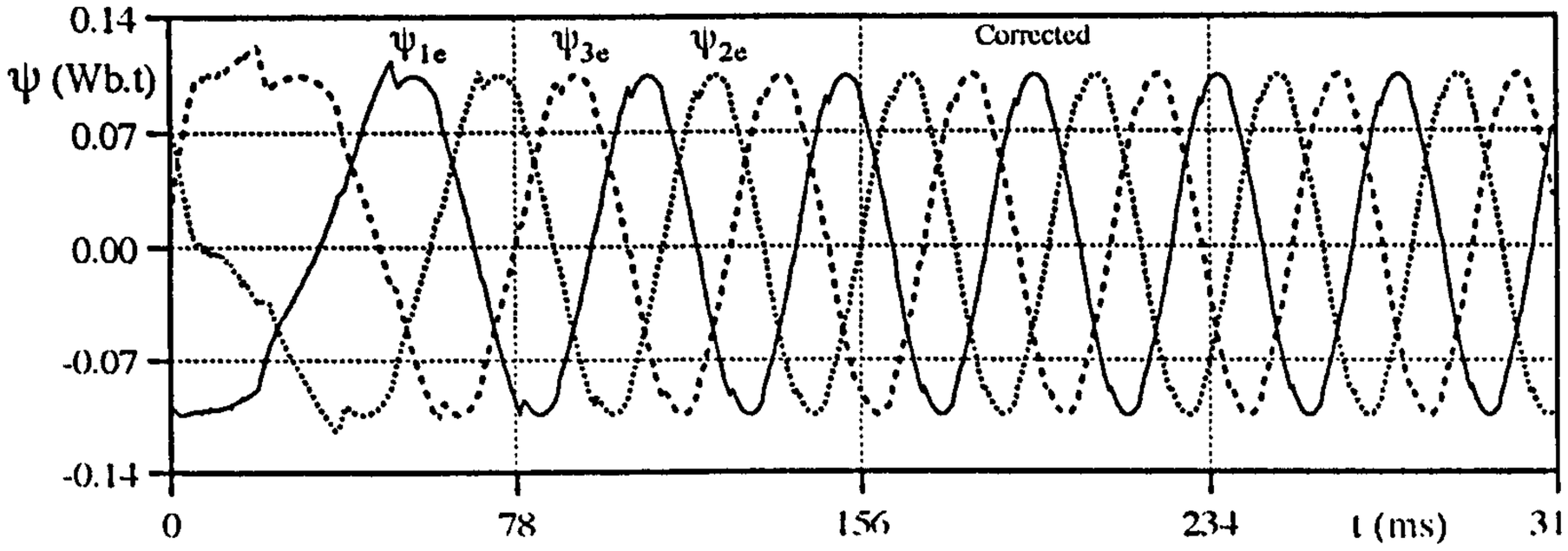

a

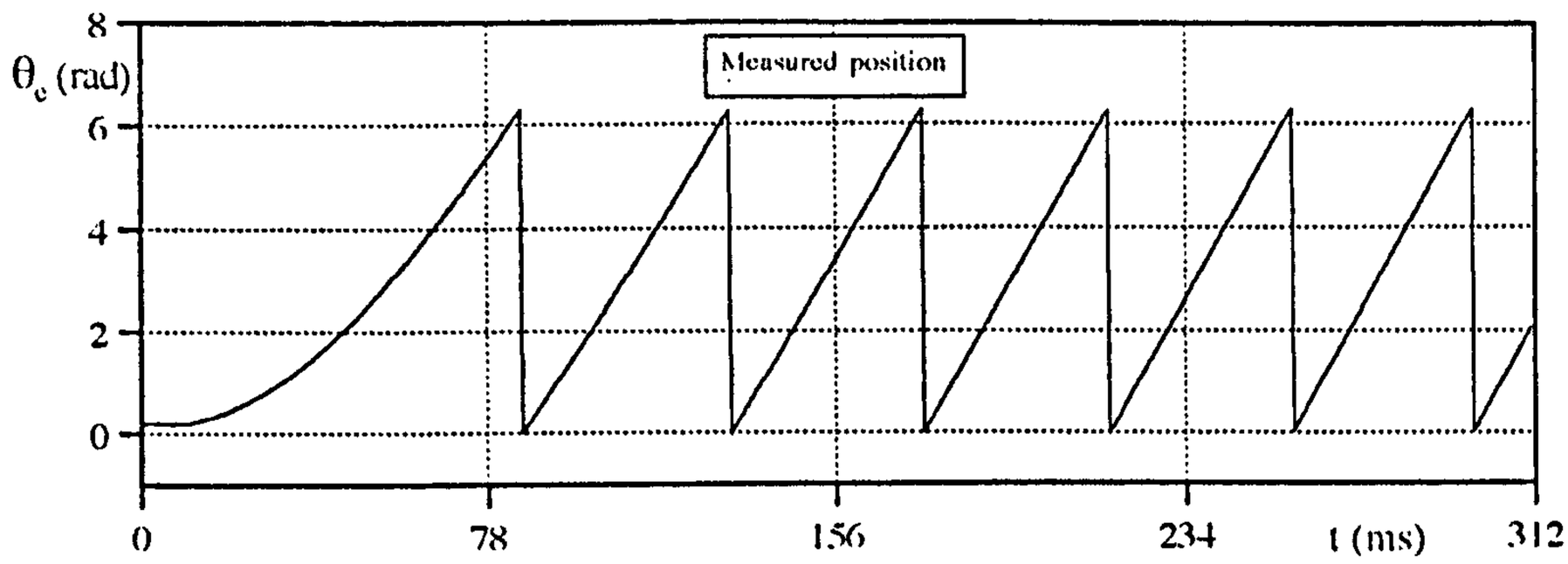

b

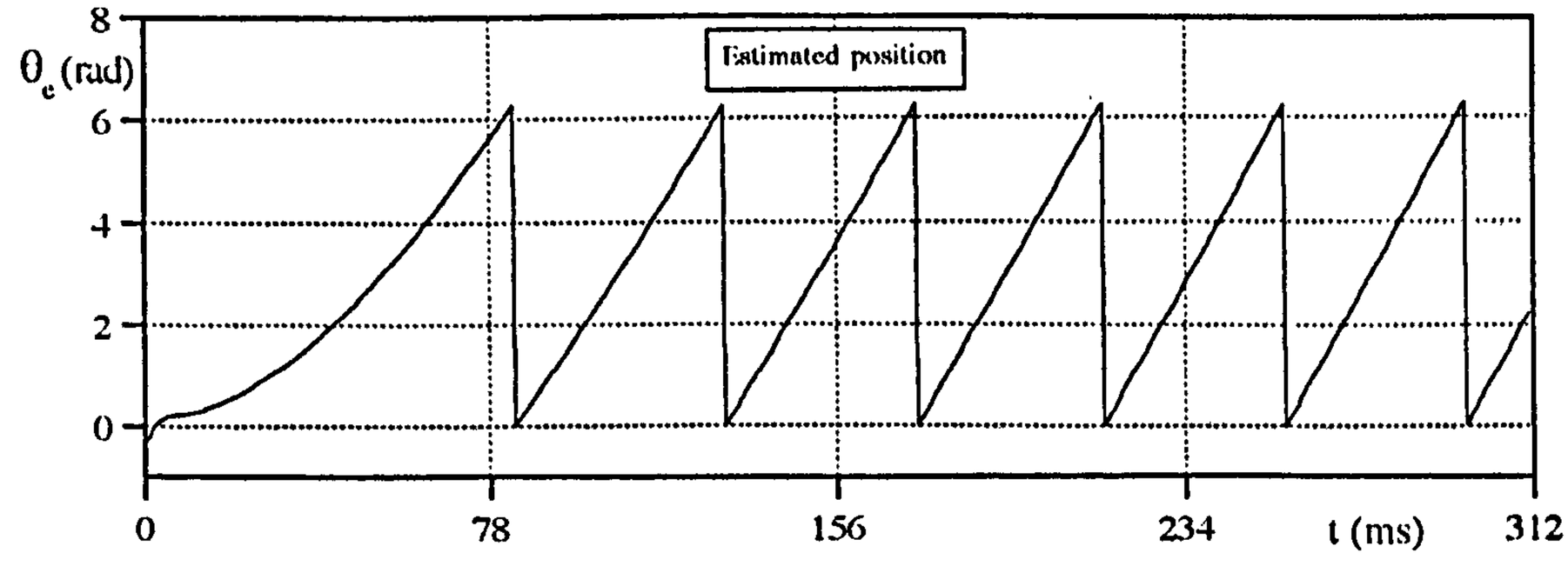

c

Figure 6.14 The transient experimental results for the operating condition shown in **Fig.6.12.**

a) Three-phase corrected flux linkage waveforms

b) Actual rotor position

c) Estimated rotor position

Figs.6.15-17 shows a similar set of results, but with a closed loop current controller causing modulation of phase voltage (**Fig.6.15a**) to maintain the current constant in excited phases (**Fig.6.15b**). Since the current is controlled, the voltage waveform involves fast switching transients. Therefore, the back EMF waveforms can not be distinguished easily within the zero current interval as in **Fig.6.12**, and the drive accelerates from standstill of a lower rate than in **Fig.6.12**, since current levels are lower. The total measured flux linkages are shown in **Fig.6.15c**. The flux linkage associated with the current is superimposed onto the magnet flux linkage, and does not vary within the current conduction interval since the current is limited by the hysteresis controller. Therefore, the dips on the total flux linkages have the same amplitude (**Fig.6.15c**).

The effect of switching action on the position estimation algorithm can be seen clearly in **Fig.6.16**. Due to the fast switching current control, the estimated errors also involve fast variations. The initial error in the starting position increases the flux linkage errors (**Fig.6.16c**).

In **Fig.6.17**, the measured and the estimated positions show the algorithm's ability. As seen in **Fig.6.16c**, a high flux linkage error indicates initial position error. As simulated in **Chapter IV** (**Fig.5.18**), the initial error in the actual position (**Fig.6.17b**) is recovered by the algorithm, and the estimated position is given in **Fig.6.17c**. Although, the estimated position gives negative values, it reflects the initial position error, and since the flux linkage correction loop is involved, it is recovered within 30 ms.

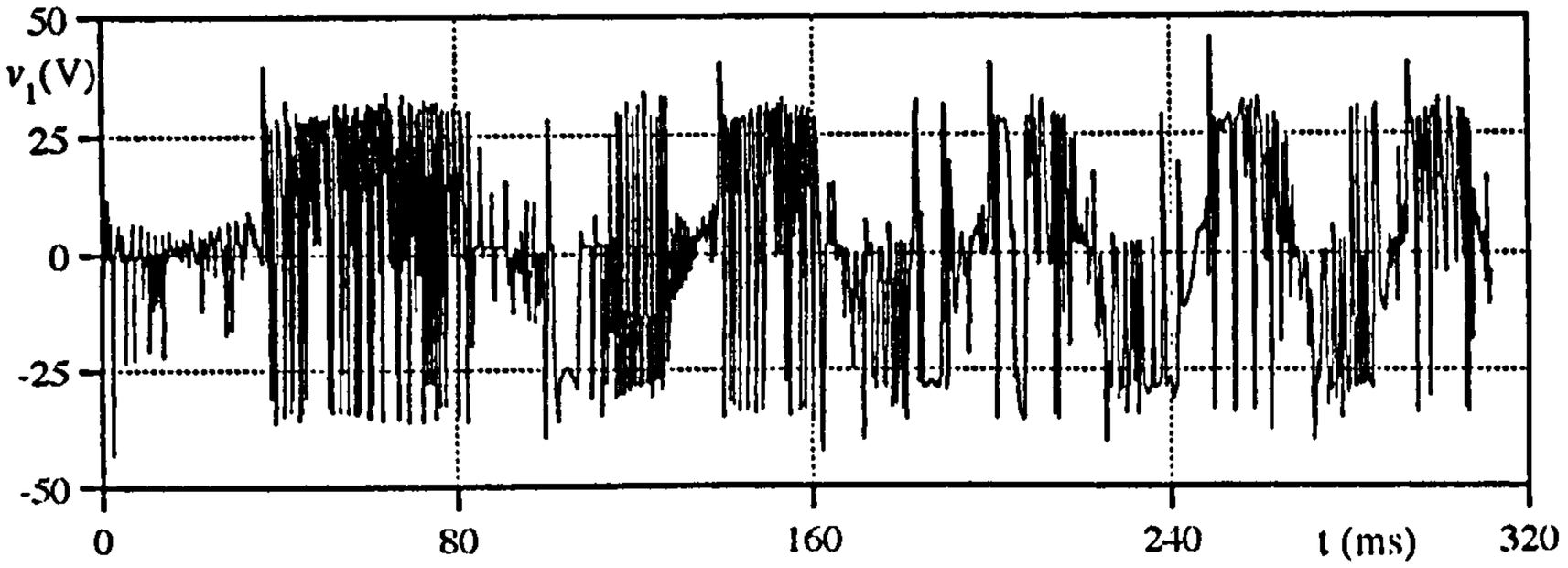

a

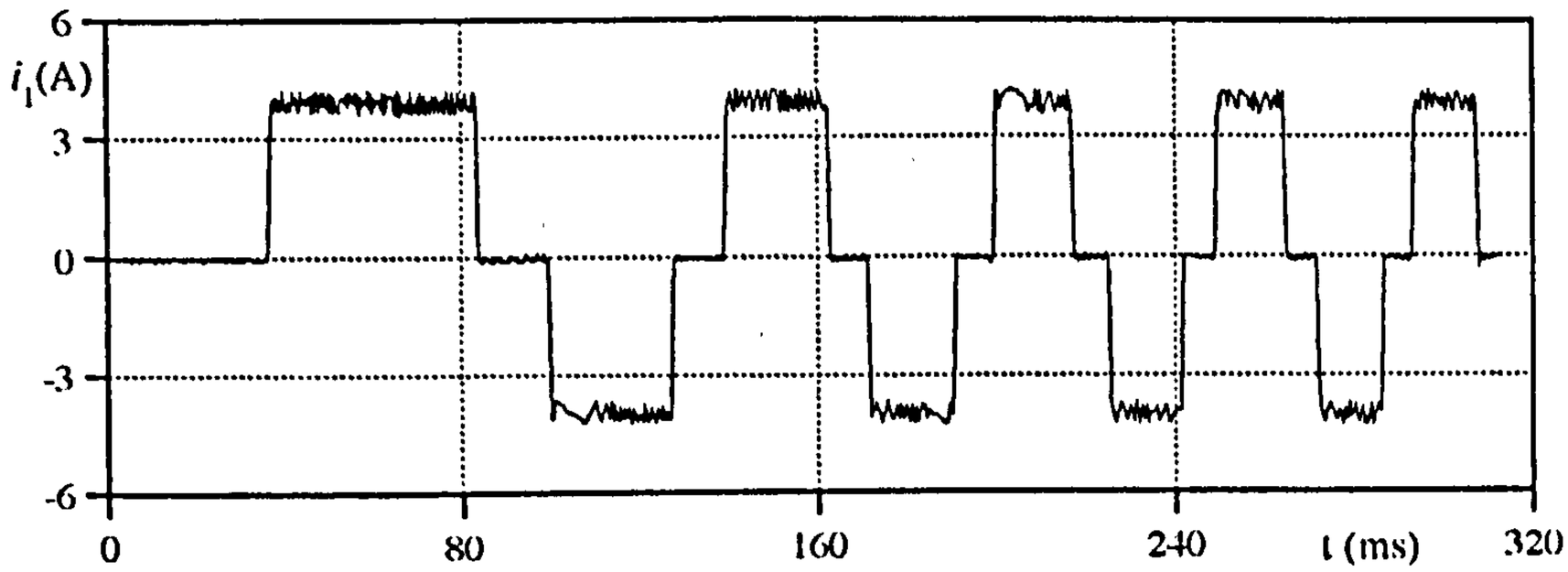

b

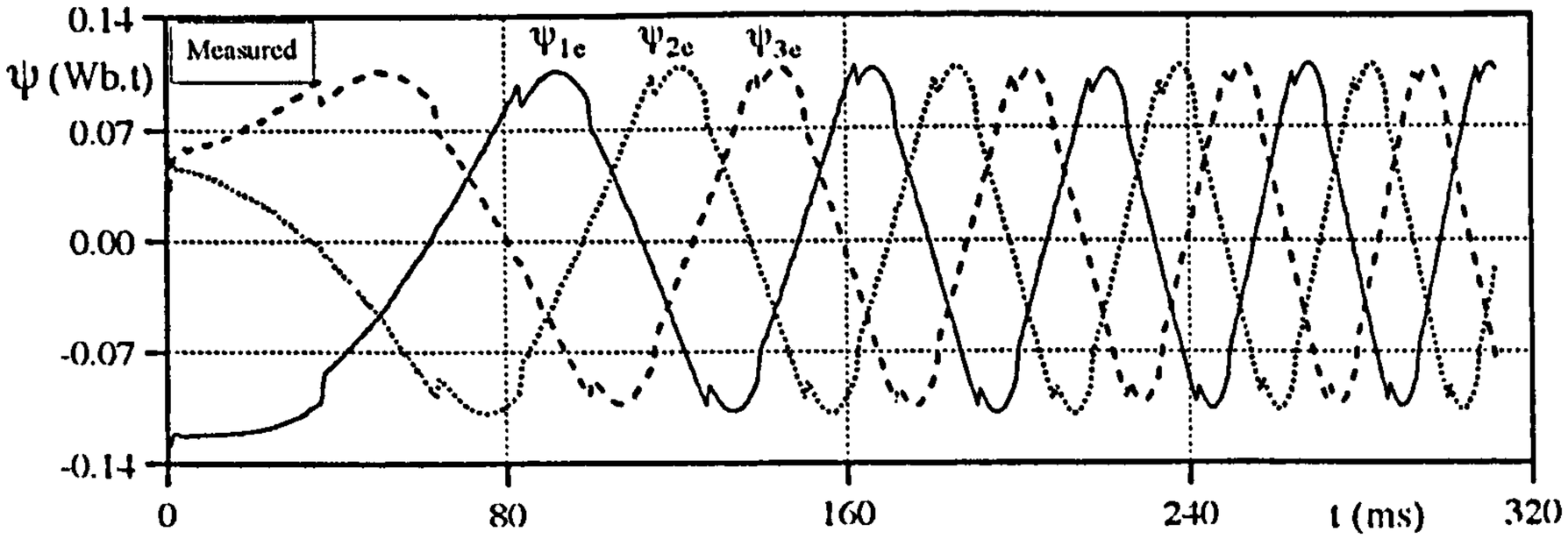

c

Figure 6.15 The transient experimental results, starting from rest, with current control, rectangular demand current, V_{dc}= 66.2V (at rest), V_{dc}= 60.6V (at steady-state).

a) Phase 1 voltage waveform

b) Phase 1 current waveform

c) Three-phase estimated flux linkage waveforms

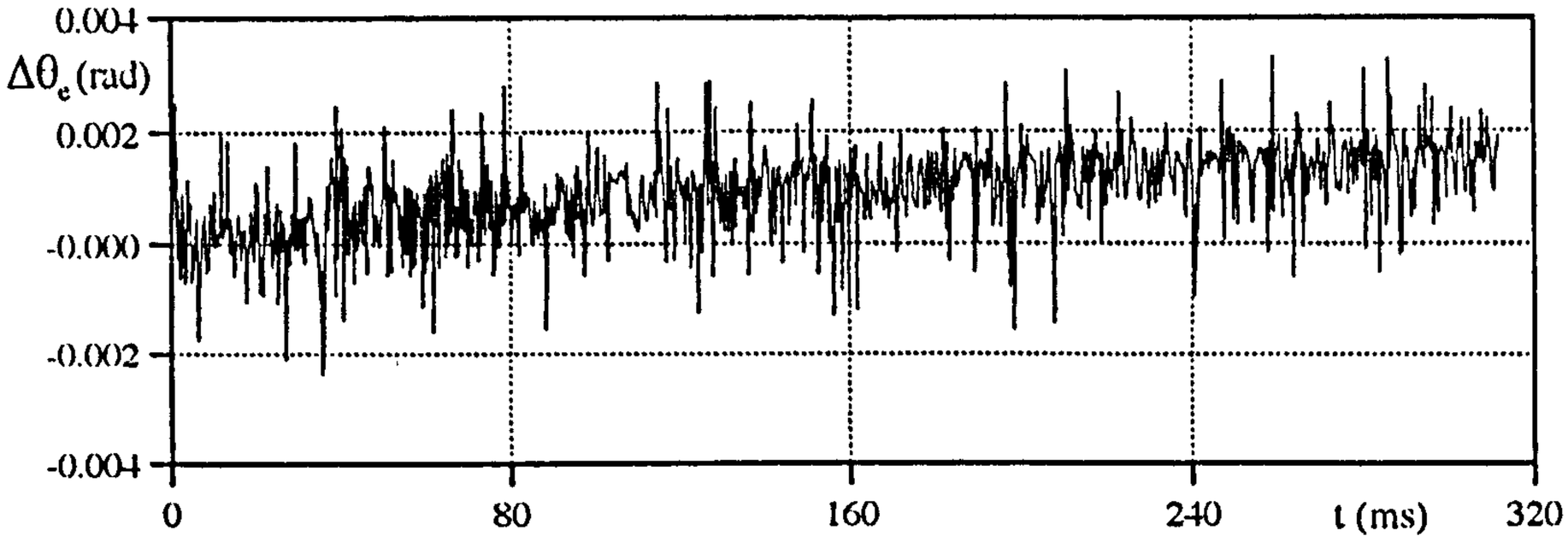

a

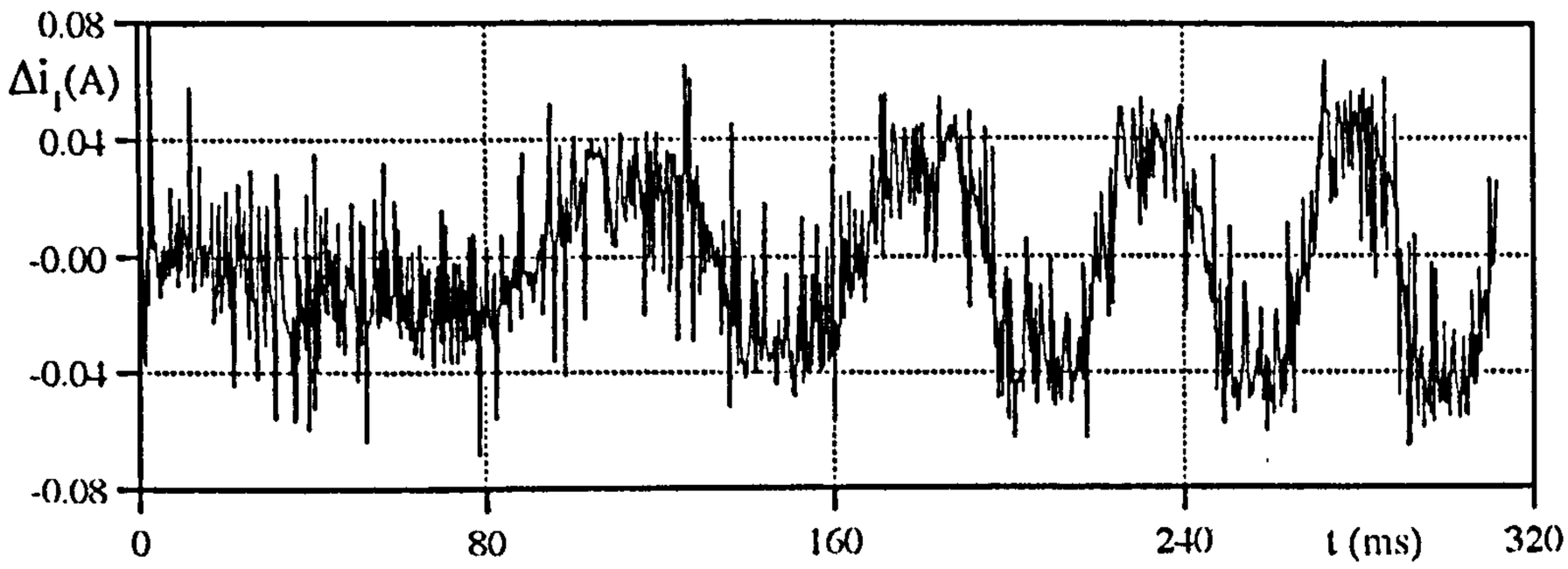

b

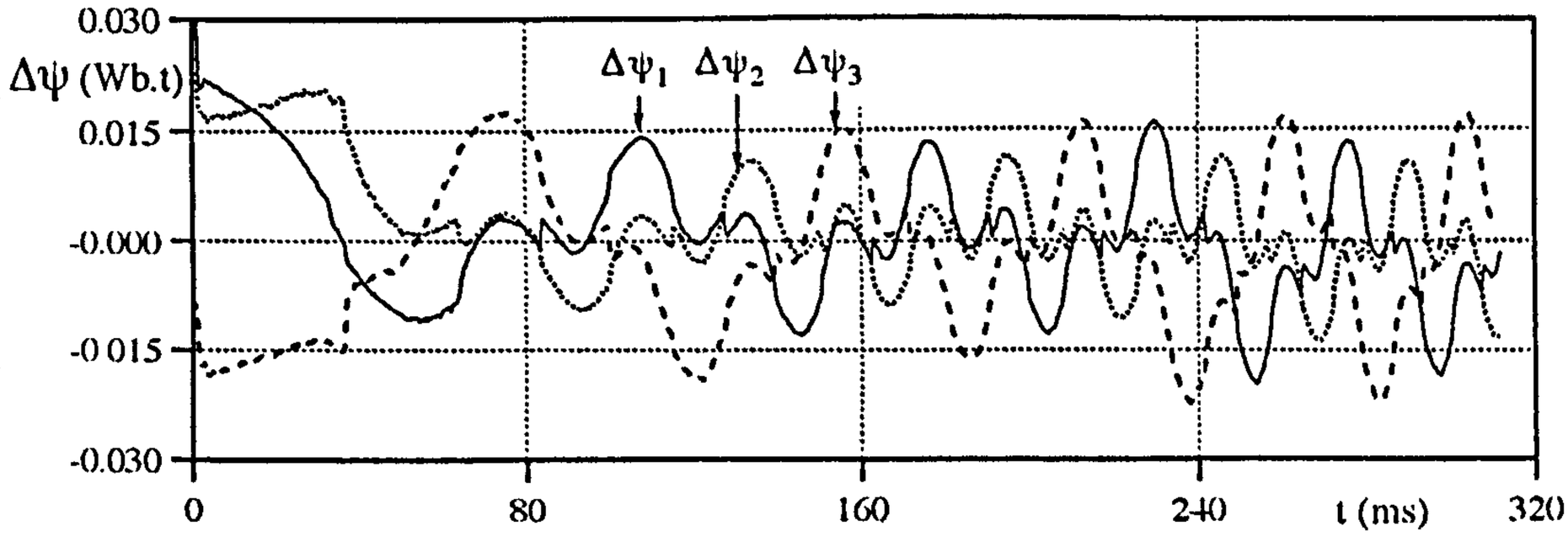

c

Figure 6.16 The transient experimental results for the operating condition shown in **Fig.6.15.**

a) Position error

b) Current error variation with time

c) Three-phase estimated flux linkage errors

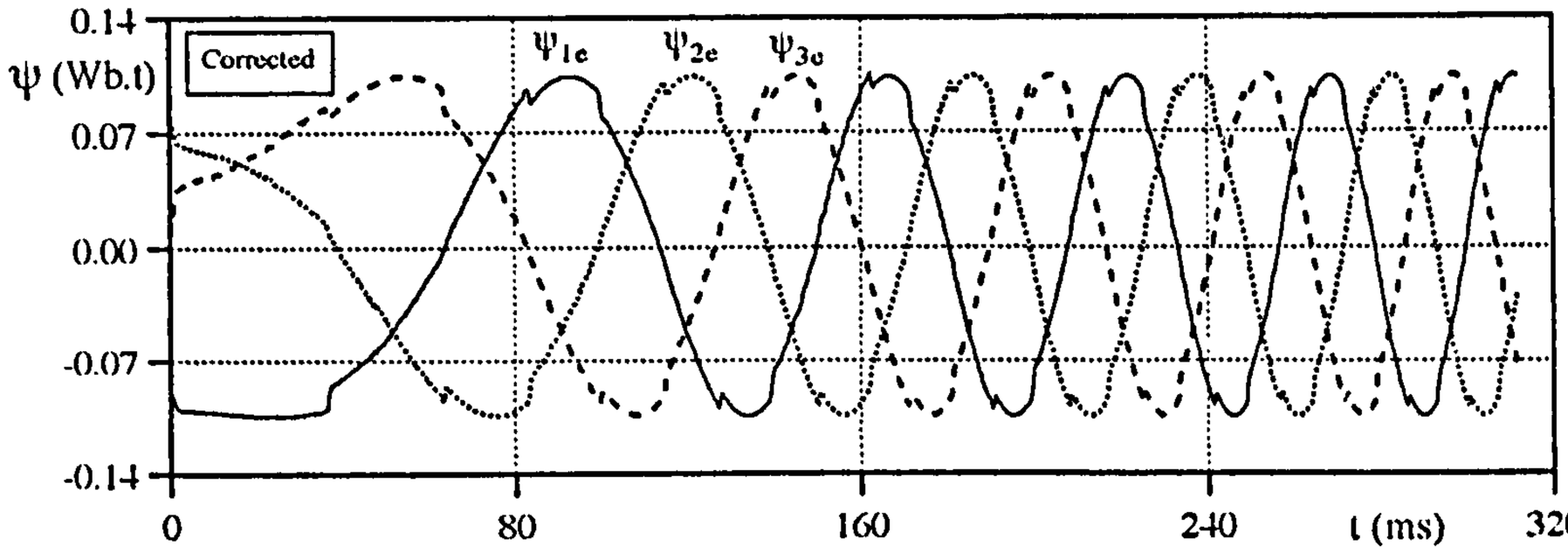

a

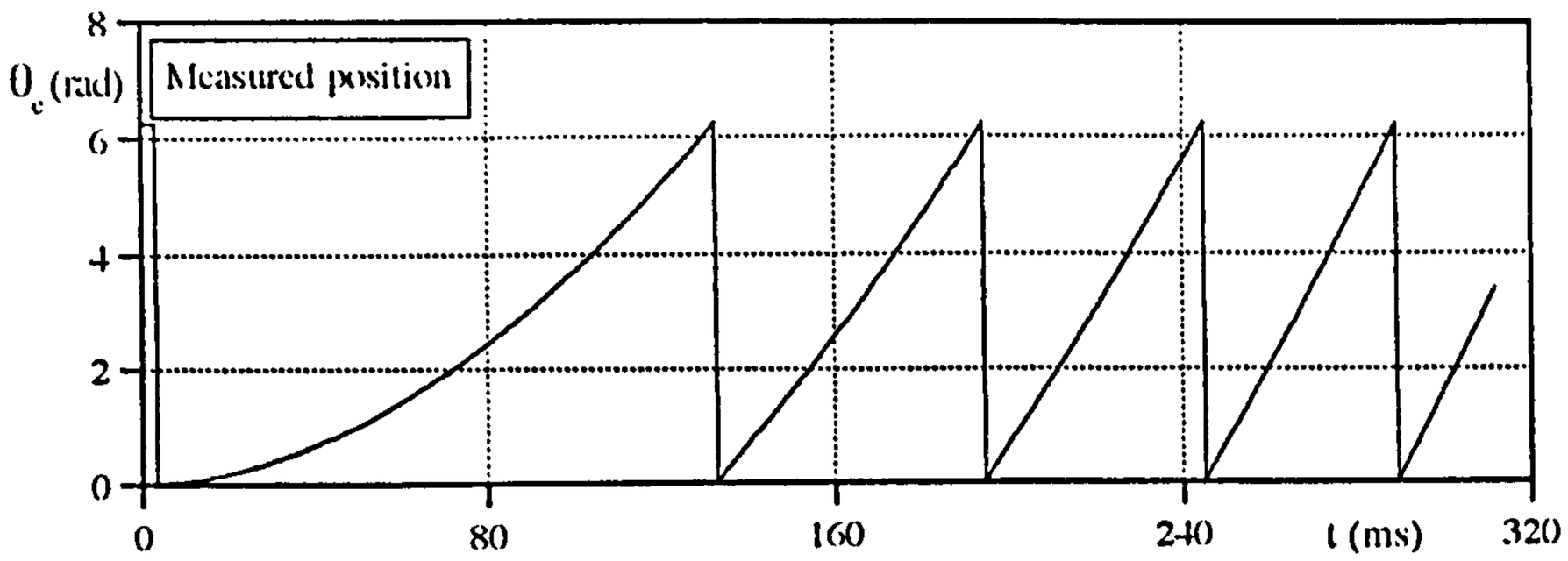

b

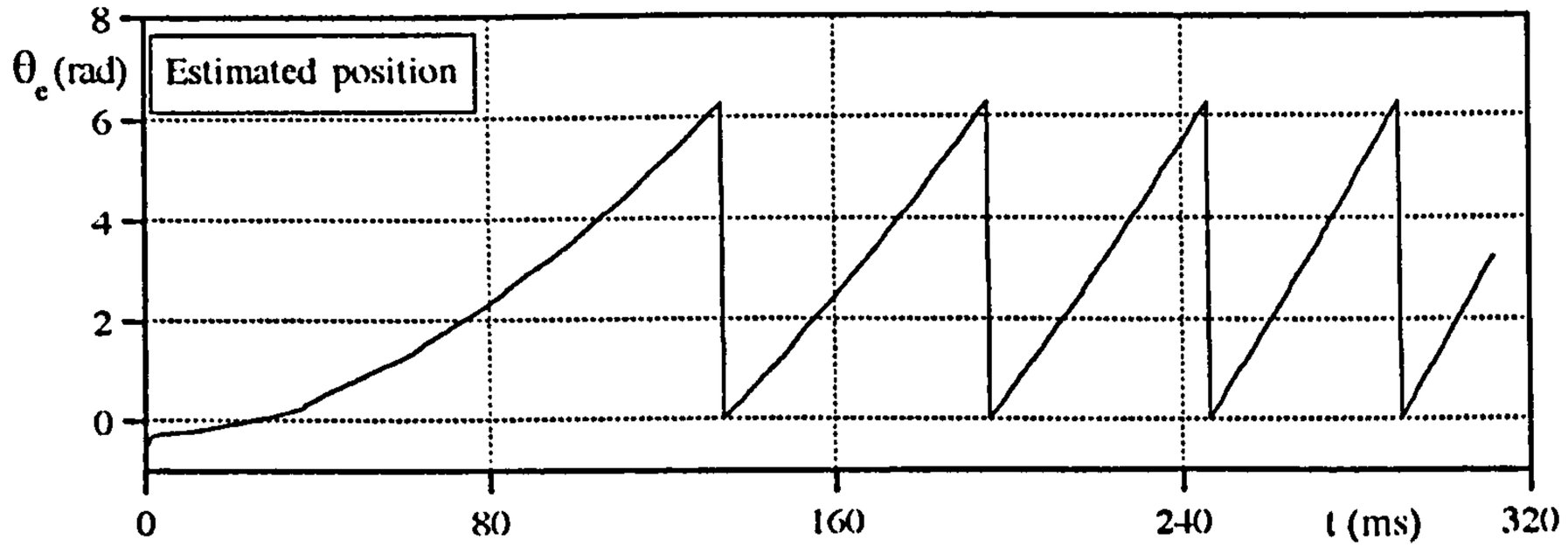

c

Figure 6.17 The transient experimental results for the operating condition shown in **Fig.6.15**.

a) Three-phase corrected flux linkage waveforms

b) Actual rotor position

c) Estimated rotor position

A third class of transient operating conditions arises from load changes. **Fig.6.18** illustrates the response of the algorithm to a step load change in the system. As said earlier, since the deceleration of the machine is defined mainly by the mechanical time constant of the system, to reduce the mechanical time constant of the drive, another axial field brushless PM machine was used as a load. The terminals of the brushless PM generator were connected to a power resistor via a three-phase diode rectifier.

As seen in the current waveform (**Fig.6.18b**), the operation of the drive deviates following the step in load at 100ms. Since there is no speed feedback on the drive, while the line current rises in amplitude, the speed of the motor reduces until the new steady-state speed, defined by the DC rail voltage, is reached. The measured speed variation during this operation was ≈30% (from 553 rpm to 384 rpm). The DC rail voltage was 45.2V before loading, falling to 39.1V after loading (at steady-state).

As seen in the waveform of measured flux linkage of **Fig.6.18c**, since the current level is small before loading, no noticeable dips occurred at current commutation. However, after loading, the dips showing the commutation instants on the flux linkage become apparent. The corrected flux linkage waveform is also given in the same figure for comparison. The estimated position is presented in **Fig.6.18d**. The verification of operation can be seen in the estimated position comparing with the actual line current waveform.

To examine the effect of lower sampling rate (more than 10μs sampling interval), the operating mode described in **Fig.6.18** was used. While **Fig.6.19** shows the estimated errors at minimum sampling rate 10μs, **Fig.6.20** presents the similar results with 200μs sampling rate. The results

are potentially valuable, since they also indicate the resolution of the position estimation algorithm and minimum number of samples per electrical period. It was observed that, even a 200μs sampling rate is enough to determine the position for this particular operation. From this examination, the following conclusions can be drawn:

The resolution of position estimation is ~0.15° electrical at high speed operation and ~0.1° electrical at low speed for 10μs sampling rate.

The resolution of position estimation is ~3° electrical before loading and ~2° electrical after loading for 200μs sampling rate.

Since the sampling rate is bigger in **Fig.6.20** than in **Fig.6.19**, the commutation instants are randomly missed during position estimation, and cause relatively large position error in amplitude. However, the estimated position error still remains small in these instants.

It is found that, the estimated flux linkage error for Phase I is unaffected by off-set effects in the integration, even with a lower sampling rate.

In both cases, it is observed that, while the speed reduces the amplitude of current error reduces. This could be expected, since the number of samples within an electrical period increases.

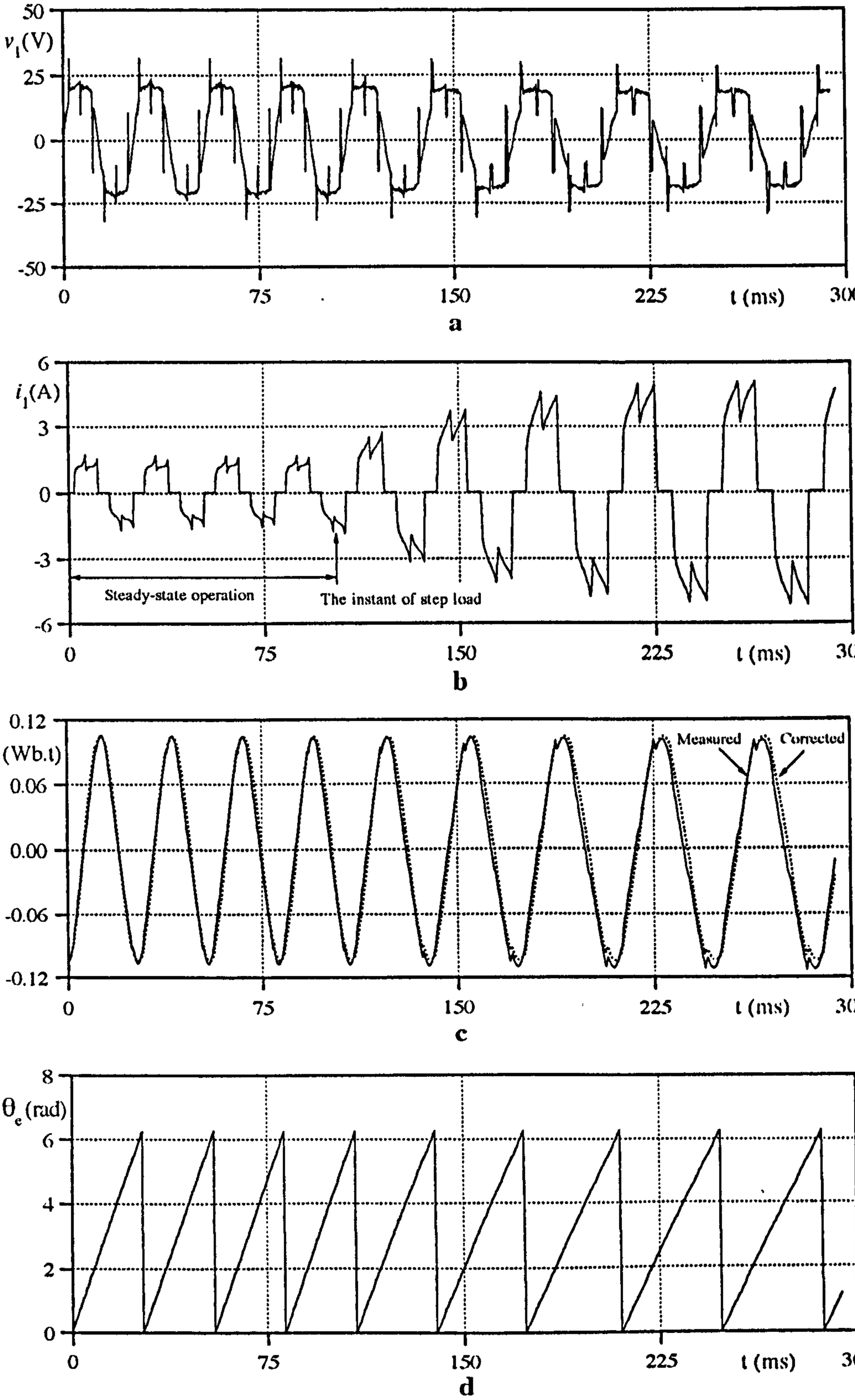

Figure 6.18 The deceleration test from 553 rpm to 384 rpm

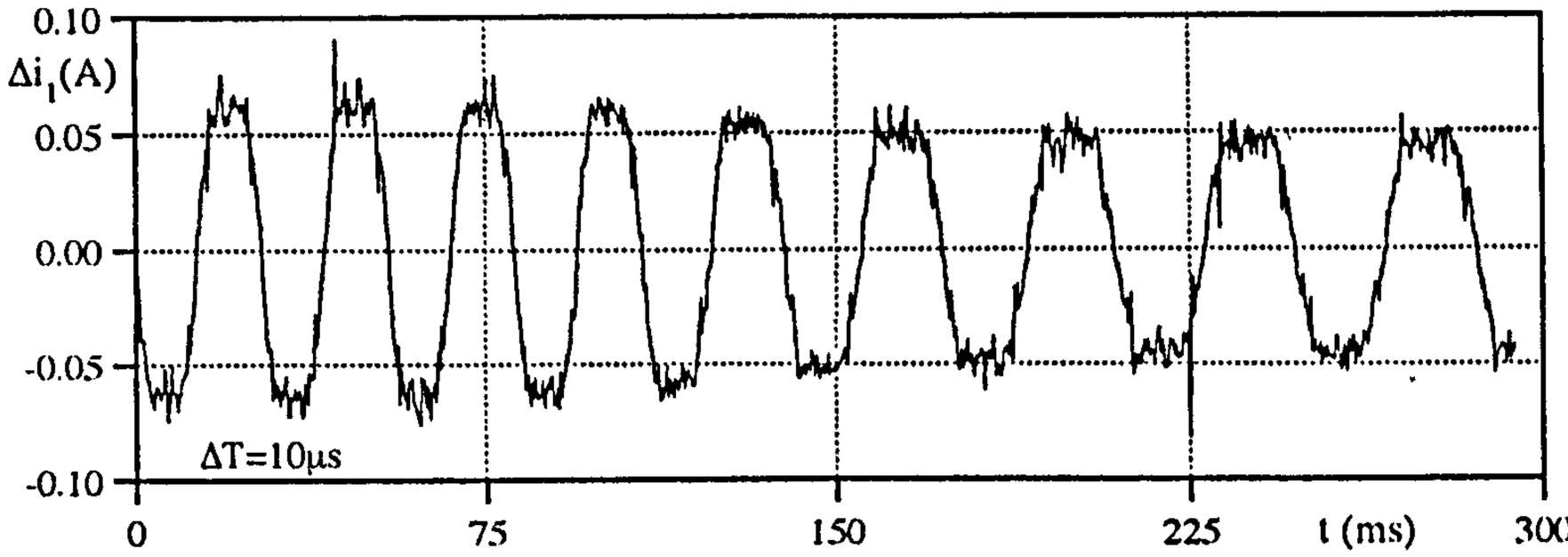

a

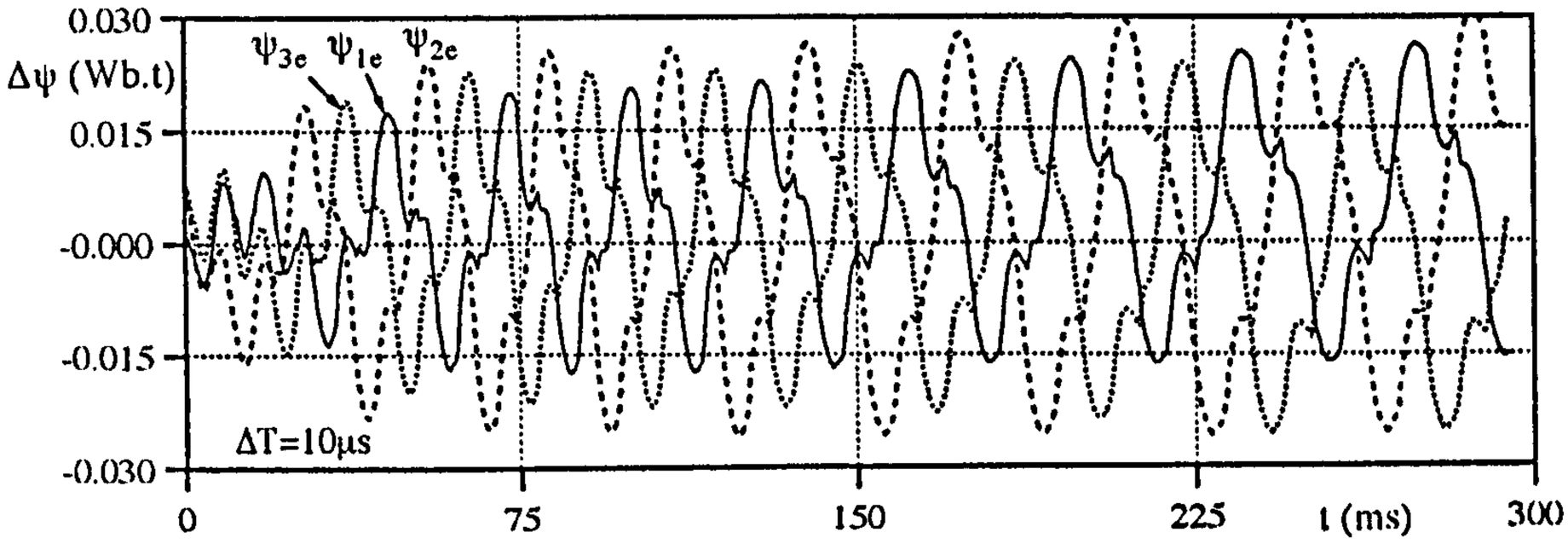

b

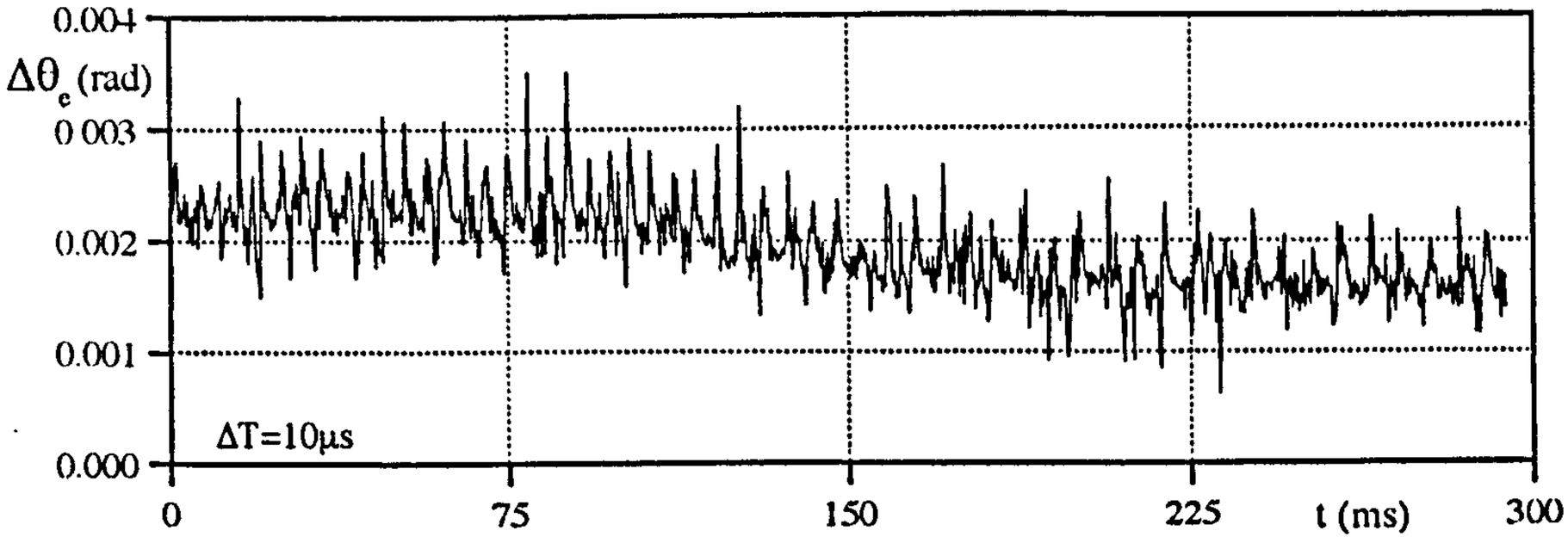

c

Figure 6.19 The transient results for the case given in **Fig. 6.18**, 10μs sampling rate.

a) Estimated current error for Phase 1

b) Estimated flux linkage error for Phase 1

c) Estimated position error

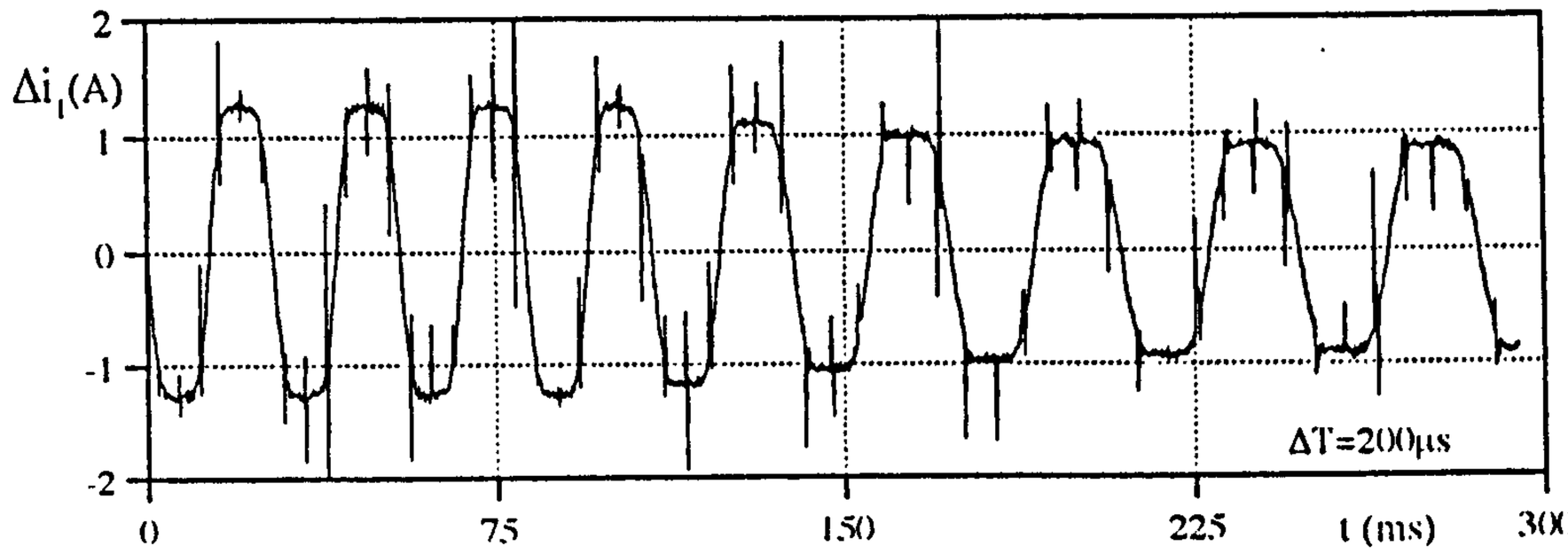

a

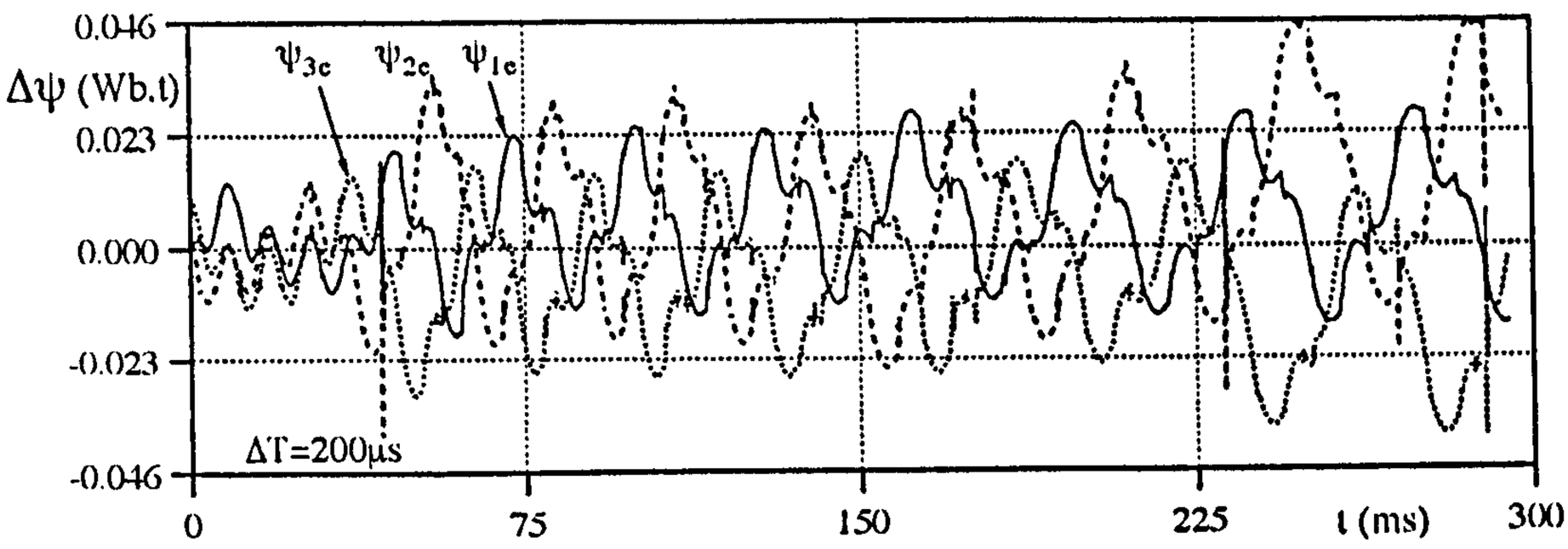

b

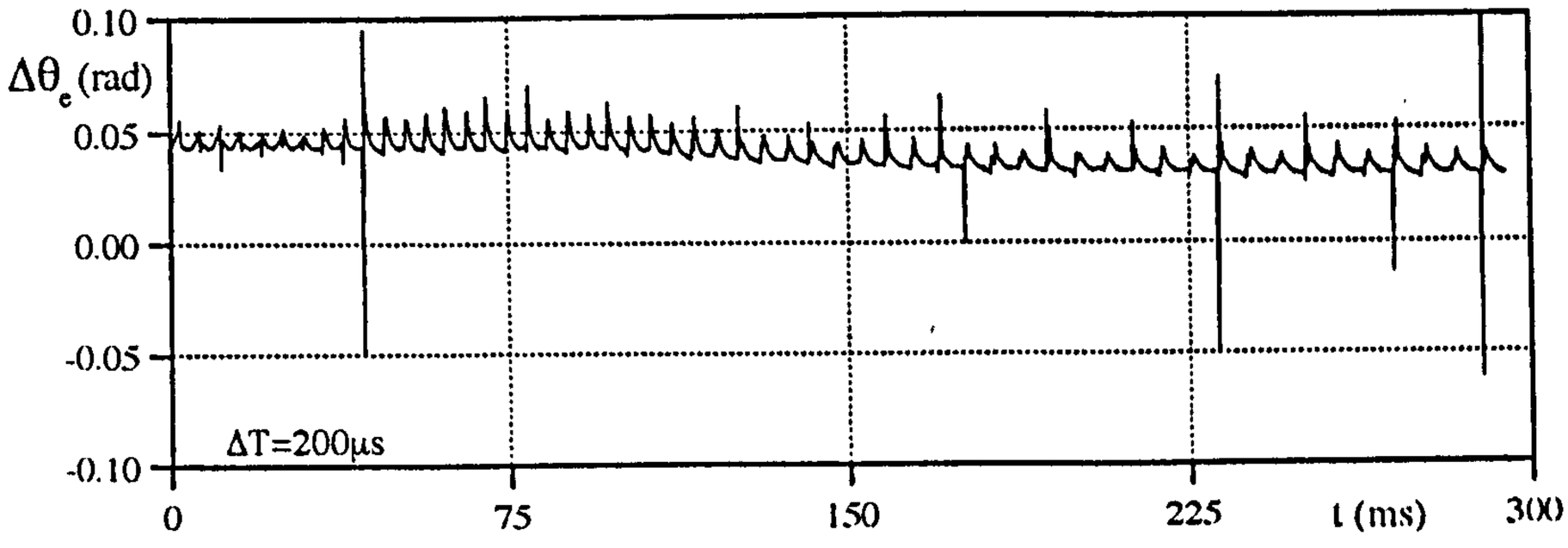

c

Figure 6.20 The transient results for the case given in **Fig.6.18**, 200μs sampling rate.

a) Estimated current error for Phase 1

b) Estimated flux linkage errors

c) Estimated position error

6.3 ON-LINE POSITION ESTIMATION AND RESULTS

The real-time position estimation is also implemented by a digital signal processor. In this section, the experimental results acquired by on-line estimation will be given. **Fig.6.21** illustrates the hardware details of the implemented real-time position estimation system using a DSP (TMS320C30). In the following subsections, the blocks shown in **Fig.6.21** will be briefly described, and three sets of experimental results will be shown.

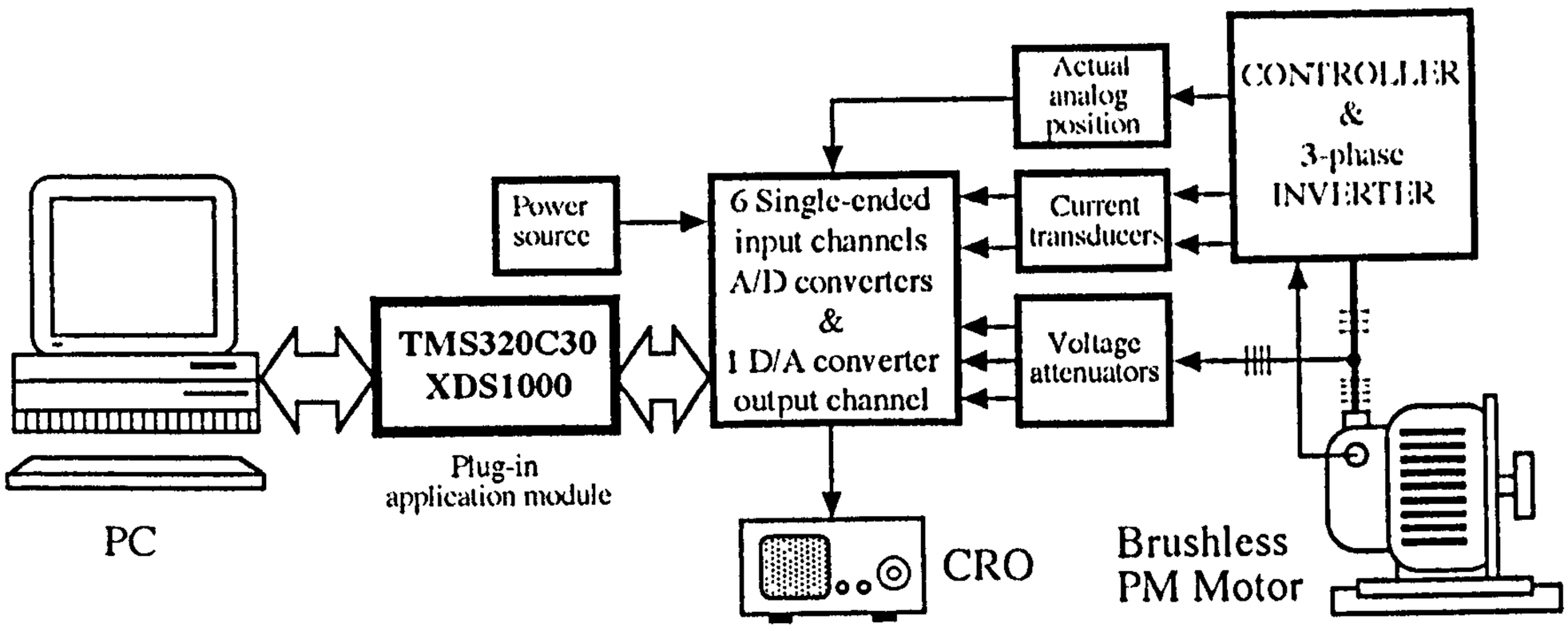

Figure 6.21 Hardware details using TMS320C30 for the real-time position estimation.

6.3.1 Implementation Details Of The DSP Based System

The analog voltage and current signals are sampled using analog-to-digital converters, and then input to the DSP (TMS320C30). The DSP performs a series of math intensive position estimation functions and generates the digital position signal.

TMS320C30 digital signal processor is a considerable enhancement from its predecessors, and its key features can be summarised as in **Table 6.2.**

Table 6.2 Some key features of TMS320C30

60ns single cycle instruction execution time
33.3 million floating-point operations per second
16.7 million instruction per second
One 4K x 32 bit single cycle dual access on-chip ROM
Two 1K x 32 bit single cycle dual access on-chip RAMs
64 x 32 bit instruction cache
32 bit instruction and data words, 24 bit addresses
Integer, floating point, and logical operations
Two 32 bit timers
Two external interface ports

The XDS1000 used in these experiments is a complete development environment, and consists of XDS500 emulator, a predefined target board with an on-board TMS320C30 DSP, assembler/linker, C/assembly source debugger.

In **Fig.6.21**, the block prior to the TMS320C30 is the data acquisition board which includes 7 channels and a switched mode power supply. Data acquisition is accomplished by digital-to-analog (D/A) converters. Since the D/A s' conversion speed relates directly to the required sampling rate of the application, they should be determined by the need to sample fast enough to prevent excessive phase lag, and to sample slow enough to avoid unnecessary expense.

The system is similar to the off-line data acquisition experimental set-up given in **Fig.6.1**: the 6 input channels are used in the real-time

implementation to measure two line currents, three phase-to-star point voltages, and the actual analog shaft position of the motor simultaneously for comparison. Since the off-line data acquisition system consists of two current and three voltage measurement units, no extra sensors were needed.

For the highest possible resolution, the measured current and voltage signals should be equal to the maximum input range of the A/D converters. Although the variable gains on the data acquisition boards give the opportunity to increase the accuracy of the measurement, they are set to a fixed value which represents a predefined operating condition.

The system from which the measurements are derived contains fast transients, therefore the inputs are isolated by using separate power sources (DC/DC converters). Although, as explained earlier, the input signals can be filtered for unwanted variations, since integration is involved, the effect of fast varying disturbances are removed from the flux linkage waveform. Therefore, it is found that a prefilter is not necessary.

The discrete position data produced by the DSP are translated back into continuous-time signals, using digital-to-analog (D/A) converters, and the signal is displayed on an oscilloscope (**Fig.6.21**) or applied back to the drive to replace the mechanical position sensor.

6.3.2 The Results of On-Line Data Processing

In real-time operation, the signal processor has to finish all of its processing before it takes the next sample. Therefore, sampling time should be chosen according to this limitation. Moreover, certain functions (such as sin, cos) in the DSP may be too time consuming to perform. Since the position

estimation algorithm involves a number of sin and cos functions, using a look-up tables reduces the execution time dramatically. The 60 ns instruction cycle time of the DSP provides a significant advantage for the position estimation, and in this particular application, processing time is 90μs. Despite the simplicity of the algorithm, the processing time might seem excessive. However, it is mainly due to programming in the language C. The processing time can be further reduced by programming in assembly language.

Three sets of results are given to display the effect of load changes in the drive. It should be noted that the results presented in **Figs.6.22-25** are also important in showing current controlled and uncontrolled cases in the same figure. The results were taken while the position estimation was performing continuously by DSP.

In **Fig.6.22**, while the drive was operating at steady-state, a power resistor was connected to the rectifier to increase the load (**Fig.6.4**), giving the effect of a step load change. As a result of loading at constant DC rail voltage (Vdc=58.8V), and since there is no speed feedback in the drive, the motor slows down while the line current increases (**Fig.6.22b**). The initial speed (629rpm) reduces by 55%, and reaches the new steady-state speed (283rpm) within two electrical cycles. As seen in **Fig.6.22b**, the loading also activates the hysteresis current controller giving the effect of current control around the predefined commanded current (5A). The effect of current control action can also be seen on the voltage waveform (**Fig.6.22a**).

The corrected flux linkage waveform is given in **Fig.6.22c**. Since the flux linkage correction is done, DC offsets in the measured quantities are not

reflected onto the measured flux linkage waveforms. Clearly, the comparison of the actual position (**Fig.6.23a**) and the estimated position (**Fig.6.23b**) indicates very close agreement. The very fast speed change does not introduce clear deviation from the actual position, and the position estimation algorithm performs well with the help of fast execution of the DSP.

Fig.6.24 represents the effect of unloading. The opposite test is applied to the drive by removing the previously added load at DC rail voltage 53V. The initial steady-state speed (329rpm) of the motor increases by 73%. The response of the position estimation to the acceleration test is excellent, and the measured and the estimated position are given in **Fig.6.25**.

The last set of result given in **Figs.6.26-27** shows the effect of sudden load change in the drive. The previous step loading tests were combined in this test to create the effect of worst possible load change in the drive. While the drive was operating at constant speed, a step load was added (at 60ms), and removed (at 250ms). The performance of the algorithm is remarkable. Both the actual and the estimated positions are shown in **Fig.6.27**. During the sudden load change, while the steady-state speed of the motor was 636rpm it reduced to 389rpm. After the load had been removed, the motor's speed reached to previous steady-state speed again.

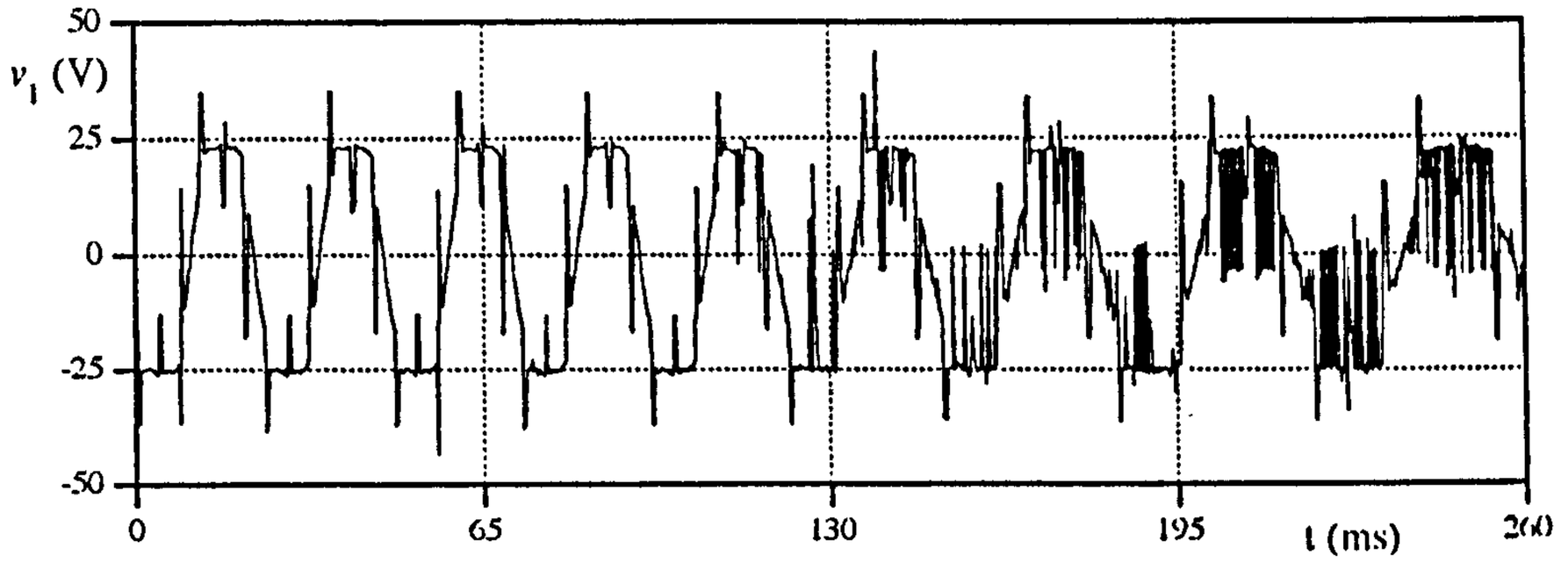

a

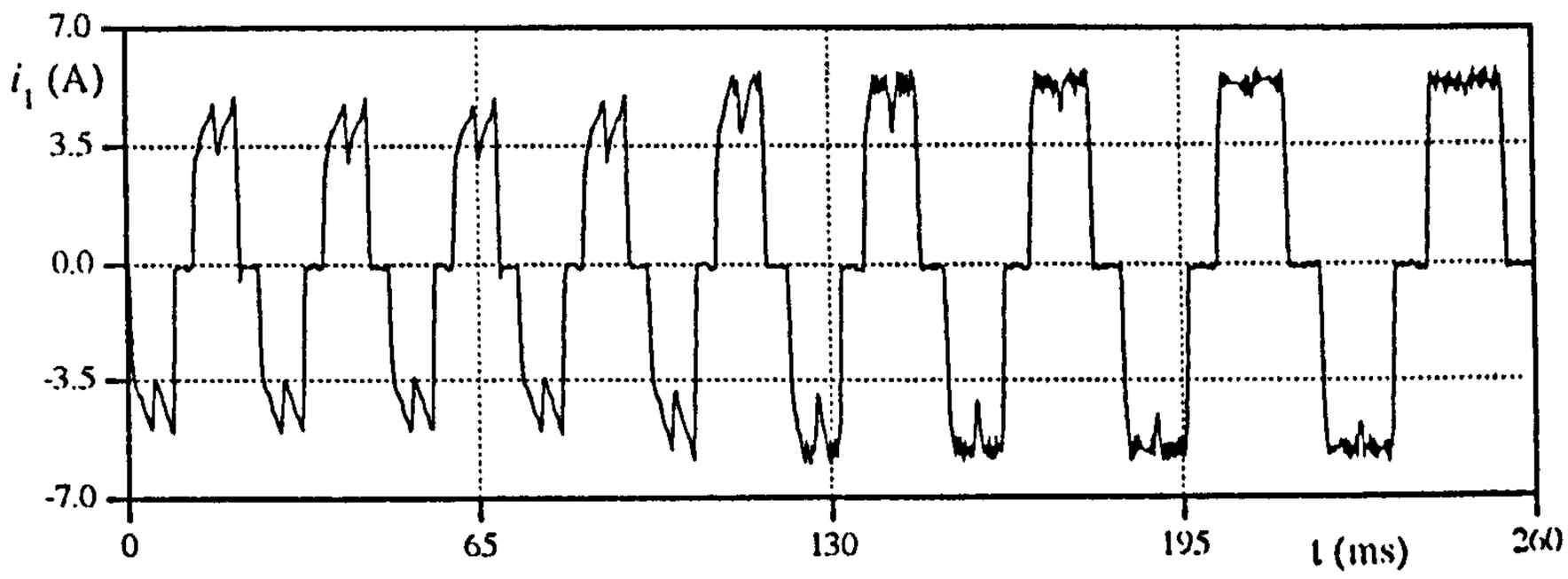

b

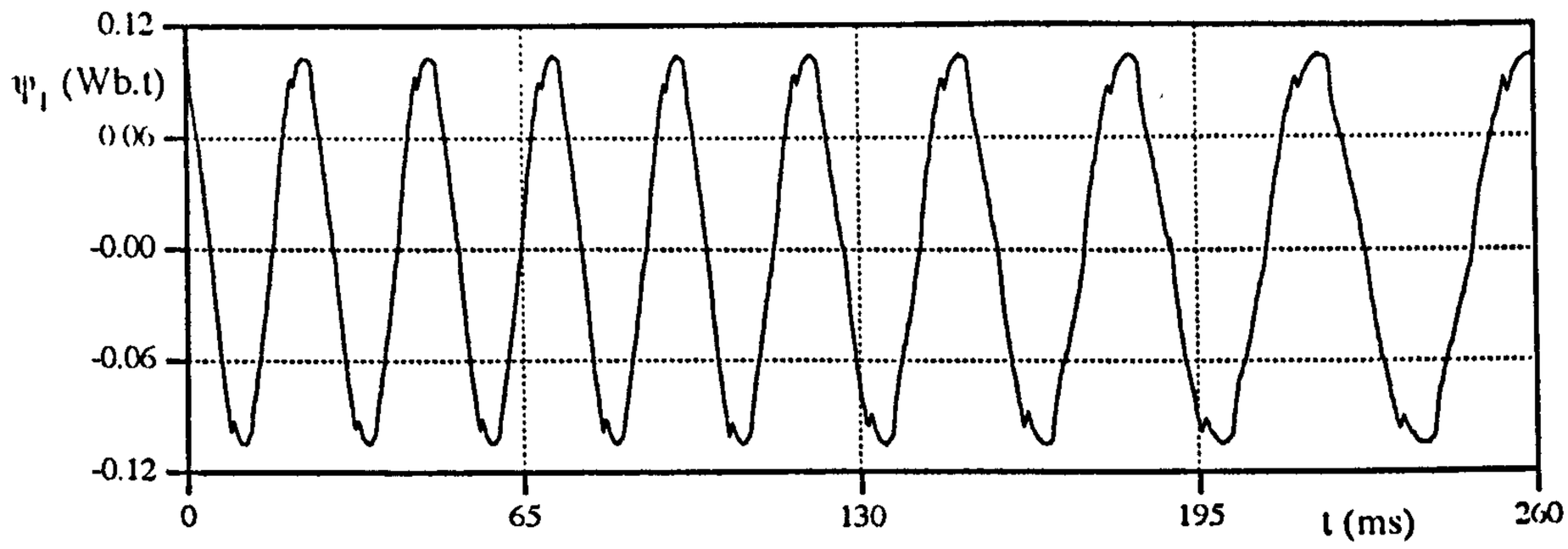

c

Figure 6.22 Real-time deceleration test results, from 629rpm to 283rpm.

a) Measured Phase 1 voltage

b) Measured Phase 1 current

c) Estimated (corrected) flux linkage

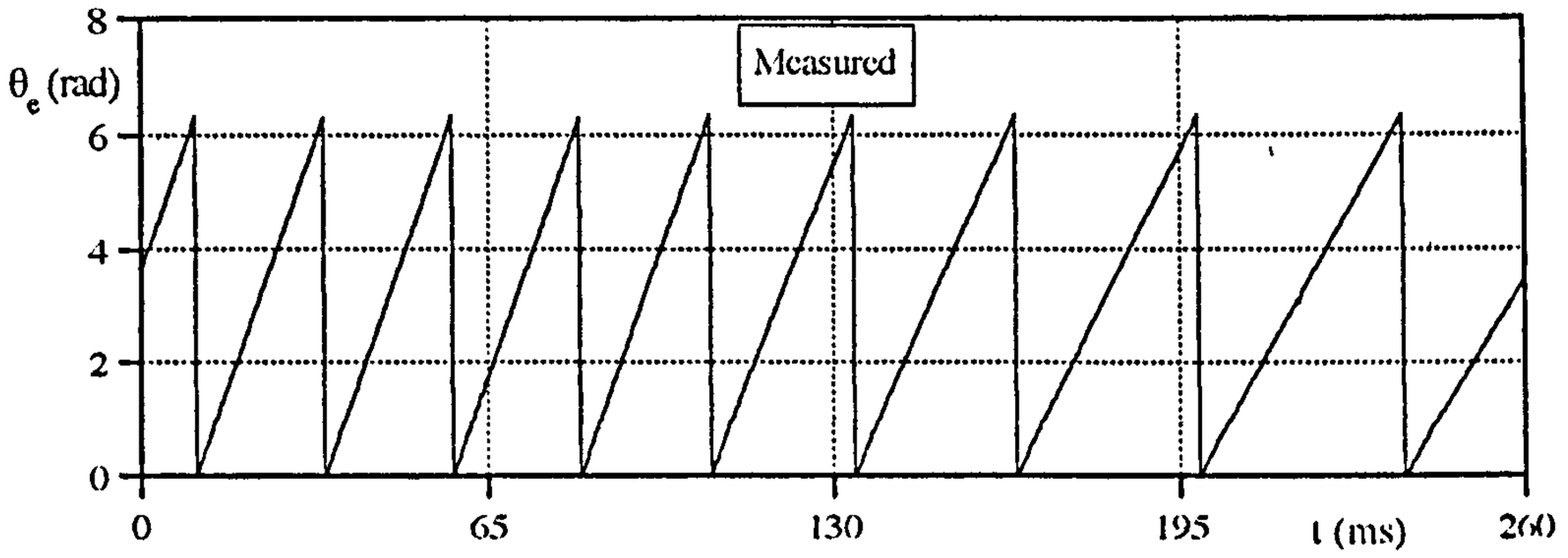

a

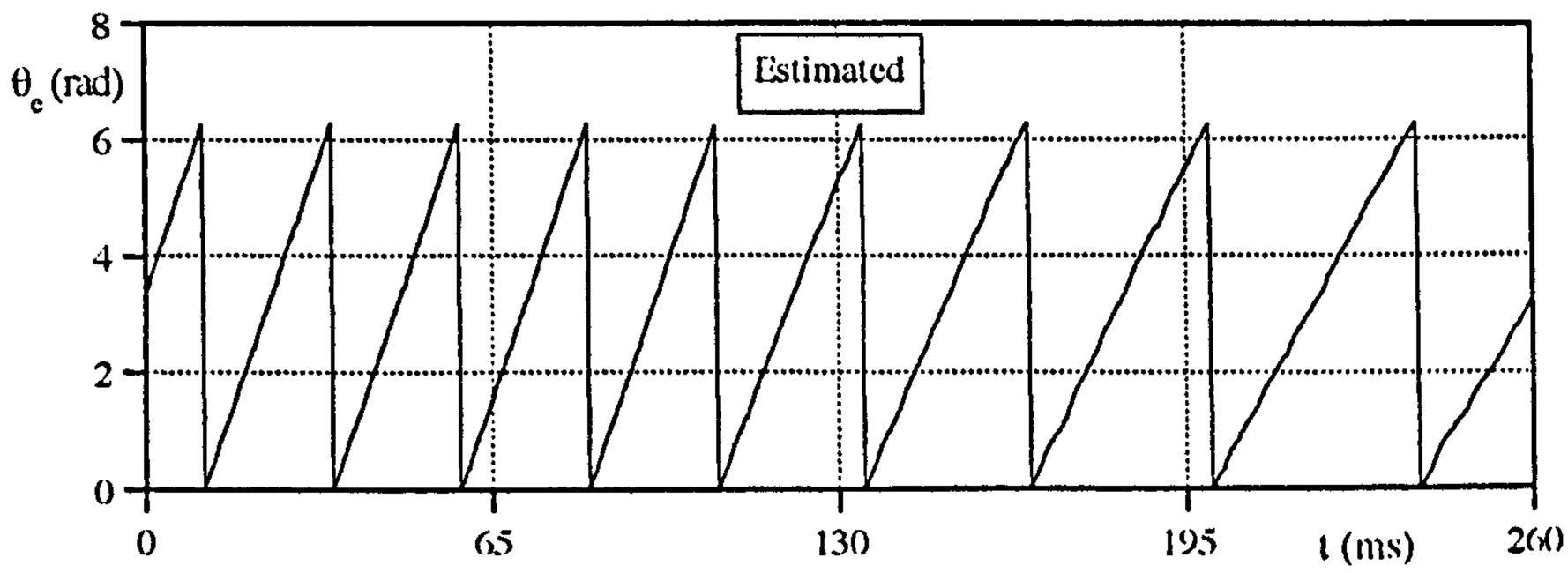

b

Figure 6.23 Real-time deceleration test results corresponding to **Fig.6.22**

a) Actual position reference to Phase 1

b) Estimated position

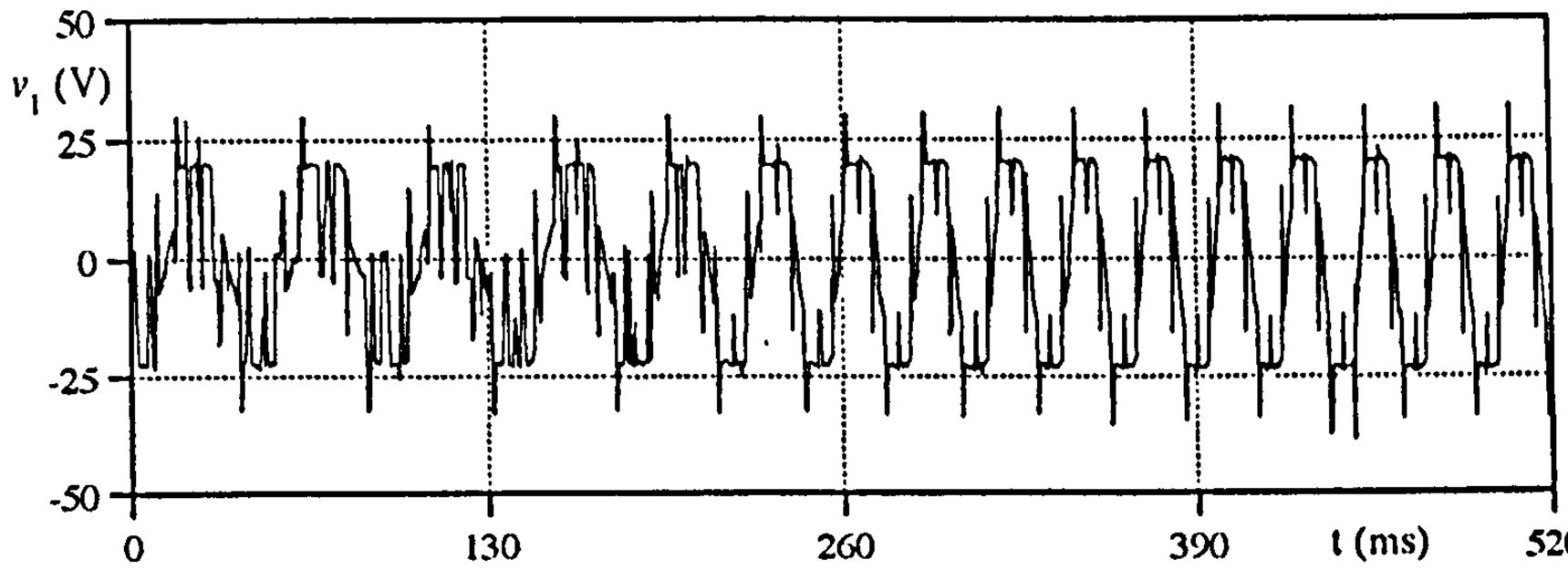

a

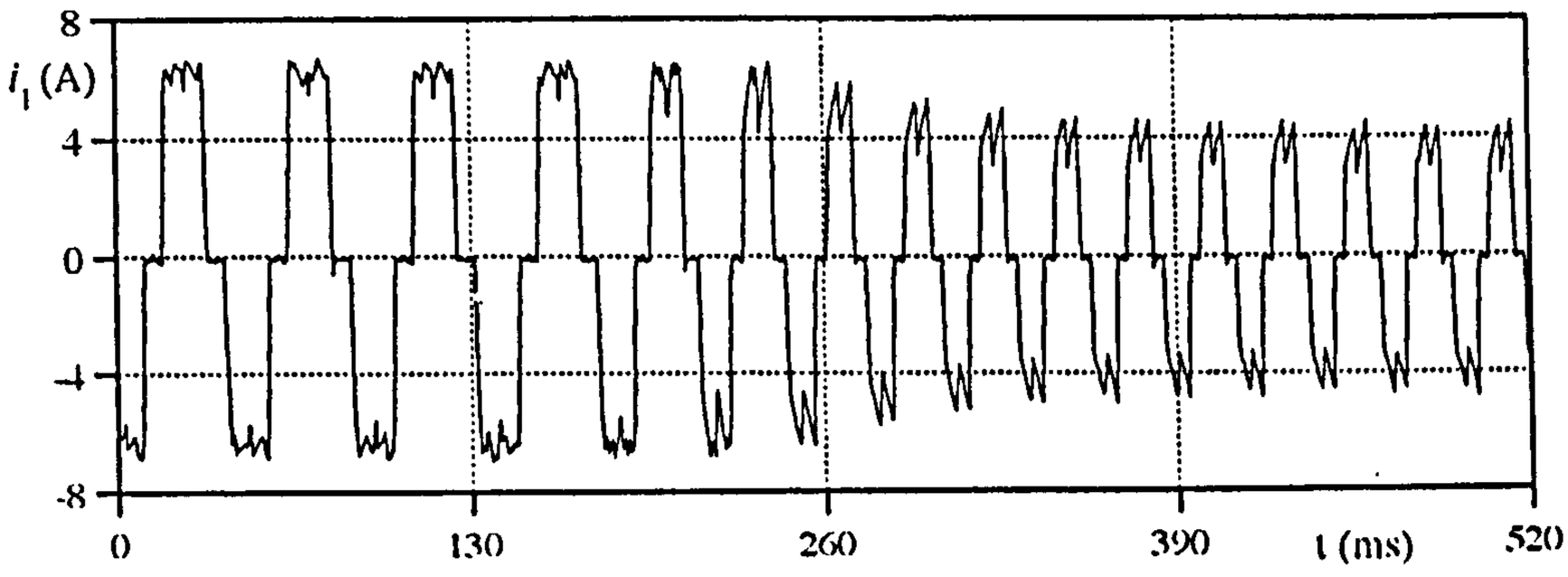

b

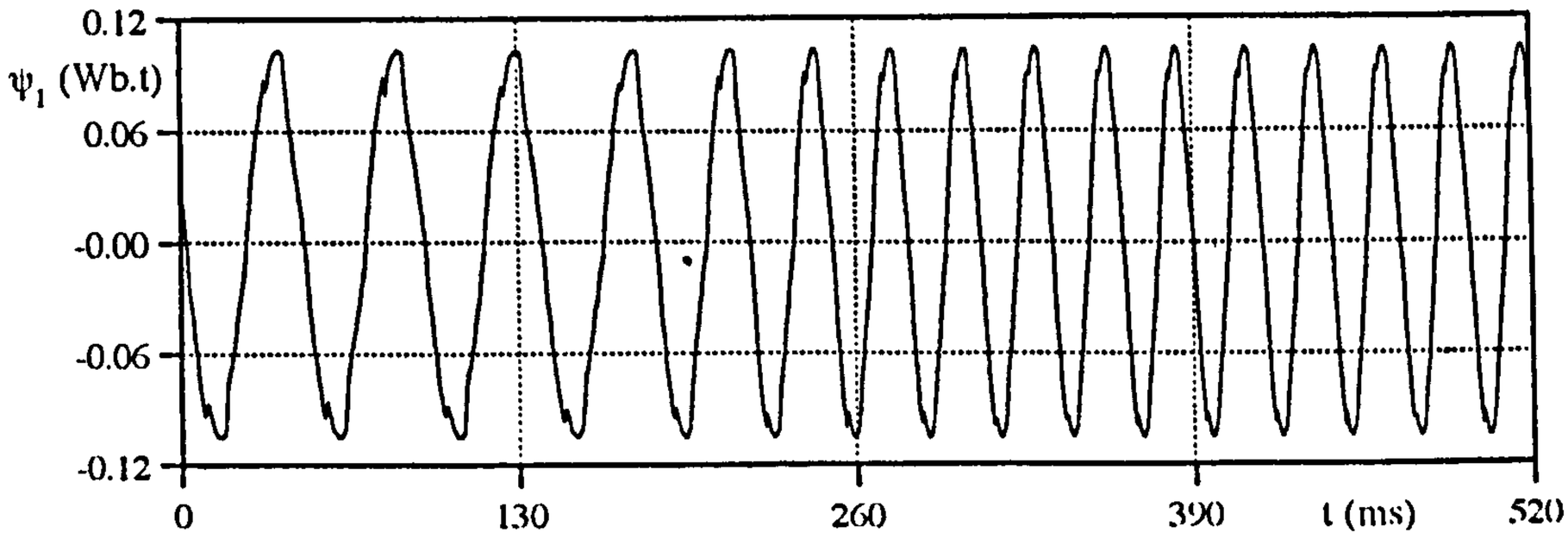

c

Figure 6.24 Real-time acceleration test results, from 329rpm to 570rpm.

a) Measured Phase 1 voltage

b) Measured Phase 1 current

c) Estimated (corrected) flux linkage

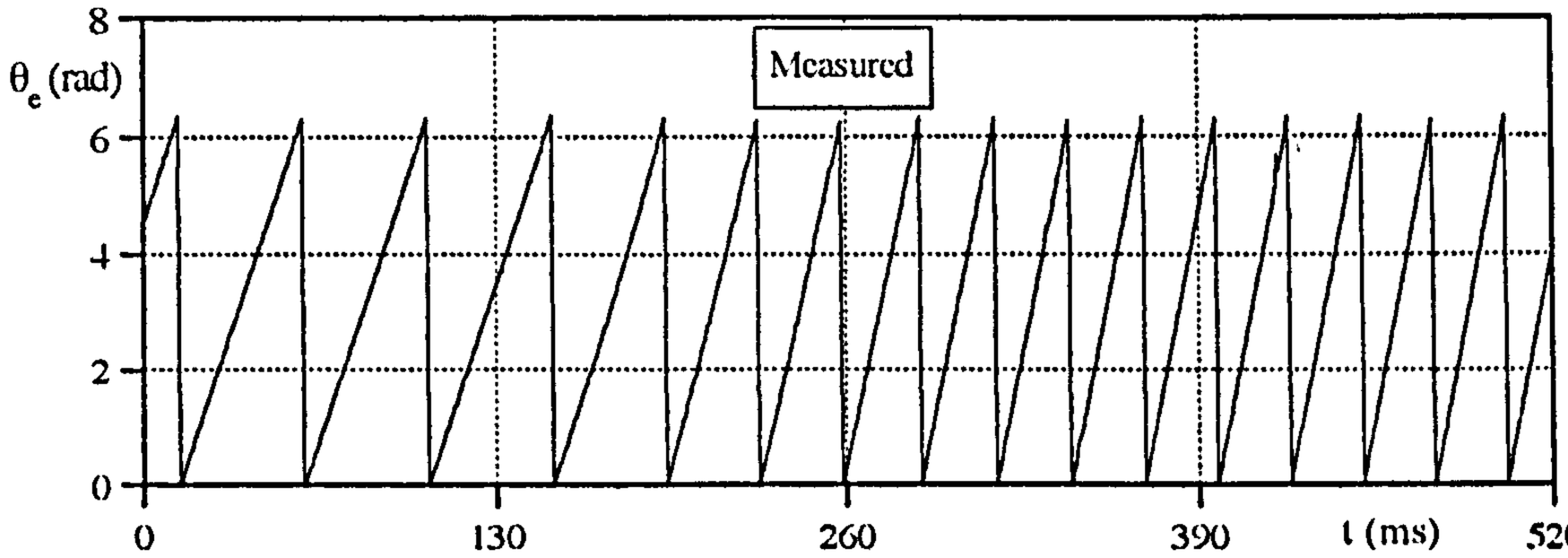

a

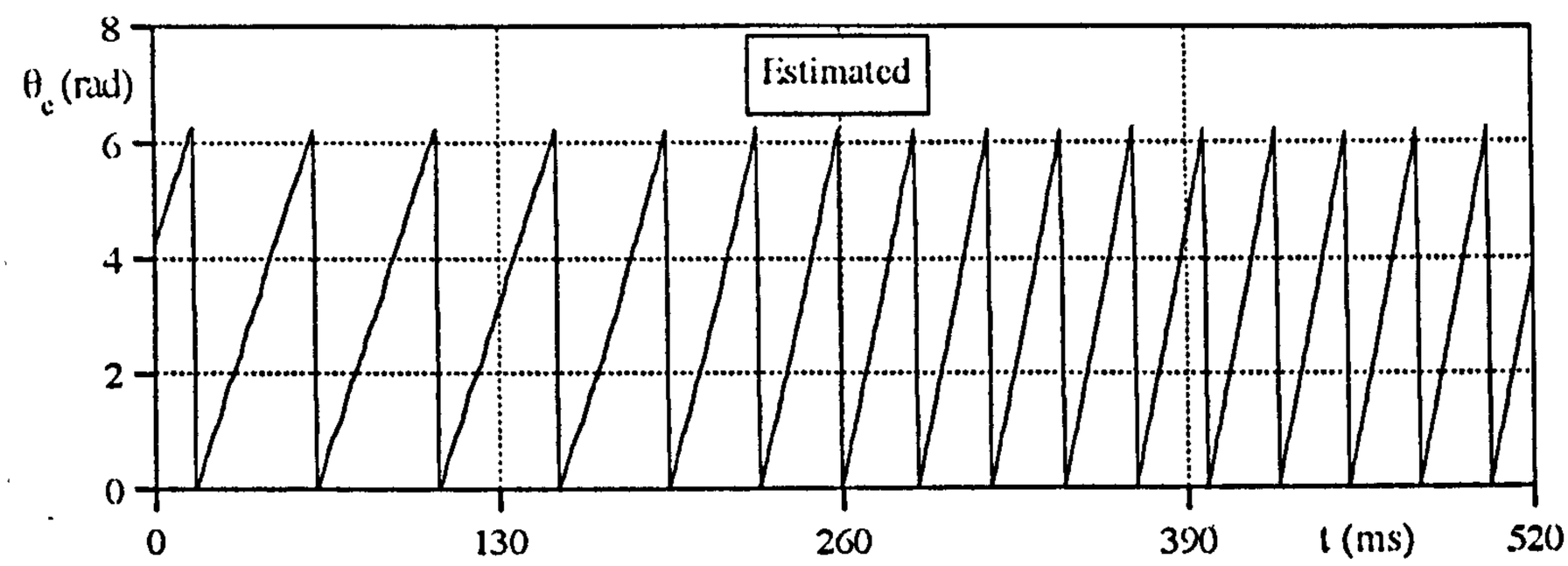

b

Figure 6.25 Real-time acceleration test results corresponding to **Fig. 6.24**

a) Actual position reference to Phase 1

b) Estimated position

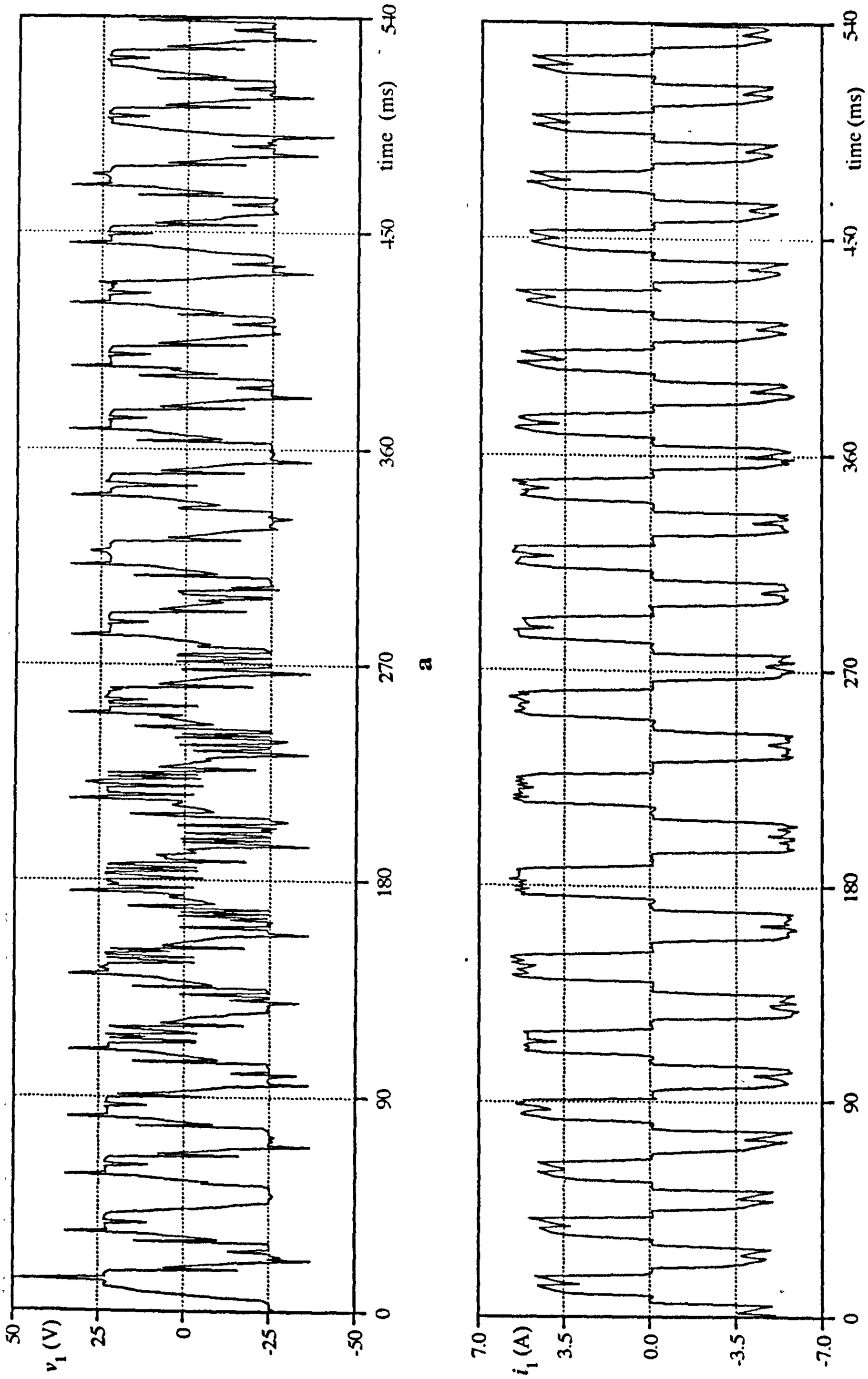

Figure 6.26 Transient results showing the sudden load change

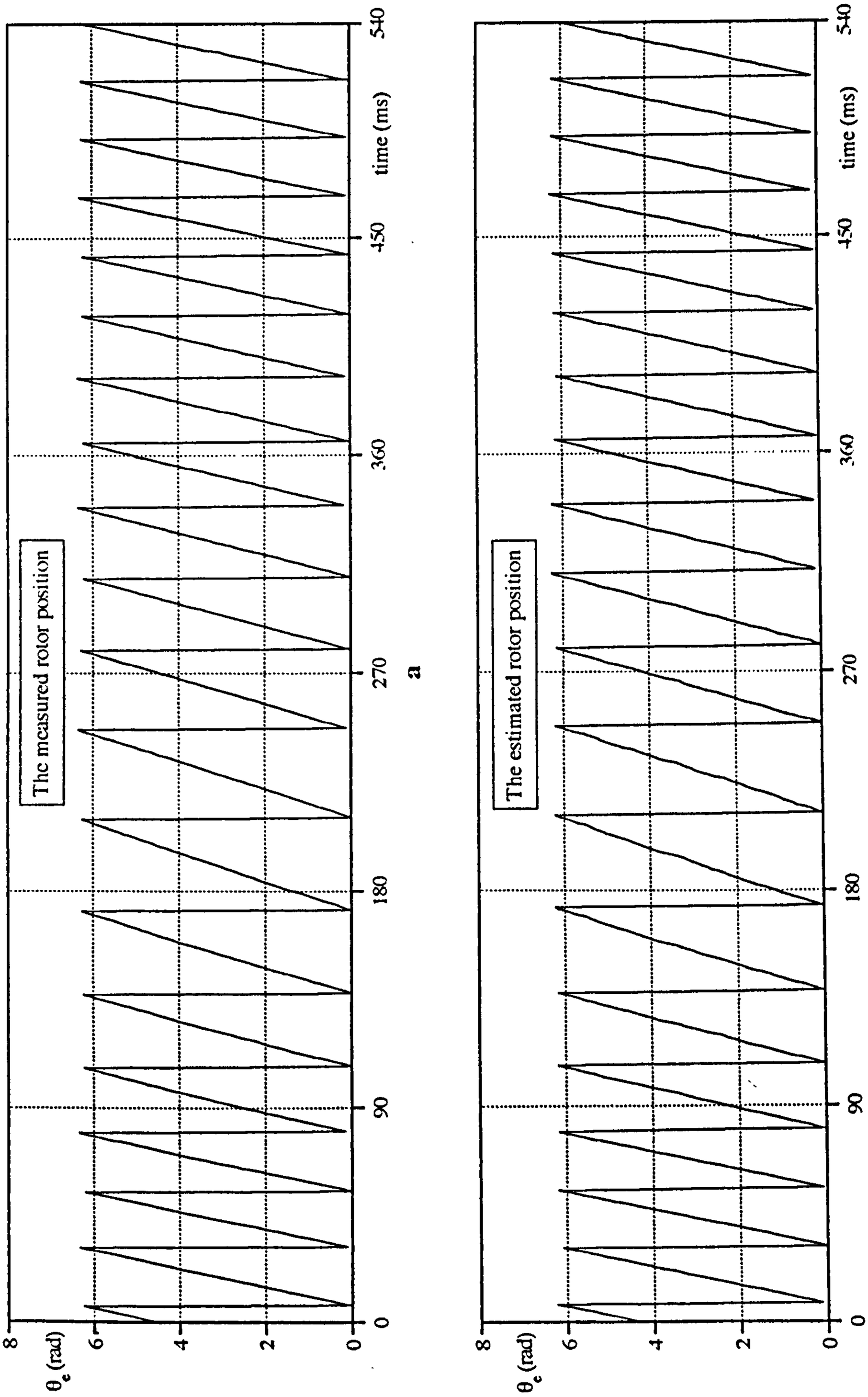

Figure 6.27 Measured and estimated rotor positions for the operating condition shown in Fig.6.26

6.4 MEASUREMENT ERRORS AND PARAMETER DEVIATIONS

6.4.1 Error Analysis

Since the proposed algorithm is implemented by calculating the flux linkage based on the phase voltage and the line current, the performance of the algorithm also depends on the quality and accuracy of the estimated flux linkages and measured currents. In addition to this, parameter deviations due to variations in temperature and saturation should be considered.

Although the state equations of the PM motor are expressed in **Eq.5.2**, and the flux linkage variables are defined in **Eq.5.5** (for constant winding inductance), disturbances occur in the flux linkage estimations due to measurement errors and parameter variations. The generalised error terms in the flux linkage estimation and flux linkage variables may be expressed as follows:

$$\psi = \int (v - Ri)\, dt + \psi_0 + \mathbf{E1} \tag{6.1}$$

$$\psi = Li - \lambda_m(\theta) + \mathbf{E2} \tag{6.2}$$

Here, **E1** and **E2** are the errors due to measurement and parameter deviations. The corruption sources on the flux linkage estimation may be classified under term **E1** as follows:

1. Measurement errors in the terminal quantities,
   a) phase shift in the measured values due to measurement devices,
   b) magnitude error due to conversion factors and gain,

c) offset in the measurement system.

d) quantisation error in the digital system.

2. Temperature effect on the winding resistance R.

The error term **E1** in **Eq. 6.1** mainly includes measurement errors. In both voltage and current measurement, one has to ensure that the measurement device will not introduce a phase shift, offset or a magnitude error. Another problem in the measurement system is the noisy computer connection to the IEEE bus. The sensitive analog front end of the instrument can also be corrupted by a noisy computer connection. One solution is to place an isolation amplifier between the input side and the measurement system. However, the isolation amplifier often limits the performance of the system particularly for high frequency measurements.

Moreover, in star connected systems, if the current regulation in the third phase is reconstructed from the regulation of the other two phases, errors in the third line current might be increased. The error in flux linkage estimation is mainly due to measurement errors, but it may not be separated from deviation of the winding resistance R.

The resolution of the measurement can be increased by reducing the quantisation. Although a faster sampling rate and a higher resolution might acquire more and accurate data points in a given time and therefore can form a better representation of the original signal, they are limited by the algorithm's processing speed and the number of bits of A/Ds.

For comparison, the following simple calculations can be introduced to determine maximum current variation in the drive at rated operation

conditions. All calculations ignore the iR voltage drop, and assume the DC rail voltage V_{dc} at rated speed is twice the maximum value of phase back EMF E_m . The calculations were given based on 120° operation. In the test motor, the maximum current variation with time at standstill (or low speed) can be written as

$$\frac{di}{dt} = \frac{(2/3)V_{dc}}{L} = \frac{4E_m}{3L} = \frac{4x131}{3x0.00312} = 0.06\ A/\mu s \qquad (6.3)$$

During running, the current variation can be given for **Phase 1** by,

$$\frac{di_1}{dt} = \frac{1}{L}(v_1 - e_1) \qquad (6.4)$$

When the hysteresis current control activates, the highest rate of current change within the current control interval can be estimated by substituting maximum value of the term (v_1 - e_1) into **Eq.6.4**. For the **Phase 1**, the phase voltage v_1 can be written:

$$v_1 = \pm \frac{V_{dc}}{2} + \frac{(e_2+e_3)}{2} \qquad (6.5)$$

and within the commutation interval, the phase voltage is

$$v_1 = -\frac{2V_{dc}}{3} + \frac{(e_1+e_2+e_3)}{3} \qquad (6.6)$$

In above equations, e_1, e_2, and e_3 are the back EMFs of the motor, and as known they vary with time. In **Table 6.3**, the estimated current changes for **Phase 1** are summarised assuming trapezoidal back EMF.

Table 6.3 Summary of highest current change with time in 120° inverter

The current control interval				REMARKS
e_1	$\pm \frac{V_{dc}}{2}$	$\frac{e_2+e_3}{2}$	$\frac{di_1}{dt}$	
E_m	$+E_m$	$-E_m$	0.04A/μs	Two phases are conducting via the power transistors
E_m	$-E_m$	$-E_m$	0.12A/μs	Two phases are conducting through a pair of complimentary reverse parallel diodes
The commutation interval				
e_1	$-\frac{2V_{dc}}{3}$	$\frac{(e_1+e_2+e_3)}{3}$	$\frac{di_1}{dt}$	
E_m	$-\frac{4E_m}{3}$	E_m	0.06A/μs	Phase commutation instant, three phases are conducting

As seen in **Table 6.3**, if the signal changes too fast, as in switching instants, the acquired data is subject to large errors. In order to retain enough data to be able to replicate the fast variation, the signal must be sampled at a rate more than twice its highest frequency (the Nyquist Theorem). It is clear that, while the highest resolution and the fastest acquisition of data increase the performance of the method, they require higher cost. A test has been carried out to determine the maximum sampling interval which can also define the minimum number of sample per electrical period. Although, the high resolution position estimation requires more data points per electrical period, it is found that, approximately 300 data samples per electrical period are enough to estimate the rotor position.

The error term **E2** also includes current measurement error. However, it is mainly affected by magnet flux linkage and winding inductance. For PM motors which have large air gap, saturation effects caused by current level may be ignored. Deviations in the magnet flux linkages and changing back EMF constant with temperature may be taken into account.

6.4.2 Examination of Parameter Variations in the Drive

The effects of parameter variations have been studied with reference to initially measured motor parameters. In order to check the ability of the method to perform in the presence of parameter variations, a test has been carried out which involves changing the value of the winding resistance, the back EMF constant, and the winding inductance within a ±10% range.

Changing the resistance value causes small phase shift and noticeable dc offset in the estimated flux linkage waveform which can be overcome by the flux linkage correction. Referring to the initially estimated position, measurements have shown that changing the resistance value ±10% for the operating condition in **Fig.6.12** changes the first electrical period by about 2ms. When the motor reaches the steady state, the difference becomes smaller. During constant speed operation, the zero crossing points in the position waveform shifted 2.5° electrical which corresponds to ±0.7% position error.

Changing the back EMF constant causes a magnitude difference between estimated and corrected flux linkage. The deviation can be recovered by flux linkage correction. Changing the back EMF constant ±10% affects the position estimation about 3° electrical during constant speed operation for the case in **Fig.6.12.**

Both changing the value of the inductance and offset effect does not introduce noticeable position error, However, small errors can be eliminated by flux linkage correction. Two typical waveforms of outer current loop error and errors in flux linkage estimation for acceleration from rest were given in **Fig.6.13b** and **Fig.6.13c** respectively. The high initial current

error in **Fig.6.13b** is related to an error in the initial position of the motor. Static friction in the mechanical system and incorrect initial value of the integration may cause this error in real system applications.

The effect of sampling rate was examined in **Section 6.2.2**. As seen in the same section, while the highest resolution in the position estimation can be achieved with a high sampling rate, the overall cost and performance limitations in hardware should also be considered in the implementation.

6.5 CONCLUSIONS

The experimental results have demonstrated that stator voltages and current signals from a PM motor can be used to obtain position information. The proposed algorithm for shaft position sensorless operation has been tested with a commercially available PMSM operating with both 120° electrical degrees conduction and sinusoidal excitation.

The method is based on flux linkage estimation, so the algorithm can be applied to any other machine, such as the trapezoidal permanent magnet machine and reluctance-type machines. A more versatile approach may be implemented using machine specific look-up tables for rotor flux linkage variations.

The method can also be applied to motors which have position dependent inductance, and allows detection of rotor position over a wide speed range including acceleration from rest. The position estimation method effectively moves the position measurement point in the drive from the mechanical side to the motor's terminals.

The actual rotor position information was obtained accurately from the output of the resolver-digital converter for comparison. It has been observed from a wide range of experimental results that there is very close agreement between the measured and the estimated rotor position.

The position estimation algorithm has also been verified by on-line experiments, and some transient results have been given. It is found that, the proposed method is simple, is easily designed and applied, since the DSP is programmed directly in a high level language (C), and performs satisfactorily. The processing time of the algorithm is 90 μs. Despite the simplicity of the algorithm, the processing time might be seen as excessive, it is mainly due to programming in the language (C). The processing time can be further reduced by programming in assembly language.

The DSP has played an important role in this application by reducing the development time. With the DSP solution, since the hardware is straightforward, and only the algorithm or software differentiates a system, additional system features such as overall control of the brushless PM motor may be added for little or no additional cost. On the other hand, if a DSP control system is already implemented in the drive, the position estimation algorithm can be implemented at low cost.

The high frequency spikes in the error waveforms are relatively small when they are compared with the amplitude of the actual signals. It is possible to minimise them by noise free design and reducing the execution time of the DSP. As said earlier, the performance of the real-time implementation can be further improved by using the actual magnet flux linkage variation in a look-up table.

CHAPTER VII

CONCLUSIONS AND SUGGESTIONS FOR FUTURE RESEARCH

There are many different types of motors which operate on electromagnetic principles. Of these, brushless PM motors have remarkable characteristics, allowing them to drive many advanced motion systems. Their motion is governed by control circuits such as microprocessors or pure analog circuit. However, between a control circuit and a motor there is the very important power electronic stage, which receives control signals from the microprocessor and deals with the electric power to be supplied to the motor to control its motion. Moreover, brushless PM motor drives require a rotor position sensor to synchronise the PM motor's current to the rotor position so that the back EMF is maintained at a fixed angle to generate maximum torque or/and speed. In practice, the rotor position sensing devices have limited resolution, operating condition, and operating characteristics. These limitations often restrict the performance and application type.

In this thesis, the overall control system was implemented in semi-digital form. Two types of inverter (IGBT and bipolar transistor) were designed with corresponding drive and protection circuits. In the past, positioning by using a brushless PM motor has been mainly performed by the so-called

serial pulse train method, or absolute encoders. However, in this work, the actual rotor position was measured by a resolver for the initial phase of the work, and for comparison reasons. Some of the circuit details and explanations have been given for future developments.

This thesis has developed and successfully tested a simulation model, and a position estimation method for brushless PM motors without a mechanical shaft position sensor being involved. In the context of these developments, both fundamental issues and details have been addressed.

In **Chapter II**, a comprehensive study of different features of brushless PM motors and drive systems has been presented. The study provides background knowledge and gives the mathematical model. Some practical considerations about measuring the motor parameters, and initial ideas about the control system have been explained. It is believed that the major remaining problems in this area relate to establishing the best techniques for proper control and position sensing in brushless PM motor by using higher level system integration which is subject to advance research by manufacturers.

Chapter III presented a straightforward analytical method of calculating the steady-state behaviour of the brushless PM motor for 120° inverter operation. The symmetrical nature of the applied voltages and resulting symmetry in line currents of the inverter driven brushless PM motor have been used to solve the differential equations. Throughout the analysis it has been assumed that the machine air gap is free of saliency effects, and has sinusoidal back EMF. The fundamental switching procedure of the inverter has been explained schematically for better understanding.

The analytical solution has been derived for 60° electrical of the whole period, and the resultant complex function has been solved by a hybrid Newton-Raphson method (a combination of bisection and Newton-Raphson). As a result of the comparison, it has been shown that the method of analysis presented in **Chapter III** is adequate to predict the instantaneous line currents and the electromagnetic torque of the motor for typical operating points including phase advance and phase delay operation. As explained in the conclusion of the chapter, discrepancies in the measured and estimated values of waveforms are mainly due to fluctuations in DC rail voltage, non-ideal motor parameters, small variations in winding inductance, imbalance between phases, and the assumption of ideal power switches in the inverter.

A computer simulation model for prediction of both the dynamic and the steady-state performance of brushless PM motors was presented in **Chapter IV**. The **abc** modelling approach has been used to simulate the drive, and the system's five differential equations (three electrical, two mechanical) have been solved simultaneously by the Kutta-Merson numerical method. The model allows a direct examination of the motor's current, speed, position, and torque behaviour. Although, the performance prediction has been done only for 120° inverter operation of the brushless PM motor, the drive simulation program can be modified easily for any excitation and motor type. The equations and diagrams has been put into a convenient form for the simulation and future developments. Since IGBTs were used in the actual drive, the off-times of the power transistors were not taken into account. Investigation of the delay time has shown that the IGBTs used in the inverter have a maximum 150ns delay time. Comparing with the usual time step in the simulation (2μs), the delay time could be ignored. However, if it is desired, after the switching command is received from the hysteresis

current comparator, the switching action could be delayed by the amount of measured delay time of the switching transistor. It should also be noted that, the time step of the simulation should be reduced down to the measured delay time for better performance prediction.

Due to the large number of available motor sizes and drive ratings, it would be a large and expensive task to obtain experimentally T-n characteristics and phase current variations of a brushless PM motor for all possible operation conditions. The computer package can be an excellent tool for simulating the complete drive without implementing the actual system.

The overall experimental system has been found to operate correctly in both steady-state and transient state. The simulation and experimental results presented in **Chapter IV** have been specifically chosen to understand the drive, and to demonstrate some capabilities of the model, and to provide confirmation of the validity of current and voltage estimation which has been used in **Chapter V.**

Chapter V summarised the earlier developed methods of shaft position sensorless operation and classified them by giving brief explanations. The chapter presented a new position estimation method for brushless PM motors without a mechanical shaft position sensor. As well as expanding the description of the position estimation procedure presented in the chapter, a wide range of simulated results have been given.

As seen in the chapter, the position estimator is essentially an observer, incorporating a simple mathematical model of the motor. The terminal phase voltages of the motor are sensed and stator voltage drops are subtracted to generate the flux linkages. The synthesis of these signals is accurate if the

voltage and current waveforms are balanced and back EMF waveforms are ideal. However, in practice, these assumptions are far from true. The back EMF signals contain harmonic ripple, there is drift in current and voltage measurement, and motor parameters are subject to inaccuracies. All of these will appear in flux linkage estimation. Therefore a more reliable position estimation method should be able to take all these imperfections into account.

The incremental position averaging was the most critical point in the algorithm. This is a problem mainly driven by unequal winding parameters in the actual motor. However, the proposed averaging method based on the actual line current level of the motor is satisfactory.

Two flux linkage correction routines were developed in order to help DC offset, and to eliminate measurement and modelling errors in the drive: the flux linkage correction by using last predicted rotor position , and the flux linkage correction based on measured currents. Since the latter method uses the measured current, significant position error might occur. Therefore, for better performance, a second flux correction method must be accompanied by a position error tolerance checking routine. However, it should be noted here that, for ideal motor and measurement system, there is no need to correct the estimated total flux linkage.

In **Chapter V**, simulation studies have also demonstrated the robustness of the developed algorithm and determined:

- the effects of errors in the initial conditions of the magnet flux linkages and the rotor position, and the effects of subsequent variation.

- the effect of noise in the measured values of voltages and currents supplied to the position estimator.

Analysis of the position estimation reveals sensitivities to initial values of the position and flux linkages specifically during starting. In fact, it has been shown that these factors are not series limitations in terms of overall performance of the method.

Chapter VI concentrated on the implementation and experimental results of the developed position estimation method in **Chapter V**. The chapter has been given the implementation details of the position estimation method, and presented two sets of experimental results including real-time data analysis by DSP (TMS320C30).In the chapter, real-time studies have demonstrated the algorithm's ability under very extreme operating conditions (sudden load change).

Since the PM motors have a low electrical time constant, as a result of their low value winding inductance relative to the winding resistance, the current measurement should be done using a wide bandwidth transducer.

To examine the effect of wider sampling time in the position estimation algorithm, the sampling time of the input signals (voltages and currents) was varied between 10μs and 200 μs for the operation given in **Fig.6.18**. Although the high resolution position estimation requires more data points per electrical period, it was found that, approximately 300 data samples per electrical period are enough to estimate the rotor position.

Very small fluctuations on the estimated position are mainly due to discontinuous current conduction mode of operation, and idealised (sinusoidal) assumptions of the back EMF and the magnet flux linkage waveforms. In a practical sense, it seems rather difficult to achieve the ideal sinusoidal back EMF in PM motors. Therefore the effect of non-ideal back

EMF and resulting magnet flux linkage waveform corrupt the flux linkage and position estimation. It can be solved using machine specific look-up table for each phase.

The proposed position estimation method:

- does not impose limits on the drive's operation (e.g. discontinuous and continuous current operation);
- requires no modifications to the motor (e.g. additional windings);
- is effective over the complete speed range;
- avoids the injection of additional signals into the machine windings;
- requires less computational effort than other math intensive full-order observer methods;
- can be used in drives based on different types of motor (e.g. switched-reluctance motors) and in brushless PM motors with variable winding inductance;

Removing the mechanical sensor from the rotor will basically move the sensor to the electrical side which is accessible via the motor's power terminals. The mechanical shaft position sensorless operation not only eliminates the number of connections between the motor and controller, it can also increase the noise immunity of position sensing.

As said earlier, the angular position of the motor should be continuously determined within acceptable accuracy to maintain the switching phase relationship in the drive. The position estimator should effectively monitor the position to generate the desired reference current. **Fig.7.1** illustrates an imaginary sinusoidal commanded current waveform produced by the estimated position which was given in **Fig.6.10**. The estimated position can be used to generate rectangular or any other desired current waveform.

With reference to the actual current waveform in **Fig.7.1**, discrepancies are due to the non-ideal sinewave (reference current) which was stored in EPROMs.

To get total flux linkage variation, analog integrators can be used instead of the discrete model. This method may avoid sampling difficulties of high switching voltage signals (produced by the hysteresis current controller).

Using a d-q model of the motor and line voltage measurements will reduce the number of variables to be measured. This will make the new method more competitive. Possible future developments might also include applying the method to reluctance type machines. It is thought that, in switched reluctance drives, using a look-up table of flux linkage versus position curves (as a function of current levels) might be the first step to predicting and estimating rotor position.

Speed controlled brushless PM drives are often equipped with a tachogenerator for speed detection, in addition to the position sensors. With the position estimation method, the speed of the motor can be achieved by the differentiation of the estimated position (**Eq.7.1**). However, since differentiation is involved, high resolution speed estimation can be achieved with faster sampling, and faster execution of the position estimation algorithm.

$$\omega = \frac{\Delta\theta}{\Delta T} \qquad (7.1)$$

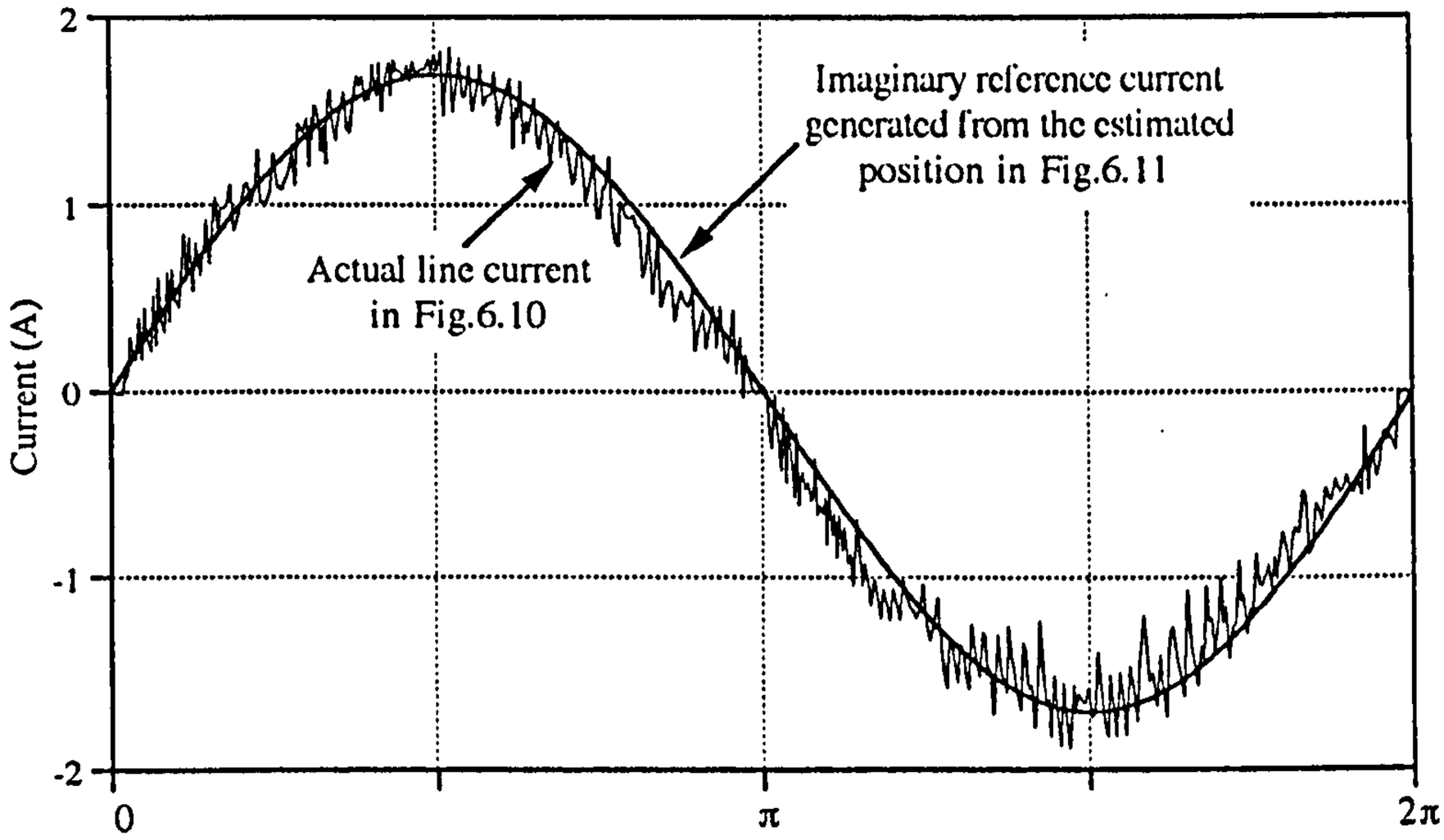

Figure 7.1 The actual line current and the generated demand current waveform by using the estimated rotor position.

Moreover, since the instantaneous torque feedback signal in the brushless PM motor control can be estimated from the measurements of instantaneous currents and measured rotor position (in conventional control), the method developed here is potentially valuable in high performance torque control of brushless PM motors by designing appropriate control algorithms [*Low et al*, 1992, *Takahashi and Ohmori* 1989, and *Dote* 1990].

The DSP has been proven itself for efficiently manipulating digital data at high speed. The cost of DSPs is decreasing, and faster cycle times are making them an affordable option for the position estimation method, as well as overall control of the brushless PM motor. Overall control of the brushless PM drive can be achieved by a microcomputer. The simplification of control hardware is the principal advantage of microcomputer control. This trend is evident as microprocessor speed is improving and more functions, with increased volume of each function, are being integrated.

Custom or semicustom application specific chips with integration of total control hardware for sensorless operation can be economical. If a DSP control system is already implemented in the drive [*Pillay* et al, 1990], the position estimation algorithm can be added at low cost.

It is also necessary to stress the importance of the tests applied to measure the parameters of the motor. Without these tests, poor parameter measurements would be passed to the position estimation algorithm or to the simulation model. Such erroneous parameters will certainly lead to poor estimation performance.

PUBLICATIONS

[1] Acarnley P.P. and Ertuğrul N., (1992), "*Rotor Position Estimation in PM Motors*", ICEM, Manchester, UK.

[2] Ertuğrul N. and Acarnley P.P., (1992), "*A New Algorithm for Sensorless Operation of Permanent Magnet Motors*", IEEE, IAS Annual Meeting, Houston, Texas, USA.

[3] Ertuğrul N. and Acarnley P.P., (1992), "*Analytical Solution of the System Equations of the Axial Field Permanent Magnet Synchronous Motor Drive*", ICEM, Manchester, UK.

[4] Ertuğrul N., Acarnley P.P., and French C.D., (1993), "*Real-Time Estimation of Rotor Position in PM Motors During Transient Operation*", accepted for EPE Conference, Brighton, UK, 13-16 September.

[5] Ertuğrul N. and Acarnley P.P., "*A New Algorithm for Sensorless Operation of Permanent Magnet Motors*", accepted for publication in IEEE Transactions on Industry Applications (expected to be published at the end of 1993).

REFERENCES

Acarnley P.P., Hill R.J., and Hooper C.W., (1985), "*Detection of Rotor Position in Stepping and Switched Motors by Monitoring of Current Waveforms*", IEEE Trans., IE-32, No.3.

Ackermann B., Janssen J.H.H., Sottek R., and van Steen R.I., (1992), "*New Technique for Reducing Cogging Torque in A Class of Brushless DC Motors*", IEE Proceedings-B, Vol.139, No.4.

Akiyama Y., Hitomi T., Tsukihashi A., and Nagasu S., (1990), "*Sensorless Brushless DC Motors*", Intelligent Motion Proceedings.

Analog Devices, (1980), "*Synchro and Resolver Conversion*", Edited by Boyes G.S.

Antiognini L., (1985), "*Dynamic Torque Optimisation of Step Motor by Back EMF Sensing*", Proceedings of Annual Symposium on Incremental Motion Control Systems and Devices.

Antognini L., and Veignat N., (1990), "*Self Synchronisation of PM Step and Brushless Motors, a New Sensorless Approach*", ICEM.

Bartlett P.M., (1984), "*The Development of Design Specifications for Brushless DC Servo Motors*", Drives/Motors/Controls Conference Proceedings.

Bartos F.J, (1990), "*Brushless DC Technology Comes Down to Earth*", Control Engineering, March.

Bartos F.J., (1988), "*Speciality Motors Provide A Variety of Control Choices*", Control Engineering, October.

Bass J.T., Ehsani M., Miller T.J.E., (1986), "*Robust Torque Control of Switched-Reluctance Motors Without a Shaft-Position Sensor*", IEEE Trans., IE-33, No.3.

Baudon Y., Jouve D., and Ferrieux J-P., (1992), "*Current Control of Permanent Magnet Synchronous Machines. Experimental And Simulation Study*", IEEE Trans., PE-7, No.3, July.

Benkhoris M.F., Doeuff R.Le, and Saadate S., (1990), "*Modelling And Simulation of A Synchronous Motor Supplied By A GTO Voltage Inverter*", IEE, 4th Conf. on PE & VSD, London.

Binns K.J., Al-Aubidy, and Shimmin D.W., (1990-A), "*Implicit Rotor Position Sensing Using Search Coils for A Self-Commutating Permanent Magnet Drive System*", IEE Proceedings, Vol.137, Pt.B, No.4.

Binns K.J., Shimmin D.W., and Al-Aubidy K.M., (1990-B), "*Implicit Rotor Position Sensing for Permanent Magnet Self-Commutating Machine Drives*", ICEM.

Binns K.J., Shimmin D.W., and Al-Aubidy K.M., (1991), "*Implicit Rotor-Position Sensing Using Motor Windings for a Self-Commutating Permanent-Magnet Drive System*", IEE Proceedings-B, Vol. 138, No.1.

Bolton H.R. and Ashen R.A., (1984), "*Influence of Motor Design and Feed-Current Waveform on Torque Ripple in Brushless DC Drives*", IEE Proceedings, Vol.131, Pt.B, No.3, May.

Bosch P.P.J. van den and Visser H.R., (1990), "*Simulation of State-Events in Power Electronic Devices*", IEE, 4th Conf. on PE & VSD, London.

Bose B.K., (1986), "*Power Electronics and AC Drives*", Prentice-Hall, Englewood Cliffs, New Jersey.

Boyes G.S., (1980), "*Synchro and Resolver Conversion*", Analog Devices, Memory Devices Ltd.

Brod D.M., and Novotny D.W., (1985), "*Current Control of VSI-PWM Inverters*", IEEE Trans., IA-21, No.4.

Carlson R., Tavares A.A., Bastos J.P., and Lajoie-Mazenc M., (1989), "*Torque Ripple Attenuation in Permanent Magnet Synchronous Motors*", IEEE, IAS Annual Meeting.

Comstock R.H., (1990), "*Comparing Trapezoidal And Sinusoidal Servo Controllers*", Control Engineering, March.

Control Techniques, (1992), "*IGBT Modules Provide Quite Motor Drive*", New Electronics on Campus, Spring.

Deleroi W. and Woudstra J.B., (1990), "*Analytical Versus Numerical Calculation Method For Simulation of Machine Converter Models*", ICEM.

Dhaouadi R., and Mohan N., (1990), "*Application of Stochastic Filtering to A Permanent Magnet Synchronous Motor-Drive System without Electro-Mechanical Sensors*", ICEM.

Dhaouadi R., Mohan N., and Norum L., (1991), "*Design and Implementation of an Extended Kalman Filter for the State Estimation of a Permanent Magnet Synchronous Motor*", IEEE Trans., PE-6, No.3.

Dote Y. and Kinoshita S., (1990), "*Brushless Servomotors: Fundamentals and Applications*", Clarendon Press-Oxford.

Dote Y., (1990), "*Servo Motor and Motion Control Using Digital Signal Processors*", Prentice Hall Englewood Cliffs, New Jersey.

Ehsani M. and Husain I., (1992), "*Rotor Position Sensing in Switched Reluctance Motor Drives by Measuring Mutually Induced Voltages*", IEEE, IAS Annual Meeting.

Ehsani M., Husain I., and Kulkarni A.B., (1992-A), *"Elimination of Discrete Position Sensor and Current Sensor in Switched Reluctance Motor Drives"*, IEEE Trans., IA-28, No.1.

Ehsani M., Mahajon S., Ramani K.R., and Husain I., (1992-B), "*New Modulation Encoding Techniques for Indirect Rotor Position Sensing in Switched Reluctance Motors*", IEEE, IAS Annual Meeting.

Electro-Craft , (1990), Heights at Performance, Data Catalogue.

Endo T., Tajima F., Okuda H., Iikuza K., Kawaguchi Y., Uzuhashi H., and Okada Y., (1983), "*Microcomputer Controlled Brushless Motor Without A Shaft-Mounted Position Sensor*", IPEC, Tokyo, 1983.

Faure E. and Jufer M., (1990), "*Cogging Torque Suppression by A Current Control*", ICEM.

Flett F.P., (1991), "*Silicon Control Algorithms For Brushless Permanent Magnet Synchronous Machines*", Analog Devices Inc.

Fouad F.A., Nehl T.W., and Demerdash N.A., (1981), "*Magnetic Field Modelling of Permanent Magnet Type Electronically Operated Synchronous Machines Using Finite Elements*", IEEE Trans., PAS-100, No.4.

Freere P. and Pillay P., (1990), "*Design and Evaluation of Current Controllers for PMSM Drives*", IEEE, IECON'90, pp 1193-1198.

Fuji Electric, (1992), "*IGBT Data Book*".

Furuhashi T., Sangwongwanich S., and Okuma S., (1992), "*A Position -and-Velocity Sensorless Control for Brushless DC Motors Using an Adaptive Sliding Mode Observer*", IEEE Trans., IE-39, No.2.

Gorman S.F., Chen C., and Cathey J.J., (1988), "*Determination of Permanent Magnet Synchronous Motor Parameters for Use in Brushless DC Motor Drive Analysis*", IEEE Trans., EC-3, No.3.

Hemati N., and Leu M.C., (1992), "*A Complete Model Characterization of Brushless DC Motors*", IEEE Trans., IA-28, No.1.

Henneberger G., (1987), "*Servo Drives for Machine Tools and Robotics*", Microcomputer Control of Power Electronics and Drives, IEEE Press, Edited by Bose B.K..

Hesmondhalgh D.E., and Tipping D., (1990), "*An Electromagnetic, Motor-Integrated Position Sensor for Brushless DC Motors, Capable of Operation at Standstill*", ICEM.

Hopkins T., and Philips C., (1988), "*Numerical Methods in Practice: Using The NAG Library*", Addison-Wesley.Publishing Company.

Horner G.R., and Freund W., (1991), "*A New Approach to Multi-Turn Absolute Position, Velocity and Motor Commutation Signals*", Drives/ Motors/Controls'91, Conference Proceedings, pp.155-158.

Houldsworth J.A. and Schmickl H., (1981), "*Electrolytic Capacitors for Industrial Applications*", Electronic Components and Applications, Philips, Vol.3, No.3, May.

Iizuka K., U zuhashi H., Kano M., Endo T., and Mohri K., (1985), *"Microcomputer Control for Sensorless Brushless Motor"*, IEEE Trans., IA-21, No.4.

International Rectifier, (1990), "*Preliminary Bulletin on IGBTs, E2987B-E29100C*".

Jahns T.M., (1989), "*Flux Weakening Operation of PM Drives*", Performance and Design of Permanent Magnet AC Drives, IEEE, IAS Publication, Edited by Pillay P.

Jones L.A., and Lang J.H., (1989), *"A State Observer for the Permanent-Magnet Synchronous Motor"*, IEEE Trans., IE-36, No.3.

Kassakian J.G., Schlecht M.F., and Verghese G.C., (1991), "*Principles of Power Electronics*", Addison-Wesley Publishing Company.

Kenjo T., (1991), "*Electric Motors and Their Controls, An Introduction*", Oxford University Press.

Krause P.C., (1986), *"Analysis of Electric Machinery"*, McGraw-Hill Book Company.

Krishnan R. and Beutler A.J., (1985), "*Performance and Design of An Axial Field PM Synchronous Motor*", IEEE, IAS Annual Meeting.

Krishnan R. and Ghosh R., (1989), "*Starting Algorithm and Performance of a PM DC Brushless Motor Drive System with no position Sensor*", PESC, Vol.2.

Krishnan R., (1986), *"Selection Criteria for Servo Motor Drives"*, IEEE, IAS Annual Meeting.

Krishnan R., and Rim G-H, (1989), *"Performance and Design of Variable-Speed Constant Frequency Power Conversion Scheme with a Permanent Magnet Synchronous Generator"*, IEEE, 24th IAS Annual Meeting, Part 1.

Kulkarni A.B., and Ehsani M., (1992), *"A Novel Position Sensor Elimination Technique for the Interior Permanent-Magnet Synchronous Motor Drive"*, IEEE Trans., IA-28, No.1.

Kuo B.C., and Butts K., (1982), *"Closed-Loop Control of a 3.6° Floppy-Disk Drive PM Motor by Back-EMF Sensing"*, 11th Proceedings SIMCSO, Champaign.

Kuo B.C., Lin W.C., and Goerke U., (1979), *"Waveform Detection of Permanent Magnet Step Motors, Part II"*, Proceedings of Annual Symposium on Incremental-Motion Control Systems and Devices.

Le-Huy H., Jakubowicz A., and Perret R., (1980), *"A Self-Controlled Synchronous Motor Drive Using Terminal Voltage Sensing"*, IEEE, IAS Annual Meeting, pp. 562-569.

Le-Huy H., Perret R., and Feuillet R., (1985), *"Minimization of Torque Ripple in Brushless DC Motor Drives"*, IEEE, IAS Annual Meeting.

Ledermann W., (1981), *"Handbook of Applicable Mathematics, Volume III, Numerical Methods"*, John Wiley & Sons.

Lee R., Wilson L., and Carter C.E., (1988), *"Electronics Transformers and Circuits"*, Third Edition, John Wiley and Sons.

Lin R-L, Hu M-T, and Lee C-Y, (1989), *"Using Phase-Current Sensing Circuit as the Position Sensor for Brushless DC Motors without Shaft Position Sensor"*, IEEE, IECON'89, Part 1.

Lipo T.A., (1981), "*The Analysis of Induction Motors With Voltage Control by Symmetrical Triggered Thyristors*", Adjustable Speed AC Drive System, IEEE Press, Edited by Bose B.K., pp.40-48.

Lipo T.A., and Cornell E.P., (1981), "*State-Variable Steady-State Analysis of A Controlled Current Induction Motor Drive*", Adjustable Speed AC Drive System, IEEE Press, Edited by Bose B.K., pp.218-226.

Liu S., and Stiebler M., (1990), "*State Estimation of an PWM Inverter Fed Synchronous Motor by Using Stochastic Filtering Techniques*", IEEE, IAS Annual Meeting.

Low T-S., Lee T-H, Tseng K-J, and Lock K-S, (1992), "*Servo Performance of a BLDC Drive with Instantaneous Torque Control*", IEEE Trans., IA-28, No.2.

Lumsdaine A., Lang J.H., and Balas M.J., (1985), "*A State Observer Variable Reluctance Motors: Analysis and Experiments*", 19th ASILOMAR Conference on Circuits, Systems and Computers, PacificGrove, CA.

Luneau J.R., (1985), "*New Developments In Feedback Devices For Brushless DC Servo Systems*", Motor-Con Proceedings, October, pp.86-95.

Matsui N., and Shigyo M., (1992), "*Brushless DC Motor Control without Position and Speed Sensors*", IEEE Trans., IA-28, No.1.

Mavilor Motors, (1991), Brushless DC/AC Servomotors, Data Catalogue.

McMurray W., (1980), "*Selection of Snubbers and Clamps to Optimize the Design of Transistor Switching Converters*", IEEE Trans., IA-16, No.4.

Mellor P.H., Chaaban F.B., and Binns K.J., (1991), *"Estimation of Parameters and Performance of Rare-Earth Permanent-Magnet Motors Avoiding Measurement of Load Angel"*, IEE Proceedings-B, Vol.138, No.6.

Miller T.J.E., (1989), "*Brushless Permanent Magnet and Reluctance Motor Drives*", Clarendon Press-Oxford.

Min-Ho P. and Hong-Hee L., (1989), "*Sensorless Vector Control of Permanent Magnet Synchronous Motor Using Adaptive Identification*", IEEE, IECON.

Mohan N., Undeland T.M., and Robbins W.P., (1989),"*Power Electronics: Converters, Applications, and Design*", John Wiley & Sons.

Motorola, Silicon Rectifiers Data Manual, (1980), Motorola Inc.

Murai Y., Kawase Y., Ohashi K., Nagatake K., and Okuyama K., (1987), "*Torque Ripple Improvement for Brushless DC Miniature Motors*", IEEE, IAS Annual Meeting.

Mvungi N.H., Lahoud M.A., and Stephenson J.M., (1990), *"A New Sensorless Position Detector for SR Drives"*, IEE, 4th Conf. on PE&VSD Conference, London.

Naunin D., and Reuss H-C., (1988), "*Synchronous Servodrive: A Very Compact Solution of Conrol Problems By Means of A Single-Chip-Microcomputer*", IEEE, IAS Annual Meeting.

Nehl T.W., Demerdash A., and Fouad, F.A., (1985), "*Impact of Winding Inductances and Other Parameters on the Design And Performance of Brushless DC Motors*", IEEE Trans., PAS-104, No.8, August.

Nehl T.W., Fouad F.A., Demerdash A., and Maslowski E.A., (1982), *"Dynamic Simulation of Radially Oriented Permanent Magnet-Type Electronically Operated Synchronous Machines with Parameters Obtained from Finite Element Field Solutions"*, IEEE Trans., IA-18, No.2.

Nerowski G., Plackner K., Piepenbreier B., and Tolle H.J., (1990), *"New Permanent-Field Synchronous Motor with Integrated Inverters"*, ICEM, MIT, Cambridge, Massachusetts, USA.

Nicholson D.S., (1991), *"Understanding Integrated Brushless DC Drives"*, Drives/Motors/Controls Conference Proceedings.

Nucera R.R., and Krause P.C., (1986), *"Computation of Steady-state Performance of An Electronically Commutated Motor"*, IEEE, IAS Annual Meeting.

Ogasawara S., and Akagi H., (1991), *"An Approach to Position Sensorless Drive for Brushless DC Motors"*, IEEE Trans., IA-27, No.7.

Pacific Scientific, (1990), Brushless Servosystems, Data Catalogue.

Panda S.K. and Amaratunga G.A.J., (1993), *"Waveform Detection Technique for Indirect Rotor-Position Sensing of Switched-Reluctance Motor, Part II: Experimental Results"*, IEE Proceedings-B, Vol.140, No.1.

Philips Components, (1989), *"Integrated Circuits Designer's Guide"*.

Pillay P., (1989), *"Modelling and Performance of Sinusoidal and Rectangular-Fed Permanent Magnet Motor Drives"*, Performance and Design of Permanent-Magnet AC Motor Drives, IEEE-IAS Press, Edited by Pillay P.

Pillay P., Allen C.R., and Budhaphathi R., (1990), "*DSP-Based Vector and Current Controllers for a Permanent Magnet synchronous Motor Drive*", IEEE, IAS Annual Meeting.

Pillay P., and Krishnan R., (1987), *"Modelling, Simulation and Analysis of a Permanent Magnet Brushless DC Motor Drive"*, IEEE, IAS Annual Meeting, Atlanta, USA.

Pillay P., and Krishnan R.,(1991), *"Application Characteristics of Permanent Magnet Synchronous and Brushless DC Motors for Servo Drives"*, IEEE Trans., IA-27, No.5.

Press W.H., Flannery B.P., Teukolsky S.A, and Vetterling W.T., (1992), *"Numerical Recipes, The Art of Scientific Computing-Fortran Version"*, Cambridge University Press.

Sattler Ph.K., and Starker K., (1989) , *"Estimation of Speed and Pole Position of an Inverter fed Permanent Excited Synchronous Machine"*, EPE, Aachen.

Schroedl M., (1988), *"Detection of the Rotor Position of a Permanent Magnet Synchronous Machine at Standstill"*, ICEM, Pisa, Italy.

Schroedl M., (1990), *"Operation of the Permanent Magnet Synchronous Machine without a Mechanical Sensor"*, IEE, Conf. on PE&VSD Conference, London.

Sepe R.B., and Lang J.H., (1992), "*Real-Time Observer Based (Adaptive) Control of a Permanent-Magnet Synchronous Motor Without Mechanical Sensors*", IEEE Trans., IA-28, No.6.

Shipley G.H., (1982), "*Brushless DC Motor For A Miniature Pneumatic Pump*", MOTORCON Proceedings, March.

Siefert W., (1985), "*Selfsynchronisation of Permanent Magnet Energized Stepper Motor With Detection of Position By Evaluation of the BEMF*", Motor-Con Proceedings.

Stefanovic V.R., (1986), "*Selecting A High Performance AC Drive*", IEEE Press-Introduction to Field Orientation and High Performance AC Drives, Edited by Novotny D.W. and Lorenz R.D..

Tadros Y., Junge G., and Salama S., (1991), "*Design Aspects of High Power PWM Inverters With IGBT*", EPE, Firenze.

Takashashi I. and Ohmori Y., (1989), "*High-Performance Direct Torque Control of An Induction Motor*", IEEE Trans., IA-25, No.2.

Texas Instruments, (1990), "*Digital Signal Processing Techniques-The ABC of DSP*", Data Book.

Texas Instruments, (1990), "*TMS320C3x User's Guide*", Data Book.

Wallace A.K. and Spee R., (1987), *"The Effects of Motor Parameters on the Performance of Brushless DC Drives"*, IEEE, Power Electronics Specialist Conference.

Watanabe H., Ishii T., and Fujii, (1987), "*DC-Brushless Servo System Without Rotor Position and Speed Sensor*", IEEE, IECON, Cambridge, MA.

Weinmann D., Nicoud G., and Gallo A., (1984), *"Advantages of Permanent Magnet Motors"*, Drives/Motors/Controls Conference Proceedings.

Wu R. and Slemon G.R., (1991), "*A Permanent Magnet Motor Drive without a Shaft Sensor*", IEEE Trans., IA-27, No.5.

APPENDICES

A-1. PM MOTOR PARAMETER MEASUREMENTS

Inductance Variation with Rotor Position

The bridge instrument was placed across the terminals of the motor, and inductance variation was measured directly. The measurement was repeated for every 5° mechanical rotor position, and since the motor has 8 poles, the measurement was carried out at 45° mechanical position intervals. **Fig. A. 1** illustrates the change of inductance in **Phase 1** of the test motor (see **Table 2. 1**) with mechanical position. The inductance variation can be approximated by a cosine function, though as seen in **Fig. A. 1**, the inductance variation can be reasonably ignored since it is only a small proportion (1.3%) of the average value.

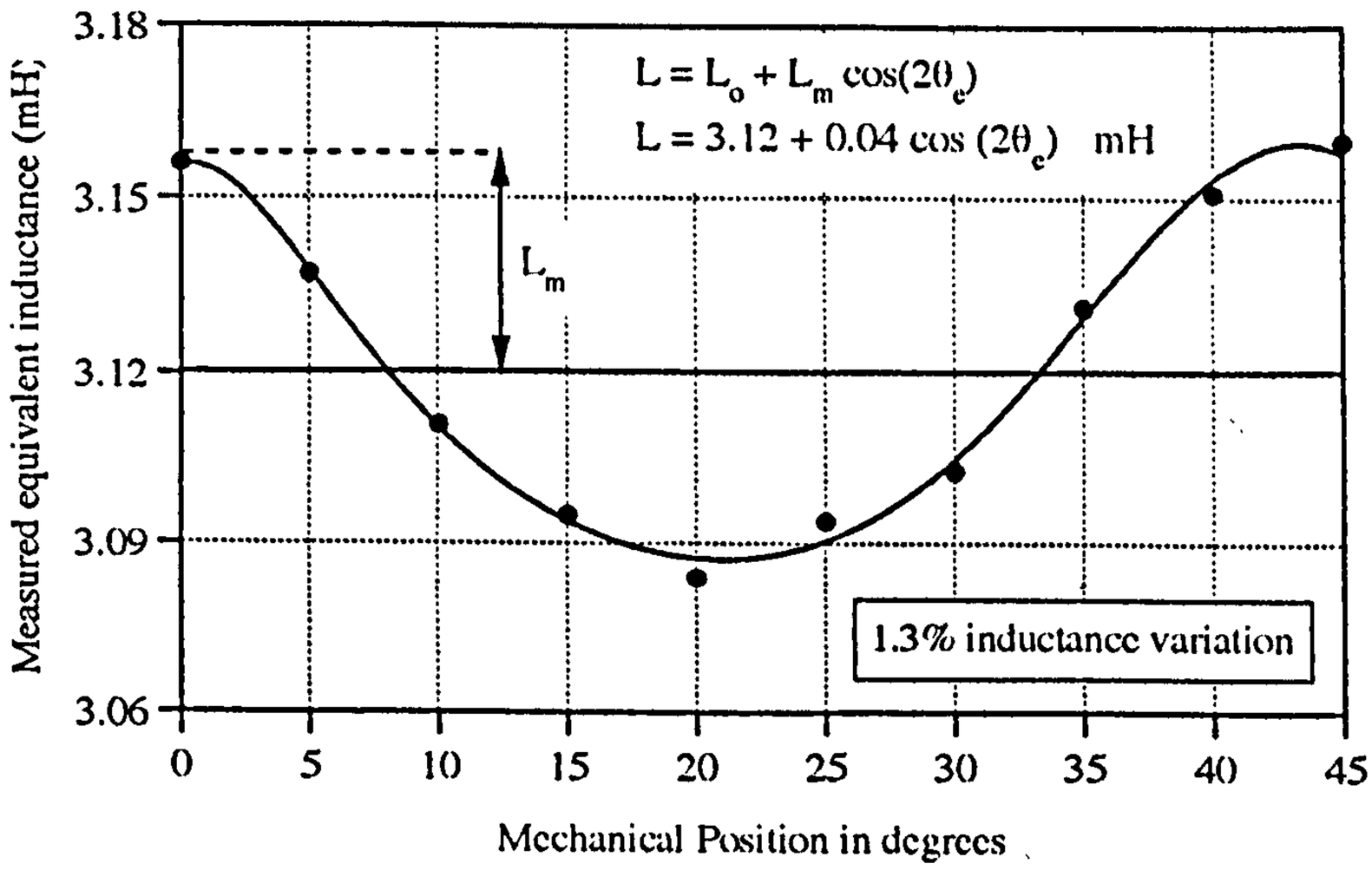

Figure A. 1 Measured equivalent winding inductance

Determination of Back EMF Constant

In this research, the back EMF constant of the test motor was estimated from the measured quantities given in **Table A.1.** While the motor is driven as a generator at different speeds, the measurements were recorded in two different ways. The results of the first method are measured by a true rms voltmeter and shown in the first two columns of **Table A.1.** The peak values of the back EMF constants were calculated for every speed measurement by **Eq.2.15** and **Eq.2.16**, and to get a unique value they were averaged. As explained in the earlier chapters, a better representation of back EMF can be obtained by harmonic analysis (see **Eq.4.10**). Peak values of back EMF at various speeds were observed with a Brüel&Kæjr Signal Analyser, and the peak values of the back EMF constants were obtained as above.

Table A.1 Measured back EMF voltages for **Phase 1** in the test motor

MEASURED BY A TRUE RMS VOLTMETER		MEASURED BY THE SPECTRUM ANALYSER (BNK) (peak values)					
e (V)	n(rpm)	f(Hz)	E_{1st} (V)	E_{3rd} (V)	E_{5th} (V)	E_{7th} (V)	E_{9th} (V)
4.51	158	10	4.52	0.78	0.07	0.04	0.04
9.07	295	20	9.05	1.56	0.18	0.02	0.07
13.62	443	30	13.50	2.32	0.26	0.03	0.11
18.19	592	40	18.10	3.12	0.36	0.04	0.14
22.72	739	50	22.50	3.88	0.44	0.05	0.18
27.23	886	60	27.00	4.64	0.53	0.06	0.21
31.79	1035	70	31.50	5.43	0.62	0.07	0.25
40.74	1320	90	40.40	6.92	0.79	0.09	0.32
49.89	1620	110	49.70	8.52	0.98	0.11	0.39
58.90	1910	130	58.60	10.10	1.15	0.13	0.46
68.08	2220	150	67.60	11.70	1.34	0.14	0.52

Fig. A. 2 shows the back EMF variation as a function of motor speed which is drawn from **Table A. 1**. As seen in the figure, the back EMF of the motor gives a linear characteristic over a wide range of speed variation.

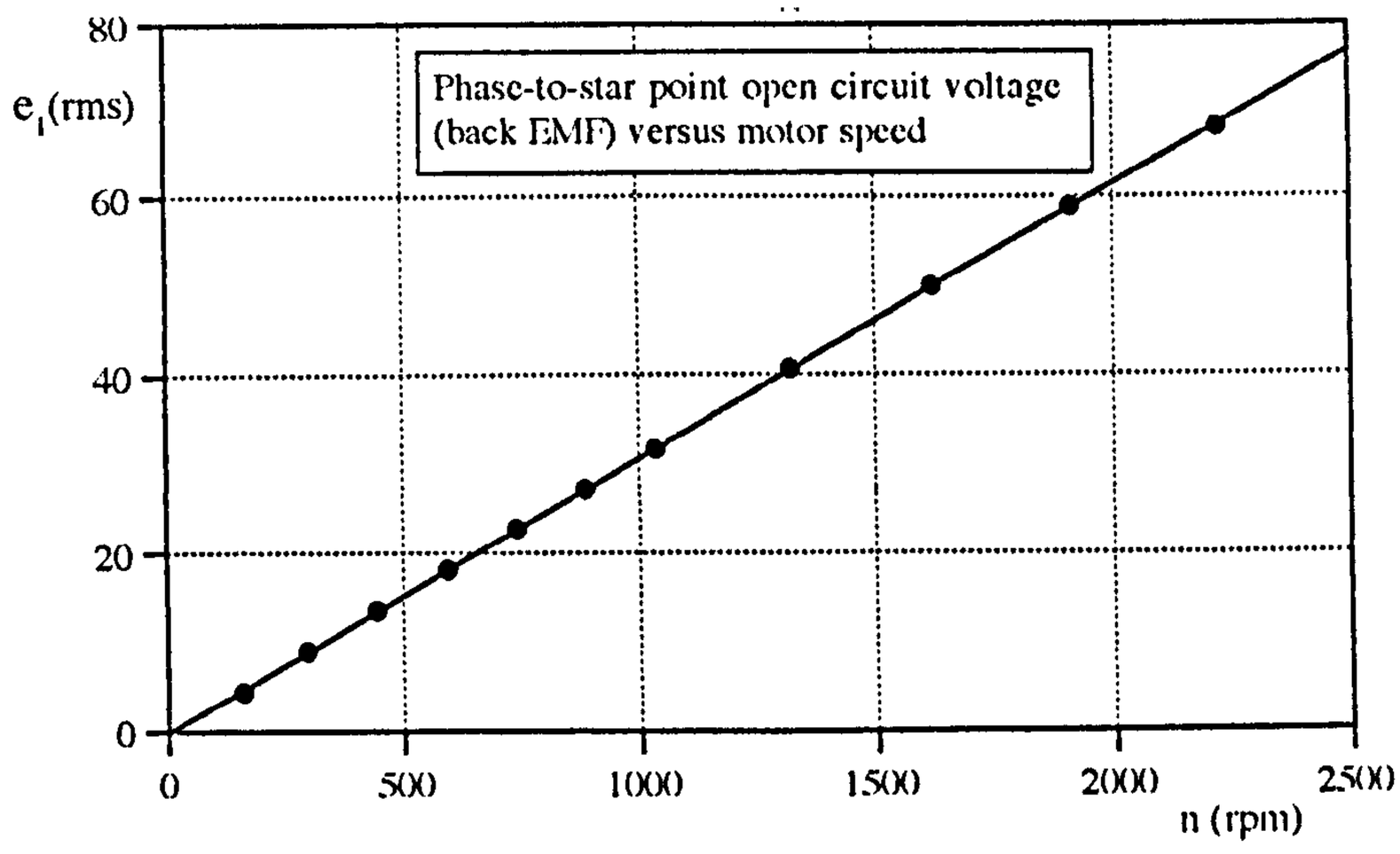

Figure A. 2 The rms value of the measured back EMF versus motor speed.

A-2. DERIVATION OF THE AVERAGE ELECTROMAGNETIC TORQUE EQUATIONS

Fig. A.3 illustrates idealised back EMF waveforms for the three-phase BSPM motor and corresponding current waveforms for the zero phase advance operating condition.

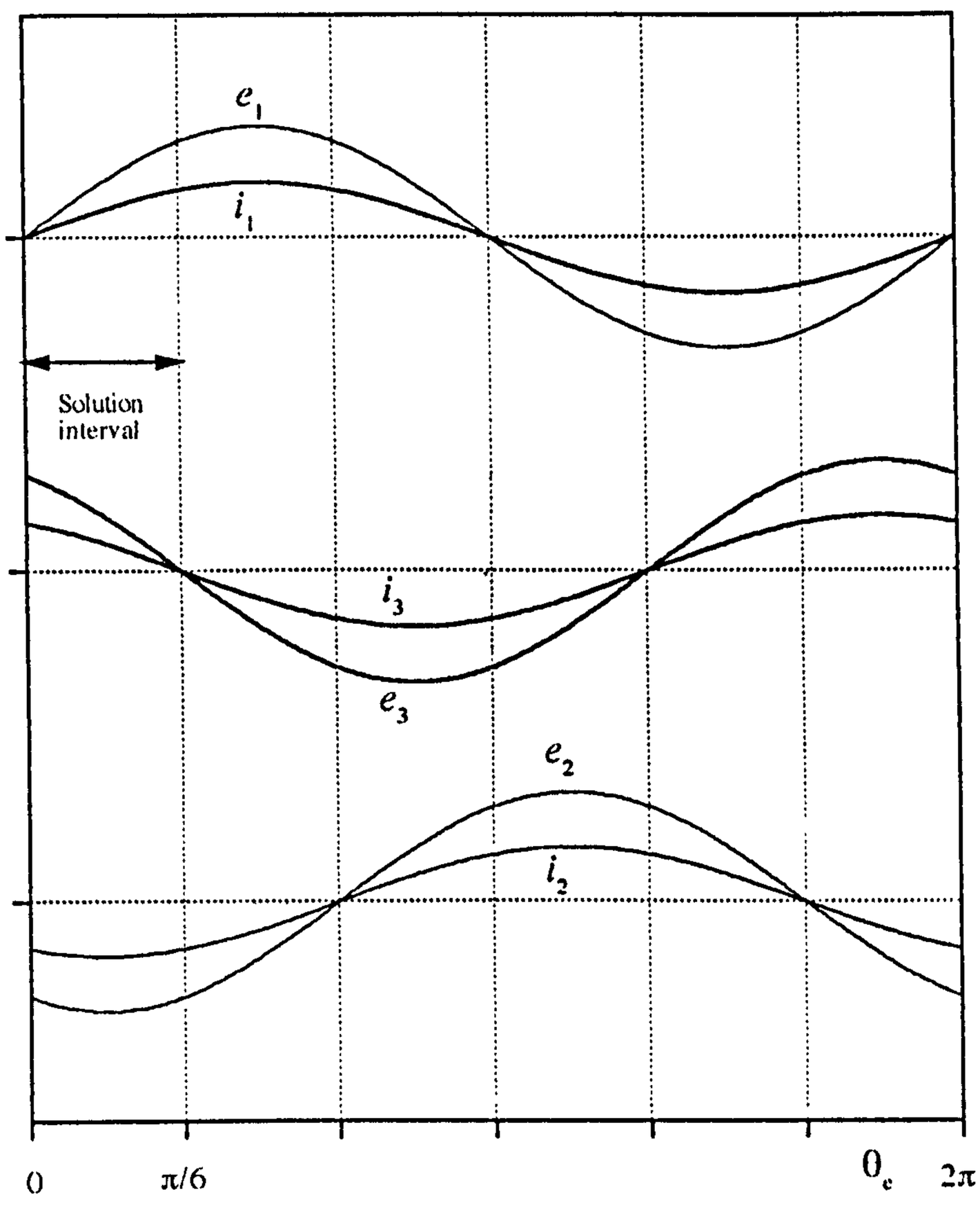

Figure A.3 Three-phase back EMFs and current waveforms for BSPM motor.

For the sinusoidal brushless PM motor, the three-phase back EMFs are:

$$e_1 = E_m \sin(\theta_e) = k_e \omega_r \sin(\theta_e)$$
$$e_2 = E_m \sin(\theta_e - 2\pi/3) = k_e \omega_r \sin(\theta_e - 2\pi/3) \qquad \text{(A-2.1)}$$
$$e_3 = E_m \sin(\theta_e - 4\pi/3) = k_e \omega_r \sin(\theta_e - 4\pi/3)$$

and, assuming sinusoidal current excitation in the drive, the line currents are given by

$$\begin{aligned} i_1 &= I_m \sin(\theta_e) \\ i_2 &= I_m \sin(\theta_e - 2\pi/3) \\ i_3 &= I_m \sin(\theta_e - 4\pi/3) \end{aligned} \qquad \text{(A-2.2)}$$

The average electromagnetic torque is

$$T_e = \frac{1}{T}\int_0^T \frac{1}{\omega_r}(e_1\, i_1 + e_2\, i_2 + e_3\, i_3)\, d\theta \qquad \text{(A-2.3)}$$

The average electromagnetic torque can be obtained by substituting **Eqns. A-2.1** and **A-2.2** in **Eq. A-2.3**, and from **Fig. A.3**,

$$T_e = \frac{3}{\pi\omega_r}\int_0^{\pi/3} [k_e\, \omega_r\, I_m \sin^2(\theta_e) + k_e\, \omega_r\, I_m \sin^2(\theta_e - 2\pi/3) + k_e\, \omega_r\, I_m \sin^2(\theta_e - 4\pi/3)]\, d\theta_e \qquad \text{(A-2.4)}$$

The expression may be reduced further,

$$T_e = \frac{3k_eI_m}{\pi}\int_0^{\pi/3} [\sin^2(\theta_e)+\sin^2(\theta_e-2\pi/3)+\sin^2(\theta_e-4\pi/3)]d\theta_e \qquad \text{(A-2.5)}$$

and, evaluating **Eq. A-2.5** by using the trigonometric relation given in **Appendix A-4**, the final form of the average electromagnetic torque,

$$T_e = \frac{3}{2}k_eI_m \qquad \text{(A-2.6)}$$

Here k_e is the back EMF constant and I_m is the maximum value of the current.

As summarised in **Chapter II, Table 2.4**, BSPM motors can be excited by rectangular current waveforms. **Fig. A.4** shows ideal current waveforms for BSPM motors with the rectangular excitation referenced to the back EMFs.

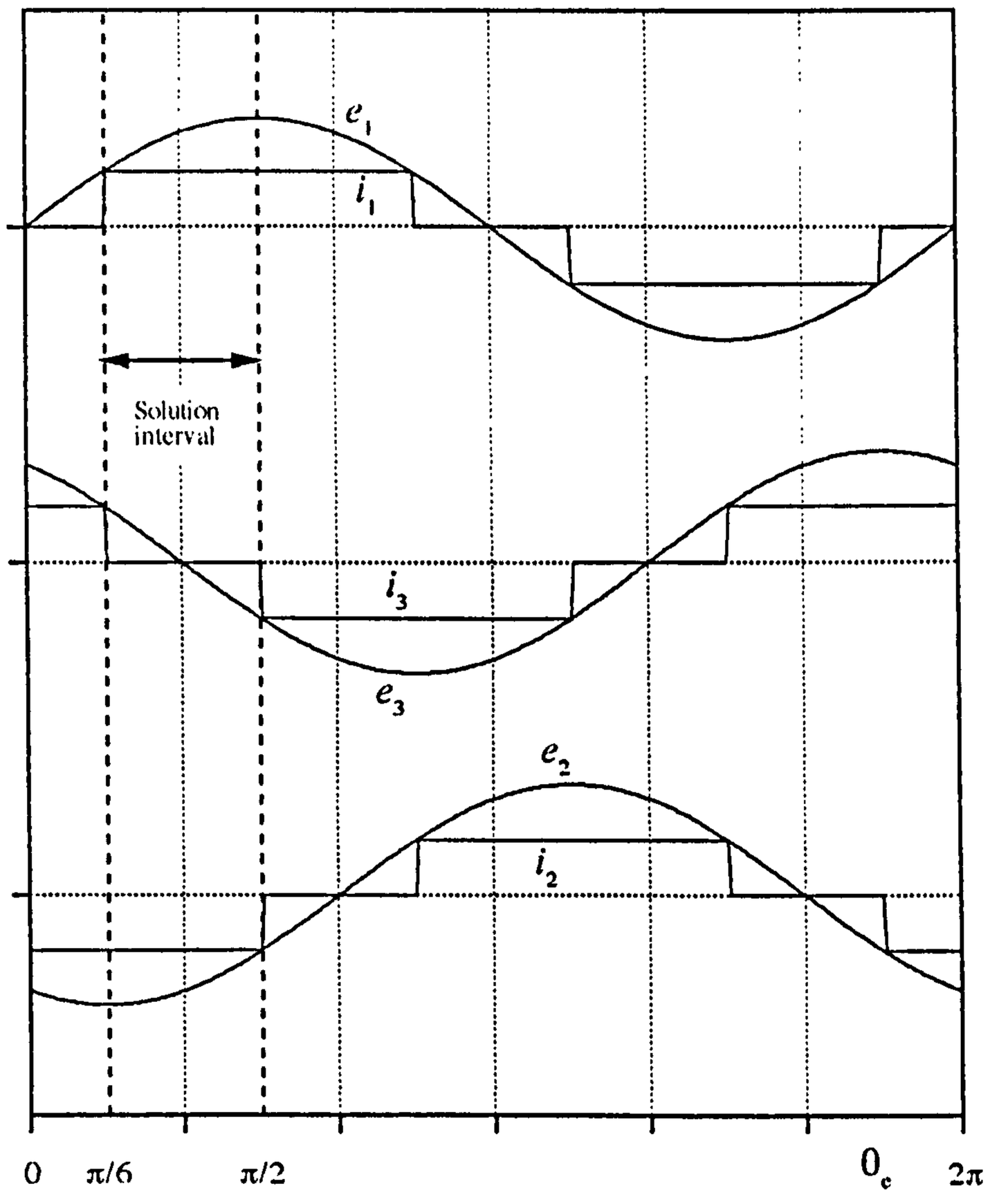

Figure A.4 The waveforms for rectangular current excited BSPM motor.

The average electromagnetic torque can be calculated easily within the interval $\pi/6<\theta_e<\pi/2$:

$$T_e = \frac{3k_eI_m}{\pi}\int_{\pi/6}^{\pi/2}[\sin(\theta_e)-\sin(\theta_e-2\pi/3)]d\theta_e \qquad \text{(A-2.7)}$$

$$T_e = \frac{3\sqrt{3}}{\pi}k_eI_m = 1.65\ k_eI_m \qquad \text{(A-2.8)}$$

Fig. A. 5 shows back EMFs and idealised current waveforms for a BTPM motor. As in previous calculations, the average electromagnetic torque is estimated within the interval $\pi/6<\theta_e<\pi/2$.

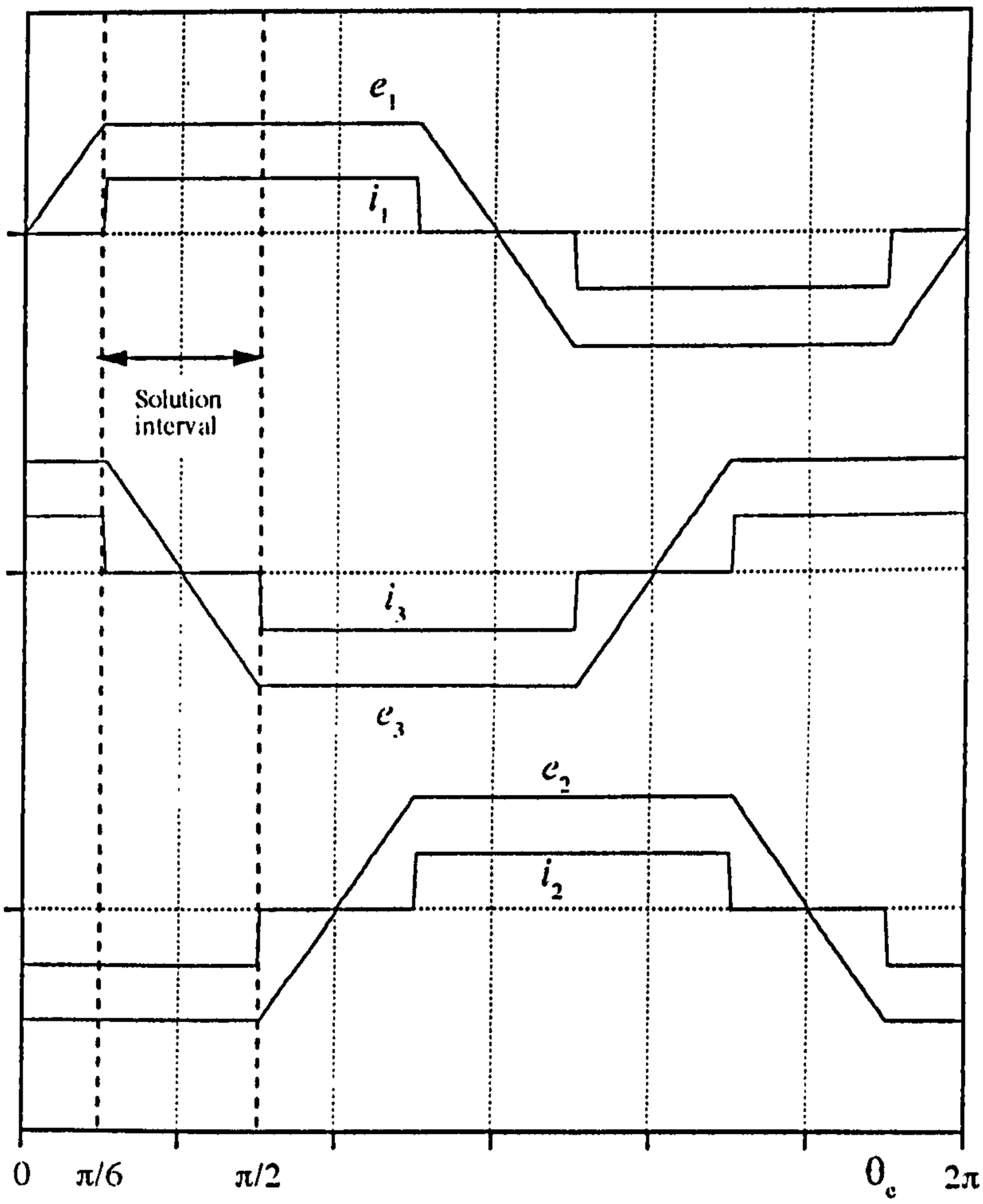

Figure A. 5 The back EMF and current waveforms for BTPM motor.

The average electromagnetic torque is

$$T_e = \frac{3}{\pi\omega_r}\int_{\pi/6}^{\pi/2}[(-E_m)(-I_m)+E_mI_m\,]d\theta_e \qquad \text{(A-2.9)}$$

$$T_e = \frac{3}{\pi\omega_r}\int_{\pi/6}^{\pi/2}[(-k_e\,\omega_r)\,(-I_m)\,+(k_e\,\omega_r)\,(I_m)\,]d\theta_e \qquad \text{(A-2.10)}$$

$$T_e = 2k_eI_m \qquad \text{(A-2.11)}$$

A-3 CONVERTER DESIGN

The typical converter structure for a three-phase brushless PM motor consists of four parts: rectifier, filter, braking circuit, and inverter. The fixed frequency AC supply voltage is rectified by using diodes, and the DC bus voltage is smoothed (in the voltage-fed inverter) by using a filter (LC), and is inverted by power switches (such as in **Fig.2.16**).

A-3.1 Rectifier And Filter Design

The rectifier must be capable of holding the DC bus voltage within limits while the inverter is supplying its peak current capability. The continuous current rating of the rectifier should be at least the peak value of the current waveform in the inverter. In choosing the diodes of the rectifier, the peak current and the supply voltage must be known.

The main purpose of rectification is to produce a steady DC output voltage (in the voltage-fed inverter). In the analysis of the inverter-fed brushless PM motor, the input voltage of the inverter is usually defined to be a DC voltage without a ripple. In applications, however, the DC voltage waveform has a ripple because of the rectifier's behaviour.

Polyphase rectifiers are preferred where the DC power required is in the order of 1kW or more [*Motorola Silicon Rectifier Data Manual*, 1980]. Moreover, the three-phase full-wave diode rectifier is preferred because of conversion high efficiency and low ripple.

The DC rail voltage of the rectifier should be at least twice the maximum value of back EMF of the PM motor at rated speed, and the diode peak inverse voltage should be at least 5% greater than the rectified voltage, or maximum supply voltage. However, if a dynamic braking circuit is used, the

safety margin of voltage must be higher than by a value which depends on hysteresis bandwidth of controller (see **Section A-3.3**). Neglecting AC source leakage inductance, the rectified average output voltage of the three-phase bridge rectifier can be found from,

$$V_d = 1.35\ V_s \qquad \text{(A-3.1)}$$

Where V_s is the line to line rms supply voltage. If the voltage drops are considered, the output DC voltage of the rectifier is less than the value given in **Eq. A-3.1**.

The maximum current per diode depends on the type of filter and also the load current. In the voltage-fed inverter, a capacitor filter is used to hold the load voltage constant. However, use of the capacitor filter alone is impractical. The high charging current of the capacitor increases the peak forward current per diode and also the ripple voltage increases with increasing load current.

The use of either the inductor filter alone or the capacitor filter alone is impractical, because of the high voltage drop across the inductor and the high charging current of the capacitor.

Moreover, during the switch on, the very large instantaneous charging current may destroy the diodes in the rectifier. In order to prevent the large instantaneous charging current, one possible solution is to charge the filter capacitor before operating the inverter by using a series resistor in the ac supply to the rectifier, the terminals of the resistor being shorted by a power switch such as a contactor or a thyristor after a few cycles.

The ripple voltage increases with increasing load current. In the inductor filters, the ripple is independent of the load current [*Motorola Silicon*

Rectifier Data Manual, 1980] and the inductor filters have the advantage of giving continuous diode conduction. This result reduces the peak forward current rating of the diodes. Unfortunately, the inductors are bulky and expensive. Therefore, in the most applications, both the capacitor and the inductor are used together for powers greater than about 4 kW [*Houldsworth and Schmickl*, 1981].

Minimum Value Of The Filter Inductor

Assuming the filter capacitor C is large, the average current through the filter capacitor in the steady state is zero, and ignoring the resistance of the inductor and AC-side inductance, for continuous current operation, the minimum value of the inductance is [*Mohan et al*, 1989],

$$L_{d\,min} = \frac{0.013 V_s}{2\ f_s\ I_d} \qquad \text{(A-3.2)}$$

Here, I_d is the average value of the rectifier current. In the filter design, L_d should be chosen bigger than $L_{d\,min}$ and its resistance must be small.

Choosing The Filter Capacitor

As given above, the minimum value of the filter inductance can be computed by **Eq. A-3.2**. In fact, C is not infinite. For estimation of the value of current flowing through the inductor, the harmonic composition of the DC voltage must be known. If C is finite, there is a ripple voltage that is superimposed on the average value of the voltage.

Series resonance between the filter inductor and the filter capacitor is also important. To avoid resonance [*Motorola Silicon Rectifier Data Manual*, 1980], it is sufficient to ensure that,

$$\omega_r^2 LC > 2 \qquad \text{(A-3.3)}$$

Where ω_r is the lowest ripple frequency in radians per second. This is $6f_s$ in the three phase bridge rectifier.

A power resistor should also be placed in parallel with the filter capacitor to discharged it when the rectifier is turned off. A reasonable discharge time should be chosen according to the value of the filter capacitor and the parallel resistor.

A-3.2 Selection Of The Power Switches And The Snubber Components

The inverter device ratings are the forward voltage blocking, the maximum inverter current and the switching frequency. A suitable power switching device is to be selected for the specified output power. In choosing the voltage rating, typically 50% overvoltage is added to the value of the estimated voltage of the power switch.

The peak current value of the power switch should be the peak value of the current waveform of the load. The average value of the power switch current is less than the peak current, because of the conducting period in the three phase inverter. All the switches conduct for just 1/3 period in the three phase inverter.

In the inverter with bipolar transistors, a shunt snubber circuit is required. The choice of snubber capacitor limits the peak overshoot voltage, and also reduces the transistor turn-off switching loss. With the shunt snubber, as the transistor turns off and collector-emitter voltage begins to rises, the snubber capacitance begins to charge. The charging current is diverted from

the transistor and all the load current flows in the snubber. If the snubber capacitor is chosen according to **Eq. A-3.4** [*McMurray*, 1980], the collector-emitter voltage rises while the collector current falls. **Eq. A-3.4** is the definition of a normal snubber capacitor values.

$$C_s = \frac{I_{cm} t_f}{2V_{dc}} \qquad (A\text{-}3.4)$$

Where I_{cm} is the maximum collector current, t_f is the fall time. The stored energy in the capacitor C_s is dissipated in the snubber resistor R_s during the transistor turn-on, and if the snubber resistor R_s is chosen according to **Eq. A-3.5** [*Lee and Wilson*, 1988], no additional energy dissipation occurs in the transistor.

$$R_s = \frac{V_{dc}}{0.2I_{cm}} \qquad (A\text{-}3.5)$$

The total power dissipation of the snubber resistor is,

$$P_{Rs} = \frac{1}{2} f C_s V_{dc}^2 \qquad (A\text{-}3.6)$$

Here f is the switching frequency of the inverter.

There are several current components which flows through the switching transistor during turn-on with an inductive load: the load current, the snubber capacitor discharge current, the opposite snubber capacitor charging current and the recovery current of the inverse parallel diode. The designer must ensure that the capacitor has sufficient time to discharge down to a low voltage during the minimum on-state time of the transistor, so that the turn-off snubber will be effective at the next turn-off interval. Therefore, discharging the capacitor voltage down to 0.2V will be ensured,

$$t_{on\text{-}min} > 1.6 R_s C_s \qquad (A\text{-}3.7)$$

Substituting of **Eq. A-3.4** and **Eq. A-3.5** in **Eq. A-3.7** yields,

$$t_{on\text{-}min} \approx 4t_f \qquad \text{(A-3.8)}$$

The ratings of series and reverse-parallel diodes should also be selected in the design. The ratings for the diodes are the maximum reverse recovery voltage, which can be equal to the value of switching transistor, and the maximum forward current, which is equal to the load current. Moreover, they must be fast recovery diodes for high frequency switching operation.

Losses and Heatsink Design

All power switches, controlled or uncontrolled, generate heat due to on-state losses and switching losses. This heat must be transferred from the junction to ambient. Generated heat in the junction is transferred to the ambient by a heat sink and also the heatsink can be cooled by air or water.

As known, the thermal equation is given,

$$T_j = P_d(R_{jc}+R_{cs}+R_{sa})+T_a \qquad \text{(A-3.9)}$$

Where T_j is the junction temperature (°C), P_d is the total losses (W), R_{jc} is the junction to case thermal resistance (°C/W), R_{cs} is the case to sink thermal resistance (°C/W), R_{sa} is the sink to ambient thermal resistance (°C/W) and T_a is the ambient temperature (°C). R_{jc} and R_{cs} are specified by the manufacturers. The total power loss P_d can be found, and for a specified ambient temperature T_a, the required thermal resistance of the heatsink can be calculated. For minimum contact thermal resistance (R_{cs}), the surface of heatsink should be smooth and clean. If there is no isolation problem, in order to decrease the value of R_{cs}, the heatsink compound should be used alone. Heat sink compounds have high thermal conductivity which provides excellent heat transfer between semiconductor devices and heatsinks.

In switching applications, power losses in the bipolar transistors are:

Drive losses (base drive losses)

Conduction losses (during turn-on)

Switching losses

Base drive losses depend on the type of power switch. For example, some bipolar transistors require a high base current for switching operation. Therefore, the power supply should be designed for high rated power. The base losses are:

$$P_b = V_{be} I_b t_{on} f \qquad \text{(A-3.10)}$$

Where P_b is the average base drive loss, V_{be} is the base-emitter voltage drop, I_b is the base drive current, t_{on} is on-time of the switching pulse.

During the switching operation, delay time losses of the transistor can be added to the conduction losses. Then the total conduction loss is,

$$P_c = V_{ce(sat)} I_{cm} t_{tc} f \qquad \text{(A-3.11)}$$

Where $V_{ce(sat)}$ is the saturation voltage of the transistor, t_{tc} is the total conduction time ($t_{tc} = t_c + t_d$, t_c is the conduction time and t_d is the delay time).

Switching losses are the power dissipation of transistors during turn-on and turn-off. They should be estimated when choosing the heatsink.

$$P_r = I_{cm} t_r f \left[\frac{V_{dc}}{2}\right] \qquad \text{(A-3.12)}$$

$$P_f = I_{cm} t_f f \left[\frac{V_{dc}}{2}\right] \qquad \text{(A-3.13)}$$

where t_f is the fall time. The total loss of the transistor can be written,

$$P_d=P_b+P_c+P_r+P_f \qquad \text{(A-3.14)}$$

In the design, for simplicity, all power components in the same switching module are assembled on a common heatsink. Therefore, the snubber loss and the conduction loss of the series diode should be considered in the heatsink design. **Eq. A-3.11** is valid for the series diodes too, because the load current flows through the series diode over the same time interval,

$$P_{cd}=V_{AK}I_{cm}t_{tc}f \qquad \text{(A-3.15)}$$

Where P_{cd} is the average conduction loss of the series diode, V_{AK} is the voltage drop of the diode during the conduction.

A-3.3 The Dynamic Braking Circuit Design

Brushless PM motors are operated in the generating mode when braking. During braking, the kinetic energy stored in the system inertia is converted to electrical energy, and the power flows from the PM motor to the rectifier. Since a diode rectifier is used in the converter, the energy flows in one direction. Therefore, in dynamic braking, generated braking energy charges the filter capacitor C (**Fig. A.6**). The voltage polarity across the DC link remains the same but the voltage on the capacitor rises above no-load DC link voltage. Then, the capacitor voltage can reach destructive levels. Both for regulation of DC link voltage to a permissible maximum and for braking of the PM motor, the transistor controlled resistor is used which is connected before the inverter as shown in **Fig. A.6**. Since there is no regeneration, it is known as dynamic braking [*Bose*, 1986].

Moreover, in practice, the drive can be designed to operate the motor above the rated speed. While the drive is operating above the rated speed, the full back EMF voltage is seen across the power devices.

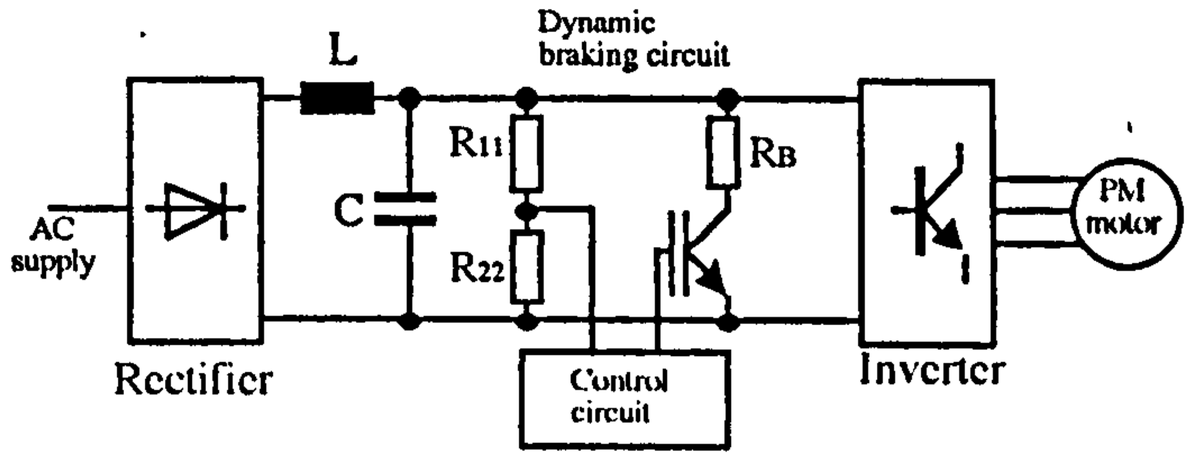

Figure A.6 The dynamic braking circuit and measuring DC rail voltage.

Fig.A.7 shows the implemented control circuit for the dynamic braking resistor. The input voltage (which is proportional with the DC rail voltage) to the hysteresis comparator comes from across the resistor R_{22}, and it is compared with a reference voltage. The reference voltage is referred to the no-load DC link voltage. The control pulses are produced by a timer separately and they are applied to an AND gate. The output of AND gate is connected to the drive circuit to activate the braking transistor.

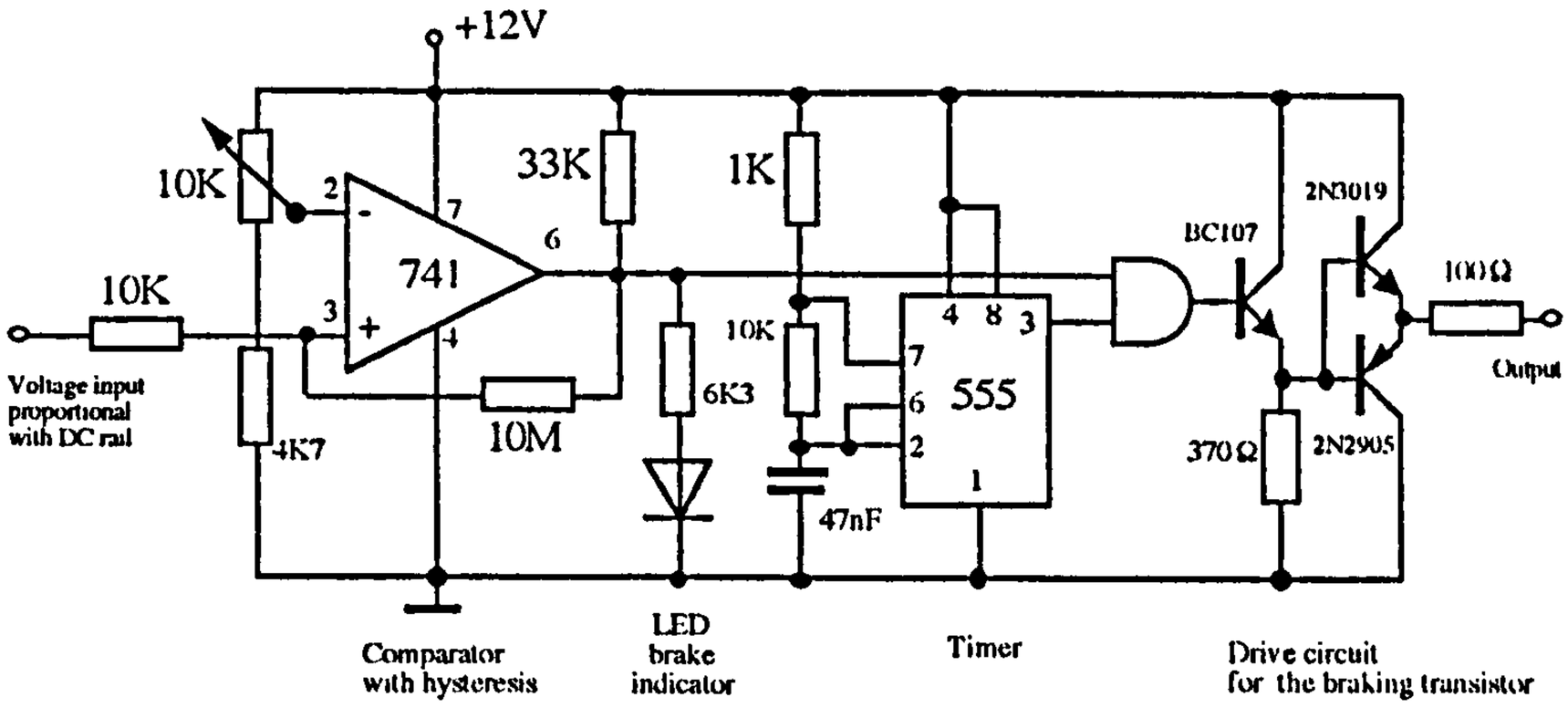

Figure A.7 The control circuit designed for dynamic braking and for overvoltage protection.

Choosing the dynamic braking resistor

Since the DC voltage output from a diode a rectifier is constant, the dynamic braking capability depends on the DC link voltage. However, the operation of the PM motor above the rated speed should also be considered in the design. The dynamic braking resistor is chosen according to the maximum rectifier current:

$$R_B = \frac{V_{dm}}{I_m} \qquad \text{(A-3.16)}$$

Here, V_{dm} is the maximum DC rail voltage, I_m is the maximum rectifier current. During braking, the dynamic braking resistor absorbs the full braking power. The maximum dynamic braking power is related to the DC link voltage, and can be given by

$$P_B = \frac{V_{dm}^2}{R_B} \qquad \text{(A-3.17)}$$

The dynamic braking capability of the drive is illustrated in **Fig. A.8**.The maximum braking power is shown by dashed horizontal line. In fact the braking power is slightly bigger than that value since the V_{dm} might reach bigger levels during operating of above rated speed. The inverter and PM motor capability is also plotted in **Fig. A.8**. It is given by a fixed-slope straight line in the constant torque region and horizontal line in the constant power region.

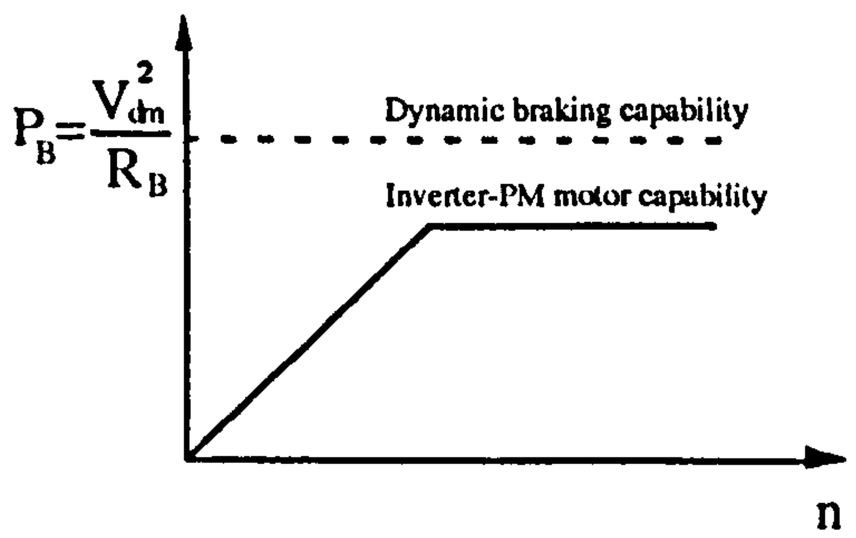

Figure A.8 Dynamic braking capability in the drive

A-3.4 The Inverter with Bipolar Transistors

Fig.A.9 shows the inverter power circuit implemented by bipolar transistors. Some darlington transistors (such as TIP 162) include a parasitic inverse parallel diode. It is built in the process of fabricating. In a power circuit with a single transistor which includes the parasitic diode, the diode seldom presents any problems. However, in a power circuit with a loop consisting of two serially connected transistors (such as the three-phase inverter) and a voltage source, the slow recovery of the parasitic diodes [*Severns, 1984*] may present a problem, such as a temporary short circuit. Since that type of power switch (TIP 162) was used in the inverter, the power circuit design differs from the conventional inverter.

The temporary short circuit was avoided in the inverter with the arrangement given in **Fig.A.9**. This arrangement requires additional diodes in series with the main power transistors in the inverter. The purpose of series diode is to prevent current flowing through the parasitic diode. Normally, for

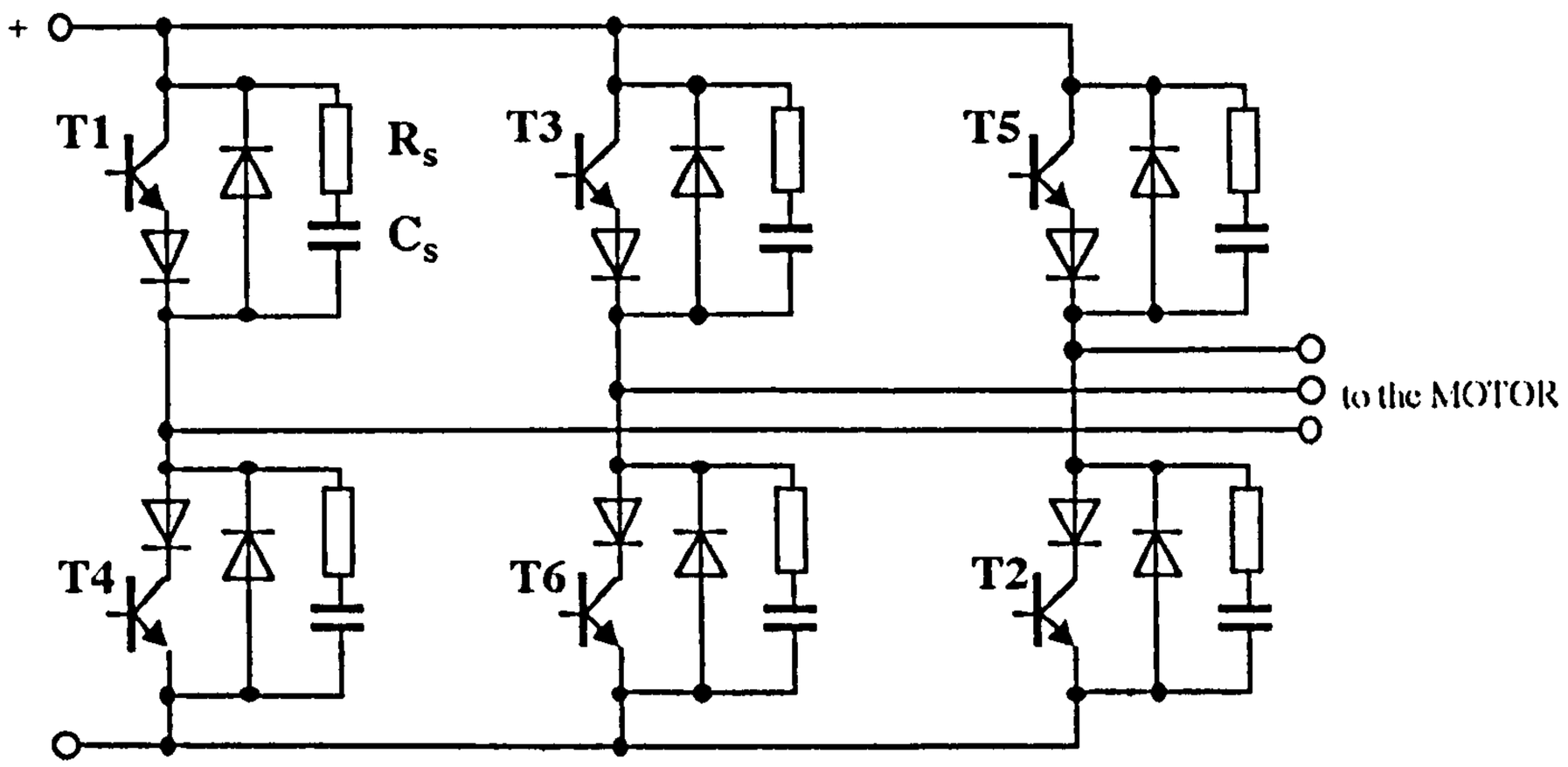

Figure A.9 The inverter configuration with bipolar transistors and diodes

a small voltage drop, Schottky diodes are used in series with each transistor. However, since Schottky diodes do not have high voltage and current ratings, fast recovery diodes were used.

In bipolar transistors, the rate of change in the collector-emitter voltage and the collector current depends on the base current. The base current determines how fast the device capacitances are charged and discharged. The drive circuit should supply these requirements. A drive circuit with a totem-pole configuration for faster turn-off times, and a high speed optocoupler for electrical isolation is shown in **Fig.A.10**. Six identical drive circuits were built to drive the power transistors in the inverter. Since the lower transistors have the same common point, a single power supply is used in these drive circuits. The upper drive circuits in the inverter are isolated by three individual power supplies designed specifically for this application.

Any failure of the input pulses of the transistors in a bridge type of inverter may cause the upper and lower transistors in the same arm to be damaged. This is usually prevented by using complementary pulses. However, storage time is also a problem in inverter applications. Storage time is the delay

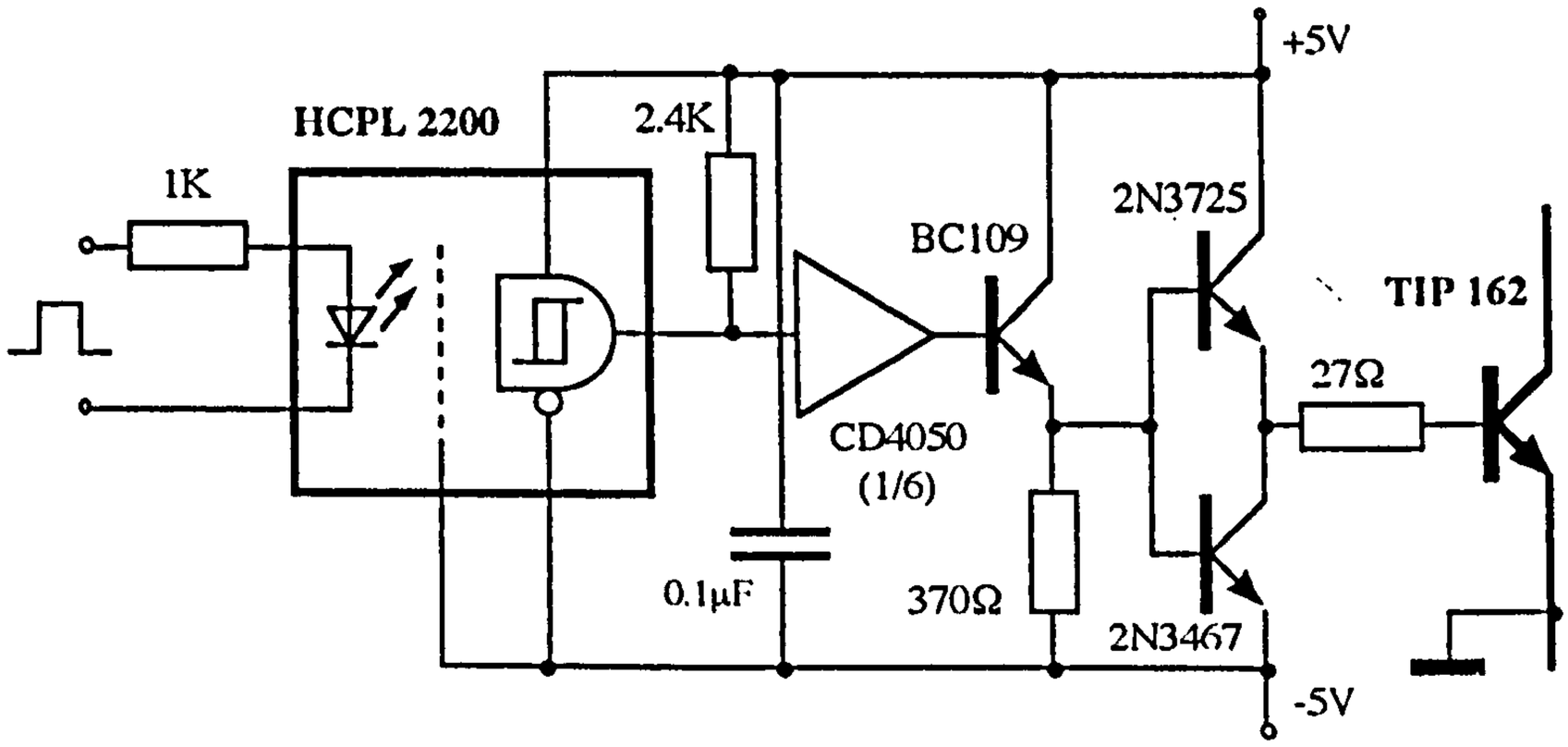

Figure A.10 The base drive circuit for the bipolar transistor.

interval between the removal of positive base current and the beginning of the decay of collector current. The worst case storage time usually occurs when the inverter is lightly loaded. Storage time causes a momentary bus to bus short circuit which could destroy the transistors in the same arm of the inverter.

In practice, a certain time (dead time) is inserted in the control circuit, and this time is sum of the storage and fall times. Some safety margin is also needed to allow for temperature effects and load changes. However if the heatsink is large enough, temperature effects can be ignored.

In this research, both the problem of temporary short circuit and inserting a dead time is solved by implementing the circuit given in **Fig.A.11**. A small value resistor is connected in series with the switching transistor to monitor the instantaneous arm current. When the current reaches a level which slightly exceeds zero level the comparator (LM311) senses this value. Two type of comparator are used in the circuit. Upper comparators are inverting and lower comparators are noninverting. The comparators are adjusted to be in negative saturation by using offset balancing. The comparators work at a value as low as one percent of the rated current.

When current flows through the low value resistor, the comparator detects the voltage across the resistor, and the output of the comparator changes from the negative to the positive voltage level. This output gives a low state at the output of the optocoupler indicating that the transistor is ON. The output of optocoupler is connected to the opposite three-input AND gate. Until the current is nearly zero, the output of the AND gate remains low level. Two low rated floating power supplies are used to power the detection circuits, one each for the positive (T1,T3,T5), and negative (T4,T6,T2) group of transistors.

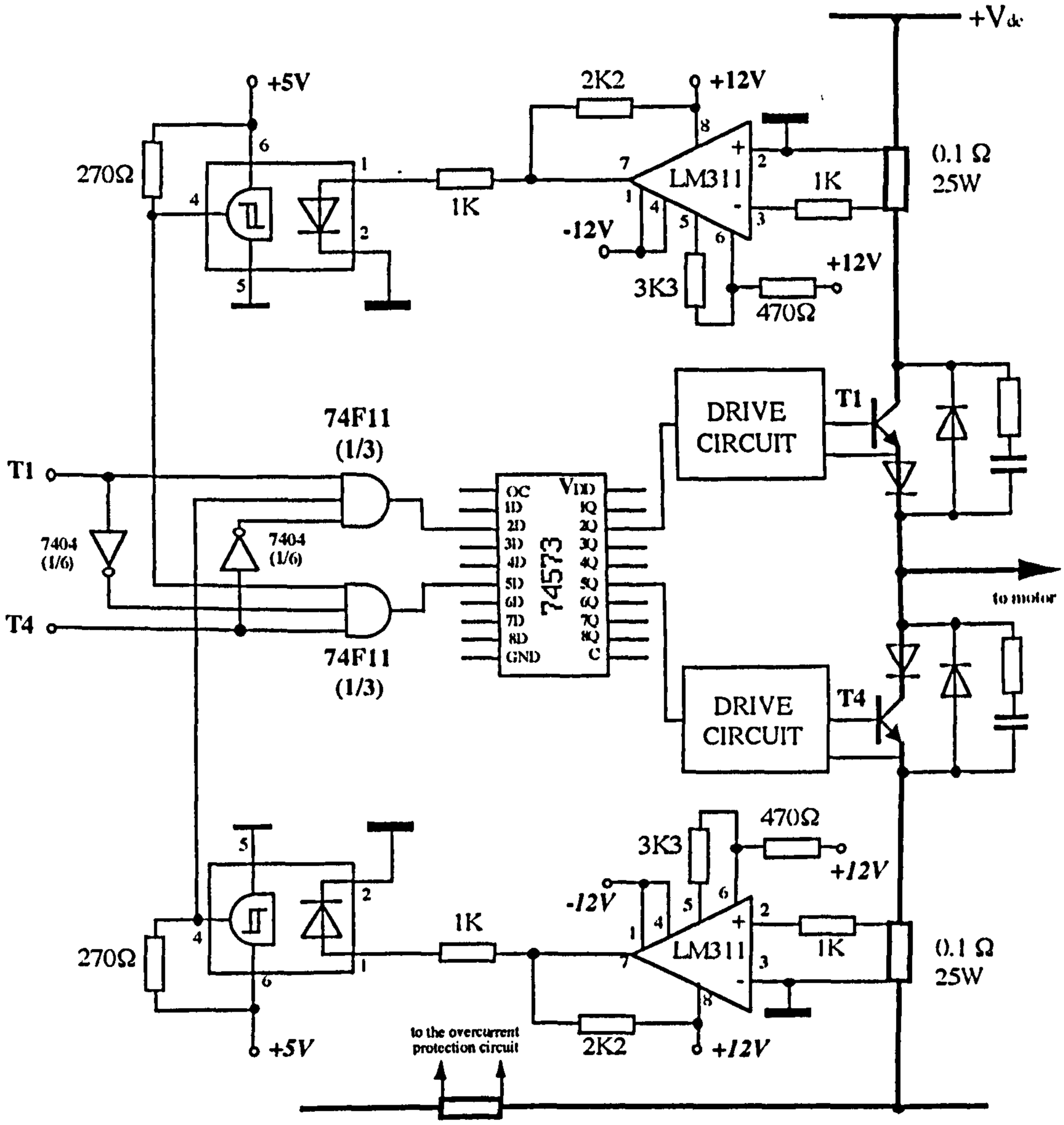

Figure A.10 The protection circuit designed for the bipolar inverter.

A-3.5 The Drive Circuit Designed for the IGBT Inverter

The power circuit for the IGBT inverter was given in **Fig.2.16.** The power switches in the inverter are isolated and driven by the circuit given in **Fig.A.12.** Since the IGBT requires a high peak current to turn on rapidly, the 7667 driver chip was used. The rest of the logic before the optocoupler is mainly to supply a push-pull signal to both ends of the optocoupler diode

increasing the speed, and to prevent non-complementary pulses to the upper and the lower IGBTs in the inverter.

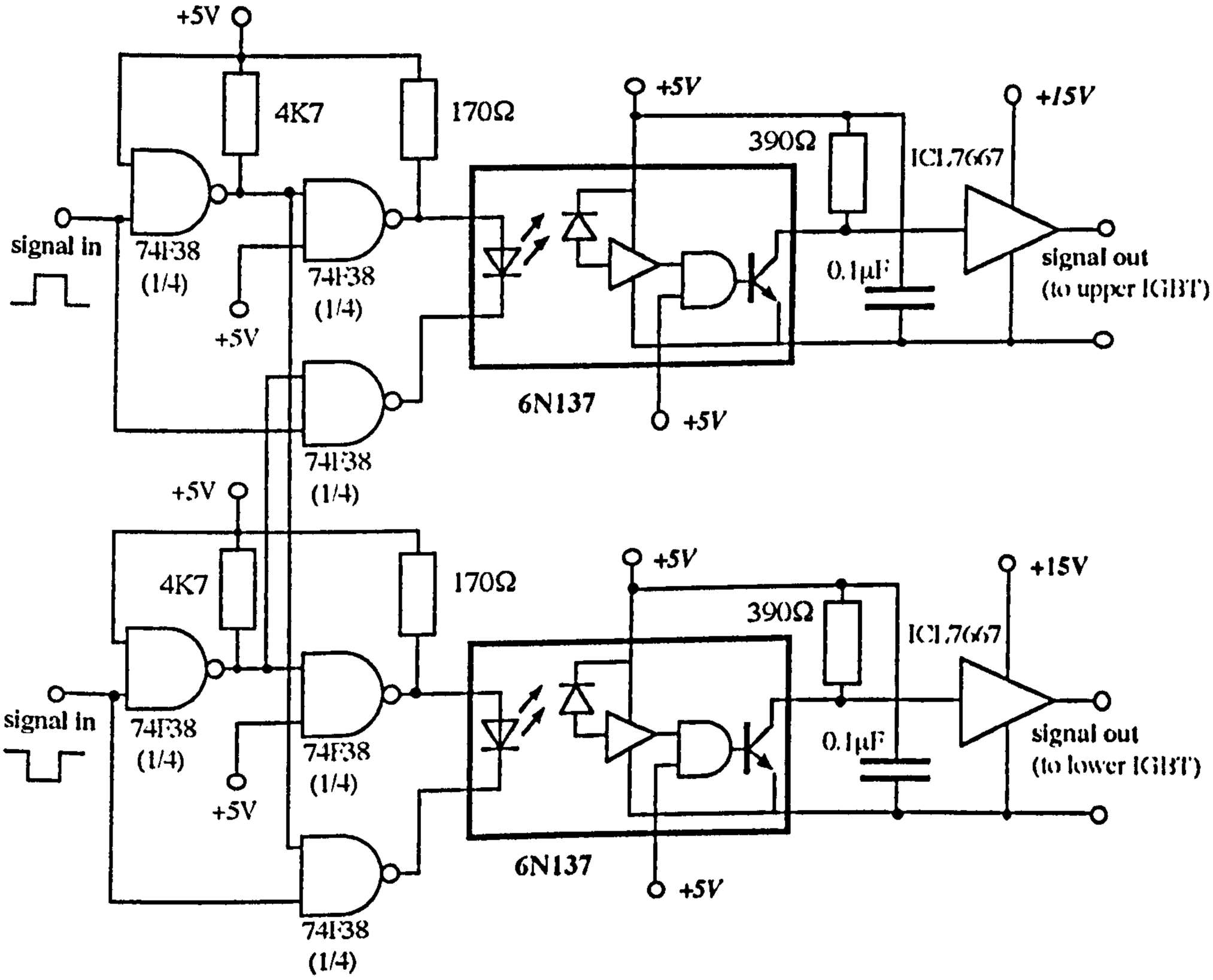

Figure A.12 The implemented drive circuits for one leg of IGBT inverter

A-4 SOME TRIGONOMETRIC RELATIONS AND INTEGRATIONS

The following trigonometric relations and integrations are used to perform the analytical solutions given in **Chapter III:**

$$\sin(a+b) = \sin a \,.\, \cos b + \cos a \,.\, \sin b$$

$$\cos(a+b) = \cos a \,.\, \cos b - \sin a \,.\, \sin b$$

$$\sin(-a) = -\sin a$$

$$\cos(-a) = \cos a$$

$$\int e^{ax}\, dx = \frac{e^{ax}}{a}$$

$$\int e^{ax} \sin(bx)\, dx = \frac{e^{ax}}{a^2+b^2}\left[a \sin(bx) - b \cos(bx)\right]$$

$$\int e^{ax} \cos(bx)\, dx = \frac{e^{ax}}{a^2+b^2}\left[a \cos(bx) + b \sin(bx)\right]$$

$$\sin^2(x) = \frac{1+\cos(2x)}{2}$$